UNIVERSITY OF ADELAIDE LIBRARY
1971-96

METEOR OBSERVATIONS WITH A NARROW BEAM VHF RADAR

By

Manuel A. Cervera, B.Sc. (Hons)

Thesis

submitted for the degree of

DOCTOR OF PHILOSOPHY

at the

UNIVERSITY OF ADELAIDE

(Department of Physics and Mathematical Physics)

3 February 1996

This work contains no material which has been accepted for the award of any other degree or diploma in any university or other tertiary institution and, to the best of my knowledge and belief, contains no material previously published or written by another person, except where due reference has been made in the text.

I give consent to this copy of my thesis, when deposited in the University Library, being available for loan and photocopying.

Signed: dated: 7/2/96

Manuel A. Cervera, B.Sc. (Hons)

Abstract

This thesis is concerned with the observations of meteors with a narrow beam, high gain, VHF radar system, operating at a frequency of 54.1 MHz. The radar, operated by the Atmospheric Physics Group in the Department of Physics at the University of Adelaide, provides an excellent tool for the investigation of meteor phenomena, and it was found that the narrow beam system offered two unique advantages over the more traditional wide beam radars used in the past. These are: (1) the sensitivity of the system is greatly increased, *e.g.* the radar is able to detect meteors with electron line densities as low as $10^{10}\ electrons/m$, and (2) the response of the radar to meteor backscatter is confined to a narrow well defined strip on the celestial sphere, which enables meteor shower radiants to be accurately determined. However, before any extensive observations and studies of meteors could be undertaken with the radar, both the transmitter and data acquisition systems were required to be upgraded. These upgrades are described together with the radar system.

A consequence of the high sensitivity of the radar to meteor backscatter is the observation of very faint meteors; and therefore phenomena, previously not noted, were expected to be detected. As such, a general survey of the meteoric phenomena observed by the radar was performed and this is discussed in detail. One particular class of echo of note was the so called "head echo" which was interpreted as being from meteors undergoing rapid diffusion so that backscatter occurs only from the region immediately behind the ablating meteoroid. Other effects investigated include those due to beating of signals received from multiple points along the trail and saturation of the signals in the receivers.

The meteor radar response function (*Elford*, 1964; *Thomas et al.*, 1988) is derived for the Buckland Park radar with the calculation being extended to include an ionization profile as given by classical ablation theory. The response function is a powerful tool for investigating various aspects of meteoric phenomena observed by the radar. These include: (1) the expected height distribution, (2) the diurnal variation of meteor echo rates, (3) prediction of the time of passage of known meteor showers, (4) calculation of the radiants of unknown showers, and (5) modeling the mass influx of shower and sporadic meteors.

A new technique to obtain speed of the ablating meteoroids was developed, and this is described. The new method makes use of the pre-t_0 phase information of the meteors echo, and it was found it has considerable advantages over previous techniques. These are: (1) speeds are able to be calculated from some 75% of all meteor echoes which is to be compared with only about 10% with methods employing the post-t_0 amplitude oscillations, (2) the reduction process is very accurate with typical accuracies almost always less than $\pm 5\%$ and often as low as $\pm 0.5\%$, and (3) selections effects which bias speed measurements against the very slow and very fast meteors are smaller with this technique. The new technique was used to obtain the speed distribution of the sporadic meteors as observed by the radar. This, after correction for various selection biases is compared with previous optical and radio results.

The capability of the radar to readily detect and measure the speeds of slow meteors is of great importance if meteors produced by re-entering space debris from geocentric orbit is to be detected and studied. A detailed discussion of this subject is made in this thesis.

The speed measurements of sporadic meteors were used together with estimations of the electron line densities of the meteor trails and classical ablation theory to obtain the masses of individual meteoroids. The resulting mass distribution of the observed sporadic meteors together with modeling using the response function yielded a cumulative mass index of $c = -0.9$ over the mass range $10^{-9} - 10^{-7}\ kg$.

Observations of two showers (the June-Librids and θ-Ophiuchids) using a new technique is described. This technique employs the meteor radar response function and is able to determine the position of meteor shower radiants to within $\pm$ 0.5°. The observation of the June-Librids is, to the best knowledge of the author, the first by a radio technique. Speed measurements were made for the θ-Ophiuchids which were observed in 1994, and a large peak in the velocity distribution was found which agreed with previous results. The mass distribution for the θ-Ophiuchids was also obtained and a cumulative mass index of $c = -1.1$ was deduced. Also, the θ-Ophiuchid stream was found to consist of two distinct radiant centres whose mean position was in good agreement with that given by *Cook* (1973).

The measurement of atmospheric wind speeds in the meteor region was performed through the determination of the radial drift velocity of the observed meteor trails. Two weeks data were obtained during September 1993 and a comparison was made with the winds obtained from the 2 *MHz* MF spaced antenna (SA) system at the same site. The results and conclusions made from this campaign are not reported in the main body of this thesis, however, see *Cervera and Reid* (1995) and Appendix A.

Acknowledgements

Well here it is at last! The road has certainly been a long one (and not very straight at that), but finally the destination has been arrived at. There are many people who deserve thanks for helping me achieve this goal, so here goes. Firstly I would like to thank my supervisor Dr. Graham Elford whose help, advice and encouragement were instrumental in getting me this far. But more than that, it has been a real pleasure to work with Graham, and I am indebted to him. Dr. Bob Vincent, who was my 'official' supervisor (Graham being retired) is deserving of thanks for his support, and together with Dr. Iain Reid was there to help, advise and keep things moving smoothly. Iain, particularly, I thank for getting the ball rolling with my first major publication (Iain is also co-author). Also deserving of thanks are Dr. Duncan Steel, who guided my first steps along this path, and Dr. Richard Thomas for his support, encouragement and helpful discussions. Dr. Susan Avery and Dr. Jim Avery from the University of Colorado I thank for collaborating with me on an interesting project, while on sabbatical in Adelaide. Finally, Dr. Andrew Taylor, while only at the Atmospheric Physics Group for the last year of my PhD candidature, provided me with many stimulating conversations and enabled me to look at old ideas in a new light.

Writing a thesis is damn hard work (as many before me will attest) and it is certainly very taxing on one's stamina, health, and indeed sanity! The support of one's loved ones goes a very long way towards keeping one from becoming a total wreck, and so I thank Emma for her continual love, support, encouragement and patience. If I may paraphrase friend and colleague David Low: "I see that Emma has kept you from going completely insane..."; and with this, I without a doubt concur. Emma has certainly made these last couple of years bearable. My parents have supported and encouraged me over the years; first through school, then though my undergrad. years, and of course throughout my PhD. For this my Mum and Dad are deserving of thanks and I am grateful for their continual interest. I would also like to thank my sister Alison and brother in–law Markus for their encouragement over the years.

I would like to thank my best mate Sean and his wife Sue for helping me keep things

in perspective. I also thank other friends outside of physics: Eddie and Helen, Steve, Rick, Stephen and Janet, and Joanne and Alex.

Having someone to share the agony of thesis writing (and simply to have someone who is in the same boat) is a great catharsis, so I thank Dave Holdsworth (Scroop!), and Dave Low (Blowy Lowy). I also thank Steve Eckermann (The UBB), who with Dave H., provided me with many a relaxing and interesting night (and very often early mornings) at those infamous Rundle St. Pubs, The Austral and The Exeter. Thanks also to Janice, Shane, Deepak, Brenton, Brian and Mike for providing me with some rather memorable occasions.

One's friends and colleagues (past and present) are certainly important to keep a workplace interesting and so I'd like to thank (in no particular order) Andrew, Archie, Dave H., Dave L., Bridget, Dorothy, Karen, Scotty, Simon, Sujata, Ali, Deepak, Trevor, Drazen, Brenton, Damian, and Laurence. I hope I haven't forgotten anybody; if so my apologies. Thanks also to Susan and Jim Avery and Todd Valentic from The University of Colorado: working with you while you were in Adelaide was an enjoyable and rewarding experience. Shane Dillon, Lesley Rutherford, Brian Fuller, Mike Shorthose, and Alex Didenko I thank for their technical support, without which I would have sunk very early on. Thanks also to Dallas Kirby and Lyn Birchby for keeping things running smoothly in the group.

Music was an integral part of my PhD life and the many bands that I or others played during those late nights certainly helped to keep me focussed. But, in particular often I found the lyrics to a song entitled Birdy Num Num by the Australian band Mr. Floppy to be quite appropriate. The lyrics in question were sampled from the Peter Sellers film The Party and read: "What's going on here? What the devil is going on?". I would like to thank TISM and Nick Cave for producing such greats as Get Thee to a Nunnery, Saturday Night Palsy, The Mercy Seat, and Lay Me Low. I also thank all the guys at Cafe Micheal for producing many delightful meals. Cafe Michael has become a great institution among certain research students, and expeditions to sample the fine food on offer a weekly event not to be missed!

Finally, I would like to thank the High Frequency Radar Division of the Defence Science and Technology Organization who has supported me financially throughout my PhD candidature.

Contents

Abstract v

Acknowledgements vii

1 Introduction 1

1.1 A General Overview of Meteoric Phenomena 1

1.2 Meteor Observing Techniques 5

1.2.1 Optical techniques 6

1.2.2 Radio techniques 8

1.2.3 Satellite borne meteoroid dust exposure experiments 11

1.3 Motivation and Scope 11

2 The Buckland Park VHF Radar 17

2.1 Introduction 17

2.2 The CoCo antenna array 18

2.3 The CoCo array antenna pattern 26

2.4 The transmitting system 35

2.5 The receiving and data acquisition system 41

2.6 The new meteor data acquisition system 44

3 Preliminary Meteor Observations and Fundamental Theory 51

3.1 Introduction 51

3.2 Fundamental Meteor Theory 52

3.2.1 Ablation theory: The effect of thermal conduction, radiation and heat capacity. 52

3.2.2 The basic Fresnel theory of radar backscatter from meteors 54

3.2.3 The effects of the initial trail radius and diffusion 59
3.2.4 Overdense meteor trails 63
3.2.5 The reflection process revisited 64
3.3 Meteor Detection with the VHF Radar 67
3.3.1 Statistics of white noise 67
3.3.2 The effect of coherent averaging on raw data 71
3.3.3 Comparison of effect of noise on the amplitude and phase information of a coherent signal 74
3.3.4 The meteor detection algorithm 76
3.3.5 Advantages of the Buckland Park VHF radar over meteor radars used in the past 79
3.4 Preliminary Meteor Observations 81
3.4.1 Introduction 81
3.4.2 Examples of meteors observed with the Buckland Park radar 81
3.4.3 The effect of receiver saturation on the returned meteor echoes 90
3.5 Summary 97

4 The Response of Radar to Meteors **99**
4.1 Introduction 99
4.2 The Development of the Response Function 100
4.2.1 The response function calculation for a uniform ionization profile . . . 100
4.2.2 The treatment of overdense echoes in the response function calculation 106
4.2.3 The full response function using classical ablation theory 108
4.3 Initial Mass and Classical Ablation Theory 112
4.3.1 Introduction 112
4.3.2 The drag, differential mass and ionization equations 112
4.3.3 An analytical solution to the classical ionization theory: the approximation of no deceleration 114
4.3.4 An analytical solution to the classical ionization theory corrected for deceleration 115
4.3.5 Minimum initial meteoroid mass detectable with the Buckland Park VHF radar 116
4.3.6 The effect of fragmentation 118

4.4 Response of the Buckland Park VHF Radar 119
4.4.1 Introduction 119
4.4.2 The response function calculation at an initial meteoroid velocity of 30 $km\,s^{-1}$ and off zenith beam tilt of 30° 120
4.4.3 Investigation of the response function for different off zenith beam angles 124
4.4.4 Velocity dependence of the response function 126
4.4.5 The complete response function - integration over the meteoroid initial velocity 135
4.4.6 The effect of the diurnal variation of the background noise 139
4.4.7 Different Antenna Configurations on Reception 141
4.5 The Response Function at Lower Frequencies 144
4.6 The Observed Height Distribution of Sporadic Meteors 147
4.7 The Diurnal Variation of Sporadic Meteor Echo Rates 150
4.8 Summary 162

5 A New Technique for Measuring Meteor Velocities 165
5.1 Introduction 165
5.2 Survey of Previous Radio Techniques 167
5.2.1 The range-time technique 167
5.2.2 The diffraction technique 169
5.2.3 Meteor velocities obtained from a UHF radar 172
5.2.4 The spaced receiver technique 174
5.3 A New Method for Measuring Meteor Velocities: The Pre-t_0 Phase Technique 175
5.3.1 Introduction 175
5.3.2 The method of reduction of meteor velocities 176
5.3.3 The measurement of meteor decelerations? 185
5.3.4 Further examples of the pre-t_0 phase technique 188
5.4 The Velocity and Mass Distributions of Sporadic Meteors 196
5.4.1 Velocity distribution 196
5.4.2 Mass distribution 201
5.5 On the Detection of Space Debris 202
5.6 Conclusion 207

6 Meteor Shower Observations with the Buckland Park VHF Radar 209

6.1 Survey of Radar Techniques Used to Observe Meteor Showers 209

6.1.1 Introduction 209

6.1.2 Range-Time envelope techniques 210

6.1.3 The shower imaging technique 212

6.1.4 Multistation radar systems 213

6.2 Meteor Shower Radiant Determination with the Buckland Park VHF radar . 215

6.2.1 Introduction 215

6.2.2 The expected rate response of meteor showers observed by the Buckland Park VHF radar 215

6.2.3 Determination of the meteor shower radiant coordinates 217

6.3 Detection of the June Librids Meteor Shower 222

6.3.1 Introduction 222

6.3.2 Observations and results 223

6.3.3 Discussion 226

6.4 Detection of the θ-Ophiuchids Meteor Shower 226

6.4.1 Introduction 226

6.4.2 Observations and results 227

6.4.3 Determination of the shower radiant coordinates 233

6.4.4 Velocity measurements of the θ-Ophiuchids meteors 235

6.4.5 The corrected velocity of the θ-Ophiuchids: an attempt to account for meteoroid deceleration by examining the velocity-height profile 240

6.4.6 An alternative method to account for deceleration: a theoretical approach based upon ablation theory 243

6.4.7 The mass distribution of the θ-Ophiuchids 246

6.4.8 Conclusions 249

6.5 Limitations and Advantages of the Technique 250

6.5.1 Identification of an anomaly 250

6.5.2 Previous measurements of the mass indices and incident fluxes for shower and sporadic meteors 251

6.5.3 Calculation of the expected rate of the δ-Aquarids relative to the sporadic background 254

6.5.4 Discussion 256

6.6 Summary 257

7 Conclusion **259**

7.1 Summary and Conclusions 259

7.2 Further Work 264

A On the Meteor Drift Technique and Comparisons with MF SA Wind Measurements **269**

A.1 Introduction 269

A.2 Comparison of simultaneous wind measurements using colocated VHF meteor radar and MF spaced antenna radar systems 271

A.3 Spaced antenna wind measurements: the effects of signal saturation 273

B Single station identification of radar meteor shower activity: the June Librids in 1992 **275**

C Meteor velocities: a new look at an old problem **277**

D A comparison of meteor radar systems **279**

E A new technique for radar meteor speed determination: inter–pulse phase changes from head echoes **281**

References **283**

List of Tables

2.1 Typical operational parameters of the VHF radar for meteor detection. . . . 18

2.2 Available pulse repetition frequencies (a) and pulse widths (b) of the VHF radar transmitting system. 36

4.1 Cumulative fluxes of meteoroids found from various experiments. 110

4.2 Modification factors applied to no-deceleration ionization profiles to produce a good approximation to the full solution. 116

4.3 Physical properties of the meteoroids and other quantities used in the response function calculation 120

6.1 Significance test of the peak observed in the superimposed rate data from $6^{th} - 9^{th}$ June 1992. 226

6.2 The time of occurrence and significance of peaks in the meteor rate data from the $5^{th} - 14^{th}$ June, 1994. 230

6.3 Time of occurrence of the peaks in the combined rate data and the expected time of passage of the θ-Ophiuchids. 233

6.4 The right ascension and declination of the meteor activity due to the activity of the θ-Ophiuchids. 234

6.5 Values of mass distribution exponents s reproduced from *Weiss* (1961, 1963) 252

6.6 Values of the mass index, K_r and $\mathcal{F}_r$ used in the calculation of the expected response of the δ-Aquarids. 255

List of Figures

2.1 Ground plan of the Buckland Park VHF radar. 19

2.2 Photograph of the Buckland Park VHF CoCo array 21

2.3 Photograph of the current probe used for checking phasing across the array . 21

2.4 Sketch of the current probe and setup for phase measurements 24

2.5 Background cosmic noise observed by the VHF CoCo array. 27

2.6 Geometry of the coordinate system used for the modeling of the CoCo array antenna pattern. 29

2.7 The radiation pattern of a half wave dipole and the geometry of an isotropic radiator situated at a height, h, above a ground plane. 30

2.8 Linear arrays of n isotropic radiators for n even (a) and n odd (b). 31

2.9 The antenna pattern of the VHF CoCo array for a 30° beam tilt Eastwards . 34

2.10 Schematic of the VHF transmitting system. 36

2.11 The 16 way power splitter used in the VHF radar and the suggested hybrid splitter to replace it. 37

2.12 Transmitter control timing pulses 39

2.13 Circuit diagram of the T/R switches used in the VHF radar 40

2.14 Circuit diagram of one of the 2 *MHz* filters, a, and where it is situated in the Rx/Tx system, b. 41

2.15 Schematic overview of the Buckland Park receiving and data acquisition system. 43

2.16 Schematic overview of the new meteor data acquisition system hardware. . . 47

2.17 Timing of the samples with respect to the transmitted pulse. 48

2.18 Circuit diagram of the trigger control for the A/D card. 48

3.1 Theoretical values of air density and altitude at the commencement of evaporation as a function of meteoroid radius (after *Hughes, 1978*). 53

3.2 The geometry of a meteoroid's path through the Earth's atmosphere with respect to an observing station. 54
3.3 The Cornu spiral of Fresnel diffraction theory. 56
3.4 The effects of diffusion on the returned echo power and phase. 58
3.5 The maximum value of the reflection coefficient as a function of electron line density. After *Poulter and Baggaley* (1977). 66
3.6 Polarization ratio, $g_\perp/g_{||}$, for various electron line densities. After *Poulter and Baggaley* (1977). 67
3.7 Distribution of 2 seconds of raw noise collected from the radar receiver. . . . 69
3.8 The effect of coherent smoothing on the amplitude data. 72
3.9 The effect of coherent smoothing on the phase data. 73
3.10 The effect of noise on various signal levels. 75
3.11 Percentage attenuation of the returned meteor echo power as a function of echo duration for underdense echoes. 78
3.12 Examples of meteors observed with the Buckland Park VHF radar. 84
3.12 Meteor examples continued. 85
3.12 Meteor examples continued. 86
3.13 Schematic of the geometry of meteor head echo detection. 88
3.14 Example of two interfering constant amplitude signals. 90
3.15 Section of the meteor echo displayed in Figure 3.12j 91
3.16 Effect of saturation on a signal of constant amplitude and varying phase. . . 92
3.17 Amplitude and phase variation of a saturated signal, case 1. 94
3.18 Amplitude and phase variation of a saturated signal, case 2. 95
3.19 Amplitude and phase variation of a saturated signal, case 3. 95
3.20 Amplitude and phase variation of a saturated signal, case 4. 96

4.1 Geometry of the echo plane for the condition of specular backscatter 102
4.2 Geometry of a reflection point from a particular radiant direction with respect to the Earth's curved surface. 103
4.3 Ionization profiles calculated from the analytical solution corrected for deceleration. 117
4.4 The response of the Buckland Park VHF radar (East beam) to meteoroids with an initial velocity of $30\,km\,s^{-1}$. 121

4.5 Contour plot of the response of the Buckland Park VHF radar (East beam) to meteoroids with an initial velocity of $30\,km\,s^{-1}$. 122
4.6 Possible meteoroid radiant directions detectable by specular backscatter of radar by the resultant meteor trails. 123
4.7 The effect of varying the off zenith beam tilt on the response function. 125
4.8 The response function of the Buckland Park VHF radar calculated for meteoroids with various initial velocities. 127
4.9 The variation of sidelobe response (as a percentage of the total response) with the initial meteoroid velocity. 128
4.10 The expected height distribution calculated for meteors with various initial velocities. 129
4.11 The response function of radar with and without the treatment of overdense meteors. 131
4.12 Ionization profiles calculated from classical ablation theory. 132
4.13 The response function calculated without the inclusion of the echo attenuation, echo selection and range cut-off factors. 134
4.14 Corrected velocity distributions of meteoroids from various researchers. 136
4.15 The response function of the Buckland Park VHF radar integrated over the Harvard Radio velocity distribution. 137
4.16 The response function of the Buckland Park VHF radar integrated over the velocity distribution determined by *Nilsson* (1962). 138
4.17 The effect of the minimum detectable power level on the response function. . 140
4.18 Calculated normalisation factors used to rescale the response function calculated at a different minimum detectable powers. 142
4.19 The modelled antenna pattern of a subset of 22 rows of the Buckland Park VHF CoCo array. 143
4.20 The response function of the Buckland Park VHF array calculated for reception on a subset of 22 rows of the CoCo array. 143
4.21 The expected height distributions of meteors calculated for the Buckland Park VHF radar and 2 fictitious radars operating at lower frequencies. 145
4.22 As for Figure 3.21, except here the expected height distributions have been calculated without the range cut off at $128\,km$. 148
4.23 Height distribution of meteors observed by the Buckland Park VHF radar. . . 149

4.24 The path which the response of the East and West pointing beams takes on the celestial sphere during the 24^{th} May 1994. 152
4.25 Observed diurnal variation from $20^{th} - 26^{th}$ May 1994 with model. 153
4.26 Observed diurnal variation from $20^{th} - 26^{th}$ May 1994 with improved model. 155
4.27 Model sporadic radiant distribution for $20^{th} - 26^{th}$ May 1994. 156
4.28 Observed diurnal variation from $10^{th} - 15^{th}$ June 1994 with improved model. 157
4.29 Model sporadic radiant distribution for $10^{th} - 15^{th}$ June 1994. 159
4.30 Observed diurnal variation from $1^{st} - 6^{th}$ February 1995 with improved model. 160
4.31 Model sporadic radiant distribution for $1^{st} - 6^{th}$ February 1995. 161

5.1 The geometry of a meteoroid's path through the Earth's atmosphere with respect to an observing station. 168
5.2 The amplitude Fresnel diffraction pattern of radiation at a straight edge. . . . 170
5.3 Typical raw meteor echo observed with the VHF radar and used for the reduction of meteor velocities 176
5.4 The effects of coherent smoothing applied to the raw data obtained from a meteor echo. 178
5.5 The effect of a constant Doppler shift over a time t on a complex signal. . . . 180
5.6 The de-trended meteor echo. 181
5.7 Fresnel diffraction pattern of the phase information from radiation at a straight edge. 182
5.8 Distance-time profile obtained from the pre-t_0 phase information of a meteor echo 185
5.9 The phase profile of a meteor echo together with the modeled pre-t_0 phase . . 186
5.10 Meteor echo observed at 12:58 CST on 6 June 1994. 189
5.11 Meteor echo observed at 12:58 CST on 6 June 1994 with 2-point coherent smoothing applied. 190
5.12 Distance-time profile obtained from the pre-t_0 phase information of the meteor echo displayed in Figure 5.10. 191
5.13 Distance-time profile obtained from the post-t_0 amplitude oscillations of the meteor echo displayed in Figure 5.10. 191
5.14 Example of a meteor echo displaying rapid diffusion of the trail 194
5.15 Slow meteor observed at 12:09 CST on 6 June 1994 195

5.16 Velocity distribution for sporadic meteors not corrected for deceleration . . . 197
5.17 Velocity distribution for sporadic meteors corrected for deceleration 199
5.18 Comparison of corrected radio and optical velocity distributions. 200
5.19 The observed cumulative mass distribution of sporadic meteors from 6-7 June 1994. 202
5.20 Geometry of radiants which may be observed with a narrow beam radar. . . . 204
5.21 Response function of the Buckland Park VHF radar for various off zenith beam angles. 206

6.1 The response function for the VHF radar with 6 fictitious radiants superimposed.216
6.2 Expected normalised count rates for six fictitious radiants 218
6.3 Polar contour plot of the response function for the VHF radar for beams tilted East and West. The loci of six fictitious radiants are superimposed. 220
6.4 The time difference between the radiant maximum activity occurring in the East and West beams of the VHF radar as a function of the radiant declination.221
6.5 Maximum normalised response for meteor shower radiants crossing the East and West response functions. 221
6.6 Time of maximum echo rate of six fictitious meteor showers detected in the East beam of the VHF radar, as a function of radiant right ascension. 222
6.7 The expected normalised count rate for the June Librid shower. 223
6.8 Meteor rates on $6^{th} - 7^{th}$, $7^{th} - 8^{th}$ and $8^{th} - 9^{th}$ of June 1992. 224
6.9 Superimposed meteor rate data from $6^{th} - 7^{th}$, $7^{th} - 8^{th}$ and $8^{th} - 9^{th}$ of June 1992. 225
6.10 The expected normalised count rate for the θ-Ophiuchids meteor shower. . . 227
6.11 Meteor rate data on the 11^{th} June 1994. 229
6.12 Background noise for a typical day in May 1994. 231
6.13 Superimposed meteor rate data from the θ-Ophiuchids meteor shower. 232
6.14 Plot of the radiant coordinates of the two bursts of meteor activity observed during early June 1994. 235
6.15 Velocity distribution of the meteors observed during the time of passage of the θ-Ophiuchids meteor shower 236
6.16 Velocity distribution of the meteors observed prior to the passage of the θ-Ophiuchids meteor shower 236

6.17 Velocity distribution of the meteors observed during the time of passage of the θ-Ophiuchids meteor shower with the sporadic distribution statistically removed 237
6.18 Velocity distribution of the Group A and Group B meteors observed during the passage of the θ-Ophiuchids meteor shower in the East beam. 239
6.19 Velocity - height distribution of the observed shower meteors. 241
6.20 No atmosphere velocity distribution of the meteors observed during the time of passage of the θ-Ophiuchids meteor shower corrected for deceleration . . . 245
6.21 Cumulative mass distribution of the θ-Ophiuchids meteor shower. 246
6.22 Observed mass distribution of the meteors detected during the time of passage of the θ-Ophiuchids meteor shower. 248
6.23 Values of mass index s, for six meteor showers (after *Elford*, 1967). 253
6.24 Mean incident flux of meteoroids capable of producing zenithal electron line densities greater than q_z for sporadics and three showers (after *Elford*, 1967). 253

UNIVERSITY OF ADELAIDE LIBRARY

Chapter 1

Introduction

Now the storm has passed over me
I'm left to drift on a dead calm sea
And watch her forever through the cracks in the beams
Nailed across the doorways of the bedrooms of her dreams
—*Nick Cave*

1.1 A General Overview of Meteoric Phenomena

Meteors are an atmospheric phenomena caused by particles of interplanetary origin (meteoroids) entering the Earth's atmosphere. These meteoroids heat up due to collisions with air molecules and eventually vapourise (ablate) each resulting in a transient luminous column which is associated with the meteor phenomena. The luminosity is caused by the de-excitation of atoms excited by the collision between air molecules and those from the ablating meteoroid. Not only is a transient luminous column produced, but the ablating particle also leaves behind a trail of ionization which acts as a scatterer for radio waves. Thus, meteors may be observed and studied by radio techniques, which is the subject of this thesis, as well as by optical methods. Some of these observing techniques will be briefly discussed later in this chapter.

The meteoroids enter the Earth's atmosphere with speeds in excess of $11\,km\,s^{-1}$ (the escape velocity of the Earth) and ablate at heights in the region between $70\,km$ and $140\,km$ above the Earth's surface. A few meteoroids are observed with speeds greater than $74\,km\,s^{-1}$, and these are termed hyperbolic as their speeds are in excess of the limit required for them to be in a bound heliocentric orbit. Thus, the possibility is raised that these meteoroids are

interstellar in origin. Most meteoroids enter the Earth's atmosphere with speeds typically around $15 - 35\,km\,s^{-1}$.

Modern meteor radars (*e.g.* the Buckland Park VHF radar) are able observe meteors with electron line densities, q, as low as $10^{10}\,electrons/m$. This limit may be related to visual magnitudes, M_V, using the expression $M_V = 36 - 2.5(log_{10}q - log_{10}V)$, where V is the meteoroid velocity (*McKinley*, 1961). For a velocity of $11\,km\,s^{-1}$ a limiting visual magnitude of +13.6 is obtained, and +15.7 for meteoroids with velocities of $74\,km\,s^{-1}$. This is to be compared to optical techniques where observations of meteors are typically limited to those brighter than visual magnitude +9.

For meteoroids whose masses are sufficiently small, heat loss due to radiation during heating becomes important and must be considered. The effect of the heat loss is to delay the onset of ablation and in the extreme case where the meteoroid mass is small enough such that the heat loss due to radiation balances the heat gained, the meteoroids do not ablate at all. This defines the micrometeoroid limit and it is strongly dependent on the meteoroid speed, *e.g.* at a speed of $11\,km\,s^{-1}$ the micrometeoroid is about $2 \times 10^{-9}\,kg$ which decreases to about $2 \times 10^{-16}\,kg$ at speeds of $70\,km\,s^{-1}$ (see *e.g. Hughes*, 1978). Meteoroids below these sizes may be studied through the deployment of meteoroid dust exposure experiments on man-made satellites in Earth orbit. At the other extreme, if the meteoroid is large enough, remnants of it (meteorites) may reach the ground. This usually occurs for meteoroids with masses greater than about $1\,kg$.

The meteoroid influx can be divided into sporadic and shower components. Meteor showers occur when the Earth crosses a stream of particles in closely related orbits. Thus, meteor showers appear as a burst of meteor activity originating from the same radiant. Showers usually appear over a period of several days with the time of passage of the shower shifted sidereally by about $3.93\,min$ on each subsequent day. If the meteoroid stream is sufficiently old, then the particles are well distributed around the orbit of the stream and the associated meteor shower occurs annually *i.e.*, when the Earth crosses the orbit of the stream in question. It is well accepted that meteoroid streams are associated with comets. *Schiaparelli* (1866) is credited by *McKinley* (1961) as the first to make such an association by showing that the Perseids meteoroid stream were moving in the same orbit as comet *Swift-Tuttle* 1862 III. Many other associations have since been made. *Hughes* (1978) gives an overview of the production of meteoroid streams from the decay of comets and further discussion on meteor showers may be found in Chapter 6.

On the other hand, sporadic meteors are, as their name implies, meteors produced from meteoroids with random orbits, although they are generally found in three broad concentrations corresponding to the Sun, Anti-sun and Apex directions. Also, in contrast to meteoroid streams, sporadic meteoroids are continuously incident on the Earth and are therefore observed at all times. However, due to the distribution of sporadic meteoroids around the Sun, the sporadic meteor echo rate does vary diurnally.

It is generally accepted that the sporadic population of meteoroids is produced by the decay of meteor streams. Processes that lead to this decay include collisions of the stream particles with both the existing sporadic background and with other particles within the same stream, gravitational perturbation due to the close approach with a planet, and solar perturbation due to the Poynting-Robertson effect.

Gravitational perturbations and the Poynting-Robertson effect change the orbits of stream meteoroids without affecting their physical characteristics. Collision processes, however, do physically affect the meteoroids, and furthermore *Hughes* (1993) identifies three possible outcomes which are dependent on the ratio of the impactor mass, i, to the parent meteoroid mass, m. These three cases are: (1) surface erosion, (2) low velocity fragmentation, and (3) high velocity fragmentation. *Hughes* states that at a collision velocity of $20\,km\,s^{-1}$, surface erosion occurs for $i/m < 0.00002$. If this value is only just exceeded, then low velocity fragmentation occurs and produces fragments with orbits that are similar to the parent meteoroid *i.e.* this process does not produce sporadic meteoroids. When $i/m \gg 0.00002$ high velocity fragmentation occurs and the fragments are scattered randomly, although the orbits of the fragments do pass through the point of the collision. A comparison of the mass distribution data, of both the stream and sporadic populations shows that the sporadic population has a much greater abundance of small meteoroids. From this *Hughes* (1993) concluded that surface erosion is the dominant collisional process.

The fact that that the sporadic population of meteoroids have a greater abundance of small particles than do most meteoroid streams, is of great interest with respect to the observation of meteors with the Buckland Park VHF radar. The greater sensitivity of this system over traditional wide beam meteor radars means that meteors produced from smaller meteoroids are observed. Thus, considering that the cumulative number of sporadic meteoroids above a given mass is roughly inversely proportional to the mass, the question is raised as to whether or not the shower meteors will be swamped by sporadics. In addition, a radar with this level of sensitivity may be biased towards the observation of showers with

a preponderance of small meteoroids *i.e.* towards younger streams. These two questions are addressed in later in this thesis.

Mass distribution data obtained by satellite, radar and optical techniques has been summarised by *Hughes* (1978) who showed that the estimated total mass influx of sporadic meteors to the Earth was some 50 times smaller than that observed by the satellite experiments. This "missing mass" problem remained unexplained until the work of *Olsson-Steel and Elford* (1987), *Elford and Olsson-Steel* (1988) and *Steel and Elford* (1991). Their observations at 2, 6, 27 and 54 MHz showed that the lower the radar frequency, the mean altitude of the meteor height distribution. This is a consequence of low frequency radars being able to observe meteors even when subject to the rapid diffusion rates which occurs at high altitudes. Thus their results suggested that previous researchers, in deriving the sporadic mass influx, inadequately corrected their observations for the effects of diffusion. The mass distribution obtained by *Thomas et al.* (1988) from their observations with the HF Jindalee over the horizon radar was calculated with the results of *Olsson-Steel and Elford* (1987) in mind. Their calculated mass influx, not surprisingly, showed consistency with the satellite derived meteor influx.

The atmospheric density below which meteoroids do not ablate is dependent on the the ablation temperature and the velocity (*Jones and Kaiser*, 1966). This translates to a maximum beginning height of meteors of about 115 km for chondritic meteoroids with an ablation temperature of 2100° K and velocity of 70 $km\,s^{-1}$.

To obtain greater beginning heights lower ablation temperatures are required. For example, a 70 $km\,s^{-1}$ meteoroid with an ablation temperature of say 1000° K would have a beginning height of about 155 km, and a meteoroid with an ablation temperature of 500° and a velocity of 30 $km\,s^{-1}$ would commence ablating at 160 km.

This implies that the high altitude meteors observed by *Olsson-Steel and Elford* were due to volatile meteoroids with possibly a "tar–like" composition. *Lebedinets* (1991) addressed the subject of volatile meteoroids with the view to explaining (amongst other things) the anomalous high altitudes of the Draconids meteors which were first noted by *Jacchia et al.* (1950). *Lebedinets* made use of the mass-spectrometer measurements of submicron dust particles in the coma of Halley's comet by the Vega and Giotto space probes (*Langevin et al.*, 1987) to postulate the existence of meteoroids composed of organic materials. The mass-spectrometer measurements showed that 35% of the particles in the coma where similar to carbonaceous chondrites; 30% contained mostly the elements C, H, O, N (and where

therefore labeled as "CHON–particles"; and 35% a mixture of carbonaceous chondrite and CHON material. As the lifetime of ice particles is small out to distances of 1 A.U., the CHON material must be polymeric (or organic) in nature (stable at temperatures up to $500°K$) if "CHON-meteoroids" are to exist.

Through consideration of the likely thermal properties of CHON–particles, *Lebedinets* shows that the anomalous high altitudes of the Draconids may be explained, and he concludes that at least 90% of the meteoroids in the Draconids stream must be comprised of these particles. Further, analysis of photographic meteors with anomalous heights, performed by *Lebedinets* with some assumptions on the metallic content of the CHON–particles, predicts that organic particles comprise about 50% of all meteoroids. This, *Lebedinets* points out, is similar to the relative content of organic particles in the coma of Halley's comet.

It is clear that the study of meteors produced from CHON's would be impossible with traditional meteor radars operating at VHF; the CHON's ablate at high altitudes where the effect of diffusion on the meteor trail precludes them from being detected by VHF radars. However, *Olsson-Steel and Elford* (1987) have shown that radars operating at much lower frequencies may be employed to study these meteors. While it is impossible to use the Buckland Park VHF radar to observe and study CHON's, the techniques developed in this thesis to study meteoric phenomena in general, may be readily extended to radars operating at lower frequencies and this would be vital for any useful study of organic meteoroids to be made.

1.2 Meteor Observing Techniques

A variety of techniques have been applied to the observation of meteoric phenomena. These may be broadly classified into two groups: optical and radar. This thesis is concerned primarily with the the second group; however, in this section an overview on the various optical methods of meteor observation will also be made. The observation of meteoroids from dust impact experiments carried by satellites in Earth orbit have also been an important tool in the study of the influx of meteoroids to the Earth and a brief discussion on this technique is made at the end of this section.

1.2.1 Optical techniques

Optical techniques that have been used to observe and study meteors include visual, photographic, telescopic, television and spectroscopic techniques. Visual techniques date back to over 3700 years ago when observations of meteors were recorded by the ancient Chinese and Japanese. The first such known record was from 1809 B.C., but it was not until the nineteenth century that serious scientific studies of meteors were undertaken. In 1798 two students, *Brandes and Besnzenberg*, from the University of Göttingen showed from observations of meteors at distant locations, that they occurred at altitudes of about 95 km and had speeds consistent with them having an interplanetary origin. Prior to these observations, meteors were believed to be an extra-terrestrial phenomenon.

During the first half of this century many visual studies of meteors by dedicated groups of observers were carried out. Most of these observations involved the recording of the positions of the meteors in relation to the star background. Radiant positions, hourly rates and magnitude distributions were able to be obtained from these observations. Accurate visual speed measurements of meteors was made possible through the use of a rocking mirror device developed by *Öpik* (1934).

The most probable magnitude of meteors observed visually is about +2.5 with around 75% of occurring in the range from 0.75 Mag. to 3.75 Mag. The magnitude limit of meteors observed visually is about +5.0 on a clear dark night. This limit may be extended to fainter meteors through use of binoculars or telescopes, although the field of view is much reduced and therefore lower hourly rates are achieved. The use of $7 \times 50\,mm$ binoculars and similar small telescopes extends the limiting magnitude to about +8 – +9 Mag., whilst the hourly rate is reduced to around 3–4. More powerful telescopes, while enabling fainter meteors to be observed, are not of much use as the field of view is reduced to the extent that the meteor rates are far too low for useful studies to be performed.

Although the naked eye has a large field of view, typically around 120°, visual observations still have field of view problems. This due to the sensitivity of eye, and hence the meteor limiting magnitude, drastically falling off with angle from the direct line of vision. This field of view restriction may be alleviated by using photographic techniques. For example, the wide aperture Baker Super-Schmidt cameras used by *Whipple* (1949) and *Jacchia and Whipple* (1956), had circular fields of view about 55° in diameter and were able to photograph meteors as faint as +4 Mag, while the system employed by *Halliday* (1973) was able to photograph

meteors as faint as +6.0 Mag. If two cameras are used in conjunction with rotating shutters, then the meteor speed and trajectory may be determined (*e.g. McCrosky and Posen*, 1961; *Jones and Hawkes*, 1975); such systems have been used extensively to obtain meteor orbits

Observations of meteors using television systems were first carried out at the Marshall Space Flight Center with an image orthicon using a 105 mm $f/0.75$ lens (*Clifton*, 1971, 1973). This system had a field of view of 13° by 16° and was capable of detecting up to 60 meteors per hour with a limiting magnitude of about +9. The image orthicon was soon superseded by an secondary electron conduction (SEC) vidicon camera coupled to a single-stage image intensifier. The field of view and limiting magnitude of this system were identical, but over twice the meteor rate was achieved. This was due to the smaller selection biases of this system against high speed meteors. As television systems effectively take photographs of the meteors every 1/25 sec, relatively high time resolution data are obtained. If two cameras are employed to observe the meteors, then the height profile of the light intensity of the meteors may be obtained. Other researchers who have employed television systems include *Hawkes and Jones* (1975a, 1986), *Jones and Hawkes* (1975), and *Sarma and Jones* (1985).

The composition of meteoroids may be studied through the spectroscopic observations of meteor trails and this has been done extensively in the past (see *e.g. Ceplecha*, 1964, 1973; *Harvey*, 1971, 1973a, 1973b; *Millman*, 1972). Spectroscopic observations may be performed through the use of slitless spectroscopes employing objective prisms or diffraction gratings (*e.g. Ceplecha*, 1968). *Millman et al.* (1973), in their observations of the Geminid meteor shower, used a slightly different system which employed a spectroscope with orthicon image enhancement. Spectroscopic techniques are able to observe the following species in the meteor spectra (1) neutral and singly ionized atoms: Iron, Magnesium, Calcium, Silicon and Oxygen; (2) neutral atoms only: Nickel, Sodium, Manganese, Chromium, Aluminium and Hydrogen; and (3) molecular species: N_2, FeO, MgO, CaO, CN, C_2 and CO. By quantitatively analysing the meteor spectra, the chemical abundances of the elements constituting the meteoroid may be found. Thus not only the composition of the meteoroid may be inferred but also the density. For example, *Ceplecha* (1966) showed from the the spectra of two meteors that the composition of the ablating meteoroids were similar to an average stony meteorite, while the observations of five meteors (one from each of the sporadic population and the Taurid, Geminid, Perseid and Leonid meteor showers) by *Harvey* (1973c) showed that the compositions were similar to that of carbonaceous chondrites.

1.2.2 Radio techniques

Radars have been used extensively since the end of World War II to study meteoric phenomena, but in this section only a brief overview will be given; more detailed discussions on the various aspects of radar observations of meteors may be found in the subsequent chapters. Radars are able to observe meteors by transmitting radio waves which are reflected by the column of ionization produced by the ablating meteoroid, and then received at a site which may be co-located with the transmitter (backscatter) or situated some distance away (forward scatter). For the case of backscatter the echo is only observed if the meteor trail is at right angles to the radar beam; the point of closest approach is known as the t_0 point. Radio techniques used to observe meteors include continuous-wave (CW), pulse, single and multi-station techniques.

The observation of meteors using radar has been generally carried out at frequencies within the range from 20 MHz to 70 MHz, although a few observations have been carried out with frequencies as low as 2 MHz (*Olsson-steel and Elford*, 1986; *Steel and Elford*, 1991) and as high as 900 MHz (*Pellinen-Wannberg and Wannberg*, 1994). The upper limit is determined by: (1) the well known echo height ceiling effect - as the diameter of the trail becomes comparable to the wavelength, severe attenuation of the echo occurs due to interference of the signal reflected from the front and back portions of the column of ionization; and (2) the intensity of the returned echo being proportional to the cube of the wavelength. The lower limit to usable frequencies is a consequence of avoiding confusion with ionospheric echoes. The observations at UHF rely on a different scattering mechanism than observations at the usual lower frequencies to detect meteoric ionization, and this is described later in this section.

The reflection coefficient of a section of ionized trail depends on the electron volume density. If the density is sufficiently low, then the electrons scatter independently and secondary interactions are negligible. In this case the trail is termed underdense. If the electron density is sufficiently large, then secondary scattering between electrons becomes important; the dielectric of the ionized column is negative and the radio waves become evanescent within the trail. The meteor trail for this situation is called overdense and the scattering is equivalent to that from a metallic cylinder. As the meteor trail expands, due to ambipolar diffusion, the returned echo from underdense trails decays exponentially. For the overdense case, the returned echo power is almost unaffected by diffusion of the trail until the electron density

has fallen sufficiently for the trail to become underdense; whence again decay of the returned echo power occurs.

The transition from underdense to overdense is conventionally defined as occurring when the evanescent wave amplitude has fallen to $1/e$. From this condition it may be shown (*e.g. McKinley*, 1961) that this corresponds to a transitional electron line density, q_{tr}, of about $10^{14}\,electrons/m$ which is independent of the wavelength of the radiation. However, the full-wave treatment of radio wave scattering from meteor trails (*Poulter and Baggaley*, 1977, 1978) shows that this transition actually occurs slowly over a large range of electron line densities. The meteor trail may be considered as fully underdense for electron line densities less than $10^{13}\,electrons/m$ and fully overdense for electron line densities greater than $10^{15}\,electrons/m$.

The reflection coefficient of the radio wave scattering process also depends on the polarization of the radio wave electric field vector with respect to the trail. If the radio wave polarization is perpendicular to the trail then, due to the separation of ions and electrons within the trail, resonant oscillation occurs. The full-wave theory of *Poulter and Baggaley* shows that for this case, the maximum reflection coefficient is about twice that for the case of parallel polarization.

Speeds of the ablating meteoroids may be determined from the analysis of the returned echo. The echo amplitude profile versus time for a meteor trail during formation is essentially that due to Fresnel diffraction at a straight edge and is analogous to the familiar optical case. Of course, as the trail is diffusing, the Fresnel diffraction pattern also exhibits an exponential decay. For the pulsed radar systems, the characteristic Fresnel oscillations are only seen post-t_0. However, with CW systems the transmitting and receiving are separated by about 10–30 km and the combination of a weak ground wave with the signal returned from the meteor trail produces both post-t_0 and pre-t_0 oscillations. Whichever system is employed, the period of the Fresnel oscillations are dependent on the speed, wavelength and range to the meteor trail. As the wavelength is known, and the range can be readily found, the application of standard Fresnel diffraction theory enables the speed of the meteoroid may be determined.

If three or more spaced receiver sites are used with a common transmitter (either pulsed or CW), then the time delay in the observation of the meteor echo at each site may be used together with the measured speed to obtain the trajectory of the ablating meteoroid. The speed together with the trajectory allows the orbit of the meteoroid to be determined

(*Gartrell and Elford*, 1975). Meteor orbit data has been used to study both the meteor shower and sporadic meteor populations. Indeed the determination of the orbital parameters of sporadic meteors has allowed the radiant distribution of these meteoroids to be determined (*Elford and Hawkins*, 1964; *Elford et al.*, 1964).

Other studies of meteors include: (1) The determination of the height distribution of meteors and how this is affected by the echo height ceiling, the atmosphere (*Elford*, 1980), and the operational frequency of the radar (*Steel and Elford*, 1991). (2) The diffusion of the meteor trails and subsequent decay of the echo as a function of the height of ablation, and how this is affected by the Earth's magnetic field. (3) The determination of atmospheric wind speeds through the observation of the radial body Doppler of the trail (*e.g. Cervera and Reid*, 1995). (4) Diurnal and seasonal variations in the meteor echo rate. (5) The determination of ionospheric electron densities through the measurement of the degree of Faraday rotation of the reflected signals from the meteors (*Elford and Taylor*, 1995).

As stated previously most radar observations of meteors have been performed at frequencies between 20 MHz and 70 MHz. However, meteors have also been observed with high power radars operating at UHF. *Evans* (1965, 1966) used the Millstone Hill radar, operating at 440 MHz, to observe and obtain accurate velocity and deceleration measurements of shower and sporadic meteors. Due to the high frequency, reflections are limited to the short region of trail immediately adjacent to the ablating meteoroid. As a consequence, the echoes displayed the characteristics of moving-ball targets rather than Fresnel diffraction patterns. Thus, the speeds of the meteors were unable to be obtained in the usual manner, instead the radar's capability of measuring the Doppler shift of a single returned pulse was employed. The high transmitter power of this radar (about 2 MW) was important for the observation of the meteors as the returned echo power from the short length of trail is much less than that for lower frequency radars which obtain reflections from a much longer portion of trail.

Meteors have also been observed by incoherent scatter radars (ISR) operating at UHF (*e.g. Zhou et al.*, 1995). The incoherent scatter process occurs when the incident electromagnetic field interacts with free electrons, via Thompson scatter, which are then forced to oscillate with the electric field. The oscillating electrons re-radiate at a similar frequency to the incident radiation, and if the wavelength is short enough the re-radiated signal is phase incoherent. As the Thompson scatter cross section of the electron is small, ISR are required to have large power-aperture products.

ISR do not observe meteors in the usual manner as with other radars, instead they measure the electron content of a certain volume of atmosphere illuminated by the beam. When a meteor passes through this volume the electron content increases as the ablating meteoroid is ionized and ionizes the air molecules along its path. ISR are able to detect the increase in the electron content and therefore indirectly observe the meteor. Once recombination and attachment of the meteoric ionization occurs, the electron content returns to its background level. ISR observations of meteors are limited in application with only the diurnal and seasonal variations and height distributions able to be investigated. As such these observations are not part of the mainstream methods used to investigate meteors. However, as ISR are not subject to the height ceiling effect of other radars, they are able to detect meteors at any and all heights. Thus, they may be an important tool for the study of CHON-particles.

1.2.3 Satellite borne meteoroid dust exposure experiments

Meteoroid dust exposure experiments, which have been carried on board satellites in Earth orbit since the 1960's, are an important tool in the study of the influx of meteoroids to the Earth as they detect meteoroids of much smaller masses than those that produce most radar and optical meteors. In addition they don't suffer from many of the various selection effects (radio: ionization efficiency, diffusion effects; optical: luminosity efficiency) that meteor observation techniques are subject to.

Typically the meteoroid dust detectors take the form of thin metallic foils with thicknesses of only a few millimeters. For example, *Love and Brownlee* (1993), describe a meteoroid dust detector, which was carried aboard the Long Duration Exposure Facility (LDEF), consisting of 1.6 mm thick sheets of 6061-T6 aluminium alloy. They were able to observe craters in the foil down to 20 μm in diameter which, from their calculations, corresponded to a particle mass of under $10^{-12}\,kg$. This is by no means the lower limit to the meteoroid masses detectable by satellites. The data obtained by *Alexander and Bohn* (1974), which is summarised by *Hughes* (1978), shows that particles with masses as low as $10^{-15}\,kg$ are detectable.

1.3 Motivation and Scope

This thesis is concerned with the observation of meteors with the Buckland Park 54.1 MHz narrow beam radar system, situated about 40 km North of Adelaide. Whilst the Buckland Park radar was originally designed for studies of the lower atmosphere (*Vincent et. al.*,

1987), it is also an excellent tool for the investigation of meteor phenomena. The narrow beam system offers two advantages over the more traditional wide beam radars used in the past. The first is that the sensitivity of the system is greatly increased, *e.g.* the Buckland Park radar is able to detect meteors with electron line densities as low as $10^{10}\,electrons/m$ even though the transmitter is relatively low power (about $30\,kW$). The second advantage is that the response of the radar to meteor backscatter is confined to a narrow well defined area of the sky, which enables meteor shower radiants and the distribution of sporadic radiants, to be accurately determined.

Early meteor research undertaken by *Steel and Elford* (1991) with the Buckland Park VHF radar during its development stage involved the investigation of the meteor height distribution at VHF, and a comparison with with the height distribution observed by a $2\,MHz$ radar at the same site. These observations constituted the limit that could be achieved by the system at that time. In order to be able to continue useful research with the radar, both the transmitter and data acquisition systems were required to be upgraded. The transmitter power output was increased from $4\,kW$ to $32\,kW$. However, it was found that the existing data acquisition system was completely inadequate and not readily upgraded, and therefore a new data acquisition system was constructed.

The upgraded radar with the new meteor detection system came fully on line in early September 1993. In addition to astronomical applications, the meteor data from this period formed part of a campaign, the objective of which was to compare the atmospheric wind speeds determined from the drift of the meteor trails with those obtained from the Full Correlation Analysis (FCA) of Spaced Antenna (SA) data with an MF radar situated at the same site. The results from this campaign are not presented in the main body of this thesis, however see *Cervera and Reid* (1995). This paper is reproduced in Appendix A.

A second 'meteor-wind' campaign, which involved the University of Colorado, was undertaken from June 29 to July 15, 1994. The object of this campaign was to compare two meteor radar systems with the view to improving the wind estimates derived from both of them. The two meteor systems were the one developed by the author at Adelaide, and the other the University of Colorado's meteor detection and collection (MEDAC) system. The MEDAC system is designed as a low-cost add-on to collect and analyse meteor echoes detected with existing wind profilers (*Avery et al.*, 1990; *Valentic et al.*, 1995). Thus, the two systems were able to operate in parallel and observe the same meteor echoes. Again, the results from this campaign do not appear in this thesis, but are described in detail by

Valentic et al. (1996) which is reproduced in Appendix D.

The meteor radar response function (*Elford*, 1964; *Thomas et. al.*, 1988) is an extremely important tool for the interpretation of meteor backscattered radio signals. As such, the response function of the Buckland Park radar is developed in considerable detail in this thesis. Previous derivations of the response function have assumed a constant ionization profile of meteor trails. Here the response function calculation is extended by including an ionization profile as given by classical ablation theory. The response function is used extensively throughout the thesis, and applications include the modeling of the expected height distribution and diurnal variation observed by the radar, prediction of the time of passage of known meteor showers and the calculation of the radiants of unknown showers, and modeling of the mass influx of both shower and sporadic meteors.

To set this work in context, a general survey of short wavelength observations of meteors is presented. As discussed earlier, as the height of ablation increases, the greater diffusion causes the length of a trail contributing to a coherent backscatter signal to decrease. In the extreme case, meteors occurring above about 98 km, have an observable trail length of less than a Fresnel zone, and the returns from these meteors are as though from the head of the trail. These "head echoes" have been difficult to observe in the past due to the large attenuation factors at these heights (due to the initial radius of the trail and the diffusion of the trail during the finite time of its formation). However, the greater sensitivity of the Buckland Park VHF radar allows such echoes to be readily observed.

A new technique for the deduction of meteor velocities using radar is developed. This method makes use of the pre-t_0 phase information available from the phase coherent receivers of the Buckland Park radar. The technique may be considered a diffraction technique as it makes use of the Fresnel diffraction theory which characterises the meteor echoes. Considerable advantages arise from using pre-t_0 phase information as opposed to the post-t_0 amplitude oscillations used in the past: velocities are able to be calculated from some 75% of all meteor echoes (*c.f.* 10% with the post-t_0 amplitude oscillations), and the process used for the reduction of velocities is very accurate, with typical accuracies almost always less than 5.0% and often as low as 0.5%. It is also shown that the head-echo like returns from meteors ablating at large heights can be used to deduce velocities by applying the pre-t_0 phase technique. In the past these echoes, if observed, would have been discarded.

Generally the greater the velocity of the meteoroids entering the Earth's atmosphere the higher altitude of ablation. The sensitivity of the upgraded radar combined with the

power of the new velocity reduction technique enables the velocities of these meteoroids to be measured more readily, despite the selection effects operating against the detection of high velocity meteors. While the echo height ceiling is still about 100 km, the significant number of high speed meteors able to be observed with the system (generally those produced by the larger meteoroids that ablate at lower altitudes) raises the possibility of observing and studying meteoroids of interstellar origin.

Equally if not more important, slow meteors are readily detected and their speeds able to be determined. Such observations are of vital importance in determining the flux of meteoroids on the Earth as the most probable velocities lie in the range from 15 to 25 $km\,s^{-1}$.

The ability of the system to detect low speed ablating particles is also the first requirement for the observation of ablating re-entering space debris. The observation of ablating space debris is important for the study of the impact it has on the near Earth environment, in particular the risks it poses for space craft in Earth orbit, both manned and unmanned. With this in mind, a discussion on the possibility of the observation of space debris as a meteoric phenomenon is given in Chapter 5.

The velocity distribution of the sporadic meteors is a key quantity in interpreting space craft data and modelling the response of radars to meteor backscatter, and strong emphasis is placed on obtaining an accurate velocity distribution. The correction of the velocity distribution obtained from observations with the Buckland Park radar for various selection effects and a comparison with previous results is also considered to be a reliable and important outcome of the work.

The mass distribution of meteoroids encountered by the Earth is also an important quantity, and a considerable effort is made to determine this in the mass range of meteoroids that produce most meteors able to be detected by the Buckland Park radar. It will be demonstrated that the initial mass of individual meteoroids are able to be determined from electron line density measurements of the meteor trails, the velocity, and ablation theory. This is important as work of this nature enables the mass distribution of the sporadic meteors as observed by the radar to be determined. The observed mass distribution may be modelled using the radar response function, and this technique enables the cumulative mass index of sporadic meteoroids encountered by the Earth to be determined. This process will be discussed in detail and the determined cumulative mass index of the sporadic meteoroids is compared with previous results.

Observations of two showers (the June-Librids and θ-Ophiuchids) were made using a

new technique which employed the meteor radar response function. This technique is very accurate with the position of a shower radiant able to be determined to within $\pm 0.5°$. The observation of meteor showers is of interest for two reasons: (1) to check the validity of the new technique developed to measure meteoroid speeds, and (2) as described earlier, to examine the possibility that for radars with high sensitivities, many meteor showers would be swamped by the sporadic background, and also the detection of showers would be biased towards those produced by meteoroid streams containing a greater abundance of small particles, *i.e.* newer meteoroid streams.

The observations of the June-Librids are to the best knowledge of the author, the first by a radio technique. Unfortunately, the observation of this shower was made prior to the upgrade of the radar which enabled velocity measurements to be made. The subsequent year (1993) the radar was not operational due to a hardware problem. A search for the June-Librids was made in the year after this (1994), but there was no evidence for its activity during that year.

Velocity measurements are made for the θ-Ophiuchids (observed in 1994) and a large peak in the velocity distribution is found. This peak is in agreement with the velocity of the stream as determined by previous researchers, and therefore the new method of determinating meteor speeds is verified. A technique is developed which enables the cumulative mass distribution of the stream to be determined, and this relies on a geometrical approach to correct the individual mass determinations which are corrupted by the polar diagram of the antenna. The results support the working hypothesis that radars with high sensitivities to meteor backscatter are biased towards the detection of meteor showers produced by streams with a preponderance of small particles.

Finally, the radiant coordinates of the θ-Ophiuchids are calculated and it will be shown that the stream actually consists of two distinct radiant centres. The mean position of the two radiant centres is obtained and this is compared with previous results.

Chapter 2

The Buckland Park VHF Radar

Oh give me a good guitar, and you can say that my hair's a disgrace
Or, just give me an open car, I'll make the speed of light outta this place

—*Tenement funster, Queen*

2.1 Introduction

The VHF radar is situated some 40 km North of Adelaide, at Buckland Park (lat. $-34.5°$, long. 138.5°), and located adjacent to the 2 MHz radar (*Briggs et al.*, 1969). The radar was designed to study tropospheric winds, the first results appearing in *Vincent et al.*, (1987). However, the versatility of the radar enables it to be used for detection of meteors, and a variety of meteor experiments are now able to be performed with the system. With this in mind, the Adelaide VHF radar was reconfigured to investigate meteor height distributions (*Steel and Elford*, 1991), meteor shower radiant determinations (*Elford et al.*, 1994), measurement of atmospheric winds at meteor altitudes using the meteor drift techniques (*Cervera and Reid*, 1995), and also the study of space debris and measurement of meteoroid velocities (both currently underway and addressed in later chapters).

The VHF radar antenna is a collinear coaxial (CoCo) array which can be used for both transmission and reception. The array is approximately 90 m square and consists of 32 North-South rows, each of 48 dipoles, and produces a beam with a half-power half-width of approximately 1.6°. Phasing the rows of antennas appropriately tilts the beam in an Eastward or Westward direction. There are also three sets of 16 Yagi antennas which are used for spaced antenna measurements of tropospheric winds. These Yagis are used for

Wavelength :	54.1 MHz
Pulse width :	12.8 μs
Pulse repetition frequency (PRF) :	1024 Hz
Beam tilt :	30° off zenith
Range resolution :	2 km
Sampling of raw data :	2 km range intervals
Sampling start range (height) :	80 km (70 km)
Sampling end range (height) :	128 km (110 km)
Peak power (rms) :	32 kW

Table 2.1: Typical operational parameters of the VHF radar for meteor detection.

reception only, and are not used for meteor detection. Figure 2.1 shows an overview of the VHF radar.

During 1992/93 the power and time resolution of the VHF radar was upgraded. The transmitted peak power was increased from 4 kW to 32 kW, so that fainter meteors (down to +13.5 Mag.) are now detectable. The time resolution of the receiving system was reduced from 16 ms to 1 ms. This latter improvement is very important in detecting the short duration echoes from meteors that occur at altitudes above 90 - 95 km. Both these upgrades will be discussed in a subsequent section of this chapter.

For meteor detection the beam is tilted 30° off zenith, either Eastwards or Westwards; the optimum tilt angle of the beam is determined from a compromise between collecting area and range. An increase in tilt angle increases the collecting area but reduces the sensitivity of the system to faint meteors. Ideally, a beam tilt of $60° - 70°$ is appropriate for meteor detection. This is readily seen from inspection of the meteor response function (*Elford*, 1964; *Thomas et al.*, 1988). The effect of the tilt angle on meteor detection is discussed in detail in chapter 4 on the meteor radar response function. Although a large off zenith beam tilt is ideal, hardware limitations with the present system means that the off zenith beam tilt is limited to only 30° if meteor data is to be obtained up to a height of 110 km.

The operational parameters typical for meteor work with the Buckland Park VHF radar are listed in table 2.1.

2.2 The CoCo antenna array

The VHF array comprises 32 rows of CoCo antennas. Each CoCo antenna is simply a length of 52 Ω coaxial cable with the inner and outer conductors of the cable interchanged every

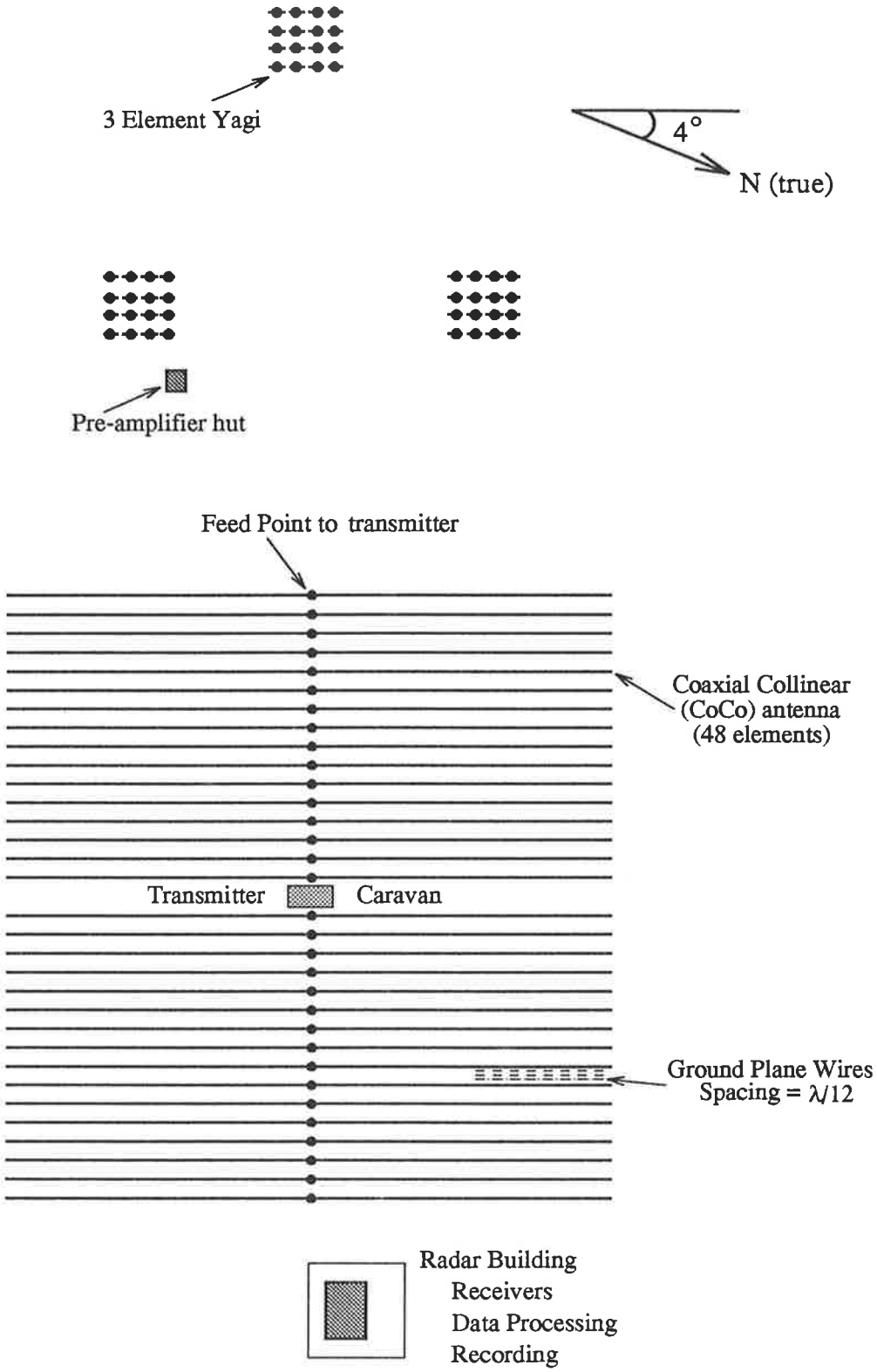

Figure 2.1: Ground plan of the Buckland Park VHF radar. The operating frequency is 54.1 MHz and the geographical coordinates are : 34° 38′ S, 138° 29′ E

half wavelength (*Wheeler*, 1956; *Balsley and Ecklund*, 1972). CoCo arrays are widely used as they are relatively cheap to build, and easy to maintain. However they are less efficient than Yagi arrays. The VHF CoCo array is only 30% efficient (due to the loss of signal in the coaxial cable used for the CoCo rows and feeders) compared to an estimated 80% if a similar aperture array was constructed from Yagi's. Each CoCo row is centre fed and has 23 inner/outer interchanges either side of the centre feed. Thus each CoCo antenna is comprised of 48 half wavelength dipoles. Each segment of coaxial cable is cut to 0.67 of a wavelength to take into account the propagation velocity of the signal in the coaxial cable. This gives a physical antenna length of 88.7 m. The bandwidth of each antenna is approximately 700 kHz. The 32 rows of CoCo antennas are spaced by half a wavelength except for the centre two which are 1.5 wavelengths apart. The transmitting caravan occupies the space between the two centre antennas (see Figure 2.1). The distance between the two end rows is then 88.7 m, this gives a square array with sides of length 88.7 m. Figure 2.2 is a photograph of the VHF CoCo array. The transmitting caravan can be seen in the centre of the array; in the background is one of the yagi arrays.

The centre feeds to the CoCo antennas have 70 pF fixed capacitors across the inputs together with small lengths of coaxial cable or "capacitive tuning stubs" in parallel with the 70 pF capacitors. Trimming the stubs to the required length provides fine tuning for each of the antennas, which are tuned to an impedance of 200 Ω and zero phase at 54.1 MHz. The centre feeds are balanced by 4:1 baluns which take the form of quarter wavelength loops of 52 Ω coaxial cable. This gives a balanced impedance for each antenna of 50 Ω and zero phase. For a vertically directed beam the electrical length of the feeder cables to each of the rows of antennas are all of integral wavelengths. If the beam is required to be tilted in either an Eastward or Westward direction, phasing cables of the appropriate length are introduced to successively delay the signal to or from each row. For example if a beam tilt of 30° is needed, then cables of length $\lambda/4$, $\lambda/2$, $3\lambda/4$ and λ are used to give successive 90° phase differences to each CoCo antenna, where λ is the wavelength. Relays controlled by a microprocessor are used to switch the phasing cables in or out, or to switch the direction of the phase delay, so that the beam may be vertically directed or tilted, East or West. To change the amount of tilt from zenith requires a different set of phasing cables to be used. The phase delay, δ, between rows of antennas spaced by $\lambda/2$, required to tilt the beam to an off zenith angle, α, is given by:

$$sin\,\alpha = \delta/\pi\,. \tag{2.1}$$

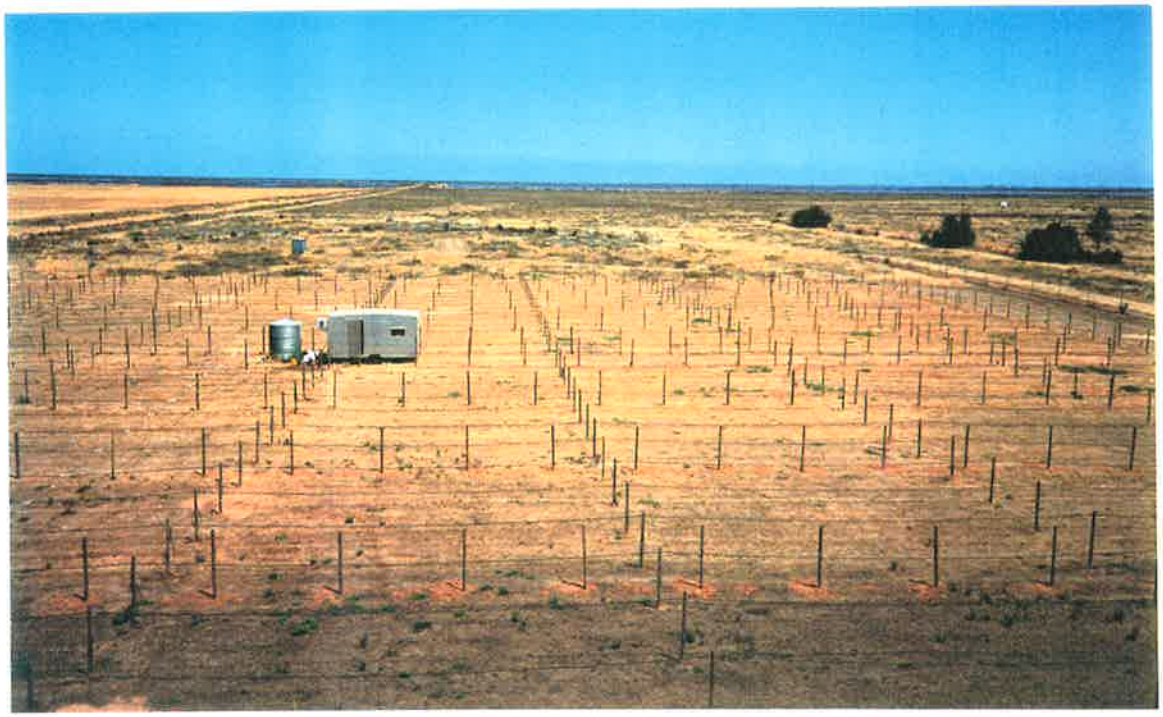

Figure 2.2: A photograph of the Buckland Park VHF CoCo array. In the centre of the array the transmitting caravan can be seen. The yagi arrays can be seen in the background together with the preamp hut. See text for details.

Figure 2.3: Photograph of current probe used for checking the phasing across the CoCo array. The centre feed of the CoCo antenna together with its balun can also be seen. See text for details.

This can be derived from a simple geometrical argument which is not reproduced here.

The CoCo array is elevated a quarter of a wavelength above the ground. Copper wire with a spacing of $\lambda/12$ strung out on the ground, parallel to the CoCo antennas, produces a ground plane that is independent of the reflectivity of the ground. This is necessary so that array's efficiency is maximised. The significance of the ground plane is discussed in Section 2.3

Throughout 1992 a major mechanical and electrical refurbishment of the CoCo array was undertaken; work of this nature had not been performed since its construction in 1984. The array needed significant mechanical repairs as many of the parts used to support the antennas (such as cable ties, staples *etc.*) were worn due to weathering. These were replaced and the antennas retensioned. Also many of the centre feeds had become exposed to the weather; these were sealed with an all-weather silastic. Although the mechanical repairs were time consuming, the electrical refurbishment was far more difficult and intricate. The entire array needed retuning which required the replacement of many tuning capacitors and stubs, and trimming of most of the remaining stubs. All the antennas were able to be tuned to within $\pm 5\,\Omega$ and $\pm 5°$ of $50\,\Omega$ and zero phase. The relay chassis, used to switch the beam tilt from East to West, also underwent minor repairs although this was generally in good working order.

Once various signs of wear and tear were repaired and the array was retuned, it was considered advisable to check the phasing across the array to ensure there were no anomalies. This was performed by feeding a 54.1 *MHz* signal into each of the CoCo antennas from the Tx caravan. A current transformer was place as near as possible to the centre feed of the CoCo antenna in question to measure the strength and phase of the current feeding each antenna. This was then compared with a reference signal, using a vector voltmeter, to determine the phase difference between the received signal and the reference (see Figure 2.4c). This process was then repeated on the next CoCo antenna, making sure that all cable lengths remained the same to preserve the phase reference. Also it was necessary to make sure that the measurements on successive antennas were made in a similar geometrical location. This is because the phase of the transmitted signal varies along the CoCo antenna. This procedure was performed for the beam vertically directed and tilted East and West with 11° phasing cables. Figure 2.4 shows a sketch of the loop antenna and the set up for measuring the phases. In Figure 2.3 a photograph of the loop antenna shows it in use.

When the current transformer was in use, a grounded copper tube was placed around

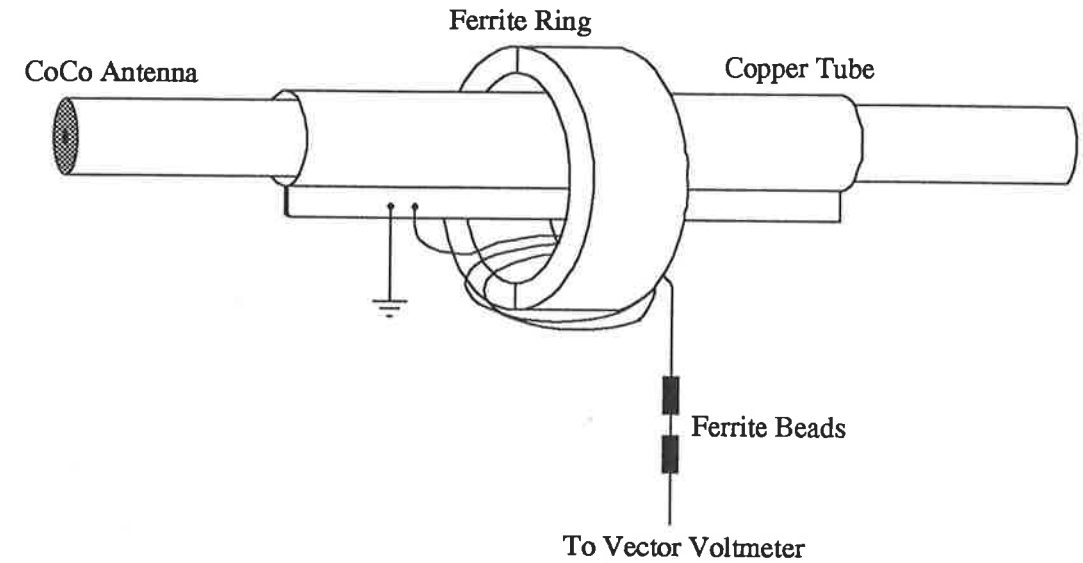

a)

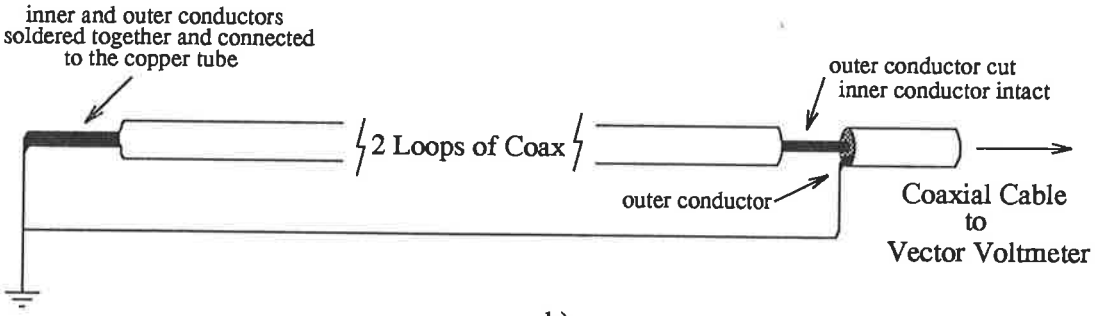

b)

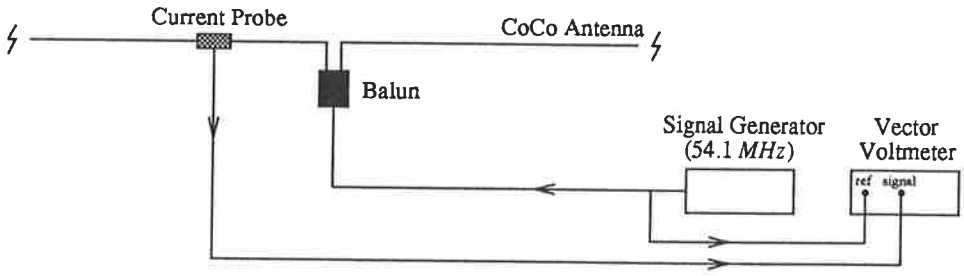

c)

Figure 2.4: This figure shows a sketch of the current probe in panels (a) and (b). Panel (c) shows the setup for checking the phasing across the CoCo antenna array. See text for further details.

the CoCo antenna in question (see Figure 2.4a). This shielded the loop antenna from any electrical radiation of the CoCo antenna and also from any other background electrostatic effects, thus a current was induced in the loop antenna by the radiated magnetic field only. The loop antenna is then basically a current detector and will from now on be referred to as a current probe. The current probe was constructed from two turns of 50 Ω coaxial cablet. It was found, from measurements in the laboratory, that 2 - 3 turns for the current probe gave the best results, any more turns and the antenna became too inductive. A ferrite core was used to increase the coupling between the CoCo antenna and the current probe (see Figure 2.4a). As the ferrite core was required to be placed around the CoCo antenna, it was cut in half and held together with cable ties. The raw surfaces of both halves of the ferrite core were ground smooth so as to minimise the loss of efficiency in coupling between the two antennas. One end of the current probe had the inner and outer conductors soldered together and joined to the copper tube. The other end of the loop had the outer conductor cut, the end of the outer conductor which led back to the vector voltmeter was soldered to the copper tube also. This grounded the copper tube, as required, and provided a ground reference for the probe. It also caused the outer conductor of the coax of the current probe to be grounded, thus providing additional electrostatic shielding. Figure 2.4b shows in detail the composition of the current probe. Note this antenna was unbalanced, however for its purpose, a balanced load was not required. Ferrite beads were placed on the cable back to the vector voltmeter to help in shielding the signal from stray pickup.

The phasing across the CoCo array (*i.e.* row to row) for a vertical beam was measured and found to be normal, *i.e.* the phase differences between the CoCo antennas was negligible. However, when the beam was tilted 11° either East or West, it was found that half of the array was phased to point the beam in one direction, and the other half phased to point the beam in the opposite direction. This meant that for either beam direction selection, two beams would be formed, one pointing East and one West, and this was not the normal operation of the radar. The problem could either have been simply with the phasing cables cut incorrectly or something wrong further into the receiving system. Fortunately, for ease of repair, the problem was with the phasing cables. Once the problem had been rectified, the measurements were repeated, and the phasing across the array for either an East or West pointing beam was as expected. Once it had been verified that there was no problem with phasing across the array for one beam angle, it was not required to repeat the measurements for others beam angles. It was only required to measure the electrical lengths of the other

groups of phasing cables and ensure that they gave the correct phase delays for each antenna.

It is important to examine the background noise received by the CoCo array. This is necessary to ensure the the CoCo array is performing as expected, to determine if there is any man made interference, for the establishment of the meteor detection criteria, and also for the calculation of the meteor radar response function (see Chapter 4). The main source of noise is due to background cosmic sources, which varies from an equivalent temperature of around $2000\,K$ to $8000\,K$ at $54\,MHz$ (see *e.g. McKinley*, 1961). Noise is also contributed to the overall observed background noise by the radar receivers, however, this contribution is small being about $400\,K$ (see Section 2.5). Figure 2.5 displays noise observed by the CoCo array for three consecutive days in August 1993. It can be seen that the noise has a background temperature of about $2000\,K$ rising to $10000\,K$ with the passage of the galactic centre, which passes close to the main beam of the CoCo array in the zenith position. The peak in the noise, due to the galactic centre, occurs at 19:24 local time on the first day and occurs 4 minutes earlier on each subsequent day as expected from the sidereal shift of cosmic sources. There also appears to be a cosmic radio source detected at 05:20 on the first day which has the expected sidereal shift to the time of its passage on subsequent days. From about 07:00 to 09:00 on the third day, one may observe a significant amount of short duration noise bursts. These noise bursts do not appear in abundance at other times. Considering that the 30^{th} August, 1993, was a Monday and that a major highway passes close (approximately $5\,km$) to Buckland Park, one possible cause of these noise bursts are automobile engine noise and the increase in abundance, during the above time, is of course due to commuters.

2.3 The CoCo array antenna pattern

For experimental work it is important that the antenna pattern of an array is known. In particular, with regard to meteor studies, the antenna pattern is required in order to calculate the response of the radar meteor echoes (see Chapter 4). In this section the model of the CoCo antenna pattern is derived on the basis of a two-dimensional array of half wavelength dipoles situated a quarter of a wavelength above a ground plane. The current distribution across the array, feeder losses, and random amplitude and phase errors in the current supplied to the elements are included. Figure 2.6 shows the geometry of the coordinate systems used for the modeling. In this diagram, β and γ are the angles that the point P makes with the y

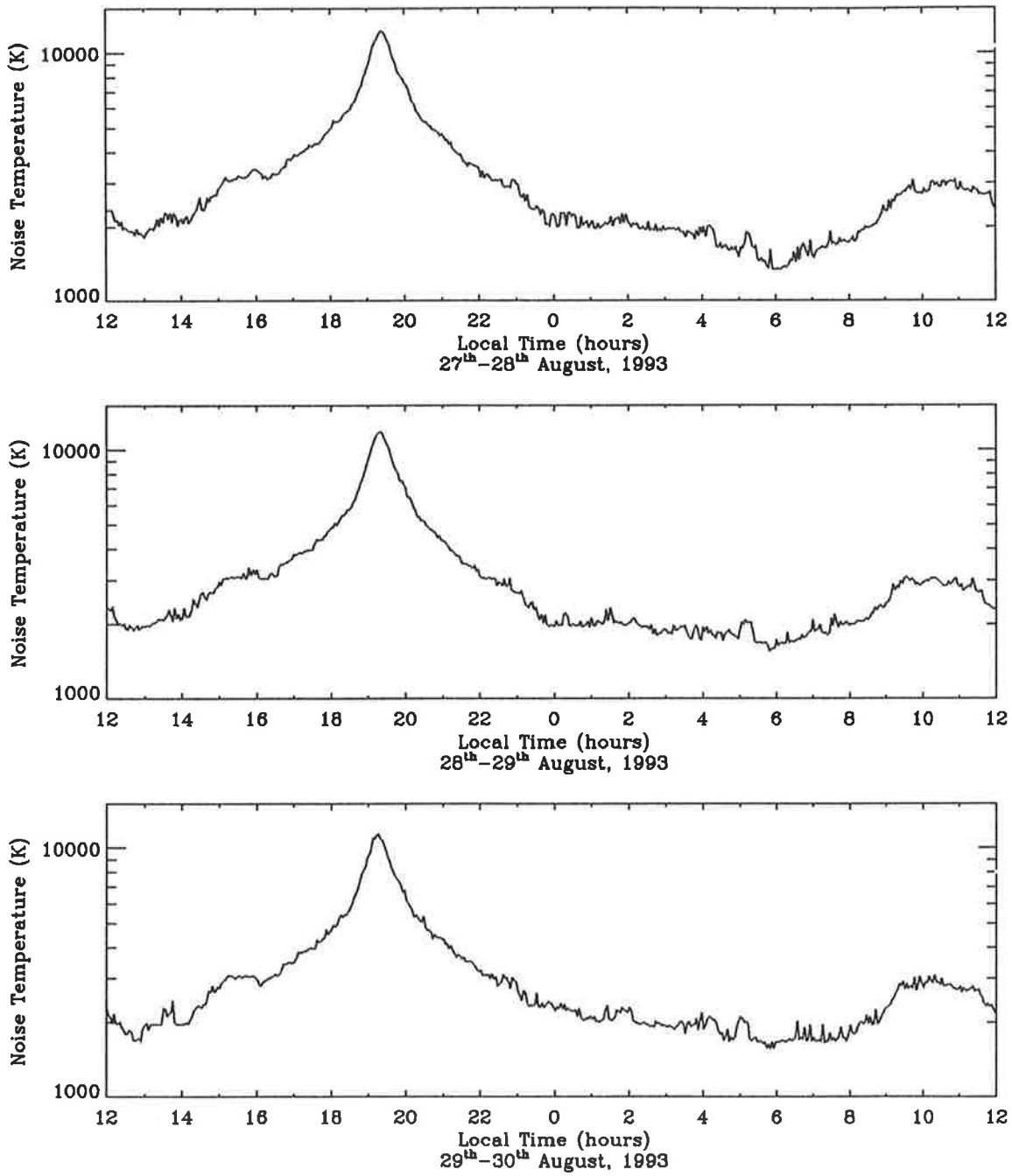

Figure 2.5: Background cosmic noise observed by the VHF CoCo array.

and x-axes respectively, θ is the North/South off zenith angle, ϕ is the East/West off zenith angle, and θ' and ϕ' are the zenith and azimuth angles respectively. Simple trigonometry gives the following relations:

$$\begin{aligned} tan\theta &= tan\theta' \, sin\phi' \\ tan\phi &= tan\theta' \, cos\phi' \\ cos^2\theta' &= \frac{1}{1+tan^2\theta+tan^2\phi} \\ sin^2\beta &= \frac{1+tan^2\phi}{1+tan^2\theta+tan^2\phi} \\ cos^2\beta &= \frac{tan^2\theta}{1+tan^2\theta+tan^2\phi} \\ cos^2\gamma &= \frac{tan^2\phi}{1+tan^2\theta+tan^2\phi} . \end{aligned} \tag{2.2}$$

The various factors (*e.g.* dipole, ground plane and array factors) that contribute to the polar diagram are defined in terms of these angles. The above equations are used to transform these factors into the (θ, ϕ) coordinate system.

The antenna pattern for a 1/2 wave dipole directed North/South in free space is shown in Figure 2.7a and is mathematically given by (see *eg. Kraus*, 1988) :

$$G_{dipole}(\beta,\phi) = G_0 \frac{cos^2[(\pi/2)sin\beta]}{cos^2\beta} \tag{2.3}$$

where the value of G_0 is 1.64 with respect to an isotropic radiator. The effect of a ground plane is to modify the dipole radiation pattern. Consider Figure 2.7b where an isotropic radiator is situated at a height, h, above a ground plane. This is equivalent to a situation where the ground plane is replaced by an image source at a distance h below the ground plane. The image source radiated with a π phase reversal. The electric field in any general direction (θ', ϕ') is given by:

$$E(\theta',\phi') \sim e^{i\psi} - e^{-i\psi} , \tag{2.4}$$

where

$$\psi = \frac{2\pi h}{\lambda} cos\theta' ,$$

and λ is the wavelength of the radiation. The above equation for the electric field can be rearranged to give :

$$E(\theta',\phi') \sim sin\left(\frac{2\pi h}{\lambda} cos\theta'\right) , \tag{2.5}$$

and thus the following equation for the gain pattern is yielded :

$$G_{gp}(\theta',\phi') = sin^2\left(\frac{2\pi h}{\lambda} cos\theta'\right) . \tag{2.6}$$

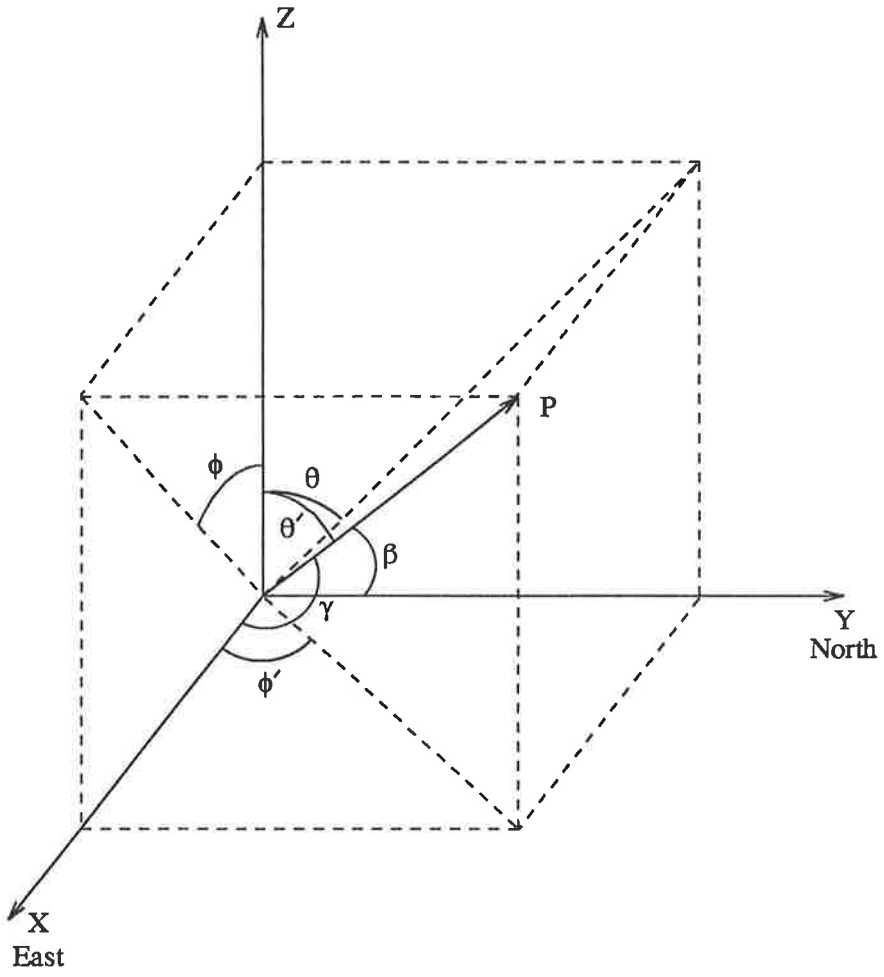

Figure 2.6: Geometry of the coordinate system used for the modeling of the CoCo array antenna pattern. The angles denoted by θ and ϕ are the off zenith angles in the North/South and East/West directions respectively. The angles denoted by $\theta^{'}$ and $\phi^{'}$ are the zenith and azimuth angles respectively.

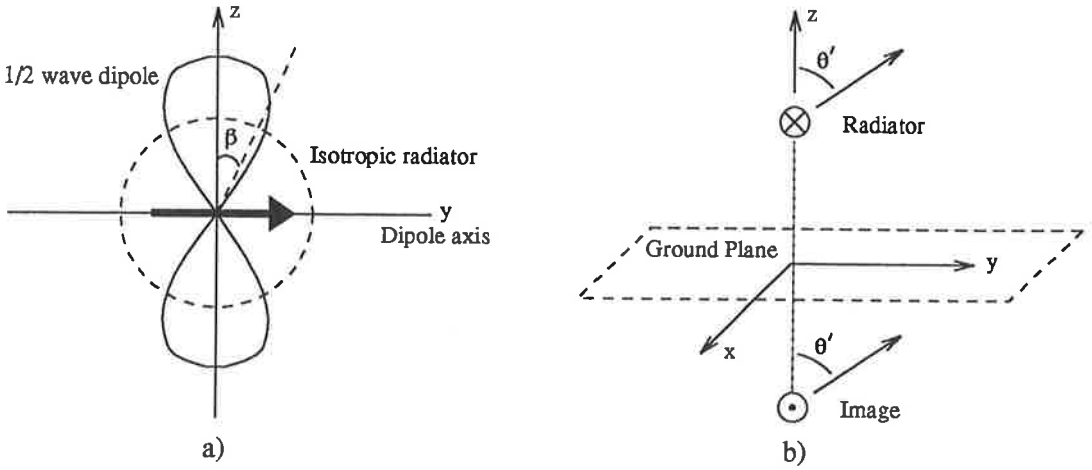

Figure 2.7: This figure shows, in panel (a), the yz cross-section of the radiation pattern of a half wave dipole in free space. The maximum gain of the dipole is 1.64 times that of an isotropic radiator. Panel (b) shows the geometry of an isotropic radiator situated at a height, h, above a ground plane. The image radiator is also shown. Note the image radiator has a π phase reversal.

Using the principle of pattern multiplication (see *eg. Kraus*, 1988), the antenna gain pattern for a 1/2 wave dipole situated 1/4 of a wavelength, above a ground plane (*i.e.* h is set to $\lambda/4$), is then given by :

$$G(\theta,\phi) = G_{dipole}(\beta,\phi)\, G_{gp}(\theta',\phi') = G_0 sin^2\left(\frac{\pi}{2}cos\theta'\right)\frac{cos^2[(\pi/2)sin\beta]}{cos^2\beta}\,. \qquad (2.7)$$

In the North/South and East/West planes this reduces to:

$$\left.\begin{aligned} G_{NS}(\theta) &= G_0\, sin^2\left(\frac{\pi}{2}cos\theta\right)\frac{cos^2[(\pi/2)sin\theta]}{cos^2\theta} \\ G_{EW}(\phi) &= G_0\, sin^2\left(\frac{\pi}{2}cos\phi\right) \end{aligned}\right\}\,. \qquad (2.8)$$

Now consider an array of identical elements. The principle of pattern multiplication simplifies the calculation of the antenna pattern to that of a pattern of a single element multiplied by the pattern from an array of isotropic radiators at the positions of the elements. For the CoCo array, this can be simplified further as the array is rectangular. The antenna pattern now becomes the pattern of a single element multiplied by the patterns of two separate linear arrays of isotropic radiators, one in the x direction and one in the y direction. Thus in general we have :

$$G(\theta,\phi) = G_e(\theta,\phi)\, G_{gp}(\theta,\phi)\, G_{lx}(\theta,\phi)\, G_{ly}(\theta,\phi)\,, \qquad (2.9)$$

where G_e is the radiation pattern of a single element, G_{gp} is the effect of a ground plane, and G_{lx} and G_{ly} are the radiation patterns of the linear arrays in the x and y directions

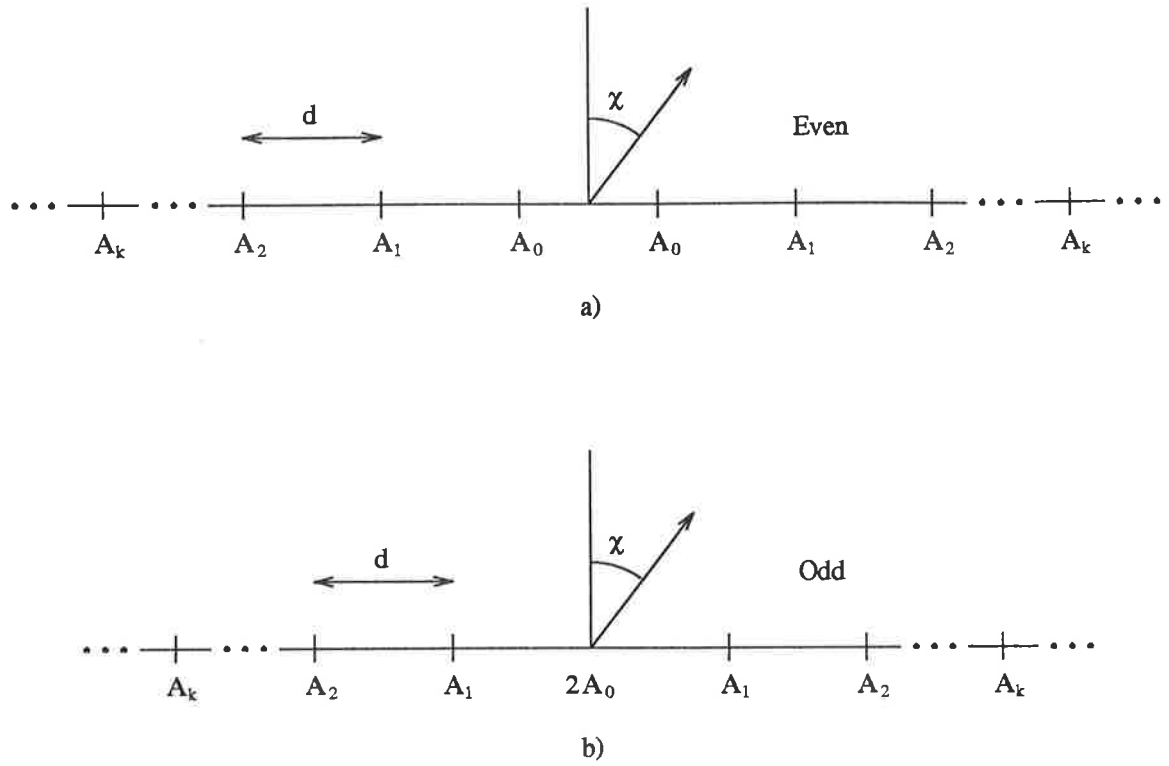

Figure 2.8: Linear arrays of n isotropic radiators for n even (a) and n odd (b).

respectively. The radiation pattern for a centre fed linear array of isotropic radiators which are in phase (refer to Figure 2.8), is given by (*Kraus*, 1988) :

$$G_{linear}(\chi) = \begin{cases} 4 \sum_{k=0}^{(n/2-1)} A_k \, cos^2 \left[(2k+1)\frac{\psi}{2} \right] & \text{if } n \text{ is even} \\ 4 \sum_{k=0}^{(n-1)/2} A_k \, cos^2 \left[2k\frac{\psi}{2} \right] & \text{if } n \text{ is odd} \end{cases} , \tag{2.10}$$

where n is the number of elements in the linear array, A_k is the power supplied to the to the k^{th} element, and ψ is given by the following expression :

$$\psi = \left(\frac{2\pi d}{\lambda} \right) sin\chi \, . \tag{2.11}$$

For the case of a linear array oriented parallel to the x-axis (*i.e.* East–West) χ is replaced by $90 - \gamma$ with the orthogonal coordinate being θ. Similarly for a linear array oriented North–South, χ is replaced by $90 - \beta$, and the orthogonal coordinate by ϕ.

The factor of 4 in 2.10 may be dropped as we are dealing with relative antenna gains. As mentioned previously, the beam of the CoCo array can be tilted in the East/West plane by introducing successive phase differences to the antennas. If the phase shifts are given by

δ_k, then the antenna pattern for an odd number of linear elements becomes :

$$G_{linear}(\chi) = 4 \sum_{k=0}^{(n-1)/2} A_k \cos^2 [k\psi - \delta_k] , \tag{2.12}$$

and again the factor of 4 may be dropped. The antenna pattern described by (2.12) is that of a vertically oriented "fan beam" if the phase shift, δ_k, of the signal to each element, is zero for all the elements. If the phase difference between each element, $\delta_{k+1} - \delta_k$, is non-zero and constant, and the element spacing is $\lambda/2$, then the fan beam is tilted in the θ plane by an off zenith angle defined by (2.1). The antenna pattern for the VHF CoCo array is given by :

$$G_{coco}(\theta, \phi) = G_{dipole}(\beta, \phi)\, G_{gp}(\theta', \phi'\, G_{lx}(\gamma, \theta)\, G_{ly}(\beta, \phi) , \tag{2.13}$$

where $G_{lx}(\gamma, \theta)$ and $G_{ly}(\beta, \phi)$ are given by :

$$\left.\begin{aligned} G_{ly}(\beta, \phi) &= \sum_{k=0}^{23} C_k \cos^2[(k + 1/2)\pi f \cos\beta] \\ G_{lx}(\gamma, \theta) &= \sum_{j=0}^{16} B_j \cos^2[j\pi(\cos\gamma - \sin\alpha)] \end{aligned}\right\} , \tag{2.14}$$

where f is the speed of propagation of electrical signals in the coaxial cable relative to the speed of light in a vacuum, and has a value of 0.67, and α is the beam tilt off zenith angle. The values B_j, are the powers supplied to each pair of rows of CoCo antennas equidistant from the centre of the array. Note that as the centre row of the CoCo array is absent, $B_0 = 0$. The values C_k, are the powers supplied to each pair of dipoles equidistant from the centre feed along a given CoCo antenna, relative to the power at the CoCo antenna centre feed. Note, the values C_k are assumed to be the same for each CoCo antenna row as all the rows are identical. The power supplied to the (j_{th}, k_{th}) dipole is then given by $B_j C_k$.

Power is supplied to each pair of rows of CoCo antennas from one of 16 transmitter modules. All of these modules produce the same power output ($2\,kW$). For the type of coaxial cable used in feeder cables to the centre feeds of the CoCo antennas, an attenuation in power of $0.0518\,dB\,m^{-1}$ was measured. From this value and the length of the feeder cables to each of the CoCo antennas, the values of B_j were calculated. Similarly, the values of C_k were calculated. It must be noted here that *Judasz* (1983) found that for an antenna constructed of 24 dipoles, resonant at 50 MHz, and with a velocity factor of 0.66, the current distribution in the antenna was of the following form: The amplitude appearing at each dipole, for successive dipole triplets, was in the approximate ratio 1:2:1. Since the Buckland Park VHF

CoCo antennas have exactly twice the number of elements as the antenna described above, the values of C_k were modified accordingly.

The effect of the cable losses is to significantly reduce the sidelobes (a form of tapering). From modeling, with and without the cable losses included, it was found that the sidelobes were reduced by about 3 dB. The side effects of tapering are: (1) the width of the main beam is broadened slightly (by less than 0.1°), and (2) the overall efficiency of the array is only about 30%.

The antenna pattern developed so far, for the CoCo array, has been calculated on the assumptions that there are no random errors in amplitude and phase of the current supplied to the elements, and that the ground plane is perfect. This is of course not the case. Addressing the first point, *Ruze* (1952, 1957) showed that assuming the random errors in the amplitude and phase are independent of each other, are independent from element to element, and are described by a Gaussian distribution, the "average" radiation pattern in the (θ', ϕ') coordinate system may be expressed as :

$$\overline{G(\theta',\phi')} = G(\theta',\phi') + S(\theta',\phi')(\overline{\Delta_a^2} + \overline{\Delta_p^2}) \frac{\sum_{m=1}^{M}\sum_{n=1}^{N} I_{mn}^2}{\left[\sum_{m=1}^{M}\sum_{n=1}^{N} I_{mn}\right]^2}, \tag{2.15}$$

where, Δ_a^2 is the relative mean square error in amplitude, Δ_p^2 the mean square phase error in radians, I_{mn} the current supplied to the mn_{th} antenna, and $S(\theta', \phi')$, the "obliquity factor" which is given by :

$$S(\theta',\phi') = cos\theta[cos^2\theta' \; cos^2\phi' + sin^2\phi'] \, . \tag{2.16}$$

It was found, from measurements on the VHF CoCo array, that Δ_p^2 is approximately 0.17 radians, and Δ_a^2 negligible compared to Δ_p^2. Also, for the CoCo array, I_{mn} may be replaced with $(B_m C_n)^{1/2}$. Thus 2.15 becomes :

$$\overline{G(\theta',\phi')} = G(\theta',\phi') + 0.17 \, S(\theta',\phi') \frac{\sum_{n=1}^{48}\sum_{m=1}^{32} B_m C_n}{\left[\sum_{n=1}^{48}\sum_{m=1}^{32} (B_m C_n)^{(1/2)}\right]^2} . \tag{2.17}$$

Note that in 2.15, the coordinates used are the off zenith angle and azimuth; to convert these to the θ, ϕ system used so far, 2.2 must be applied. It was found that in applying the random errors to the antenna pattern calculation, the sidelobes were elevated slightly (less

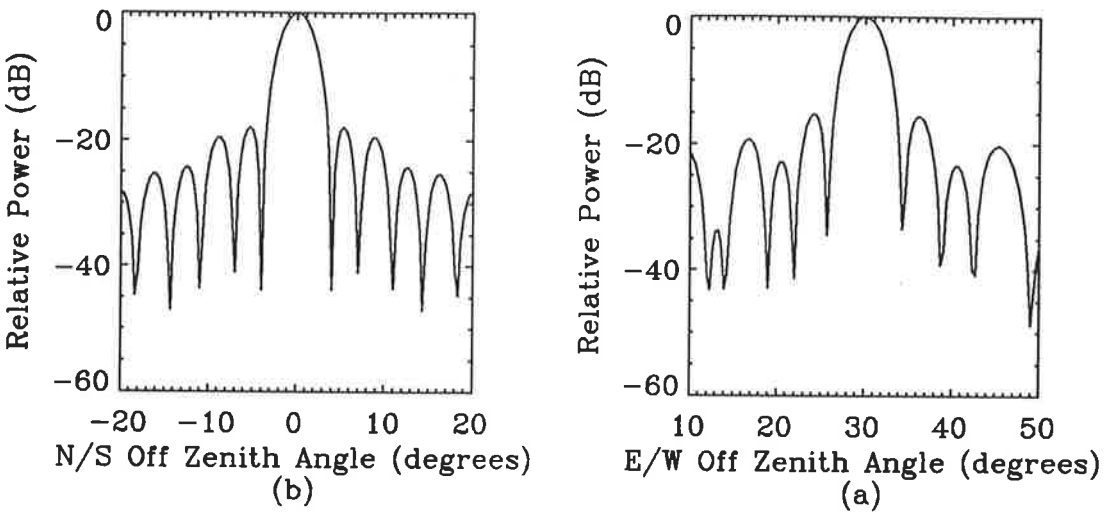

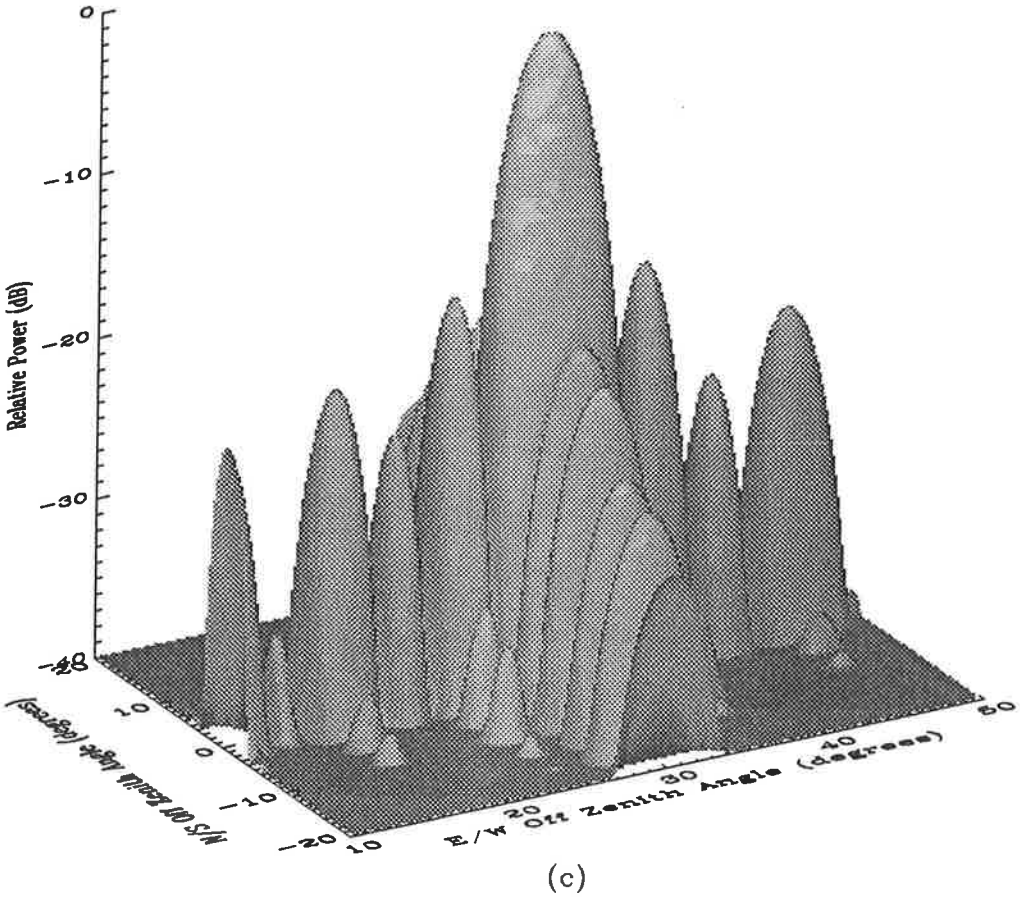

Figure 2.9: The one way antenna pattern of the VHF CoCo array for a 30° beam tilt Eastwards. Panels (a) and (b) show the cross-sections of the antenna pattern in the North/South and East/West planes respectively. The North/South half power half width is 1.7°, the East/West is 1.9°. See text for further details.

than $0.1\,dB$) and also smeared out to a small degree. The changes to the shape of the main beam were negligible.

For completeness the effect of an imperfect ground plane, consisting of only clay soil, on the antenna radiation pattern has been considered. The equations describing this may be found from *Kraus* (1988). It was found that the effects on the shape of the antenna pattern were negligible; however, there was a significant reduction in the gain of the array of almost $2.5\,dB$. As stated earlier, the ground plane comprised of copper wires spaced at intervals of $\lambda/12$. *Briggs* (private communication), showed that a such a ground plane has a complex reflection coefficient approaching that of a perfect ground plane. Thus the antenna pattern was modeled assuming a perfect ground plane.

The antenna pattern of the VHF CoCo array appears in Figure 2.9 for a beam tilt of 30° off zenith. This beam tilt was chosen as most of the meteor observations were performed with this configuration. The half power half width is 1.70° in the North/South plane through the main beam , and 1.88° in the East/West plane. The first set of sidelobes are suppressed by at least $15\,dB$ from the main beam. Figure 2.9 displays only the one way antenna pattern, *i.e.* the antenna pattern on either transmission or reception. The combined antenna pattern for transmission and reception with the CoCo array (two way antenna pattern) is, from the principle of pattern multiplication, the square of the one way antenna pattern. For the two way antenna pattern, the sidelobes are suppressed by at least $30\,dB$. The large sidelobe suppression and also the narrow beam, is important for meteor observations, so that there is as little ambiguity as possible in the position of the returned meteor echoes. To address this issue fully requires the development of the meteor radar response function (see Chapter 4).

The beam width was confirmed, in a somewhat unusual manner, from the amplitude response of a very rapidly decaying meteor which presented, in effect, a small moving-ball type target. From the analysis of the amplitude response of this echo (see Chapter 3), the two way half width of the radar was found to be 1.4° ± 0.2°. This corresponds to a one way half width of 2.0° ± 0.3°, which confirms the beam width as obtained from the model.

2.4 The transmitting system

The Buckland Park VHF transmitting system was upgraded in three stages during 1992 and 1993, from $4\,kW$ (rms envelope) to the design specification of $32\,kW$. There are 16 channels in all, each capable of supplying $2\,kW$ of power (rms envelope) to an East and West pair of

PRF (Hertz)
256
512
1024
2048
4028
8192

(a)

Pulse Width (μs) and Range resolution	
1.3	(0.20 km)
2.4	(0.36 km)
3.5	(0.53 km)
6.7	(1.01 km)
12.8	(1.92 km)

(b)

Table 2.2: Available pulse repetition frequencies (a) and pulse widths (b) of the VHF radar transmitting system.

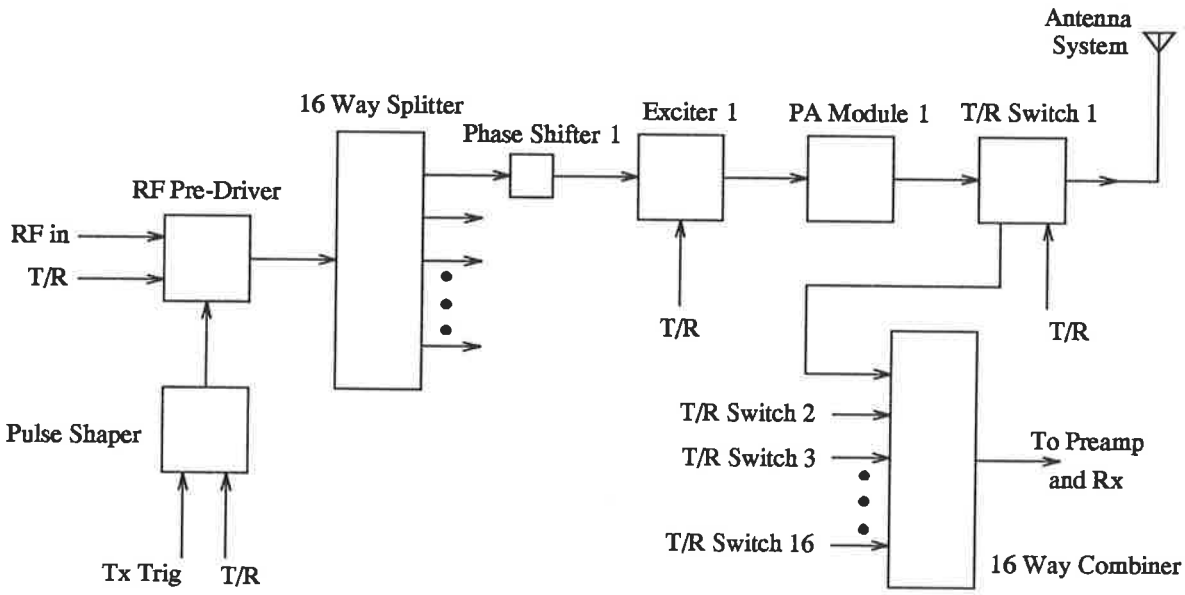

Figure 2.10: Schematic of the VHF transmitting system.

rows of the CoCo array. The pulse repetition frequency (PRF) and pulse width of the output power may be independently selected. The variable pulse width feature was only available from 1993, and formed part of the upgrade to the transmitting system. Previously a pulse width of 6.1 μs was only available. Table 2.2 lists the available values which may be selected for both parameters; all combinations of PRF and pulse width can be selected without any degradation in pulse power.

The transmitting system is modular in design, a single channel comprises a power amplifier (PA) module, exciter and a transmit/receive (T/R) switch. Figure 2.10 shows a schematic overview of the transmitting system. The exciter modules are driven by a single pre-driver via a 16 way splitter and phase shifters. The pre-driver produces bursts of RF

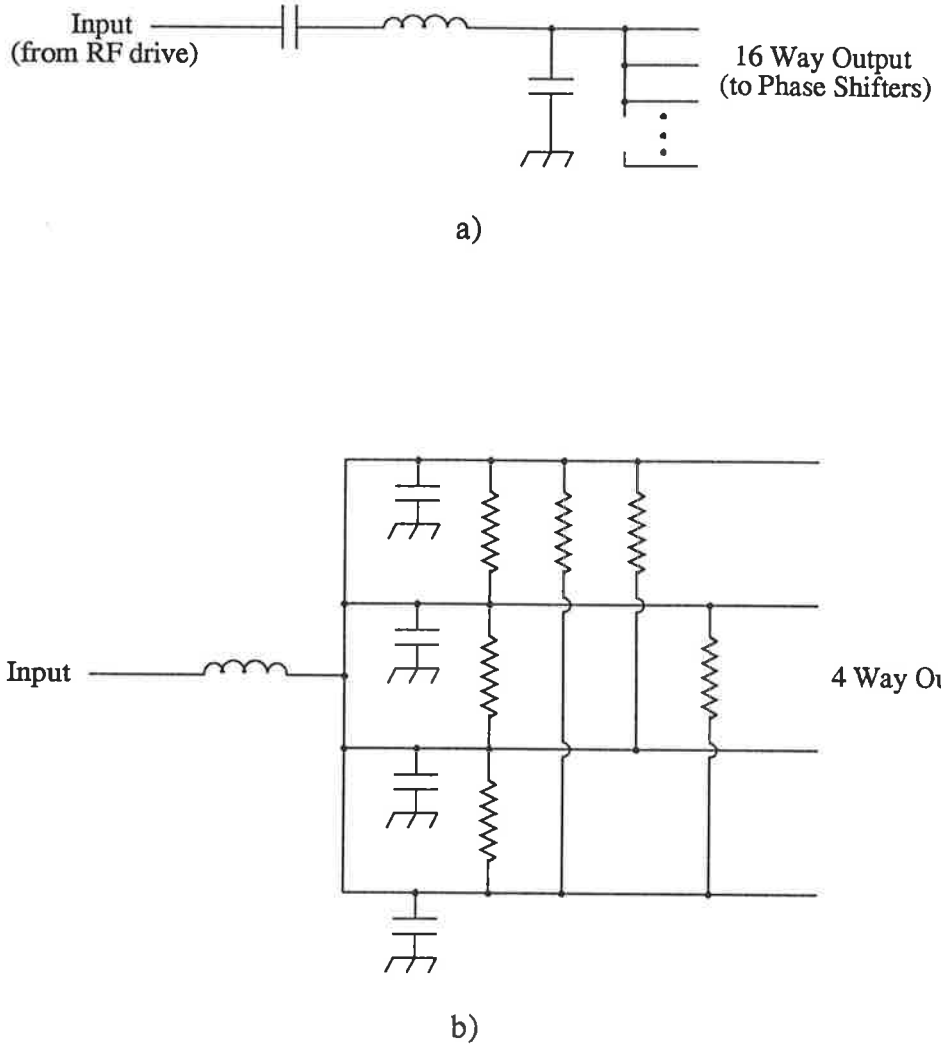

Figure 2.11: The top figure (a) shows the 16 way splitter that is used in the VHF transmitting system. The 4 way hybrid splitter in the bottom figure (b) is a suggested improvement. In practice, five 4 way hybrid splitters would be used to form a 16 way splitter. See text for further details.

with an envelope shape and width governed by a pulse shaper, and controlled by a microprocessor. The shape of the pulse is rectangular to increase power received per pulse. Each exciter module then further refines the pulse shape before being amplified in the PA modules. The phase shifters are a simple network of variable inductances and capacitances. These are used to shift the phase of the RF pulse input to the PA modules, the phase of each channel is appropriately shifted such that the signal is in phase with a phase reference. Usually the signal from channel 1 is used as the phase reference, although any channel would serve. Although the 16 way splitter performs the task of providing RF drive to the exciter modules adequately, its simple design (see Figure 2.11a) does lead to the following difficulties. If any of the outputs of the splitter has its impedance changed (*eg.* by changing the phase of the

signal via the phase shifters), then the impedance of the other outputs will also change by a small amount. This in turn changes the phase of the signal from these outputs and naturally means that the 16 transmitter channels are difficult to bring into phase. Generally what is required is to iterate around the 16 phase shifters manually, until a solution is achieved (usually 3 to 4 times is sufficient). Due to the interdependence of all the channels, any phase drift, or the failure, of a channel, would affect the phase of the others. The phase of the transmitter modules are checked regularly (2 to 3 months) to make sure no drift has occurred, and so far this has not been a problem. A better design for a 16 way splitter would be to use a hybrid splitter which has the property that each output channel is independent of the others. Thence phase aligning the transmitter channels would be a much easier task. Also maintaining the system once set up is much simpler and easier; phase drifts or the failure of any channel would leave the other channels unaffected. Figure 2.11b shows an example of a 4 way hybrid splitter, which can easily be extended directly to give a 16 way splitter, or used to drive four other hybrid splitters. The latter is probably the simpler.

The PA modules, as with the exciter modules, all use solid state technology which has only been available since the mid to late 1980's. Although these modules are reliable and compact, the transistors used are heat sensitive, failing at approximately $50° C$. With this in mind, it is necessary to have a sophisticated cooling system for the PA modules. The entire transmitter caravan is air conditioned. The PA modules are mounted in pairs, back to back, on an aluminium frame which is sealed by a cork gasket. In addition to the general cooling to the PA modules supplied by fans, water, cooled to the ambient air temperature in a large reservoir, is pumped between each pair of PA modules.

The PA modules are comprised of 6 sub-modules, each of which are able to supply $1/3\,kW$. The outputs of these sub-modules are combined through a 6 way combiner to give the output of the PA module. Again these 6 way combiners suffer the same flaw as the 16 way splitter, *i.e.* the outputs are not independent. If one sub-module should fail, the added stress on the other 5 increases the probability of one of these failing well. Also, the phase of the entire module would be affected. This of course could be alleviated by the use of 6 way hybrid combiners. Similarly 6 way hybrid splitters should be used on the inputs to the sub-modules. This is contemplated for future system upgrades.

The transmitting system requires 3 separate timing pulses to operate. These are: (1) the T/R pulse which determines whether the transmitter is on or off (radar in receive mode), (2) gate-tx which governs the length of the burst of RF to the transmitters, and (3) tx-trigger

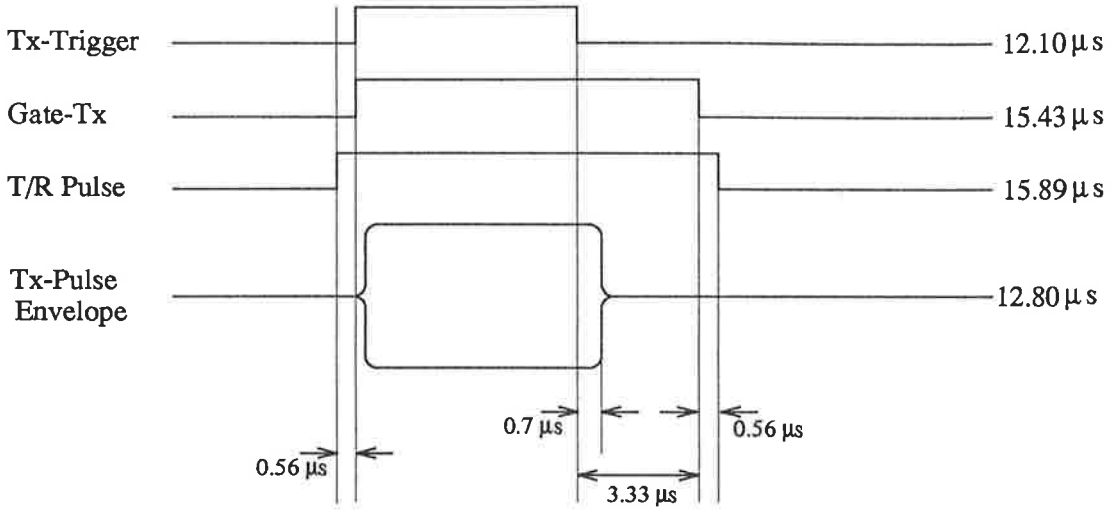

Figure 2.12: Transmitter control timing pulses. The duration of the transmitted pulse is about $0.7\,\mu s$ longer than tx-trigger. Gate-tx is $3.33\,\mu s$ longer than tx-trigger, and the T/R pulse starts $0.56\,\mu s$ before tx-trigger and finishes $0.56\,\mu s$ after gate-tx.

which governs the duration of the transmitted pulse. Figure 2.12 shows the relative timing and duration of these pulses required in the case of a $12.8\,\mu s$ transmitted pulse. The T/R pulse is used by the RF pre-driver, exciters and T/R switches. These are all switched off, or in the case of the T/R switches to receive mode, when the T/R pulse is low. It is of course necessary that the T/R pulse goes high before and stays high longer than the other two timing pulses. Gate-tx is used by the frequency synthesis unit to generate the RF drive, when it is low the RF drive to the transmitter is switched off. The pulse shaper then uses the tx-trigger to govern the width of the transmitted pulse. Finally, for all pulse selections, gate-tx is $3.33\,\mu s$ longer than tx-trigger and the T/R pulse starts $0.56\,\mu s$ before tx-trigger and finishes $0.56\,\mu s$ after gate-tx. The duration of the transmitted pulse is about $0.7\,\mu s$ longer than tx-trigger.

The T/R switches isolate the transmitting system from the receiving system. They employ state of the art solid state pin diodes to enable extremely fast switching (less than $1\,\mu s$). This is of prime importance for the investigation of the lower atmosphere boundary layer region, where very short duration pulses and hence high range resolutions are needed, although for meteor work this is not so important. The heart of the T/R switches are two pin diodes and an L/C network designed to resemble a $50\,\Omega$, $\lambda/4$ piece of coaxial cable (see figure 2.13). When the pin diodes, D1 and D2, are switched on (*i.e.* forward biased), they are able to conduct RF. Thus when tx-trig is high, the transmitter has a low resistance path to the antenna array, but the receiver and the $\lambda/4$ line are shorted to ground. The other end

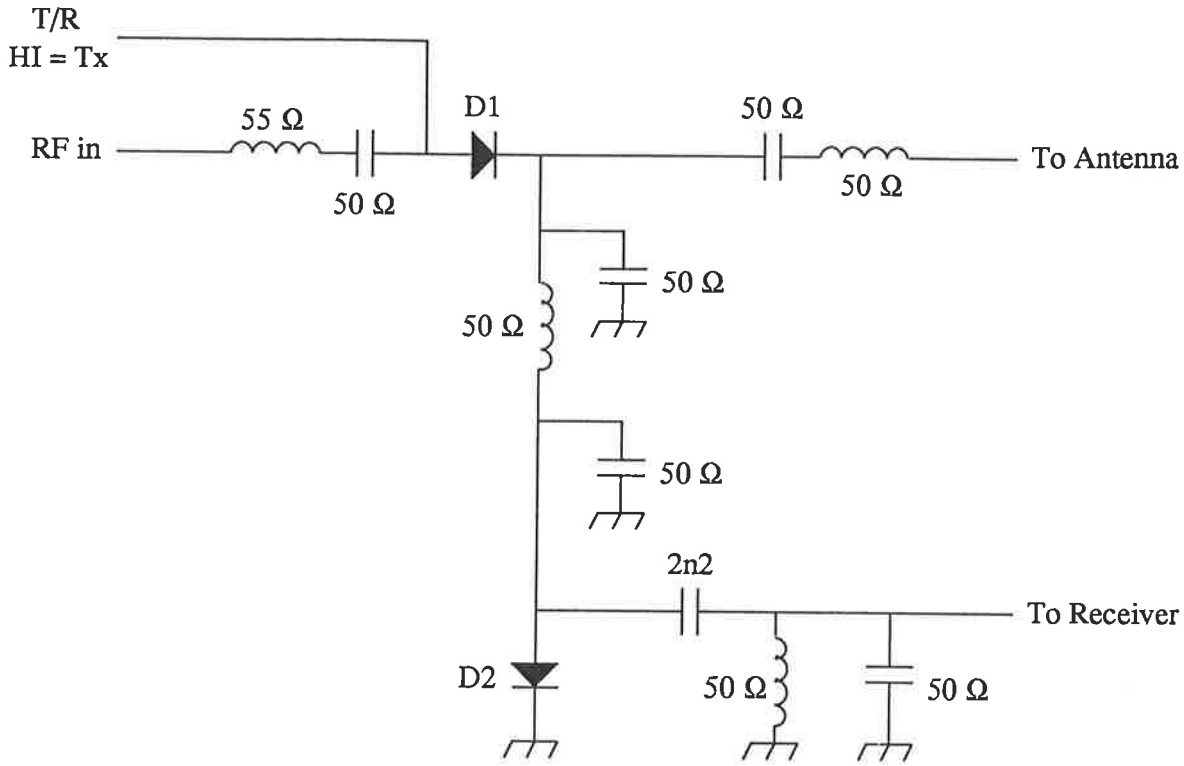

Figure 2.13: Circuit diagram of the T/R switches used in the VHF radar. For operational details, see text.

of the $\lambda/4$ line appears open to RF in this state. The receiver is therefore isolated from both the transmitter and antenna as required. When tx-trig is low, both pin diodes are biased off, thus the transmitter is now isolated and the $\lambda/4$ line is no longer grounded. In this case the receiver is connected to the antenna array as required.

It was discovered that there was a problem with the T/R switches. As the VHF CoCo array is situated in the near field of a 2 MHz transmitter (also operated by the Atmospheric Physics group), the 2 MHz transmitter pulse is picked up by the CoCo antennas. This should be filtered out by the bandpass filters of the receiving system, however the 2 MHz noise cross-modulates with the 54.1 MHz signal in the T/R switches. This produces 52 MHz and 56 MHz signals which are beyond the capabilities of the bandpass filters to remove. These signals are so strong that they actually saturate the receivers. The 2 MHz noise is manifest in the raw time series as a noise spike lasting for about 20 μs with a PRF of 80 Hz. These of course are the operational parameters of the 2 MHz transmitter. The 2 MHz noise is not a problem for lower atmospheric work as much coherent averaging of the data is performed. However, for meteor work, no coherent averaging is performed as the meteor echoes are of short duration. The 2 MHz noise then causes significant interference and so the problem was required to be

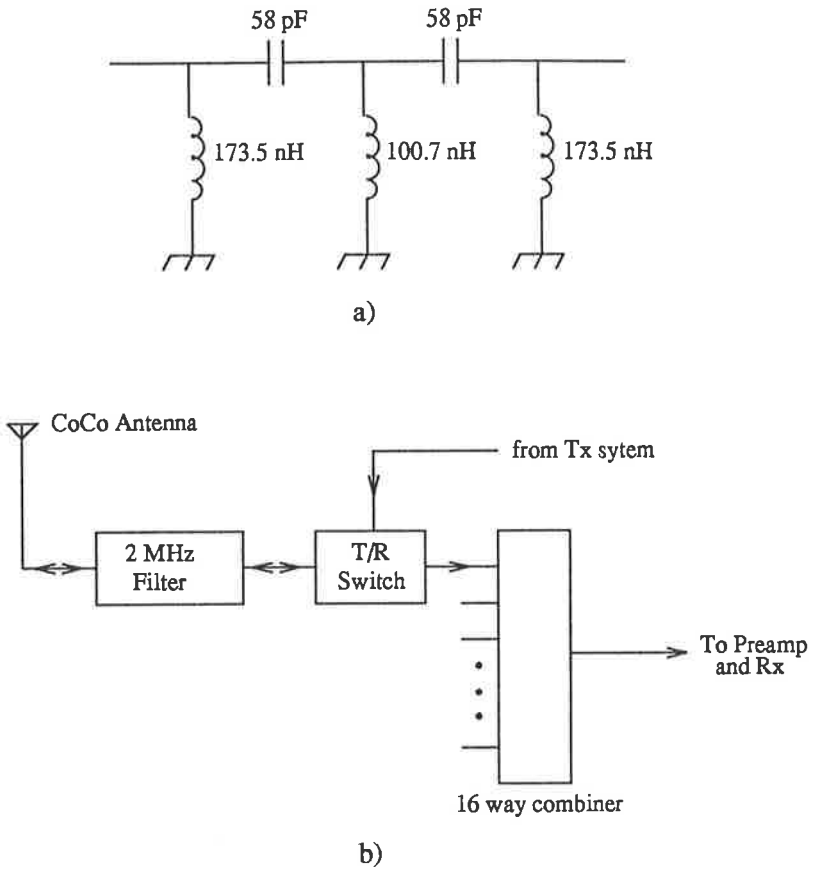

Figure 2.14: Circuit diagram of one of the 2 MHz filters, a, and where it is situated in the Rx/Tx system, b.

addressed. The simplest solution was to build 16 high pass filters and place these directly on the feeders to the CoCo antennas. Each filter is a 5 pole high pass π filter and is required to handle the 2 kW of power supplied by each transmitter module. The circuit diagram for these filters is shown in Figure 2.14. The filters attenuate 2 MHz signals by about 50 dB, while 54 MHz signals are attenuated by a factor of about 1%.

2.5 The receiving and data acquisition system

The Buckland Park VHF receiving and data acquisition system comprises 3 receiving channels, each with in-phase and in-quadrature outputs, and 6 digitizing channels and 6 coherent averagers. The three receiving channels are required for the original operational design specification of the radar, *i.e.* studies of the troposphere. Data are transferred via direct memory access (DMA) to an IBM compatible PC for analysis and storage. The usual operation of the radar is in one of two modes:

- Doppler Mode: Receiver 0 (Rx0) connected to the CoCo array, Rx1 and Rx2 are not used. The radar in this mode is used for either tropospheric research (vertical beam) or meteor observations (East or West pointing beam). A bank of 16 T/R switches are used to isolate Rx0 from the transmitter.

- Spaced antenna mode: Rx0, Rx1 and Rx2 are each connected to one of the spaced yagi arrays. Transmission is on the CoCo array with a vertical beam. This mode is used to study tropospheric winds using Full Correlation Analysis (*Briggs*, 1984) of spaced antenna data.

Figure 2.15 shows a block diagram of the receiving and data acquisition system.

A frequency synthesis unit generates 54.1, 44.1, 10 and 9 MHz signals necessary for the operation of the radar, from a 40 MHz master oscillator. The 54.1 MHz signal is only produced when the tx-gate is high and provides the RF drive required by the transmitting system (see Section 2.4). The 44.1 and 10 MHz signals are used by the receivers to produce the intermediate frequency (IF) signal and detected output respectively. The 9 MHz signal is used by the digitizing system, averagers and the system clock for timing. It is important for all of the generated signals to remain phase locked.

During the 1993 refurbishment of the receiving system it was found that the master oscillator had drifted from its specified frequency to the extent that one of the phase locked loops (PLL) of the frequency synthesis unit was unable to remain in lock. This had the effect of the 44.1 MHz signal drifting over a range of some 3 kHz thus degrading the performance of receivers significantly. The source of the problem was the crystal of the master oscillator which was found to have degraded in performance due to overheating in a temperature controlled oven designed to prevent drift due to temperature fluctuations. When the master oscillator crystal was replaced, it was found that the oven was too unreliable. Finally, it was decided to replace the master oscillator with a commercial version. These are relatively inexpensive, extremely reliable and operate over a wide temperature range ($-10°\,C$ to $50°\,C$) thus negating the need for a temperature control oven. The new master oscillator is accurate to 10 Hz at 40 MHz.

Each receiver can be connected to either the CoCo array or to one of the Yagi arrays via a pre-amplifier. The pre-amplifiers all have a have a gain of approximately 20 dB and a bandwidth of about 1.5 MHz. The output signal level of a preamp due to background cosmic noise from the CoCo array is approximately 350 μV. The noise temperature of the

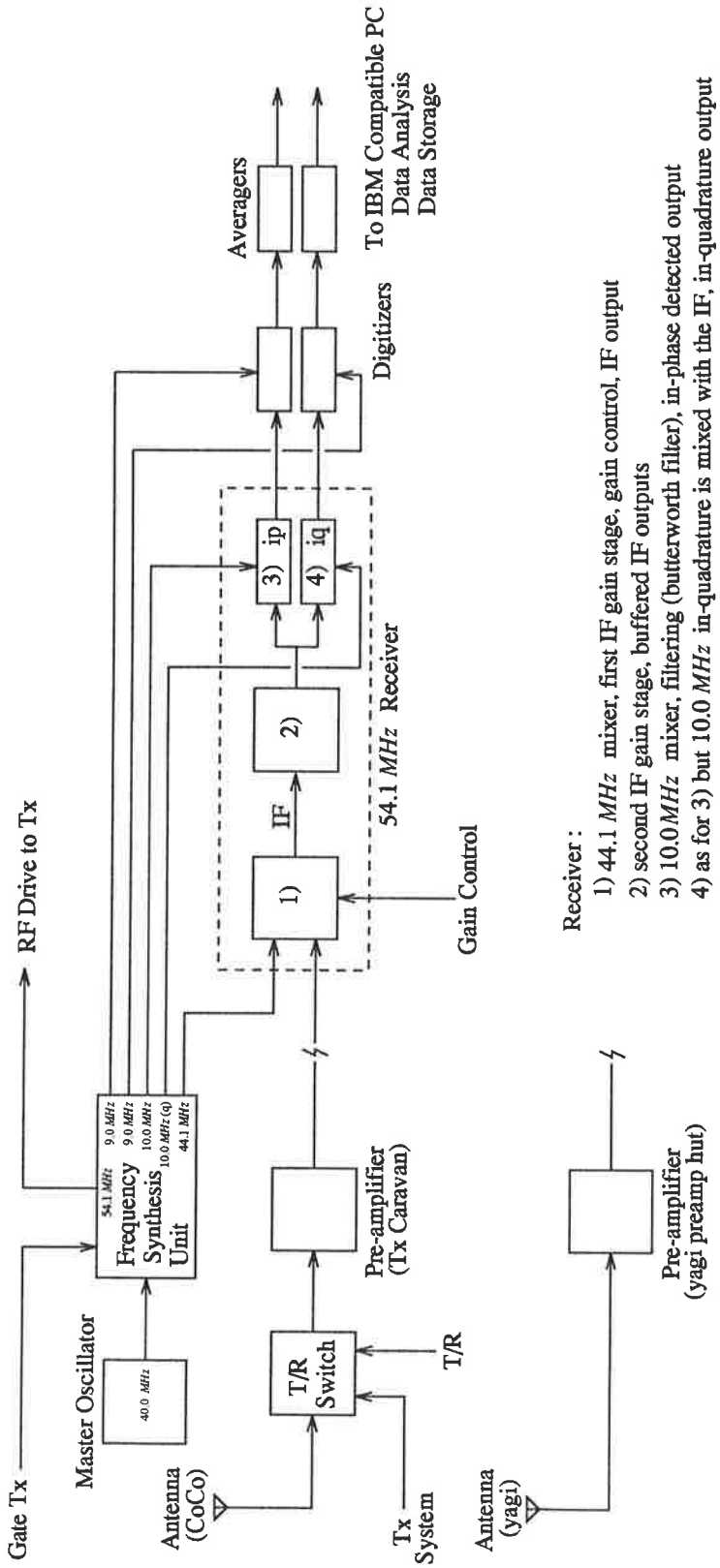

Figure 2.15: Schematic overview of the Buckland Park receiving and data acquisition system. Note this shows a single channel only, which can be connected to either the CoCo array or one of the spaced antenna yagi arrays. For further details, see text.

receivers is low, being about 400 K which is much less than the equivilent temperature of the background cosmic noise. The signal from the preamp is first mixed with a 44.1 MHz sine wave. This produces the 10 MHz IF signal which is then amplified in two stages. The first stage is a low gain amplifier with manual gain control. The second IF amplifier saturates at a level of $\pm 5\,V$ which limits the level of amplification. The level at which the gain is set, depends upon the experiment being performed. Weak atmospheric returns need a higher level of amplification than the much stronger specular echoes of meteors. Meteor echoes have a large range of returned echo powers, thus the receiving system is required to have a large dynamic range, and for most of the meteor work with the VHF radar a dynamic range of about 70 was used. This corresponded to a receiver gain of approximately 38 dB (*c.f.* 45 dB for Doppler tropospheric work). The IF signal, after it is amplified to the appropriate level, is then buffered to give two outputs. These are mixed with 10 MHz sine and cosine signals to give the in-phase and in-quadrature signals respectively. These two signals are filtered and buffered to give the in-phase and in-quadrature detected outputs. The filters used are butterworth filters with a $3dB$ cutoff of 75 kHz. This corresponds to an RF bandwidth of 150 kHz for the receiver, which is matched to a transmitted pulse width of 6.67 μs.

The digitizers used by the original data acquisition system are 10 bit, thus rendering the raw data to a digitized range of 0 - 1023. The averagers are controlled by a microcomputer and 16, 32, 64, 128 or 256 pulse coherent averaging can be selected to be performed on the digitized data. The possibility of using 2, 4 or 6 point coherent averaging was not built into the system as it was considered that these would not be useful for atmospheric experiments. Before any coherent averaging is performed, every second data record is phase inverted in order to complement the phase inversion of every second pulse on transmission. This process, known as instrumental-dc elimination (*Röttger*, 1984), removes any systematic instrumental interference signal introduced to the data. Of course any random noise introduced to the data in the receiving process is not removed.

2.6 The new meteor data acquisition system

The data acquisition system, described in Section 2.5 and which was used for preliminary meteor research with the VHF system, had significant limitations for extensive meteor research. In particular, the least amount of coherent averaging that was possible with the original data acquisition system was 16 point. This limited the time resolution of meteor

data to 15.6 ms for a PRF of 1024 Hz. The limitation was overcome by the development of a new meteor data acquisition system throughout late 1992 and the first half of 1993; the new system was in its final operational form by September 1993 (barring ongoing minor modifications to software).

Meteor echoes are generally short lived events usually lasting for less than 100 ms and many have life times of the order of 10 ms at VHF. On the other hand, there are occasional long enduring meteor echoes lasting up to 2000 ms, but these will not discussed here, (see Chapter 3). Assuming all meteor echoes are short duration events, it is necessary to have data acquisition and analysis systems that are capable of collecting and processing data with a time resolution appropriate to the shortest duration echo. With this in mind, the VHF radar is operated at the highest possible PRF that will give unambiguous meteor echoes. Within the choice available, the PRF is 1024 Hz. As a beam tilt of 30° is normally used for meteor observations, a PRF of 1024 Hz allows unambiguous sampling up to a height of 127 km (range of 146 km). This height limit is appropriate for most meteor experiments with the VHF radar, since at these frequencies, meteor echoes generally occur from trails at heights between 70 and 110 km, with relatively few echoes above 100 km. Clearly then, it was desirable not to perform any coherent averaging of raw meteor data.

The option of modifying the existing data acquisition system to remove coherent averaging when the radar was operating in a meteor observation mode, would have required very significant modifications to the system. Thus, it was decided to increase the flexibility of the system by developing a new entirely separate data acquisition system that could be used exclusively for meteor observations. Other reasons for the development of a separate meteor data acquisition system were simplicity and cost. Also, a new interface card would have been required to cope with the greater data throughput to the computer for analysis and data storage, further increasing the complexity and cost of implementing this option.

Considering that PC's based on the 80486 microprocessor are able to process large amounts of data very rapidly and are easy to interface to equipment, the new data acquisition system was realised by the use of a commercial A/D card with an 80486 PC. The A/D card, which is designed for use with PC's, fits simply in one of the 16 bit expansion slots of a PC's external expansion bus. Necessary features of a suitable A/D card are:

- The ability to digitize at least 2 channels.
- The A/D conversions for each channel to be performed at a rate of at least 75000 Hz,

corresponding to a range resolution of $2\,km$.

- The ability to be triggered externally.
- Two control ports which can be configured to output or input modes. These are required for control of the triggering of the A/D conversions (see text for further details).

Figure 2.16 shows a schematic overview of the new meteor data acquisition system. The new A/D card was supplied by Boston Technologies. It is capable of digitizing 4 channels at a combined A/D conversion rate of $200\,kHz$ ($100\,kHz$ per channel if 2 channels are used). Triggering for A/D conversions was supplied by the samples port of the controller rack of the VHF radar data acquisition system. The samples port produces a high TTL level whenever the VHF radar digitizers sample the raw data. At the present time, the samples are limited to a maximum range of $128\,km$ (height of $110\,km$ for a beam tilt of 30°) due to hardware limitations of the earlier data acquisition system. As triggering of the A/D card required CMOS levels, suitable buffering was necessary. The A/D card also has three 8 bit ports which can be designated as output or input. One of these was used for the control of the start of the triggering to the A/D card. The other two ports could be used for control of additional experimental equipment if necessary. The four-channel digital to analogue converter, also supplied on the A/D card, is not used.

The operation of the new system initially requires the radar to be setup to the correct configuration (beam tilt, PRF and data sampling). This is carried out by using the PC to program the radar controller appropriately via the interface system. Once this is done the operation of the new meteor data acquisition system is totally self contained. The only time the radar controller needs to be reconfigured is either after a power failure (done automatically) or if a meteor experiment involving beam swinging was performed. For the latter case, the radar controller would be reconfigured after a certain number of preset data runs with a given beam direction, were completed. This would be performed by a controlling batch file program from the PC DOS.

The operation of the new meteor data acquisition system is as follows. First DMA is initialized and the A/D converter setup such that each A/D strobe produces two simultaneous A/D conversions. This is necessary so that two channels, *viz.* the in-phase and in-quadrature receiver outputs, are digitized simultaneously. Once the initial setup has been performed, bit 0 of port A is taken high. This arms the trigger control, and blanks out the samples line to

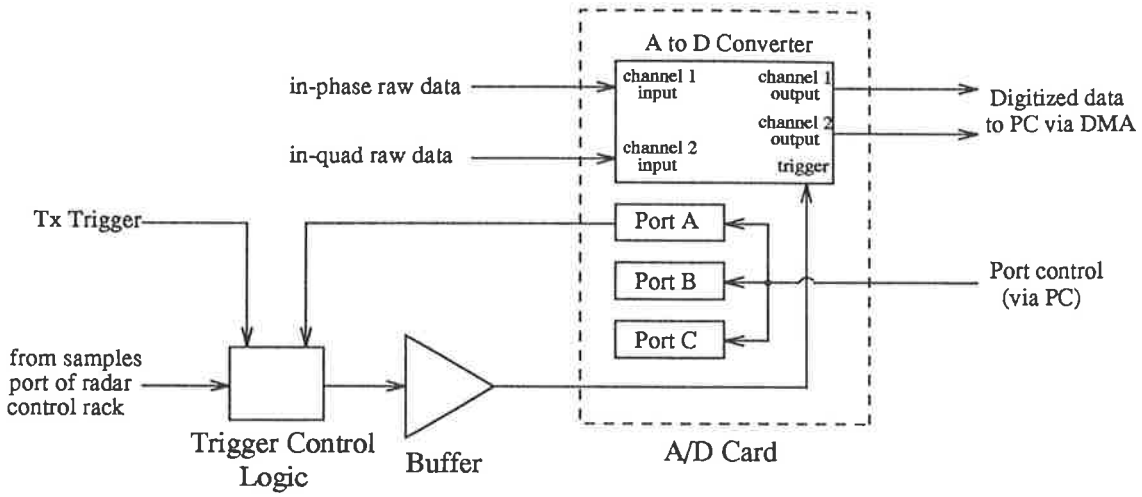

Figure 2.16: Schematic overview of the new meteor data acquisition system hardware. Not shown, for the A/D card, are the other two digitizing channels and the four D/A channels as these are not used. For a description and details of operation, see text.

the A/D card so no strobing of the A/D converter is available. Gap free dual DMA[1] to the PC's extented memory is then started, however the A/D card "waits" until the A/D card is strobed. Bit 0 of port A is then taken low, the trigger controller remains off until a tx-trigger pulse (which occurs when the radar transmits a pulse of RF) is received, it then latches on and the A/D card is strobed whenever the samples line goes high. The trigger control is important so that the strobing of the A/D card occurs at the correct time. Figure 2.17 shows the timing of the samples with respect to the transmitter pulse, and one can see that the duration over which the samples occurs is approximately 1/3 that of the total time between transmitted pulses. Starting the A/D conversions at any time will then have about a 30% chance of occurring between the first and last sample pulse. This means that there is a 30% chance per data run of the height information of the returned echoes being ambiguous. The trigger control forces the A/D strobes to start at the first sample pulse and thus alleviates the above problem.

Figure 2.18 shows the circuit diagram of the trigger control. The nand gates used are from the HCT series of CMOS devices. These are able to accept TTL levels for their inputs and produce CMOS level outputs, thus giving the required buffering to the A/D card. The heart of the trigger controller is a type D CMOS flip-flop. The preset and data inputs of

[1]Gap free dual DMA refers to the mode of DMA used. The number of samples which can be acquired in a single block is limited by PC hardware to 32768. As about 50000 samples are required to be transferred per second, a single channel DMA is not sufficient for a reasonable length data set. Gap free dual DMA is then simply two DMA channels which are instantly switched by a DMA controller when one has finished transferring data, thus enabling large amounts of data to be transferred.

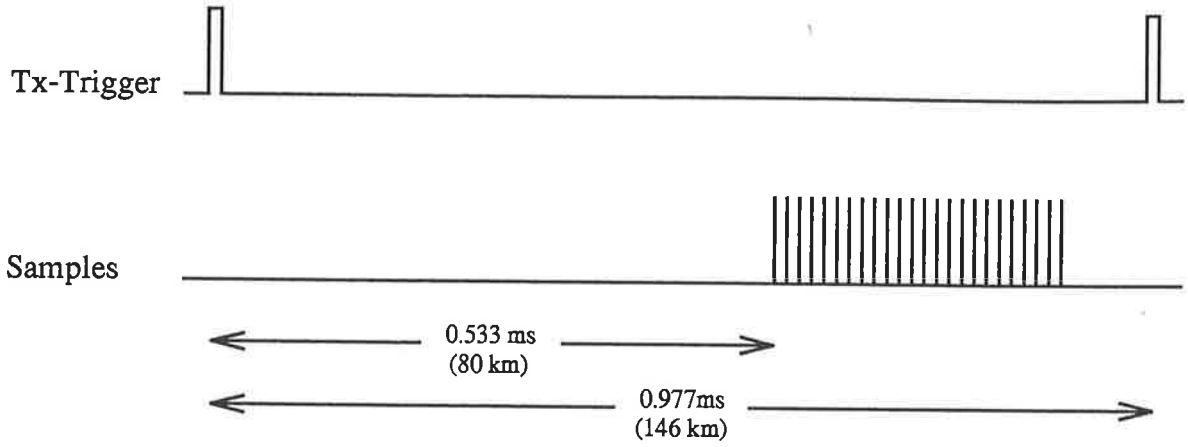

Figure 2.17: Timing of the samples with respect to the transmitted pulse (pulse width of $12.80\,\mu\,s$) for a PRF of $1024\,Hz$. The time interval between each sample is $13.33\,\mu s$ (or $2\,km$ in range). The samples are not available to strobe the A/D card until the trigger control has been armed.

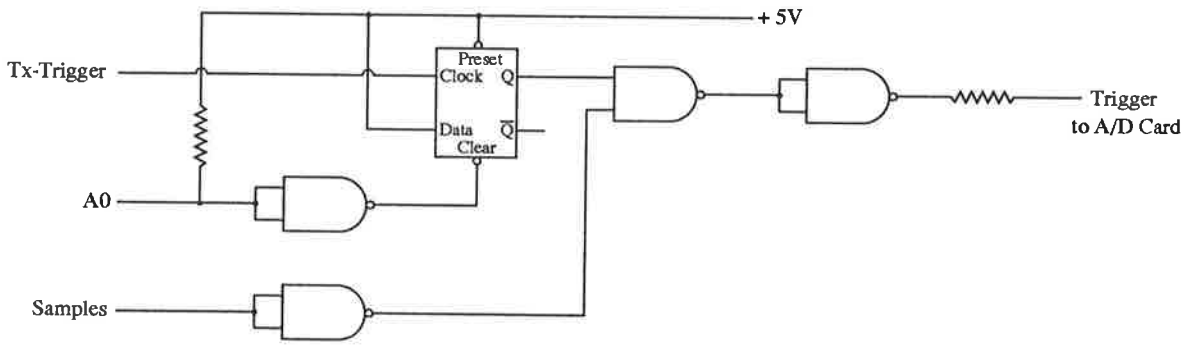

Figure 2.18: Circuit diagram of the trigger control for the A/D card. The logic gates accept TTL inputs and produce CMOS level outputs to give the required buffering to the A/D card. The flip-flop is a CMOS type D flip-flop. See text for details on operation.

the flip-flop are held high, thus control to the flip-flop is only available via the clear and clock inputs. When clear is low, the output of the flip-flop is also low, however when clear goes high, the output goes high when the clock receives a high pulse. Bit 0 of port A of the A/D card is connected to the clear input via an inverter. Thus when A0 is taken high, the samples line is masked out from the A/D card trigger by a nand gate. When A0 is then taken low, the output of the flip-flop goes high as soon as the clock receives a high pulse from the tx-trigger, and remains high until A0 is again taken high at the start of the next data run. The trigger to the A/D card is then supplied whenever the sample line goes high as required.

As stated previously, the raw data once digitized, is transferred to the extended memory

of the PC via DMA. Typically 16 seconds of data are collected and transferred. This corresponds to 786,432 data points or 1,572,864 bytes of data (each datum is a 2 byte integer). The above data set is formed from in-phase and in-quadrature information from 24 heights ($80\,km$ to $128\,km$) over the 16 seconds at a PRF of $1024\,Hz$. The data once collected, is then transferred in 49152 byte blocks to conventional memory of the PC for meteor detection and analysis. The size of the block transferred is convenient as this corresponds to 0.5 seconds of data for all 24 heights. A larger block cannot be transferred as there is a 65536 byte limit to the size of the block of data. The meteor detection and analysis procedures will not be discused here (see Section 3.3.4), except to say that with a 486DX microprocessor running at 66 MHz, generally 2 seconds are required to do this. Once the meteor detection and analysis routines are complete, the extended memory of the PC is released from control by the A/D card and another 16 seconds of data are collected.

Chapter 3

Preliminary Meteor Observations and Fundamental Theory

The only genuine philosophy that I have been able to expound,
Is that the world is not a stage but a primary school playground.

—Leo's Toltoy, T.I.S.M.

3.1 Introduction

This chapter is concerned with the preliminary observations of meteors with the Buckland park VHF radar. Firstly, theory which is fundamental to meteoric phenomena will be described. A short discussion of the effect of thermal conduction, radiation, and heat capacity on the ablation process and how this modifies the classical ablation theory described in Chapter 4, will be followed by discussions on basic Fresnel diffraction theory, underdense and overdense trails, the effects of initial trail radius and diffusion, and finally the radio wave scattering process.

The meteor detection algorithm will be detailed along with a discussion of the effects of coherent averaging on the raw data, echo rates and the sensitivity of the system. The radar employs a high gain narrow beam antenna array, this together with the use of high PRF's gives the radar considerable advantages over the wide beam systems used in the past.

Examples of various meteor echoes observed by the radar will be displayed including those displaying typical underdense and overdense characteristics, echoes which are affected by receiver saturation and "beating" echoes. The effects of noise and receiver saturation on

the meteor echoes, and in particular the phase, will be discussed.

3.2 Fundamental Meteor Theory

3.2.1 Ablation theory: The effect of thermal conduction, radiation and heat capacity.

Classical ablation theory (described later in Chapter 4) neglects the effects of thermal conduction, radiation and heat capacity on the ablation process. Before the meteoroid begins to ablate, it must first acquire enough energy to raise the temperature to its boiling point. Prior to this temperature being reached, the kinetic energy it loses due to collisions with atmospheric molecules goes into heating the meteoroid and radiation. Thus, we may write the following (see *e.g. Hughes*, 1978)

$$\frac{1}{2}\Lambda\rho_a V^3 \pi r^2 = 4\pi r^2 \epsilon\sigma(T_s^4 - T_e^4) + \frac{4}{3}\pi r^3 \rho_m c \frac{dT_m}{dt}\,, \tag{3.1}$$

where r, ρ and V are respectively the meteoroid radius, density and velocity; T_s, T_m and T_e are the surface temperature, mean temperature and environmental temperature respectively; c and ϵ are the specific heat and emissivity of the meteoroid; σ is Stefan's constant and ρ_a is the density of the atmosphere.

The above equation may be used to investigate the starting height of ablation for meteoroids of various sizes, compositions and speeds (*Jones and Kaiser*, 1966). This is shown in Figure 3.1 for a stony meteoroid which has been reproduced from *Jones and Kaiser's* work. *Kaiser and Jones* (1968) and *Jones and Kaiser* (1966) identify four critical values for the meteoroid radius: R_1, R_2, R_3 and R_4, which appear in Figure 3.1. For radii less than R_2, the thermal capacity term in Equation 3.1 may be neglected, and the heating process is dominated by the radiative term. This delays the onset of ablation due to heat loss. If the meteoroid radius is small enough, deceleration becomes important. The reduction in the speed further delays the onset of ablation; we define R_1 such that for $r < R_1$ the meteoroid does not ablate at all. This is the micro-meteoroid limit. Most meteors detected by the Buckland Park radar lie on the flat portion of the curve (of a given speed) between the R_1 and R_2 limits.

If the meteoroid radius lies between R_2 and R_3, then the thermal capacity term becomes important and radiative effects may be neglected. In this case the onset of ablation is delayed due to finite heat capacity of the meteoroid. Meteoroids with radii greater than R_3 develop

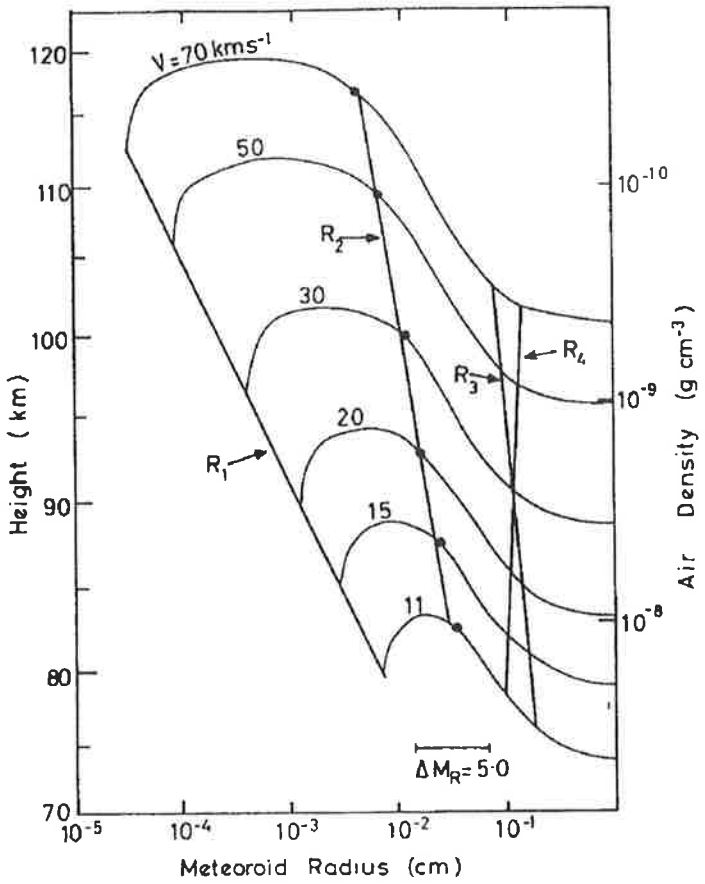

Figure 3.1: Theoretical values of air density and altitude at the commencement of evaporation of a stony meteoroid as a function of radius The solid circles denote the size of a meteoroid that produces a +10.0 magnitude radio meteor (after *Hughes, 1978*).

a thermal gradient which may be enough to cause fragmentation of the meteoroid. However, it is observed that meteors brighter than magnitude +10 do not commence at the heights given in given in Figure 3.1 where the expected altitude of commencement falls away with increasing mass. Rather the altitude of commencement is similar to that for meteors fainter than magnitude +10, the reason being attributed to the continuous fragmentation of the meteoroid (*Hawkes and Jones*, 1975b).

The inclusion of radiation and heat capacity not only delays the onset of ablation, but also causes the height of maximum ionization (or luminosity) to occur lower down and to have a greater value than given by the classical ablation theory. If $\rho_{a(max)}$ is the density of the atmosphere at maximum ionization as given by classical ablation theory, then the new density of maximum ionization ρ_{max} is given by (*Hughes*, 1978)

$$\rho_{max} = \rho_{a(max)}(1 + \gamma/3)\,, \tag{3.2}$$

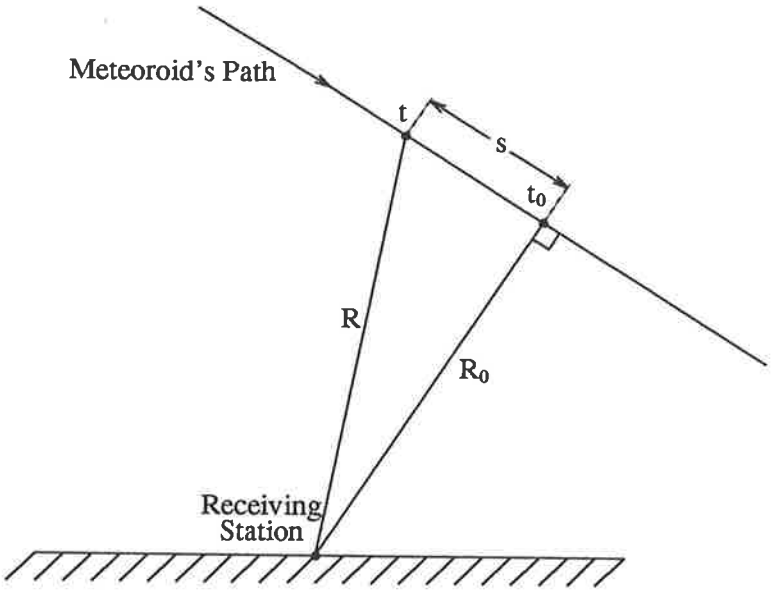

Figure 3.2: The geometry of a meteoroid's path through the Earth's atmosphere with respect to an observing station.

where γ is

$$\gamma = c(T_b - T_e)/\zeta \approx 0.35\,, \tag{3.3}$$

and T_b is the boiling point of the meteoric material. The maximum ionization is larger by a factor $(1+\gamma/3)^3$ or about 40%. In effect the meteor trail has a finite length (instead of starting at infinity) and is slightly more intense or brighter. In addition the peak ionization occurs about 0.5 km lower than that predicted by classical theory. Typically for meteors of magnitude +10 to +15, the beginning and end heights differ by about 10 km.

3.2.2 The basic Fresnel theory of radar backscatter from meteors

Consider the idealized case of a meteor trail where the diameter of the trail is small in comparison with the wavelength and the diffusion of the trail is negligible. In addition, it is assumed that the trail is underdense, *i.e.* the incident radio waves are scattered by individual electrons, and secondary radiative and absorptive effects may be neglected. The geometry of the situation is displayed in Figure 3.2. The flux of power incident on the trail is $\Phi_i = P_T G_T/4\pi R^2$, where P_T is the transmitted power, G_T is the antenna gain relative to an isotropic radiator and R is the range to the trail. The scattering cross-section of a free electron is $\sigma_e = 4\pi r_e^2 sin^2(\gamma)$, where r_e is the classical radius of an electron and γ is the scattering angle. For the case of backscatter, $\gamma = \pi/2$, $\sigma_e \approx 1 \times 10^{-28}\, m^2$ and the flux of power appearing at the receiving antenna is $\Phi_i \sigma_e/4\pi R^2$. The effective absorbing area of the

receiving antenna is $G_R\lambda^2/4\pi$, where G_R is the gain of the receiving antenna gain relative to an isotropic radiator. Thus the power of the backscattered signal appearing at the input of the receiver due to a single electron is given by:

$$P_e = \frac{P_T G_T G_R \lambda^2 \sigma_e}{64\pi^3 R^4} \,. \tag{3.4}$$

Consider a small segment of the trail, ds. If q is the electron line density of the trail segment and Z_0 is the wave impedance of free space, then as the assumption has been made that trail diameter is much smaller than the wavelength of the incident radio waves, the maximum possible amplitude of the returned electric field from the segment of trail is $(2Z_0P_e)^{1/2}q\,ds$. The distance the received wave has travelled is $2R$, therefore the received electric field is modulated by the expression $e^{i4\pi R/\lambda}$. The optical convention of describing phase, in which the *phase angle* increases with with the path length, has been used. Alternatively, one may use the electrical engineering convention where all phases are regarded at an instant in time. In this case, the *phase lag* increases with path length and the modulation factor is $e^{-i4\pi R/\lambda}$. The choice of convention doesn't matter as long as one is consistent.

The electric field phasor amplitude received from the electrons in a segment ds of the trail is:

$$dE_R = (2Z_0P_e)^{1/2} q e^{i4\pi R/\lambda} ds \,, \tag{3.5}$$

which upon integration from $-\infty$ to a point s along the meteoroid's path, yields the total received electric field at the time when the meteoroid has reached point distance s from the t_0 point, *i.e.*

$$E_R(s) = (2Z_0P_e)^{1/2} q \int_{-\infty}^{s} e^{i4\pi R/\lambda} ds \,, \tag{3.6}$$

where the assumption has been made that the electron line density of the trail is constant. The integral may be made more tractable by using the approximation $R \approx R_0 + s^2/2R_0$. For a trail length $s = 10\,km$, and a range $R_0 = 100\,km$, the error is about 0.001%. Thus,

$$E_R(s) = (2Z_0P_e)^{1/2} q e^{i4\pi R_0/\lambda} \int_{-\infty}^{s} e^{i2\pi s^2/(R_0\lambda)} ds \,. \tag{3.7}$$

The transformation $x = 2s/\sqrt{R_0\lambda}$ is employed to obtain:

$$E_R(x) = (2Z_0P_e)^{1/2} q e^{i4\pi R_0/\lambda} \frac{\sqrt{R_0\lambda}}{2} \int_{-\infty}^{x} e^{i\pi x^2/2} dx \,, \tag{3.8}$$

which may be recast to give:

$$E_R(x) = (2Z_0P_e)^{1/2} q e^{i4\pi R_0/\lambda} \frac{\sqrt{R_0\lambda}}{2} (C + iS) \,, \tag{3.9}$$

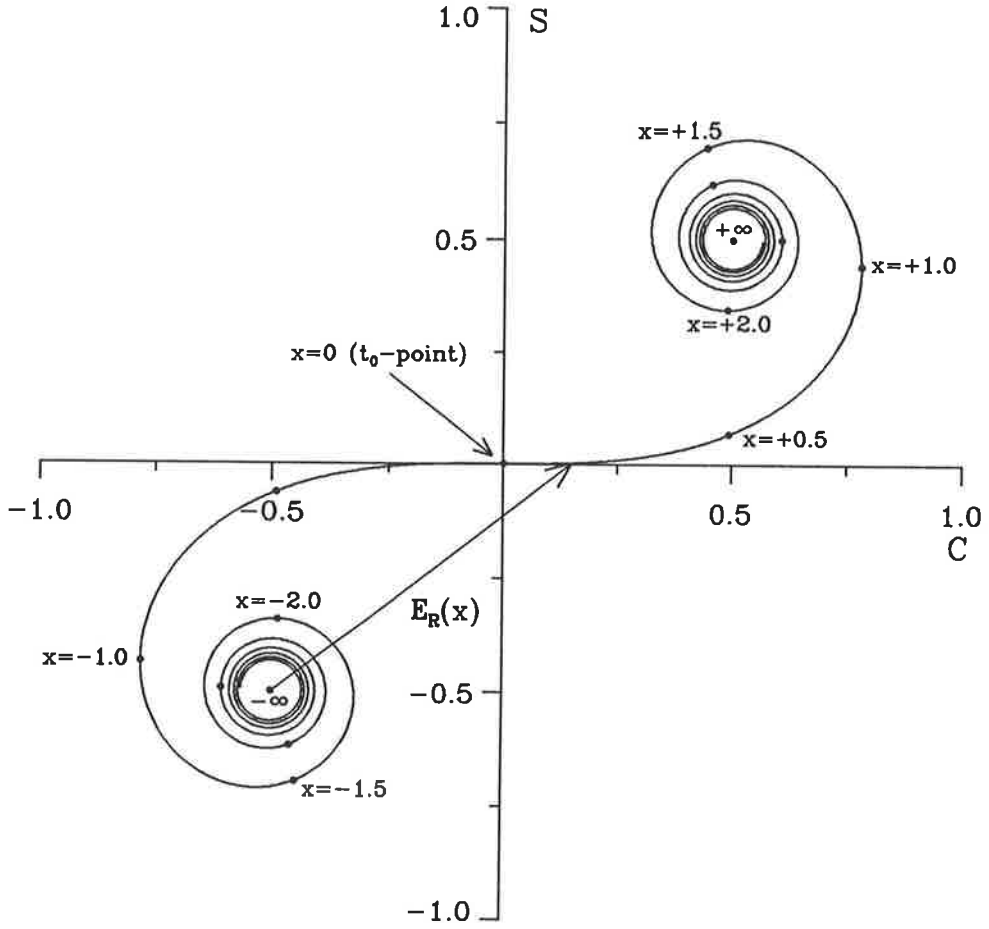

Figure 3.3: The Cornu spiral of Fresnel diffraction theory. The curve is formed from the locus of the time varying electric field phasor of the meteor echo (assuming no decay), whose origin is at $x = -\infty$. Values of x from -3.0 to +3.0 have been noted on the curve (solid circles). In this diagram, the displayed electric field phasor $E_R(x)$ has been normalised such that its final amplitude is equal to $\sqrt{2}$. Note, the origin has been shifted to the point $(-1/2 - i/2)$.

where

$$C = \int_{-\infty}^{x} cos\left(\frac{\pi x^2}{2}\right) dx \quad \text{and} \quad S = \int_{-\infty}^{x} sin\left(\frac{\pi x^2}{2}\right) dx \,, \tag{3.10}$$

and are the Fresnel integrals of diffraction theory. The normalised variable x, is often referred to as the Fresnel length.

In Figure 3.3, S and C have been plotted orthogonally resulting in the familiar Cornu spiral of Fresnel diffraction theory[1]. Values of the normalised x parameter are indicated along the Cornu spiral. The origin of the meteor echo is held at the centre of the lower spiral ($x = -\infty$). As the electric field phasor traces out the lower spiral, the amplitude of

[1]Note, if the electrical engineering convention of the definition of phase angle had been adopted, the resulting Cornu spiral would be reflected in the S axis (see *eg. Gartrell*, 1971).

the returned signal increase continuously while the phase angle decreases. The amplitude reaches its maximum value as the meteor crosses the first Fresnel zone past the t_0-point, which occurs at $x = +1.21$. Past this point, the amplitude oscillates (with decreasing magnitude and increasing frequency) about its final (at $x = +\infty$) value as the electric field phasor traces out the upper spiral. A similar situation applys for the phase, a minimum value is reached at $x = +0.6$, past this point oscillations of decreasing magnitude and increasing frequency occur. Note that the phase and amplitude oscillations are in quadrature with the phase leading. The intensity of the returned echo at any time may be found by squaring the length of the electric field phasor.

Although the Cornu spiral provides a useful graphical means for examining the behaviour of the power and phase of the returned echo, more formally the power is given by $P_R(x) = |\boldsymbol{E}_R(x)|^2/(2Z_0)$, which upon evaluation and substitution for P_e yields:

$$P_R(x) = 2.5 \times 10^{-32} P_T G_T G_R q^2 \left(\frac{\lambda}{R_0}\right)^3 \frac{C^2 + S^2}{2} . \tag{3.11}$$

Similarly the phase of the echo is given by[2]:

$$\phi_R(x) = tan^{-1}\left(\frac{S}{C}\right) . \tag{3.12}$$

The maximum returned power is found by evaluating C^2+S^2 at $x = +1.21$ ($C^2+S^2 = 2.72$), the final normalised echo power (at $x = +\infty$) is given by $C^2+S^2 = 2.0$, while at the t_0-point ($x = 0$) $C^2+S^2 = 0.5$. The calculated power (a) and phase (b) as a function of x is displayed in Figure 3.4 (curve A) together with other echoes where the effects of trail diffusion have been included (curves B to D). A discussion on these effects follows in the next section.

The echo power and phase variations may be found as a function time through the use of the transformation $2s = x\sqrt{R_0\lambda}$ and knowledge of the velocity of the meteor. If the velocity is assumed to be constant, the echo profiles are effectively scaled as $x = (2V/\sqrt{R_0\lambda})t$. Alternatively, one may use the observations of the meteor echo as a function of time to calculate the speed of the meteor. This is usually done from measurements of the post-t_0 amplitude oscillations (*e.g. Ellyett and Davies*, 1948), although a new technique has been developed using the pre-t_0 phase variation (see Chapter 5). However, if either of these techniques are to be used to calculate meteor speeds, it must be shown that the effect of diffusion on the relevant portions of the echo is either negligible or can be adequately accounted for.

[2]For the electrical engineering convention, the expression for phase becomes $\phi_R(x) = tan^{-1}(-S/C)$.

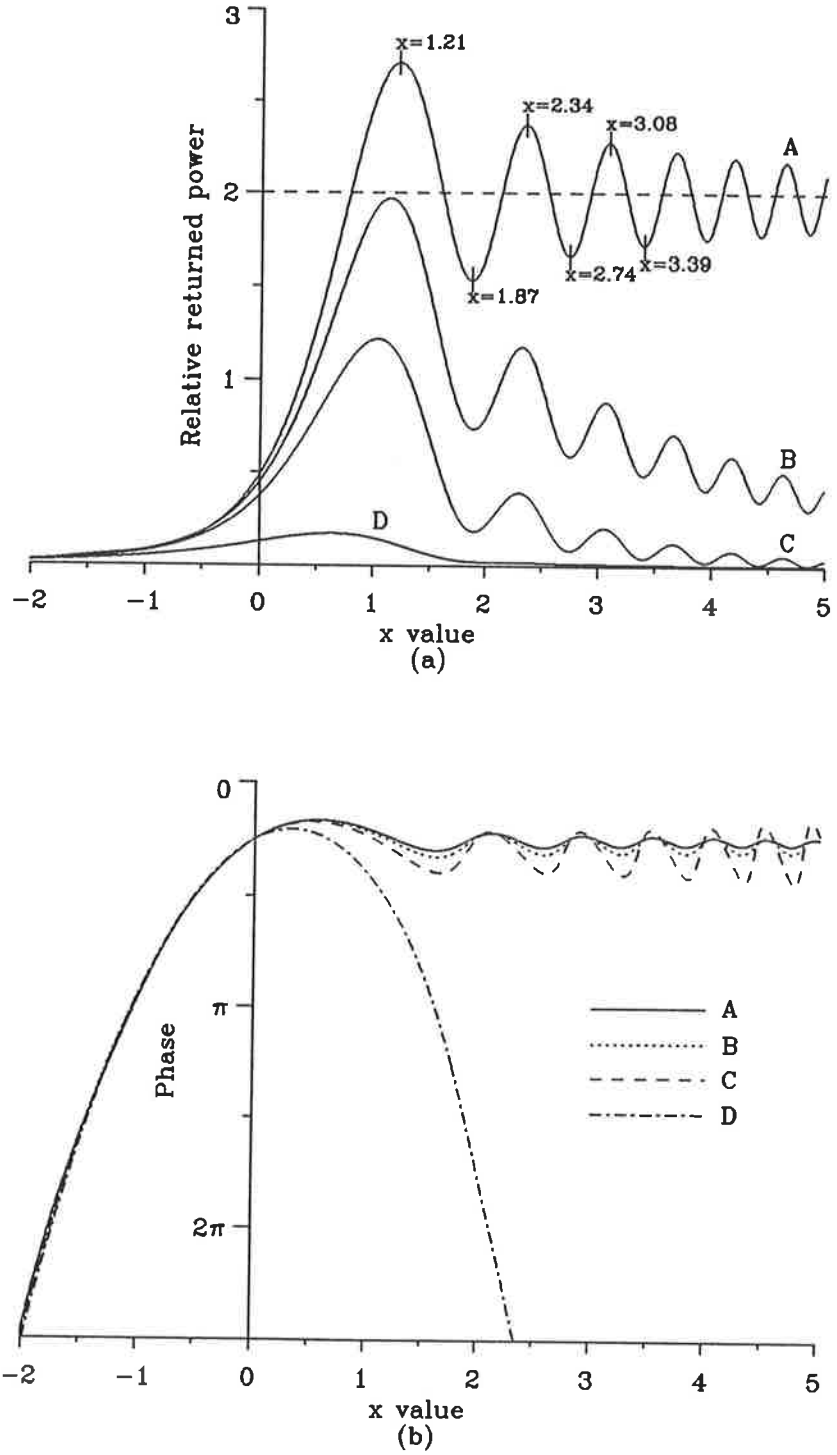

Figure 3.4: The effects of diffusion on the returned echo power (a) and phase (b). Curve A displays the case for no diffusion, while curves B to D display the effects of increasingly severe diffusion. The dashed line in panel (a) indicates the final echo power level for a meteor with no diffusion.

3.2.3 The effects of the initial trail radius and diffusion

The evaporating meteoric species from an ablating meteoroid, initially have velocities close to the translational velocity of the meteor. In contrast, the diffusive velocities of the atmospheric species in the region where meteors ablate, is about 2 orders of magnitude less (*Greenhow and Hall*, 1960; *McKinley*, 1961) than this velocity. The ablated atoms spread rapidly via collisions with the atmospheric species and are 'thermalized' after about 10 such collisions (*Jones*, 1995). Thus, the meteor train (a mixture of ions and electrons) is formed with an initial radius which, for most applications, can be considered to occur instantaneously (about $1\,ms$). *Baggaley* (1970), estimated the initial radii of meteors from observations at two different wavelengths (see also *Baggaley and Fisher*, 1980). He found that for meteors with speeds of $54\,km\,s^{-1}$, the initial radius was about $0.5\,m$ at height of about $90\,km$, rising to $3\,m$ at $115\,km$. Additionally *Baggaley* found that the initial radius doubled at all heights for an increase in the meteor speed from 40 to $65\,km\,s^{-1}$. Clearly the initial radius of a meteor trail depends strongly on both the height of ablation and the velocity of the meteor.

The trail, once formed, diffuses radially through ambipolar diffusion. The diameter of a cross-sectional segment (width ds) of the trail will at any time be dependent on both the initial radius of the trail and the amount of time the segment has been diffusing. If the trail is underdense, then the returned echo from this segment will be attenuated due to the radiation backscattered from the far parts of the trail being delayed in phase compared to that from the near part. The degree of attenuation is of course dependent on the radius of the segment, as the radius approaches $\lambda/4$ the attenuation becomes severe.

If one assumes the radial density distribution of electrons to be Gaussian then through the consideration of the radial diffusion equation and the contribution to the returned echo from annular rings of width dr within a thin slice of the trail of width ds, one may show that the total echo power from slice of the trail is given by (McKinley, 1961)

$$dP_R^d = dP_R e^{-(8\pi^2 r_0^2/\lambda^2)} e^{-(32\pi^2 Dt/\lambda^2)} ds\ , \tag{3.13}$$

where r_0 is the initial radius and dP_R is the echo power for the case of no diffusion and the electrons concentrated at the axis ($r_0 = 0$). Integration along the trail using amplitudes from each segment, ds, and applying the appropriate phase shifts, yields the echo due to the entire trail.

Recently *Jones* (1995) showed that the radial distribution of the electrons is more correctly described by a model which has a denser narrower central region and a more diffuse

outer region than that given by a Gaussian profile. *Jones* also showed that the decay part of the signal is unaffected by the initial radius and Equation 3.13 is still valid if r_0 is replaced by r_{eff}, the effective initial radius given by computer simulations of the initial collisions of meteoric material immediately after their ablation. The initial radii given by *Jones'* computer simulations were in much better agreement with experiment results than previous theoretical values based upon the analysis of collision cooling (see *e.g. Bronsten*, 1983).

The first exponential term in Equation 3.13, due to the initial radius of the trail, causes the immediate attenuation of the received power and defines the attenuation factor:

$$\alpha_r = exp\left(-\frac{8\pi^2 r_0^2}{\lambda^2}\right) , \tag{3.14}$$

and this becomes more severe for shorter wavelength observations.

The second exponential term is the time varying attenuation factor due to the radial diffusion of the trail. This causes the returned echo power of the trail once fully formed, to decay exponentially. The echo decay time, T_{un}, of underdense trails is defined as the time taken for the echo power to decay by a factor of e^{-2}. Thus we have the following relation for T_{un}:

$$T_{un} = \frac{\lambda^2}{16\pi^2 D} . \tag{3.15}$$

The radio echo is dominated by the contribution of the first Fresnel zone of the trail, which has a length equal to $\sqrt{R\lambda/2}$. If the meteor trail has diffused such that the trail width is comparable to the wavelength by the time the meteor has traversed the first zone, the returned power will be severely attenuated. If the meteor speed is assumed to be constant, then the length of time required to traverse the first Fresnel zone is $(R\lambda/2)^{1/2}/V$. Clearly, the attenuation is dependent on the speed of the meteoroid, with the echo from meteor trails formed from slow meteoroids being more severely attenuated. *Peregudov* (1958) derived the following formula for the attenuation of the echo due to the finite velocity of formation of the trail:

$$\alpha_v = \frac{1 - e^{-\Delta}}{\Delta} , \qquad \text{where} \qquad \Delta = \frac{16\pi^2 D}{V}\left(\frac{R}{2\lambda^3}\right)^{1/2} , \tag{3.16}$$

which again is more severe for shorter wavelength observations. The two attenuation factors, α_r and α_v, are the cause of the well known height ceiling effect of radar meteor trails.

The amplitude (a) and phase (b) of four typical meteors have been calculated for increasing levels of trail diffusion, and the results are presented in Figure 3.4, with curve A being the case for no diffusion. Although the values used for the diffusion coefficients are arbitrary,

a feel for the amount of diffusion applied in each calculation may be gained through the dimensionless quantity $D/(V\lambda)$. This was, in the calculations, set in the ratio 1 : 2.7 : 13.3 for curves B, C and D respectively.

The echo amplitude is examined first. One immediately notices that curves B and C behave in the expected manner decaying exponentially, with C having a smaller time-constant due to the greater diffusion. Although the position of the first maxima is shifted back towards the t_0-point, for these two curves, their subsequent oscillations occur at almost exactly the same x value as for the no-diffusion case. This is an important result and the calculation of meteor speeds from the measurement of the positions of these oscillations relies on this (see *e.g. Ellyett and Davies*, 1948). Amplitude curve D, however, shows no oscillations at all, displaying a smooth rise and fall with the maximum occurring just after the t_0-point. In this case, the diffusion is so great that the effective trail length is less than a Fresnel zone length and is starting to resemble a small moving target. The situation is clearly visualised with the Cornu spiral; instead of the electric field phasor being anchored at $-\infty$, diffusion effectively causes the origin of the phasor to also move around the spiral. When the length of the phasor becomes sufficiently short, no amplitude oscillations will be evident. Note that as the diffusion is increased further, the trail increasingly resembles a small moving target and the peak in the amplitude moves further back towards the t_0-point.

Turning now to the phase curves displayed in Figure 3.4b, the most striking feature is that the effect of diffusion on the pre-t_0 phase is very small. This is an important result and is particularly significant to the pre-t_0 phase method of calculating meteor speeds, that is developed in Chapter 5. Curve D displays an almost parabolic behaviour which is not surprising given that it arises from a trail whose effective length is very short. As the trail length decreases further, the phase behaviour becomes more parabolic with the point of minimum phase occurring closer to the t_0-point. It is interesting to note that for curves B and C the post-t_0 phase oscillations have a greater magnitude than for the no-diffusion case. This may be understood by again appealing to the Cornu spiral; as the origin of the electric field phasor moves towards $x = 0$, the shortened length of the phasor causes the phase fluctuations to increase as the tip of the phasor moves around the upper spiral. It is also interesting to note that for curve C, the phase oscillations have lost their symmetry becoming skewed such that the minima occur earlier and the maxima later. This is to be compared to the amplitude oscillations which displayed no such effect.

Finally, the effect of the geomagnetic field upon the diffusion coefficient for electrons in

the meteor trail must be commented upon. If the geomagnetic field is ignored (valid for heights below about 95 km) the effective diffusion coefficient for the electrons is given by:

$$D = D_i(1 + T_e/T_i)\,, \tag{3.17}$$

where D_i is the diffusion coefficient for the positive ions and T_e and T_i are the electron and ion temperatures respectively (*McDaniel and Mason*, 1973). Clearly, in the absence of magnetic fields, the diffusion of the electrons is controlled by the ionic diffusion. The electrons and ions rapidly come into thermal equilibrium with the ambient temperature once the trail has formed, therefore the diffusion coefficient for the electrons is $D = 2D_i$. This may be written as:

$$D = 6.39 \times 10^{-2} KT^2/p\,, \tag{3.18}$$

where p and T are the atmospheric pressure and temperature respectively, and K is the zero field mobility of the ions and is taken to be about $2.2 \times 10^{-4}\, m^2\, s^{-1}\, V^{-1}$ (*McDaniel and Mason*, 1973). This value for the zero field mobility of meteoric ions is derived from values for various alkali ions in Nitrogen determined from laboratory experiments.

In the absence of positive ions the diffusion coefficient of the electrons parallel to the magnetic field, $D_{e\|}$, is much larger than the value of D_i at all heights. Perpendicular to the magnetic field, the diffusion coefficient of the electrons is given by $D_{e\perp} = D_{e\|}\nu^2/(\nu^2 + \omega^2)$ where ν is the collision frequency and ω the gyro-frequency. Below 95 km $D_{e\perp}$ is greater than D_i, while above 95 km $D_{e\perp}$ rapidly becomes much less than D_i. Thus, below 95 km the radial diffusion of the electrons in all directions is controlled by the ionic diffusion, and the usual ambipolar diffusion coefficient applies. However, while the radial diffusion of the electrons parallel to the magnetic field is still controlled by the positive ions at heights above 95 km, the radial diffusion of the electrons perpendicular to the magnetic field is suppressed. Therefore, above 95 km the meteor trails become elliptical in cross-section

Jones (1991) found that for angles from 90° to about 5° between the meteor trail and magnetic field lines, the radial diffusion in the direction lying in the plane defined by the trail and magnetic field is unaffected; and that the radial diffusion in the orthogonal direction is suppressed with the degree of suppression decreasing with decreasing angle. For angles less than 5°, the diffusion becomes severely depressed, such that trails aligned within 2° of the magnetic field lines have life times much greater than is usual (assuming of course the trail formed above 95 km).

3.2.4 Overdense meteor trails

The limiting electron line density of meteor trails observable by the Buckland Park VHF radar is about $10^{10}\,electrons/m$, which is about 3 orders[3] of magnitude less than the start of the transition from the underdense to overdense regime. Thus, most meteors detected by the radar are underdense. With this in mind, only a brief discussion on the overdense trails is given here. For a fuller account, see *eg. McKinley* (1961).

If the electron density of the meteor trail is large enough, secondary scattering between electrons becomes important. The electrons no longer scatter the radio waves independently and the dielectric constant of the ionized column becomes negative. The meteor trail, in this case, is termed overdense and the reflection of incident radio waves is equivalent to that due from a metallic cylinder. The essential difference between metals and ionized gasses is that the conductivity is real for the former and imaginary for the latter. As with metals, the overdense meteor trail has a "skin depth" which is defined as the depth where the amplitude of the penetrating wave has fallen to $1/e$ of the surface amplitude.

The transition from the underdense to the overdense case is not sharply delineated, although various researchers have derived values for a critical value of the electron line density q_c which marks this transition. For example, a value for q_c of $2.4 \times 10^{14}\,electrons/m$ is calculated by *Kaiser and Closs* (1952) and *McKinley* (1961); while *Manning and Eshleman* (1959) derive a value of $1.1 \times 10^{14}\,electrons/m$. However, the work of *Poulter and Baggaley* (1977), shows that the transition region starts at electron line densities much lower than this, being at about $10^{13}\,electrons/m$, with the trail not becoming fully underdense until an electron line density of $10^{15}\,electrons/m$ is exceeded.

The received echo power for a fully formed, purely overdense meteor trail is (see *eg. McKinley*, 1961)

$$P_R = 1.6 \times 10^{-11} P_T G_T G_R \left(\frac{\lambda}{R_0}\right)^3 q^{1/2}\,. \tag{3.19}$$

Clearly, for overdense meteor trails, the received echo power is relatively insensitive to the electron line density ($P_R \sim q^{1/2}$) as compared with the underdense case ($P_R \sim q^2$). While the meteor trail is overdense, the returned echo is not subject to the effects of the initial radius and diffusion of the trail, although it is of course the diffusion which causes the 'reflecting surface' to expand. However, once the trail has diffused such that the electron density has fallen to the underdense regime (note the electron line density remains constant), the meteor

[3] Based on recent work by *Elford* (private communication).

echo will begin to decay as usual. The duration over which the echo is overdense is given by (*McKinley*, 1961)

$$T_{ov} = \frac{\lambda^2 q}{4\pi^3 D q_c} \,. \tag{3.20}$$

It is restated here that this is a simplification of the situation, the transition from the overdense to the underdense regime being a gradual one, a full treatment requires extensive modelling. A brief discussion follows.

3.2.5 The reflection process revisited

The treatment of the underdense and overdense cases of meteor trails has, so far, been a simplified one. For the underdense case the trail electrons were treated as independent scatterers, while in the overdense case the meteor trail was considered to be a metallic cylinder. As will be shown shortly, these two simple cases do give an accurate model of the reflection of parallel polarized radio waves from meteor trails with electron line densities less than $10^{13}\, electrons/m$ (independent scatterers), and greater than $10^{15}\, electrons/m$ (metallic cylinder). However, they fail for meteor trails with electron line densities within the above limits. In addition they do not account for the polarization of the radio wave.

In order to fully model the returned echo power from a meteor trail, the reflection coefficient, g, of radio waves scattered from the meteor trail, is required. This depends on the polarization of the radio waves with respect to the trail, the electron line density of the trail, and the length of time the trail has been diffusing. The returned amplitude of the electric field vector from radio waves backscattered by a short length of trail, ds, is given by:

$$dE_R = \frac{(2Z_0 P_T G_T G_R)^{1/2} \lambda g(s)}{4\pi R_0^2} e^{-i4\pi R/\lambda} ds \,. \tag{3.21}$$

This is similar to Equation 3.5, the difference being that the q and σ_e terms have been replaced by $g(s)$. Upon integration along the trail and substituting for the Fresnel length, x, one obtains:

$$E_R = \frac{1}{8\pi} \left(\frac{2Z_0 P_T G_T G_R \lambda^3}{R_0^3} \right)^{1/2} e^{-i4\pi R_0/\lambda} \int_{-\infty}^{x} g(x)\, e^{-i\pi x^2/2} dx \,, \tag{3.22}$$

for the electric field vector appearing at the receiver. Again, the received power is given by $|E_R|^2/(2Z_0)$.

Various researchers since the 1940's have formulated theories of radio wave reflection from meteor trails. It was *Lovell and Clegg* (1948) who first developed such a theory; based on

the assumption that each electron scatters independently and coherently. *Herlofson* (1951) discussed the validity of this with his full wave treatment and showed that the independent scatterers assumption only applied to trail of low electron line densities. *Herlofson's* full wave theory also showed that resonance effects could occur when the incident radio waves were polarized perpendicular to the trail. The metallic cylinder model (*i.e.* total reflection taking place at critical radius) was first suggested by *Greenhow* (1952) for dense meteor trails, and this was refined by *Manning* (1953) to include refractive effects in the region outside the critical radius. *Kaiser and Closs* (1952) also considered resonance effects, their approximate solutions showed a maximum increase in the amplitude by a factor of two. They also predicted (incorrectly) that radiation damping in the column would cause the resonance only to be observed in underdense trails.

Numerical solutions to the wave equations became possible when the speed of digital computers increased. One of the first researchers to take advantage of this was *Keitel* (1955) who, employing *Herlofson's* wave matching technique, found results in agreement with *Kaiser and Closs* (1952). Other researchers who have used numerical techniques include *Brysk and Buchannan* (1965), *Lebedinets and Sosnova* (1968) and *Jones and Collins* (1974). The formulation of *Brysk and Buchannan* (scattering from a Gaussian potential) excluded polarization effects and hence resonance was not observed. The latter two researchers employed the wave matching technique and found that (1) the resonance effect was not damped at large electron line densities, and (2) the resonance peaked at $q \approx 2 \times 10^{14} electrons/m$ with a polarization ratio of about 100. In addition *Jones and Collins* found an addition resonance peak at $q \approx 10^{16} electrons/m$.

Poulter and Baggaley (1977) reported that while polarization ratios greater than 2 had been observed, the large resonances predicted by *Lebedinets and Sosnova*, and *Jones and Collins* are over an order of magnitude greater than any recorded experimentally. They showed that the discrepancy may be explained as follows: for the perpendicular polarized case, the path taken by an integration in the complex plane was in the wrong direction around a singularity. Physically, taking the wrong path in the integration, is equivalent to a negative collision frequency. For this situation, collisions of the electrons with neutral particles would supply energy to the electrons instead of damping them, thus giving rise to large resonances. *Poulter and Baggaley* (1977, 1978) calculated numerically the complex reflection coefficients, and polarization ratios for trails with various electron line densities using the wave matching technique and made detailed comparisons with previous experimental results.

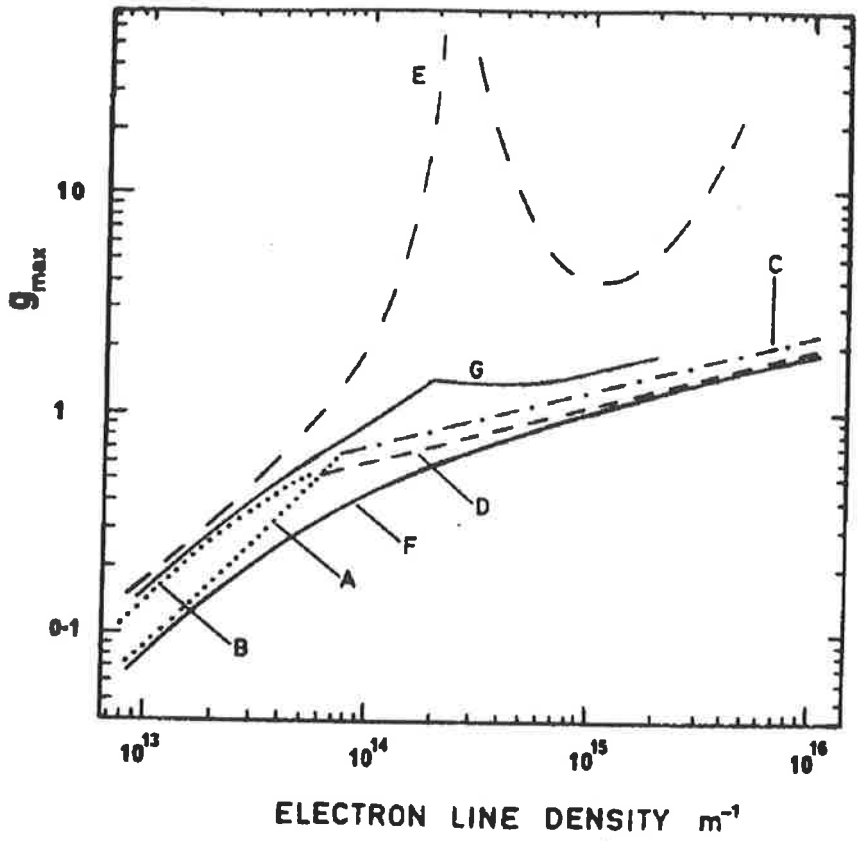

Figure 3.5: The maximum value of the reflection coefficient g_{max} as a function of electron line density. (A) $g_{\|max}$ independent scatterer model. (B) $g_{\perp max}$ *Kaiser and Closs* (1952). (C) metallic cylinder model. (D) metallic cylinder model with refraction. (E) $g_{\perp max}$ *Jones and Collins* (1974). (F) $g_{\|max}$ *Poulter and Baggaley* (1977). (G) $g_{\perp max}$ *Poulter and Baggaley* (1977). After *Poulter and Baggaley* (1977).

With particular regard to resonance, they found that resonance effects were not limited to trails with low electron line densities as for the theoretical prediction by *Kaiser and Closs* (1952) from their approximate solutions, and the resonance polarization ratio was generally a factor of about 2 with a peak of about 2.6 at $q \approx 2 \times 10^{14}\, electrons/m$. To date, the work of *Poulter and Baggaley* on the reflection of radio waves by meteor trails remains the most comprehensive.

In Figure 3.5 the maximum value of the reflection coefficient for parallel and perpendicular polarization ($g_{\|max}$ and $g_{\perp max}$ respectively) is shown as a function of electron line density as calculated by various researchers (from Figure 3. of *Poulter and Baggaley*, 1977). The work of *Poulter and Baggaley* clearly shows that for electron line densities less than $10^{13}\, electrons/m$ the independent scatterer model is valid. Likewise for $q > 10^{15}\, electrons/m$, the metallic cylinder model modified for refraction is a good approximation. The Buckland Park VHF

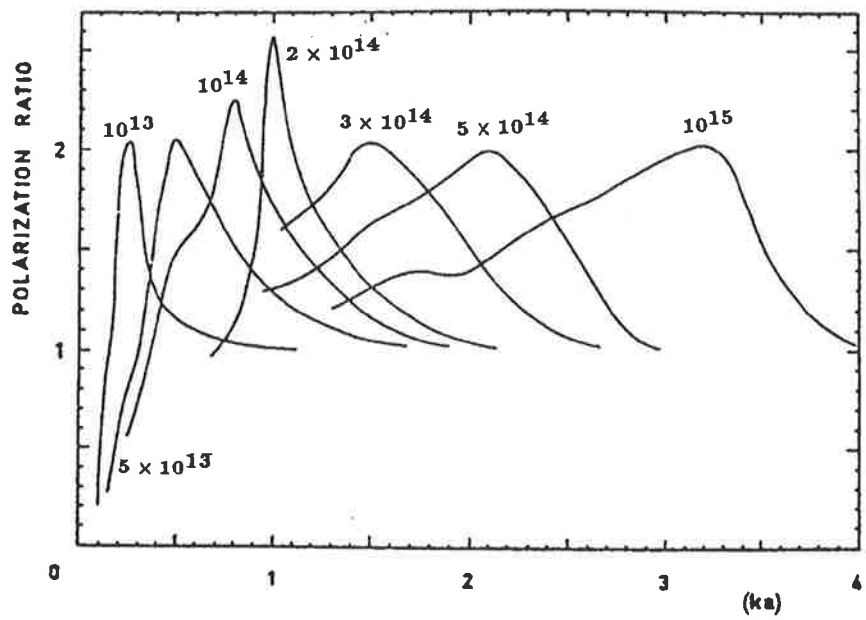

Figure 3.6: Polarization ratio, $g_\perp/g_{||}$, for various electron line densities. After *Poulter and Baggaley* (1977).

radar generally observes meteors with q in the range 10^{10} to $10^{12}\,electrons/m$, and thus for our purposes we may freely use the independent scatterer model.

It should be noted that for electron line densities less than $10^{13}\,electrons/m$, the effect of resonance on $g_\perp$ lasts for only a very short period of time and therefore resonance can be neglected. This is clearly displayed in Figure 3.6 which shows the polarization ratio, $g_\perp/g_{||}$ as a function of time for various electron line densities. In this diagram the abscissa is ka where $k = 2\pi/\lambda$ and $a = r_0^2 + 4Dt$, and λ is the wavelength, r_0 is the initial radius, D the diffusion coefficient, and t is time. Thus, for meteor trails with $q < 10^{13}\,electrons/m$ one can assume that $g_\perp = g_{||}$.

3.3 Meteor Detection with the VHF Radar

3.3.1 Statistics of white noise

In order to be able to develop a meteor detection algorithm, the statistics of the background noise from the receiver must first be investigated. It will be assumed that the noise output from both the in-phase and in-quadrature channels of the receiver has a Gaussian distributed. This is reasonable and indeed from an inspection of the distribution of digitized receiver noise in in each channel in Figures 3.7a and 3.7b, one may observe that this is true. In each case

the solid line is a fitted Gaussian. The receiver in-phase and in-quadrature output levels can vary from -5 to $+5\,V$ and the A/D converter employs a 12 bit digitizer. Thus, a digitized signal over a range of ± 2048 A/D units is rendered (1 A/D unit $\equiv 2.44\,mV$). From the coefficients of the fit to the noise data it is found that the in-phase and in-quadrature signals have peaks of 19.5 and 19.4, means of -0.4 and +0.6 A/D units, and $1/e$ widths of 112 and 114 A/D units respectively. Thus, the noise characteristics of the in-phase and in-quadrature channels are identical to within experimental uncertainty (the A/D noise is about 3–4 A/D units).

Now that the distribution of the raw in-phase and in-quadrature noise has been established to be Gaussian, we may proceed to calculate the probability of obtaining a signal above a certain threshold. Let x, y denote the noise level output from the in-phase and in-quadrature channels respectively. The probability density function describing the noise from the in-phase channel, $f(x)$, is Gaussian and is given by:

$$f(x) = \frac{1}{\sqrt{2\pi}\sigma} e^{-x^2/2\sigma^2} , \tag{3.23}$$

where σ^2 is the variance of the noise. Thus, the probability of obtaining a noise level $x > x_0$, is given by:

$$P(x > x_0) = \frac{1}{\sqrt{2\pi}\sigma} \int_{x_0}^{\infty} e^{-x^2/2\sigma^2} dx . \tag{3.24}$$

One may obtain a similar expression for $P(y > y_0)$. The probability of obtaining a noise level greater than x_0 from the in-phase channel, and greater than y_0 from the in-quadrature channel is then given by:

$$\begin{aligned} P(x > x_0, y > y_0) &= P(x > x_0).P(y > y_0) \\ &= \frac{1}{2\pi\sigma^2} \int_{y_0}^{\infty} \int_{x_0}^{\infty} e^{-(x^2+y^2)/2\sigma^2} dx dy . \end{aligned} \tag{3.25}$$

The following transformation is now made: $x = rcos(\theta)$ and $y = rsin\theta$. Therefore $r = \sqrt{x^2 + y^2}$ and $\theta = tan^{-1}(y/x)$, and these are respectively the amplitude and phase of the noise. Thus the following equation is obtained:

$$P(r > r_0, \theta > \theta_0) = \frac{1}{2\pi\sigma^2} \int_{r_0}^{\infty} \int_{0}^{\theta_0} J e^{-r^2/2\sigma^2} d\theta dr , \tag{3.26}$$

where J is the Jacobian of the transformation and is given by:

$$J = \begin{vmatrix} \frac{\delta x}{\delta \theta} & \frac{\delta x}{\delta r} \\ \frac{\delta y}{\delta \theta} & \frac{\delta y}{\delta r} \end{vmatrix} = r . \tag{3.27}$$

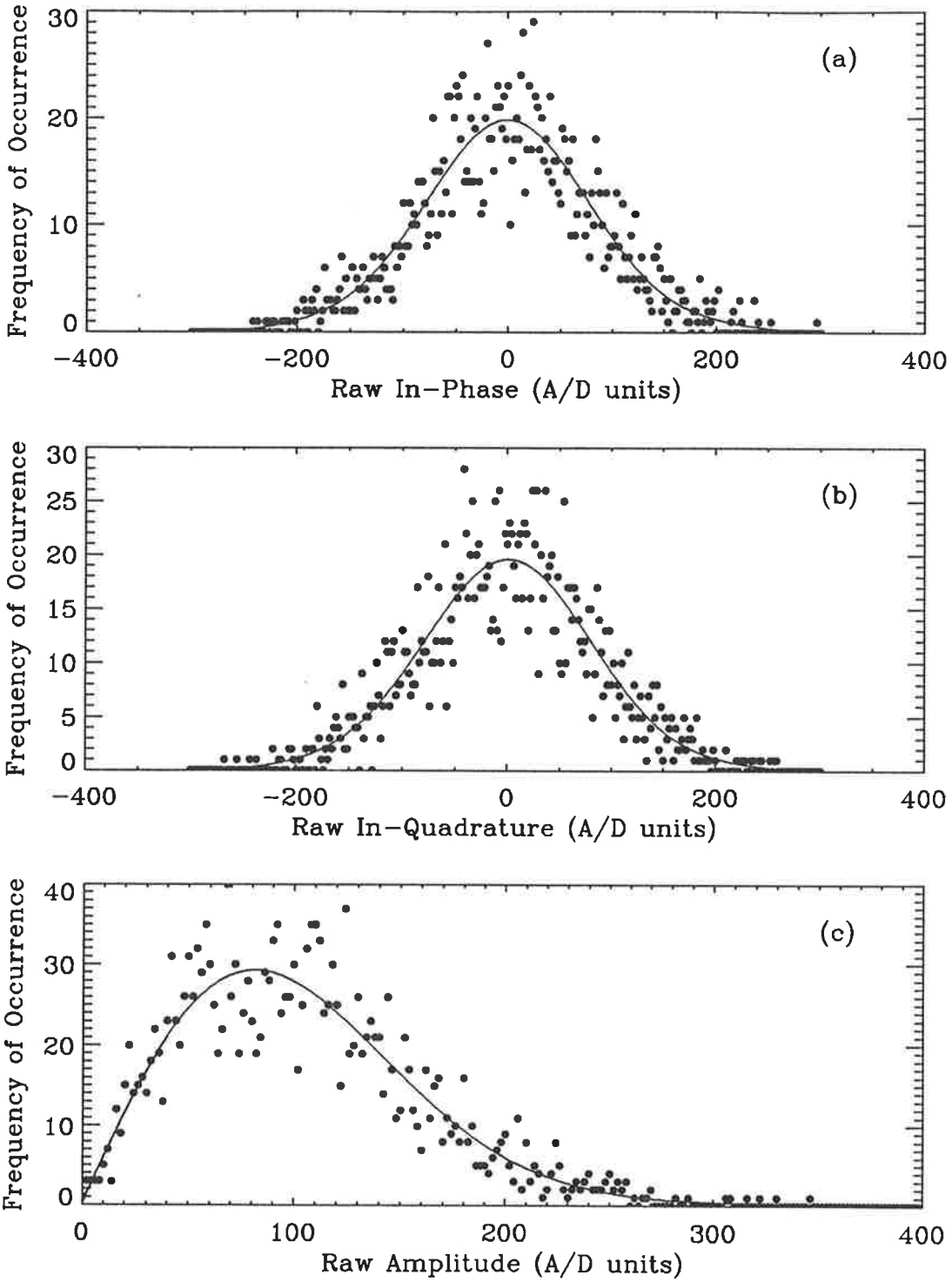

Figure 3.7: Distribution of 2 seconds of raw noise collected from the radar receiver. The in-phase noise distribution is shown in (a), the in-quadrature noise distribution in (b), and the amplitude distribution in (c). The solid lines are fitted Gaussian functions for (a) and (b), and a fitted Rayleigh function for (c).

By integrating θ over the range from 0 to 2π, one obtains the probability of observing a noise amplitude above a given level:

$$P(r > r_0) = \frac{1}{\sigma^2} \int_{r_0}^{\infty} r\, e^{-r^2/2\sigma^2} dr = e^{-r_0^2/2\sigma^2} . \tag{3.28}$$

The probability density function for the noise amplitude is given by:

$$f(r) = \frac{r}{\sigma^2} e^{-r^2/2\sigma^2} , \tag{3.29}$$

which is a Rayleigh function. Thus, one would expect that the amplitude of the noise obtained from the receiver to be Rayleigh distributed. This is in fact the case as seen in Figure 3.7c which displays the distribution of the raw noise amplitude calculated from the in-phase and in-quadrature noise data (see Figures 3.7a and 3.7b). The solid line is a fitted Rayleigh distribution.

It is more convenient to rewrite Equation 3.28 in terms of the mean noise amplitude, $\overline{r}$, instead of σ. The mean noise is given by:

$$\begin{aligned} \overline{r} &= \int_0^{\infty} r f(r) dr \\ &= \frac{1}{\sigma^2} \int_0^{\infty} r^2 e^{-r^2/2\sigma^2} dr , \end{aligned} \tag{3.30}$$

and the following solution can be found from any standard table of integrals:

$$\sigma = \overline{r}\sqrt{2/\pi} . \tag{3.31}$$

Upon the substitution of σ into Equation 3.28 and putting $L = r_0/\overline{r}$, the following expression is obtained for the probability of observing a noise amplitude greater than the mean noise by a factor of L:

$$P(r > L\overline{r}) = e^{-L^2\pi/4} . \tag{3.32}$$

This equation may be used to predict the number of false triggers a detection algorithm observes due to random noise (receiver noise and galactic noise). For example, if data is collected for 1 hour with a PRF of 1000 Hz and 20 range gates are sampled, then for a threshold level of $L = 4.780$, one false trigger due to random noise is expected. Equation 3.32 forms the basis of the detection algorithm developed to collect meteor echo data which is described in Section 3.3.4. However, caution must be exercised in the application of this equation as interference from other noise sources (especially impulsive noise) will affect the expected false trigger rate significantly.

3.3.2 The effect of coherent averaging on raw data

The process of coherently averaging of raw data will now be described. Coherent averaging is a simple process which involves the averaging of blocks of raw in-phase and in-quadrature data separately before any other signal processing takes place. This of course reduces the time resolution of the data, but has the advantage of increasing the signal to noise ratio by a factor of $\sqrt{N}$, where N is sufficiently large and is the number of points in the block of data to be averaged over.

The central limit theorem (given in any standard text on statistics and probability density functions) states that the average of N independent random variables each with mean, μ, and variance, σ^2, is normally distributed with mean, μ, and variance, σ^2/N, for N sufficiently large. Thus, the probability density function of the in-phase data after a boxcar average over successive blocks of N data points has been applied, denoted by $f_N(x_a)$, is given by:

$$f_N(x_a) = \frac{\sqrt{N}}{2\pi\sigma} e^{-Nx_a/2\sigma^2} \; . \tag{3.33}$$

Following the procedure of the previous section, the probability density function of the noise amplitude after coherent averaging has been applied, denoted by r_a, may be found. This is given by the following:

$$f_N(r_a) = \frac{N}{\sigma^2} r e^{-Nr_a^2/2\sigma^2} \; . \tag{3.34}$$

Thus the mean noise amplitude of the coherently averaged data, $\overline{r}_a$, is given by

$$\overline{r}_a = \sigma \left(\frac{\pi}{2N}\right)^{1/2} = \frac{\overline{r}}{\sqrt{N}} \; , \tag{3.35}$$

i.e. a factor of $\sqrt{N}$ less than the mean noise amplitude of the unprocessed data.

The effect of coherent averaging on raw data is displayed in Figure 3.8. About two seconds of raw noise data were recorded from the radar receiver, and an artificial "signal" introduced by adding a constant level of 100 A/D units to the in-phase and in-quadrature data over a time interval defined by 500 to 1000 radar pulses. The amplitude of this signal is 141.4 A/D units. The raw amplitude of the resulting data set is displayed in panel (a). The mean noise level is 110.29 A/D units and the artificial signal is just discernible above this. In panel (b) a 16 point running boxcar average has been applied to the amplitude data. The signal is now more easily discerned, however the the mean noise level is essentially unchanged now being 110.27 A/D units. Contrast this to amplitude data displayed in panel (c), which was produced by applying a 16 point running boxcar coherent average to the raw data. The

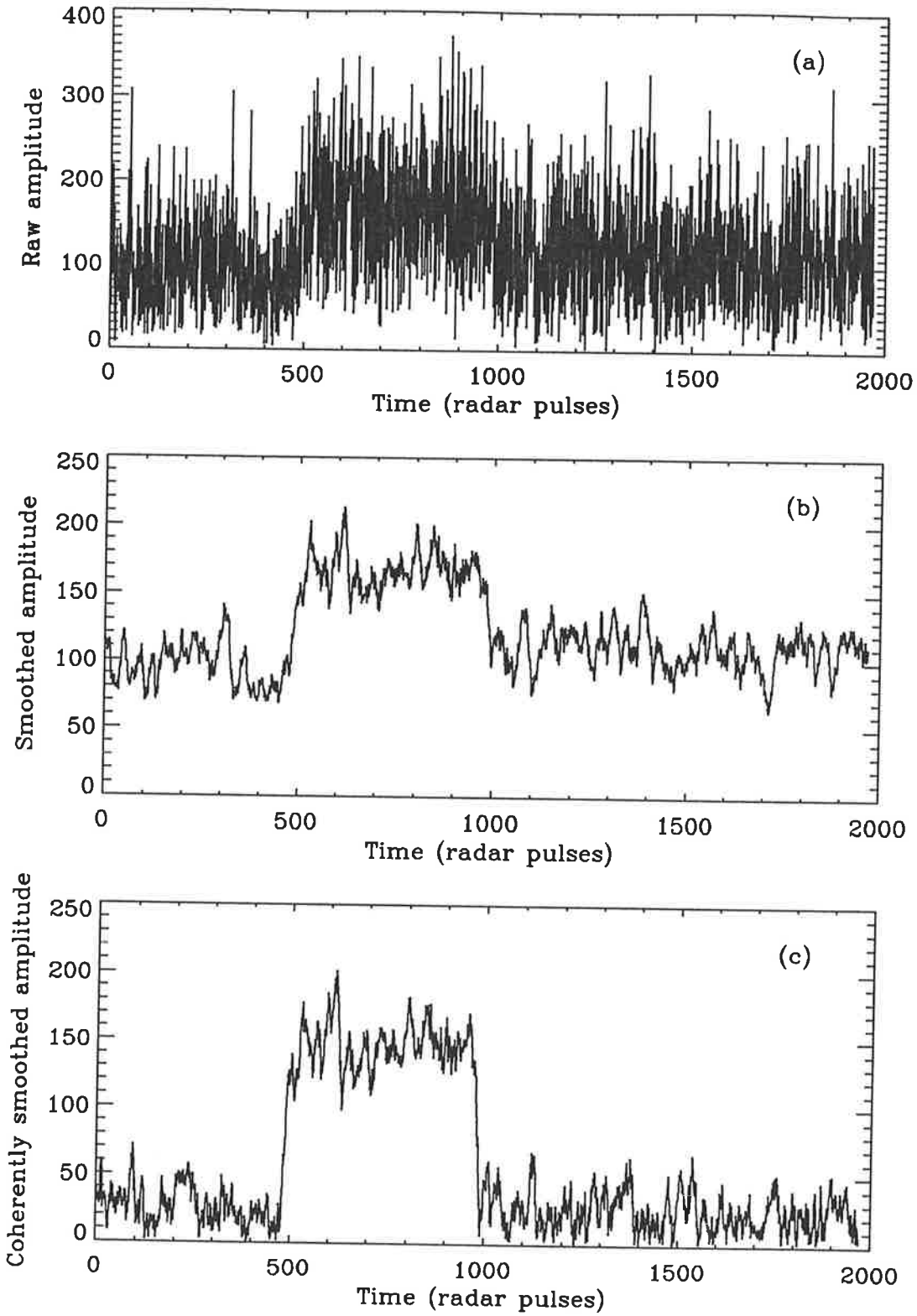

Figure 3.8: The effect of coherent smoothing on raw data. The raw noise amplitude with an introduced artificial signal signal is shown in (a), a 16 point sliding boxcar average is applied to the raw amplitude data and is displayed in (b), and in (c) the amplitude data is shown after a 16 point sliding boxcar coherent average has been applied to the raw data. See text for further details.

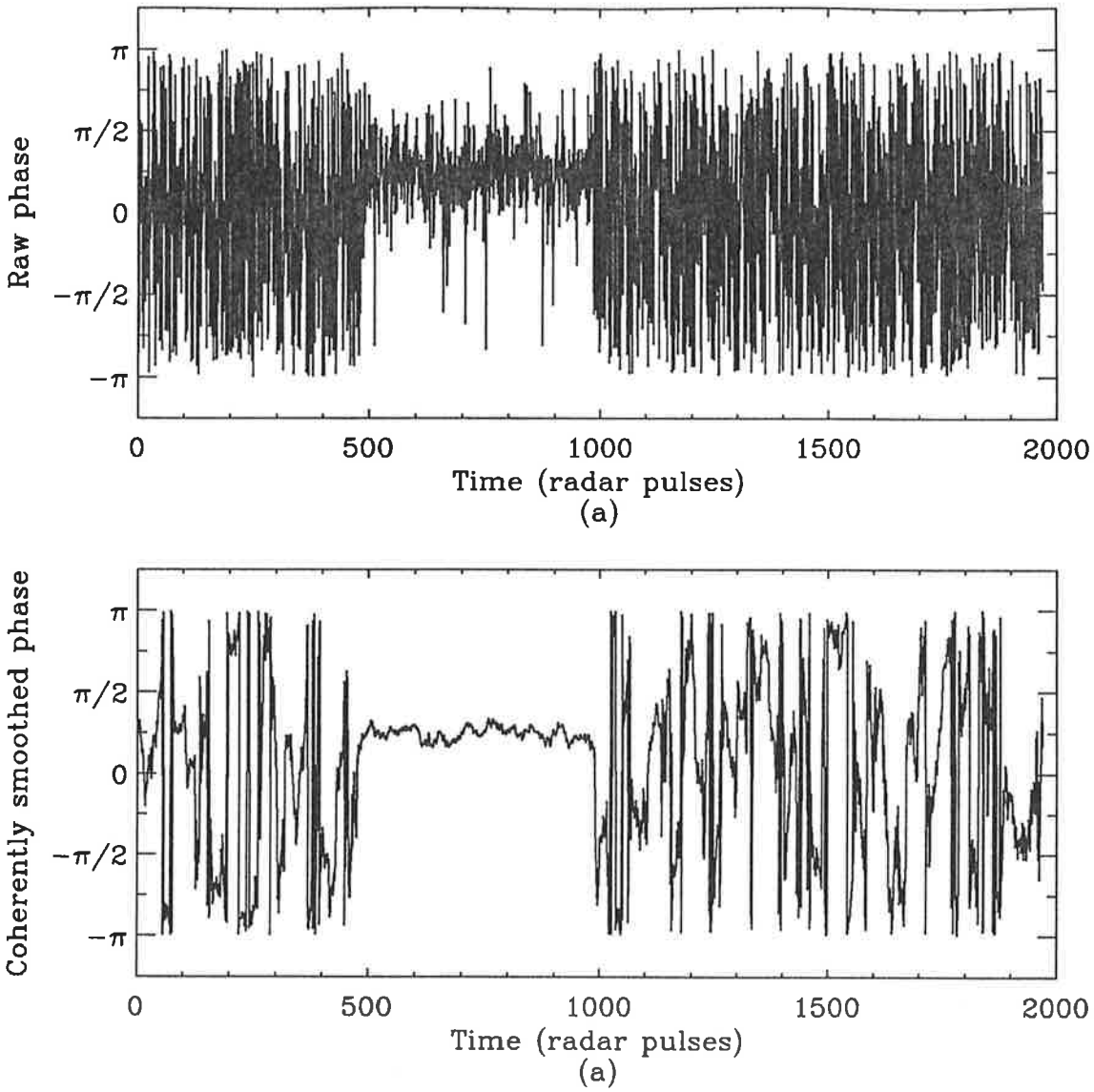

Figure 3.9: The effect of coherent smoothing on raw data. The raw phase information obtained from 2 *sec* of noise recorded from the radar receiver with an introduced artificial signal signal is shown in (a). A 16 point sliding boxcar coherent average was applied to the raw data and the result displayed in (b). See text for further details.

mean noise level has now been reduced to 24.77 A/D units, a reduction by a factor of 4.4, the signal is essentially unaffected by this process and is now much more easily discerned.

Figure 3.9 displays the effect of coherent averaging on the phase information. The raw phase is displayed in (a), while in (b) the resulting phase is shown after a running 16 point box car average had been applied to the raw data. The effect of the coherent averaging, as with the amplitude information, is to make the phase information of the signal much more readily discernible.

One interesting point, which is noted from a comparison of the raw phase and amplitude

information, is that even in the absence of averaging the signal is more apparent in the phase data than in the amplitude data. This is also apparent in all the meteor echoes observed with the radar. A discussion on why this is the case follows in the next section.

3.3.3 Comparison of effect of noise on the amplitude and phase information of a coherent signal

The fact that the phase information of a signal is more easily discerned from the noise than the amplitude information has significant implications for the detection of meteor echoes and the use of the data. The situation can be examined by considering Figure 3.10 where, in the first instance, raw in-phase and in-quadrature noise data was recorded from the radar receiver and are plotted against each other (a). The distribution of points is randomly distributed about the origin (as expected) and the spread is about $\pm$200 A/D units.

Various artificial signal levels were then added to the noise data and the effect of the noise on the signals examined. For simplicity, and without loss of generality, the signal is added only to the in-phase component. This is effectively a signal with zero phase (compared to the in-phase reference) and an amplitude which is given by the level which is added to the in-phase component. The signal amplitudes are 200 (b), 400 (c) and 800 A/D units (d). The effect of adding the signal is to restrict the values that the resultant phase may take. In (b) where the signal level is only half that of the spread in the noise, the signal amplitude is swamped and therefore difficult to discern. However the phase information is another matter. While the phase for the noise only situation is random between -π to π, the addition of the weak signal has restricted the phase to -$\pi/2$ to $\pi/2$, and this is much more apparent than the change to the amplitude data.

This effect is even more apparent in Figure 3.10c where the signal level has increased to 400 A/D units which is equal to the spread in the noise. The amplitude is still hard to discern from the noise, the phase is now restricted to about 20% of the available range. This falls to 11% in Figure 3.10d where the signal is twice noise. One obvious and advantageous effect of the reduction in the extent of values that the phase information may take, is the manner in which weak amplitude signals can be so easily discerned from the phase data. A detection algorithm based on phase would appear to be the logical outcome of this analysis. However, this phase characteristic was only appreciated in hind-sight, well after the equipment was built and operating.

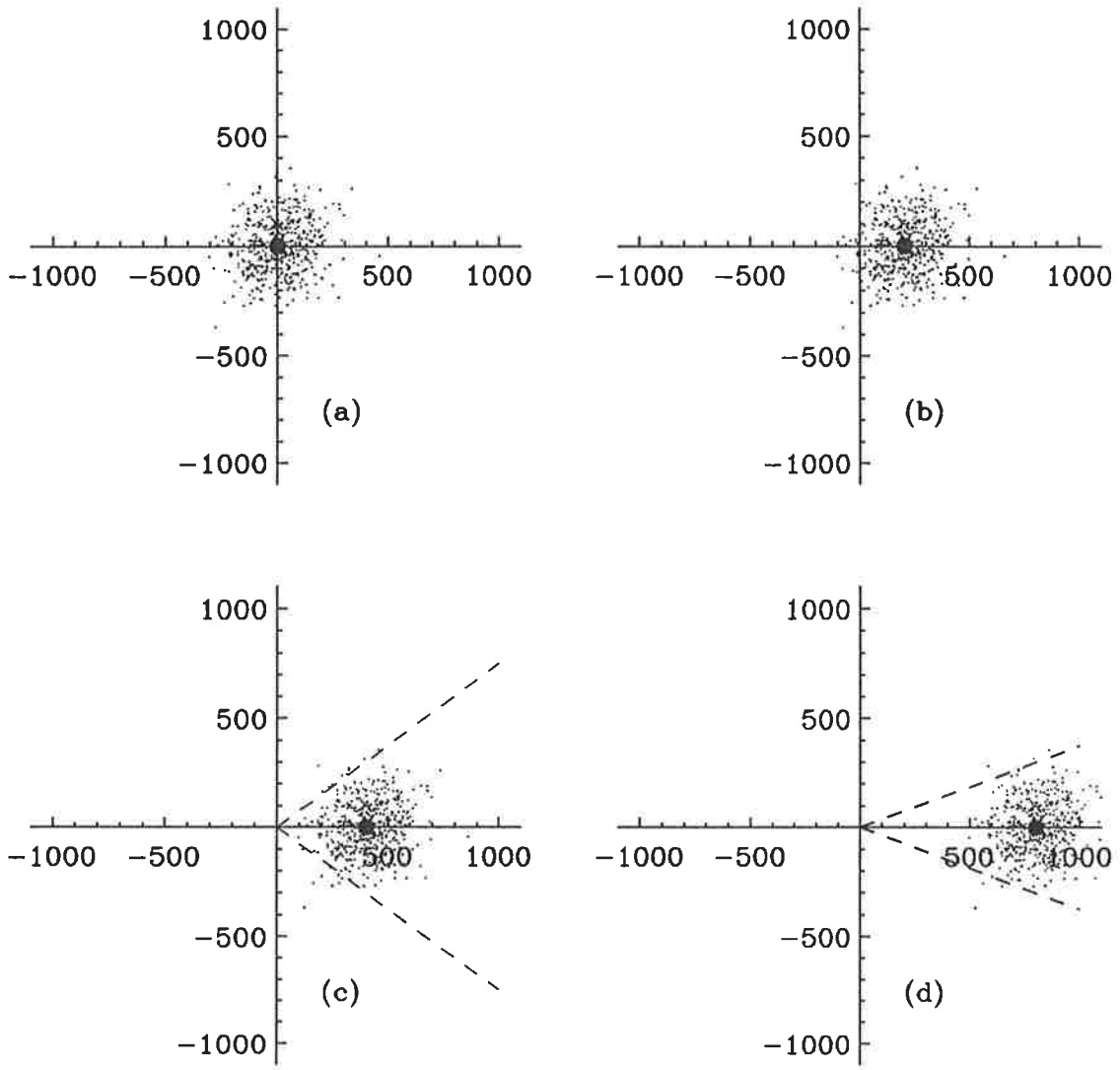

Figure 3.10: The effect of noise on various signal levels. In (a) raw in-phase (abscissa) and in-quadrature (ordinate) noise data is plotted. Artificial signals are introduced to the noise data by adding constant levels of 200 (b), 400 (c), and 800 A/D units (d) to the in-phase component. The solid circles indicate the signal added to the noise data, the distance from the origin gives the amplitude level of the signal. The dashed lines in (c) and (d) delineate a region whose angle at the origin is subtended by the spread of the data, the calculated phase of the data lays within this region.

3.3.4 The meteor detection algorithm

Now that the noise characteristics of the radar receiver has been examined, and the effects of coherent averaging on the noise discussed, the meteor detection algorithm may be developed. The algorithm is based upon Equation 3.32 derived in Section 3.3.1. The choice of an appropriate amplitude level, above which a meteor is deemed to have been detected, sets a false alarm rate based on the assumption that the noise is purely random in nature. For example, if an amplitude threshold of 4.811 above the mean background noise is set, then for the usual operating parameters of the radar (PRF = 1024 Hz, 24 range gates sampled, 2 sec analysis time required for 16 sec of data), one false alarm is expected per hour. This may be checked experimentally by running a detection routine for one day with the transmitter off, the number of detections should be the expected number of false alarms. This was performed and in the absence of any other noise source or interference, the prediction was confirmed.

It would of course be naive to assume that the noise is purely random white noise and thus try to detect meteors on only one data point. Other noise sources such as lightning and man-made interference would trigger the detection algorithm. The latter is especially true for the Buckland Park VHF radar which resides in the near field of a 2 MHz radar also operated by the University of Adelaide. As described in Chapter 2 the 2 MHz transmitter pulses are picked up by the VHF antenna array. Cross-modulation with 54 MHz signals in the T/R switches of the VHF radar produces 52 MHz and 56 MHz signals which are impossible to remove with the receiving system's band pass filters. The effect is observed in the raw data from the receiver as noise spikes occurring with a frequency of 80 Hz, the PRF of the 2 MHz transmitter. As discussed earlier in Chapter 2, a hardware solution to this problem was developed which involved the construction of high pass filters to attenuate the 2 MHz at the input of the T/R switches. This was only partially successful as occasionally the noise spikes produced by the 2 MHz transmitter pulse were still evident in the raw data. Indeed, even with the 2 MHz in place, false alarm rates of 1000 to 10000 detections per day where obtained when the 2 MHz transmitter was operating and the detection threshold adjusted so that only one false alarm per hour was expected.

It is clear that even if the 2 MHz transmitter noise problem could be eliminated entirely, there is still the possibility of receiving impulsive noise from other sources. The solution to this was to check the next data point in the time series once the amplitude had exceeded a certain threshold. The detection algorithm rejected those candidates where the second

pulse was less than half the amplitude of the previous pulse. The choice of this level is somewhat arbitrary, but from trial and error this was just above the minimum level required to eliminate most of the impulsive noise. With meteor detection being performed on two pulses, the choice of the threshold level for the first point is not as important, a level of around 4.5 times the mean background noise was found to give satisfactory results.

Other forms of noise were rejected by recognising that the noise is spread over several range gates whereas meteors generally occur only in one range gate and occasionally (about 2%) in two. Thus, once an event is detected, the adjacent range bins are examined as well using the same threshold criteria. If the detection algorithm was also triggered in these range gates, the event was regarded as noise and discarded, otherwise the event was assumed to be a meteor and recorded for further analysis. The false alarm rate for this detection algorithm was found to be less than 1 event per 24 hours on quiet days (*i.e.* the $2\,MHz$ transmitter not operational) and under about 10 events per day otherwise.

So far the effect of coherent averaging on the raw data has not been discussed. If the detection algorithm is applied to the raw data directly, then only relatively strong echoes (at least 4.5 times above the mean background noise) will be detected. However, the weaker echoes can be detected by first coherently averaging the raw data to improve the signal to noise ratio, and therefore increase the meteor detection rates. Once a meteor has been detected, the raw data[4] is recorded so as to retain the high time resolution of the data. Of course the very short duration events are lost, but with careful consideration of the length of the coherent average, these can be minimised. For the purpose of detection, most routine meteor observations were performed with two successive sets of 16 point coherent averages applied to the raw data. With this procedure echo rates during June/July 1994 were about 800 per day which is to be compared with about 250 per day when no coherent averaging was applied.

Consider the usual case of 16 point coherent averaging of the raw data for detection purposes. With the radar operating at a PRF of $1024\,Hz$, a lower limit to the echo duration of observable meteors is about $20\,ms$, 16 times greater than if no averaging was applied. The above limit is about what is observed experimentally. The echo amplitude decay time, T_{un}, for underdense meteor echoes is given by (*McKinley*, 1961):

$$T_{un} = \frac{\lambda^2}{16\pi^2 D}\,, \tag{3.36}$$

[4]The raw data is held in a temporary store in the PC's extended memory

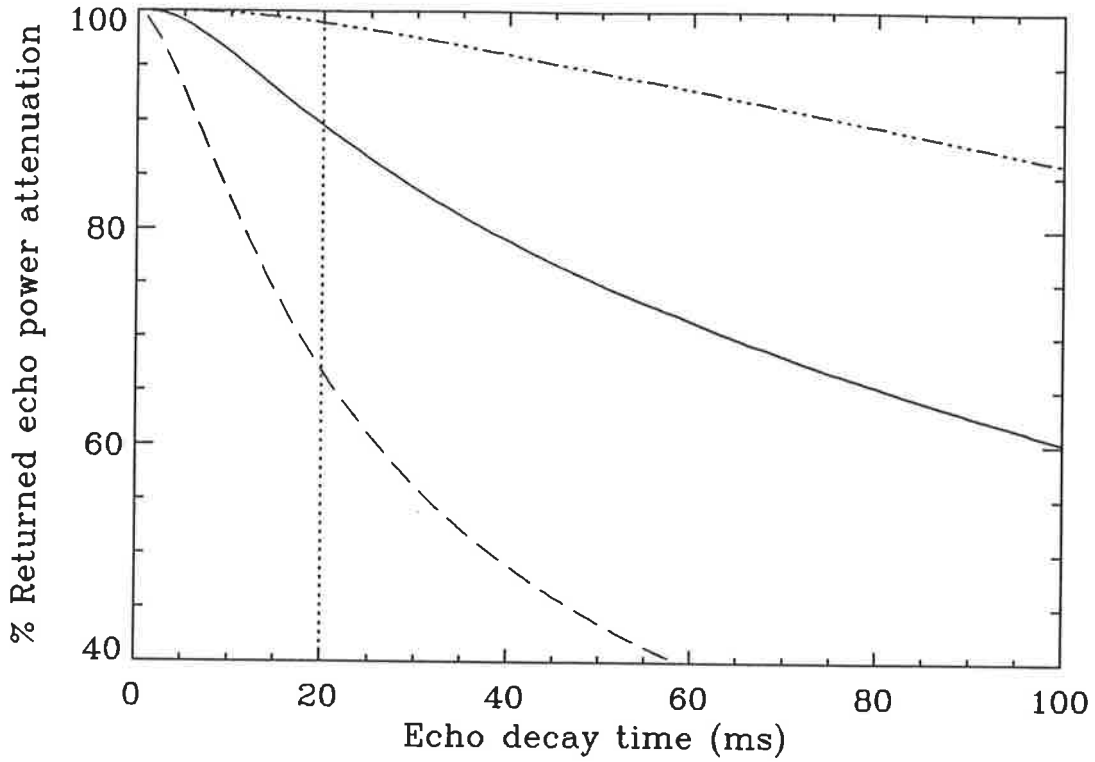

Figure 3.11: Percentage attenuation of the returned meteor echo power as a function of echo duration for underdense echoes. The dashed line indicates a velocity of 20 km, the solid line a velocity of 40 km, and the broken line 60 km. The vertical dotted line indicates the minimum echo decay time for meteors able to be detected with the Buckland Park VHF radar meteor detection routine.

where λ is the radar wavelength, and D is the ambipolar diffusion coefficient. Thus, the upper limit of the ambipolar diffusion coefficient is about $10\,m^2\,s^{-1}$. Using this value for D, the echo attenuation factors (see Equations 3.14 and 3.16), α_r and α_v, are calculated to be 0.15 and 0.72 for meteors with speeds of $40\,km\,s^{-1}$. Thus, the attenuation of meteors with a duration of 20 ms is about 89%. For meteors lasting 15 ms, this increases to 93%, and 96% for meteors with durations of 10 ms. In both cases a meteor velocity of $40\,km\,s^{-1}$ was assumed. In Figure 3.11, the percentage attenuation of meteor echoes as a function of echo duration and velocity is displayed.

The discussion so far on the attenuation of short duration echos only applies to underdense echoes. Overdense echoes are not affected in the same manner, as radio wave scattering from these trails takes place near the surface of the column of ionization. Thus, short duration overdense echoes should be observable if the coherent averaging is reduced. The duration of overdense trails, as seen from Equation 3.20, depends on both the height

of ablation and the electron line density of the trail. An overdense trail with an electron line density of $10^{15}\,electrons/m$ occurring at a height of $110\,km$ has a duration of $20\,ms$. Meteor trails are generally accepted to be overdense when the electron line density exceeds $1-2\times10^{14}\,electrons/m$ (*eg. McKinley*, 1961). However the work of *Poulter and Baggaley* (1978) indicates that the transition from underdense to overdense is a gradual process over electron line densities of $10^{13}-10^{15}\,electrons/m$. Whichever the case, the radar observes most meteors in the range $10^{10}-10^{12}\,electrons/m$ (see Chapter 4 and Section 3.3.5). As the cumulative flux of meteors is proportional to q_{min}^{-1} the contributions of overdense echoes to the data base is so small that their presence or absence will not affect the rate statistics.

Clearly from Figure 3.11, if the 16 point coherent averaging of the raw data was removed or reduced, the number of extra short duration echoes observed would be small, and in any case they are too short in duration to be of any use in the reduction of data from them such as meteor velocities, wind drifts or echo decay rates. The large increase in the count rates from applying the coherent averaging in the detection algorithm far outweighs the loss of the relatively few number of short duration echos that otherwise would be missed. On the other hand, an increase in the coherent averaging, although it would reduce the noise and therefore increase the meteor detectability further, is not desirable as the number of meteors echoes lost due to excessive averaging is too great to be a viable option. The author felt that 16 point coherent averaging struck the best balance - increased detectability without the loss of too many short duration meteor echoes.

Finally, although already mentioned in the above discussion, it is repeated here that the 16 point coherent averaging of the raw data was performed for the purpose of meteor detection only. Once a meteor had been detected, the raw data was recorded.

3.3.5 Advantages of the Buckland Park VHF radar over meteor radars used in the past

There are three main differences between the Buckland Park VHF radar and other traditional radars used in the past. These are the narrow pencil beam, high PRF, and the ability to record in-phase and in-quadrature data resulting in the determination of the phase as well as the amplitude information from returned echoes. Each of these features will be addressed in turn.

The narrow beam of the radar has two advantages over the wide beam systems used in the past. The first is that the narrow beam constrains the response of the radar to

meteors radiants from a narrow, well defined strip of the sky (see Chapter 4). This is of great importance for the study of meteor showers as their radiants are able to be determined with a high degree of accuracy (see *Cervera et al.*, 1993; *Elford, et al.*, 1994); the method is detailed in Chapter 6 together with the observations of two showers.

The second advantage of narrow beam radars is the greatly increased sensitivity of the system. For example, as will be seen in Chapter 4, even though the transmitter power is relatively low (about $30\,kW$), which is reduced further by the low efficiency of the CoCo antenna array (about 30%), the limiting meteoroid mass which produces meteor trails observable with the radar is about $10^{-6}\,kg$ (see also Chapter 5). The limiting electron line density of the system is about $10^{10}\,electrons/m$ which is equivalent to radar magnitudes of +13.6 and +15.6 for meteoroids with speeds of $11\,km\,s^{-1}$ and $76\,km\,s^{-1}$ respectively. Sensitivities as low as this were not achieved with the wide beam radars used in the past.

The high PRF of the Buckland Park radar plays two important roles. The first, and most obvious, is the resulting high time resolution of the meteor data. This enables data of very high quality to be recorded which is important for the reduction of accurate meteor speeds (*Cervera et al.*, 1995; *Elford et al.*, 1996) as detailed in Chapter 5. *Cervera and Reid* (1994, 1995) also make use of the high time resolution data to obtain accurate wind determinations in the meteor region with this radar using the meteor drifts technique (see Appendix A). The high PRF is also important in the meteor detection algorithm. In the previous section, it was pointed out that 16 point coherent averaging of the raw data was usually performed in order to reduce the background noise and therefore enable weaker echoes to be detected. This is made possible only through the use of a high PRF. If, for example, the PRF was only $100\,Hz$ then 16 point coherent averaging of the data would mean that only echoes lasting for more than $150\,ms$ would be detected! Clearly for low PRF systems the use of coherent averaging to increase the system sensitivity is not a viable option.

Finally, the phase coherent receivers, which produce in-phase and in-quadrature outputs, enables the phase of the signal to be recorded as well as the amplitude. As will be seen in Chapter 5, it was the phase information from the meteor echoes that enabled a new technique for the reduction of meteor velocities to be developed. This technique, as discussed in Chapter 5, is far more powerful and versatile than previous methods that use the Fresnel amplitude oscillations. The phase information is also used to determine the meteor winds discussed above.

3.4 Preliminary Meteor Observations

3.4.1 Introduction

This section is concerned with preliminary observations of meteors with the Buckland Park VHF radar. Before any research into the various aspects of meteor phenomena could be undertaken, a large sample of meteor echoes was required to be inspected visually so that the various types of echoes observed by the radar could be broadly classified. Examples of various type of echoes (*e.g.* classical underdense echoes, weak, overdense, saturated and beating echoes) are presented in this section and are discussed in detail. The effects of receiver saturation by strong meteor echoes are significant and need to be recognised, and a discussion on this follows.

A large body of information is now available on meteor fluxes, showers, heights, and velocities collected over many decades of optical and radio observations. It is shown that the VHF observations are in general consistent with what is expected from previous studies and that the VHF system makes possible a unique and highly significant contribution to all four areas.

3.4.2 Examples of meteors observed with the Buckland Park radar

In Figure 3.12 eight examples of various types of meteor echoes observed by the Buckland park radar are displayed, with amplitude at the top and phase at the bottom in each case. The first echo shown (a), is that of a typical underdense meteor echo with a good signal to noise ratio detected at 12:58 Australian Central Standard Time (CST) on the 6^{th} June 1994 at a range of $100\,km$. The amplitude profile is that of a classical decaying Fresnel diffraction pattern which shows the relatively fast rise and, in this case, slow exponential decay due to diffusion of the trail. About 18 Fresnel oscillations are evident in the post-t_0 amplitude information from which a velocity may be determined (see Chapter 5). The phase information prior to the t_0 point shows a high degree of coherency and this is used by the new technique described in Chapter 5 to deduce velocities. The echo decay time (time for amplitude to fall to $1/e$) is found by fitting a straight line to the log of the exponential portion of the echo, and the value is $43 \pm 2\,ms$. Thus the ambipolar diffusion coefficient is calculated to be $4.5 \pm 0.2\,m^2\,s$ which gives a decay height of $94.5 \pm 0.3\,km$. This is some $8\,km$ greater than the height of $87\,km$ obtained by multiplying the range at which the meteor was observed by the cosine of the off zenith beam tilt (30°). The higher than expected rate of

diffusion could be explained by fragmentation of the meteoroid orthogonal to the direction of motion although it is more likely that this meteor was detected in a sidelobe.

The next echo displayed (b) is another strong underdense echo (detected at 05:54 CST on the 11^{th} June 1994 at a range of $110\,km$), but here the post-t_0 amplitude oscillations are not well defined at all. They have been smoothed out and this is probably due to fragmentation of the meteoroid. *Elford* (private communication) has shown from a model that a simple two body fragmentation argument explains the smearing out of the amplitude oscillations seen in many echoes where the decay rate is not high enough to do this. Typically *Elford* has found that the two fragments are only required to be separated by some $40\,m$ along the direction of motion for significant smearing of the oscillations to occur. Spread of the fragments orthogonal to the direction of motion is negligible in this case, as this would increase the rate of decay and therefore the decay height would be larger than the observed height. This is not the case, the decay height is measured to be $92.6 \pm 0.2\,km$ which compares well with the observed height of $95\,km$. This echo also shows the strong phase coherence well before the t_0 point.

In panel (c) an example of a weak underdense echo is displayed which was detected at 15:28 CST on the 6^{th} June 1994 at a range of $102\,km$. The next figure (d) shows the same echo but with a 16 point coherent running boxcar average applied to the raw data. Note that the mean noise level of the coherently smoothed smoothed data is much lower and therefore the meteor echo is much more apparent. This raw echo would have been ignored by the detection algorithm if the coherent averaging had not been applied, and the useful data able to be deduced from this echo would be lost. The pre-t_0 phase exhibits strong coherence and a velocity for this meteor is able to be obtained by the new technique developed in Chapter 5. The height of this echo, as obtained from the echo decay, is $86 \pm 1.0\,km$ (*c.f.* $88\,km$ as obtained from the range).

Overdense echos are also observed with the radar, but as the electron line densities are high these echoes generally saturate the receiver. The example shown in panel (e) is one that has not caused receiver saturation, probably because it was detected right at the very edge of the beam (or possibly in a sidelobe). This echo was detected at 21:54 CST on the 7^{th} June 1994 at a range of $110\,km$ (height of $95\,km$). The rise of the amplitude is typical of a Fresnel diffraction pattern, but the amplitude does not immediately decay due to the trail being overdense. Once the trail has diffused sufficiently such that it becomes underdense, the amplitude starts to decay. The height of this meteor, found from the decay rate of the echo,

is $92.1 \pm 0.5\,km$ which agrees with the height as calculated from the range. This suggests that the meteor was detected at the edge of the beam instead of in a sidelobe. As previously stated, this is a well behaved overdense echo. This is not the usual case, many overdense echoes are very long enduring (sometimes up to 10's of seconds) and become distorted by the background wind. Multiple reflection points may be produced, and this causes large fluctuations in the echo amplitude and phase records. An example of this type of overdense echo is displayed in panel (f) which represents the first $2\,sec$ of the echo (duration of $5\,sec$ in total).

Meteors which occur at high altitudes diffuse rapidly. The effect is to limit that region of the trail whose radius is less than $\lambda/2\pi$ to a short length back from the head of the trail. When the effective length of trail that may be observed becomes less than a Fresnel zone length, the echo starts to behave as if it was that from a small moving ball target. An example of this type of echo, which will be referred to as a "pseudo head echo" (to distinguish it from "traditional" head echoes) is displayed in panel (g). It was observed at 12:14 CST on the 6^{th} of June 1994 at a range of $112\,km$. Both the amplitude and phase are symmetric about the point of closest approach and in particular the phase is parabolic as expected for a moving ball type of target. Note that the phase has been unwrapped (*i.e.* the 2π phase jumps removed) so as to show the parabolic nature of the phase. Fitting a parabola to the phase enables the velocity to be determined (see Chapter 5), although the more general velocity reduction technique developed in Chapter 5 produces a more accurate result. The amplitude profile, in this case, is a cross section of the antenna pattern. This echo is discussed in greater detail in Chapter 5.

Strong meteor echoes may cause saturation of the receiver. An example of this type of echo, which was observed at 20:01 CST on the 6^{th} June 1994 at a range of $96\,km$ is displayed in panel (h). The maximum output level of the in-phase and in-quadrature outputs of the receiver is $\pm 5\,V$ which corresponds to a digitised range of ± 2048 A/D units. Thus, the maximum amplitude that may be recorded is $\sqrt{2048^2 + 2048^2} = 2896$ A/D units. However, only amplitudes less than 2048 A/D units are definitely not saturated; amplitudes within these two limits may be saturated depending on the phase of the signal. As an example, in-phase and in-quadrature levels of 2000 A/D units each are not saturated and give an amplitude of 2828 A/D units, but an in-phase level of 1000 A/D units and a saturated in-quadrature signal (level truncated at 2048 A/D units) gives a saturated amplitude of 2279 A/D units. This is less than the previous amplitude level which was not saturated. For

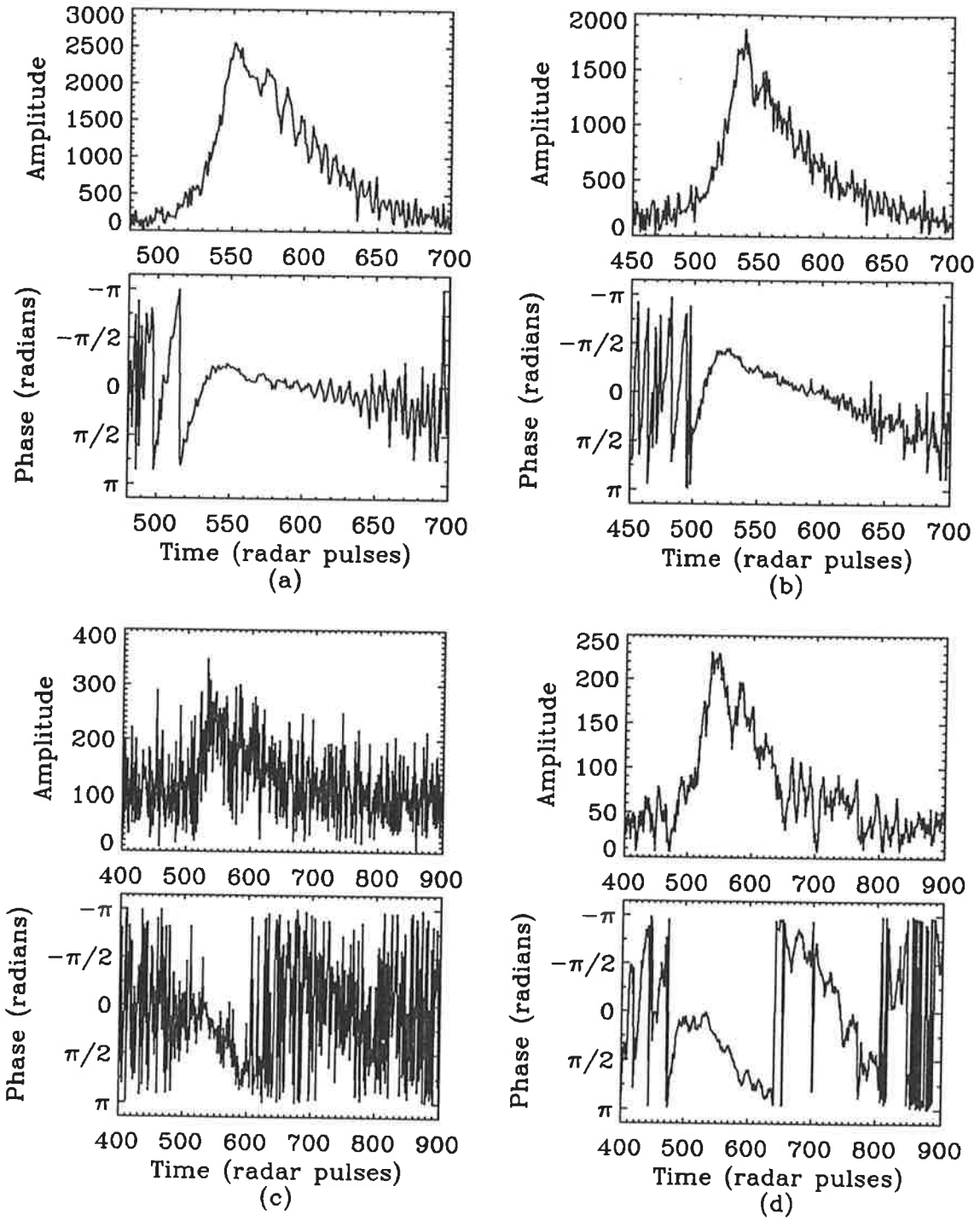

Figure 3.12: Examples of meteors observed with the Buckland Park VHF radar. Meteors (a) to (d) are shown on this page, meteors (e) to (j) are shown on the subsequent 2 pages. For each meteor echo the amplitude (top) and phase (bottom) information is shown. See text for further details.

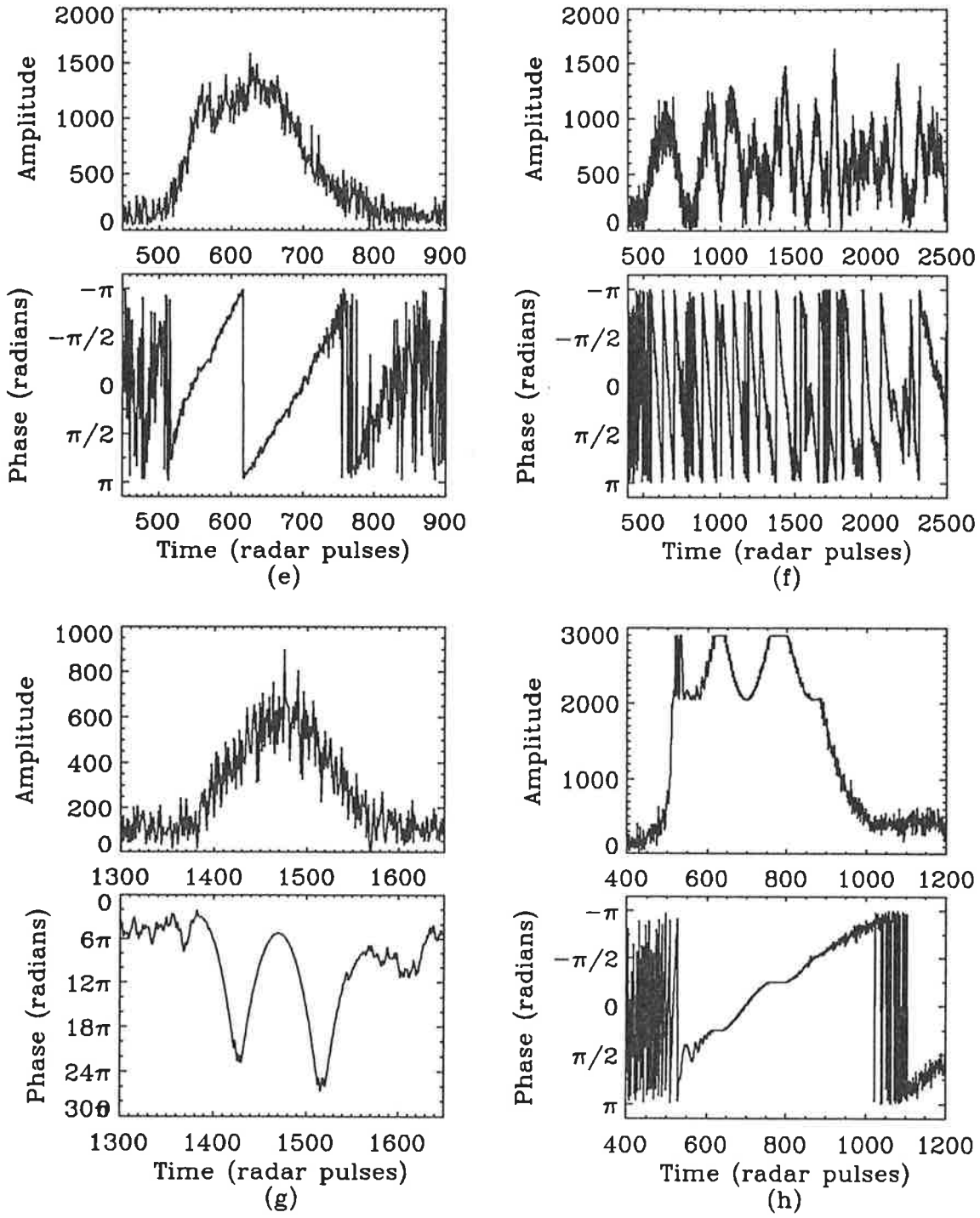

Figure 3.12: Meteor examples continued.

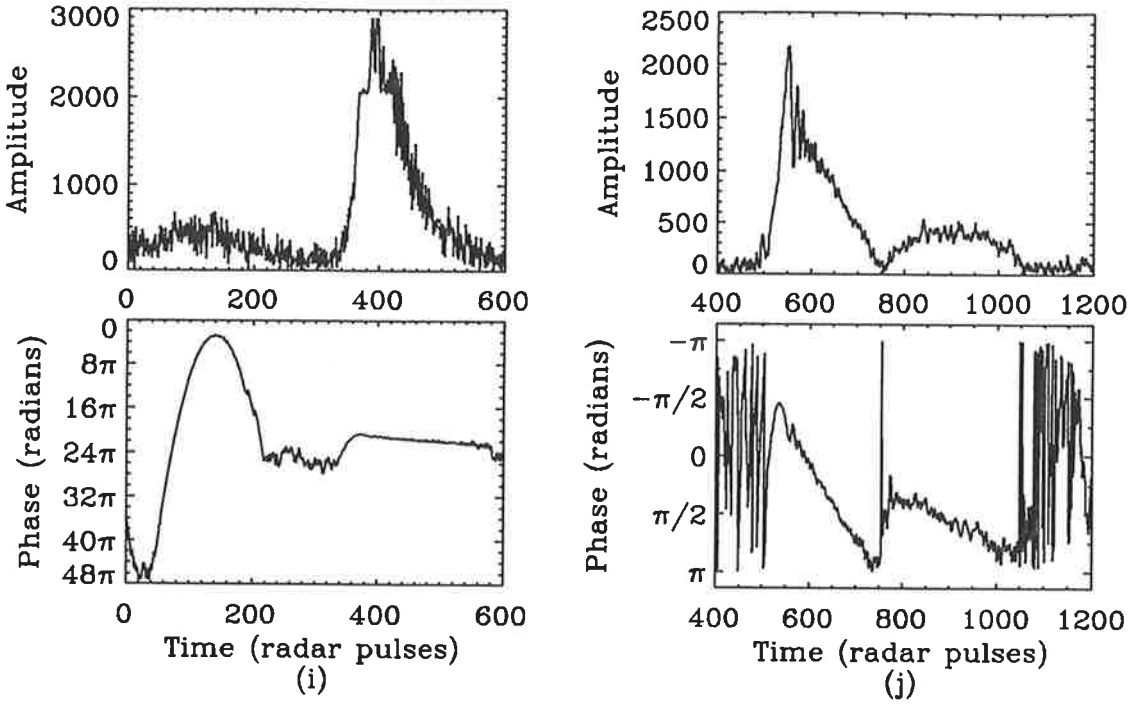

Figure 3.12: Meteor examples continued.

this reason, the saturated amplitude of the echo from 510 to 890 radar pulses, displays a "scalloped" profile, and a flat truncated level is observed only when both the in-phase and in-quadrature signals are saturated. The saturated phase information displays a flat constant level when the amplitude is truncated, while at other times the phase appears to retain some valid information although it is distorted to some extent. Clearly saturated meteor echoes are not simple to interpret and the analysis must be undertaken with care. The saturation of signals in the receiver and how they affect the meteor echoes is discussed in more detail in the next section.

The next meteor example (i) displays what appears to be two echoes, a typical underdense echo (although the peak saturated the receiver) and an echo some 220 ms prior similar to that displayed in (g) which was interpreted as being due to a very short (in radio terms) trail. This meteor was detected at 23:22 CST on the 6^{th} June 1994, at a range of 100 km. The phase information has been unwrapped so as to show the parabolic nature of the first portion of the phase record. One explanation of this record is that there are indeed two echoes, which are detected at the same range within a short period of time. The fact that the two echoes show very different decay characteristics may be explained by assuming one was detected in a sidelobe and thus occurred at a different height. For example, if a meteor is detected in one of the first sidelobes (about 7° from the bore) at a range of say 100 km,

then the meteor will be interpreted to have ablated at a height either 5.5 km lower or 6.5 km higher (dependent on which sidelobe) than the actual height. The range gates are 2 km wide, therefore this adds a possible extra 4 km to the height difference. This would be enough to explain the different decay rates of the two echoes.

If the above interpretation of the record displayed in panel (i) as a double event is correct then one would expect to observe meteors detected within very short short time intervals of each other, in the same range bin, and both in the main beam of the radar, and therefore displaying about the same decay rates. While such records have been observed, they are about 1 - 2 orders of magnitude less frequent than the type of record displayed in panel (i). This suggests, that the "two events" in (i) are associated with a single meteor and the first portion of the echo is due to the aspect insensitive head of the meteor prior to the formation of the trail, *i.e* this echo is a "traditional" meteor head echo. If this is the case, then the following two points must be verified: (1) the meteor velocity obtained from the head and the trail portions of the echo must be the same, and (2) both portions of the echo must be shown to occur within the same range gate.

The method used to deduce the meteor velocity from the trail and head portions of record (i) was a new technique which uses the pre-t_0 phase, developed in Chapter 5. The velocity obtained from the meteor head is $38.1 \pm 0.5\, km\, s^{-1}$, while the velocity obtained from the trail is slightly smaller being $37.3 \pm 0.3\, km\, s^{-1}$. Note, the meteor head echo occurs from a region further back along the meteoroid's path than the trail echo and the trail in this region is no longer orthogonal to the beam. Therefore only a component of the velocity is measured (see 3.13). The velocity obtained from the meteor must be multiplied $1/cos(\theta)$, where θ is the off beam axis angle subtended by the meteor head (see 3.13). Using the velocity obtained from the trail, the distance, s, back along the meteoroid's path where the meteor head is detected, is about 8.2 km. Thus a value for θ of 4.3° is obtained, and the velocity determined from the meteor head is found to be $38.2 \pm 0.5\, km\, s^{-1}$, which is about $0.9\, km\, s^{-1}$ greater than the velocity obtained from the t_0 region. The lower velocity obtained from the t_0 region is of course due to deceleration of the meteor, and a mean deceleration of $4\, km\, s^{-2}$ is obtained for this meteor (see Chapter 5 for a detailed discussion on meteor decelerations).

The range to the meteor head is calculated to be about 300 m greater than the range to the t_0 point, therefore the meteor head and trail echoes occur within the same range gate as required. The half-power full-width of the beam is about 3.8° which means that it is unlikely

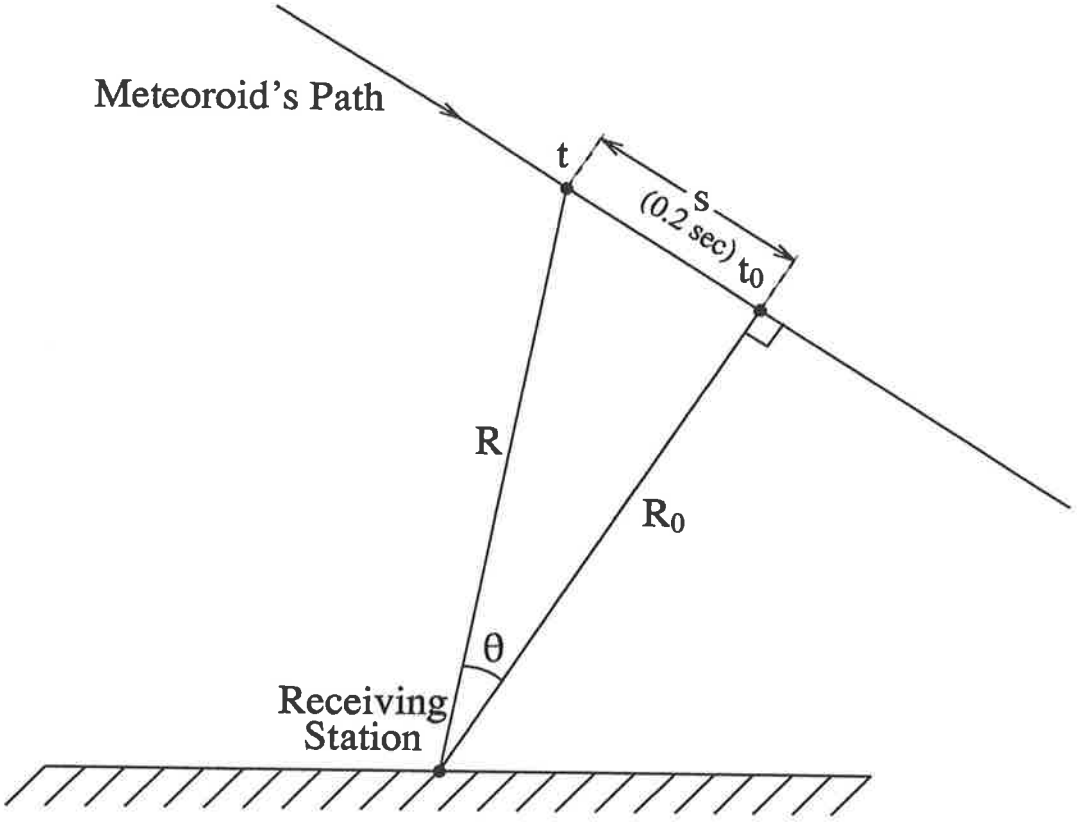

Figure 3.13: Schematic of the geometry of meteor head echo detection. The meteor head is observed at a distance, s, back from the t_0 point at time, t.

that the head and trail portions of the echo both occur in the main beam (considering that $\theta = 4.3°$). It is more probable that the meteor head was detected in the first sidelobe and the trail in the main beam of the radar.

Further confirmation that the echo displayed in Figure 3.12i is a head echo, may be gained through the prediction of the position of the phase minima associated with the meteor head, from the information provide by the phase information associated with the trail. From panel (g) we see that the when the rate of change of phase exceeds the Nyquist frequency, the phase still behaves in a well behaved manner that may be modeled. In fact if the phase record is long enough, the phase will pass through successive minima each of which occurs at a frequency given by an integer multiple of twice the Nyquist frequency. If the signal were sufficiently strong then cusps, the same as that which occur at the Nyquist frequency, would appear at every odd integer multiple of the Nyquist frequency (*Elford*, private communication). These features are due to the aliasing of the phase information and is easy to verify using a simple model which will not be reproduced here. Using this information, the phase minima associated with the head in panel (i) must occur at an aliased frequency of 1024 Hz (Nyquist

frequency is half PRF or $512\,Hz$). Now the rate of change of phase is given by:

$$\begin{aligned} \frac{d\phi}{dt} &= \frac{2}{\lambda}\frac{dR}{dt} \\ &= \frac{2V sin(\theta)}{\lambda}, \end{aligned} \tag{3.37}$$

where R is the range and V is the meteor velocity. From geometry, the following equation holds:

$$sin(\theta) = \frac{VT}{R_0}, \tag{3.38}$$

where R_0 is the range at the t_0 point ($110\,km$) and T is the time interval between the occurrence of the head and trail phase minima (measured to be $0.225\,sec$). Thus from substitution the following equation is obtained:

$$T = \frac{R_0}{2V^2}\frac{d\phi}{dt}. \tag{3.39}$$

Therefore the predicted time interval between the head and trail phase minima is predicted to be $0.224\,sec$ which agrees well with observation.

The final echo which will be examined was observed at 20:52 CST on the 7^{th} June 1994, at a range of $98\,km$, and is displayed in Figure 3.12j. This echo is believed to be from a trail that has become deformed such that there are two scattering points, whose signals beat with each other. One may observe the "bite-out" in the amplitude information at around 750 radar units, and the corresponding jump in the phase at this time. Consider Figure 3.14, this displays in panel (a) an example of two signals with amplitudes A_1 and A_2. The first signal (A_1) has a fixed phase, ϕ, while the second (A_2) varies at a constant rate with respect to the first. The sum of the two signals is a vector whose locus describes the dashed circle as a function of time. The amplitude of the resulting vector varies sinusoidally as a function of time (top panel of Figure 3.14b), with maximum and minimum amplitudes of $A_1 - A_2$ and $A_1 + A_2$ respectively. The phase of the resulting vector (bottom panel of Figure 3.14b), also varies sinusoidally. The minimum and maximum values of the phase (ϕ_{min} and ϕ_{max} respectively) are defined by the angles which the two tangents to the circle passing through the origin, make with the real axis. Also noted from Figure 3.14b is that the resulting amplitude and phase variations are in quadrature. This is typical of beating signals.

The model described above is an over simplification; in reality both signals not only have a varying phase but also varying amplitudes. Although this is the case, meteor echoes which have been modified by two beating signals should display the basic characteristic of amplitude and phase variations from the expected "no-beat" echo which are in quadrature.

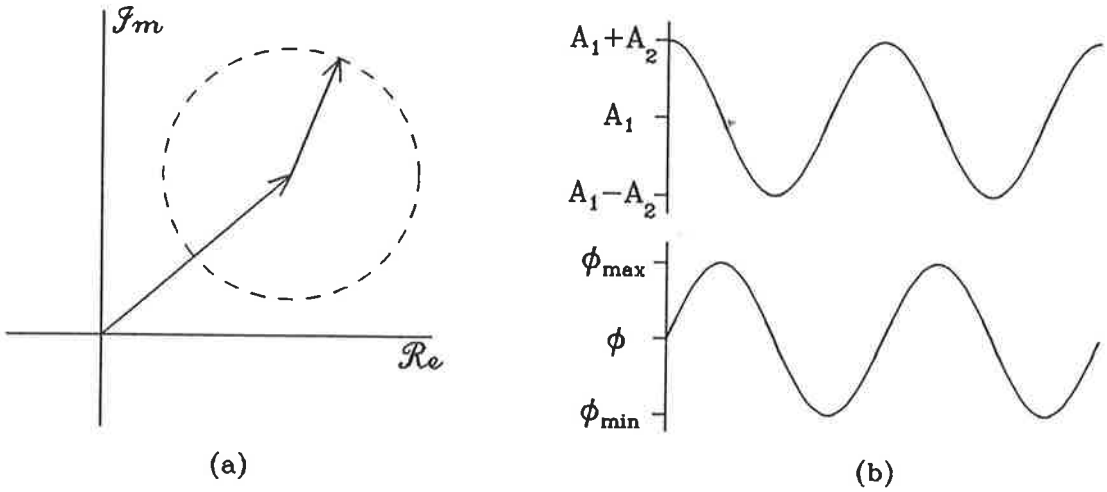

Figure 3.14: Example of two interfering constant amplitude signals (a) and the resulting amplitude (top b) and phase (bottom b). The first signal (amplitude A_1) has a constant phase, ϕ, while the second signal (amplitude A_2) has a phase which varies at a fixed rate. The dashed circle in (a) is the locus of the resulting sum of the two signals.

This characteristic may be observed in the echo shown in Figure 3.12 when the section of the echo from 700 to 800 radar pulses is redisplayed in Figure 3.15. The smooth line in each panel is a fitted 3^{rd} order polynomial to the data. The phase variation is clearly in quadrature with the amplitude variation suggesting that this echo was indeed the product of two beating signals.

3.4.3 The effect of receiver saturation on the returned meteor echoes

In the previous section, an example of a meteor echo which has saturated the radar receiver was shown (Figure 3.12h). A brief explanation of the form of the echo was given. In this section the effects of receiver saturation will be treated more fully.

In Figure 3.16, the phasor 'A' describes a signal with a constant unsaturated amplitude A, and a phase which varies at a constant rate. The dashed box in each panel delineates the range over which the in-phase and in-quadrature components of the signal is not saturated. In panel (a), we see that the signal has a phase such that the in-quadrature component is less than the upper bound of the dashed box and is therefore not saturated. However, the in-phase component exceeds the right bound of the box and therefore is saturated. The actual signal that is observed may be found by truncating the in-phase component to the limiting level (dotted line parallel to the in-phase axis), and this saturated signal has a amplitude A'.

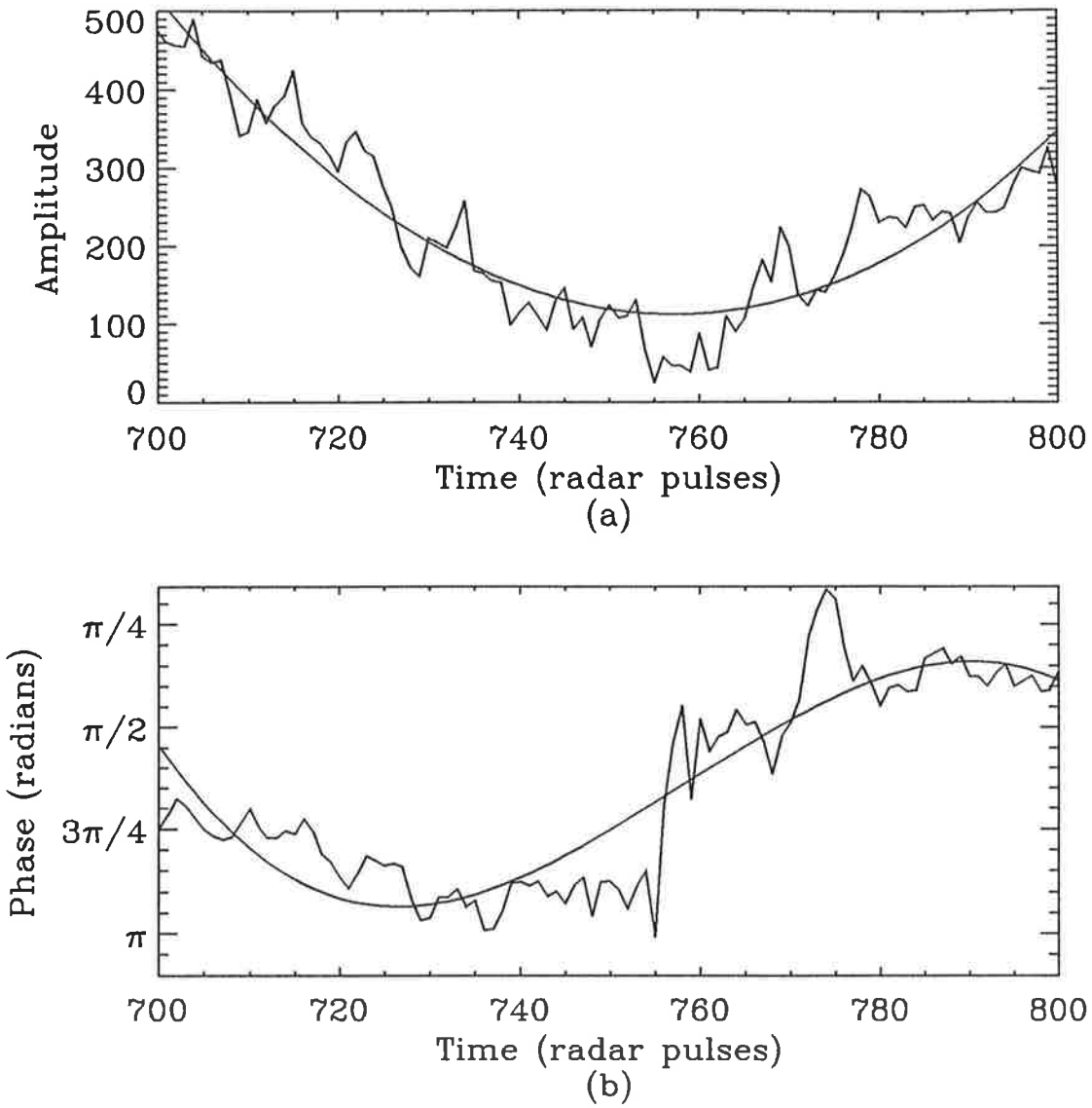

Figure 3.15: Section of the echo displayed in Figure 3.12j (from radar pulse 700 to radar pulse 800). The smooth line in each panel is a fitted 3^{rd} order polynomial to the data.

There are two things to note from panel (a); the first is that $A' < A$, and the second is that the phase of the saturated signal is different (in this case advanced) from the true phase of the signal. Note that if the signal had a zero phase (*i.e.* the in-quadrature component is zero), then the saturated amplitude, A', would be smaller (in fact the minimum value), but the phase error would be zero.

Panel (b) shows the situation a short time later; although the in-quadrature component has not started to saturate, it is observed that the saturated amplitude and the error in the phase have both increased. In panel (c), it is observed that the error in the phase has decreased from that in panel (b), this error will actually become zero when the phase of the

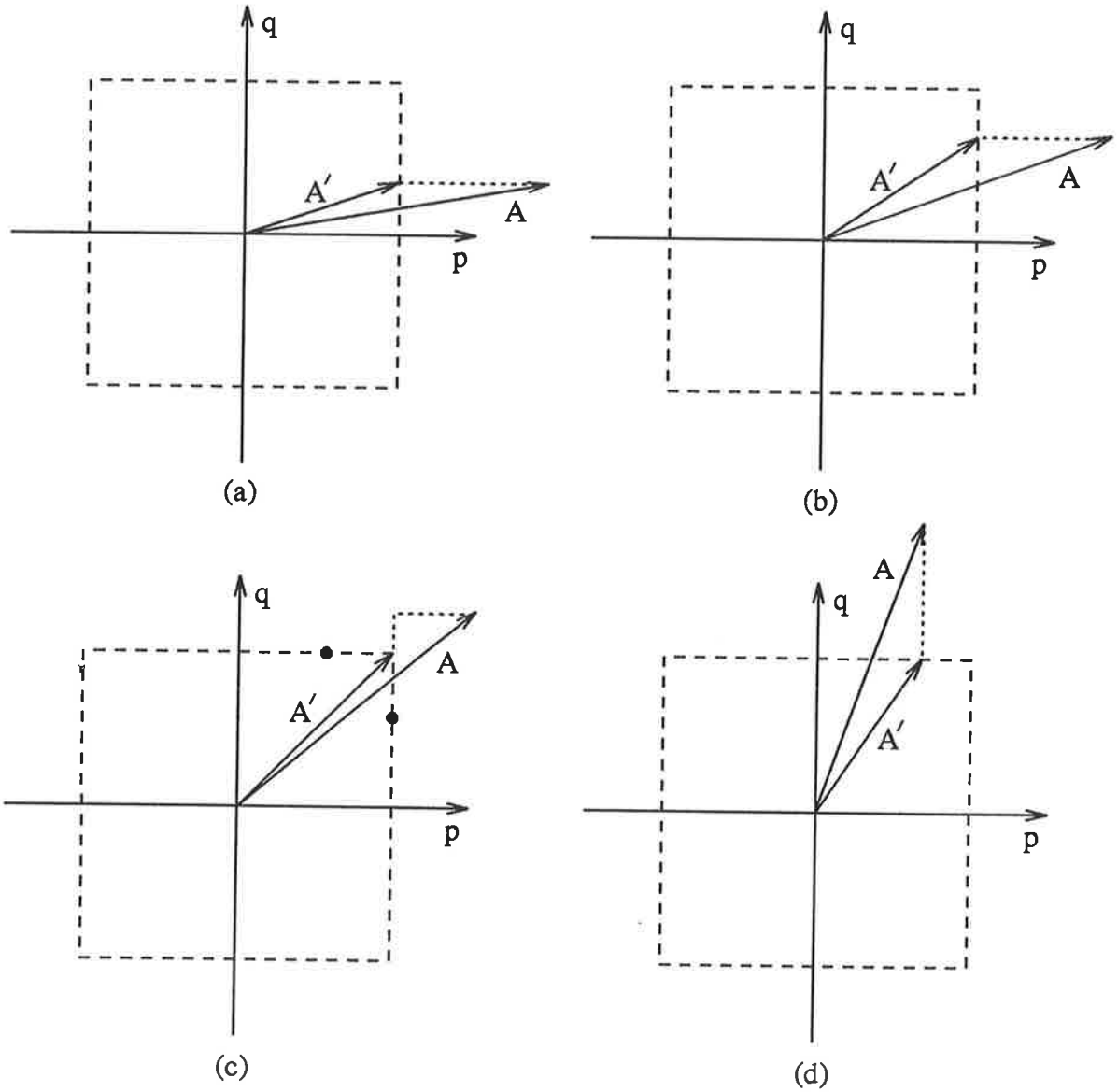

Figure 3.16: Effect of saturation on a signal of constant amplitude and varying phase. Each panel shows the signal at successively increasing times, the dashed box in each case delineates the region where the in-phase and in-quadrature components are not saturated. The original signal is the vector labeled A, while the saturated signal is the vector labeled A'. The two solid circles in panel (c) delineates the region within which the saturated signal has a constant amplitude and phase.

unsaturated signal is $\pi/4$ radians. The point where the phase error stops increasing and starts to decrease is where the phase of the original signal is $\pi/8$ radians. The other point to note is that when the unsaturated signal lies between the two solid circles, both the in-phase and in-quadrature components are saturated. Thus, in this region the saturated signal has both a constant amplitude (the maximum possible) and a constant phase ($\pi/4$ radians).

Finally in panel (d), the phase of the signal has increased so that now only the in-phase component is saturated. The amplitude of the saturated signal has decreased, and the phase error has increased, the phase of the saturated signal now lagging the actual phase. As the phase of the original signal increases further, the amplitude of the saturated signal will continue to decrease until the in-phase component is zero in which case the amplitude will be at a minimum again. The phase error will increase up to a point (where the phase of the original signal is $3\pi/8$ and then decrease to zero when the in-phase component is zero.

The above process is repeated as the signal rotates through the other three quadrants. Thus, over one complete phase cycle, the saturated signal completes four identical sub-cycles. The saturated amplitude and phase are plotted as a function of time for one complete phase cycle in Figure 3.17. In this figure the in-phase and in-quadrature saturation levels were set to 2048 units, and the amplitude of the original signal is 3500 units. Note the "scalloped" profile of the amplitude which truncates at an amplitude given by the square root of the sum of the squares of the saturation levels (2896 units). The minimum amplitude is of course 2048 units. This amplitude profile is identical to that observed in the meteor echo displayed in Figure 3.12h. The phase information (bottom panel) displays a much smaller effect due to saturation than the amplitude. In fact the error induced in the phase information is quite small even though the amplitude information is greatly distorted. The maximum error in the amplitude is about 41% while the maximum error in the phase is only about 3.1% over one complete phase cycle. Thus, despite the amplitude showing a high degree of saturation, the phase is still well behaved, with information (such as radial drift velocities) being able to be deduced from it. It should be noted that the phase information displayed in Figure 3.17 displays a constant value (plateau) when the amplitude is truncated as explained in the discussion about Figure 3.16. This characteristic is also observed in the meteor echo shown in Figure 3.12h.

Consider now a reduction in the amount of saturation, either through a reduction in amplitude of the original signal, or an increase in the level at which the in-phase and in-quadrature components saturate. The two solid circles in Figure 3.16c move in closer to

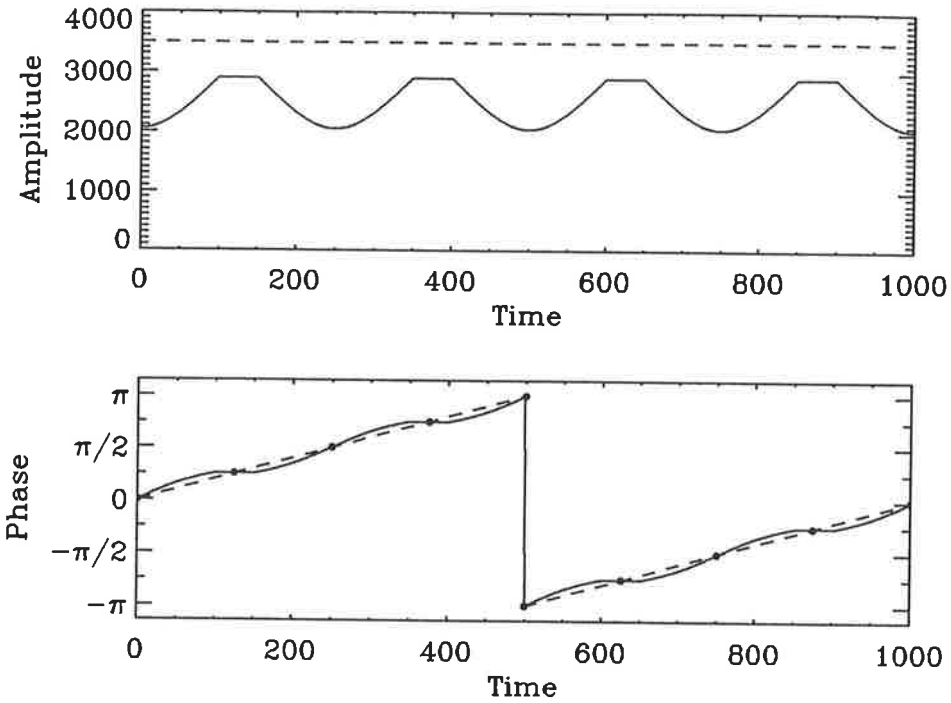

Figure 3.17: The amplitude (top) and phase (bottom) variation of a constant amplitude saturated signal for one phase cycle. The dashed line in each panel refers to the true amplitude and phase of the signal. The amplitude and time scales are in arbitrary units. The solid circles in the bottom panel denote where the phase of the saturated signal agrees with the true phase. The in-phase and in-quadrature saturation levels were set to 2048 units, and the amplitude of the original signal is 3500 units.

the corner of the square, thus reducing the amount of time the amplitude and phase are constant. The critical case is when the amplitude of the signal is equal to the square root of the sum of the squares of the saturation levels. This case is shown in Figure 3.18. For this situation the saturated amplitude agrees with the actual amplitude of the signal at discreet points. These points occur whenever the phase is an integer multiple of $\pi/4$. The maximum error in the amplitude is still large, being about 32%, but the error in the phase is now under 1.7% over one complete phase cycle.

If the amount of saturation is decreased further (the signal amplitude is now less than the square root of the sum of the squares of the saturation levels) the amplitude agrees with the actual amplitude for a length of time and then "drops out" when one of the components saturates. An example of this is shown in Figure 3.19, again the in-phase and in-quadrature components saturate at 2048 units, but now the unsaturated signal amplitude is 2300 units. One may observe that the amplitude gives the correct value about 41% of the time. The maximum error in the amplitude is still relatively large (about 11%) but the error in the

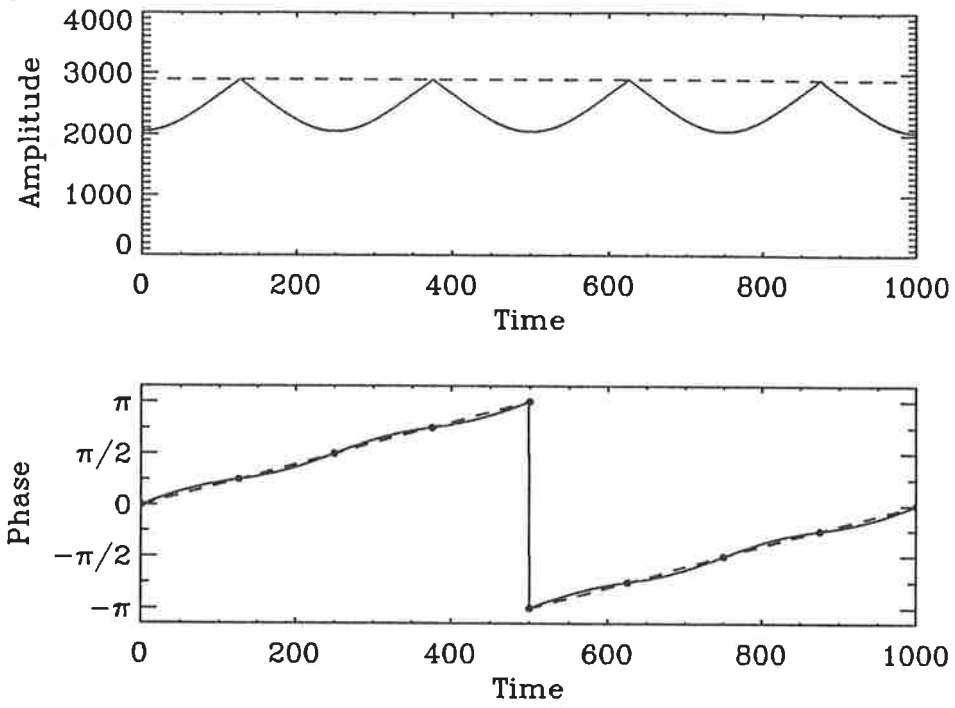

Figure 3.18: As for Figure 3.17, except the amplitude of the original signal is now equal to the square root of the sum of the squares of the saturation levels (2896 units).

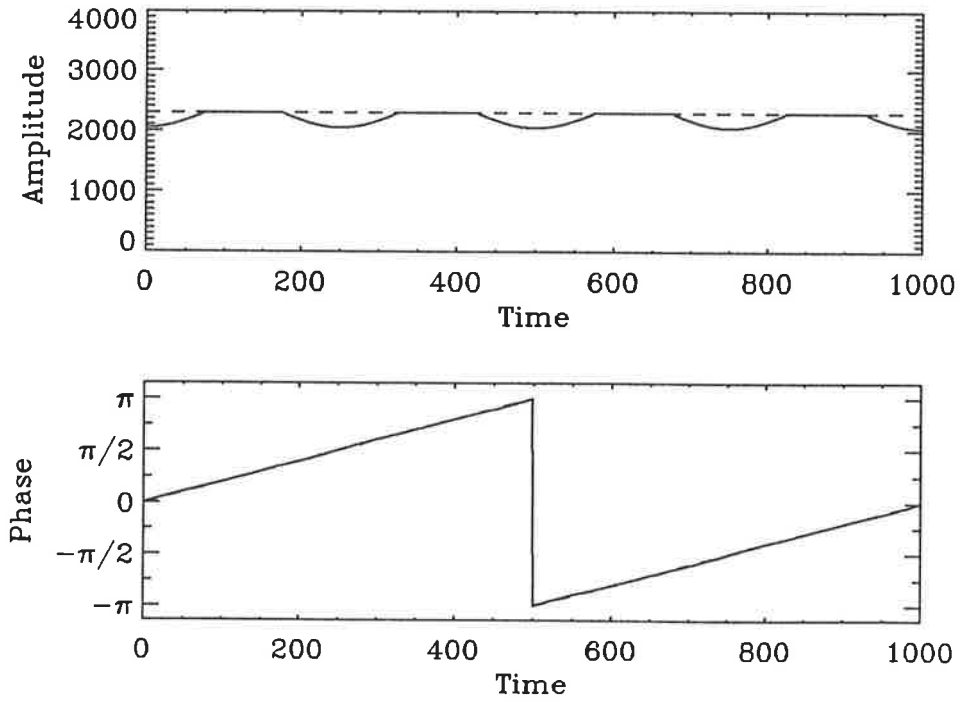

Figure 3.19: As for Figure 3.17, except the amplitude of the original signal is now less than the square root of the sum of the squares of the saturation levels (2896 units) being 2300 units.

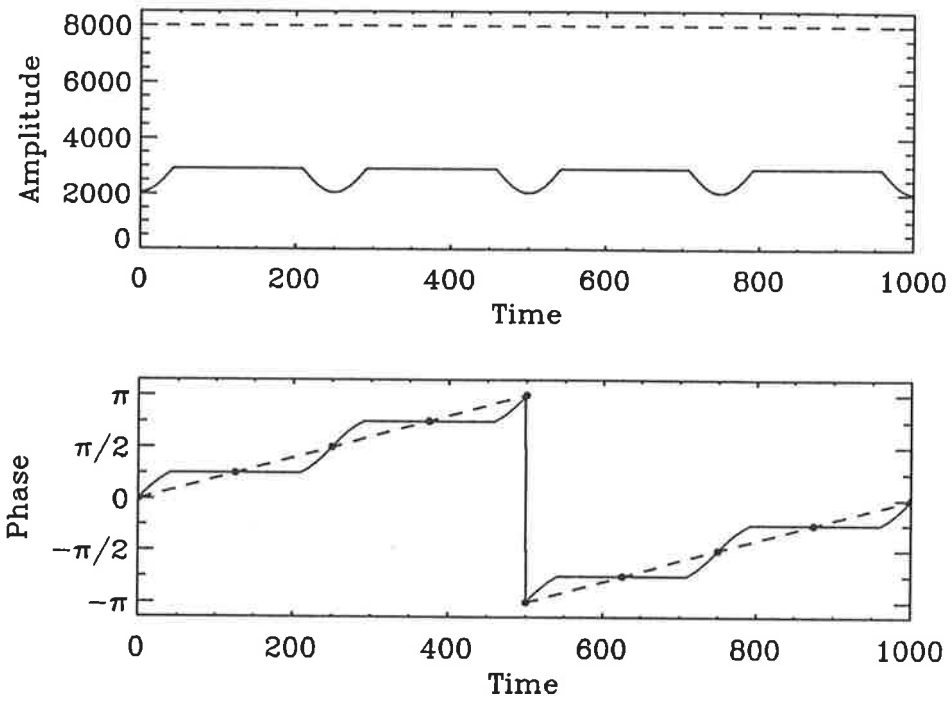

Figure 3.20: Example of extreme saturation. Details are as for Figure 3.17, except the amplitude of the original signal is now 8000 units.

phase is now negligible (about 0.3% over one cycle) and is generally less than the error in the phase due to random noise in most meteor echoes.

The case of extreme saturation is now examined. In Figure 3.20 the in-phase and in-quadrature saturation levels are again 2048 units, but now the signal amplitude is well in excess of this being 8000 units. One may observe that the amplitude information is highly saturated, while the phase profile is approaching a step function. Even so the original phase information may be retrieved (dashed line) from the saturated phase by fitting a straight line to the points denoted by the solid circles where the saturated phase is known to be correct. In fact one may fit the straight line to the *entire* saturated phase record and still obtain the correct phase due to the symmetry of the saturated phase variations.

In addition, not only can the original phase be recovered, it is possible to also recover the original amplitude! This is realised through the consideration that the length of time which the saturated phase is constant, increases with the level of saturation. However, first consider again Figure 3.16c. Recall the two solid circles delineates the region over which the saturated signal has a constant phase (and amplitude). At the time the original signal is just entering this region, the amplitude of this signal may be expressed as $A = L/sin\theta$,

where L is the saturation level, and θ the phase of the original signal at this time. As the original phase has already been recovered, θ is known. More formally, one may show from consideration of the phase record displayed in Figure 3.20, that $\theta = \pi(T - T_c)/4T$, where T is the time between points where the saturated phase is correct and T_c is half the time over which the saturated phase is constant. Thus, the original amplitude of the signal is:

$$A = L\left[sin\left(\frac{\pi(T - t_c)}{4T}\right)\right]^{-1} . \tag{3.40}$$

For the example displayed in Figure 3.20, $T = 125 \pm 0.5$ units, $T_c = 41 \pm 0.5$ units, and $L = 2048$ units. Therefore the recovered amplitude is calculated to be 8040 ± 100 units, which is in agreement with the original signal amplitude.

3.5 Summary

In summary, this chapter has been concerned with the fundamental theory of meteoric phenomena, the observing routine used to detect meteors, and preliminary observations of meteors with the upgraded Buckland Park radar.

The effects of noise, coherent averaging, and receiver saturation on the returned meteor echo were examined in detail and the following were discovered: (1) The phase of a signal is more readily discerned from the noise than the amplitude, (2) Coherent averaging of the data may be performed to increase the signal-to-noise ratio, the trade-off being a reduced time resolution, and (3) While the effects of receiver saturation on the echo amplitude are large, the effects on the phase are quite small. In fact, even for cases of extreme saturation, the phase was shown to be correct at intervals of $\pi/4$, and therefore the actual phase may be interpolated from the saturated case. This can then be used to recover the amplitude.

Preliminary observations of meteors were detailed so as to build a case study of the various types of echoes detected with the Buckland Park VHF radar. These included underdense and overdense echoes, meteor echoes which displayed the effects of saturation, the effect of beating on the echo due to scattering at two or more distinct points on the trail, and meteor head echoes. Rapidly diffusing meteor trails were also observed. In these cases the radio length of the trail is less than a Fresnel zone length and the resultant echo is head echo like, that is the echo appears to be that from a moving-ball target.

Chapter 4

The Response of Radar to Meteors

When too much sport is barely enough, it's not enough!

—Roy Slaven and H. G. Nelson

When too much beer is barely enough, it's not enough!

—Roy and H. G.'s quote restated by some Research Students

4.1 Introduction

In order to be able to interpret radar observations of meteor showers and back-ground sporadic meteors, it is necessary to know the response of the radar to meteors associated with a particular radiant. The response as a function of radiant position over the sky is known as the response function. The factors that determine the response function are: the antenna pattern of the radar, the flux of meteors as a function of mass or zenithal electron line density (usually assumed to be a power law), the ionization profiles of meteors, the polarization of the radio waves with respect to the meteor trail, the elevation of the meteor radiant, the minimum detectable electron line density of the radar system, attenuation factors due to the reflection properties of the trail and the detection criteria for a particular system.

The response function, once fully developed, will be used to model the height distribution and diurnal variation of meteors observed by the Buckland Park radar. More importantly, it will be shown that the knowledge of the response function of a narrow beam radar system may be used together with observations of the diurnal variation of meteor echo rates with that system to model the sporadic meteor radiant distribution. This may be performed

for each month of the year and for various meteoroid velocities. Thus, the distribution of sporadic meteoroids around the Earth's orbit may be described in much greater detail than previously possible.

Other applications of the response function include its use in the study of space debris, prediction of the time of passage of meteor showers, and the mass distribution of the meteoroid influx to the Earth. These will be detailed in Chapters 5 and 6.

4.2 The Development of the Response Function

The derivation of the response function for a backscatter radar has already been carried out (*Elford*, 1964; *Thomas* et al., 1988). The basis for this model was set down by *Kaiser* (1960) for the case of meteors with an idealized ionization profile, assumed to have a constant line density over a height range δh, and zero outside this range. The value of δh is taken to be $6.0\,km$ and the mean height, h_m, of the equivalent trail to be $90 - 95\,km$. The response function calculation using this model is reproduced here, and then generalized to the case of an ionization profile as given by classical ablation theory.

4.2.1 The response function calculation for a uniform ionization profile

The flux of meteoroids from a unit area of sky producing trails with electron line densities above a certain zenithal value[1], q_z, per steradian per second, is assumed to be a power law of the form :

$$N(q_z) = K {q_z}^c \quad . \tag{4.1}$$

Various estimates of the parameter c have been made from radar observations of meteors (*McKinley*, 1951; *Weiss*, 1961; *Kaiser*, 1953; *Kaiser*, 1961; *Elford*, 1964 and *Thomas et al.*, 1988). There is some uncertainty in these values. For example c appears to lie in the range -1.2 to -1.0 for meteors with electron line densities between 10^{10} and $10^{14}\,electrons\,m^{-1}$, while *Weiss* (1961) found from radar observations that for electron line densities in excess of 10^{15}, the value of c decreases to -1.5. Photographic observations of meteors by *Hawkins and Upton* (1958), give a value of c of -1.34 for meteor with electron line densities above $1.4 \times 10^{14}\,electrons\,m^{-1}$. However for underdense radar meteors, most results tend to point to a value for c of approximately -1.0 and it is this value that we shall use in the subsequent

[1]The zenithal electron line density is the electron line density that would be produced if the meteoroid was incident vertically (see Equation 4.10).

UNIVERSITY OF ADELAIDE LIBRARY

calculations.

If one is only interested in relative rate responses then the actual value of K is not needed as K is only a multiplicative factor in the response function; however as a point of reference, K has been calculated by *Thomas et al.* (1988) to be 1035 *particles* $m^{-2}s^{-1}ster^{-1}$ based on meteor observations with the Jindalee radar operating near 10 *MHz*.

Consider now Figures 4.1 and 4.2. These show the geometry for radio reflections from meteors from a particular radiant. A discussion on the theory of radio reflections from meteor trails can be found in Chapter 3. Due to the condition of specular backscatter from meteors, all possible reflections points from a particular radiant, lie in a plane which is normal to the radiant direction and which passes through the receiving site. This plane is called the echo plane and is the plane defined by the points ABCD in Figure 4.1. Consider a small element dS on the echo plane surface, where dS lies between heights $h - dh/2$ and $h + dh/2$. The echo rate from radiants which lie within a solid angle of $d\Omega$ about a radiant direction with an elevation of θ_r and azimuth of ϕ_r is then given by :

$$n(\theta_r, \phi_r)\, d\Omega = \int_{echoplane} N(q_z)\, dS\, d\Omega\,. \tag{4.2}$$

The function $n(\theta_r, \phi_r)$ is then the response of the radar to a meteor radiant of unit density in the direction (θ_r, ϕ_r) and is termed the meteor radar response function or simply the *response function.*

If R and Φ are the polar coordinates of the reflection point, P, in the echo plane, then a small element of area, dS, in the echo plane is given by :

$$dS = R\, d\Phi\, dR\,, \tag{4.3}$$

From Figure 4.1 we may also obtain the following relations between the elevation and azimuth, (θ, ϕ), of the reflection point, and the elevation and azimuth, (θ_r, ϕ_r), of the radiant.

$$\left.\begin{array}{ll} sin\theta = cos\theta_r\, cos\Phi\,, & 0 \le \theta \le \pi/2 \\ sin(\phi - \phi_r - \pi) = sin\Phi\, sec\theta\,, & |\phi - \phi_r - \pi| \le \pi/2 \end{array}\right\}. \tag{4.4}$$

The curvature of the Earth must be taken into account in the response function calculation. The geometry of this situation is shown in Figure 4.2. From this diagram we obtain the following expression :

$$(R_E + h)^2 = R_E^2 + R^2 + 2R_E R sin\theta \tag{4.5}$$

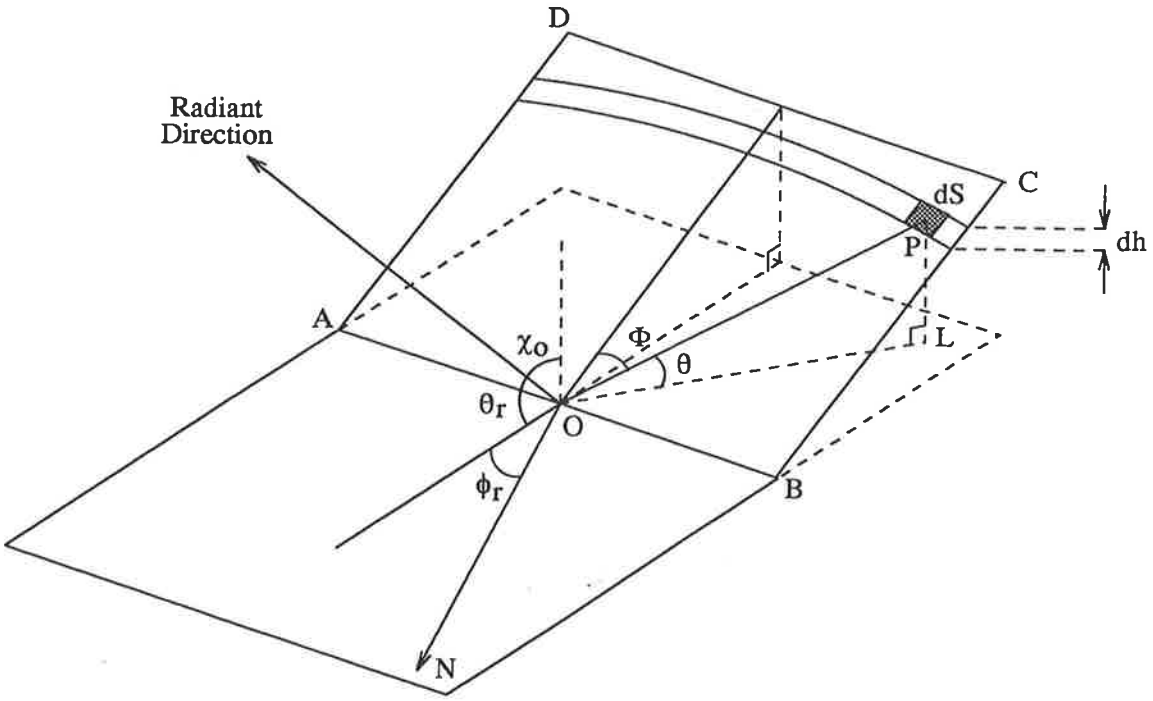

Figure 4.1: Geometry of the echo plane for the condition of specular backscatter

where θ is the elevation of the reflection point with respect to the observing station and R_E is the radius of the Earth. This may be rearranged to give the following expression for the range :

$$R = R_E \left[\left(sin^2\theta + \frac{2h}{R_E} + \frac{h^2}{R_E^2} \right)^{1/2} - sin\theta \right] . \tag{4.6}$$

Substituting 4.6 and 4.3 into 4.2 and rearranging, gives the following expression for the response function :

$$n(\theta_r, \phi_r) = R_E \int_{h1}^{h2} \int_{-\pi/2}^{\pi/2} N(q_z) f \left(1 + \frac{h}{R_E} \right) d\Phi dh . \tag{4.7}$$

where f is given by:

$$f = 1 - sin\theta \left(sin^2\theta + \frac{2h}{R_E} + \frac{h^2}{R_E^2} \right)^{-1/2} . \tag{4.8}$$

This may be rewritten using 4.4 to give the following expression for f for a given radiant elevation θ_r:

$$f(\Phi) = 1 - cos\theta_r \, cos\Phi \left(cos^2\theta_r \, cos^2\Phi + \frac{2h}{R_E} + \frac{h^2}{R_E^2} \right)^{-1/2} . \tag{4.9}$$

The final piece information required for the response function calculation is an appropriate value for the zenithal electron line density. Since the response function is the total

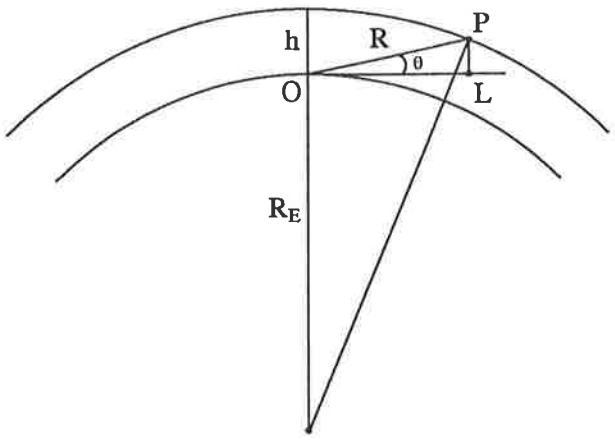

Figure 4.2: Geometry of a reflection point from a particular radiant direction with respect to the Earth's curved surface.

number of meteors detected from a radiant of unit density, the minimum detectable zenithal electron line density must be used. The zenithal electron line density is the electron line density produced if the meteoroid is incident vertically. Thus q_z is related to the electron line density, q, by the following equation:

$$q_z = \frac{q}{cos\chi} , \tag{4.10}$$

where χ is the zenith angle of the meteor radiant at the point of reflection. Due to the curvature of the Earth, χ, is actually slightly greater that the zenith angle of the radiant as measured at the observing station, which is denoted by χ_0 (see Figure 4.1). It can be shown that the following relation exits between the two quantities :

$$cos\chi_0 = \left(1 + \frac{h}{R_E}\right) cos\chi , \tag{4.11}$$

therefore, as $cos\chi_0 = sin\theta_r$, 4.10 may be rewritten as :

$$q_z = \frac{q}{sin\theta_r}\left(1 + \frac{h}{R_E}\right) . \tag{4.12}$$

The minimum detectable electron line density by a radar system for underdense meteors is given by the following (*Thomas et al.*, 1988) :

$$q_{min} = 4.5 \times 10^{15} \left(\frac{R}{\lambda}\right)^{3/2} P_R^{1/2} (P_T\, G_T(\theta,\phi)\, G_R(\theta,\phi)\, \alpha_r\, \alpha_v\, \alpha_d)^{-1/2} , \tag{4.13}$$

where λ is the wavelength, P_T the transmitted power, P_R the minimum detectable signal of the receiving system, G_R and G_T are the power gains of the receiving and transmitting arrays with respect to an isotropic radiator, α_r and α_v are the attenuation factors of the

echo power for underdense meteors. These attenuation factors are respectively due to the initial radius, r_0, of the meteor trail and the diffusion of the trail during the finite time of its formation. A discussion on α_r and α_v may be found in Section 3.2.3; however, due to their importance in the response function calculation a brief discussion on these attenuation factors follows in the next two paragraphs. The quantity α_d is an echo selection factor due the diffusion of the trail once formed and the meteor detection criteria. Equation 4.13 only applies to underdense meteors, the overdense case will be considered in the next section.

The finite initial radius, r_0, of the meteor trail causes attenuation in the echo power returned by underdense meteors given by (*McKinley*, 1961) :

$$\alpha_r = exp\left(-\frac{8\pi^2 r_0^2}{\lambda^2}\right), \tag{4.14}$$

and *Thomas et al.* (1988) derive from the results of (Baggaley, 1980, 1981) the following expression for the initial trail radius:

$$log_{10} r_0 = 0.019h - 1.92 + log_{10}(V/40), \tag{4.15}$$

where h is height in kilometers and V is the meteor velocity in km/s.

The attenuation due to the finite meteor velocity is given by (*Peregudov*, 1958; *Baggaley and Webb*, 1980):

$$\alpha_v = \frac{1 - e^{-\Delta}}{\Delta}, \qquad \text{where} \qquad \Delta = \frac{16\pi^2 D}{V}\left(\frac{R}{2\lambda^3}\right)^{1/2}, \tag{4.16}$$

where V is the meteoroid velocity, D the ambipolar diffusion coefficient and λ the wavelength of the radar. *McDaniel and Mason* (1973) show that the ambipolar diffusion coefficient is given by:

$$D = 6.39 \times 10^{-2} T^2 \frac{K}{p} \tag{4.17}$$

where T is the temperature, p the pressure of the atmosphere and K is the zero field reduced mobility of the ions. The value of K is not known for the actual case of meteoric ions in air, but experimental studies of alkali ions in atomic nitrogen give a value of $K \approx 2.2 \times 10^{-4} m^2 s^{-1} V^{-1}$. In the subsequent response function calculations detailed here, the temperature and pressure are obtained from the CIRA86 model of the middle atmosphere.

Once the trail has formed, the returned echo power from an underdense trail will decay exponentially due to the diffusion of the trail. *McKinley* (1961) gives the reduction in echo

power after a time t to be:

$$P(t) = P(0)exp\left(-\frac{t}{\tau}\right) , \tag{4.18}$$

where the decay time constant, τ, is given by :

$$\tau = \frac{\lambda^2}{16\pi^2 D} . \tag{4.19}$$

Clearly this causes a selection bias against short duration echoes. The selection effect is dependent on f_{prf}, the pulse repetition frequency of the radar, and also on the meteor echo detection criteria. The selection effect is more severe for systems with lower PRF's. *Elford* (private communication), has shown for the detection criteria used by the Buckland Park VHF radar (see Chapter 3), that α_d is given by:

$$\alpha_d = \frac{e^{\omega} - 1}{\omega\, e^{\omega}} , \tag{4.20}$$

where ω is a function of f_{prf}, τ, and the mass index, c, as given by the following expression:

$$\omega = \frac{-c}{f_{prf}\ \tau} . \tag{4.21}$$

On substitution of 4.12 into 4.2 and using 4.13, the following expression for the response function is obtained :

$$n(\theta_r, \phi_r) = \int_{h1}^{h2} A \int_{-\pi/2}^{\pi/2} [G_T(\theta,\phi)\, G_R(\theta,\phi)]^{-c/2} F(\Phi) \left(1 + \frac{h}{R_E}\right)^{c+1} d\Phi\, dh , \tag{4.22}$$

where

$$A = R_E \left[4.5 \times 10^{15} \left(\frac{R_E}{\lambda}\right)^{3/2} \left(\frac{P_R}{P_T \alpha_r \alpha_v \alpha_d}\right)^{1/2} cosec\theta_r\right]^{c} , \tag{4.23}$$

and

$$\begin{aligned} F(\Phi) \;=\; & \left[\left(cos^2\theta_r cos^2\Phi \;+\; \frac{2h}{R_E} + \frac{h^2}{R_E^2}\right)^{1/2} \;-\; cos\theta_r cos\Phi\right]^{3c/2+1} \\ & \times \left[cos^2\theta_r cos^2\Phi \;+\; \frac{2h}{R_E} + \frac{h^2}{R_E^2}\right]^{-1/2} . \end{aligned} \tag{4.24}$$

In the above expression for the response function, $(1+\frac{h}{R_E})^{(c+1)} \approx 1$ to within 0.3% therefore this term may be ignored. The quantity A is a function of height through α_r, α_v and α_d.

Using the approximation described previously for the electron line density profile, the expression for the response function becomes :

$$n(\theta_r, \phi_r) = \Delta h\, A \int_{-\pi/2}^{\pi/2} [G_T(\theta,\phi)\, G_R(\theta,\phi)]^{-c/2} F(\Phi)\, d\Phi , \tag{4.25}$$

and

$$F(\Phi) = \left[\left(cos^2\theta_r cos^2\Phi + \frac{2h_m}{R_E} + \frac{h_m^2}{R_E^2}\right)^{1/2} - cos\theta_r cos\Phi\right]^{3c/2+1} \times \left[cos^2\theta_r cos^2\Phi + \frac{2h_m}{R_E} + \frac{h_m^2}{R_E^2}\right]^{-1/2} . \quad (4.26)$$

Calculation of the response function described by Equation 4.22 requires integration over height with a suitable height distribution of electron density being used (see *eg. Thomas et al.*, 1988). While integration over velocity with a suitable velocity distribution is also required for the full solution, this was not performed by *Thomas et al.* Calculations of the response function for the Buckland Park VHF radar show that the shape of the response function is not a function of velocity (as can be seen from 4.22), nor does it change at different heights over which meteors typically ablate (*i.e.* 70 - 110 km). Only the magnitude of the response is height and velocity sensitive. Therefore if one is interested in the relative response function only (*eg.* for meteor radiant determination, and theoretical diurnal variation calculations), integration over height and velocity is not required and the response function can be normalised to the peak response.

4.2.2 The treatment of overdense echoes in the response function calculation

Attention is now turned towards the treatment of overdense echoes in the response function calculation. The model that shall be employed is simple; meteor trails with an electron line density under a certain transitional value, q_{tr}, are regarded as underdense, while above this value they are regarded as overdense. This is, in actuality, a rather crude approximation; the transition from underdense to overdense is a gradual one taking place over electron line densities in the region 10^{13}–$10^{15}\, electrons/m$. To model this fully the consideration of the reflection coefficients of the scattering process (*Poulter and Baggaley*, 1977, 1978) is required. In addition, the effect of the polarization of the incident radio waves with respect to the trail, which is not included in the existing response function calculation, may be modeled through the consideration of the reflection coefficients, although for $q < 10^{12}$ the reflection coefficients perpendicular and parallel to the trail are approximately equal. A more detailed discussion on the radio wave scattering process from underdense and overdense trails may be found in Chapter 3.

A discussed in Section 3.2.4, radio wave scattering from a fully overdense meteor trail may

be modeled as scattering due to a metallic cylinder (see *eg. McKinley*, 1961) which expands as the trail diffuses. When the electron density falls below the critical level, the trail becomes underdense and decay of the echo takes place as usual. Typically values for the transitional electron line density, lie in the range 1–2 $\times$ $10^{14}\,electrons/m$; however, for our purposes a value of $0.75 \times 10^{14}\,electrons/m$ will be used. This is because at this value, the returned echo power as calculated for the overdense case (Equation 4.27) and the underdense case are equal. The returned echo power, P, from an overdense trail is given by (*eg. McKinley*, 1961):

$$P = 1.6 \times 10^{-11} P_T G_R G_T \left(\frac{\lambda}{R}\right)^3 q^{1/2} \,. \tag{4.27}$$

Note that the echo attenuation factors, α_r and α_v, do not affect the returned echo power as for the underdense case. Equation 4.27 may be recast to give the minimum detectable electron line density of an overdense trail, q^{od}_{min}. Thus,

$$q^{od}_{min} = 3.9 \times 10^{21} \left(\frac{R}{\lambda}\right)^6 \frac{P_R^2}{P_T^2 G_R^2 G_T^2} \,, \tag{4.28}$$

and this equation is used in place of Equation 4.13 for the calculation of the response to overdense meteors, *i.e.* when the electron line density exceeds q_{tr}. However, before this can be done the effect of any echo selection factors which could modify Equation 4.28 must be considered.

Echo selection factors for the overdense case could become important when the duration of the echo becomes comparable to the data sampling period, T, of the detection algorithm. If T_{ov} is greater than the data sampling period then clearly echo selection effects do not apply. However, they must be considered if T_{ov} is less than the sampling period. For overdense meteors occurring at high altitudes, the subsequent decay once they become underdense, is so rapid the echo profile may be approximated by a boxcar of duration T_{ov}. This would suggest that for short duration overdense trails an echo selection factor could be derived based on its duration as compared to the sampling period. For example, if $T_{ov} < T$, then it may be shown that the probability of detecting the meteor on a single pulse is T/T_{ov}.

In practice, it is not necessary to consider this effect. The width of the radar beam at a range of say $100\,km$, is about $7\,km$. Therefore even a high speed meteoroid (say $70\,km\,s^{-1}$) will be within the beam for a relatively long period of time ($0.1\,s$ in this case) as compared to the sampling rate. The meteor will resemble a moving ball-target and the echo profile is directly related to the antenna pattern. Thus, Equation 4.13 was not required to be modified for the calculation of response to overdense meteors.

4.2.3 The full response function using classical ablation theory

The response function derivation is now reworked to take into account of the ionization profile. In deriving the expression for the response function, as given by 4.22, the cumulative flux of meteors above a given zenithal electron line density, q_z, was used. From 4.22, it is difficult to see how to include the ionization profile of meteors, hence the use of the approximation which leads to 4.25. With this in mind, a different approach to the derivation of the response function is required Instead of starting with the cumulative flux per unit solid angle of meteors above a zenithal electron line density given by 4.1, the cumulative flux of meteors from an element $d\Omega$ on the celestial sphere above a given mass is used. The cumulative mass flux per unit solid angle, $N(m)$, is assumed to be:

$$N(m) = K' m_\infty^c \tag{4.29}$$

where the previous discussion on c holds here as well. However, the value of c must be examined as a function of mass. *Hughes* (1978) summarises the results of various observations from satellite, radar, visual and photographic experiments. For masses greater than $10^{-2} gm$, meteors are detected by visual techniques and c has a value of $\sim$-1.6. For masses in the range of 10^{-2} to $10^{-6}\, gm$, meteors are detected by radar and c has a value of -1.03. Satellite results give c to be -0.55 for masses less than $10^{-6}\, gm$. The results of *Thomas et al.* (1988) with the Jindalee radar, give c to be -1.0 for masses between 10^{-7} and $10^{-4}\, gm$. This mass range overlaps with the upper end of the satellite results. The Buckland Park VHF radar detects meteors produced by meteoroids with initial masses greater than $1 \times 10^{-6}\, gm$ (see discussion on classical ablation theory later), thus a value for c of -1.0 is appropriate for the radar.

The value of K' may be estimated as follows: the flux of particles ablating in the Earth's atmosphere, $\mathcal{F}$, may be expressed as $n_t/4\pi\mathcal{R}^2$, where n_t is the total number of meteoroids with masses $\geq\ m_\infty$ entering the Earth's atmosphere per second and $\mathcal{R}$ is the radius of the Earth plus the height at which meteors typically ablate ($95\, km$). The rate of meteoroids ablating in the Earth's atmosphere is also given by :

$$n_t = \sigma_E \int_{4\pi} N\, d\Omega\,, \tag{4.30}$$

where σ_E is the area of the target that the Earth presents to meteoroids, and is given by $\pi\mathcal{R}^2$. Therefore the following expression may be obtained for n_t :

$$n_t = 4\pi^2 K' m_\infty^c \mathcal{R}^2\,, \tag{4.31}$$

hence the cumulative flux of particles above a mass, m_∞, incident on the Earth's atmosphere is given by :

$$\mathcal{F} = \pi K' m_\infty^c \ . \tag{4.32}$$

Elford and Hawkins (1964) operated a radar at 41 *MHz* and observed a cumulative flux of $1.0 \times 10^{-8}\, m^{-2}s^{-1}$ for meteors with zenithal electron line densities exceeding $4.5 \times 10^{10} m_\infty^{-1}$. *Hughes* (1978) has summarised the data on the relationship between the ionization line density and initial mass of the meteoroid to obtain the following relation :

$$log_{10}q = 16.58 + log_{10}m_\infty \ , \tag{4.33}$$

which is independent of velocity. In this relation, the units of q and m_∞ are *electrons* m^{-1} and *gms* respectively. Using 4.33, a value for K' of 3.82×10^{-18} is obtained from the results of *Elford and Hawkins* (1964), (the corresponding mass is 1.2×10^{-6} *g*). The radar data summarised by *Hughes* (1978) gives a cumulative flux of $3.3^{+7.7}_{-2.9} \times 10^{-9}\ m^{-2}s^{-1}$ for initial masses above 1.0×10^{-6} *g*, thus a value for K' of $1.05^{+2.45}_{-0.92} \times 10^{-18}$ is obtained. In comparison, the cumulative flux above the same mass limit as measured by satellites (summarised by *Hughes*, 1978) is $1.7^{+2.3}_{-0.8} \times 10^{-7}\ m^{-2}s^{-1}$, some 50 times larger. The value for K' in this case is $5.4^{+7.3}_{-2.5} \times 10^{-17}\ m^{-2}s^{-1}$. *Thomas et al.* (1988) using the Jindalee radar operating near 10 *MHz*, obtain a value of the cumulative flux for particles above 1.0×10^{-6} *g* to be $8.7 \times 10^{-8}\ m^{-2}s^{-1}$ thus rendering a value for K' of 2.8×10^{-17}. Table 4.1 summarises these results.

There is a large spread in the cumulative flux for different types of experiment (satellite, MF radar and VHF radar), and a corresponding spread in the values for K'. Satellites and MF radar measure fluxes some 50 and 27 times larger respectively, than VHF radar. This is not surprising and is now understood to be due to the echo height ceiling effect implicitly associated with radar observations of meteors. The echo height ceiling of meteors is directly attributable to the attenuation factors α_r and α_v, and the echo selection factor α_d (*Steel and Elford*, 1991). From 4.14, 4.16 and 4.20 one can see that each of these factors cause a bias against detecting echoes at large heights, thus producing a ceiling above which meteors are unable to be observed, if they indeed ablate at those altitudes. The effect of the attenuation factors is also larger for radars operating at higher frequencies, and thus with these radars the echo ceiling occurs at lower altitudes.

Steel and Elford (1991) investigated the effect of the attenuation factors as a function of height for various frequencies. It is clear that traditional meteor radars, which operate

Experiment	$\mathcal{F}\ (m^{-2}s^{-1})$	K'
Summarised satellite, *Hughes* (1978)	$1.7^{+2.3}_{-0.8} \times 10^{-7}$	$5.4^{+7.3}_{-2.5} \times 10^{-17}$
10 *MHz* radar, *Thomas et al.* (1988)	8.7×10^{-8}	2.8×10^{-17}
41 *MHz* radar, *Elford and Hawkins* (1964)	1.2×10^{-8}	3.82×10^{-18}
Summarised radar, *Hughes* (1978)	$3.3^{+7.7}_{-2.9} \times 10^{-9}$	$1.05^{+2.45}_{-0.92} \times 10^{-18}$

Table 4.1: Cumulative fluxes, $\mathcal{F}$, of particles above a limiting mass of 1.0×10^{-6} g found from various experiments, and the associated values of K', as calculated by 3.29. Note, the cumulative flux measured by *Elford and Hawkins* (1964) was extrapolated back from a limiting mass of 1.2×10^{-6} g to 1.0×10^{-6} g by the use of 3.29 and the assumption of $c = -1.0$. The original mass of 1.2×10^{-6} g was estimated from *Elford and Hawkins* measured value of limiting electron line density, q, and 3.30.

at VHF (around 50 *MHz*), are unable to detect underdense echoes above $\sim$ 100 *km* as the backscattered echo power is severely attenuated. On the other hand, *Steel and Elford* find that radars operating at lower frequencies, for example at 2 *MHz*, can detect meteors at altitudes up to $\sim$ 140 *km*, if they indeed ablate at these heights. *Olsson-Steel and Elford* (1987) have observed meteor echoes at 2 *MHz* with the Buckland Park MF radar situated near Adelaide, and also at 6 *MHz* (*Elford and Olsson-Steel*, 1988), with the same radar receiving array operating on its 3rd harmonic. The results indeed show that there are significant numbers of meteors observed up to observing limit of 140 *km* and that at 2 *MHz*, the peak of the height distribution has moved up to an altitude of 105 *km*. These results are summarised together with their meteor observations at 54.1 *MHz* with the VHF radar at the same site (see chapter 2), and also with 26.4 *MHz* observations in New Zealand (*Baggaley and Webb*, 1980), by *Steel and Elford* (1991). The results show that as the frequency at which a radar operates decreases, meteors at higher altitudes are able to be observed, as well as the peak of the height distribution increasing in altitude.

It is to be expected then, based on the discussion of the previous paragraph, that radars operating at lower frequencies than previously used for meteor observation, will measure higher cumulative fluxes above a given limiting mass. This is exactly the case with the Jindalee radar which was operated at 10 *MHz*. However, even at this low frequency, the

Jindalee radar still underestimates the mass influx of meteoroids to the Earth. The basis for this conclusion is from the fact that the mass influx, as measured by the Jindalee radar, is less than the value from satellite observations which detect meteoroids in the vicinity of the Earth. Although it is advantageous to observe meteors with radars operating at low frequencies, significant problems occur due to echoes from the ionosphere saturating the receivers during the day, thus restricting the time of observations (*Olsson-Steel and Elford*, 1987; *Elford and Olsson-Steel*, 1988). While this is not a problem with the Jindalee radar (*Thomas et al.*, 1988), the inherent multi-mode propagation characteristics of the Earth-ionosphere cavity complicates the analysis of the meteor echo data.

Clearly, an appropriate value of K' for the Buckland Park VHF radar is the value determined from satellite observations with all the attenuation factors included in the response function calculation. However, in specific cases such as the response function calculated using an idealized ionization profile without the attenuation factors as in described in Section 4.2.1, a value of K' as measured by radars operating near the frequency of the Buckland Park VHF radar must be used. For this case, K' calculated from either the results of *Elford and Hawkins* (1964) or the summarised radar data of *Hughes et al.* (1978) is appropriate.

The response function of the radar may now be developed from 4.29 in a similar manner that 4.1 was to give 4.7. Thus the following equation for the response function in terms of the limiting mass is obtained :

$$n(\theta_r, \phi_r) = R_E K' \int_{h1}^{h2} \int_{-\pi/2}^{\pi/2} m_\infty^c f \left(1 + \frac{h}{R_E}\right) d\Phi \, dh \, , \tag{4.34}$$

where f is given by 4.9 and m_∞ is the limiting initial mass of the meteoroid. The limiting initial mass is obtained from the minimum detectable electron line density, q_{min} (given by 4.13 for the underdense case and 4.28 for the overdense case), and classical ablation theory. How this is performed is detailed in Section 4.3. Note, q_{min} for the underdense case is a function of velocity and height due to the attenuation and selection factors, also velocity is introduced to the calculation from the classical ablation theory. Hence integration of 4.34 is required over velocity with a suitable velocity distribution. Thus the response function becomes :

$$n_t(\theta_r, \phi_r) = R_E K' \int_V N_V(V) \int_{h1}^{h2} \int_{-\pi/2}^{\pi/2} m_\infty(q_{min}, V)^c f \left(1 + \frac{h}{R_E}\right) d\Phi \, dh \, dV \, , \tag{4.35}$$

where $N_V(V)$ is the velocity distribution of meteoroids with respect to the Earth's reference frame. The last requirement for the completion of the response function calculation is how m_∞ is related to q_{min}.

4.3 Initial Mass and Classical Ablation Theory

4.3.1 Introduction

In order to complete the response function calculation implied by Equation 4.35, a model of the ionization profile of meteors is required. The model that will be used, which is described in this section, is based on the classical ablation theory of meteoroids. Note, this applies only for single particles. No attempt is made to include fragmentation, although a short discussion on the effects of fragmentation will be given.

4.3.2 The drag, differential mass and ionization equations

A recent summary of the classical equations for the luminosity and ionization distributions along a meteor trail is given by *Ceplecha* (1993). The meteoroid, once it enters the Earth's atmosphere, will decelerate due to collisions with air particles. This gives rise to the drag equation which is found by equating the loss of momentum of the meteoroid to that gained by the intercepting air particles. If m and V are the mass and velocity of the meteoroid at any time after it has entered the atmosphere, the rate of change of momentum, p_m, of the meteoroid is then given by:

$$\frac{dp_m}{dt} = -m\,\frac{dV}{dt}\,. \tag{4.36}$$

In a small time interval dt, the mass of air intercepted by the meteoroid is dm_a, and the momentum gained is $dp_a = \Gamma V dm_a$, where Γ is a dimensionless quantity called the drag coefficient. The drag coefficient depends on the shape of the meteoroid and also the velocity, V, and scale height, $\mathcal{H}$, to a small extent. Typically Γ lies between 0.5 and 1.0. The rate of change in momentum of the air particles intercepted by the meteoroid is given by:

$$\frac{dp_a}{dt} = \Gamma V \frac{dm_a}{dt}\,. \tag{4.37}$$

The meteoroid travels a distance $ds = Vdt$ in a time dt, thus the mass of air intercepted in a time, dt, by the meteoroid is given by :

$$dm_a = \sigma_m \rho_a ds = \sigma_m \rho_a V dt\,, \tag{4.38}$$

where ρ_a is the density of the atmosphere and σ_m is the effective cross-sectional area of the meteoroid which may be expressed as $\sigma_m = A\mathcal{V}^{2/3} = A(m/\rho_m)^{2/3}$. Here, $\mathcal{V}$ and ρ_m are the volume and density of the meteoroid respectively, the quantity A is dimensionless and called the shape factor. For spherical particles, it can easily be shown that the shape factor

is $A \approx 1.2$. Elongated particles have a range of values for A, depending on the aspect of the particle; $A = A_{min} < 1$ for the "end on" aspect, and $A = A_{max} > 1$ for the "broadside" aspect. Generally, irregularly shaped meteoroids will have $A \approx 1.2$ due to rotation. Combining Equations 4.36, 4.37 and 4.38 yields the drag equation:

$$\frac{dV}{dt} = -\frac{\Gamma A}{m^{1/3}\rho_m{}^{2/3}}\rho_a V^2 \,. \tag{4.39}$$

The meteoroid, as it collides with the air molecules, loses kinetic energy. The lost kinetic energy is converted mainly to heat; small amounts are converted to light and ionization. Since the meteoroid intercepts a mass of air given by dm_a in time dt, the amount of kinetic energy lost by the meteoroid will be :

$$dE_{KE} = -\frac{1}{2}\, dm_a\, V^2 = -\frac{A}{2}\left(\frac{m}{\rho_m}\right)^{2/3} \rho_a V^3 dt \,. \tag{4.40}$$

If Λ is the heat transfer coefficient, then the amount of heat energy gained in time dt by the meteoroid is $dE_H = -\Lambda\, dE_{KE}$. The meteoroid loses mass $dm = -dE_H/\zeta$ through its surface atoms vapourising due to the heat transfer, where ζ is the heat of ablation of the meteoroid. Thus the differential mass equation may be expressed as :

$$\frac{dm}{dt} = -\frac{\Lambda\, A}{2\,\zeta}\left(\frac{m}{\rho_m}\right)^{2/3} \rho_a\, V^3 \,. \tag{4.41}$$

The heat transfer coefficient typically lies in the range 0.1 to 0.6, (*McKinley*, 1961) and the heat of ablation of the meteoroid is taken to be $8.0 \times 10^6\, JKg^{-1}$, (*Bronshten*, 1983). *Nicol et al.* (1985) use a value of ζ of $6.0 \times 10^6\, JKg^{-1}$ in their modelling of meteor ablation.

Ablated atoms from the meteoroid, on collision with the air particle, produce free electrons. The meteoroid in a time dt, travels a distance Vdt and loses mass dm. If β is the probability that a single ablated atom of mass μ produces a free electron on collision with an air molecule, and q is the number of electrons produced per unit path length, then the following is obtained :

$$q\, V dt = -\frac{\beta}{\mu} dm \,. \tag{4.42}$$

Rearranging this equation and substituting for dm/dt from 4.41, the ionization equation is arrived at :

$$q = \beta \frac{\Lambda A}{2\zeta\mu}\left(\frac{m}{\rho_m}\right)^{2/3} \rho_a V^2 \,. \tag{4.43}$$

The value of β depends on the material of the meteoroid and also on the velocity of the meteoroid. *Bronshten* (1983) summarises the results of various experiments to obtain the

following expression for β applicable to stony meteoroids :

$$\beta(V) = 3.02 \times 10^{-17} V^{3.42} , \tag{4.44}$$

where the units of V are ms^{-1}.

4.3.3 An analytical solution to the classical ionization theory: the approximation of no deceleration

The three equations, 4.39, 4.41 and 4.43, describing the classical ablation theory are simple to solve for an ionization profile produced by a meteoroid of a given initial mass, m_∞, and a given initial velocity, V_∞. One numerically integrates down from a starting height (say $150\,km$) to where ionization production has stopped (about $60\,km$). However a numerical solution to the classical ionization profile is not desirable for the response function calculation. The reason for this may be seen from inspection of the form of the response function (see 4.35). One can see that a triple integral is required to calculate the response at each radiant position, thus the response function calculation is time consuming. The ionization profile calculation is nested inside the innermost integral of 4.35, therefore, from time constraints, an analytical solution to the classical ionization theory is desirable.

Starting with 4.41, this equation may be rearranged and integrated from $t = -\infty$, where the mass of the meteoroid is m_∞, to a time t where the mass of the meteoroid has decreased to a value m. Thus the following equation is obtained :

$$\int_{m_\infty}^{m} m^{-2/3} dm = -\frac{\Lambda A}{2\zeta\rho_m} \int_{-\infty}^{t} \rho_a V^3 dt , \tag{4.45}$$

which upon using $dh = -cos\chi\ V dt$ becomes :

$$m^{1/3} = {m_\infty}^{1/3} + \frac{\Lambda A}{6\zeta\rho_m cos\chi} \int_{h}^{\infty} \rho_a V^2 dh , \tag{4.46}$$

where dh is a small change in height and χ is the angle the path of the meteoroid makes with the zenith. Now over much of the meteor path the deceleration is small. Carrying out the above integration on the assumption of no deceleration, the following is obtained :

$$m^{1/3} = {m_\infty}^{1/3} - \frac{\Lambda A V_\infty^2 \mathcal{H}}{6\zeta\rho_m cos\chi} \rho_a , \tag{4.47}$$

where $\mathcal{H}$ is the scale height of the atmosphere at the geometrical height, h. Note, both $\mathcal{H}$ and ρ_a, and hence m, are functions of the geometrical height.

On substituting 4.47 into the ionization equation as given by 4.43, the following relation between m_∞ and q is obtained at a height h :

$$q(h) = k_2\, \rho_a(h) \left(m_\infty^{1/3} - \frac{k_1\, \mathcal{H}(h)\, \rho_a(h)}{cos\chi} \right)^2 , \tag{4.48}$$

where k_1 and k_2 are constants for a given meteoroid composition, and are given by :

$$\left.\begin{aligned} k_1 &= \frac{\Lambda A V^2}{6\zeta \rho_m^{2/3}} \\ k_2 &= \frac{\beta \Lambda A V^2}{2\zeta \mu \rho_m^{2/3}} \end{aligned}\right\} . \tag{4.49}$$

Equation 4.48 may be rearranged to give m_∞ in terms of q, thus :

$$m_\infty = \left[\left(\frac{q(h)}{k_2\, \rho_a(h)} \right)^{1/2} + \frac{k_1\, \mathcal{H}(h)\, \rho_a(h)}{cos\chi} \right]^3 \tag{4.50}$$

This equation may be used in the response function calculation (see 4.35), however as will be seen, the approximation of no deceleration of the meteoroid is poor at low meteoroid velocities and thus not appropriate.

4.3.4 An analytical solution to the classical ionization theory corrected for deceleration

As described previously, an ionization profile may be obtained by integrating downwards the drag, differential mass an ionization equations. This has been performed and compared with the approximate no-deceleration analytical solution (Equation 4.48), by *Elford* (private communication). Comparisons were made with initial masses of 10^{-6}, 10^{-7}, 10^{-8} and $10^{-9}\, kg$ and a range of velocities from 11 to 70 $km\, s^{-1}$. *Elford*, found that a good approximation to the full solution may be obtained from the no-deceleration approximation by applying the following two modifications to the no-deceleration approximation ionization profile.

1. The electron line density at any point on the no-deceleration profile is reduced by a multiplication factor, $\mathcal{S}$.

2. The effective height is increased by an amount, δh.

The modifications were found to be essentially independent of the initial mass, depending only on the initial velocity. Table 4.2 shows values of $\mathcal{S}$ and δh for selected initial velocities.

Initial Velocity ($km\,s^{-1}$)	$\mathcal{S}$	$\delta h\,(km\,s^{-1})$
11	0.38	+5.5
20	0.68	+1.5
30	0.80	+1.0
40	0.87	0
50	0.91	0
60	0.93	0
70	0.95	0

Table 4.2: Modification factors applied to no-deceleration ionization profiles to produce a good approximation to the full solution.

The ionization profiles for various initial masses and velocities are now calculated using no-deceleration profile from 4.48 and applying the appropriate modifications. In doing so, 4.48 becomes the following equation :

$$q(h) = \mathcal{S}(v)\, k_2\, \rho_a(h - \delta h(v)) \left(m_\infty^{1/3} - \frac{k_1\, \mathcal{H}(h - \delta h(v))\, \rho_a(h - \delta h(v))}{cos\chi} \right)^{1/2}, \qquad (4.51)$$

The scale height and atmospheric density for these calculations may be obtained from any atmospheric model; for these calculations, the CIRA86 model of the middle atmosphere was used. The ionization profiles calculated from 4.51 appear in Figure 4.3.

Again the above equation may be rearranged to give m_∞ in terms of q, which is required for the response function calculation, thus :

$$m_\infty = \left[\left(\frac{q(h)}{\mathcal{S}(v)\, k_2\, \rho_a(h - \delta h(v))} \right)^{1/2} + \frac{k_1\, \mathcal{H}(h - \delta h(v))\, \rho_a(h - \delta h(v))}{cos\chi} \right]^3 . \qquad (4.52)$$

This is the solution for the ionization profile which will be used in subsequent response function calculations.

4.3.5 Minimum initial meteoroid mass detectable with the Buckland Park VHF radar

The minimum initial meteoroid mass detectable with the Buckland Park VHF radar may now be estimated. Equation 4.13 gives the minimum detectable electron line density; this is a function of initial velocity (due to the echo attenuation and selection factors) and range. The range may be obtained through Equation 4.6 and is a function of height, h, and the elevation angle of the reflection point on the meteor trail which depends on the angle Φ.

The procedure used to obtain the minimum detectable initial meteoroid mass, was to calculate q_{min}, and then the initial mass from Equation 4.52 for a range values of V and h.

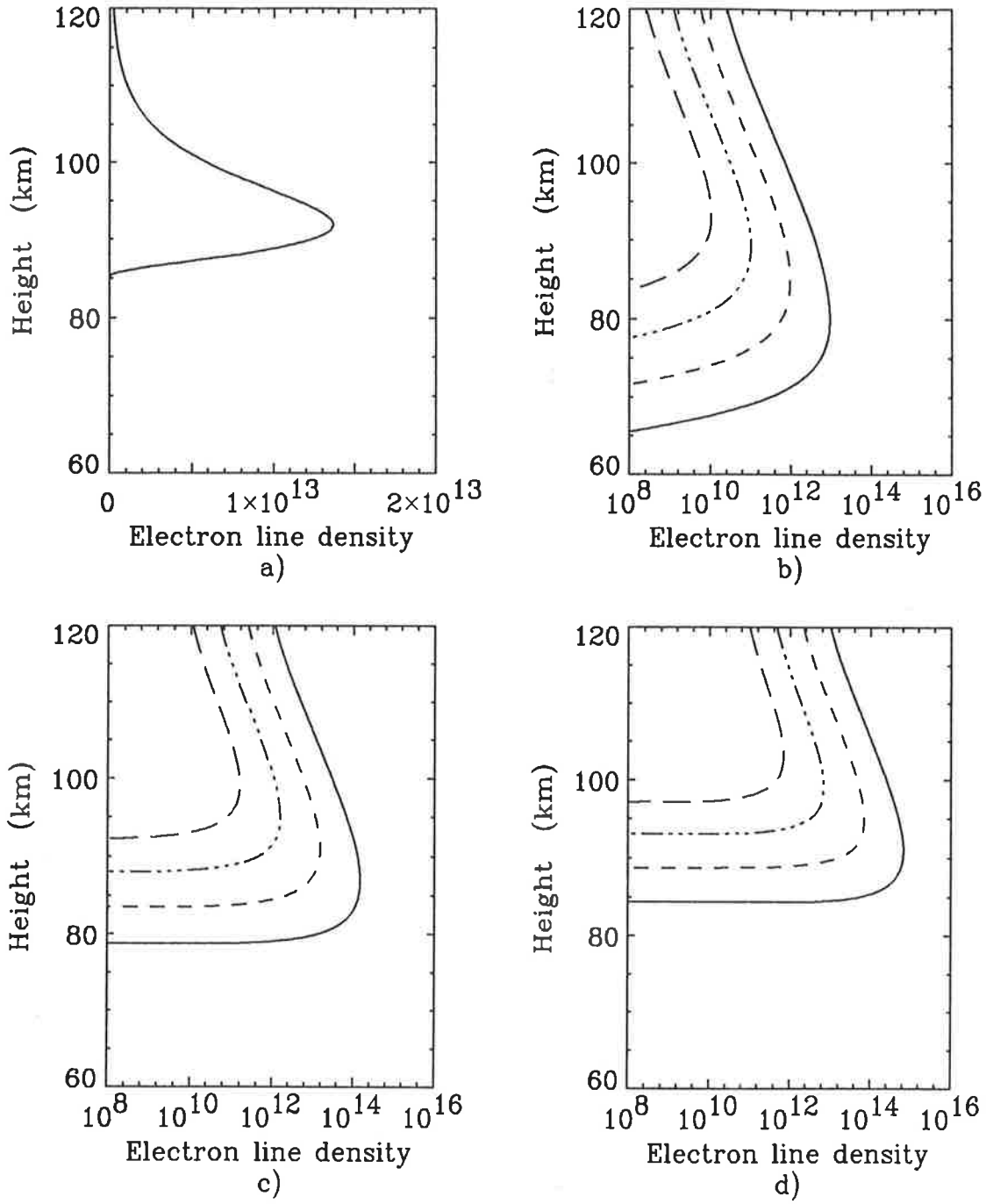

Figure 4.3: Ionization profiles calculated from the analytical solution corrected for deceleration (see text). Panel (a) shows a single profile (linear plot) for an initial mass and initial velocity of $10^{-7}\,kg$ and $40\,km\,s^{-1}$ respectively. Displayed in (b), (c) and (d) (all log plots), are ionization profiles with various initial masses for initial velocities of $20\,km\,s^{-1}$ $40\,km\,s^{-1}$ and $60\,km\,s^{-1}$ respectively. In each of these panels, the solid line indicates an initial mass of $10^{-6}\,kg$, short dashed $10^{-7}\,kg$, broken $10^{-8}\,kg$, and the long dashed line an initial mass of $10^{-9}\,kg$.

The extent of values used for V and h were $11 - 70\,km\,s^{-1}$ and $60 - 120\,km$ respectively, *i.e.* typical meteoroid velocities and typical height range over which they ablate. It was not necessary to repeat the calculation over values of Φ, because the range and hence q_{min}, is at a minimum for $\Phi = 0$, and increases monotonically as $|\Phi|$ increases. Thus it was only required to calculate the initial mass for $\Phi = 0$ and repeat over V and h only. The physical properties of the meteoroid, needed for this calculation are listed in Table 4.3. The gain of the VHF radar antenna is about 2700, and the minimum detectable power around $1.0 \times 10^{-13}\,W$ (see Section 4.4). Finally the operational parameters and detection criteria required for the calculation of echo attenuation and selection factors are given in Chapters 2 and 3 respectively. A table of minimum detectable initial masses at various heights and velocities, $m_{min}(V, h)$ was calculated for the radar. From this table, the minimum mass was found to be about $1 \times 10^{-9}\,kg$.

4.3.6 The effect of fragmentation

Fragmentation of the meteoroid will affect the meteor trail. A short qualitative discussion of these effects follows. No attempt is made to model the effects of fragmentation on the meteor trail and the associated ionization profile.

Two main types of fragmentation have been identified by *Babadzhanov* (1993) and *Ceplecha* (1993); quasi-continuous and gross fragmentation. Quasi-continuous fragmentation is the gradual release of small fragments from the surface of the meteoroid which subsequently evaporate. Gross fragmentation occurs when the meteoroid breaks into two particles of similar mass. The produced particles may then fragment further.

The effects of fragmentation may be examined by decomposing the situation into two cases: fragmentation orthogonal to the direction of the meteoroid, and fragmentation parallel to the meteoroid's motion. For the first case it is reasonable to assume that the electron line density is unchanged, however the ionization is spread over a larger meteor trail cross-section. The effect of this is to increase the initial radius, r_0, and hence attenuate the meteor echo to a greater degree. The second case, *i.e.* fragmentation parallel to the direction of the meteoroid's motion, will not affect r_0, however the meteor echo will have several contributions to it which are spatially separated along the meteoroids path. *Elford* (private communication) has modeled this and has shown that the effect of this is to wash out the post t_0 Fresnel oscillations. It is also expected that the ionization profile would be affected to some degree.

4.4 Response of the Buckland Park VHF Radar

4.4.1 Introduction

In this section the radar response function to meteors developed in Section 4.2 is applied to the Buckland Park VHF Radar. There are, however, two points relevant to the Buckland Park VHF Radar which must be noted. The first is the effect of range cut-off. Due to hardware limitations, the raw data was only sampled up to a maximum range of 128 km (height of 111 km for an off zenith beam tilt of 30°). Thus in the response function calculation, contributions from a range greater than 128 km are ignored.

The second point regards the minimum detectable echo power, P_R, of the radar. The total noise power is given by the following expression :

$$P_N = k\,\Delta f\,(T_r + T_e)\,, \tag{4.53}$$

where k is Boltzmann's constant, Δf the bandwidth of the receivers, T_r, the noise temperature of the receivers and T_e is the noise temperature of external noise sources (mainly due to background cosmic noise). A meteor echo is detected only if the the echo amplitude exceeds a certain discrimination level. This level is taken to be ~ 4.5 times that of the background noise. The choice of this level is from statistical considerations and will be discussed further in Chapter 3. The minimum detectable echo power is then given by :

$$P_R = (4.5)^2\,P_N = 20.25\,k\,\Delta f\,(T_r + T_e)\,. \tag{4.54}$$

The values of Δf and T_r are known quantities dependent on the receiver: for the VHF radar, these are 150 kHz and 400° K respectively. However, the background cosmic noise varies diurnally due to different cosmic sources entering the field of view of the radar beam. From observations (see Chapter 2), the cosmic noise varies from some 2000 to 8000 K. Thus the minimum detectable echo power varies diurnally from 1.0×10^{-13} to $4.0 \times 10^{-13}\,W$.

Since the minimum detectable power varies diurnally and considering the large amount of computing resources required to calculate the response function, an average value is used in the subsequent response function calculation. It will be shown later that the effect on the response function is minimal and thus an average value for P_R is an acceptable approximation.

Quantity	Value used for response calculation
meteoroid density, ρ_m	$3500\,kg\,m^3$
meteoroid mean molecular weight, μ	$6.6 \times 10^{-26}\,kg$
heat of ablation of meteoroid, ζ	$8.0 \times 10^6\,J\,kg^{-1}$
heat transfer coefficient, Λ	0.4
shape factor, A	1.2

Table 4.3: Physical properties of the meteoroids and other quantities used in the response function calculation

4.4.2 The response function calculation at an initial meteoroid velocity of $30\,km\,s^{-1}$ and off zenith beam tilt of $30°$

The response function for meteoroids of a given initial geocentric velocity may be calculated using 4.34, 4.52 and the CIRA86 model of the middle atmosphere. The initial geocentric velocity of the meteoroids was chosen to be $30\,km\,s^{-1}$, and the results are shown in Figures 4.4 and 4.5. In each figure, the response rate has been normalized to the peak response. Values of certain physical properties of the meteoroid, required for the calculation, are listed in Table 4.3.

As described in Chapter 2, the beam of the radar may be tilted either Eastwards or Westwards, however as the array is actually aligned 4° anticlock wise from true North (see Figure 2.1), the beam is directed at azimuth angles of either 86° or 266°. The response function calculations were performed with the beam of the radar directed at an elevation of 30° and azimuth of 86° (East/West 'axis' of the antenna). These coordinates were chosen for the beam direction as most of the meteor observations, described later in this thesis, were made with a beam directed as such. It is noted, but not shown here, that the response function calculated with the beam pointed in the other direction (at the same elevation), is identical but with a 180° shift in azimuth. This applies for all azimuths in general; changing the beam azimuth by a certain amount but maintaining a constant elevation, shifts the response function in azimuth by the same amount.

In general, it is desirable, for meteor observations via specular backscatter, to have a beam tilted far off zenith, say $60 - 70°$. The reasons for this are as follows :

1. As the beam is tilted further off zenith, the meteor collecting area in the echo plane increases, thus increasing the echo rate.

2. A beam orientation close to zenith implies detection of meteor radiants close to the

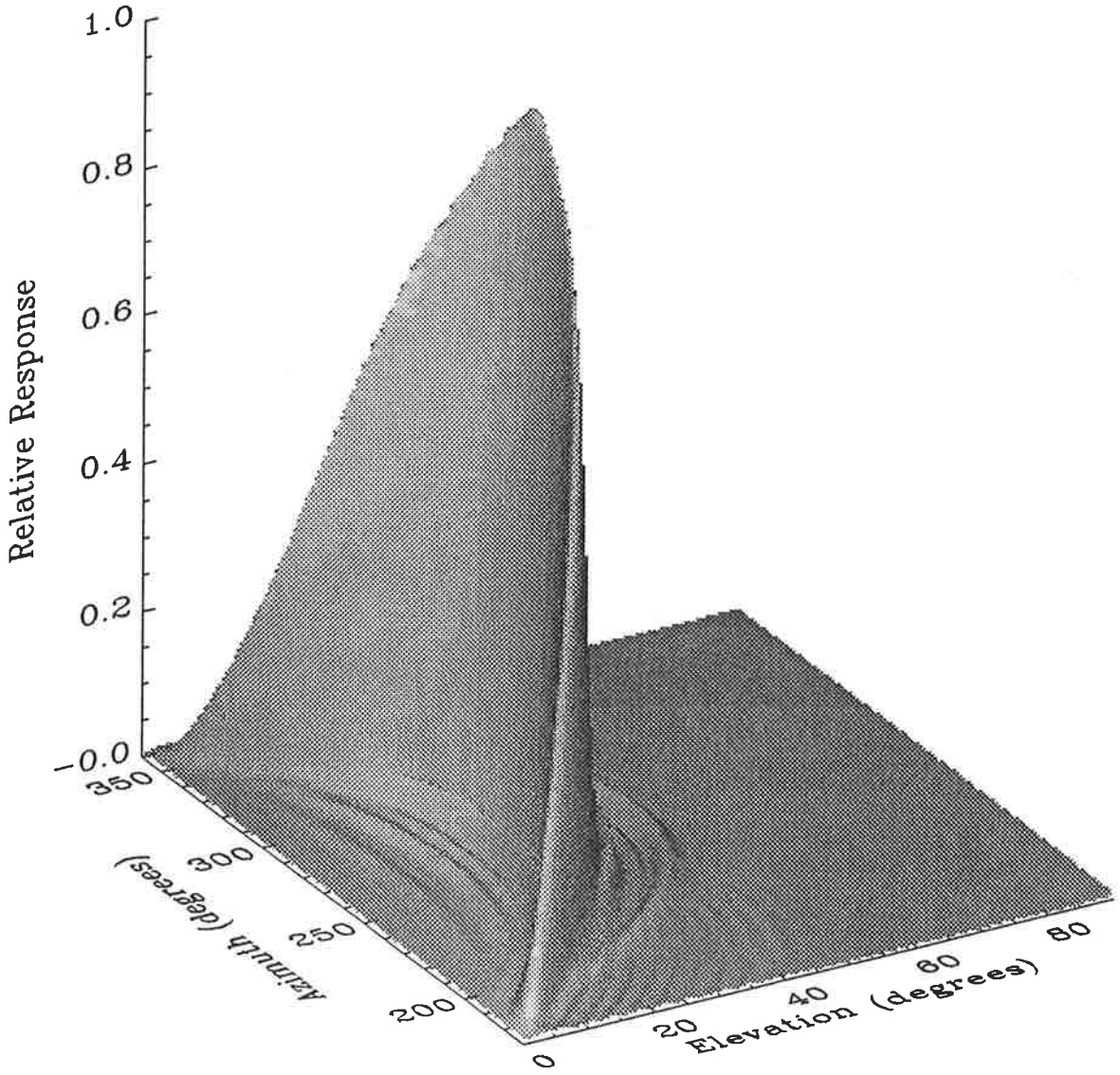

Figure 4.4: The response function (normalized to the peak response) of the Buckland Park VHF radar for an Eastward pointing (azimuth : 84°) beam. The initial geocentric velocity of the meteoroid is $30\,km\,s^{-1}$.

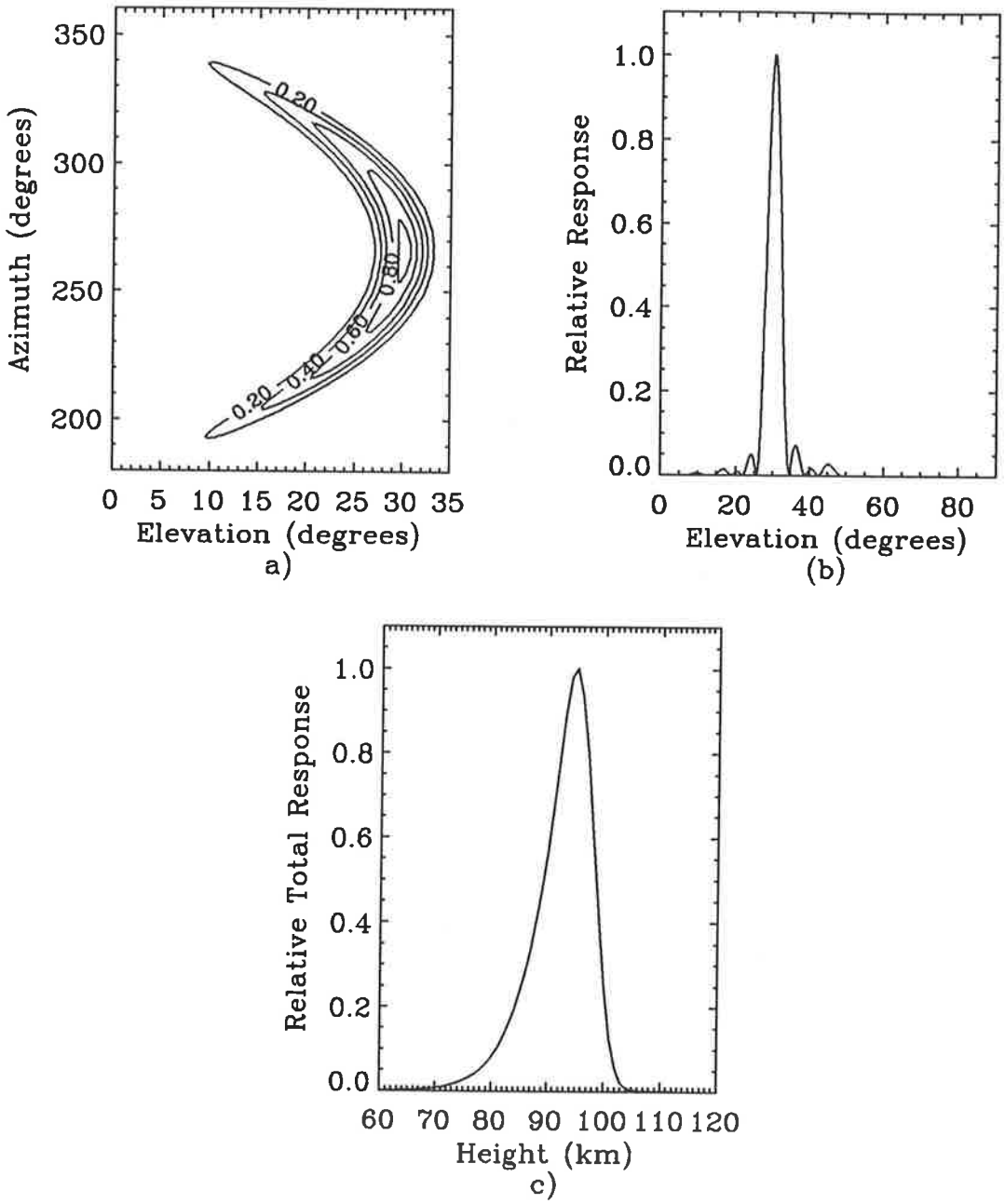

Figure 4.5: Contour diagram of the response function (normalized to the peak response) of the Buckland Park VHF radar for meteoroids with an initial geocentric velocity of $30\,km\,s^{-1}$ (a). Panel (b) shows a cross-section through the response function at a azimuth of 266°. Panel c shows the spatially integrated response as a function of height (see text for details).

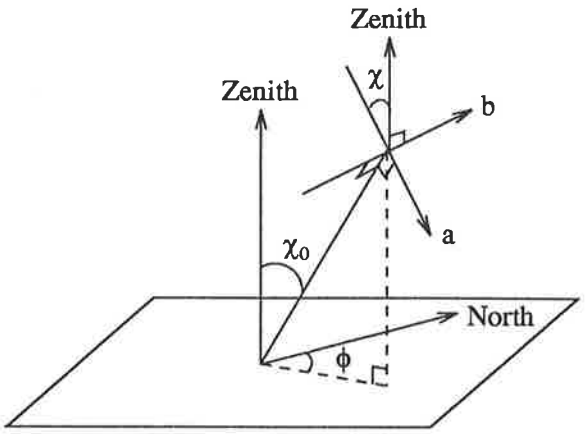

Figure 4.6: Possible meteoroid radiant directions detectable by specular backscatter of radar by the resultant meteor trails. Radiant 'a' has an elevation and azimuth of χ and ϕ, the relation between χ and χ_0 is given by equation 3.11. Radiant 'b' is from a direction whose elevation and azimuth is $0°$ and $\phi + 90°$ respectively. The angles χ_0 and ϕ give the position of the t_0 point with respect to the observer.

horizon for the condition of specular backscatter. For meteoroids of a given mass, the electron line density varies as $cos\chi$, where χ is the zenith angle of the radiant (see Equation 4.10).

Although the sensitivity of the system and hence the meteor count rates, are higher for a beam tilt of $60 - 70°$, the present system has a hardware limitation (see Chapter 2) that limits the sampling of the data to ranges less than $128\,km$. Thus, a beam tilt of about $30°$ is appropriate with the existing system.

Figure 4.4 displays the response function as a surface, in which the main lobe is due to the main lobe of the radiation pattern of the radar array. The ripples that can be seen in this figure correspond to the sidelobes of the antenna pattern. Figure 4.5a is a contour diagram of the main lobe of the response function. It can be seen from these two diagrams that the main feature of the response function, is a narrow curved wedge extending from azimuth $176°$ to $356°$. The maximum response occurs for radiants from an azimuth of $266°$, and decreases to a minimum at azimuths $176°$ and $356°$. The reason for this can readily be seen from the geometry of situation (see Figure 4.6). The condition of specular backscatter requires that the meteor trail be perpendicular to the beam direction, and is met for a range of radiant directions. For the extreme radiant azimuths, *i.e.* those which are away from the beam azimuth by a $90°$, the elevation of the radiant is required to be zero. Hence from point two of the previous paragraph, they produce a minimal response. Conversely, radiants with azimuths equal to the beam azimuth, have a maximal elevation, *viz* the elevation of the

beam, and thus produce the maximum possible response.

Figure 4.5b, shows the cross-section through the response function at an azimuth of 266°. A detailed examination of the response function shows that the maximum occurs at an elevation of 30.25° rather than 30° (the off zenith angle of the main beam of the radar). This is of course due to points 1 and 2 discussed earlier, these two effects outweighing the decrease in the antenna gain thus shifting the maximal response to a slightly higher elevation. This effect is also seen in the relative strengths of the first sidelobes on either side of the main lobe of the response function. The sidelobe which is at the larger elevation observes some 2 – 3 times more meteors than that of the other sidelobe closer to the zenith.

In the last diagram of Figure 4.5, the response function at each height is integrated over the sky. This gives the height response or the expected height distribution of meteoroids, with the given physical properties of Table 4.3, entering the Earth's atmosphere at a velocity of 30 $km\,s^{-1}$. It can be seen from this diagram, that the height distribution for these particles peaks at 95 km with few being detected above 100 km. Summation of similar diagrams over all velocities, with an appropriate velocity distribution, gives the expected height distribution of meteors as observed by the radar.

4.4.3 Investigation of the response function for different off zenith beam angles

The effect of using different off zenith beam angles on the response function is now investigated. In Figure 4.7, the response function, at an azimuth of 266° is displayed for a beam tilted off zenith by 4, 7, 11, 15 and 30° (panels (a) to (e) respectively). Each of these response functions have been normalised to their peak response. Panel f shows the response function, at an azimuth of 266°, integrated over the elevation angle, displayed as a function of off zenith beam angle. This has been normalised to the total response (*i.e.* total number of echoes) of a beam tilt of 30° and therefore gives a measure of the expected rate for various beam tilts with respect to a 30° off zenith beam angle.

The beam tilts listed above were chosen because all these elevations (except $\chi = 15°$) are available with the present radar; the 4, 7 and 11° tilts are used for tropospheric work. If these beam tilts are to be used for meteor experiments such as detection of space debris (see Section 5.5), their response functions must be fully explored.

There are two things to note from Figure 4.7. The first is that the side lobe contribution rises dramatically with smaller off zenith beam tilts. The second can be seen from

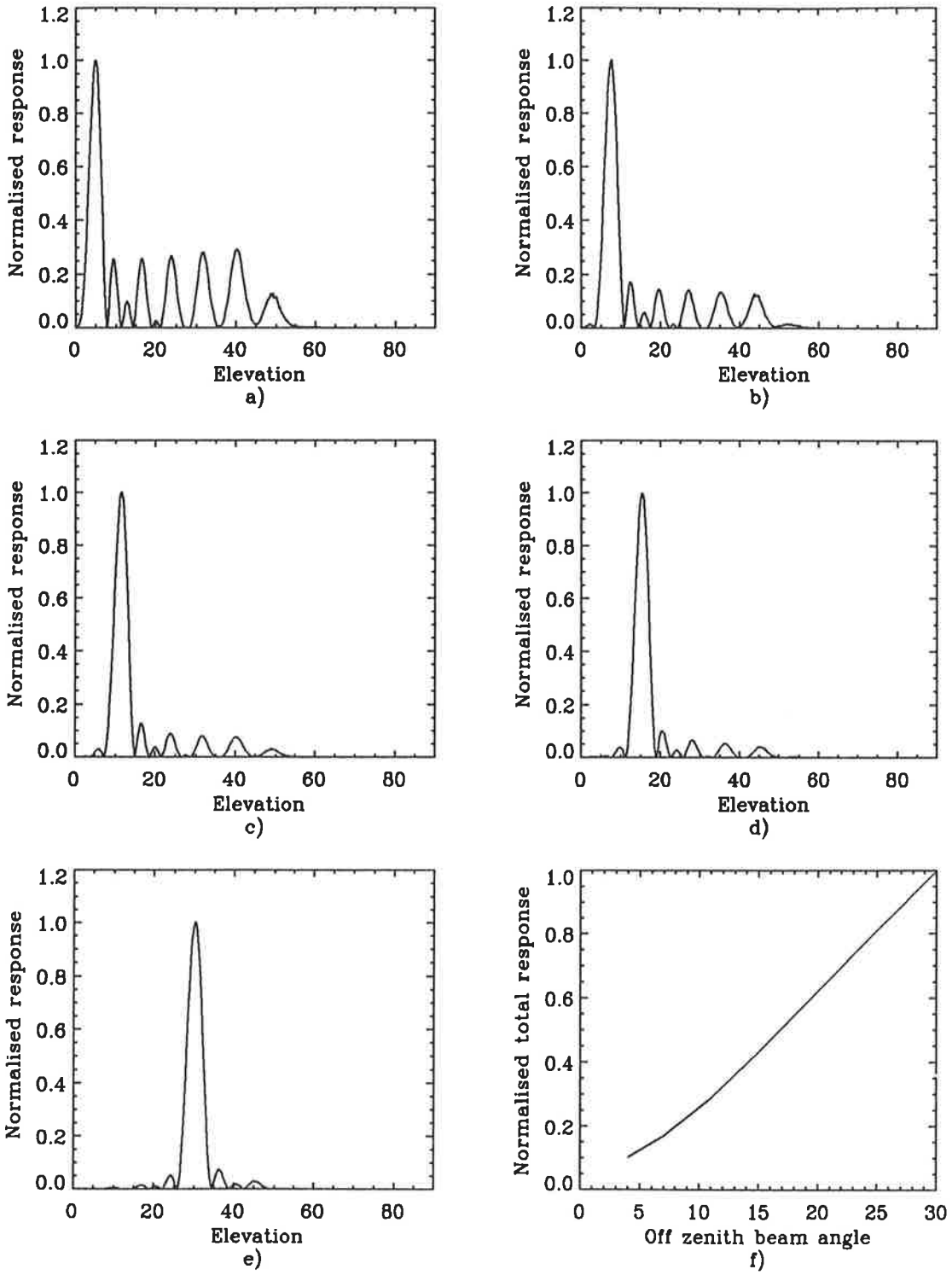

Figure 4.7: The response function (normalised to the peak response) at an azimuth of 266° for beam tilts of 4, 7, 11, 15 and 30° off zenith (panels (a) to (e)). In panel (f), the results of the five previous panels are integrated over elevation and plotted against the off zenith beam angle. Here normalisation is with respect to the integrated response for a beam tilt of 30°.

Figure 4.7f: the sensitivity of the system to meteors falls almost linearly with decreasing off zenith beam tilts. Again the reasons for this are due the changes in the meteor collecting area and minimum detectable electron line density discussed in Section 4.4.2. This figure also demonstrates the need to have a beam geometry such that the beam is tilted significantly off vertical to be of use for observing meteors. This creates problems for the study of meteors produced by space debris as most of their radiants are close to the horizon. This problem is looked at more fully in Section 5.5.

4.4.4 Velocity dependence of the response function

The velocity dependence of the meteor response function is now examined. Figure 4.8 shows a section through the response function a an azimuth of 266° for initial meteoroid velocities of 11, 20, 40 and 60 $km\,s^{-1}$ (panels (a) to (d)). The off zenith beam angle was 30° for each case, and all are normalised to their respective peak rates. The peak response in all cases occurs at 30.25°. Figure 4.8e shows the total response, *i.e.* the response function integrated over the sky, as a function of velocity, while panel f of Figure 4.8 shows how the maximum response rate varies with velocity.

The two most striking features of figure 4.8 are the increases in side lobe response as the initial velocity increases, and the rise of the peak response to a maximum at a velocity of about 40 $km\,s^{-1}$ followed by a fall off. The reasons for these features are as follows. As the initial velocity of the meteoroids increase, the ionization efficiency increases as v^n, where n is between 3.5 and 4 (*Bronshten*, 1983; *McKinley*, 1961; *Verniani*, 1973). Thus, a greater amount of ionization is produced by meteoroids with larger velocities. The height of ablation of a given meteoroid also increases as the initial velocity increases. Both these effects are described by classical ablation theory and are seen in Figure 4.3. These two effects compete against each other with respect to the response function. As the amount of ionization produced increases, so too does the detectability of the meteor, hence the response is greater for higher initial meteoroid velocities. However, as the height of ablation increases, the attenuation factors play a greater role thus reducing the number of underdense echoes which may be detected. This explains the general form of Figure 4.8f, for velocities less than 40 $km\,s^{-1}$, the effect of increasing ionization production dominates, therefore the peak response increases. For velocities greater than 40 $km\,s^{-1}$ the effect of the attenuation factors dominates, therefore the peak response decreases. The increase in the sidelobe response with velocity is also explained. The sidelobe sensitivity is much lower than the main beam

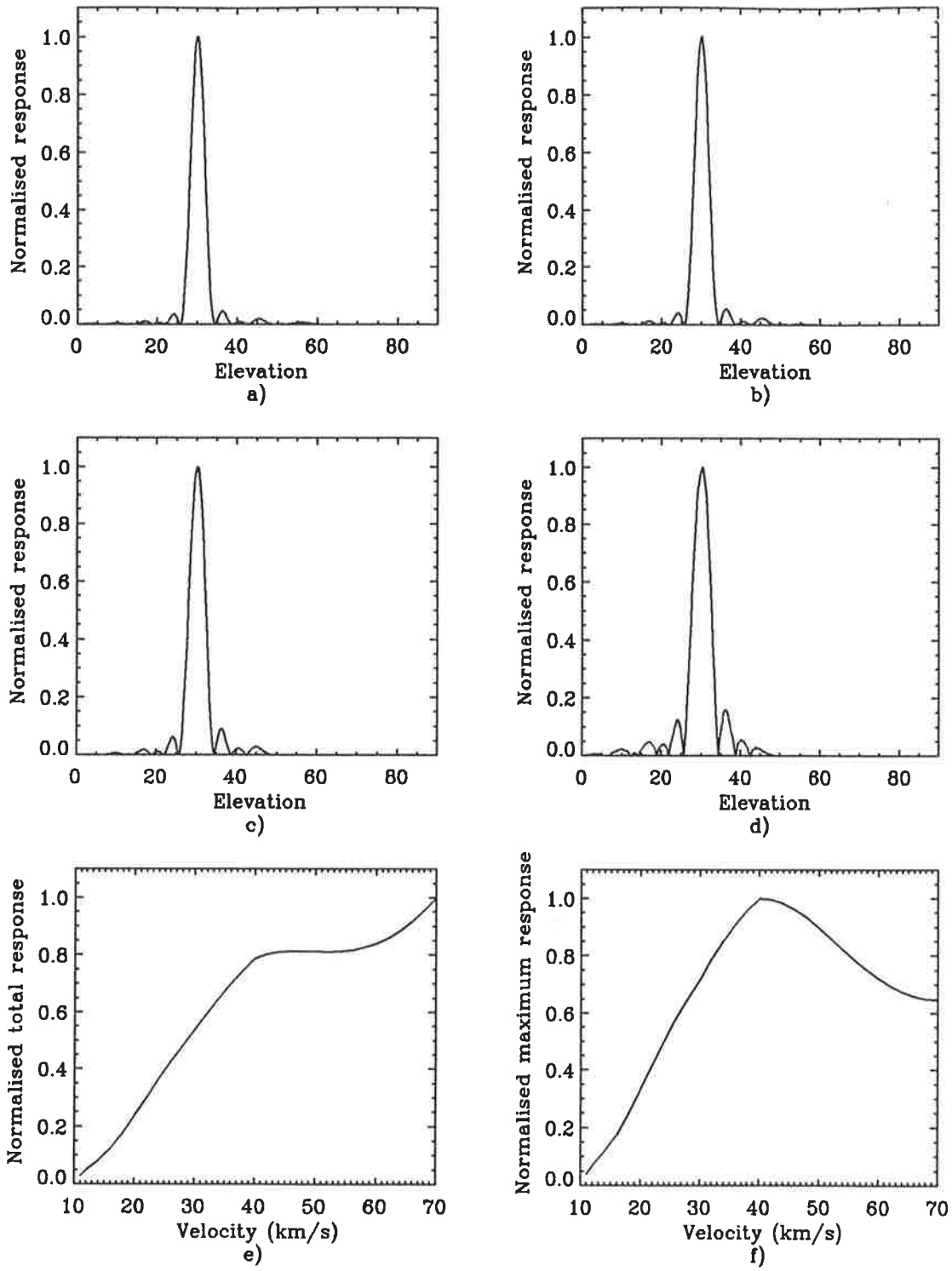

Figure 4.8: The response function (normalised to the peak response) at an azimuth of 266° with a beam 30° off zenith for initial meteoroid velocities of 11, 20, 40 and 60 $km\,s^{-1}$ (panels (a) to (d)). In panel (e), the response function is integrated over the sky to obtain the total response as a function of velocity (normalised to the maximum total rate). Panel (f) shows the peak response rate (which occurs at an elevation of 30.5° and azimuth of 266°) plotted as a function of velocity. This is normalised to the peak (which occurs at 40 $km\,s^{-1}$).

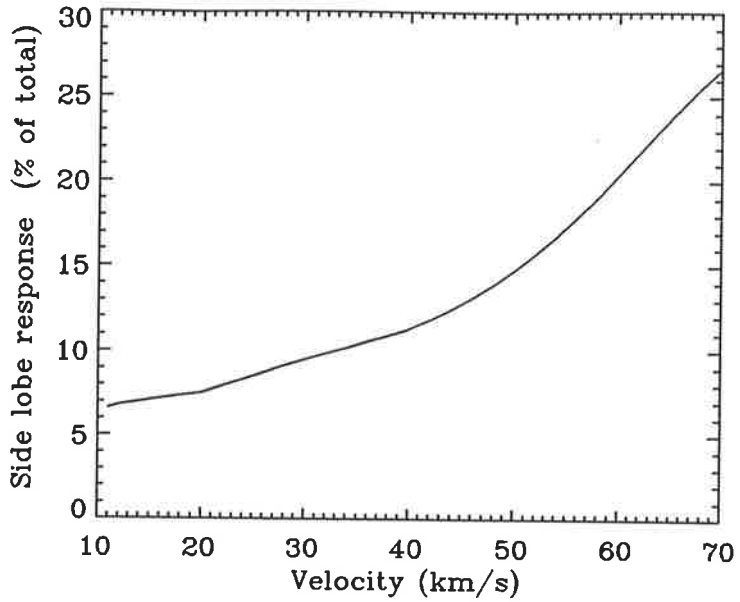

Figure 4.9: The variation of sidelobe response (as a percentage of the total response) with the initial meteoroid velocity.

and primarily overdense echoes are detected by the sidelobes. Thus the sidelobe response is not affected by the attenuation factors. The increase in ionization production is the only factor to consider when determining the effect on the sidelobe response as the initial velocity increases. Thus the sidelobe response, unlike the main beam, increases monotonically with increasing initial velocity. Figure 4.9 shows the response of the sidelobes (percentage of the total response) as a function of the initial meteoroid velocity. One can see that the sidelobe response increases slowly until the velocity reaches $\sim 40\,km\,s^{-1}$. The sidelobe response past this point increases more rapidly as the fraction of underdense trails fall.

On examining Figure 4.8e, one may observe that the response function integrated over the sky increases with the initial velocity of the meteoroids, except in the region from 43 to $55\,km\,s^{-1}$. In this region of velocities, the integrated response reaches a plateau. This is not surprising in the light of the arguments detailed in the previous paragraph. Clearly, in this region of velocities, the effect of the decreasing sensitivity of the main beam, and increasing sensitivity of the sidelobes with velocity, balances. Thus the net effect is a constant integrated response over the velocity range of 43 to $55\,km\,s^{-1}$.

The variation of the expected height distribution as a function of meteoroid velocity may also be investigated. Figure 4.10 shows the expected height distribution calculated at initial meteoroid velocities of 11, 20, 40 and $60\,km\,s^{-1}$ (panels a to d respectively). Panel (e) of

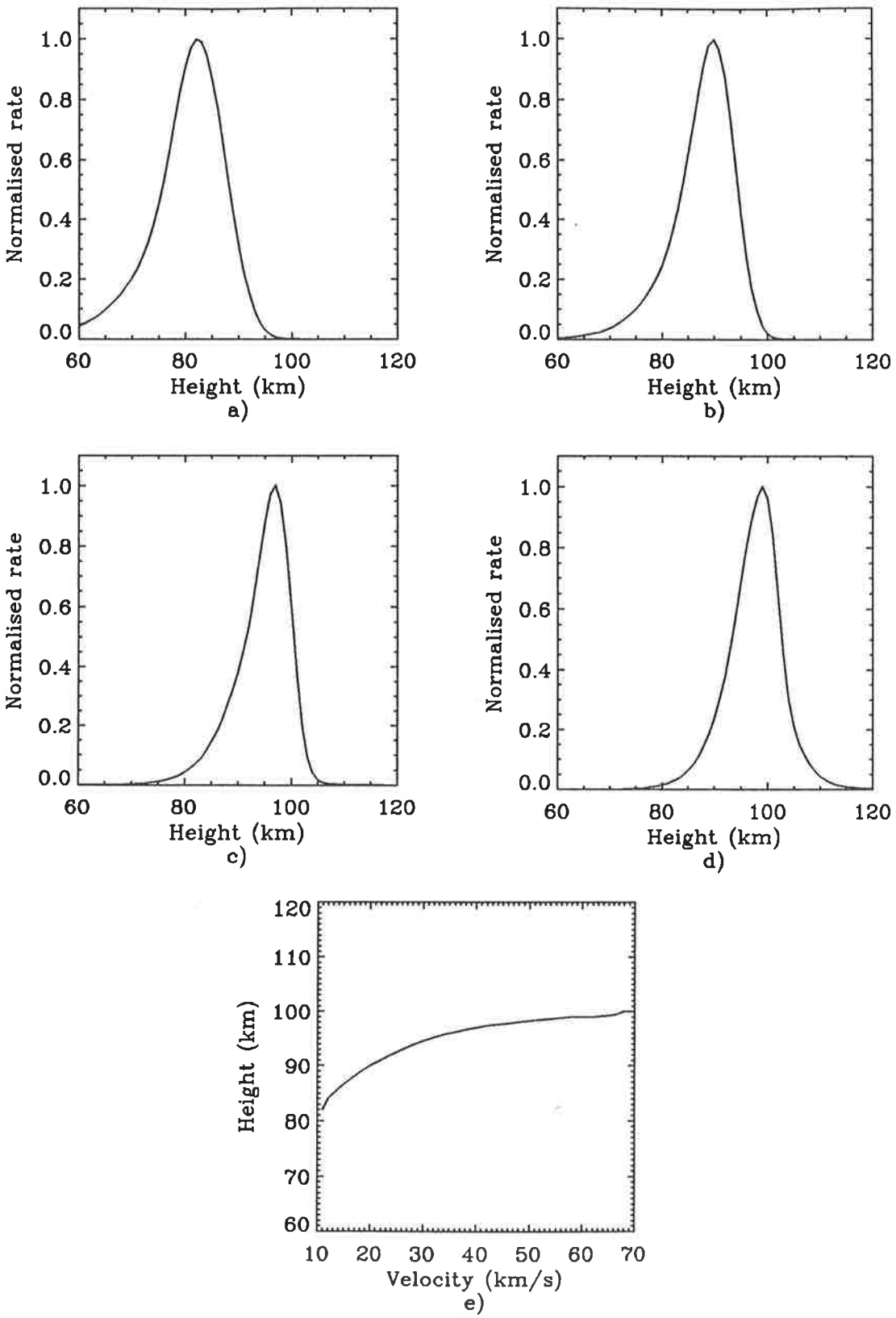

Figure 4.10: The expected height distribution calculated at initial meteoroid velocities of 11, 20, 40 and 60 $km\,s^{-1}$ (panels (a) to (d) respectively) and the height of the peak as a function of velocity (e).

Figure 4.8 shows the altitude of the peak of the height distribution as a function of velocity. As expected the height distribution shifts to higher altitudes with increasing velocity. This is of course due to both the meteoroids with larger velocities ablating at higher altitudes and the increase in ionization efficiency with velocity. Above a velocity of $30\,km\,s^{-1}$, the rate of increase of the peak with velocity falls considerably, so that even at $70\,km, s^{-1}$ the peak of the height distribution is limited to an altitude less than $100\,km$. The reason for this is due to the echo attenuation and echo selection factors.

Consider now Figure 4.11. Here, in panels (a) and (b), the response function (at an azimuth of 266°) is shown for an initial velocity of $60\,km\,s^{-1}$. In panel (b), the calculation was performed such that all meteors, regardless of their electron line densities, are treated as underdense and the attenuation factors applied appropriately. Panels (c) and (d) are a repeat of panels (a) and (b) at an initial velocity of $30\,km\,s^{-1}$. All of the responses have been normalised to the peak response of that in panel (a). It can be seen from this figure that treating all echoes as underdense, affects the response function significantly at large meteoroid velocities. However, at low meteoroid velocities the effect is negligible. At a meteoroid velocity of $60\,km\,s^{-1}$, treating all echoes as underdense reduces the total response (*i.e.* response integrated over the entire sky) by 33.7% and the sidelobe response decreases from 20.3% to 14.0% of the total response. When the meteoroid velocity decreases to $30\,km\,s^{-1}$, the reduction factor of the total response to has fallen to 1.1% and the side lobe response decreases fro 9.6% to 9.3% upon treating all echoes as underdense. This demonstrates the importance of considering how the overdense echoes contribute to the response function at large meteoroid velocities. However, there are two important points to note from Figure 4.11 in conjunction Figure 4.9 which indicate that the overdense echoes are not the only contribution that requires consideration. These points are :

1. Although the sidelobe contribution is reduced for the case of all meteors treated as being underdense, the response function for an initial meteoroid velocity of $60\,km\,s^{-1}$ still has a higher sidelobe contribution than the response function calculated at an initial meteoroid velocity of $30\,km\,s^{-1}$. Thus the argument detailed at the start of this section, does not explain entirely why the the sidelobe response increases with the initial meteoroid velocity.

2. At low initial meteoroid velocities, treating all meteors as underdense has a negligible effect on the response function. From Figure 4.9, it can be seen that at low initial

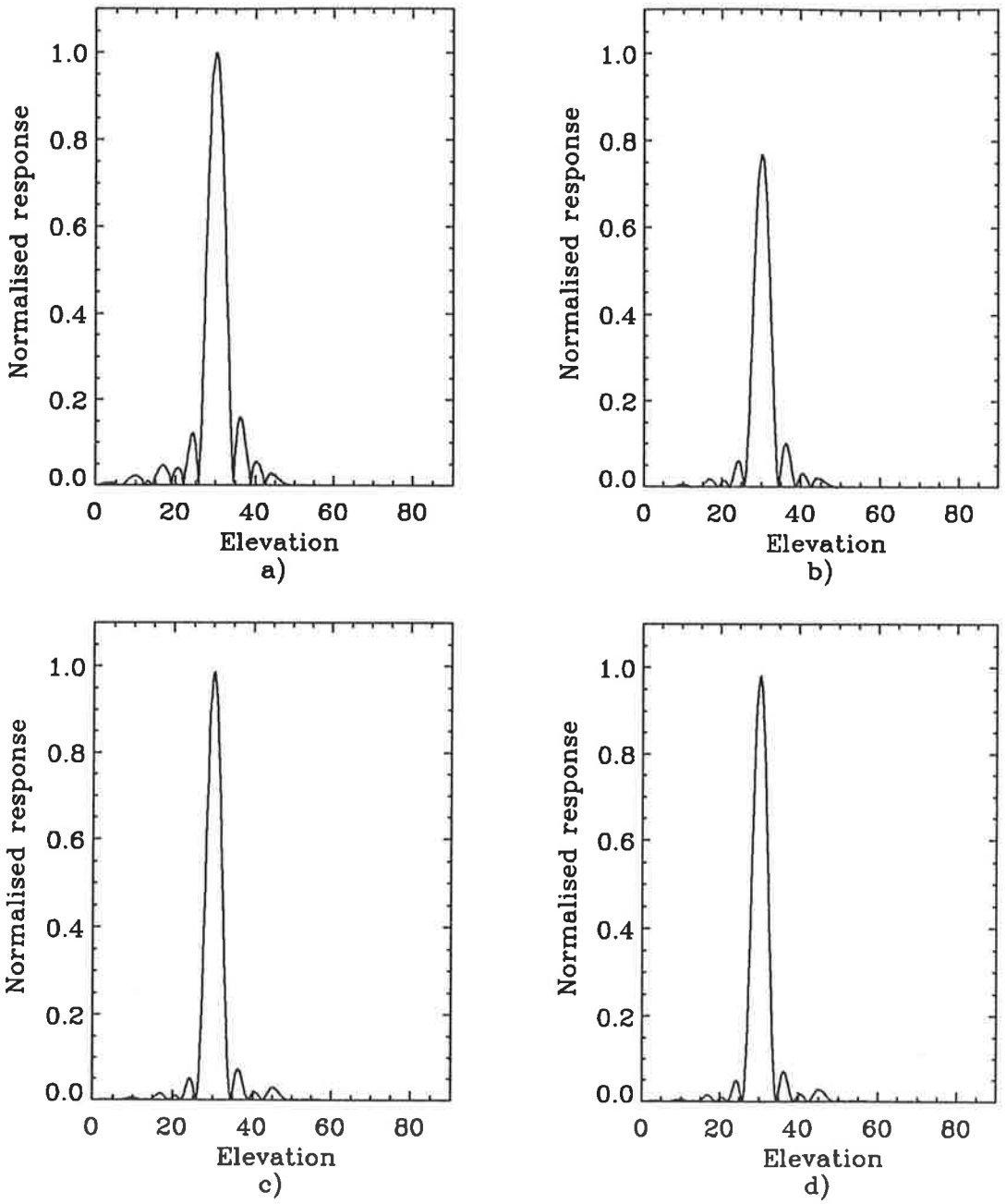

Figure 4.11: The response function at an azimuth of 266° calculated for initial velocities of $60\,km\,s^{-1}$ (panels (a) and (b)), and $30\,km\,s^{-1}$ (panels (c) and (d)). In panels (b) and (d), the calculations have been performed such that all meteors are treated as underdense and the attenuation factors applied. All have been normalised to the peak response of that in panel (a).

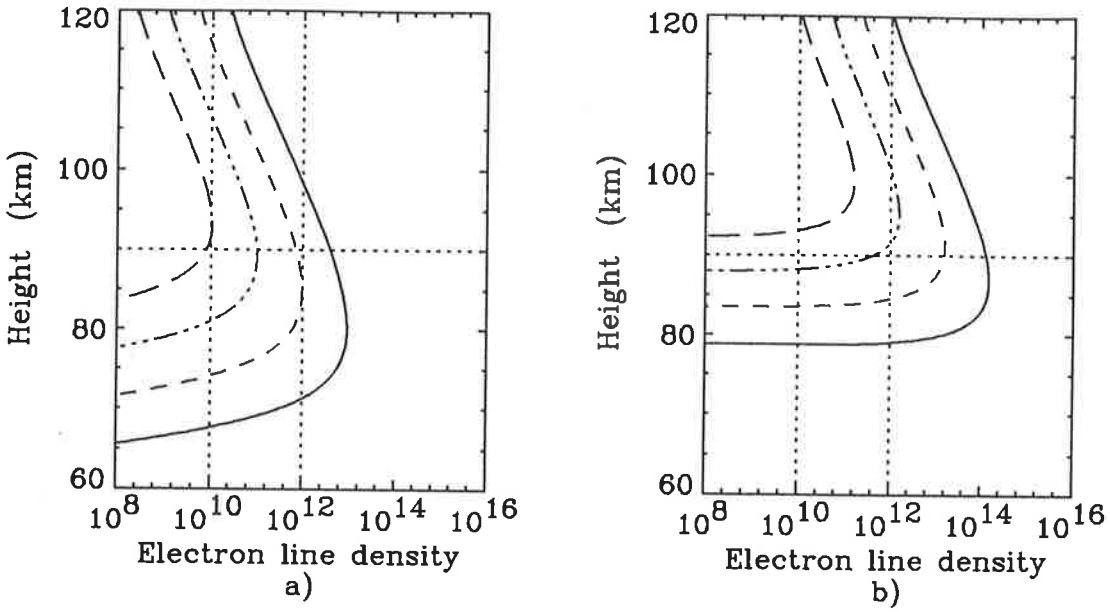

Figure 4.12: Ionization profiles calculated from classical ablation theory (see section 3.3) for initial meteoroid velocities of $20\,km\,s^{-1}$ (a) and $40\,km\,s^{-1}$ (b). In each of these panels, the solid line indicates an initial mass of $10^{-6}\,kg$, short dashed $10^{-7}\,kg$, broken $10^{-8}\,kg$, and the long dashed line an initial mass of $10^{-9}\,kg$. The dotted lines indicate electron line densities of 10^{10} and $10^{12} electrons\,m^{-1}$ and a height of $90\,km$.

meteoroid velocities the side lobe response increases with the meteoroid velocity. Again the argument described at the start of this section does not explain this.

It is clear that the role of overdense meteors is not the whole story regarding the sidelobe response, and further investigation is required.

Consider the ionization profiles calculated from classical ablation theory for initial meteoroid velocities of $20\,km\,s^{-1}$ and $40\,km\,s^{-1}$ (see Figure 4.12). In this figure, ionization profiles are plotted for initial meteoroid masses of 10^{-9}, 10^{-8}, 10^{-7} and $10^{-6}\,kg$. Consider, also, the two limiting electron line densities; 10^{10} and $10^{12}\,electrons\,m^{-1}$, indicated by vertical dotted lines in Figure 4.12). For meteoroids with initial velocities of $20\,km\,s^{-1}$, the limiting masses are approximately 10^{-9} and 10^{-7}, at a height of $90\,km$, for the two respective limiting electron line densities. These two limiting masses (at the same height and limiting electron line densities as above) become about 3×10^{-8} and 10^{-8} for meteoroid velocities of $40\,km\,s^{-1}$. Thus, assuming a mass index of $c = -1$, the ratio of the number of meteors detected above the respective limiting electron line densities at a height of $90\,km$, decreases from around 100 to about 3.5 for the given increase in the meteoroid initial velocity. This demonstrates that at a particular height, increasing the sensitivity of the system (*i.e.* reducing the minimum detectable electron line density) has less of an affect on the meteor count rates at higher

velocities. Of course what happens is that the ionization profile is pushed up in height as the meteoroid velocity increases. Thus at the height of interest there are fewer meteors since the less massive meteors have already ablated at higher altitudes. Now, the response function requires integration over height and the attenuation factors must be taken into account. The effect of the attenuation factors is to suppress the number of echoes detected at high altitudes. Thus one can immediately see that the sidelobes of the radar have a greater response with respect to the main beam at higher meteoroid velocities. Also, if one was to ignore the attenuation factors in the response function calculation, one would expect the effect of the increased sidelobe response with meteoroid velocity not to occur.

In Figure 4.13, panels (a) and (b), the response function has been calculated at initial velocities of $20\,km\,s^{-1}$, $40\,km\,s^{-1}$ and $60\,km\,s^{-1}$, with the attenuation factors set to a value of 1.0 at all heights (thus they play no role in the calculation). The response functions are normalised to the peak rate at $60\,km\,s^{-1}$ in panel (a) of Figure 4.13; one can see the large difference in the meteor rates due to the increase in ionization efficiency at larger velocities. Panel (b) shows the response functions calculated at $20\,km\,s^{-1}$ and $60\,km\,s^{-1}$, each of which are normalised to their respective peak rates. It can be seen that there are significant differences between these two responses, especially at large elevation angles. This appears to contradict the arguments of the previous paragraph.

There are two other curious features to note. First, the peak of the response function calculated at $60\,km\,s^{-1}$ occurs at 29.75° and second, examining the first side lobes, shows that the side lobe at the larger elevation is smaller than the one at the lower elevation. These two points are opposite to what is observed if the attenuation factors are included in the calculation. The explanation of these three effects is straight forward. One must consider the range cutoff at $128\,km$. If the the response function is calculated with no attenuation factors, meteoroids ablating at higher altitudes will contribute. However at a given height the range cut off will apply and essentially this is a selection effect for meteors with radiants from lower elevation angles. The selection effect is of course worse for meteoroids with larger initial velocities, due to these ablating at higher altitudes, which is observed in Figure 4.13b. Given the importance of considering the range cutoff, panels (a) and (b) of Figure 4.13 are repeated in panels (c) and (d) of the same figure, except here the response functions have been calculated without the range cutoff as well as removing the attenuation factors. Now it may be observed that the response function, when normalised to it's peak, is the same at all velocities. The two other points mentioned (*i.e.* the shift of the peak response to a lower

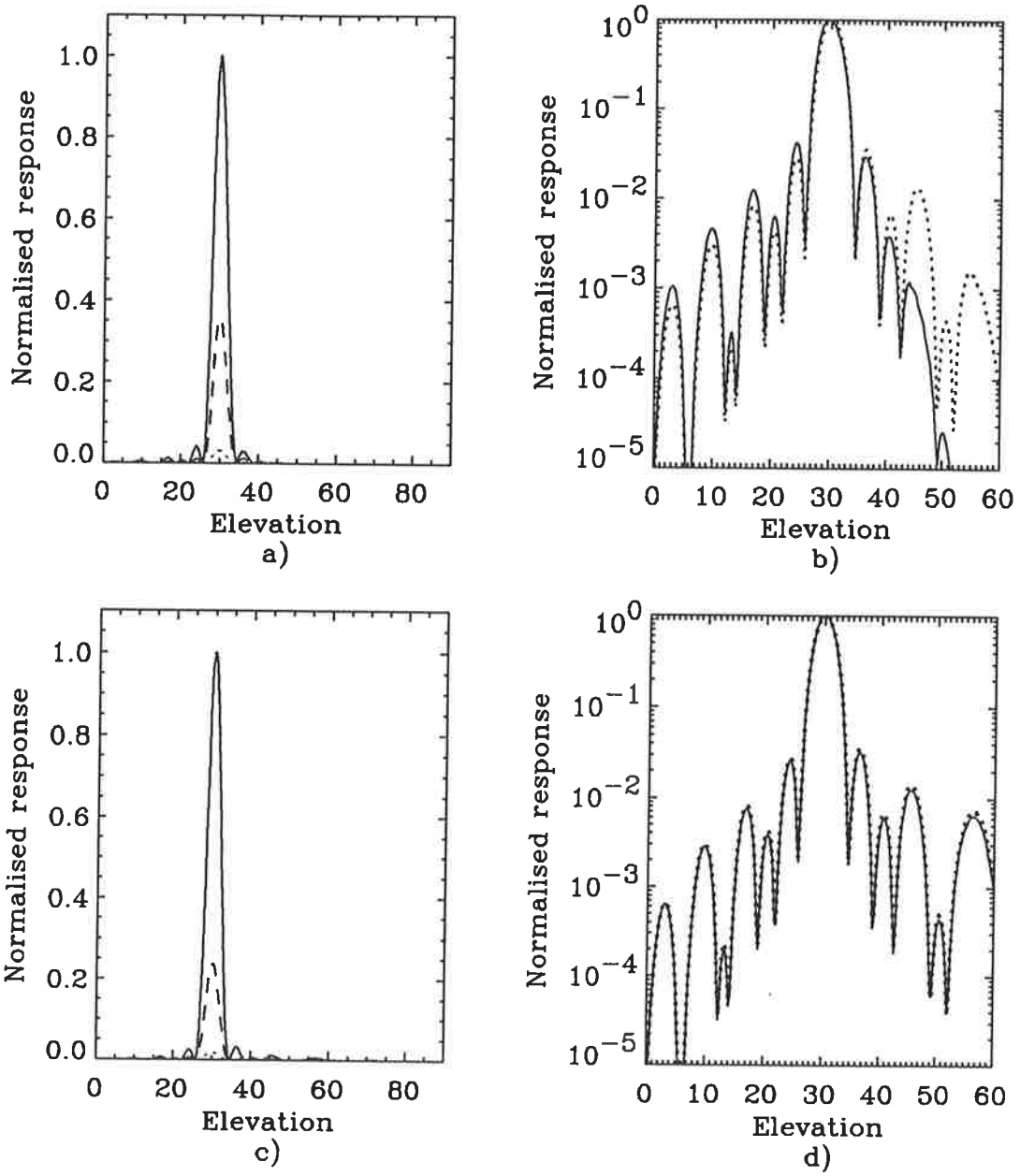

Figure 4.13: Response functions (displayed at an azimuth of 266°) calculated with no attenuation factors applied to the returned echo power at initial velocities of $20\,km\,s^{-1}$, $40\,km\,s^{-1}$ and $60\,km\,s^{-1}$. Panel (a) displays these response functions (dotted, dashed and solid lines respectively) normalised to the peak rate at $60\,km\,s^{-1}$. Panel (b) displays the response calculated at $20\,km\,s^{-1}$ (dotted line) and $60\,km\,s^{-1}$ (solid line), each are normalised to their respective peak rates. Panels (c) and (d) are repeats of (a) and (b) except here the effect of the range cut off has been removed also.

elevation angle and the reversed response levels of the first sidelobes) are also resolved. The ratio between the peak response rates is 1.0 : 12.6 : 59.0 for the corresponding velocity ratio of 1.0 : 2.0 : 3.0. Thus the meteor rate increases as V^n, where n is 3.6 - 3.7. Clearly, the meteor rate increase with velocity is due to the increase in ionization efficiency, which varies as V^x, where x is generally accepted to lie between 3 and 4.

This completes the discussion on the velocity dependence of the response function of the Buckland Park VHF radar. The complete response function, *i.e.* the response function integrated over a suitable velocity distribution, is now required to be calculated. This is performed and discussed in the next section.

4.4.5 The complete response function - integration over the meteoroid initial velocity

Integration of the response function over the meteoroid initial velocity requires, of course, a suitable meteoroid velocity distribution. Two meteoroid velocity distributions, as observed by radar techniques, will be used. The first is the Harvard Radio Meteor Project velocity distribution (*Sekanina and Southworth*, 1973), the second is that obtained by *Nilsson* (1962, 1964a) from his meteor orbit survey at Adelaide. The velocity distribution as observed by radar must be corrected for velocity selection effects such as the ionization probability and trail diffusion. *Cook* (1972) gives an ionization probability of V^4, and this is used by *Sekanina and Southworth* (1973) to correct the Harvard Radio Meteor Project velocity distribution. *Nilsson* (1962, 1964a) also used a correction factor of V^4.

Taylor (1995) has noted that the correction factor applied by *Sekanina and Southworth*, is not the value that they state in their paper. *Elford et al.* (1996) in their paper on meteoroid velocities, have revised the correction applied to the Harvard Radio Meteor Project velocity distribution based upon the investigation of *Taylor*. They then compare the revised corrected Harvard radio distribution together with *Nilsson's* corrected distribution and the Super-Schmidt observations (optical) reported by *McCroskey and Posen* (1961). This comparison of the three meteoroid velocity distributions appears in Figure 4.14.

Elford et al. find considerable disagreement between the two radio velocity distributions. The optical and Harvard radio distributions do agree from 20 to 55 $km\,s^{-1}$ but the Harvard radio distribution is a order of magnitude less than the optical results above velocities of 55 $km\,s^{-1}$. Conversely *Elford et al.* find that for low velocities (less that 30 $km\,s^{-1}$) the velocity distribution obtained by *Nilsson* disagrees with the Super-Schmidt results, but agrees

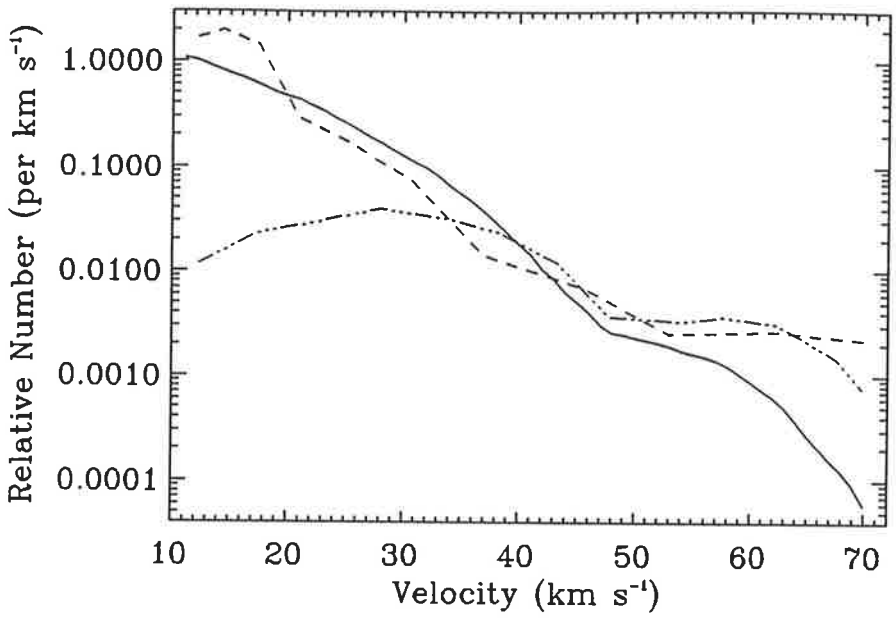

Figure 4.14: Corrected velocity distributions of meteoroids. The solid line is the revised Harvard Radio distribution (see text), the dashed line the Super-Schmidt observations of *McCroskey and Posen* (1961), while the dashed line indicates the distribution observed by *Nilsson* (1962) at Adelaide. This diagram is reproduced from *Elford et al.*, [1996].

well above this velocity.

Elford et al. put forward one possible explanation for the disagreement of the Harvard radio observations at large velocities: the Harvard correction for diffusion is underestimated. This is based on the height distribution of meteors observed at MF (*Steel and Elford*, 1991). These results show that at MF, meteors may be observed at greater heights than with traditional VHF meteor radars. Thus the diffusion meteors plays a greater role in meteor selection at the upper heights than previously thought. At larger velocities, meteors ablate at larger altitudes, thus if the effect of diffusion is underestimated, the corrected velocity distribution would be biased against meteoroids with larger velocities. The results of *Nilsson* at low velocities remains unexplained. No biases against low velocity meteors in either of *Nilsson's* system or method were found.

Figure 4.15 shows the response function (normalized to the peak response) integrated over the revised corrected Harvard Radio velocity distribution. In panel (a) the response function is displayed as a contour diagram, panel b shows a cross-section through the response function at an azimuth of 266°. The percentage of meteors detected in sidelobes as opposed to the main beam is 8.5%. Panel (c) shows the expected height distribution of meteors for an isotropic distribution of meteors. This was calculated as follows : the response function at

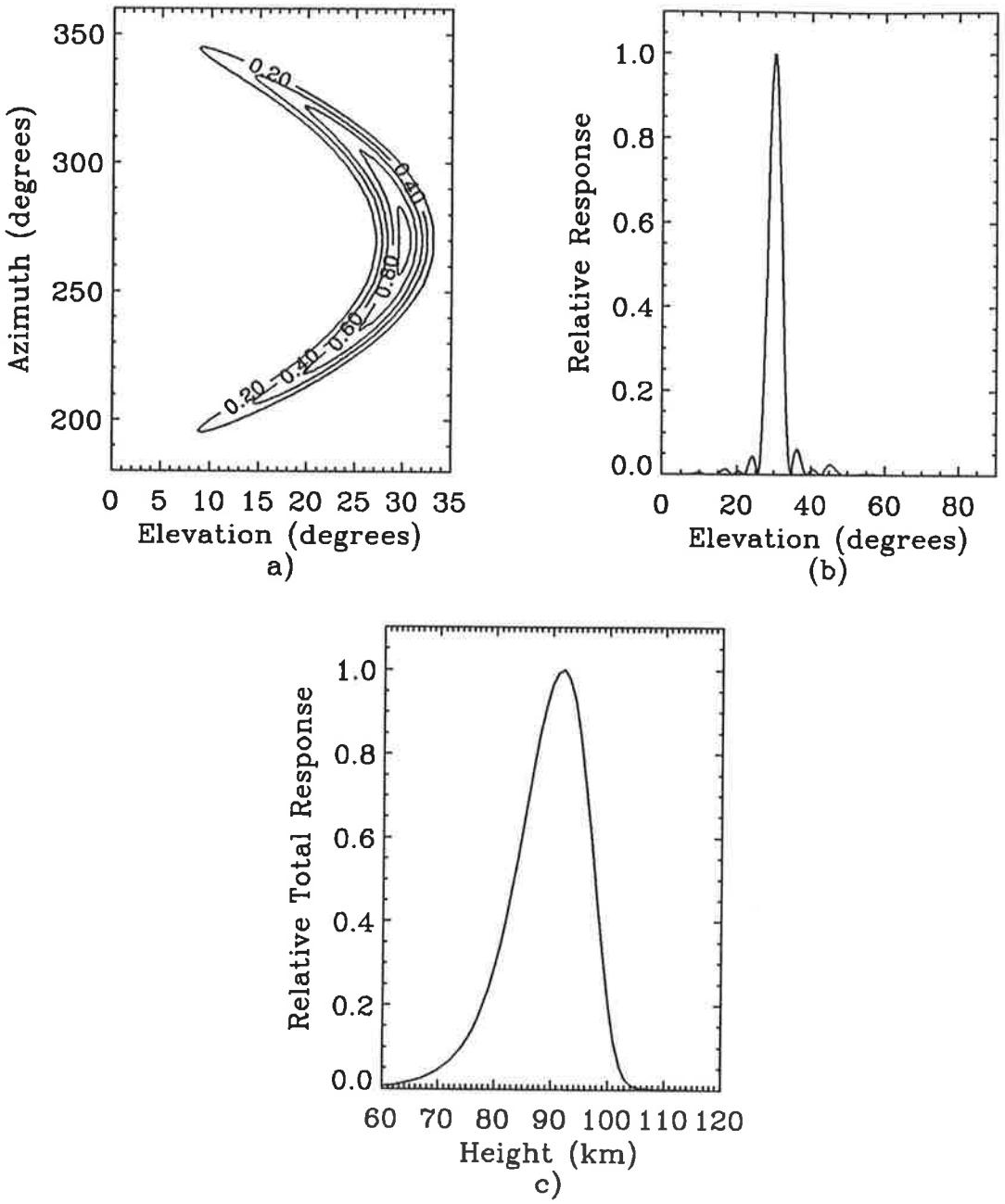

Figure 4.15: Contour diagram of the response function (normalized to the peak response) of the Buckland Park VHF radar integrated over meteoroid velocity (a). The revised corrected Harvard Radio velocity distribution was used. Panel (b) shows a cross-section through the response function at a azimuth of 266°. Panel (c) shows the expected height distribution of meteors.

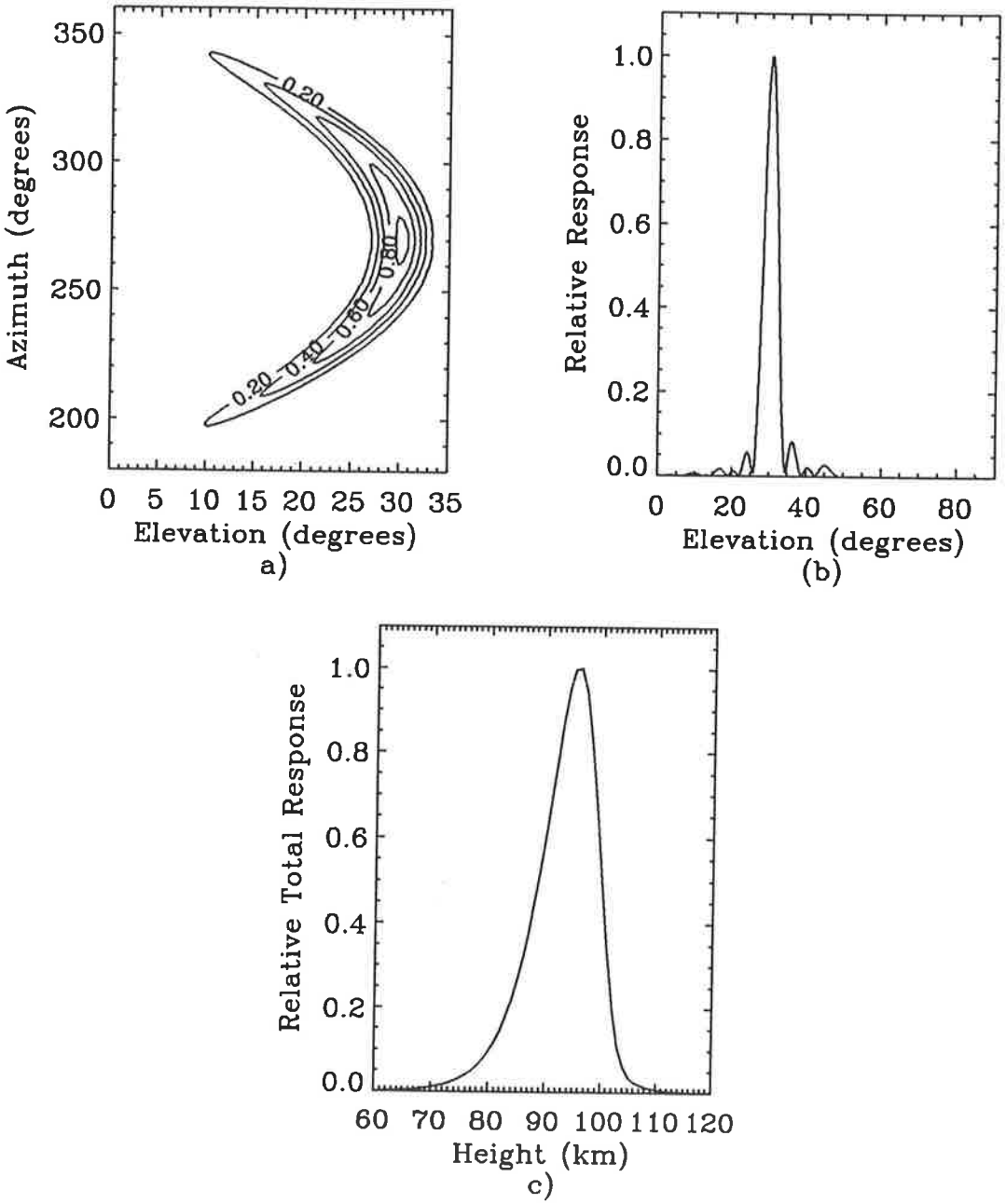

Figure 4.16: As for figure 3.15 except here integration over meteoroid velocity has been performed using the velocity distribution obtained by *Nilsson* (1962).

each height and meteoroid velocity was integrated over the sky, thus yielding the response as a function of both height and velocity. Subsequent integration over velocity with a suitable velocity distribution, gives the expected height distribution plotted in Figure 4.15c. This height distribution is of the form expected for a radar operating at VHF. The peak of the height distribution occurs at 92 km with few meteors detected above at height of 100 km and none above 105 km.

There is no particular reason to use the Harvard velocity distribution over that obtained by *Nilsson* in the integration over velocity. Thus integration of the response function over meteoroid velocity using *Nilsson's* velocity distribution is also performed. The results of this are presented in Figure 4.16, the same format of Figure 4.15 is used. The sidelobe contribution here is 10.9% and the peak of the height distribution has moved up to 96 km. These results are not surprising, since using *Nilsson's* velocity distribution means that meteoroids with larger velocities have a greater contribution to the response function integrated over velocity than with the Harvard velocity distribution. It was shown previously that the response function calculated at larger meteoroid velocities had both a larger sidelobe response and a height distribution peaking at larger altitudes.

In Chapter 5, the velocity distribution of sporadic meteors is determined by the author from observations with the Buckland Park radar. It is shown in Chapter 5 that this velocity distribution is in better agreement with the optical results than those from the two radio techniques described above. The response function was calculated using the Buckland Park velocity distribution, and a sidelobe contribution of about 8.7% was found. This response function is not displayed as only negligible differences were found between it and the response function calculated with the Harvard velocity distribution.

4.4.6 The effect of the diurnal variation of the background noise

As stated in the introduction to this section, the background cosmic noise varies diurnally, thus causing a similar variation in the minimum detectable power due to the method of the echo detection employed. The value of P_R may vary from 1.0×10^{-13} to $4.0 \times 10^{-13}\,W$ depending on when the galactic centre passes through the main beam of the antenna pattern. As all the response function calculations conducted so far have used an average value of 2.5×10^{-13} for P_R, now the effect of the variation of P_R on the response function needs to be examined.

In Figure 4.17, the response function calculated at a velocity of 20 $km\,s^{-1}$ and at minimum

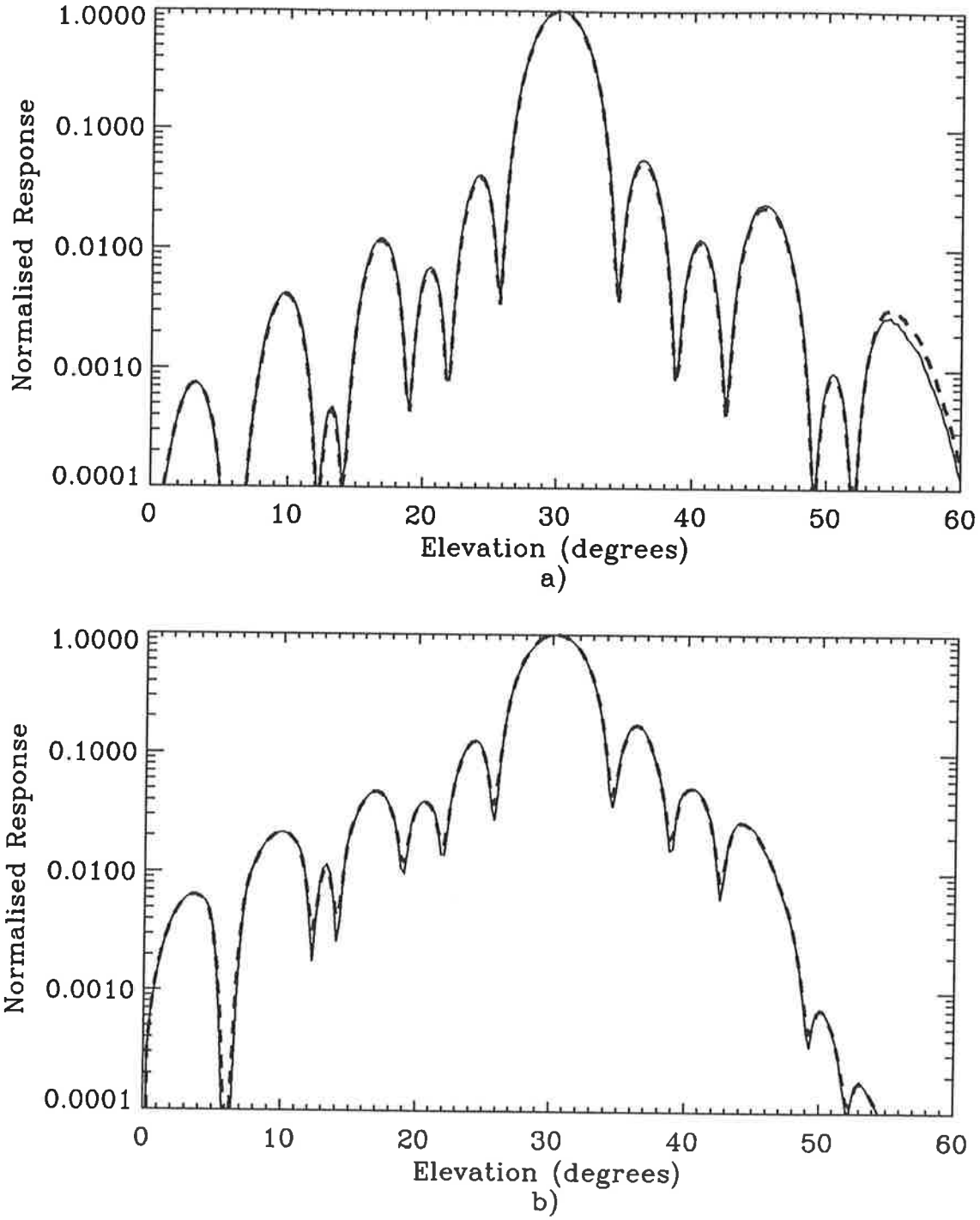

Figure 4.17: Panel (a) shows the response function calculated a velocity of $20 km\, s^{-1}$ and minimum detectable power levels of $1.0 \times 10^{-13} W$ (solid line) and $4.0 \times 10^{-13} W$ (dashed line). Panel (b) is a repeat of panel (a), except here the response functions are calculated at a velocity of $60\, km\, s^{-1}$.

detectable power levels of 1.0×10^{-13} and $4.0 \times 10^{-13} W$ are displayed in panel (a) (solid and dashed lines respectively). In both cases the response functions were normalised to their respective peaks. Panel (b) is a repeat of panel (a), except here the response functions have been calculated at a velocity of $60\, km\, s^{-1}$. These response functions have been plotted on log scales and it is immediately clear that at $20\, km\, s^{-1}$ there are negligible differences between the two response functions calculated at different levels of P_R. Furthermore these differences only occur in the sidelobes of the response function. At a velocity of $60\, km\, s^{-1}$, there is no discernible difference between the response functions at all.

On the basis of Figure 4.17, it is then reasonable to calculate the response function at an average value for the minimum detectable power, and then apply a multiplicative factor to obtain the response function at other values of P_R. Figure 4.18 shows normalisation factors appropriate for response functions calculated at velocities of 20, 40 and $60\, km\, s^{-1}$ (solid, dashed and broken lines respectively), as a function of the minimum detectable power. These normalisation factors have been scaled to unity for a minimum detectable power of $2.5 \times 10^{-13} W$. Multiplying the response function calculated at this P_R by the appropriate normalisation factor will rescale the response function to that calculated at the required level of P_R. This only becomes significant when comparing a shower observed in the East and West beams or examining the sporadic flux.

4.4.7 Different Antenna Configurations on Reception

Now that the discussion on the response function calculated for the Buckland Park VHF radar is complete, the effect of different receiving and transmitting configurations on the response function may be investigated. The motivation for this is to see if the side lobe contribution can be reduced. Since the VHF radar transmitting system is modular in design (see Chapter 2), it is possible to transmit on the entire 32 rows of the CoCo array and receive on subset of the same array. For this configuration, the antenna pattern in the East/West direction is broadened on reception. However, this may be advantageous; if the antenna pattern is broadened sufficiently on reception, the first set of nulls match the first sidelobes of the transmit antenna pattern. This, of course, reduces the contribution of these lobes to the response function calculation.

The receiving configuration required to suppress the first sidelobes of the response function as described above, is to receive on a subset of 22 rows of the CoCo array. The physical

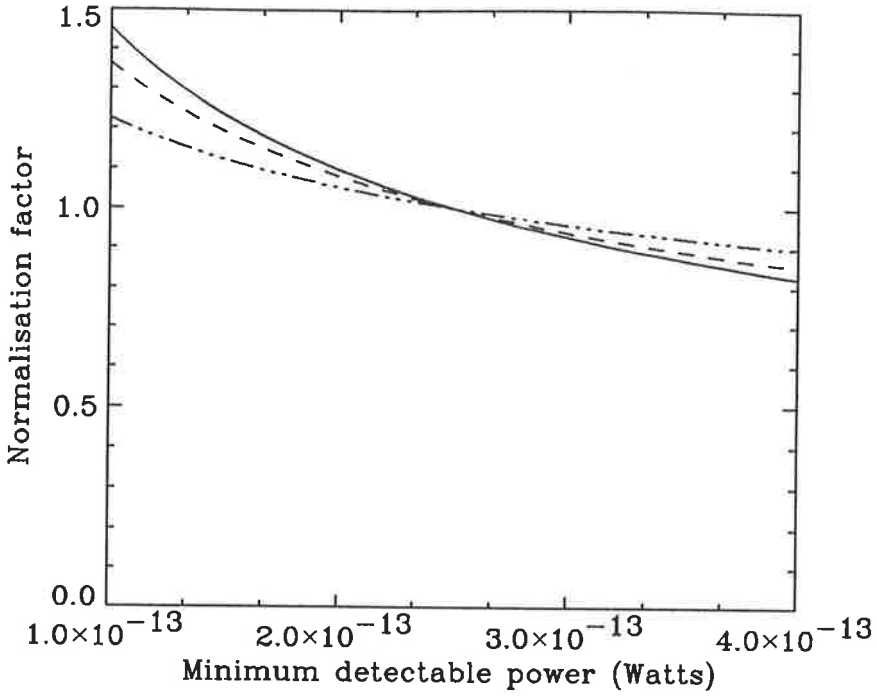

Figure 4.18: Normalisation factors to rescale the response function calculated at a minimum detectable power of $2.5 \times 10^{-13} W$ to the required minimum detectable power level. The solid line is the normalisation factor calculated at a velocity of $20\,km\,s^{-1}$, the dashed and broken lines are calculated at velocities of $40\,km\,s^{-1}$ and $60\,km\,s^{-1}$ respectively.

arrangement of this subset is 11 rows on either side of the transmitting caravan (see Figure 2.1), *i.e.* the outer 5 rows on either side of the caravan are not used. Figure 4.19 shows the modelled antenna pattern for a subset of 22 rows of the CoCo array (solid line) for a 30° beam tilt. The modelled antenna pattern for the entire array is also shown (dashed line). One can see that the antenna pattern is broadened significantly when a subset of the entire array is used. The first nulls of the subset array match the first side lobes of the entire array as required, however one can see that other lobes (such as the second set of sidelobes) will be enhanced in the response function calculation.

The response function using the above configuration on reception and transmission is now calculated. An off zenith beam tilt of 30° was used and the calculation was performed for meteoroids with an initial velocity of $30\,km\,s^{-1}$. This response function is displayed in Figure 4.20 (solid line) together with the response function calculated using the usual antenna configuration (*i.e.* transmission and reception on the entire array). One can see that the response function calculated for this configuration has a broader main lobe and a "bite out" in the first sidelobes, these sidelobes are suppressed by approximately 15%. However, as expected, the second set of side lobes have been enhanced. Subsequent sidelobes are also

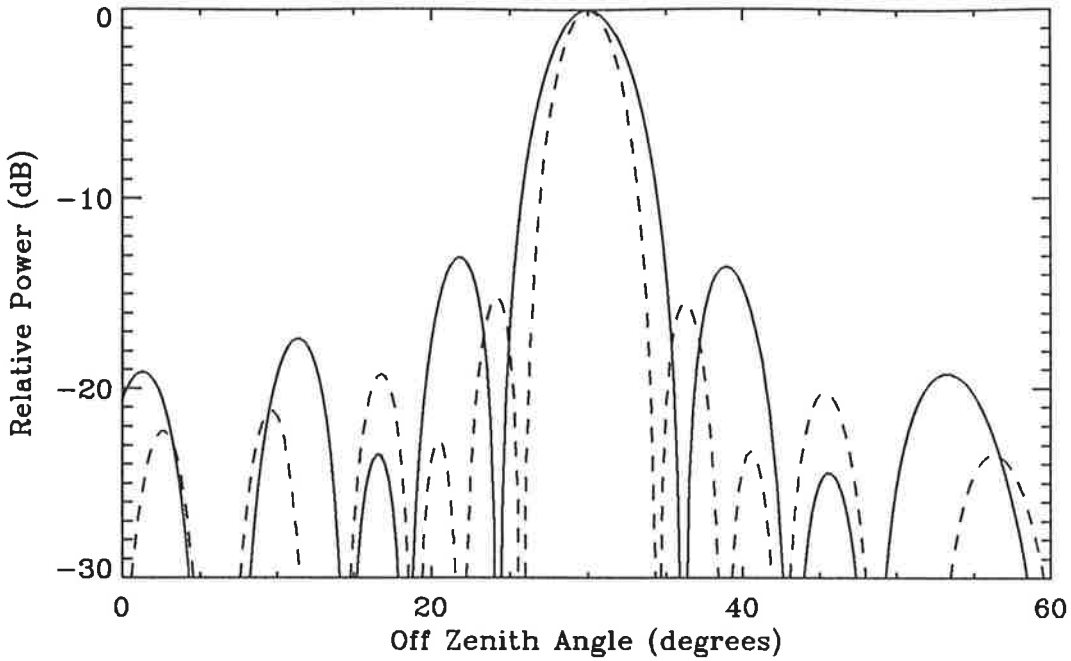

Figure 4.19: The modelled antenna pattern for a subset of 22 rows of the Buckland Park VHF CoCo array (solid line). The dashed line shows the modelled antenna pattern of the entire array.

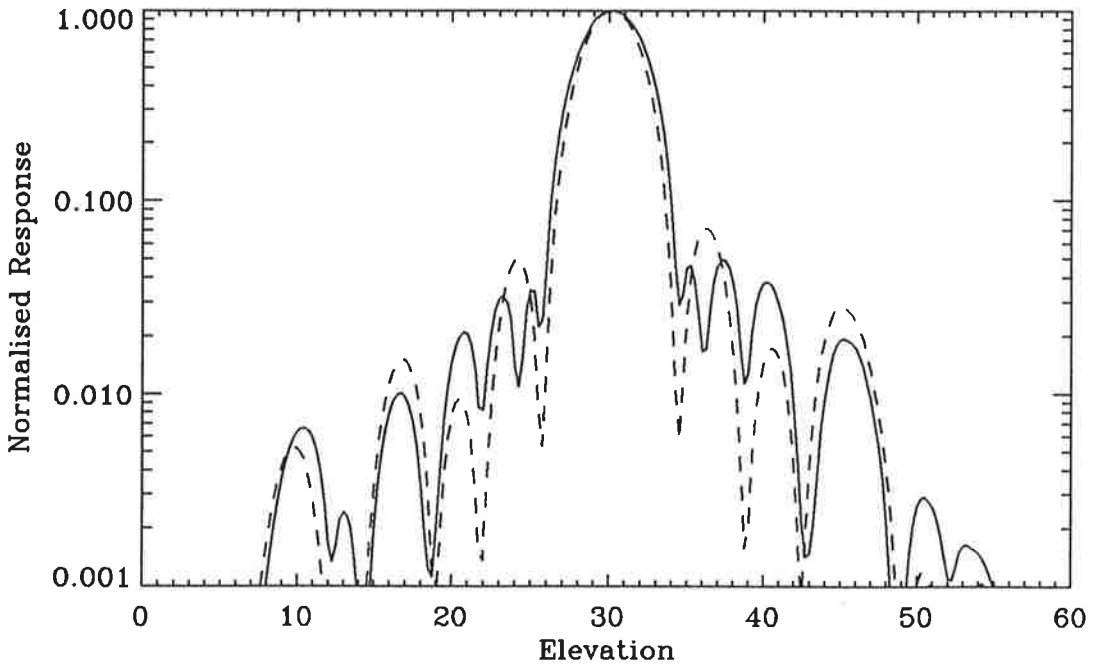

Figure 4.20: The response function of the Buckland Park VHF array calculated for reception on a subset of 22 rows of the CoCo array (solid line). The dashed line is the response function calculated for the usual reception configuration (the entire CoCo array). Transmission in both cases is on the entire CoCo array, an off zenith beam tilt of 30° was used and the calculation was performed at a velocity of $30\,km\,s^{-1}$.

either enhanced or suppressed. It is necessary, then, to quantify the effect to the side lobes by using this configuration. The sidelobe response for the usual configuration is 9.9% of the total response. This reduces to 8.9% for reception on only 22 rows of the CoCo array. One can see then that the benefit of sidelobe suppression using this configuration is small. Performing this calculation for different numbers of CoCo rows on reception, has a negligible effect on this result. It was therefore deemed unnecessary to use these sort of antenna configurations on reception, and all meteor observations were performed using the entire CoCo array for both reception and transmission.

4.5 The Response Function at Lower Frequencies

The final topic to discuss concerning the meteor radar response function, is the effect of operating a radar at lower frequencies. The operating frequency of the radar affects the response function through the attenuation and echo selection factors. These three factors are discussed in Section 4.2.1 and are summarised below.

$$\alpha_r = exp\left(-\frac{8\pi^2 r_0^2}{\lambda^2}\right), \qquad [log_{10} r_0 = 0.019h - 1.92 + log_{10}(V/40)] \quad (4.55)$$

$$\alpha_v = \frac{1 - e^{-\Delta}}{\Delta}, \qquad \left[\Delta = \frac{16\pi^2 D}{V}\left(\frac{R}{2\lambda^3}\right)^{1/2}\right] \quad (4.56)$$

$$\alpha_d = \frac{e^{\omega} - 1}{\omega\, e^{\omega}}, \qquad \left[\omega = \frac{-16\pi^2 Dc}{\lambda^2 f_{prf}}\right] \quad (4.57)$$

(4.58)

Clearly, as the wavelength of the radar increases (decrease in operating frequency), these factors approach unity and thus have a much smaller effect on the minimum detectable electron line density. It is expected that this should be reflected in the radar response function; more meteors should be detectable at greater altitudes.

Figure 4.21 shows the expected height distributions calculated from the response function for meteoroids with initial velocities of 11, 20, 40 and 60 $km\, s^{-1}$ (panels a to d respectively). At each meteoroid velocity, the expected height distribution has been calculated (from the response function) for two fictitious radars operating at frequencies of 2 and 20 MHz and also for the Buckland Park VHF radar operating at 54.1 MHz. The two fictitious radars are assumed to be identical to the Buckland Park VHF radar in all respects except for the minimum detectable power, P_R, and of course the operating frequency. The reason for this is as follows. Consider Equation 4.13 which gives the minimum detectable electron line density,

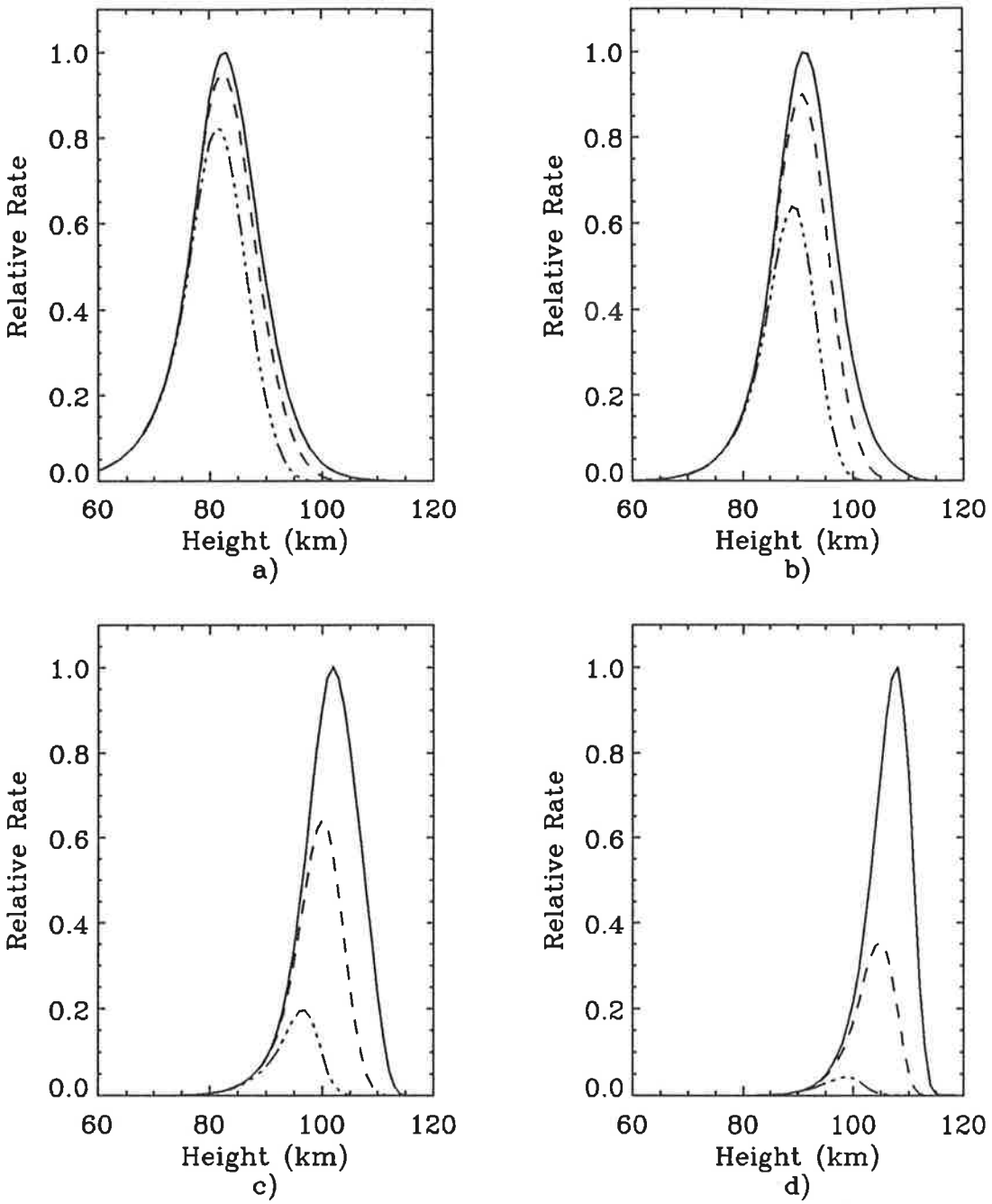

Figure 4.21: Expected height distributions calculated from the response function obtained at initial meteoroid velocities of 11, 20, 40 and 60 $km\,s^{-1}$ (panels (a) to (d) respectively). In each panel the solid line refers to the expected height distribution calculated for a fictitious radar operating at 2 MHz, the dashed line for a fictitious radar operating at 20 MHz and the broken line for the Buckland Park VHF radar. The two fictitious radars are identical to the Buckland Park VHF radar except for minimum detectable power and frequency. For each velocity, the expected height distributions have all been normalised to the peak rate of that obtained for a radar operating at 2 MHz. See text for further details.

q_{min}. This equation is repeated below:

$$q_{min} = 4.5 \times 10^{15} \left(\frac{R}{\lambda}\right)^{3/2} P_R^{1/2} (P_T\, G_T(\theta,\phi)\, G_R(\theta,\phi)\, \alpha_r\, \alpha_d\, \alpha_d)^{-1/2}\,.$$

The only concern is how α_r, α_d and α_d affect q_{min} when the frequency is changed. However, the $1/\lambda^{3/2}$ term will also affect q_{min} as the frequency is altered. This effect is of course invariant with velocity, unlike the α_r, α_d and α_d terms, so the shape of the height distributions will be unchanged. However, this is still undesirable as the absolute rates will increase with decreasing frequency. The minimum detectable power is therefore modified appropriately to counter balance the effect of the $1/\lambda^{3/2}$ term. This is not unreasonable. The minimum detectable power is proportional to the cosmic noise power if the receiver noise power is small (as is the case for the VHF radar), this may be seen from inspecting Equation 4.54. Now, the cosmic noise power is frequency dependent (see *eg. McKinley*, 1961); for a reduction in frequency from 54.1 *MHz* to 20 *MHz*, the cosmic noise power and thus P_R increases by an order of magnitude. This is within a factor of 2 of the amount required to balance the effect of the $1/\lambda^{3/2}$ term.

The height distributions calculated at 2, 20 and 54.1 *MHz*, in Figure 4.21, are displayed as solid, dashed and broken lines respectively. In each panel, the expected height distributions have all been normalised to the peak rate of that obtained for a radar operating at 2 *MHz*. At low velocities the effect of using a radar operating at lower frequencies is small. For example, at an initial velocity of 11 $km\,s^{-1}$, the peak of the height distribution moves up from 82 *km* at a frequency of 54.1 *MHz*, to 83 *km* at 2 *MHz*, and the peak rate is some 22% larger. Contrast this to the expected height distributions for meteoroids with initial velocities of 60 $km\,s^{-1}$. For this case the peak of the height distribution moves up from 99 *km* at a frequency of 54.1 *MHz* to 108 *km* at 2 *MHz*, and the peak rate is about 22 times larger. This figure clearly demonstrates the severity of the attenuation and echo selection factors at the upper altitudes for radars operating at VHF.

All of the height distributions described in this section so far, have been calculated with the range cut off at 128 *km*. Radars operating at lower frequencies may also operate at lower PRF's due to the slower decay of the underdense meteor echoes. It may be seen from Equation 4.19, that the echo power decay time constant, τ, is inversely proportional to the square of the radar frequency. Thus, if the radar frequency is reduced from 54.1 *MHz* to 2 *MHz*, the same meteor echo will last about 5.2 times longer. In this case a PRF of only 20% of that used to observe the echo at 54.1 *MHz* is required to observe the same

echo with the same resolution at 2 MHz. Clearly, at low radar operating frequencies, lower PRF's may be used and thus the range cutoff effect is not as important. With this in mind, Figure 4.21 is repeated, however in this case the calculations were performed with no range cutoff in the calculations. The results appear in Figure 4.22 which are in the same format as Figure 4.21. The changes to the expected height distributions are negligible except for the two distributions calculated at a radar frequency of 2 MHz and meteoroid initial velocities of 40 and 60 $km\ s^{-1}$. For these two cases, the peaks of the respective height distributions have been shifted up in altitude by 1 – 2 km, and many more meteors are detectable above 110 km. The reason for this is as follows. As the height distribution moves up in altitude, the range cutoff plays a greater role in meteor selection thus affecting the shape of the height distribution to a greater degree. However, the range cutoff effect is small until the main beam is also affected. This occurs above a height 111 km for an off zenith beam tilt of 30°.

Figure 4.21 demonstrates that to study meteors above altitudes of 110 km, a radar operating at a low frequency is essential. An appropriate PRF must also be chosen so as not to introduce a height ceiling through the range cutoff effect, but also enable the meteor echoes to be studied in as high a detail as possible. It must be noted that at low radar frequencies, the effect of ionosphere must be considered also, this is not discussed here however see *Olsson-Steel and Elford* (1987) and *Steel and Elford* (1991).

4.6 The Observed Height Distribution of Sporadic Meteors

The height distribution of meteors as observed by the Buckland Park VHF radar is now investigated. In Figure 4.23 the height distribution of about 4200 meteors observed from the 10^{th} to 15^{th} June 1994, is displayed (solid line) together with the height distribution as modeled by the radar response function (dashed line). In this chapter the theoretical height distribution for meteors of a given velocity has been determined by integrating the response to these meteors, calculated at each height, over the entire sky. The full theoretical height distribution was then obtained by integrating over a suitable velocity distribution, in this case the sporadic meteor velocity distribution obtained with this radar (see Chapter 5). The observed height distribution is typical of that observed by VHF radars with a peak at about 94 km and relatively few meteors detected above 100 km.

The modeled distribution agrees extremely well with the observations at all heights except above 100 km, where the modeled distribution drops off much more sharply than what is

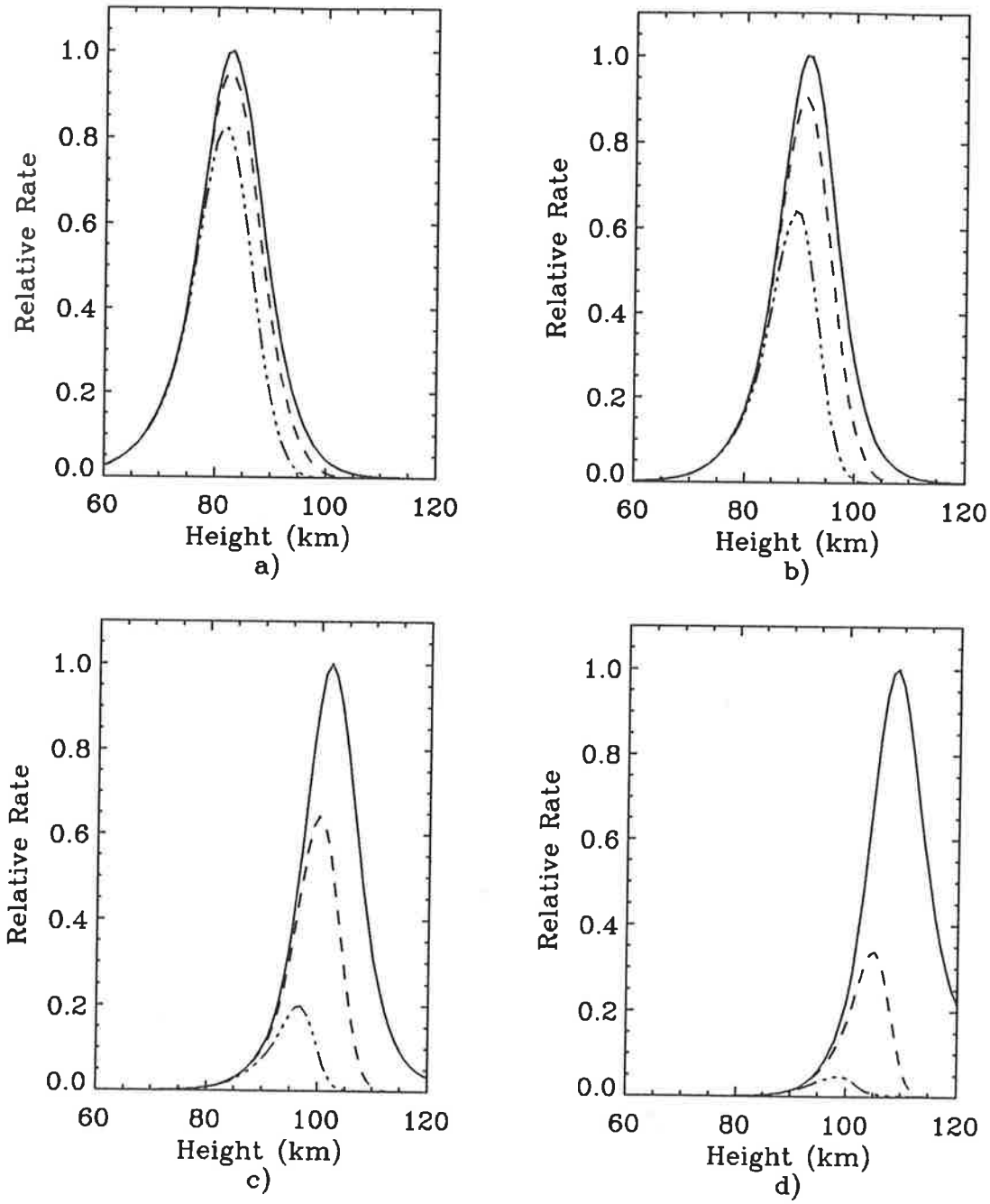

Figure 4.22: As for Figure 3.21, except here the expected height distributions have been calculated without the range cut off at 128 km.

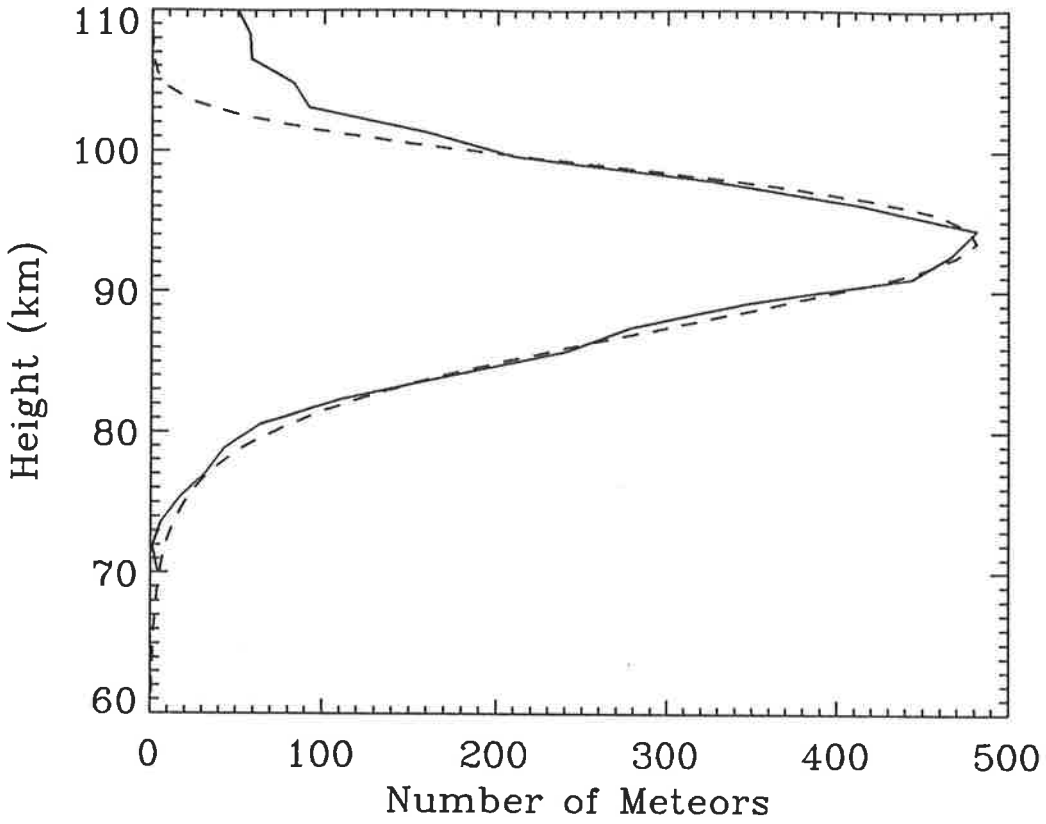

Figure 4.23: Height distribution of meteors observed by the Buckland Park VHF radar (solid line) and the modeled distribution (dashed lined) obtained from the response function. Note the departure of the observations from the model at heights above 100 km. This is due to meteors being detected in the side lobes of the beam (see text).

observed. The explanation of this is believed to lie with the detection of meteors in the sidelobes of the radar. Earlier in this chapter, it was shown from the consideration of the response function, that about 10% of meteors are detected in sidelobes. In fact this figure may be refined further, some 8% of meteors are detected in the sidelobes oriented at an angle further from the zenith than the main beam, and 2% are detected in the sidelobes closer to the zenith. This difference is of course due to the greater sensitivity of the system to meteors with trajectories further removed from the horizontal as previously described in this chapter. In the absence of a direction finding system, there is no way by which meteors detected in the main beam or the sidelobes may distinguished apart from examining the 'decay' height, but this is prone to large errors. Thus, the 8% of the meteor population which is detected in the side lobes further off zenith than the main beam are interpreted to have ablated at heights larger than the actual heights. For example, if a meteor ablates at a height of 100 km

and is detected in the first sidelobe ($6 - 7°$ off beam axis), then for a beam tilt of 30°, the range at which this meteor is observed at is about 123.6 km. The height at which the meteor is interpreted to have ablated at is therefore calculated as 107 km, some 7 km greater than the actual height.

Another possible explanation for the greater numbers of meteors observed above 100 km than predicted, is that these meteors could be overdense. This, however, is not likely due to several reasons: (1) overdense meteors were included in the response function calculation (although crudely), (2) the VHF radar observes meteors with electron line densities in a range much lower than that of meteors in the overdense regime, therefore relatively few overdense meteors are likely to be detected, and (3) some of the meteors observed above 100 km show an amplitude profile which is clearly underdense and relatively long duration with the interpretation being that they are meteors detected in the sidelobes. Thus, the larger than expected number of meteors detected above 100 km is not likely to be due to overdense echoes, and the most plausible explanation is that they are simply meteors detected in the sidelobes of the radar.

The height distribution of the observed meteors has been examined for other periods of data also. In all cases (not shown here) the height distribution is similar; good agreement with the modeled distribution below 100 km is found, and the excess numbers of meteors above 100 km attributed to meteors detected in the sidelobes.

Finally, the height distribution of radio meteor echoes is highly sensitive to the initial radius of the meteor. Therefore, as the initial radius is an important factor which is included in the response function calculation, the response function together with the observed height distribution may be employed to measure this parameter. The short study of the height distribution of radar meteors presented in this section strongly supports the expression used by *Thomas et al.* (1988) for the initial radius (see Equation 4.15). However, further investigations involving the examination of the height distribution of the meteors, as a function of speed, are desirable as this would enable the initial radius to accurately determined over the range of speeds of the meteoroids.

4.7 The Diurnal Variation of Sporadic Meteor Echo Rates

The diurnal variation in the observed meteor rate is common to all types of observation and is due to the rotation of the frame of reference of the observer with respect to the direction

of the Earth's motion around the Sun. At 0600 hours local time, the observer looks in the direction of the Earth's motion and therefore will see a peak in the meteor rates as the Earth sweeps up the meteoroids in it's path. Conversely at 1800 hours local time, the direction of observation is opposite to the direction of the Earth's motion and therefore a minima in the meteor rate is observed. In the case of radar meteors, the response function may be employed to model the expected diurnal variation.

The response function, $n(\theta, \phi)$, as previously discussed, is the response of the radar system to meteor backscatter from meteors originating from a radiant of unit density in the direction (θ, ϕ), where θ and ϕ are elevation and azimuth respectively. Let the density distribution of sporadic meteor radiants over the celestial sphere with respect to an isotropic distribution be $g(\beta, \lambda - \lambda_\odot)$, where β and λ are the ecliptic latitude and longitude of the radiant, and $\lambda_\odot$ is the ecliptic longitude of the sun. As $g(\beta, \lambda - \lambda_\odot)$ is normalised with respect to an isotropic distribution the following relation exists:

$$\iint_{sky} g(\beta, \lambda - \lambda_\odot) d\Omega = 4\pi \ . \tag{4.59}$$

The convolution of the response function with the sporadic radiant distribution gives the total expected meteor echo rate. An appropriate transformation of coordinates must be made to take the response function from the elevation-azimuth frame to the celestial coordinate frame. As this depends on the local solar time on a particular day, the total expected meteor echo rate as a function of time is obtained. Thus the expected diurnal variation of the meteor echo rate on a given day of a given year is:

$$n(t) = \iint_{sky} n(\theta, \phi) g(\beta, \lambda - \lambda_\odot) d\Omega \tag{4.60}$$

where t is the local solar time on the day in question.

In Figure 4.24 the response functions for the East pointing beam (top) and the West pointing beam(bottom) are plotted on the celestial sphere at six separate times on the 24^{th} May 1994, using the Hammer-Aitoff equal area projection. The dashed line in each plot describes the path that the peak response takes over the celestial sphere in a 24 hour period. Also displayed for each case in Figure 4.24 is the sporadic radiant distribution as determined by *Elford and Hawkins* (1964).

Figure 4.24 is useful for obtaining a qualitative feel of the expected diurnal variation by following the response function across the sporadic distribution. For example, inspection of this figure shows that a peak in the meteor rate in the West beam is expected at about

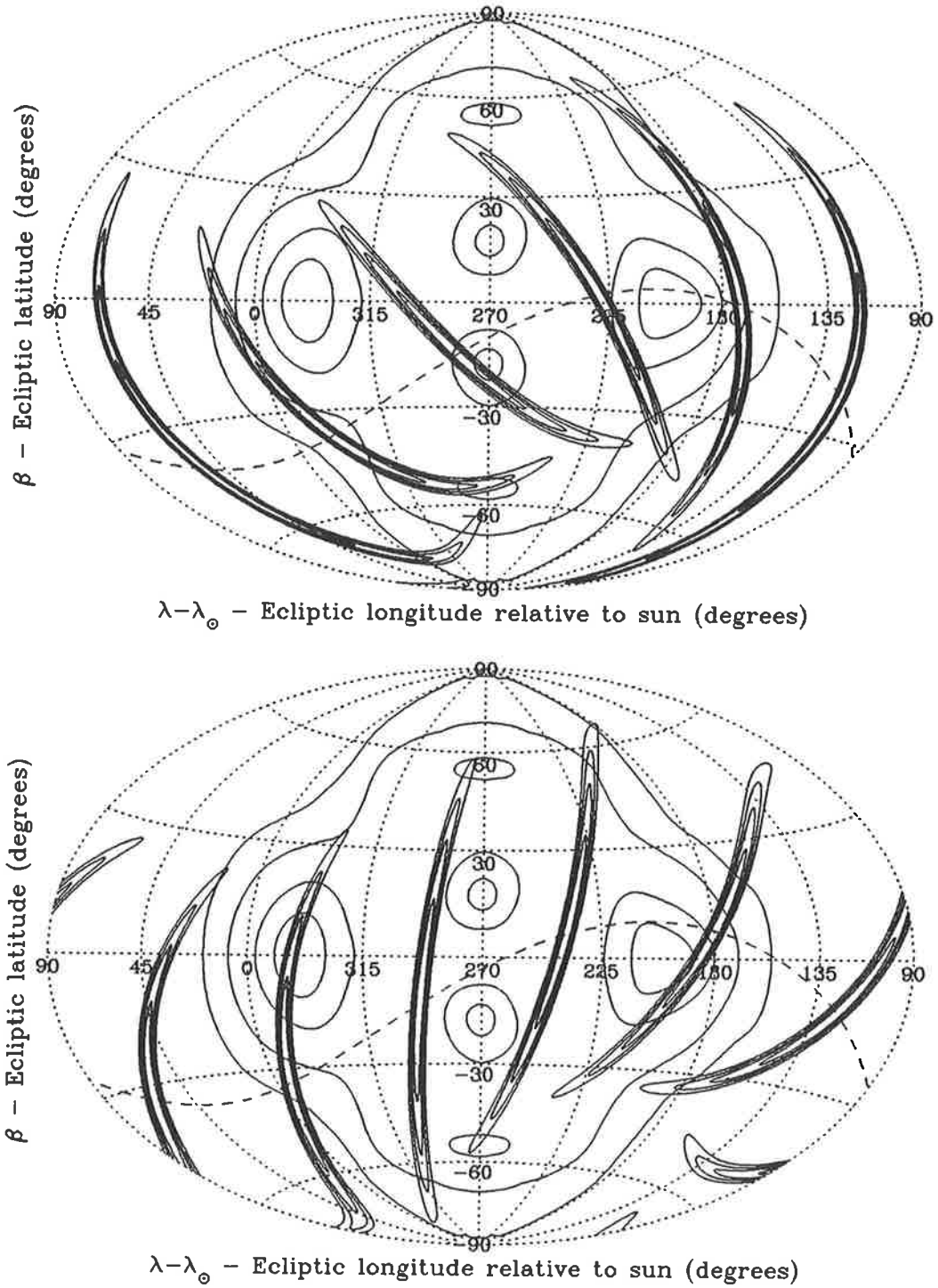

Figure 4.24: The path which the response of the East (top) and West (bottom) pointing beams take on the celestial sphere during the 24^{th} May 1994. The East (West) response function is plotted at 00:00 (16:00), 04:00 (20:00), 08:00 (00:00), 12:00 (04:00), 16:00 (08:00) and 20:00 (12:00) CST, respectively from right to left, with the dashed line in each plot indicating the path of the peak response. The contour levels for each response function are at 20%, 40%, 60% and 80%. Also displayed on each plot is the sporadic radiant distribution interpolated from *Elford and Hawkins* (1964) with contour levels at 15%, 30%, 65% and 85%.

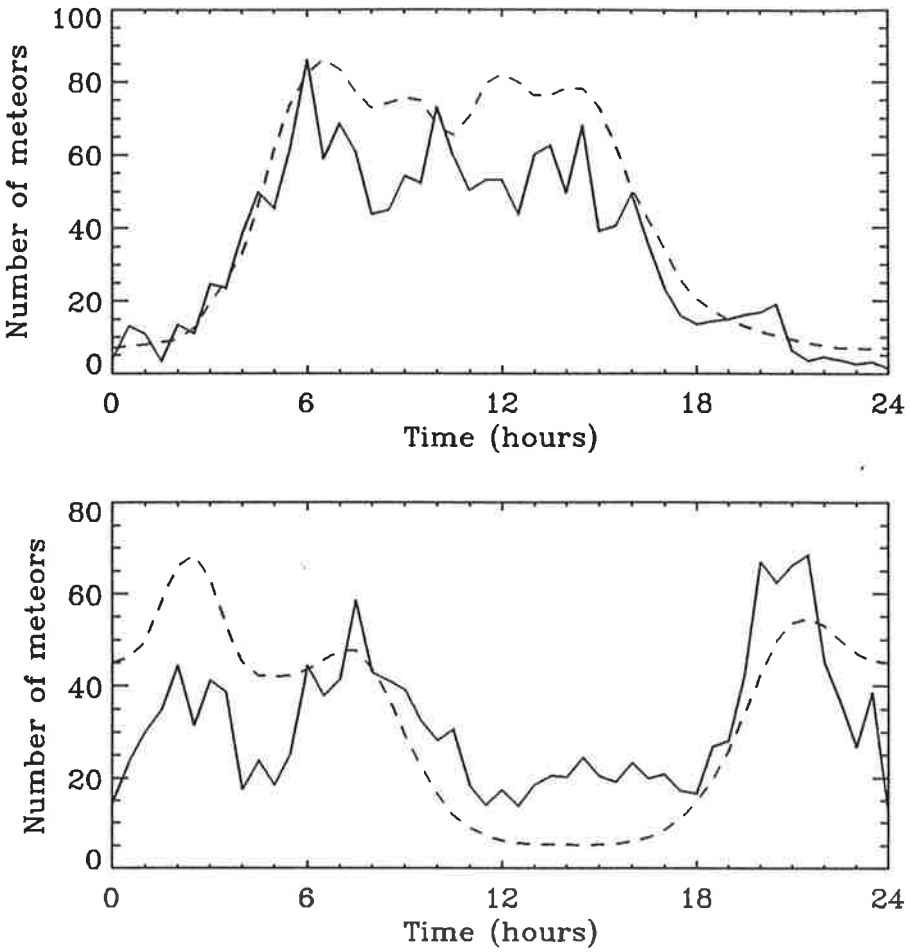

Figure 4.25: The observed diurnal variation in the meteors rates from $20^{th} - 26^{th}$ May 1994 folded into a single 24 hour period (solid line) in the East (top) and West (bottom) beams of the radar, and the expected diurnal variation calculated for the 24^{th} May 1994 (dashed line). The model diurnal variation was calculated using the average sporadic radiant distribution obtained by *Elford and Hawkins* (1964).

02:00 CST on the 24^{th} May 1994 as the response function crosses the broad source at the apex. Subsequent peaks are expected at 07:30 CST and 21:00 CST as the response function crosses the Helion and Anti-helion broad sources. Likewise in the East beam, peak rates are expected at 06:00, 10:00-12:00, and 14:00 CST as the response function of the East beam crosses the Anti-helion, Apex and Helion sources respectively. Of course, the evaluation of Equation 4.60 yields the full expected diurnal variation. This has been performed for the 24^{th} May 1994 and for both the East and West beams, and the model results (dashed line) together with the observed diurnal variation (solid line) are displayed in Figure 4.25. The observed diurnal variation was obtained from 7 days of data ($20^{th} - 26^{th}$ May 1994) folded into a single 24 hour period.

Inspection of Figure 4.25 reveals that the times at which the peak rates occur in the East and West beams agree well with the expected times, but the relative strengths of the peaks differ, to some extent, from the expected values. In particular, the peak in the West beam corresponding to the passage of the Apex is about half the expected rate. The disagreement of the observed and expected strengths of the peaks is not surprising considering that, (a) the sporadic radiant density distribution obtained from *Elford and Hawkins* (1964) was produced from meteor observations with a much higher limiting mass, and (b) the *Elford and Hawkins* distribution was an average over 8 months (from January to August 1964), and it is well established that the sporadic meteors are not uniformly distributed around the Earth's orbit.

Alternatively a model of the sporadic meteor radiant distribution over a given period may be deduced from the consideration of the observations of the meteor echo rates during this period and the response function of the radar. The essential requirement is that the model distribution, when convolved with the response function, yields a diurnal variation closely matching that observed by the radar. Although this method is not as good as deducing the radiants from the measurement of the meteor orbits directly with a multi-station meteor orbit radar, it does offer a way of obtaining a good model of the sporadic meteor radiant distribution with a single station radar. Due to the excellent coverage that the Buckland Park radar has over the celestial sphere, one would expect the model to be fairly accurate with only fine structure, if there is any, not able to be determined.

The basic model of the sporadic meteor radiant distribution that shall be used, is similar in form to that employed by *Thomas et al.* (1988). Four sources are defined, each represented algebraically by a two dimensional Gaussian, $S_i(\beta, \lambda - \lambda_\odot)$, and then superimposed on a uniform background. Thus, $g(\beta, \lambda - \lambda_\odot) = \sum_{i=1}^{5} S_i$, where the equations describing each source (S_i) are:

Helion,

$$S_1 = 175\, exp\left[-\left(\frac{\beta}{32}\right)^2 - \left(\frac{\Lambda - 345}{32}\right)^2\right] , \tag{4.61}$$

Anti-helion,

$$S_2 = 205\, exp\left[-\left(\frac{\beta}{26}\right)^2 - \left(\frac{\Lambda - 200}{26}\right)^2\right] , \tag{4.62}$$

North apex,

$$S_3 = 50\, exp\left[-\left(\frac{\beta - 15}{19}\right)^2 - \left(\frac{\Lambda - 274}{19}\right)^2\right] , \tag{4.63}$$

South apex,

$$S_4 = 150\, exp\left[-\left(\frac{\beta + 15}{19}\right)^2 - \left(\frac{\Lambda - 265}{19}\right)^2\right] , \tag{4.64}$$

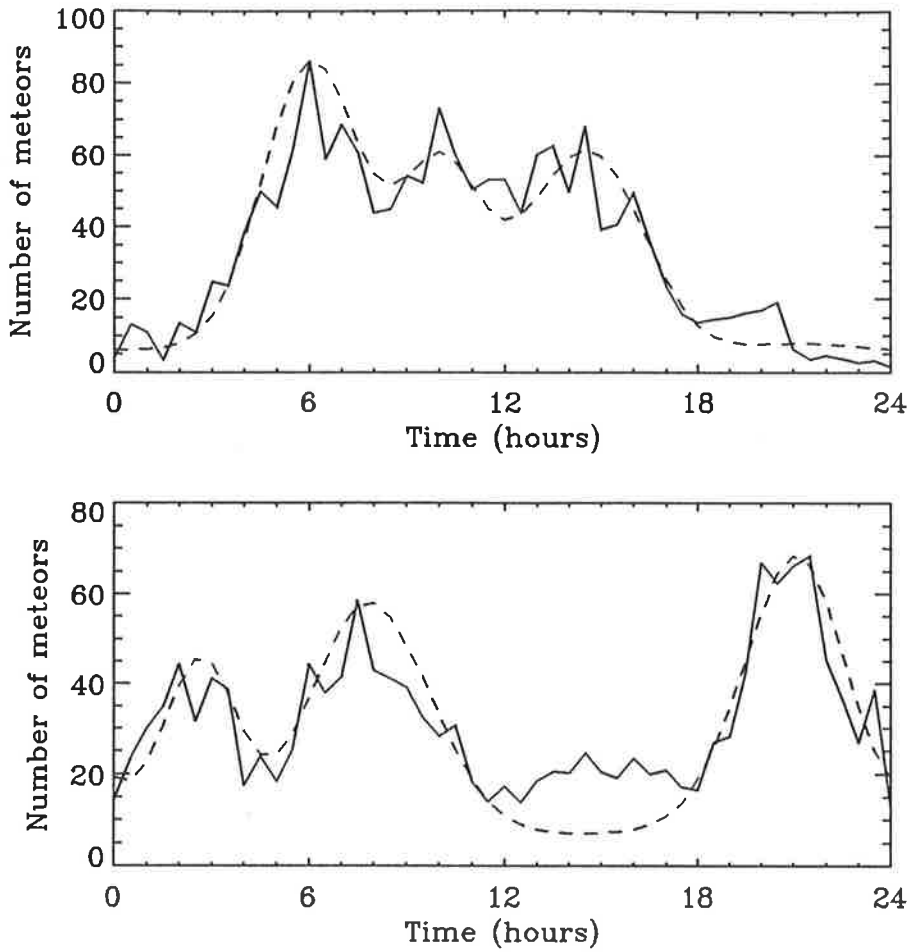

Figure 4.26: The observed diurnal variation in the meteors rates from $20^{th} - 26^{th}$ May 1994 folded into a single 24 hour period (solid line) in the East (top) and West (bottom) beams of the radar, and the expected diurnal variation calculated for the 24^{th} May 1994 (dashed line). The expected diurnal variation was calculated using the model sporadic radiant distribution defined by Equations 4.61 to 4.65.

Uniform background,

$$S_5 = 5 \,, \tag{4.65}$$

where $\Lambda = \lambda - \lambda_\odot$. The particular choice of the relative strengths, widths, and positions of the sources were made so as to give the best fit of the expected diurnal variation to the data.

The expected diurnal variation calculated from the model sporadic radiant distribution on the $24th$ May 1994 is displayed in Figure 4.26 (dashed line) over the observed diurnal variation (solid line). It is clear that the expected diurnal variation now agrees well with the observed diurnal variation in both beams except for times from about 11:30 to 17:30 CST in the West beam when the observations indicate the presence of a source of meteors at these times. However, there does not appear to be a corresponding increase in the East

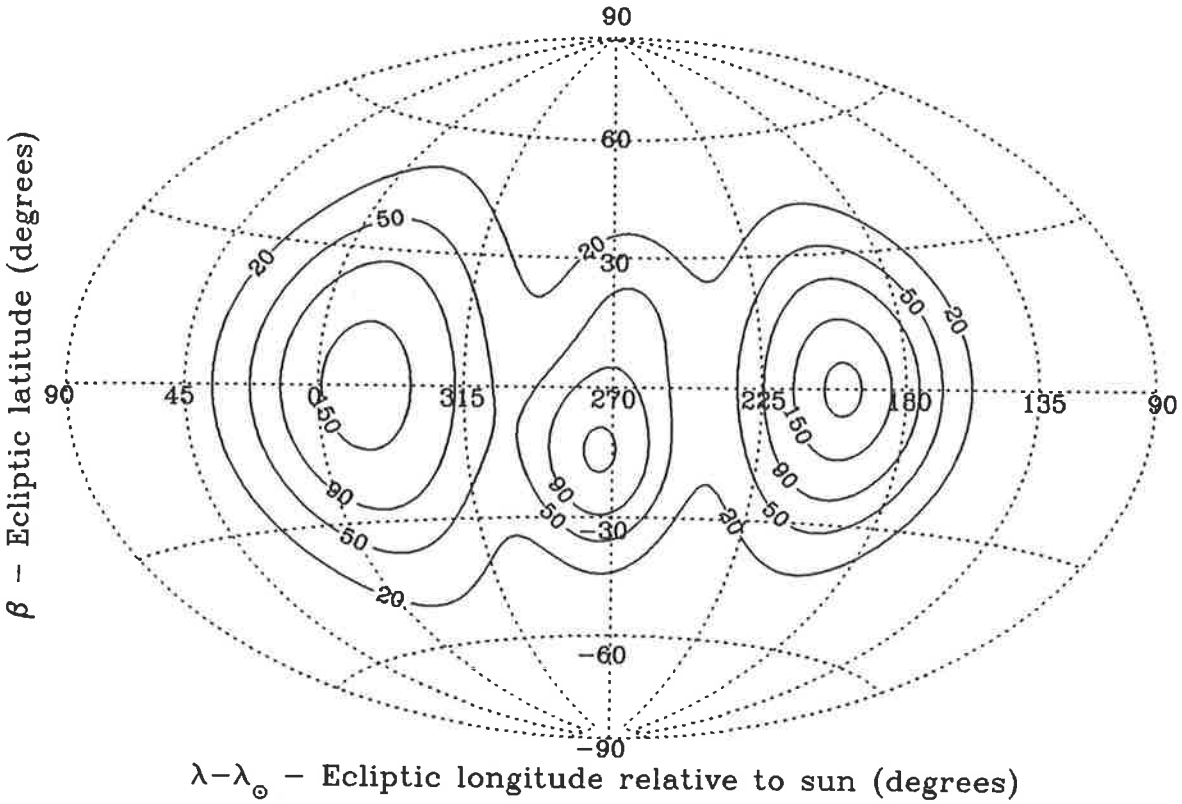

Figure 4.27: Model sporadic radiant distribution for $20^{th} - 26^{th}$ May 1994 as defined by Equations 4.61 to 4.65.

beam echo rates from around 18:00 CST of one day to 02:00 CST of the next, consistent with such a source, and as yet this feature remains unexplained. With the exception of these 6 hours, the observed and predicted rates are in excellent agreement indicating that the model distribution is a good representation of the sporadic meteor radiant distribution over the period of the observations.

The actual model distribution of the sporadic meteor radiants used to generate the predictions in Figure 4.26 ($20^{th} - 26^{th}$ May 1994) is shown in Figure 4.27. One immediately notices that while the Helion and Anti-Helion sources are similar to those from the average sporadic radiant distribution determined by *Elford and Hawkins* (1964), and shown in Figure 4.24, the Apex sources differ considerably. The North Apex is almost non-existent being only a third of the strength of the South Apex. The South apex, not only being quite intense, is also broader than that displayed by *Elford and Hawkins'* distribution. In addition, the South Apex is off center, its ecliptic longitude is about 275° from the Sun's, rather than 270°.

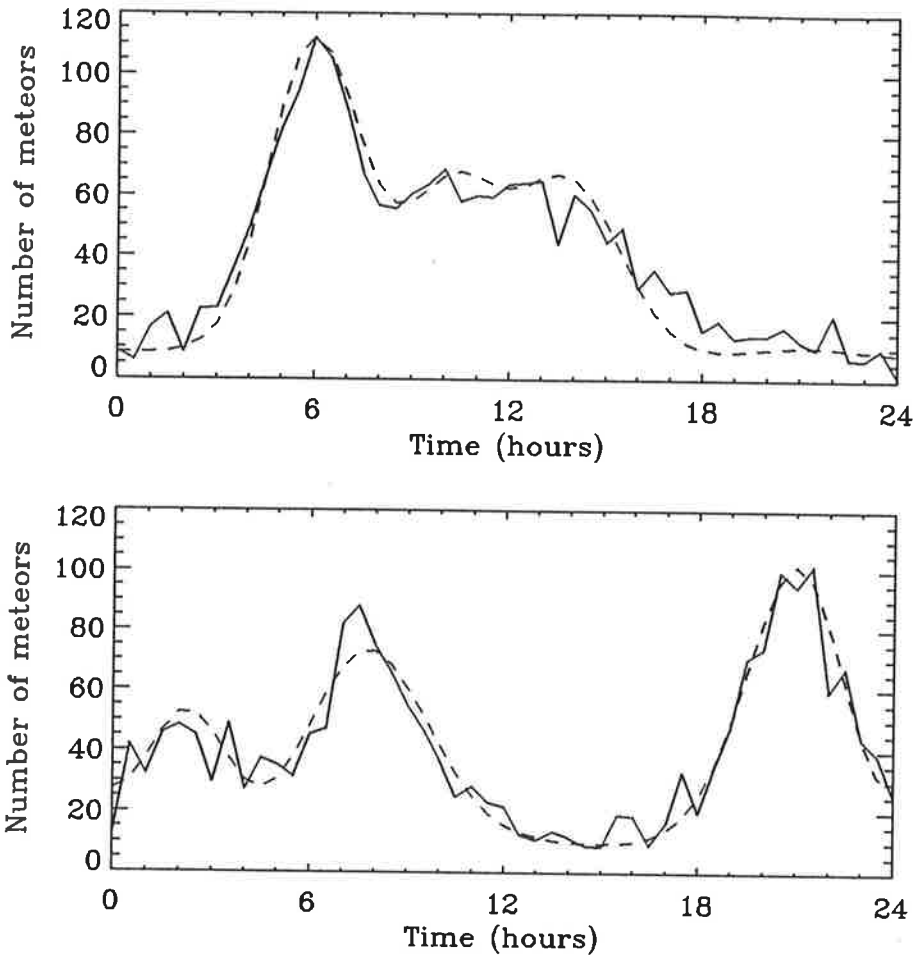

Figure 4.28: The observed diurnal variation in the meteors rates from $10^{th} - 15^{th}$ June 1994 folded into a single 24 hour period (solid line) in the East (top) and West (bottom) beams of the radar, and the expected diurnal variation calculated for the 13^{th} June 1994 (dashed line). The expected diurnal variation was calculated using the model sporadic radiant distribution defined by Equations 4.66 to 4.70.

As stated previously, it is well established that sporadic meteors are not uniformly distributed around the Earth's orbit. Therefore it is expected that the sporadic meteor radiant distribution will show changes throughout the year. This is confirmed data collected from three separate periods: $20^{th} - 26^{th}$ May 1994 (already described), $10^{th} - 15^{th}$ June 1994, and $1^{st} - 6^{th}$ February 1995. These observations are discussed below.

10^{th} – 15^{th} June 1994

Figure 4.28 displays the diurnal variation of meteor echo rate data recorded from the 10^{th} – 15^{th} June 1994, together with the modeled diurnal variation calculated for the 13^{th} June 1994. The model diurnal variation agrees well with the observations except for the peak due

to the Helion source at 07:00 CST in the west beam, which is slightly underestimated. If the intensity of this source is increased, the model agrees better with the observations in the West beam at this time, but the peak due to the Helion source in the East beam at 14:00 CST is then overestimated. The model sporadic meteor radiant distribution used for the calculation of the expected diurnal variation is displayed in Figure 4.29 and is defined by the following set of equations:

Helion,

$$S_1 = 195\, exp\left[-\left(\frac{\beta - 10}{30}\right)^2 - \left(\frac{\Lambda - 340}{30}\right)^2\right] , \tag{4.66}$$

Anti-helion,

$$S_2 = 205\, exp\left[-\left(\frac{\beta}{24}\right)^2 - \left(\frac{\Lambda - 198}{24}\right)^2\right] , \tag{4.67}$$

North apex,

$$S_3 = 35\, exp\left[-\left(\frac{\beta - 10}{22}\right)^2 - \left(\frac{\Lambda - 270}{22}\right)^2\right] , \tag{4.68}$$

South apex,

$$S_4 = 75\, exp\left[-\left(\frac{\beta + 10}{22}\right)^2 - \left(\frac{\Lambda - 265}{22}\right)^2\right] , \tag{4.69}$$

Uniform background,

$$S_5 = 5 , \tag{4.70}$$

Clearly, from a comparison of Figure 4.29 with Figure 4.27, the model sporadic meteor radiant distribution has changed somewhat from the previous month. The Apex source has been reduced in intensity by about a factor of two, become broader, and has moved closer to the apex. It also shows a greater degree of symmetry with separate North and South components not discernible. The Anti-Helion source has changed by only a small amount, now being more compact. In contrast, the Helion source shows a marked change, drifting North by about 10°, as well as being slightly more compact and intense. Figures 4.27 and 4.29 demonstrate the non-uniformity of the sporadic meteors around the Earth's orbit, although the same three basic features are evident in each case.

$1^{st} - 6^{th}$ February 1995

The change in the sporadic radiant distribution throughout the year is displayed more dramatically by the rate data obtained about 6 months later than the previous two data sets. This data was collected over a period of 6 days from the $1^{st} - 6^{th}$ February 1995. The resulting diurnal variation appears in Figure 4.30, and again the modelled variation is overlaid.

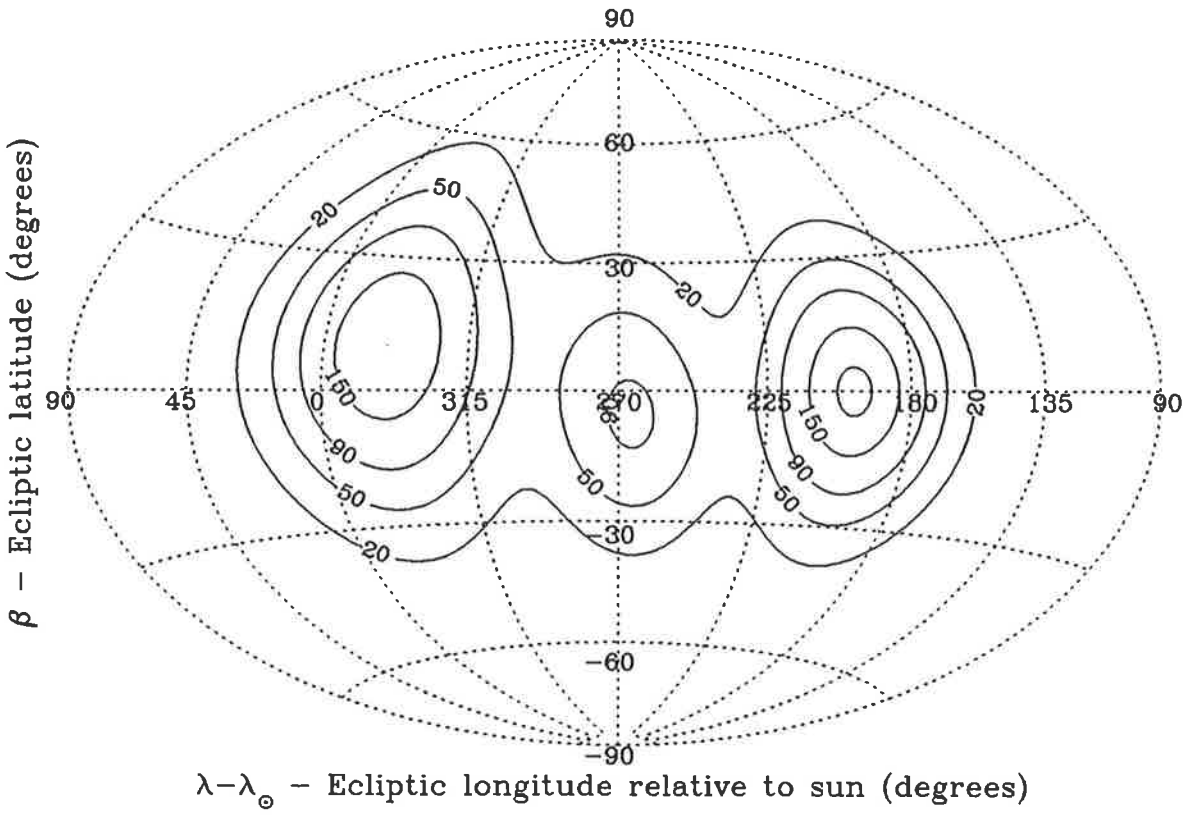

Figure 4.29: Model sporadic radiant distribution for $10^{th} - 15^{th}$ June 1994 as defined by Equations 4.66 to 4.70.

Inspection of this figure shows that the agreement between the observations and the model is generally good, although in the West beam the observed peak at 06:00 is broader than the model. Also, the peak occurring at 22:00 in the West beam is slightly narrower than the model. The model sporadic radiant distribution may be adjusted to give better agreement in the West beam, but this causes a reduction in the quality of the East beam comparison. From consideration of both East and West beam data, the model data displayed in Figure 4.30 represents the best fit to the observations.

The equations describing the model sporadic meteor radiant distribution used to calculate the expected diurnal variation are now:

Helion,

$$S_1 = 210\, exp\left[-\left(\frac{\beta+10}{23}\right)^2 - \left(\frac{\Lambda-345}{18}\right)^2\right], \tag{4.71}$$

Anti-helion,

$$S_2 = 160\, exp\left[-\left(\frac{\beta+10}{30}\right)^2 - \left(\frac{\Lambda-202}{17}\right)^2\right], \tag{4.72}$$

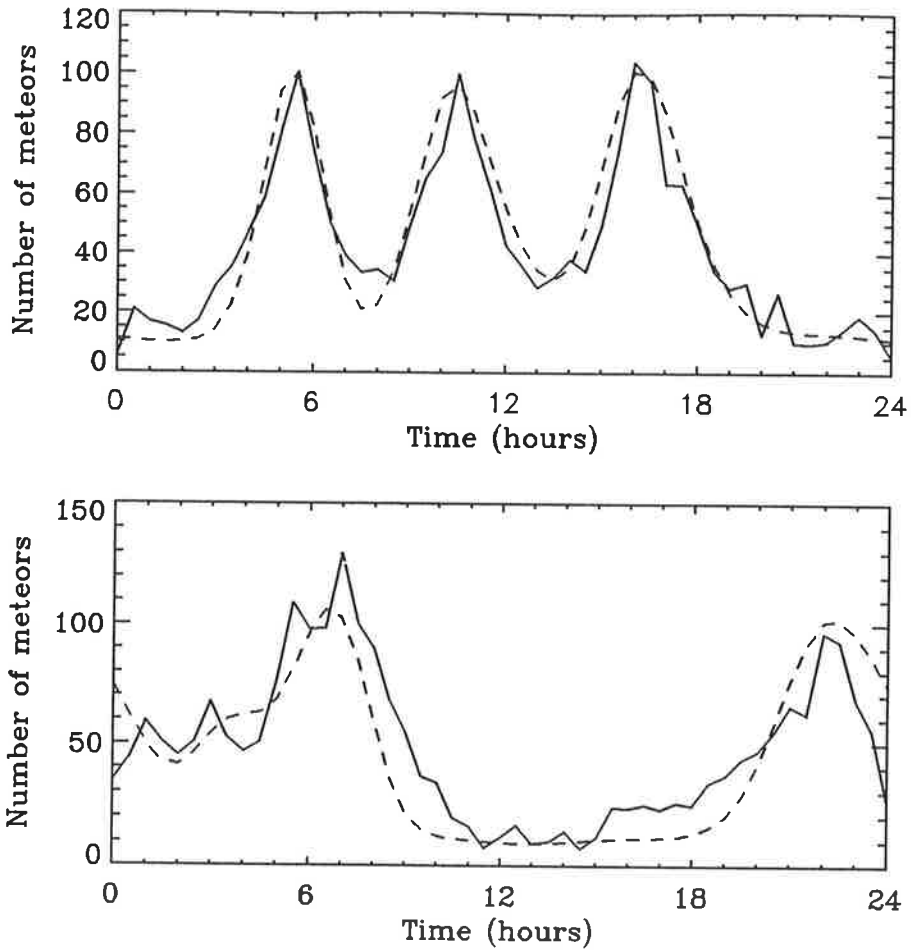

Figure 4.30: The observed diurnal variation in the meteors rates from $1^{st} - 6^{th}$ February 1995 folded into a single 24 hour period (solid line) in the East (top) and West (bottom) beams of the radar, and the expected diurnal variation calculated for the 4^{th} Feb. 1995 (dashed line). The expected diurnal variation was calculated using the model sporadic radiant distribution defined by Equations 4.71 to 4.75.

North apex,

$$S_3 = 115\, exp\left[-\left(\frac{\beta - 30}{20}\right)^2 - \left(\frac{\Lambda - 270}{20}\right)^2\right] , \tag{4.73}$$

South apex,

$$S_4 = 150\, exp\left[-\left(\frac{\beta + 30}{20}\right)^2 - \left(\frac{\Lambda - 270}{20}\right)^2\right] , \tag{4.74}$$

Uniform background,

$$S_5 = 5 , \tag{4.75}$$

One may immediately observe, from these equations and also Figure 4.31 which displays the model sporadic distribution, that the model for February is quite different from models for May and June. The most striking change is to the apex source which is much more intense

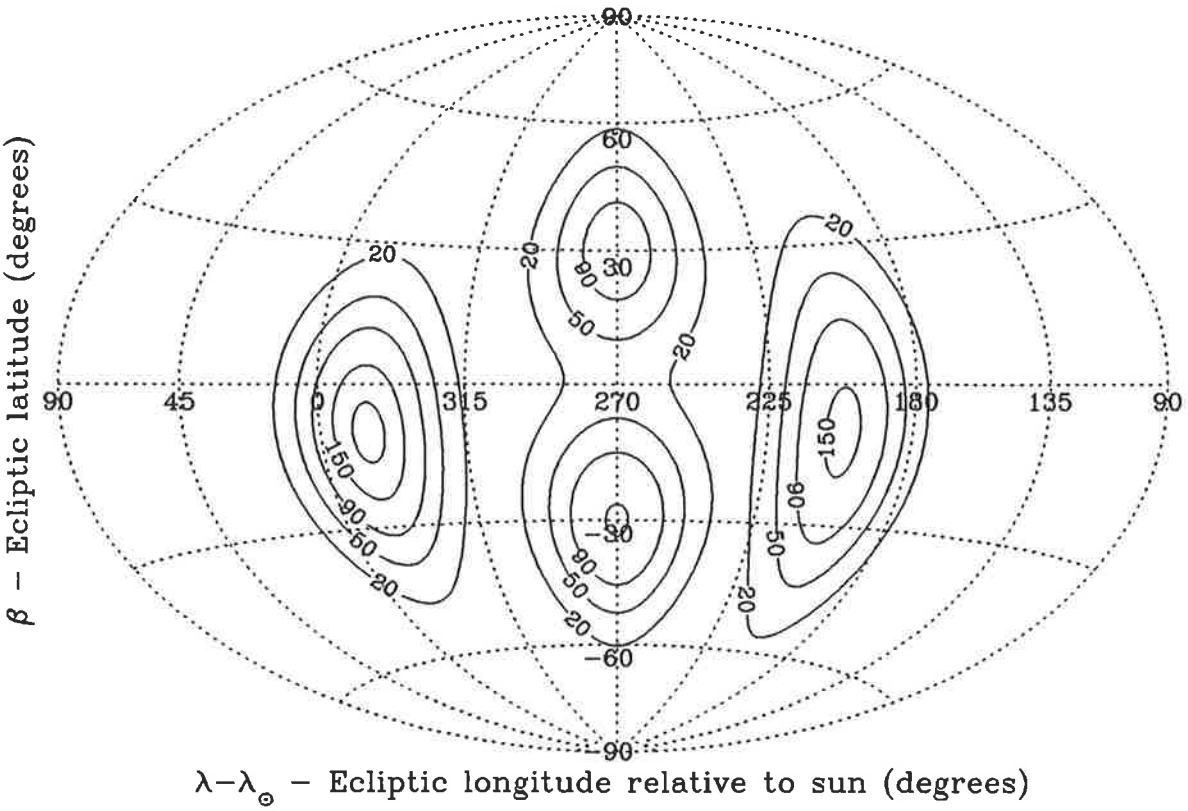

Figure 4.31: Model sporadic radiant distribution for $1^{st} - 6^{th}$ February 1995 as defined by Equations 4.71 to 4.75.

and broader than previously, also both North and South components are now clearly delineated. The Helion and Anti-helion sources have also changed, though not as spectacularly as the Apex. These two sources have both become narrower in longitude and broader in latitude. The Helion source has moved South so that its peak occurs at an ecliptic latitude of $-10°$, and it is noticeably stronger than the Anti-Helion source in contrast to six months earlier when it was marginally weaker.

In summary, the analysis of three sets of meteor echo rate data has clearly shown that observations of sporadic meteor rates obtained with a VHF radar, together with modeling using the response function of the system, enables a model of the sporadic meteor radiant distribution to be constructed for a particular time of the year. It should be noted that no attempt was made to model the sporadic meteor radiant distribution for a particular velocity range. In practice this should be relatively simple to achieve with the new velocity reduction technique developed and described in Chapter 5. The potential now exists to analyse a whole years rate data so that the distribution of sporadic meteors around the Earth's orbit may be described in better detail than known heretofore, and it should be possible to do this for

various meteoroid velocities.

4.8 Summary

In this chapter, the response of radar to meteors was developed. The classical ablation theory of meteors was used in the derivation of the response function, and no attempt was made to include fragmentation of the meteoroids. A simple model was employed to introduce overdense meteors to the response function calculation, a more detailed approach using the reflection coefficients of the scattering process (*Poulter & Baggaley* 1977, 1978) would be appropriate. Use of these reflection coefficients would also require the consideration of the polarization of the radio waves with respect to the trail.

The response function was calculated for the Buckland Park VHF radar. All of the characteristics and limitations of this radar were incorporated into the calculation. The response function was examined in detail for various beam geometries. It was found, as expected, that for off zenith beam tilts of a few degrees the radar response to meteors was low and the side lobe contribution significant. Thus, off zenith beam tilts greater than 20°–25° are required for meteor observations.

The response function was also examined as a function of the initial velocity of the meteoroids incident on the Earth's atmosphere. It was found that due to the increase in the height of ablation at large meteoroid velocities, the effects of the echo attenuation and echo selection factors cause a bias against underdense echoes. As a result, echoes from overdense trails become increasingly significant at large meteoroid velocities. Considering this, it is clear that in order to study high velocity meteoroids and/or meteoroids ablating at high altitudes, a narrow beam high gain system is not appropriate. A system with a wide beam and hence large collecting area would be more appropriate for studying these meteors. A better approach is to use a radar operating at a much lower frequency. It was found from modelling of the response function in this case, that the attenuation factors are not as severe and thus underdense meteors are detectable at much larger altitudes. This was observed by *Steel and Elford* (1991) and reported in their paper.

The full response function for the Buckland Park VHF system was determined by integrating over two velocity distributions; the revised corrected Harvard velocity distribution, and the velocity distribution found by *Nilsson* at Adelaide. There was no reason to choose one distribution over the other, and the results differ significantly. *Nilsson's* distribution

gave a peak height of 96 km and a sidelobe response of 10.9% compared to 92 km and 8.5% for the Harvard distribution.

The effect on the response function of variable background noise and hence minimum detectable power, was investigated. It was found that a variation by a factor of 4 in the minimum detectable power of the system changed the rate by a factor of about 1.6 but did not affect the form of the response function. Thus, the response function may be calculated at only one minimum detectable power level and a multiplicative correction factor applied to obtain the total response for different minimum detectable powers. This is an important result considering that the minimum detectable power of the Buckland Park VHF radar varies diurnally by a factor of 4–5 due to the variation in the background cosmic noise.

The response function of the Buckland Park VHF radar was examined for different configurations of the receiving array. It was hoped that for a broader beam on reception, that the side lobe response would be reduced if the nulls of the receiving antenna pattern occurred at the same position as the maxima of the sidelobes of the transmitting pattern. Unfortunately, it was discovered that while the first side lobes were able to be reduced, others were enhanced. Thus the nett advantage by using such a receiving configuration was negligible.

The height distribution of the observed meteors from data spanning a 24 hour period in June was examined. The response function was used to model the height distribution and it was found to be in excellent agreement with the observations below about 100 km. Above 100 km, more meteors were observed than expected from the model. Consideration of the echo attenuation factors due to the initial trail radius and diffusion suggested the detection of meteors above 100 km was unlikely at the frequency at which the radar operates. As mentioned earlier, modeling with the response function in this chapter showed that about 10% of meteors were expected to be detected in the sidelobes of the radar, and the height of such meteors would be interpreted as being about 6 km greater than in actuality. Thus, the discrepancy between the observations and the model above 100 km was attributed to meteors detected in the sidelobes.

Finally, the response function of the radar and observations of the diurnal variation of sporadic meteors were used together to model the sporadic meteor radiant distribution over three separate periods, each about a week in duration. The distributions are applicable to the last week of May and June 1994, and the first week of February 1995. It was clear that while the same general features (*viz.* the Helion, Anti-Helion and Apex broad sources) of the model sporadic meteor radiant distributions were apparent for each period, there were differences.

This is consistent with the sporadic meteors not being homogeneously distributed around the Earth's orbit. The changes to the modeled distributions took the form of small variations in the width and positions of the broad sources, and relatively large changes to their relative strengths. The differences were most apparent for the data periods which were separated by 6 months; this was not surprising. With an observing program designed to yield sporadic meteor rate data over the the entire year, it should be possible to model the sporadic meteor radiant distribution around the orbit of the Earth.

Some further applications of the response function not discussed in this chapter will be considered subsequent chapters. These include the use of the response function to interpret results in the study of space debris, prediction of the time of passage of meteor showers, and the mass distribution of the meteoroid influx to the Earth.

Chapter 5

A New Technique for Measuring Meteor Velocities

Sleep? Isn't that a completely inadequate substitute for caffeine?

—*Computer programmers saying*

(also used by many Research students).

5.1 Introduction

Since the 1940's meteor astronomy has been revolutionized by the development of several new techniques, both optical and radio. Of particular significance is the measurement of the encounter speeds of meteoroids with the Earth. Indeed the determination of the orbital parameters of meteoroids is only possible with the knowledge of their velocities. However despite the precision and reliability of the new methods developed to measure meteoroid velocities, all of have their disadvantages. Optical techniques can only be used at night and are limited to the brighter meteors; for example the photographic technique employed by *McCrosky and Posen* (1961) had a magnitude limit of +4.5 The more recent work by *Sarma and Jones* (1985), who employed the TV meteor technique for their observations, were only able to detect meteors as faint as +8.5 Mag. This limit is to be compared with that of modern meteor radars: +13.0 for AMOR operated by *Baggaley et al.* (1994) and +13.6 for the Buckland Park VHF radar (see Chapter 6). On the other hand, radio techniques suffer from the disadvantage of strong selection effects. (1) The high order dependence of ionizing efficiency with the meteoroid velocity grossly over emphasizes high velocity meteoroids in

all radio observations which must be accounted for. (2) The effect of the initial radius and diffusion of the ionized column gives a frequency dependent ceiling that causes a bias against high speed meteors as they generally ablate at larger altitudes. (3) The fact that the diffraction method may only be applied where the post-t_0 Fresnel oscillations in the echo are well defined reduces the velocity sample to only about 10% of all echoes observed. These selection effects together with the various radio techniques that have been used in the past will be discussed more fully in the next section.

Whilst the measurement of meteor velocities is essential in the determination of meteoroid orbits, it is also important in the study of the velocity distributions of meteor showers and the possible presence of interstellar meteoroids.

The velocity distribution of the sporadic meteors has also been examined by various researchers using different techniques and it has been noted (see *eg. Elford et al.*, 1996) that there is a basic discrepancy between the optical and radio results (discussed more fully later this chapter), which remains as yet unresolved. Some researchers that have investigated the sporadic velocity distribution includes: *Hawkins and Southworth* (1958), *McCrosky and Posen* (1961) (photographic); *Nilsson* (1962, 1964a), *Sekanina and Southworth* (1973) (radio); *Sarma and Jones* (1985) (TV meteors). Examples of procedures used to correct the observed velocity distribution are *Erickson* (1968), who corrected the optical data of *Hawkins and Southworth* (1958) according to the variation of luminosity efficiency of meteors with velocity; *Nilsson* (1962) which was applied to his survey of radio meteors; and *Sekanina and Southworth's* (1973) correction of the Harvard Radio Meteor Project results (later revised by *Taylor*, 1995, 1996).

In a recent paper *Baggaley et al.* (1994) employ a new technique to measure meteor velocities for the purpose of the determination of meteoroid orbits. Their technique does not suffer from the disadvantages of previous radio techniques in that it may be applied to a much larger proportion of observed meteors. However, the range of radar systems that can take advantage of their technique is limited, as only multistation systems which use fan or pencil beams may employ their method. Another recently developed technique, employs the pre-t_0 phase information to measure meteor velocities. This method (the preliminary results appear in *Cervera et al.*, 1995, and *Elford et al.*, 1996) has the advantage that it may be employed by any single station meteor radar with sufficiently high PRF, the accuracy is considerably better than previous radio techniques, and reliable results are obtained for about 75% of all observed echoes, a considerable improvement on the older techniques. This

technique is detailed later and forms the major part of this chapter.

5.2 Survey of Previous Radio Techniques

In this section previous radio techniques used to measure meteoroid velocities will be described. These techniques include the range-time technique which was first implemented by *Hey et al.* (1947), and was in fact the first time meteor velocities were measured by radar; the diffraction method developed by *Ellyett and Davies* (1948); a unique method employed by *Pettengill* (1962) which used a radar operating at UHF; and the method used by *Baggaley et al.* (1994) with their Advanced Meteor Orbit Radar (AMOR).

5.2.1 The range-time technique

The range time method was developed by *Hey et al.* (1947) to measure the velocity distribution of the Giacobinid shower meteors. These velocity measurements were the first to be performed by a radio technique and were base on the observation of the meteor head echo. Velocity determinations by this technique are restricted to the few cases (generally bright meteors) where the echo from the meteor head is evident.

Meteor head echoes are the aspect insensitive returns that appear just before the onset of the trail echo. On the range-time records they take the form of a segment of a hyperbola that lasts for about 1 *ms* at a given range, and is to be distinguished from the more persistent body or trail echo. *McKinley and Millman* (1949) defined the head echo as a moving echo having no appreciable enduring characteristics and with a range-time motion apparently corresponding to the geocentric velocity of the meteor. The echo appears to come from a cloud of ionization, with radius initially of the order of a few mean free paths, at the head of the meteor train (hence the name), and this is thought to be produced and quenched rapidly rather than being carried along with the particle. The mechanism to explain this phenomena is still not well understood and indeed head echoes pose a rather puzzling problem. *McKinley and Millman* (1949) suggested the rapid ionization production could be due to the photo-ionization of the surrounding atmosphere by ultraviolet radiation from the meteoroid. Recombination processes which remove the ionization are, however, about 50 times too slow to account for the short duration of these echoes (*Bronsten*, 1983). *Jones et al.* (1988) suggest a mechanism, involving water cluster ions, which is fast enough to account for the echoes' short durations. However this requires the cluster ions to be a constituent of the meteoroid as the atmosphere

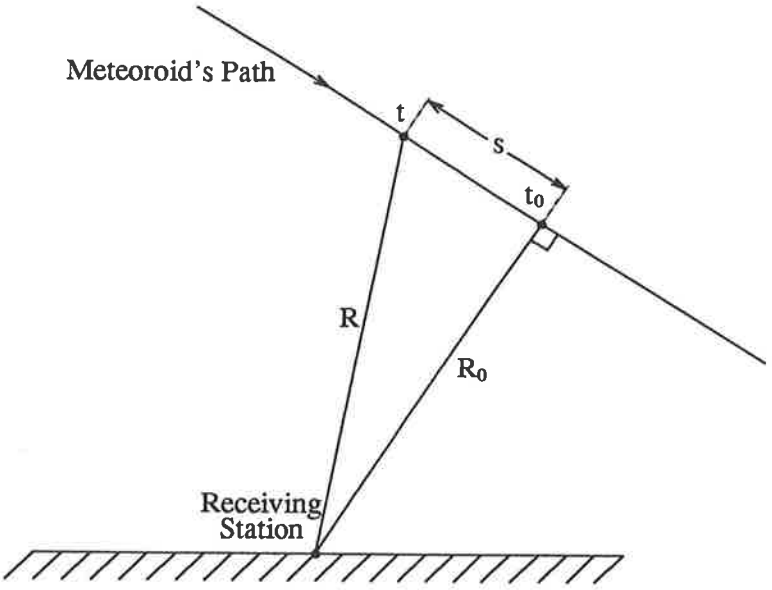

Figure 5.1: The geometry of a meteoroid's path through the Earth's atmosphere with respect to an observing station.

contains little water above 90 km (see also *Jones and Webster*, 1991). Examples of range-time records where the head echo is evident may be found in *Hey et al.* (1947), *McKinley* (1961) and *McIntosh* (1962). More recent observations of meteor head echoes have been reported by *Thomas and Netherway* (1989) with the Jindalee over the horizon radar at Alice Springs, Australia.

Consider now Figure 5.1 which shows the geometry of a moving cloud of ionization travelling along the path of the meteoroid in the Earth's atmosphere. The point of closest approach to the observing station is defined by R_0 and is labeled the t_0 point. The following equation may be immediately written:

$$\begin{aligned} R^2 &= R_0^2 + s^2 \\ &= R_0^2 + \left(\int_{t_0}^{t} V(t) dt \right)^2 , \end{aligned} \tag{5.1}$$

if the assumption is made that the velocity is constant (*McKinley*, 1961) then Equation 5.1 reduces to:

$$R^2 = R_0^2 + V^2 (t - t_0)^2 . \tag{5.2}$$

The velocity of the meteoroid may then be found by fitting a hyperbola of the form given by above equation, to the range-time record of the meteor head echo. Any departure of the data from the fit, if evident, is attributed to deceleration of the meteoroid.

McKinley and Millman (1949) extended this technique to a three station radar. This

enabled them to determine the path and therefore the radiant of individual meteors. Thus with the measurement of the velocity, they were able to calculate the orbits for individual meteoroids, the first time this was achieved by a radio technique.

As stated previously, the range-time technique for the reduction meteor velocities may only be applied where the meteor head echo is evident. Since these echoes are generally only observed for the brighter meteors, the range-time technique is severely limited in its application.

5.2.2 The diffraction technique

Herlofson (1948) suggested that the radio waves scattered from the ionization produced during the formation of a meteor trail should give a diffraction pattern analogous to that of the diffraction of light at a straight edge. This being the case, the velocity of the meteor would be able to be obtained from observation of the diffraction pattern and measurement of the Fresnel zone spacings. *Lovell and Clegg* (1948) showed that the post-t_0 echo amplitude oscillations in the signal scattered from a meteor trail were actually described by the Fresnel theory of diffraction. The first measurement of the velocity of a meteoroid from the post-t_0 radio echo was carried out by *Ellyett and Davies* (1948), and they were the first to employ this technique to successfully measure the velocities of two meteor showers: the Geminids and the Quadrantids (see also *Davies and Ellyet*, 1949). In particular, the result for the Geminid meteor shower was in excellent agreement with the photographic measurements of the velocities of visible meteors from this shower by *Whipple* (1947).

The technique developed by *Ellyett and Davies* has formed the basis for the measurement of meteor velocities by many other subsequent researchers (see *eg. Davies and Gill*, 1960; *Nilsson*, 1964a and 1964b; *Kascheyev and Lebedinets*, 1967; *Andrianov, et al.*, 1970; *Cook et al.*, 1972; and *Gartrell and Elford*, 1975). *Ellyett and Davies* pointed out that, while the relative amplitude of successive zones are not necessarily given by the Fresnel integrals due to the non linearity of the ionization along the trail, it is the only required that the zone lengths are consistent with the theory. *Ellyett and Davies* showed experimentally that this is the case. From the Fresnel integrals, *Ellyett and Davies* calculated the theoretical zone lengths (for a given range, R and radar wavelength, λ) defined by the first and second, and the second and third maxima of the post-t_0 amplitude oscillations (see Figure 5.2). The zone lengths defined by corresponding minima were also calculated. This yielded four theoretical zone lengths, and from these they calculated a total of six ratios between the zone lengths. Forming the

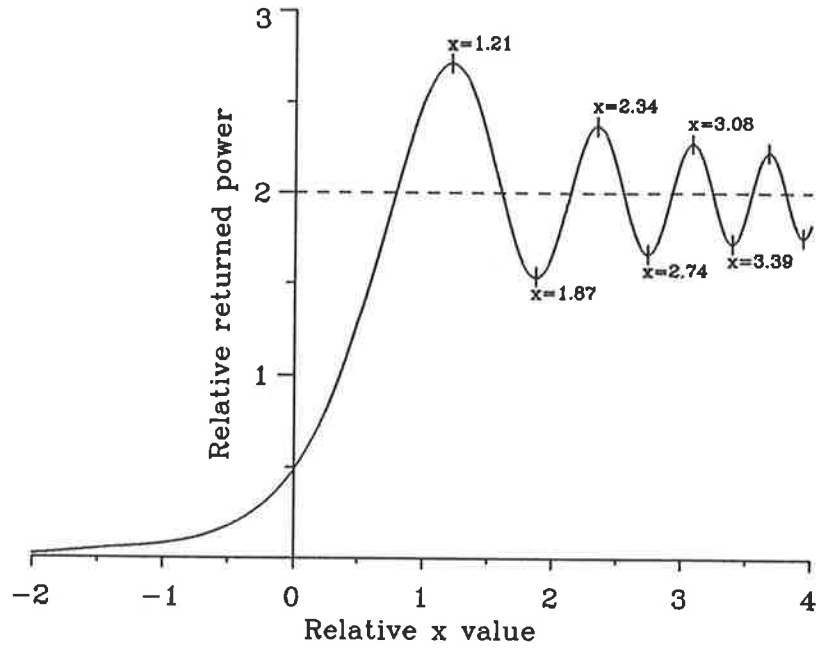

Figure 5.2: The amplitude Fresnel diffraction pattern of radiation at a straight edge. The relative x values are shown for the first 3 maxima and minima.

ratios eliminated R and λ and thus dimensionless numbers were obtained which could be compared directly to the observed diffraction patterns. The comparison of the theoretical ratios of the zone lengths to those determined from observations of several meteor echoes showed good agreement, thus indicating that the observed diffraction pattern of radio waves from the meteor trails are consistent with the Fresnel integrals, and justified their use in the calculation of meteor velocities.

Figure 5.2 shows the theoretical amplitude Fresnel diffraction pattern due to radiation incident on a straight edge. The abscissa of this plot is the relative x value derived from the Fresnel integrals (see *eg.* McKinley, 1961) and is related to the distance, s, back along the trail from the t_0 point by the following expression:

$$x = \frac{2s}{\sqrt{R_0 \lambda}} \,. \tag{5.3}$$

The positions of the first three maxima and minima of the post-t_0 oscillations in terms of the parameter x are also shown in this figure. A similar diagram may be obtained for the diffraction pattern of the phase information of the signal (see Figure 5.7). From the time difference, Δt, between the n^{th} and m^{th} maxima, the velocity is given by:

$$V = \sqrt{R_0 \lambda}\, \frac{(x_n - x_m)}{2\Delta t} \,, \tag{5.4}$$

where x_n and x_m are the positions of the n^{th} and m^{th} maxima in terms of the x parameter. If one was to measure the time difference between the n^{th} and m^{th} minima then the same expression holds. Likewise one may obtain a similar expression based on the positions of the zero crossings (see *eg. Cook et al.*, 1972). If one employs a CW radar to observe meteors, then pre-t_0 amplitude oscillations are also present in the echo diffraction pattern and these may be used in a similar manner to calculate velocities (see *eg. McKinley*, 1961).

The methods used to analyse the echo amplitude diffraction patterns by other researchers are similar to that detailed in the previous paragraph. Recently *Baggaley et al.* (1994) developed a more powerful technique of calculating the meteor velocity from the post-t_0 amplitude oscillations[1]. By using the digitized amplitude profiles and performing least fit squares fits to the oscillatory pattern, all the of available data from their echoes were used instead of only a limited number of points from the post-t_0 amplitude oscillations (such as the zero crossings, maxima or minima). The algorithm they developed to do this first obtained a mean amplitude level in the presence of the decaying oscillatory pattern. The normalized oscillatory function was then modelled as a succession of half periods each fitted to a sine function. At least three oscillatory cycles were required to be present to obtain the meteor velocity. In the cases where a large number of oscillations (at least 10) were well defined in the echo, decelerations were obtained by calculating the velocity over different subsections of the oscillatory pattern and combining the data from all three of their spaced receiving sites to produce a velocity profile over time. The deceleration was assumed to be constant in these cases, and its value was found from a linear least squares fit performed on the velocity-time profile.

All the methods employing the diffraction technique, while an improvement on the range-time method, are limited to only those echoes which show at least three clear post-t_0 amplitude oscillations. In general this requirement limits the number of velocity determinations to only about 10% of all meteor echoes observed. (see *Davies and Gill*, 1960; *Baggaley et al.*, 1994). The suppression of the oscillations may be caused by a number of factors including fragmentation of the meteoroid which produce multiple sources smoothing out the pattern, distortion of the pattern due to atmospheric winds, and larger echo decay rates at the upper heights, causing dampening of the oscillations.

[1]They used the velocities obtained by the diffraction method to verify a new technique that they developed. This technique is described later in Section 5.2.4.

5.2.3 Meteor velocities obtained from a UHF radar

A novel technique for the measurement of meteor velocities with UHF radars was developed by *Pettengill and Pineo* (1960) and *Pettengill* (1962) to investigate velocity distributions of showers and sporadic meteors with the Millstone radar operating at 441 MHz. Further meteor observations using this technique with the Millstone radar were carried out by *Evans and Brockelman* (1963, 1964). *Pettengill and Pineo's* technique was dependent on the ability of the Millstone radar to determine with a fair degree of accuracy, the Doppler shift in the transmitted frequency caused by the target motion, during a single transmitted pulse. This was achieved by employing a bank of 310 crystal filters. The filters had bandwidths of 200 Hz (matched to the transmitted pulse width of 2 ms) and were centered on frequencies stepped by 160 Hz, thus a frequency range of $\pm 24\ kHz$ about the transmitted frequency was covered. The Doppler shift of the echo was estimated by simply determining which filter in the bank gave the strongest output signal. Detailed descriptions of the radar may be found in publications by *Pettengill and Kraft* (1960) and *Arthur et al.* (1961).

Since the Millstone radar operated with a transmitter pulse width of 2 ms, the range resolution was quite poor. For a single return, the resolution was estimated to be of the order of one tenth of the pulse length, *i.e.* $\sim \pm 30\ km$. This was not a severe problem for these meteor observations as a narrow beam (2.1° half-power full-width) was employed, elevated typically 3° above the horizon. A meteor ablating at height of say 90 km would be detected at a range of about 790 km (the curvature of the Earth is required to be taken into account - see Equation 4.6), and the corresponding error in the determination of the height was about 3.5 km.

Consider now the effect on the returned echo of decreasing the radar wavelength. The effect is to reduce the amount of time (governed by the ambipolar diffusion of the trail at a given height) for which the diameter of the trail is less than the radar wavelength. Once the trail expands to a size where the diameter is greater than $\sim \lambda/(2\pi)$, destructive interference of the signal reflected from different portions of the trail will cause severe attenuation of the signal. Thus as the wavelength of the radar is decreased, the portion of a trail giving rise to significant reflections decreases until only the segment of trail immediately subsequent to the meteoroid contributes to the echo. The effect of the finite initial radius of the trail must also be considered (see Chapter 4). From Equation 4.15 the initial radius for a meteor with a velocity of 30 $km\ s^{-1}$ ablating at a height of 90 km is 0.46 m, and as the wavelength of the

Millstone radar is $0.68\,m$ severe attenuation of even the initial echoes occurs. This together with the fact that only short segments of the meteor trail are observable at these frequencies, implies that the returned echo power is correspondingly weak, thus requiring narrow beam high gain antennas and large transmitter powers. The Millstone radar had an antenna gain of $37.5\,dB$ and a peak transmitter power of $2\,MW$, and the system gave an average echo rate of 40 per hour.

The fact that the Millstone radar only received echoes from a small segment of trail was exploited by *Pettengill* (1962) in developing a method of analysis for the measurement of velocities. The length of this segment was less that a Fresnel zone at the wavelength at which the radar operated, and thus the meteor trails could be treated as a small target travelling with the velocity of the meteoroid. This, at first glance, suggests a method of analysis similar to the range-time method used for the head echoes observed by traditional meteor radars and discussed in Section 5.2.1. However, a meteor ablating at a height of $90\,km$ would be detected at range of $790\,km$ when orthogonal to the bore direction, and this increases by only about $0.1\,km$ when it is orthogonal to the direction defined by the half power points of the beam. Therefore the range resolution of the system was far too coarse to calculate meteor velocities in this manner. Instead *Pettengill* made use of the ability of the radar to measure the Doppler shift in the signal on a single pulse as described above. The deduction of the velocity from the observed Doppler shift is determined as follows. The geometry of the situation is described in Figure 5.1, where the following equation applies:

$$R^2 = R_0^2 + s^2 \,. \tag{5.5}$$

On differentiating twice with respect to time,

$$R\ddot{R} + (\dot{R})^2 = s\ddot{s} + (\dot{s})^2 \,. \tag{5.6}$$

The quantity $\dot{s}$ is of course the meteor velocity, so that the above equation may be recast to give:

$$v = \sqrt{R\ddot{R} + (\dot{R})^2 - s\ddot{s}} \,. \tag{5.7}$$

The deceleration was assumed to be negligible, and thus the term $s\ddot{s}$ was set to zero. $\dot{R}$ is related to the Doppler shift which is measured by the radar. The rate of change of radial velocity, $\ddot{R}$, was found by plotting the radial velocity $\dot{R}$ against time and performing a linear least squares fit. Thus the meteoroid velocity was found.

Pettengill produced a velocity distribution for sporadic meteors and for the Perseid meteor shower. As no attempt was made to correct the sporadic velocity distribution for various selection effects, *Pettengill's* distribution cannot be compared with velocity distributions obtained by other methods. However, the velocity which *Pettengill* obtained for the Perseids may be compared with other results and it was found to be in good agreement. Subsequently, *Evans and Brockelman* (1964) obtained the velocity for the Geminids, Quadrantids, Leonids and Orionids as well the Perseids using this radar. They also found that their measurements agreed well with results obtained using other techniques (see also *Evans* 1965).

Finally, *Evans* (1966) showed that by observing meteor showers down the beam of the radar, several precise velocity measurements could be made along the meteors' path. Subsequent analysis of the resultant velocity–time profiles yielded precise measurements of the deceleration of the shower meteors.

5.2.4 The spaced receiver technique

A new technique to obtain meteor velocities was developed recently by *Baggaley et al.* (1994) and applied in their Advanced Meteor Orbit Radar (AMOR). By deploying spaced receivers, the meteor velocities were obtained by measuring the time delays between observing meteors at three receiving stations with baselines of $8\,km$.

Multistation systems have been used in the past to obtain meteor orbits and investigate showers (see *eg. Gill and Davies*, 1956; *Davies and Gill*, 1960; also the discussion on multistation radars in Chapter 6). However, as these systems used wide beams, the elevation and azimuth of the meteor echoes were unable to be obtained. An exception was the Adelaide system (*Nilsson*, 1962) where the position of the reflection point was determined using a phase measuring system. In general the radiant coordinates and velocities of the meteors were unable to be calculated from only the measurements of the time differences between observing the meteors at the separate receiving stations. Thus, the velocity was required to be measured by a different technique (usually the diffraction technique) and then used, together with the time differences, to calculate the radiant coordinates.

The method developed by *Baggaley et al.* (1994), is quite simple, yet it represents a large step forward in the measurement of meteor velocities and thus their orbits. They use fan beams narrow in azimuth (3.2° half-power full-width) on reception thus constraining the echo azimuth, and employ a 5λ phase pair antenna to determine the echo elevation. With the position of the meteor echoes known, both their radiants and velocities may be calculated

from the measurement of the time delays between the echoes detected at each receiving site for a given meteor. The orbits of the meteors could then be calculated.

A great advantage of this method for determining orbits over previous methods is that the velocity is not required to be determined using the diffraction technique, thus greatly increasing the yield of velocity measurements and hence orbit determinations (about 60% compared with 10% for the diffraction technique). However, as discussed earlier in the section concerning the diffraction technique for the determination of meteor velocities, *Baggaley et al.* did calculate the velocities of the meteors using the post-t_0 amplitude oscillations where they could (they state about 12% of echoes). A comparison of these velocities with those calculated from the time lags gave good agreement, thus verifying the validity of their new technique.

5.3 A New Method for Measuring Meteor Velocities: The Pre-t_0 Phase Technique

5.3.1 Introduction

Recently, a new powerful method for the reduction of meteor velocities from the meteor echo profile was developed for use with meteor data obtained from the Buckland Park radar. This technique should be classified as a diffraction technique, as it makes use of the Fresnel diffraction theory applied to the observed echo. However, as will be shown later, this technique can be applied to approximately 75% of meteors observed, yielding some 7-8 times more determinations than with the previous diffraction method.

The technique exploits the phase information available from the coherent phase receivers of the Buckland Park radar. The phase information prior to the t_0 point is used for the reduction of velocities, and it is available even to the point where the amplitude has fallen to the level of the background noise (see Chapter 3). Furthermore, the pre-t_0 phase is available for reduction even in those cases where the post-t_0 amplitude oscillations have been washed out due to fragmentation, rapid echo decay or other effects. Thus the method is far more powerful and flexible than the previous diffraction method. Preliminary results using this technique have been reported by *Cervera, et al.* (1995) and *Elford, et al.* (1996).

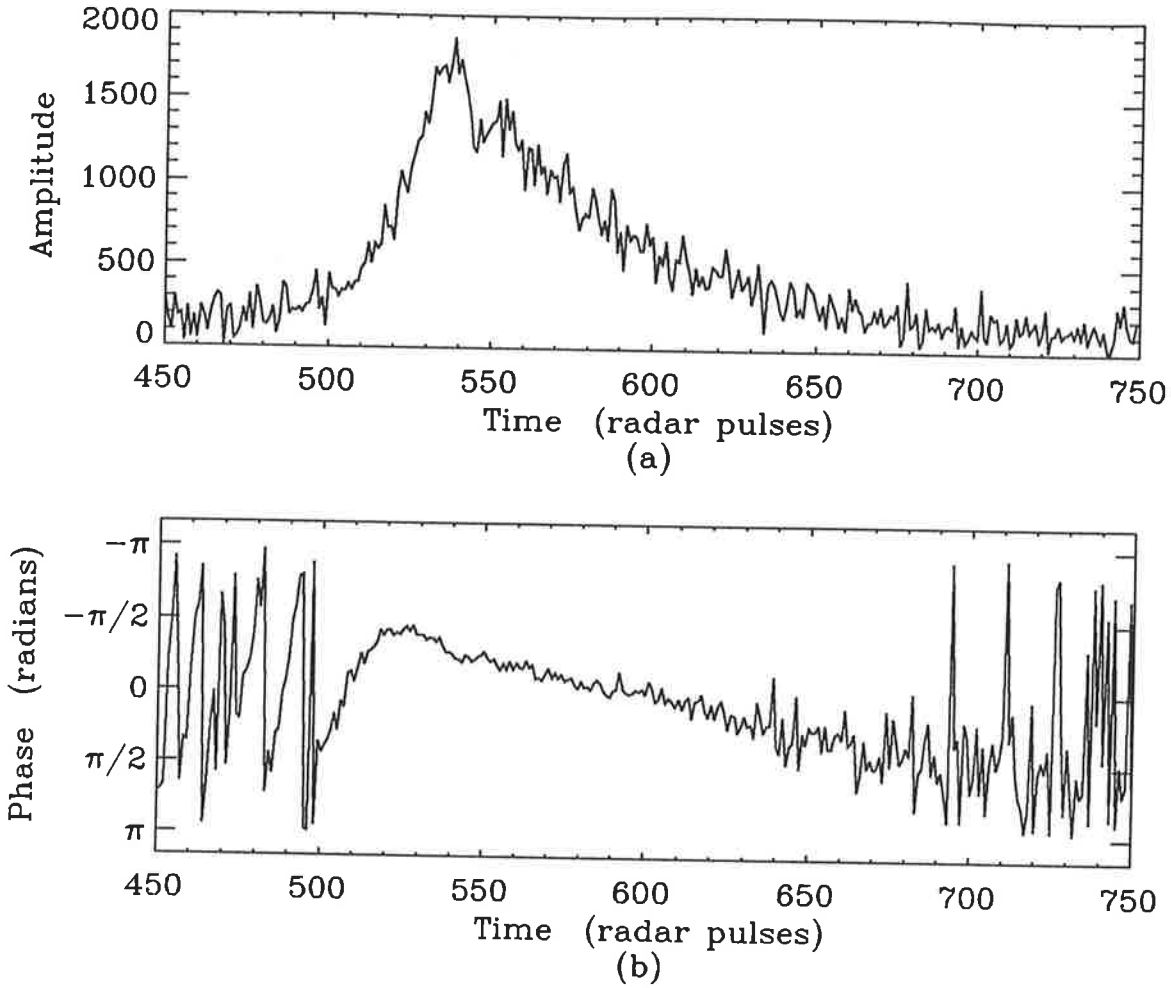

Figure 5.3: Typical raw meteor echo observed with the VHF radar and used for the reduction of meteor velocities. The abscissa is in units of radar pulses; thus, as the PRF was 1024 Hz, 1024 radar pulses $\equiv$ 1 *sec*. Also note that the origin for the radar pulse count is arbitrary. Panel (a) displays the amplitude information (scale in A/D conversion units) and panel (b) the phase. The meteor was observed at 0554 hours CST on 11 June 1994. The range was 110 km which corresponds to a height of 95.3 km if the assumption is made that the meteor was detected in the main beam of the radar. Note the lack of post-t_0 amplitude oscillations and the strong coherency in the pre-t_0 phase information.

5.3.2 The method of reduction of meteor velocities

The method of deducing meteor velocities from the pre-t_0 phase information from a meteor echo will now be discussed. Figure 5.3 shows a typical meteor echo observed by the radar at 0554 hours Australian Central Standard Time (CST) on 11 June 1994 at a range of 110 km (corresponding to a height of 95.3 km if the assumption is made that the meteor was detected in the main beam). Individual pulse returns appear at the output of the receiver as in-phase and in-quadrature components. These are digitised and recorded, converted to amplitude

and phase, and then plotted as a continuous record. The data presented in this figure is raw data, that is no post detection signal processing has been applied to it apart from converting the in-phase and in-quadrature signals from the receiver to amplitude and phase information. The time axis is in units of radar pulses where 1024 pulses is equivalent to a time interval of 1 *sec* (PRF 1024 Hz); for 'inspection purposes' the abscissa can be read as milli-seconds. Also, the origin of the time axis is arbitrary. The amplitude scale is in Analogue/Digital (A/D) conversion units. Despite the peak amplitude of the echo (found by fitting a 10^{th} order polynomial to the echo) being about 12.3 dB above the mean background noise, there is little evidence for any post-t_0 amplitude oscillations. Certainly this echo would be regarded as useless for determining a velocity from the post-t_0 Fresnel diffraction pattern.

For our purposes, the phase information displayed in Figure 5.3b is of much greater interest than the amplitude behaviour displayed in panel (a). The feature one notices immediately is the linearity of the echo phase from a time after about radar pulse 530 to where it disappears into the background noise some 150 ms later. This is of course due to fact that the meteor trail, once fully formed, drifts with the atmospheric wind, causing a smooth phase change with time. One may make use of this information to obtain atmospheric wind speeds and is described in the literature as the 'meteor drift' technique (see *e.g. Robertson et al.*, 1953; *Stubbs*, 1973; *Mathews et al.*, 1981; *Avery et al.*, 1983; *Nakamura et al.*, 1991; and *Cervera and Reid*, 1995). Further discussion of the meteor drift technique developed by the author for the measurement of atmospheric wind speeds using the Buckland Park VHF radar is found in Appendix A. The second feature, which is important for calculation of meteor velocities, is the rapid phase variation with time during the formation of the trail. One can see that the echo is phase coherent some 70 radar pulses (about 68 ms) prior to the t_0 point near radar pulse 525 (estimated to be approximately where the amplitude has risen to half the peak value). A close inspection of the record between pulse 450 and 500 indicates that the phase information undergoes four to five 2π cycles of decreasing phase[2]. To explore this phase behaviour further a suitable phase unwrapping procedure is required. It is noted that the amplitude in this region is well down into the noise.

The signal to noise ratio of the record may be improved by applying post detection signal processing. This takes the form of coherent smoothing which is a running boxcar average of the separate raw in-phase and in-quadrature signals. The signal to noise ratio is improved by a factor of $\sqrt{N}$, where N is the width of the boxcar. Typically, coherent smoothing over two

[2]Note the phase plot shows phase decreasing in the positive 'OY' direction

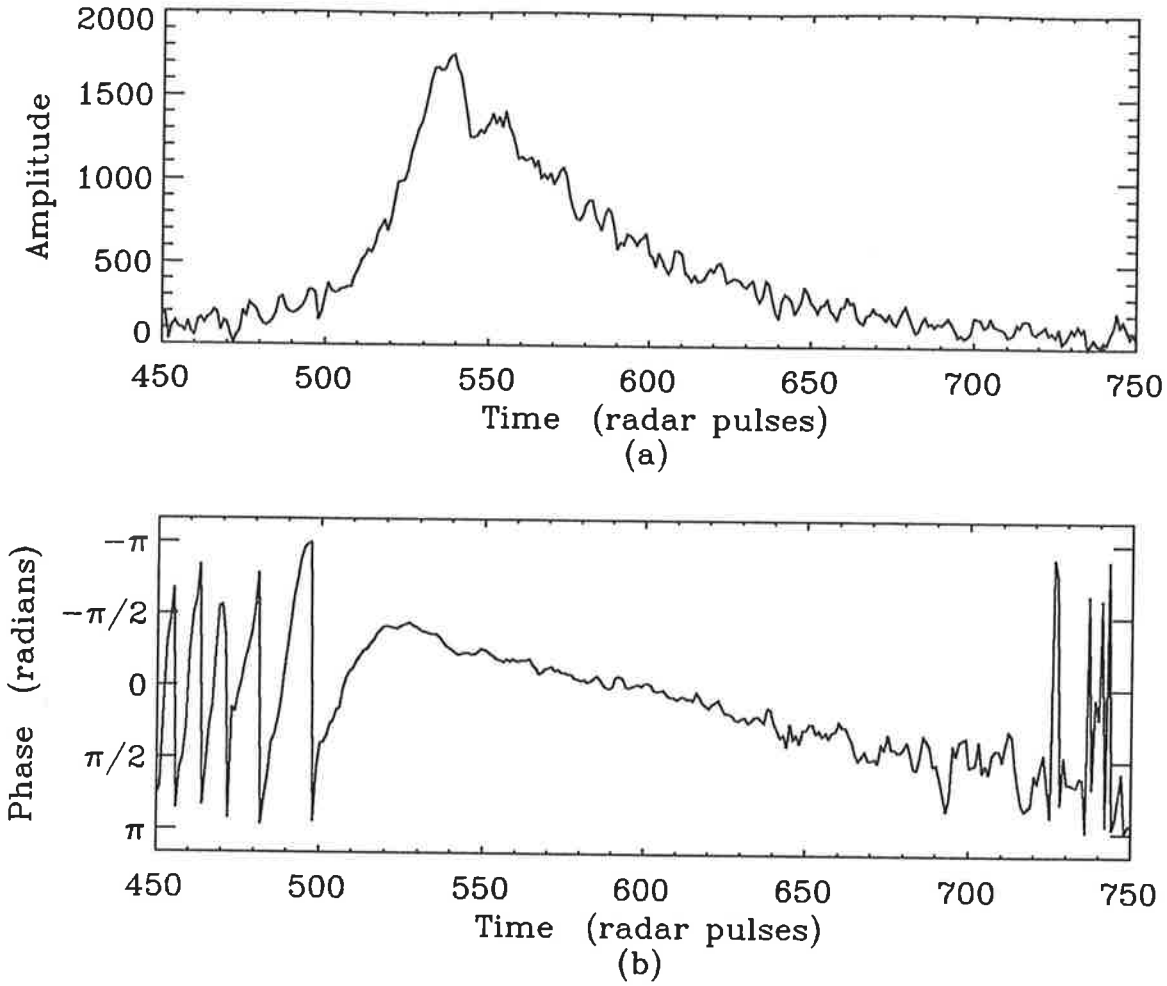

Figure 5.4: The effects of coherent smoothing applied to the raw data obtained from a meteor echo. The echo displayed here is that from Figure 5.3 with 2-point coherent smoothing applied to it.

to eight pulses is chosen. Care must be exercised when coherent smoothing is applied: one wants to increase the signal to noise ratio of the echo without smoothing out any important features. Figure 5.4 shows the effect of 2-point coherent smoothing applied to the meteor echo displayed in Figure 5.3. The effect of the coherent smoothing on the amplitude profile is to enhance the Fresnel oscillations: while they are now more apparent than in the raw echo, it is still impossible to obtain a meteor velocity from them. A still greater amount of coherent smoothing washes out entirely the little oscillation that is evident. However, the effect on the phase information is quite spectacular, the coherency of the returned signal is clearly evident during the formation of the trail, with five 2π cycles of phase well delineated. The phase information is clearly well behaved even during the early portion of the echo where the amplitude is comparable to the noise, and also the phase holds up well at the latter

end of the echo long after the amplitude has apparently decayed into the noise background. This demonstrates the power of using the phase information which is available from phase coherent receivers as was discussed in Chapter 2.

Now that the quality of the phase information from meteor echoes has been established, two points must be addressed before the phase may be used to obtain a meteor velocity. These are: (1) the meteor echo is influenced by the background atmospheric wind (*i.e.* it is Doppler shifted), and the effect on the phase is required to be removed (de-trended) from the echo; and (2) the 2π wrapped phase data must be 'unwrapped' to give a continuous and smooth phase record.

In order to remove the effect of trail drift on the phase of the returned echo, the amount of Doppler shift (denoted Δf) must first be found. This is achieved by recognising that the Doppler shift is given by:

$$\Delta f = \frac{d\phi}{dt} \tag{5.8}$$

where ϕ is the phase and t is time. The Doppler shift is readily measured from the echo by fitting a straight line to the linear portion of the phase record once the trail has fully formed. If the returned complex signal from a meteor which has experienced a constant Doppler shift over a time t, is denoted by $\boldsymbol{E}'$ and the signal with the Doppler shift 'de-trended' by $\boldsymbol{E}$, then the following equation may be written:

$$\boldsymbol{E} = \boldsymbol{E}' e^{i\xi} \,, \tag{5.9}$$

where the angle ξ is the change in phase over time t due to the Doppler shift and is given by $\xi = t\Delta f$. Figure 5.5 displays the situation. The quantities p' and q' in Figure 5.5 are the in-phase (real) and in-quadrature (imaginary) components of the returned signal and p and q are the in-phase and in-quadrature components of the de-trended signal. Thus the following equation may be written:

$$\begin{pmatrix} p \\ q \end{pmatrix} = \begin{pmatrix} cos(\xi) & sin(\xi) \\ -sin(\xi) & cos(\xi) \end{pmatrix} \begin{pmatrix} p' \\ q' \end{pmatrix} . \tag{5.10}$$

The application of this equation to the data de-trends the Doppler shift from the echo; the time interval t, that was used to calculate ξ, was found for each point in the echo from the start of the data record. The 'de-trending' is continued back to the pre-t_0 section of the echo on the assumption that the background wind is uniform over the whole of the trail contributing to the record.

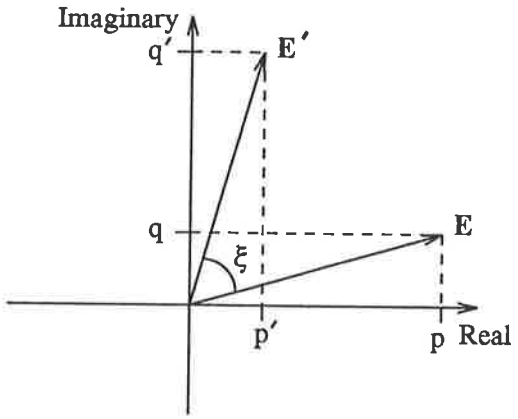

Figure 5.5: The effect of a constant Doppler shift over a time t on a complex signal. $\boldsymbol{E}$ is the signal with no Doppler shift, $\boldsymbol{E}'$ the Doppler shifted signal and ξ the change in phase over time t due to the Doppler shift given by $\xi = t\Delta f$.

The unwrapping of the phase information was achieved by a simple algorithm which was applied to the echo once the phase was calculated from the de-trended in-phase and in-quadrature data. Coherent smoothing, if applied, was performed on the de-trended data before the unwrapping procedure. The unwrapping algorithm operated by checking each point in the phase time series, and if the phase of the next point was found to greater by a value of $+\pi$ or more, then each point in the time series from that point onwards had 2π subtracted. Likewise if the difference was less than $-\pi$, 2π was added from this point to each datum in the time series. Usually this simple procedure handled most data records with no error. In the cases where it failed, a 2π phase jump was introduced to the data. This occurred when the phase data was exceptionally noisy (usually occurring simultaneously with a low signal amplitude). Usually the 2π phase jump was obvious by eye; in many cases correction of the 2π phase jumps was achieved by applying further coherent smoothing to the unwrapped data (for example see Figures 5.10 and 5.11).

Figure 5.6b displays the de-trended and unwrapped phase record of the meteor echo displayed in Figure 5.3, when 2-point coherent smoothing was applied to the de-trended data. Note that at a time of about 470 pulses, the phase does not behave as consistently as the rest of the phase record, it appears the phase loses coherency at this point. This is not surprising as the amplitude at this time has fallen to zero, thus the phase at this time is random. Nevertheless, inspection of the phase in Figure 5.6 suggests that the phase record is reliable from pulse number 450.

The meteor velocity may now be calculated from the pre-t_0 phase. This will be done by

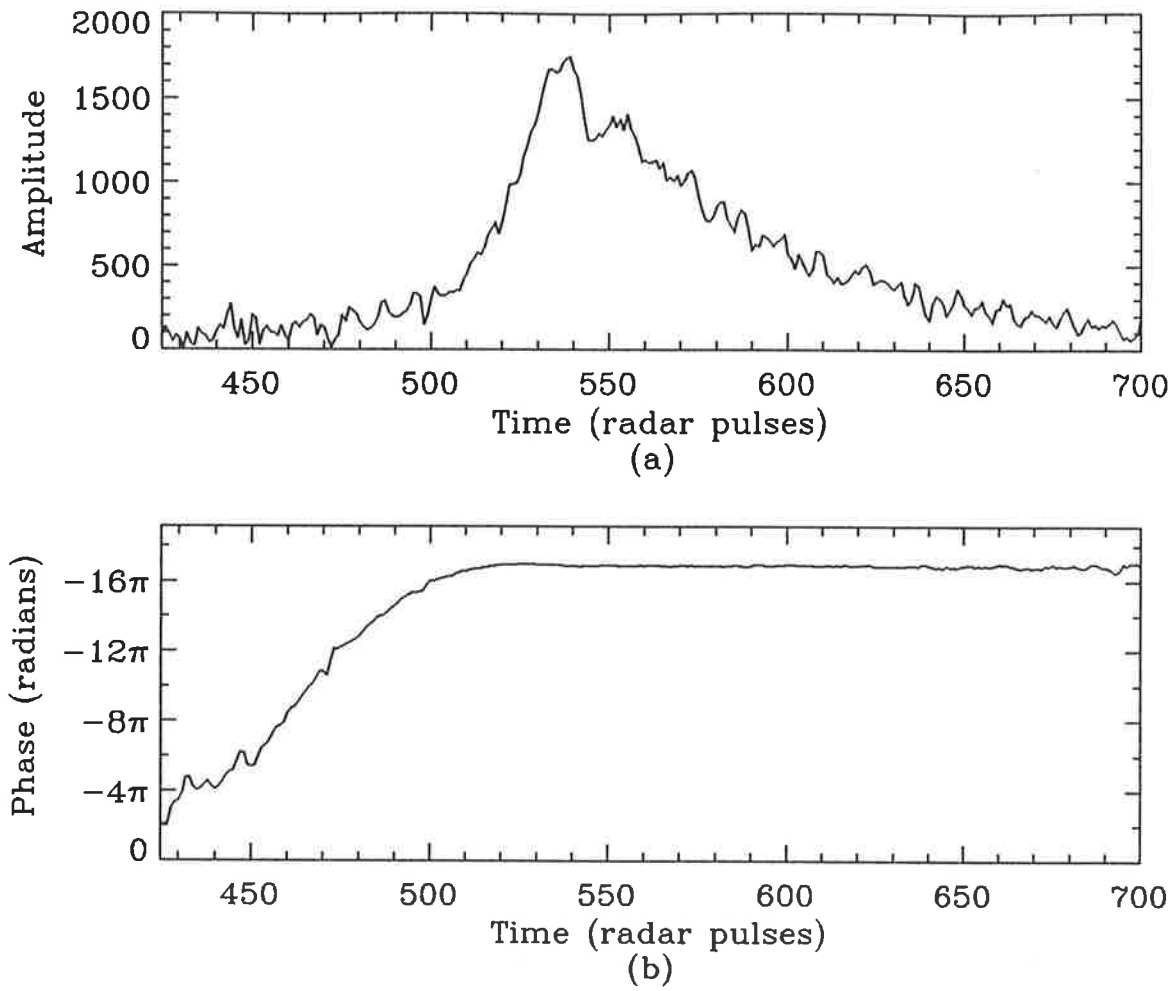

Figure 5.6: The echo displayed here is that from Figure 5.3 which has been de-trended. The phase data has also been unwrapped, 2-point coherent smoothing applied prior to this process.

two methods. The first method involves fitting a quadratic to the pre-t_0 phase (valid only for $x < -1$). This is fairly crude but simple to perform and was done to obtain an initial verification of the technique. Consider the Fresnel integrals in the following equation (see *eg. McKinley* 1961):

$$C = \int_{-\infty}^{x} cos\left(\frac{\pi x^2}{2}\right) \qquad \text{and} \qquad S = \int_{-\infty}^{x} sin\left(\frac{\pi x^2}{2}\right) , \tag{5.11}$$

the amplitude diffraction pattern is given by $\sqrt{C^2 + S^2}$ and the phase by $tan^{-1}(S/C)$. The amplitude diffraction pattern displayed in Figure 5.2 was calculated from these equations. In a similar manner the diffraction pattern of the phase information may be calculated, and this is displayed in Figure 5.7. The Cauchy approximations to Fresnel integrals are:

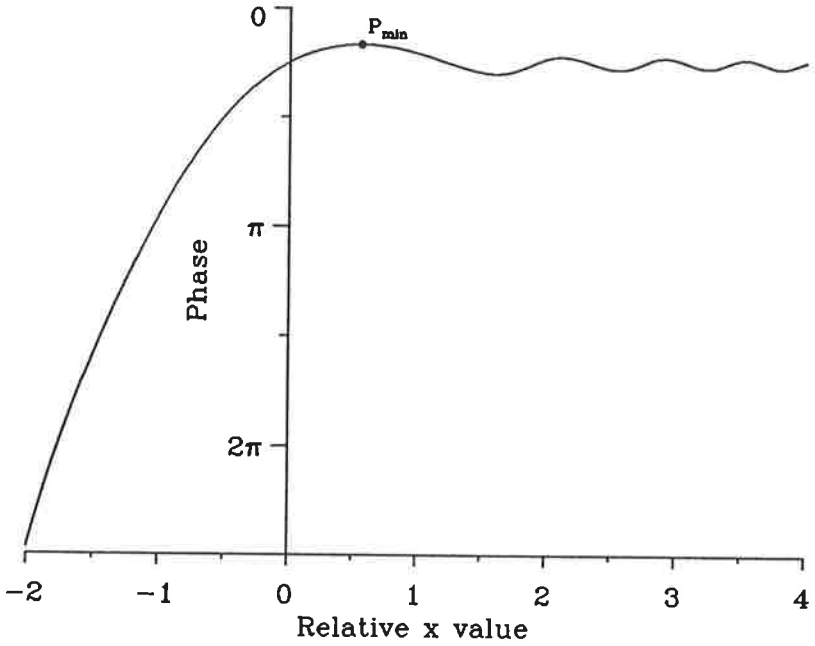

Figure 5.7: Fresnel diffraction pattern of the phase information from radiation at a straight edge. The point P_{min} denotes the point of minimum phase.

$$\begin{aligned} C &= \frac{1}{\pi x} sin\left(\frac{\pi x^2}{2}\right) \quad \text{and} \quad S = -\frac{1}{\pi x} cos\left(\frac{\pi x^2}{2}\right) \quad \text{for } x < -1\,, \\ C &= 1 + \frac{1}{\pi x} sin\left(\frac{\pi x^2}{2}\right) \quad \text{and} \quad S = 1 - \frac{1}{\pi x} cos\left(\frac{\pi x^2}{2}\right) \quad \text{for } x > 1\,, \end{aligned} \tag{5.12}$$

(the Cauchy approximations are not valid for the region $-1 < x < 1$). Therefore the phase behaviour for $x < -1$ is given by:

$$\phi_{x<-1} = \frac{\pi x^2}{2} = \frac{2s^2}{R_0 \lambda}\,. \tag{5.13}$$

With the assumption of no deceleration, this becomes (using $s = Vt$):

$$\phi_{x<-1} = \frac{2V^2}{R_0 \lambda} t^2\,, \tag{5.14}$$

and therefore the coefficients obtained from performing a quadratic fit to the phase data prior to $x = -1$ will yield the velocity. Alternatively one could obtain the slope of a linear least squares fit to $\phi^{1/2}$ vs. t and thus calculate the velocity. The velocity for the meteor echo displayed in Figure 5.6 was calculated by this method and was found to be $27 \pm 2\, km\, s^{-1}$.

The second method (and the one used for the routine calculation of meteor velocities) is a more complicated technique, but it may be applied to a greater portion of the phase information and yields a much more accurate measurement of the velocity. Once the algorithm was developed, a computer program was used to implement it for all the meteor echo data.

Consider again the Fresnel integrals, which describe the Fresnel diffraction patterns. *McKinley* (1961) shows how they are developed for meteor echoes, and apply in the idealized case where the effects of the initial radius, ambipolar diffusion and polarisation of the radio waves are not included (see also Chapter 3). One may apply the Fresnel integrals as they stand by evaluating them, and thus the expected phase, as a function of x back along the trail. By comparing the expected and observed phase one may calculate the velocity. However, it is desirable to include the above mentioned effects into the modeled phase. *Elford* (private communication) has developed a height dependent model which includes these effects. The reflection coefficients calculated by *Poulter and Baggaley* (1977) for transverse and longitudinal polarisations of the radio wave with respect to the trail (see Chapter 3) were also incorporated into the model. However, no attempt was made to factor into the model the ionization profile of the meteors, which was assumed to be constant over the length of the trail. An independent analysis by *Elford* (private communication) had shown that a trail with a "classical ionization profile" gave results for the phase as a function of x that could not be distinguished from a uniform trail. From an analysis of the results of the modelling procedure, *Elford* made the following observations:

- Prior to the point where the phase minimises (*i.e.* P_{min} in Figure 5.7), the use of transverse or longitudinal polarisation had little effect on the form of the phase information as a function of the parameter x. However, after the point of minimum phase, significant differences occurred.

- Changing the input model velocity of the ablating meteoroid had no effect on the model phase prior to the point where it minimised; however, at heights above $90\,km$ significant differences occurred in the phase after the point of minimum phase.

- As the height of ablation was increased (*i.e.* increase in the value of the diffusion coefficient), negligible changes occurred to the phase for $x < -1$. For $-1 < x < 0$ small changes were noted at heights above $100\,km$. Post-t_0 ($x > 0$), significant changes to the phase occurred as the height of ablation was increased. Eventually, the phase behaviour approached a parabolic form, as expected due to the shortened effective length of trail causing the meteor to look more like a point source.

- Finally, as the height of ablation was increased, it was noted that the point of minimum phase move closer to the t_0 point (from about $x = 0.6$ at $75\,km$ to about $x = 0.3$ at

105 km). This is consistent with the post-t_0 phase behaviour becoming more parabolic at the upper heights.

Consideration of the above points was required to develop the algorithm to reduce the meteor velocities. This will now be described.

From the model of the phase behaviour of meteor echoes as a function of the parameter x, developed by *Elford*, a look-up table of phase as a function of x and height was constructed. The height of ablation of the echo was obtained and the modeled phase was interpolated from the table at this height. For the velocity estimate, the appropriate portion of phase from the processed echo (*i.e.* de-trended, appropriate coherent smoothing applied, and unwrapped) was defined as that from the point where the phase was at a minimum value ($\equiv P_{min}$) back to where the phase first became coherent out of the noise. This gave a set of phase vs. time data. The modeled phase vs. x values were used to interpolate the corresponding x values at each point on the observed echo phase profile. Finally, using the relation $s = x\sqrt{R_0\lambda}/2$, the distance, s, back along the trail as a function of time was obtained. A linear least squares fit was then applied to the obtained distance-time profile and a parameter, denoted by χ, characterising the "goodness of fit" was calculated. The expression for χ is:

$$\chi = \frac{1}{N-2}\sum_{i=0}^{N}(f_i - s_i)^2 \,, \tag{5.15}$$

and is known as the error variance from standard statistics theory. In this equation the values of s_i are the distances obtained from the implementation of the reduction technique to the meteor echo, and the f_i are the corresponding values obtained from the linear least squares fit. The entire process was iterated over several estimated times for the position of the minimum phase. Minimising the error variance gave the best fit, and the velocity was taken as the slope of the fit to the data for this case.

Figure 5.8 shows the calculated distance-time profile prior to the point of minimum phase for the echo displayed in Figure 5.6. In this diagram, the crosses are the calculated distances, the straight line is that given by the linear least squares fit to the data. One can see that the fit is extremely good, and this is a characteristic of this technique. The velocity of the meteor is calculated to be $27.5 \pm 0.2\, km\, s^{-1}$. The departures of the calculated distance from linear behaviour at times 474 and 500 radar pulses correspond to distinct 'minima' in the amplitude record as seen in Figure 5.6a.

In Figure 5.9 the modeled phase (solid line) has been superimposed on the observed phase (solid circles) of the returned meteor echo. As the modeled phase is given as a function of

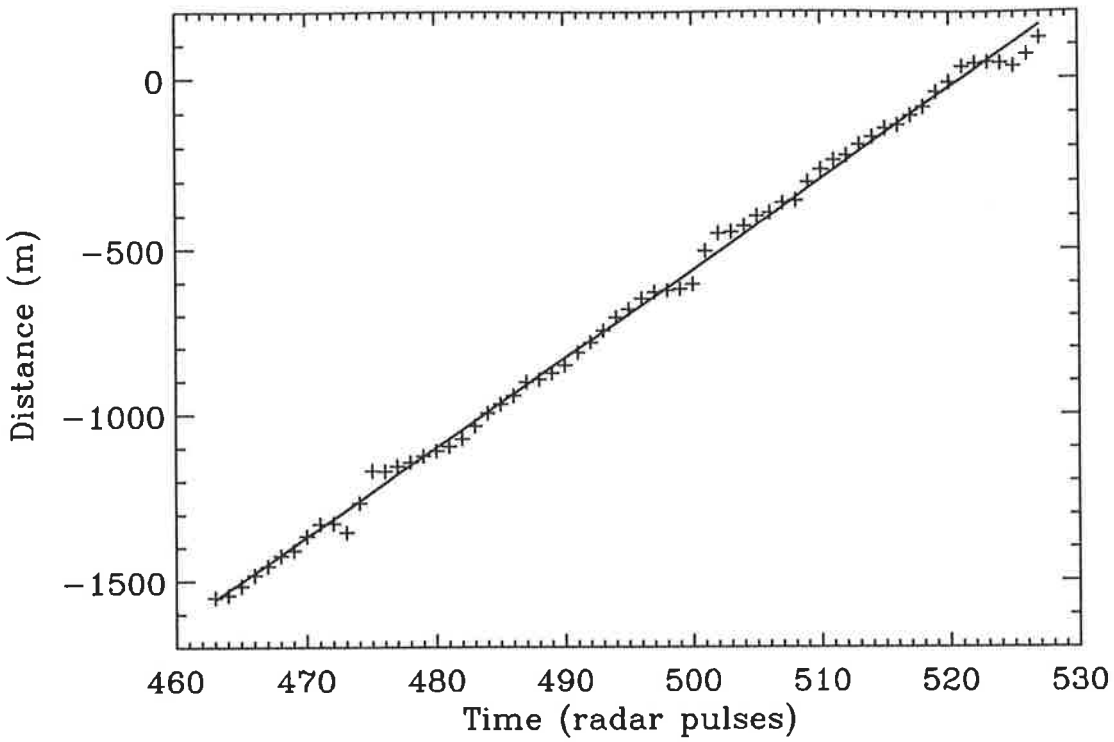

Figure 5.8: Distance-time profile obtained from the phase information (prior to the point of minimum phase) of the meteor echo displayed in Figure 5.6. The distance axis refers to the distance back along the trail. The crosses are the distances calculated from measured phase and the model (see text for details), the solid line is a linear least squares fit to the data. The slope of the line gives the velocity of the meteor which is $27.5 \pm 0.2\, km\, s^{-1}$.

the x parameter, the velocity calculated from this echo was used to convert these x values to time so that the modeled phase could be plotted over the recorded phase. Again one may observe that the model gives an extremely good fit to the basic data. (With hindsight the phase data between 'times' 450 and 460 could also have been used).

5.3.3 The measurement of meteor decelerations?

So far, in this discussion, the deceleration of the meteors has not been considered, in fact the deceleration has been assumed to be zero which, of course, is not the case. Except for the last 10% of a meteor trail, the deceleration of the meteors may be considered a second order effect. It may appear possible that instead of performing a linear least squares fit to the distance-time profile, fitting a second order polynomial would give an estimate of the deceleration. Although this is simple; in practice, it not possible as is shown by the following analysis. Consider again Figure 5.8, the data here spans a duration of 64 radar pulses or $62.5\, ms$. With the assumption of no deceleration, the distance traveled by the meteoroid

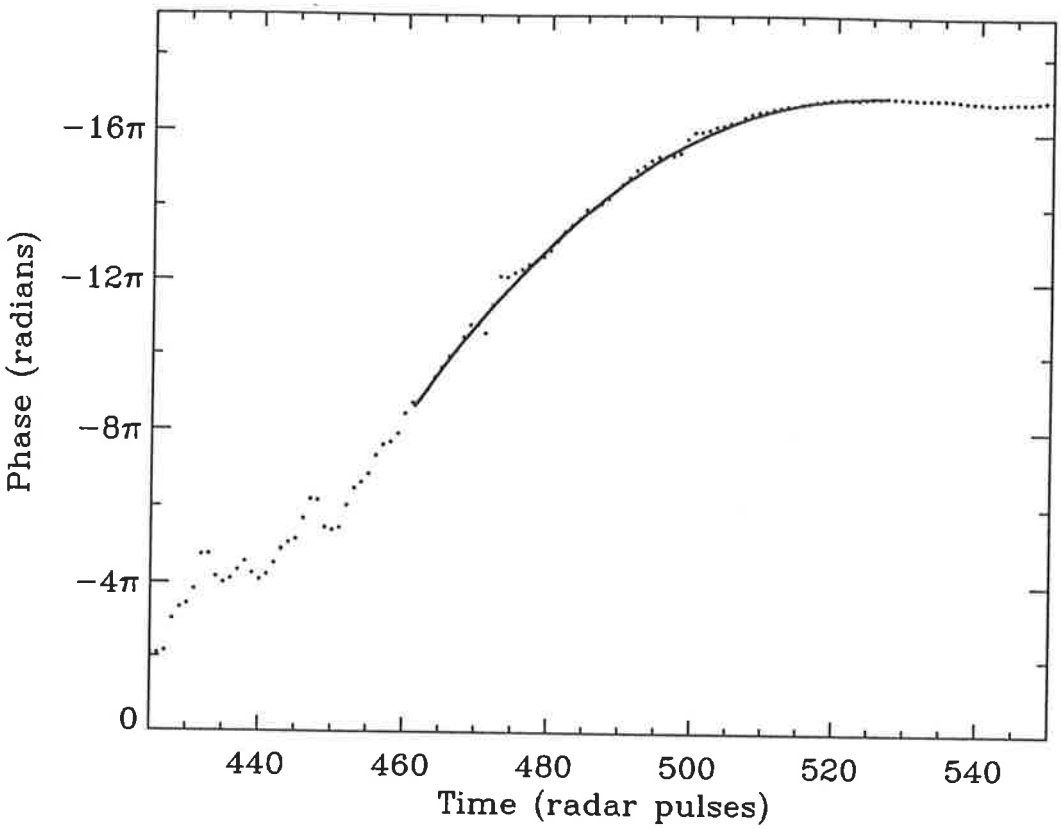

Figure 5.9: The phase profile of the meteor echo displayed in Figure 5.6 (solid circles) together with the modeled phase prior to the point where phase is a minimum (solid line).

in this time is calculated to be $1719\,m$. Now assume a velocity at time $t = 0$ to be the calculated velocity of $27.5\,km\,s^{-1}$, and a moderate constant deceleration of $10\,km\,s^{-2}$ (the choice of this value will be addressed shortly), occurring over the duration of the record. Using the following two kinematical equations:

$$s = V_0\,t + \frac{1}{2}at^2 \qquad \text{and} \qquad V_t^2 = V_0^2 + 2as\,, \tag{5.16}$$

where a is the acceleration, V_0 the initial velocity and V_t the velocity at time t, then one may calculate that in $62.5\,ms$ the meteoroid has travelled $1699\,m$, a reduction of $20\,m$ or about 1%. Also, the velocity at the end of the path has decreased to $27.49\,km\,s^{-1}$, *i.e.* a reduction of $0.01\,km\,s^{-1}$ or about 0.03%. This is over an order of magnitude smaller than the error in the velocity estimate. Clearly for the example deceleration used, the modification to the result is small, and in particular, the curvature of the distance-time profile is far too small to be calculated with a second order polynomial fit. If decelerations are to be measured from pre-t_0 phase, much greater phase paths or very much larger decelerations are required.

In Chapter 6, the velocity distribution of an observed meteor shower (the θ-Ophiuchids) is

obtained. Deceleration of the meteors are taken into account using two methods: (1) through consideration of the velocity-height scatter plot of the meteors, and (2) using a model based on classical ablation theory. These methods are discussed in detail in Chapter 6. It will be shown that the observed shower meteors have a mean measured velocity of $24\,km\,s^{-1}$ and an estimated initial velocity of $26.4\,km\,s^{-1}$. The mean height of ablation is $92\,km$. If it is assumed that the onset of ionization (and therefore deceleration) occurs at about $100\,km$[3], then a mean value for the deceleration of $7.6\,km\,s^{-2}$ is obtained for the shower meteors. This of course has assumed that the deceleration of the meteors is constant which is not the case, the deceleration increases monotonically at the onset of ablation.

The range of electron line densities over which the Buckland Park VHF radar typically observes meteors is about 10^{10}–$10^{12}\,electrons/m$. Ablation theory may be employed to estimate the amount of deceleration experienced by meteoroids, with a given velocity, producing electron line densities in this range. For example, *Elford* (private communication) estimates from his ablation model, that at the point of maximum ionization, a meteor with an initial velocity of $20\,km\,s^{-1}$ producing a maximum electron line density of $10^{12}\,electron/m$, experiences a deceleration of about $5.2\,km\,s^{-2}$. This increases to about $9.1\,km\,s^{-2}$ and $12.1\,km\,s^{-2}$ for meteoroids (velocity of $20\,km\,s^{-1}$) producing maximum electron line densities of 10^{11} and $10^{10}\,electrons/m$ respectively. The amount of deceleration that the meteor experiences at the point where it is observed, depends at what point on the ionization profile it is detected. Limits may be placed on the range of positions on the ionization curve according to the threshold for detection of the radar system, but within this range, the point on the ionization curve where the meteor is detected is random. Prior to the point of maximum ionization, the example meteoroids (above) experience a smaller deceleration than the values given, while after this point the meteoroids experience larger decelerations. Still, these values for deceleration in addition to the crude estimate of deceleration in the previous paragraph, gives a useful guide to the amount of deceleration experienced by the meteor shown in Figure 5.6. The assumed value for the deceleration of $10\,km\,s^{-2}$ used to estimate the effect on the fit to the pre-t_0 phase appears to be appropriate.

The discussion so far on deceleration indicates that it is a difficult quantity to measure using the pre-t_0 phase information. This is indeed the case. For example in an attempt to calculate decelerations by performing second order least squares polynomial fits to the

[3]This figure is based on a model of the ablation of meteoroids, developed by *Elford* (private communication), which takes into account conduction, heat capacity and radiative effects.

distance-time data resulted in values, which appear to be random, ranging from -50 to $+50\,km\,s^{-1}$ with equally large errors in the determinations. Another method to calculate the deceleration was tried which involved splitting the distance-time profile into four sections and calculating a velocity to each. However this encountered the same problem as with fitting the second order polynomial. Splitting the records into two portions instead of four did not improve the situation at all. Thus the conclusion is reached that measuring the deceleration by using the pre-t_0 phase technique alone is not possible. The amount of deceleration meteors typically experience is not great enough to cause measurable variations in the distance-time profiles. If the meteor was observed over a much greater distance then measuring decelerations may be possible. This is a possibility for meteors which display a large number of post-t_0 Fresnel oscillations as is discussed in the next section.

5.3.4 Further examples of the pre-t_0 phase technique

Several interesting examples of application of the pre-t_0 phase technique will now be examined. Figure 5.10 displays a meteor echo observed at 12:58 CST on 6 June 1994, at a range of $100\,km$ (height of $86.7\,km$). Panel (a) shows the raw amplitude profile, (b) the raw phase (no detrending applied), and (c) the processed phase. This echo is of considerable interest because the amplitude profile displays a large number of clear post-t_0 oscillations, from which a meteor velocity may be calculated and compared with the velocity as measured from the pre-t_0 phase. Note that the phase information in (b) also displays oscillations post-t_0, and these oscillations are in quadrature (lagging) with the amplitude oscillations as expected from the Fresnel diffraction theory. Meteor echoes displaying such a large number of clear post-t_0 oscillations are relatively rare, comprising about 1-2% of all meteor echoes observed.

The second interesting feature to note in Figure 5.10 is the 2π phase jump in the pre-t_0 phase information displayed in panel (c). This (as described previously) is due to the unwrapping algorithm failing at this point. The algorithm fails due to a large phase fluctuation at this point, that is coincident with the amplitude falling to zero (see Figure 5.10a). As described earlier, this problem may be rectified by appling a small amount of coherent smoothing to the raw data. In Figure 5.11 the echo from Figure 5.10 is redisplayed with 2-point coherent smoothing applied. Note that the 2π phase jump in the pre-t_0 phase information has now disappeared. The post-t_0 amplitude oscillations are also clearer. Figure 5.12 displays the distance time profile obtained from the pre-t_0 phase using the method described in Section 5.3.2; the crosses are the data points and the solid line a linear least squares fit.

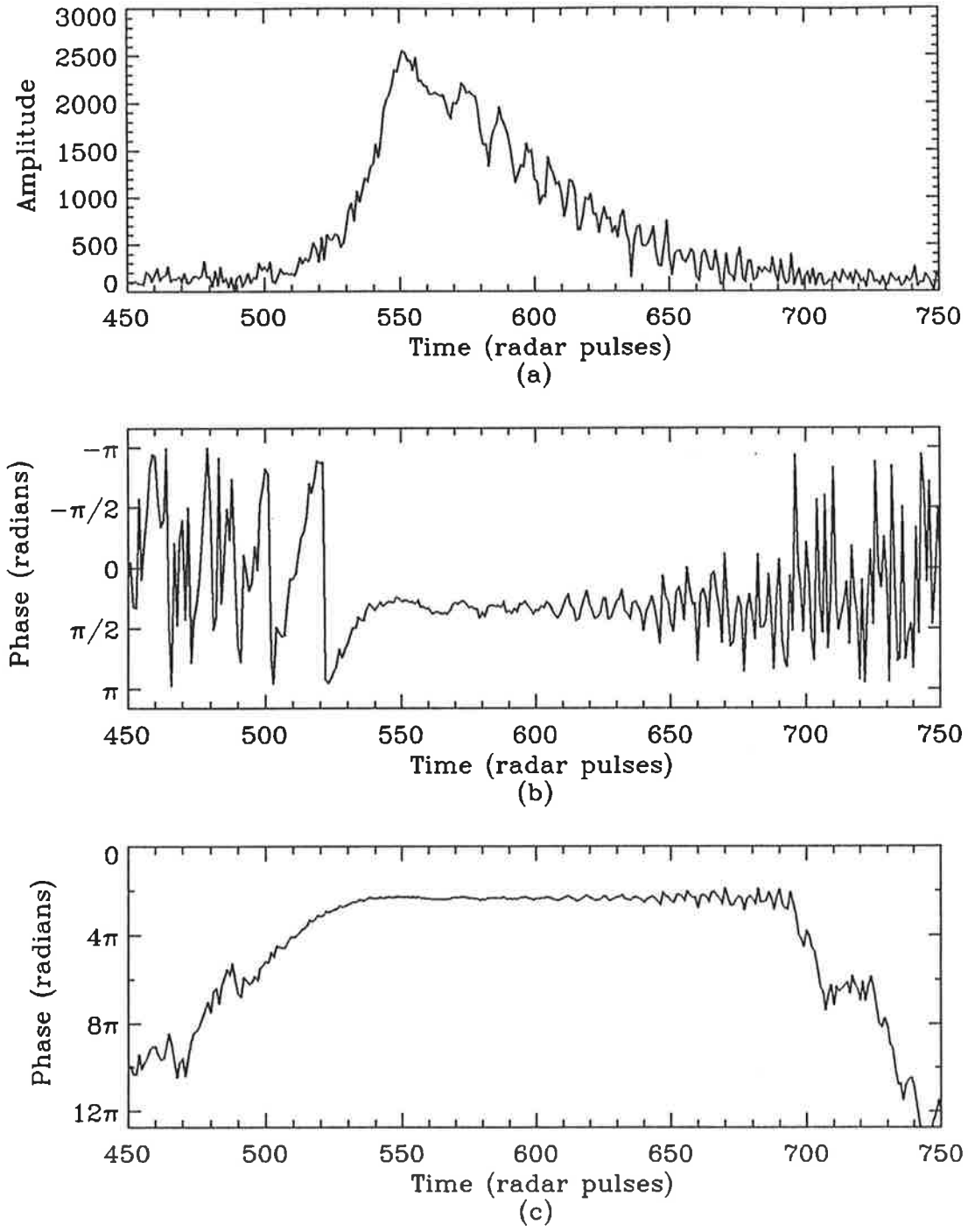

Figure 5.10: Meteor echo observed at 12:58 CST on 6 June 1994, at a range of 100 km (height 86.7 km). Note the large number of post-t_0 amplitude oscillations shown in panel (a) and the corresponding oscillations in the phase information shown in panel (b). The post-t_0 amplitude and phase oscillations are in quadrature with the phase lagging, as expected from the Fresnel diffraction theory. Also note the 2π phase jump in the processed, pre-t_0 phase information displayed in panel (c). See text for further details.

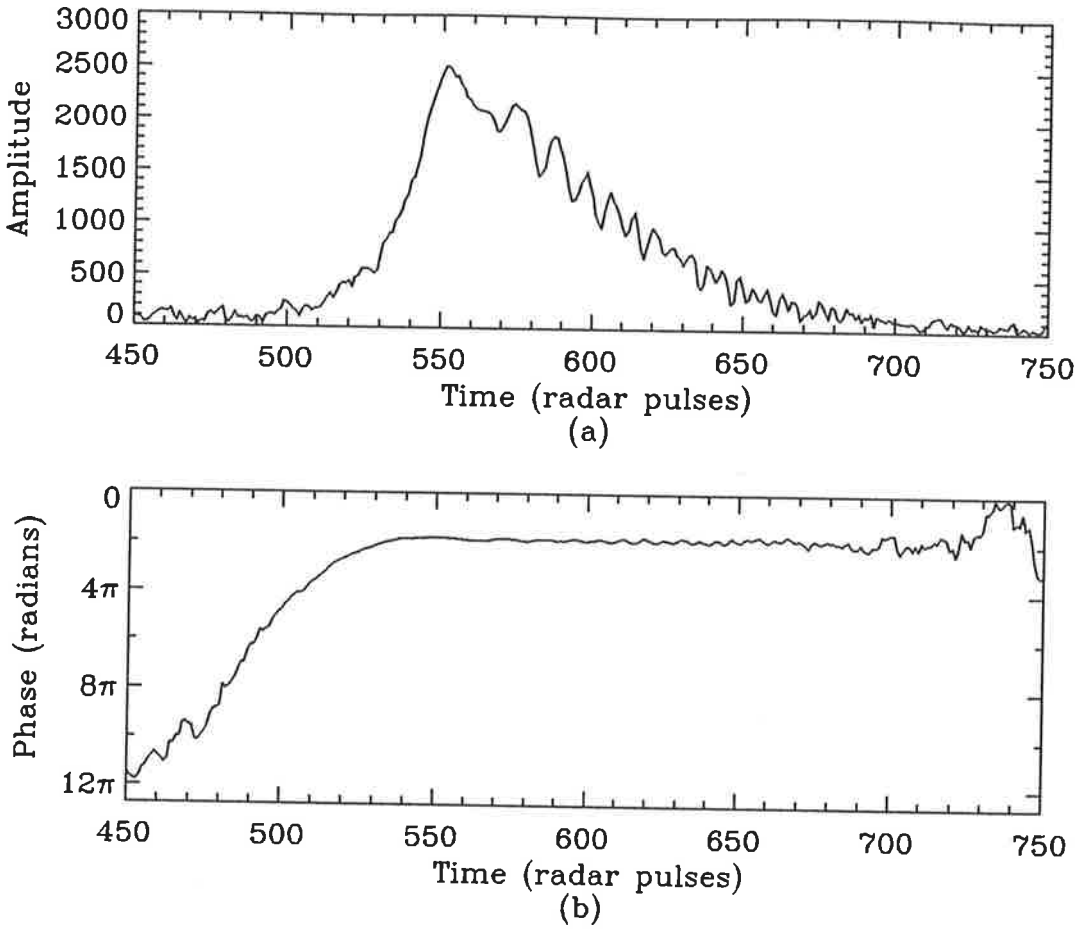

Figure 5.11: Meteor echo observed at 12:58 CST on 6 June 1994 with 2-point coherent smoothing applied. The 2π phase jump in the pre-t_0 phase information has disappeared and the post-t_0 amplitude oscillations are clearer.

A velocity of $23.6 \pm 0.1\, km\, s^{-1}$ is obtained from the fit, the error being only 0.4%.

The velocity of the echo displayed in Figure 5.11 can also be calculated from the post-t_0 amplitude oscillations. From the amplitude profile displayed in Figure 5.11a, some 19 oscillations may be observed. The time at which the maxima and minima are observed to occur are recorded. The first maximum is ignored as the amplitude at this point is at the level where the signal saturates in the receiver, causing distortion to the shape of the first Fresnel oscillation (see Chapter 3). Ignoring the first oscillation, some 35 data points are are available for an accurate determination of the velocity. From the application of Fresnel diffraction theory, the positions of the maxima and minima of the post-t_0 amplitude oscillations, in terms of the parameter x, may be found either by calculating the Fresnel integrals directly, or by applying the Cauchy approximations and calculating the positions analytically (see *eg.* Figure 5.2). The amplitude is related to the Fresnel integrals by $A^2 \propto C^2 + S^2$, therefore for

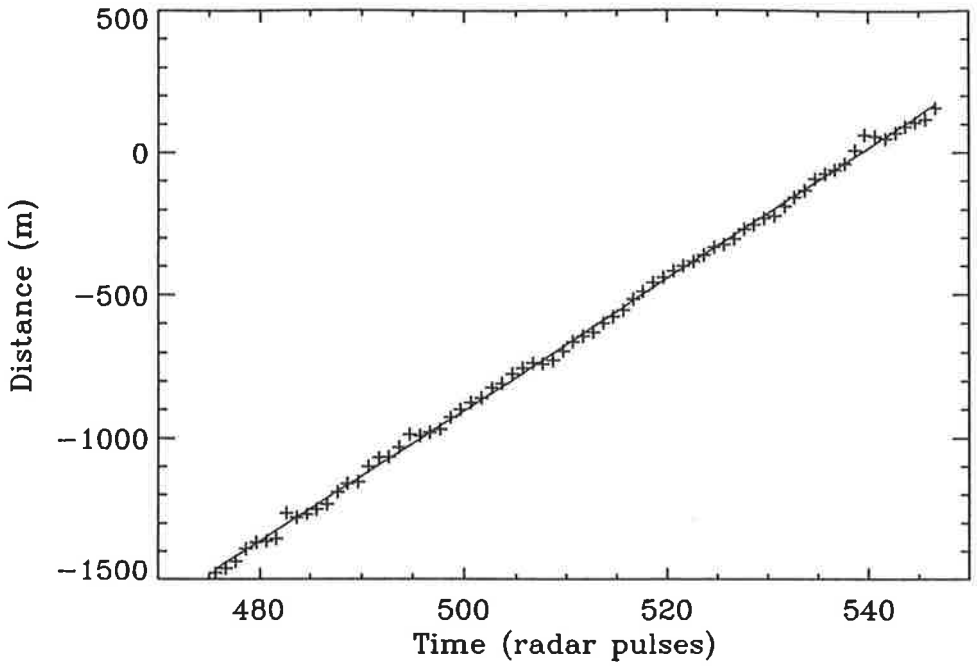

Figure 5.12: Distance-time profile obtained from the phase information (prior to the point of minimum phase) of the meteor echo displayed in Figure 5.10. The crosses are the distances calculated from measured phase and the model, the solid line is a linear least squares fit to the data. The meteor velocity is calculated to be $23.6 \pm 0.1\, km\, s^{-1}$.

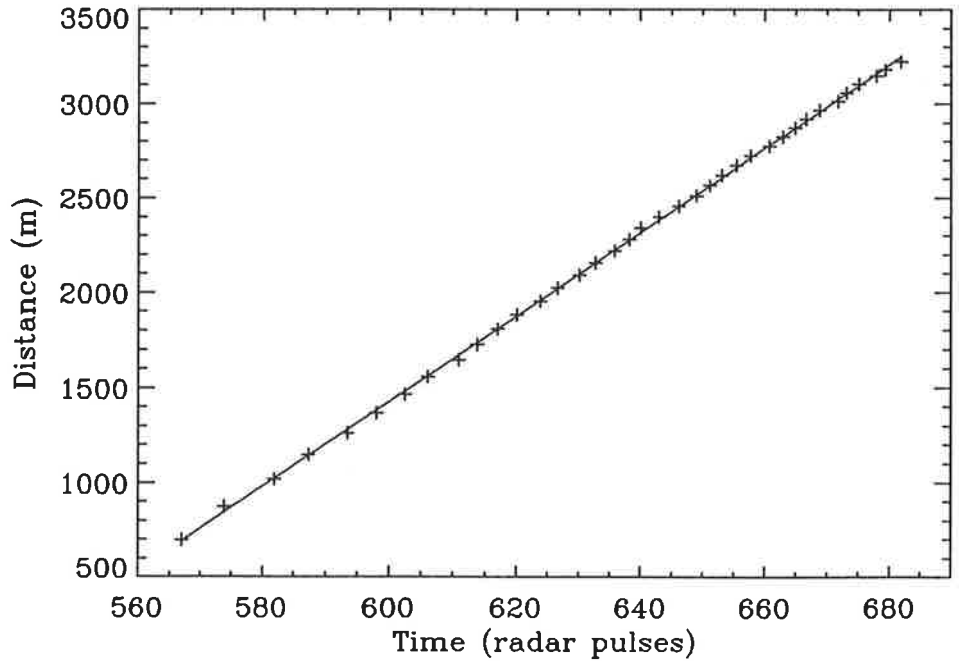

Figure 5.13: Distance-time profile obtained from the post-t_0 amplitude oscillations of the meteor echo displayed in Figure 5.10. The crosses are the distances calculated for the oscillation maxima and minima from Fresnel diffraction theory, the solid line is a linear least squares fit to the data. The meteor velocity is calculated to be $22.8 \pm 0.1\, km\, s^{-1}$.

$x > 1$, the Cauchy approximations (see Equation 5.12) give:

$$\begin{aligned} A^2 &\propto 1 + \frac{1}{2\pi^2 x^2} + \frac{1}{\pi x}\left(sin\left(\frac{\pi x^2}{2}\right) + cos\left(\frac{\pi x^2}{2}\right)\right) \\ &\propto 1 + \frac{1}{2\pi^2 x^2} + \frac{\sqrt{2}}{\pi x} sin\left(\frac{\pi x^2}{2} + \frac{\pi}{4}\right) . \end{aligned} \tag{5.17}$$

It is the oscillatory term which is of interest in this equation, differentiating this term with respect to x and equating to zero gives an expression for the positions of the maxima and minima. If x_m is the x value of the m^{th} turning point (*i.e.* maxima *or* minima) then it is simple to show that $x_m = \sqrt{2n - 0.5}$. This may be recast to give the following two equations for the positions of the maxima, x_{max}, and the positions of the minima, x_{min}:

$$x_{max} = \sqrt{4n - 3/2} \qquad \text{and} \qquad x_{min} = \sqrt{4n - 1/2}\,, \tag{5.18}$$

where n is an integer greater than zero and refers to the oscillation of interest. It should be noted that the position of the 1^{st} maxima given by the above equation differs by about 1% from that calculated directly from the Fresnel integrals ($x = 1.22$ as compared with $x = 1.21$). The error associated with subsequent oscillations decreases, the second maxima is out by 0.2%, the third by less than 0.01%. Thus Equations 5.18 gives the positions of the maxima and minima to a sufficiently high degree of accuracy for their use in the analysis of the post-t_0 data.

The distance along the trail from the t_0 point, for each maximum and minimum in the record, is calculated through the relation $2s = x\sqrt{R_0\lambda}$. These distances are then plotted against the time of occurrence of the minima and maxima of the post-t_0 amplitude oscillations. If deceleration is assumed to be zero, then the slope of the line found from a linear least squares fit to the data gives the velocity. This is shown in Figure 5.13 for the meteor echo displayed in Figure 5.11, the crosses are the data points and the solid line the linear least squares fit. A velocity of $22.8 \pm 0.1\, km\, s^{-1}$ is obtained. Again, the distance-time profile is linear to a high degree which suggests that the effect of meteor deceleration is not visible in the post-t_0 amplitude oscillations as for the case with the distance-time profile obtained from the pre-t_0 phase information. The post-t_0 velocity estimate of $22.8\, km\, s^{-1}$, is to be compared with the pre-t_0 value of $23.6\, km\, s^{-1}$ indicating a small degree of deceleration of about $7.8 \pm 0.2\, km\, s^{-2}$.

Consider now the echo displayed in Figure 5.14 which was observed at 12:14 CST on 6 June 1994, at a range of $112\, km$ (height of $97\, km$). This is an unusual echo in that the

amplitude profile (and indeed that of the phase) is not traditionally associated with that due to a meteor echo. Very little information may be obtained from the amplitude profile alone and in the past this sort of echo would have been discarded. However, through the analysis of the phase information, together with the amplitude, a wealth of information both about the echo and the radar system may be obtained. Both the amplitude and phase profiles are consistent with the target being a compact moving-ball target. The explanation of the phenomena is that, at the height where the trail formed, radial expansion of the ionization is so rapid that at the frequency used, the radar only "sees" the short segment of trail immediately subsequent to the ablating meteoroid (see Chapter 3). The first point to note is that the phase is parabolic about a point of symmetry which may be the t_0 point or alternatively a point further back on the trail where the Doppler frequency was an integer multiple of $1024\,Hz$, but the former is more likely. The velocity may be deduced by either applying the technique already discussed or by simply fitting a parabola to the phase record between times of 1425 and 1515 radar pulses. The former is a more precise method and gives a speed of $59.2 \pm 0.2\,km\,s^{-1}$. For times less than pulse 1425 and greater than 1515, the phase is changing so rapidly that it exceeds the Nyquist sampling frequency ($512\,Hz$) and has become aliased. Around the Nyquist frequency, the unwrapping algorithm clearly fails, but recovers when the Nyquist frequency has been sufficiently exceeded, and the phase again behaves smoothly. It is possible to de-alias the phase record in these regions, however the record is sufficiently long, that this is not required.

The second point of interest arising from Figure 5.14 is that the peak in the amplitude profile occurs at the same time as the t_0 point. This indicates that the path of the meteoroid is orthogonal to the direction of the beam's axis (assuming the ionization production is constant over this region). If the meteor's path was not orthogonal to the beam's axis, then the peak in the amplitude would occur earlier for radiant elevations which were larger than the off zenith angle of the beam's axis, and likewise later for radiant elevations smaller than the beam's off zenith angle. Measurement of the time difference together with the meteor's velocity would enable the angle that the path of the meteor makes with the beam's axis to be calculated.

Assuming that the rate of ionization production is approximately constant over the region where the echo is observed (reasonable as the amplitude profile shows high degree of symmetry about the t_0 point), the amplitude profile of the echo may be interpreted as the cross-section of the antenna beam radar pattern. Thus, the beam width of the antenna may

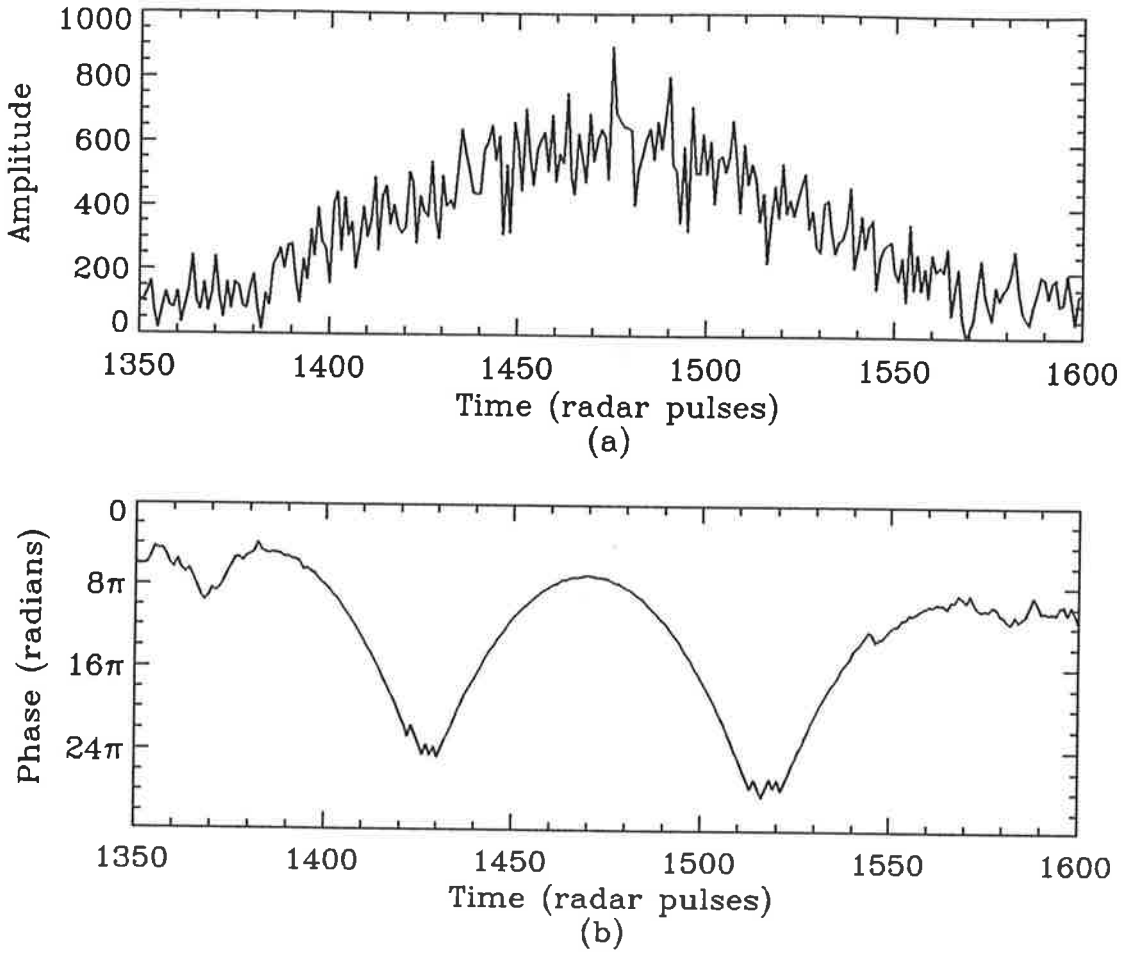

Figure 5.14: Example of a meteor echo displaying rapid diffusion of the trail. Note both the amplitude and phase are symmetric about the t_0 point which indicates (1) scattering from the trail only occurs from the short segment immediately prior to the ablating meteoroid and (2) the meteor's path is orthogonal to the axis of the beam. The velocity of the meteor may be obtained by either fitting a parabola to the phase or by the pre-t_0 phase technique and is found to be $59.5 \pm 0.2\, km\, s^{-1}$. Note the aliasing of the phase information for times less than 1425 pulses and 1515 pulses, this is due to the rate of change of phase exceeding the Nyquist sampling frequency ($512\, Hz$). The width of the beam may be obtained from the amplitude profile and the velocity and is found to be 3.4° (see text).

be found directly from measuring the time over which the amplitude is $1/\sqrt{2}$ times the peak value (the $3\, dB$ or half power points). This is found to be 96 ± 10 radar pulses, giving a half-power half-width of $1.4° \pm 0.2°$ for the two way antenna pattern (the pattern on reception and transmission) of the radar beam. In Chapter 2, a theoretical half-power half-width of 1.88° was calculated for a beam formed by the CoCo array, and tilted off vertical by 30°. This corresponds to a two way beam width of 1.35°. Thus the beam width as measured from Figure 5.14, compares very well with the beam width obtained from a theoretical model.

The last example of the application of the pre-t_0 phase technique for the reduction of

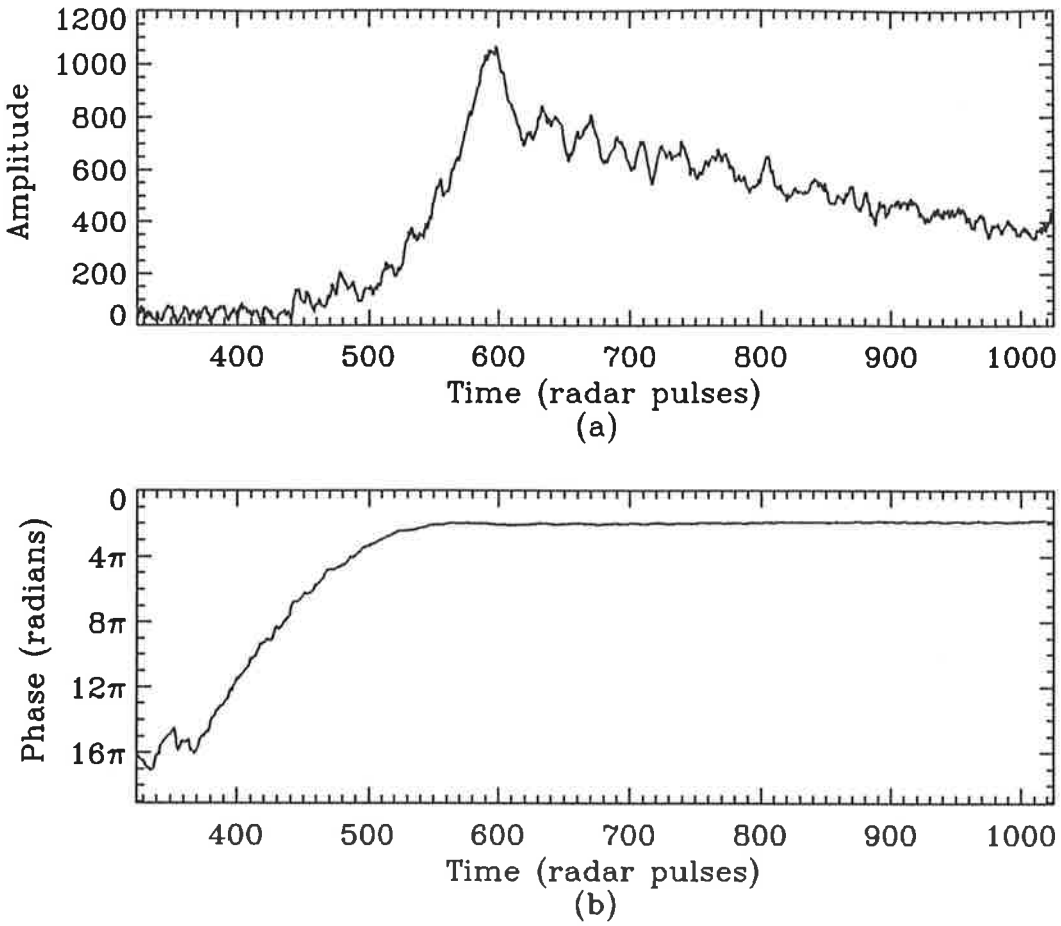

Figure 5.15: Slow meteor observed at 12:09 CST on 6 June 1994 at a range of 90 km (height of 78 km). The echo has been processed and 6-point coherent smoothing applied. The velocity was measured to be $10.20 \pm 0.05\, km\, s^{-1}$

meteor velocities is now considered. Figure 5.15 displays a meteor echo detected at 12:09 CST on 6 June 1994 at a range of 90 km (height of 78 km). The displayed echo has been processed and 6-point coherent smoothing applied. While there appears to be nothing unusual about this meteor echo, the measured velocity is $10.20 \pm 0.05\, km\, s^{-1}$, emphasising the fact that very slow meteors can be readily detected with the system. A velocity determination can also be made from the post-t_0 amplitude oscillations, that occur on average 174 ms after the pre-t_0 phase data. The result of $9.4\, km\, s^{-1}$ is consistent with a significant deceleration ($\sim 4.6\, km\, s^{-2}$). As the velocity is less than the escape velocity of the Earth ($11.2\, km\, s^{-1}$) the question is raised: was this echo due to a meteoroid or piece of ablating space debris?

Space debris is man made material in geocentric orbit. Re-entering space debris is therefore expected to have velocities less than the escape velocity of the Earth, and a trajectory close to the horizontal (*i.e.* low elevation) due to it spiraling into the Earth's atmosphere.

These two points implies that detection of space debris will be difficult as low velocity and small elevation reduce the electron line density of the trail. Also classical ablation theory shows that meteors with low velocities experience high decelerations. Therefore if a meteor is observed meeting the requirements of being consistent with ablating space debris, it still could be simply a heliocentric meteor with an encounter velocity just above the Earth's escape velocity, and which has decelerated to a velocity below this.

At present there is no reason to favour either possibility for the explanation of the record shown in Figure 5.15. However, it should be pointed out that at the observed deceleration of $4.6\,km\,s^{-2}$, the meteoroid speed $2.3\,km$ further back along its path would be $\sim 11.2\,km\,s^{-1}$, *i.e.* within the limit of a meteoroid encounter with the Earth. This suggests the explanation that the echo was caused by an ablating heliocentric meteoroid is perhaps more likely.

Clearly the identification of space debris will be difficult, however the meteor echo displayed in Figure 5.15 demonstrates that the radar is capable of measuring accurately the very slow velocities expected for space debris. The possibility of detecting space debris will be considered later in this chapter.

5.4 The Velocity and Mass Distributions of Sporadic Meteors

5.4.1 Velocity distribution

To examine the velocity and mass distributions of sporadic meteors, meteor data obtained from 12:00 CST 6 June 1994 to 12:00 CST 7 June 1994 were analysed. There was no evidence for any meteor shower during this period, and therefore all the data were assumed to be sporadic in origin. The distribution of the 586 measured velocities (about 75% of the total number of echoes observed) is shown in Figure 5.16. The observations have not been corrected for deceleration.

It is of interest to note that 41 meteors were found to have a measured velocity less than the escape velocity of the Earth. This represents 7.0% of the sample, and demonstrates that the radar is able to observe very slow meteors which are possibly caused by re-entering space debris as mentioned in section 5.3.4. However, the most interesting features of this distribution are that the proportions of meteors observed with high velocities (above $\sim 50\,km\,s^{-1}$) and low velocities (below $\sim 15\,km\,s^{-1}$), is greater than those observed by radars

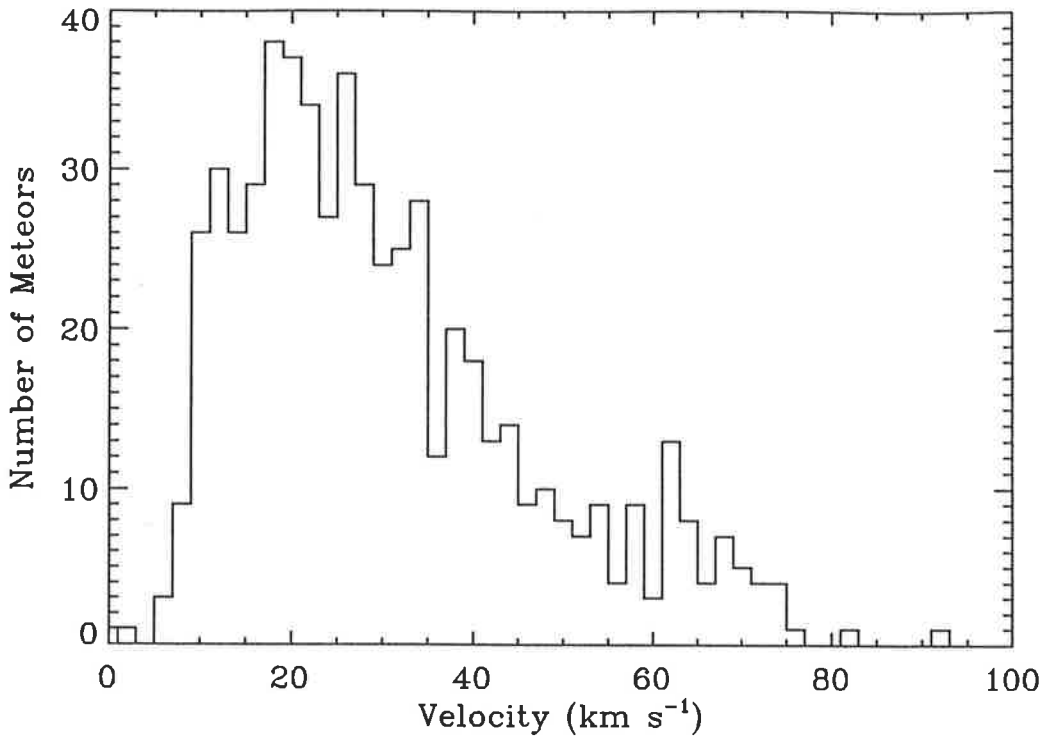

Figure 5.16: Velocity distribution for sporadic meteors observed from 12:00 CST 6 June 1994 to 12:00 CST 7 June 1994. The measured velocities were not corrected for deceleration, 586 meteors contribute.

in the past. Previous velocity measurements of high velocity meteors were difficult due to the reduction techniques being subject to large selection effects. High velocity meteors ablate at higher altitudes and thus experience greater diffusion which attenuates the post-t_0 amplitude oscillations used to calculate the velocity. In contrast, the pre-t_0 phase technique used to reduce the meteor velocities displayed in Figure 5.16 does not suffer from the effects of diffusion (as shown in the previous section), and thus this selection effect due to diffusion does not apply. It must be noted, however, diffusion causes general echo attenuation with increasing height which affects the detection of such meteors (the selection factors associated with this effect are discussed later in this section). The detection of slow meteors and the measurement of their velocities is readily achieved with this radar due to the greater sensitivity of the system (a result of the employment of a narrow beam), which allows the detection of the lower electron line densities produced by these meteoroids. Detection of these meteors with wide beam radar systems employed for meteor observations in the past, required transmitter powers of 100's of kilowatts and were only employed at a few locations (*e.g.* Ottawa, *McKinley*, 1953).

The fact that the new VHF system is able to readily measure high speed meteors is important for the study of hyperbolic meteoroids[4]. Inspection of Figure 5.16 shows that about 7 meteors ($\sim 1\%$) gave speeds greater than the escape velocity from the Solar system ($72\,km\,s^{-1}$), and the possibility is raised that these are interstellar in origin. Recent observations and studies of hyperbolic meteors have been undertaken by *Baggaley et. al.* (1993) and *Taylor et. al.* (1994) who found that data obtained with AMOR (*Baggaley et al.*, 1994) yielded about 1% of meteoroids with speeds in excess of $100\,km\,s^{-1}$.

It is of interest to obtain the velocity distribution of the observed sporadic meteors with the velocity corrected for deceleration (giving the initial or encounter velocity of the meteor). In the previous section, the possibility of measuring meteor decelerations was discussed: generally it was found that this was not feasible. Therefore another method for accounting for the meteor deceleration must be developed. The method used here is based on the classical ablation theory of meteors (described in Chapter 4) and only a brief discussion is given here. A fuller account may be found in Chapter 6 together with discussions on other methods used to account for the deceleration of shower meteors. The electron line density is first calculated from the mean noise and the maximum echo amplitude obtained from the meteor echo. This is then used with the measured velocity and the observed height of ablation to calculate the mass (at this height) from the ionization equation (see Equation 4.43). The drag and differential mass equations (Equations 4.39 and 4.41 respectively) are then integrated in height to obtain the initial velocity of the meteoroid. Note the meteoroid initial mass is also obtained from this calculation.

Figure 5.17 displays the velocity distribution of the observed meteors corrected for deceleration as calculated from the data displayed in Figure 5.16 using the method described above. The dashed line in Figure 5.17 represents a velocity of $11.2\,km\,s^{-1}$, the escape velocity from the Earth. The meteors appearing to the left of this line (25 or 4.3% in all) could be due re-entering space debris, although the failure to adequately account for deceleration is probably more likely. This will be discussed in the next section. The actual velocity distribution of particles encountered by the Earth may be obtained by correcting the velocity distribution displayed in Figure 5.17 for various meteor detection selection effects. The selection effects are caused by: (1) dependence of ionization production q, on the meteor velocity v, ($q \propto v^n$ where $n \sim 3.5-4$); (2) echo attenuation due to the initial trail radius and

[4]Hyperbolic meteoroids are those whose speed is greater than the escape velocity from the Solar system and are therefore assumed to be of interstellar origin.

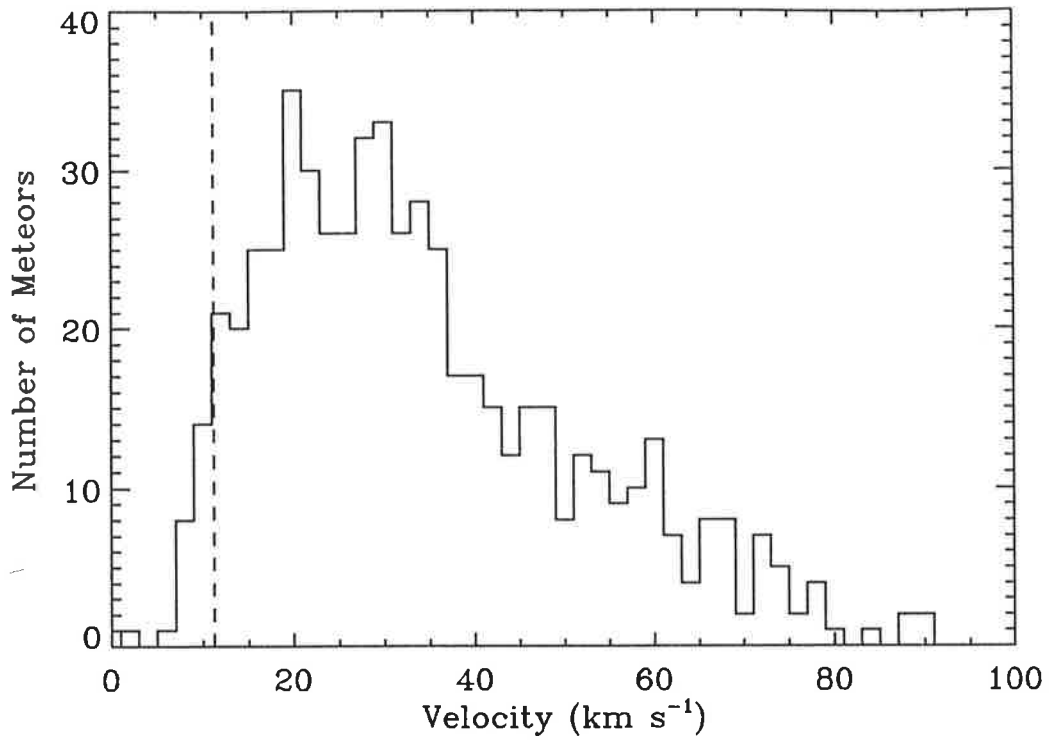

Figure 5.17: Velocity distribution for sporadic meteors observed from 12:00 CST 6 June 1994 to 12:00 CST 7 June 1994. The measured velocities were corrected for deceleration using classical ablation theory (see text), 586 meteors contribute.

diffusion of the trail during the finite time of formation; and (3) the meteor detection criteria. The first selection effect may be corrected for by applying a multiplicative correction factor to the velocity distribution of the form $1/v^n$. The other two selection effects are described in detail in Chapter 4. Briefly, the effect of the two echo attenuation factors (2) is to reduce the returned signal strength as the height of ablation and the velocity of the meteoroid increases, while the echo selection factor due to the detection criteria (3) is dependent only on the height of ablation and reduces the detectability of the echo as the height increases. Since meteors with larger velocities ablate at higher altitudes, the effect of (3) also causes a reduction in the number of high speed meteors observed. As factors associated with (2) and (3) are incorporated into the response function calculation (see Chapter 4), the response function itself may be employed to correct the observed velocity distribution. While this is probably the best approach, in practice this is not possible as convolution of the response function with the sporadic meteor radiant distribution is required, and the variation of the sporadic radiant distribution with velocity is not known. The result of correcting the velocity distribution for ionizing efficiency alone is shown in Figure 5.18 (thick solid line).

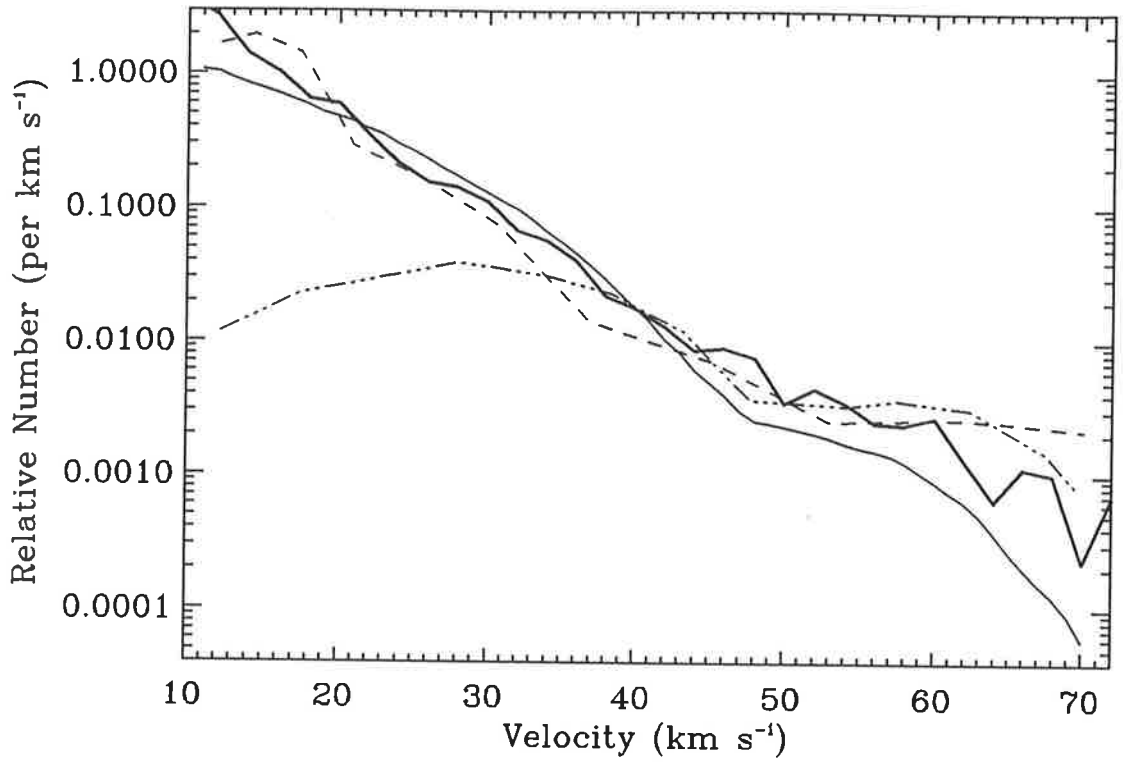

Figure 5.18: Comparison of corrected radio and optical velocity distributions. The thin solid line is the revised (*Taylor*, 1995) corrected distribution obtained from the Harvard Radio Meteor Project, the dashed line are the optical results, and the broken line the results obtained by *Nilsson* (1964) at Adelaide (after *Elford et al.*, 1995). Also displayed in this figure, is the corrected distribution obtained from the June 6-7 1994 data set observed by the Buckland Park VHF radar (thick solid line). See text for further details.

Elford et al. (1996) compared three corrected velocity distributions, two obtained by radio techniques and the third by optical means. In the case of the optical results, *Erikson* (1968) applied corrections to a random sample of 286 meteors from about 2500 collected by *McCrosky and Posen* (1961) during the Harvard Super-Schmidt campaigns; the correction used by *Erikson* was derived by *Jacchia et al.* (1965). The radio results were those of *Nilsson* (1962) obtained from his meteor orbit survey at Adelaide, and the Harvard Radio Meteor Project velocity distribution corrected by *Sekanina and Southworth* (1973); in both cases the velocity distributions were corrected according to v^4. The Harvard results shown by *Elford et al.* were in fact revised by them according to *Taylor* (1995, 1996) who pointed out that the correction factor applied by *Sekanina and Southworth* was not the value stated in their paper. The corrected distributions given in Figure 6 of *Elford et al.* are reproduced in Figure 5.18, where the thin solid line is the Harvard velocity distribution, the dashed line is

the optical result, and the broken line the results obtained by *Nilsson*.

Elford et al. in their comparison of the velocity distributions make the following observations. The Harvard Meteor Project optical and radar distributions agree to within a factor of ~ 2.5 for speeds from 20 to 55 $km\,s^{-1}$. However above 55 $km\,s^{-1}$ the radio distribution is significantly lower, and at 70 $km\,s^{-1}$ they differ by about 1.5 orders of magnitude. *Elford et al.* surmise that in view of the height distribution obtained by *Steel and Elford* (1991) with a radar operating at 2 MHz, the Harvard correction for the effect of diffusion is significantly underestimated. In contrast the results of *Nilsson* agree well with the optical results for velocities above 30 $km\,s^{-1}$, but differ by up to two orders of magnitude for low velocities. *Elford et al.* could find no reason why *Nilsson's* radio system or analysis techniques were biased against the measurement of the speed of slow meteors.

The Buckland Park VHF radar velocity distribution, in contrast to the other two radio distributions, agrees extremely well with the optical results over the entire velocity range below 60 $km\,s^{-1}$. Above 60 $km\,s^{-1}$, the Buckland Park results are lower then the optical results by about a factor of 4, but this is still a much better agreement than that shown by the Harvard results. Further, it should be noted that the biases against the high velocity meteors caused by the attenuation factors and the echo detection criteria have not been taken into account in the Buckland Park velocity distribution. Once the appropriate correction factors are derived and then applied to the data, it is expected that the agreement with the optical results above 60 $km\,s^{-1}$ will be significantly better. One further point to note is that the Harvard results are significantly lower than the optical results for slow meteors (velocities less than about 20 $km\,s^{-1}$). This is not the case for the Buckland Park velocity distribution which is an indication of the greater sensitivity of this radar to the generally weaker echoes produced by slow meteors.

5.4.2 Mass distribution

Figure 5.19 displays the cumulative mass distribution observed by the Buckland Park VHF radar (solid line) for 24 hours of data, 6-7 June 1994. The process used to derive the meteoroid mass is identical to that used to obtain the initial velocity described in the previous section. Also shown in this figure are the modelled mass distributions using the response function for mass indices of -0.7 (dotted), -0.9 (dashed), and -1.1 (broken). The modelled distributions were found by calculating the response function using appropriate assumed mass indices, and then convolving the response function with the sporadic radiant distribution at

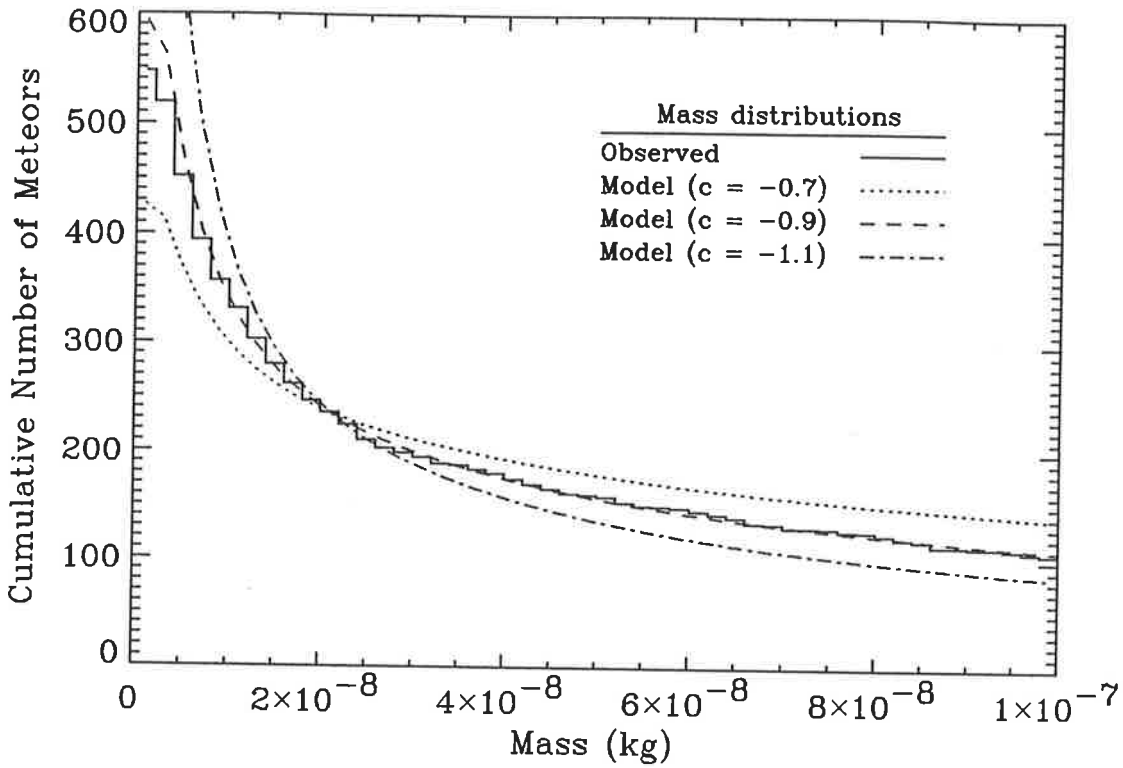

Figure 5.19: The observed cumulative mass distribution of 586 sporadic meteors from 6-7 June 1994 (solid line). The dotted, dashed and broken lines are modelled mass distributions using the response function for cumulative mass indices of -0.7, -0.9, and -1.1 respectively.

the time and date of the observations (see Chapter 3). For each case, the number of meteors above a given mass which were expected to be detected, were binned and thus the model cumulative mass distribution was found for the assumed cumulative mass index. The model mass distribution using a value for c of -0.9 represents the best fit to the observed cumulative mass distribution. Thus in the mass range where the Buckland Park VHF radar observes meteors (10^{-9}–$10^{-7}\,kg$), the cumulative mass index is -0.9.

5.5 On the Detection of Space Debris

Space debris (artificial man-made waste material in geocentric orbit) is fast becoming an important consideration in space research, especially so with the placement of satellites in Earth orbit and the launch of manned space craft. With this in mind it is necessary to learn as much about space debris as possible, and one method of doing this is with meteor radars. To date, space debris has been mainly studied through the use of impact sensors carried by satellites in Earth orbit (see *e.g. Laurance and Brownlee*). While these techniques have

been successful, *Olsson-Steel and Elford* (199?) note that they have the following drawbacks: (1) lack of temporal resolution, (2) lack of trajectory information, and (3) the inability to detect a statistically large sample of larger particles due to the small area the detector. With this in mind, *Olsson-Steel and Elford* discuss the possibility of the use of meteor radars to study space debris; and in Section 5.3 the possibility of the detection of space debris with the Buckland park VHF radar was raised. This will now be discussed in detail, taking advantage of the response function, developed in Chapter 4.

The assumption is made that most space debris re-entering the Earth's atmosphere does so because of the degeneration of their orbits (*i.e.* they spiral in), and thus it is expected their radiants will appear low on the horizon. This constitutes a problem as meteors with radiants at low elevations are much harder to detect than meteors with associated high elevation radiants (see Chapter 4) and this will be considered in detail shortly.

The speed at which space debris enters the Earth's atmosphere must be less than the escape velocity ($11\,km\,s^{-1}$) as re-entering space debris originates from bound geocentric orbits. The slow speed of the re-entering space debris could constitute a problem as the ionization produced would be much less than for meteoroids originating from heliocentric orbits (typical speeds[5] of 15–40 $km\,s^{-1}$). However, Figure 5.15 and the associated discussion clearly demonstrated that the detection of very slow meteors and the measurements of their speeds with the Buckland Park VHF is not a problem.

Figure 5.20 displays the geometry of the extreme positions of radiants available for observation with a narrow beam radar tilted off-zenith by an angle χ_0 Eastwards. The angle, χ, which the radiant makes with the zenith differs from χ_0 by a small amount (less than 2%) due to the curvature of the Earth. The relation between χ and χ_0 is given by Equation 4.11. The two radiants, "a" and "b", lie in the echo plane of the beam, and represent the maximum "a" and minimum "b" radiant elevation angles which may be observed. Radiant "a" lies in the plane of tilt of the beam (*i.e.* the East-West plane in this case), while radiant "b" lies in the orthogonal plane (*i.e.* North-South). Consideration of this figure reveals that the beam tilt usually employed for meteor observations with the Buckland Park VHF radar (*i.e.* beam tilt 30° off-zenith) may not be appropriate for the detection of space debris. While space debris with radiants close to the North and South cardinal directions would be detectable, those close in azimuth to the East-West plane would not as the off zenith beam tilt is probably too large. With this in mind, a smaller off zenith beam tilt (say 4° or 7°)

[5]These are the speeds of radar meteors. Figure 5.18 indicates that the most probable speed is 15–20 $km\,s^{-1}$.

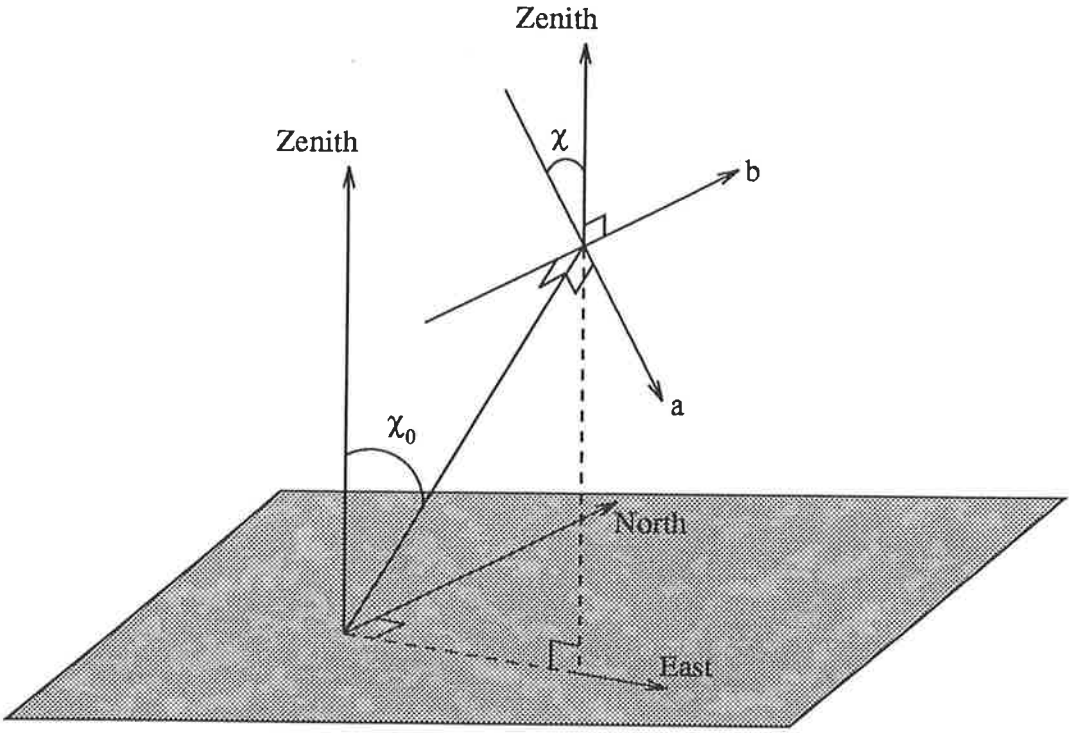

Figure 5.20: Geometry of radiants which may be observed with a narrow beam radar. The beam axis is directed Eastwards at an angle χ_0 off zenith. The two radiants (denoted by "a" and "b") are two possible radiants which may be observed with the radar. Radiant "a" has the maximum possible elevation angle for detection, and lies in the plane of tilt of the beam. Radiant "b" has an elevation angle of zero degrees and lies in the plane orthogonal to the plane of tilt of the beam.

would be more appropriate, although one must carefully consider the effect of the increased sidelobe response at these angles (see Chapter 4).

Although the usual beam geometry used for usual meteor observations is perhaps not ideal for the observation of space debris, in the previous section it was seen that 41 meteors (or 7.0%) had velocities less than the escape velocity of the Earth. After deceleration was accounted for, this was reduced to twenty-five meteors (or 4.3%). There are two possibilities which could account for these meteors: (1) they are caused by re-entering space debris, or (2) they are heliocentric in origin and their deceleration has been incorrectly accounted for. Currently neither of the the two possibilities is preferred. If observations were made with a smaller off-zenith beam tilt, and a larger number of meteors was observed with velocities less than $11.2\,km\,s^{-1}$, then the first hypothesis (*i.e.* space debris) would be strongly favoured. However, if about the same number of slow meteors were observed then the second hypothesis must be favoured. Clearly, in order to answer the question of whether space debris may be observed with radar, meteor observations at smaller off zenith angles must be made. In order

to interpret these observations, the response function must be examined.

Figure 5.21 (essentially a repeat of Figure 4.7) displays, in panels (a) to (d), slices through the response function at an azimuth of 266° for the Buckland Park VHF radar with the beam tilted 4°, 7°, 11° and 30° off zenith Eastwards (az.=86°). These beam tilts were chosen as they are readily available with the present system; other beam tilts may be used if the appropriate phasing cables are produced. The response function in each of these plots has been normalised to their respective peak response. One immediately sees from these plots that as the beam approaches the zenith, the sidelobe response increases dramatically. This is of course due to the increased response to radiants from greater elevations (for a full discussion see Chapter 4). In Figure 5.21e, the response functions have been integrated over the sky to give the total response, and plotted against the beam off zenith angle. Figure 5.21f displays the total response of the main beam as a percentage of the total (*i.e.* sidelobes included) as a function of the beam off zenith angle. These two figures clearly demonstrate the decreased response and greater sidelobe contributions for beams with small off zenith angles.

While the application of Figure 5.21 to the interpretation of the observation of meteors originating from heliocentric orbits is appropriate, caution must be exercised when space debris is considered. The reason for this is that the mass distribution of space debris is unknown, the response function calculations displayed in Figure 5.21 assume a mass index appropriate for heliocentric meteoroids (*i.e.* $c = -1$), and this is not necessarily expected to be applicable to space debris. Although the mass index used in the 'debris' response function calculations may not be appropriate, the two general points regarding lower response and greater sidelobe contributions with smaller off zenith beam tilts, still apply. If the assumption that most space debris have low radiant elevations is correct, these two points will not be an issue for space debris. One would expect that if space debris was indeed detectable then the observed number of meteors with velocities less than the Earth's escape velocity would increase, while the number of meteors with velocities exceeding this limit would decrease as the beam approached the zenith.

Clearly from the preceding discussion, the possibility of the detection of space debris may be confirmed or denied from meteor observations with smaller beam tilts. In fact observations from a range of off zenith beam tilts would be appropriate. Several days of observations would be required in each case so as to give acceptable statistics, but observations for longer than a week would not be necessary for initial confirmation. Due to the small numbers of

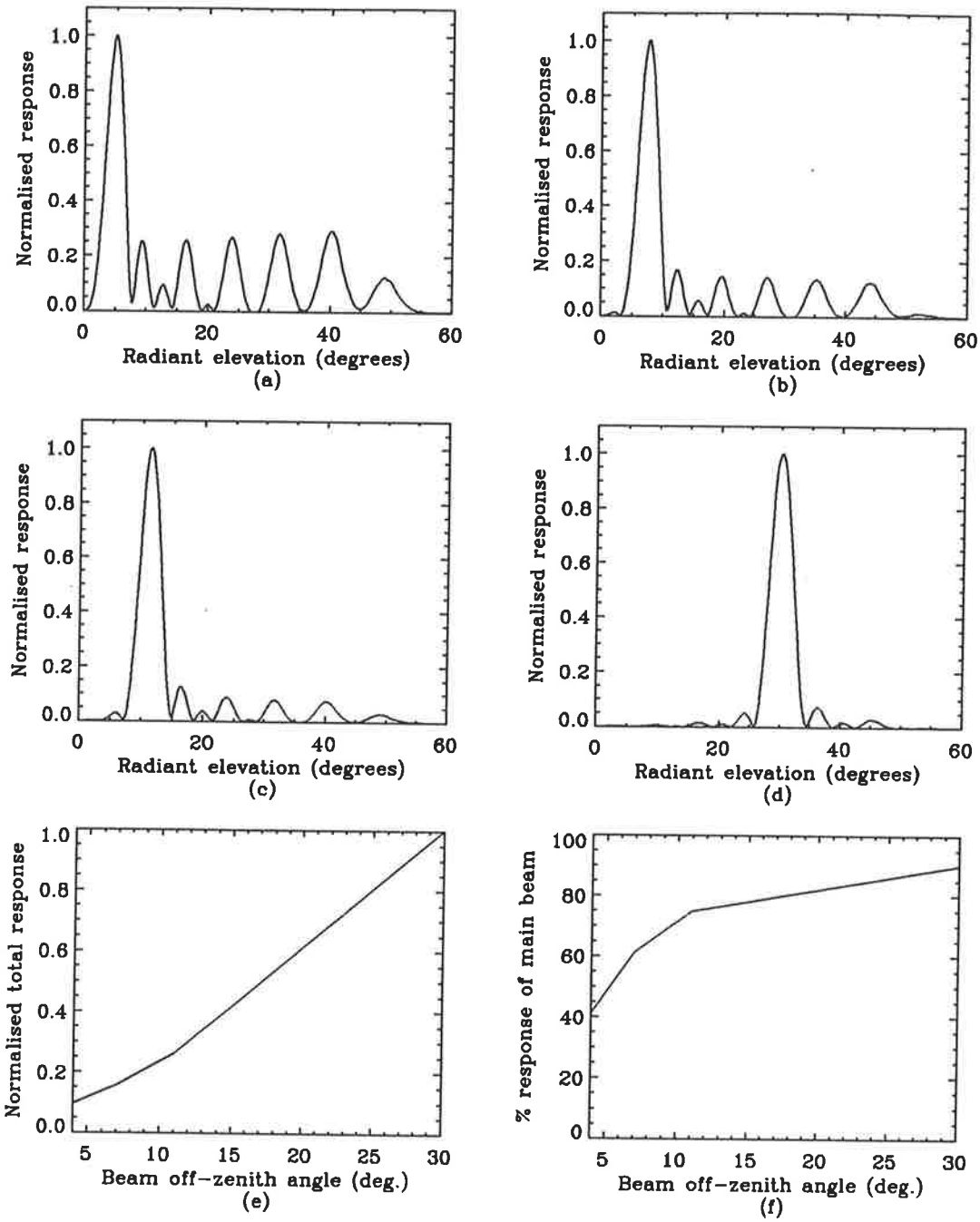

Figure 5.21: Response function of the Buckland Park VHF radar (at an azimuth of 266°) for off zenith beam angles of 4°, 7°, 11° and 30° (panels (a) to (d) respectively), in each case the beam is tilted East (az.=86°). The total response (response integrated over the sky) as a function of off zenith angle beam tilt is shown in panel (e), and the response of the main beam as a percentage of the total for various beam tilts is shown in panel (f).

space debris which are expected to be detected, no other useful information from the initial observations would be expected to be found. However, once the initial confirmation had been made, and the most appropriate off zenith beam tilt established, long term observations would enable the mass distribution of space debris to be found. This would enable the response function of the radar to space debris to be calculated fully, and the thus total mass influx of space debris to be determined. Unfortunately, the trajectory of re-entering space debris would not be able to be computed from observations with the radar, thus no information on how the space debris is distributed in orbit around the Earth may be obtained. This would require observations with a multi-station meteor orbit radar that was capable of detecting space debris. Preliminary observations with the Buckland Park VHF radar would suggest the design for such a radar system.

5.6 Conclusion

In this chapter a new robust method of reducing meteor velocities, namely the pre-t_0 phase technique, was developed. The technique is essentially a diffraction technique, but unlike previous diffraction methods which rely on the post-t_0 amplitude information, it has been shown that the phase technique does not suffer from the selection effects due to the rapid diffusion of meteor trails at large heights. As a consequence, some 75% of all observed meteors were able to have a velocity determined for them (*c.f.* about 10% with diffraction methods employing the post-t_0 amplitude information) with a very high degree of accuracy. Determination of meteor decelerations was not possible with the pre-t_0 phase technique, the information available from the meteor echoes not being available for sufficient duration for this to be realised. However, when the speed was able to be determined from the post-t_0 amplitude oscillations as well the pre-t_0 phase data, estimates of the deceleration were possible. The observation and determination of velocities for slow meteors was shown to be possible with the Buckland Park VHF and the employment of the pre-t_0 phase technique. This is the minimum requirement for the detection of space debris, if it is indeed possible, and thus the question as to whether this can be achieved was raised.

The velocity distribution of the sporadic meteors was obtained from a single day of meteor data collected during June 1994. Nearly 600 meteors contributed to this distribution. Deceleration of the meteors was accounted for through the use of classical ablation theory. This is dependent on assumptions of the physical properties of the meteoroids; however,

a better solution to the problem was not available. Once deceleration was accounted for, about 4% of meteors had velocities less than the escape velocity of the Earth. It was shown that these meteors could be due to re-entering space debris, although it is quite likely that these low velocities could be a result of inadequately accounting for the meteor deceleration. Further observations using smaller off zenith beam tilts would be required to resolve this question.

There was no solid evidence with the sample of meteor velocities examined, for meteors originating from hyperbolic orbits. Whether the study of hyperbolic meteors is feasible with the Buckland Park VHF radar will require further observations using a much larger sample (say 10,000 echoes). However, it should be noted that most meteors with speeds of the order of $70\,km\,s^{-1}$ are likely to occur at heights of about 110–120 km to which the VHF system is very insensitive. The observed velocity distribution corrected for various velocity selection effects was compared with the Harvard radio and optical distributions. It was found that the velocity distribution obtained by the VHF radar agreed very well with the Harvard optical distribution over all velocities. In contrast, the Harvard radio results disagreed with the optical results for velocities over $55\,km\,s^{-1}$ even after the revised correction (*Taylor*, 1995, 1996) was applied (*Elford et al.*, 1996). The disagreement has been attributed to an underestimation of the effects of diffusion in the correction of the Harvard radio results (*Elford et al.*, 1996).

The cumulative mass distribution of sporadic meteors observed by the radar was obtained from the data set for which the velocities were determined. The response function of the radar was employed to model the cumulative mass distribution for various mass indices and it was found that a cumulative mass index of $c = -0.9$ gave the best fit to the observations. The mass range for which this index applies is $10^{-9} - 10^{-7}\,kg$. Previous radio results give a value of about -1.0 (see *e.g. Thomas et al.*, 1988, whose results apply over a mass range from 2×10^{-10} to $8 \times 10^{-7}\,kg$).

The velocity determination of meteors originating from known showers was not discussed in this chapter. Such observations offer an additional check on the validity of the pre-t_0 technique to measure meteor velocities. In particular observations of the θ-Ophiuchids meteor shower together with velocity measurements of the detected meteors using pre-t_0 technique are presented in Chapter 6, where it is shown that the measurement of the velocity of the θ-Ophiuchid meteoroid stream agrees well with previous measurements.

Chapter 6

Meteor Shower Observations with the Buckland Park VHF Radar

So how will the slips be lining up in the field?

—Reporter's question to G. Gooch at a pre match conference

Next to the wicket keeper I expect.

—Reply by G. Gooch

6.1 Survey of Radar Techniques Used to Observe Meteor Showers

6.1.1 Introduction

Following the end of World War II, the study of meteoric phenomena using radar techniques increased dramatically. This was due, mainly, to the availability of a large number of radar installations which had previously been operated for military purposes (see *eg. Hey & Stewart*, 1947; and *Eastwood & Mercer*, 1948). One of the major thrusts of this research was the study of meteor showers. Such meteors appear as bursts of meteor activity originating from a common radiant and are produced by meteoroids with almost the same heliocentric orbits ablating in the Earth's atmosphere. When the Earth crosses the orbit of such a stream of particles, an increase in the meteor occurrence rate from that radiant direction is observed. Meteor showers may last for only a few days, *eg.* the Quadrantids which peak on January 3^{rd}, or up to a month, *eg.* the Perseids which occur during the period July 23^{rd} to August

23^{rd}, and which peak on August 12^{th}, (see *eg. Cook*, 1973). The time of passage of the shower is of course shifted sidereally on each subsequent day.

Some meteor showers are associated with the orbits of known comets. The first such association was of the Perseids meteoroid stream with the comet *Swift-Tuttle* 1862 III by *Schiaparelli*, (1866). Other well known associations are the Southern and Northern Taurids with comet *Encke* 1954 IX, the η-Aquarids and Orionids with comet *Halley*, the Giacobinids with comet *Giacobini-Zinner* 1946 V and the Leonids meteor stream with comet *Tempel* 1866 I. The latter two meteoroid streams have produced spectacular showers in the past. The Leonid "meteor storm" in 1833 initiated the science of meteor studies. The shower reappeared in 1866 with fair strength but has failed to reappear since then with any significant intensity due to perturbation of it's orbit by Jupiter. The Giacobinids which appeared spectacularly in 1933, reappeared in 1946 when a large number of ex-military radars in both North America and England together with other research installations were used by radio scientists to study the event (see *eg. McKinley*, 1961).

A wide range of different radar techniques have been used to study meteor showers. These include pulse and continuous wave (CW), wide aperture and narrow beam, single and multiple stations. The early work of *Clegg* (1948) using a single station pulsed radar determined activity and radiant positions. A statistical method is required to detect and study meteor showers with single station radars; for example *Clegg* developed the range-time envelope technique. The measurement of the speed of evaporating meteoroids exploited the range change of a moving target transverse to the beam (*Hey et al.*, 1947) or the Fresnel diffraction features of the early part of the echo (*Ellyet and Davies*, 1948). With CW systems the Fresnel characteristics of the pre-t_0 echo region could also be explored for velocity measurements (see *eg. McKinley*, 1961). Multistation systems enable the radiant coordinates of any meteoroid to be determined from individual meteor trails, and together with the measurement of the meteoroid velocity, enable their orbital elements to be determined. However, the cost and complexity of multistation systems have restricted their installation and lifetime.

6.1.2 Range-Time envelope techniques

Clegg, (1948), first showed how meteor shower radiants may be determined with a single station monostatic narrow beam system when the polar diagram of the antenna is accurately known. The method assumed that all echoes were detected under the condition of specular

reflection, and that shower meteor echoes occur within a limited range of heights. Given a certain minimum sensitivity level, *Clegg* was able to calculate the temporal variation of the maximum and minimum ranges associated with a given radiant. Thus a range-time envelope was calculated for a given radiant, within which meteor echoes associated with that radiant must occur. To enable the declination of a shower to be accurately determined by this method, the azimuth of the radar beam was required to be changed from day to day. Thus *Clegg* was only able to study meteor showers lasting several days. Under the most favourable conditions, the shower radiants were able to be determined to within 1°; however accuracies of 2° and 3° in the right-ascension and declination of the shower radiants were more common.

In order that showers could be identified from a single day's data *Aspinall et al.* (1951) extended *Clegg's* method to two fixed independent antennas directed at azimuthal bearings of 242° and 292° resectively. Pulses from the transmitter were simultaneously radiated by both antennas and range-time data recorded separately on reception. For a particular radiant, the range-time envelopes calculated for each antenna are temporally shifted (due to the antennas directed at different azimuths), enabling the coordinates of a meteor shower radiant to be unambiguously determined. For high echo rate data (greater than 50 an hour) *Keay*, (1957), extended *Clegg's* method of analysis producing rate curves for a narrow range band centred on the most probable range, and these are generally referred to as partial rate curves. Due to meteor shower echoes occurring in a limited height range, the restriction on the range from which meteor echoes are selected is equivalent to a reduction of the beam-width in the vertical plane for meteors associated with a given shower.

For over two decades the range-time envelope technique was the prime single station method for studying meteor showers and the method has been used extensively by various researchers (see *eg. Hawkins and Almond*, 1952; *Weiss*, 1955, 1957a, 1960; *McKinley*, 1961; *Belkovič and Pupyšev*, 1968 and *Hughes, 1972*). *Belkovič and Pupyšev*, (1968) attempted to improve upon the method of *Clegg* by using a radar with a rotating antenna (30° step in azimuth every 5 min.) to scan a large area of the celestial sphere. The main motivation of their work was to measure the mass index over the celestial sphere. While the technique was successful for studying sporadic meteor mass indices, the low meteor echo rates, coupled together with 15 day averaging of the data, rendered even the major meteor showers undetectable.

The range-time envelope technique suffers from the drawback that weak showers are

difficult to differentiate from the background sporadic meteors. Until recently, this method has been the only one available to the reduction of meteor echo data from single station monostatic radars. *Cervera et al.* (1993) and *Elford et al.* (1994) describe a technique where the radar response function is employed to study meteor showers with single station radars (discussed in Section 6.2). They show that this technique may be used to study weak meteor showers also.

6.1.3 The shower imaging technique

In the early 1980's, *Morton and Jones* (1982) developed a new technique of determining meteor shower radiants. Their system was based on ideas presented earlier by *Elford* (*Weiss*, 1955) and later by *Jones* (1977) and *Jones and Morton* (1977) for shower detection by single station monostatic radars. Meteors are observed with a set of at least three closely spaced antennas. By comparing the phase information of a meteor echo from the antennas, the position of the meteor may be determined. Of course the orientation of the meteor trail and hence the radiant is unknown, however by applying the condition of specular backscatter, the plane in which the radiant lies is determined. The difference between this method and that of *Clegg* is that with the *Morton and Jones* method the plane within which the radiant lies is accurately determined. Also, detailed knowledge of the radar antenna pattern is not required. *Morton and Jones* applied this technique to a continuous wave bistatic radar, where the receiver and transmitter were separated by about $38\,km$. The separation of the receiver and transmitter changed the geometry of the situation which was accounted for in the analysis. The theory of *Kaiser*, (1960), was then applied by *Morton and Jones* (using a cumulative mass flux index of $c = -1$) to obtain the activity of particular radiants as a function of the time of transit. This, together with their observations of meteor showers, enabled high resolution contour maps (better than 1°) of the shower radiant to be produced. Thus, meteor showers were able to be "imaged" with this system and the system was therefore referred to as an imaging meteor radar system. These types of studies of the structure of meteor shower radiants were not possible in the past, either with the monostatic systems based on the method of *Clegg*, or the multistation systems described later in this section (although multistation systems have other advantages such as orbit determinations for single meteors). The system developed by *Morton and Jones* also had the advantage that weak shower radiants could be determined monostatically, in contrast to the systems based on *Clegg's* method which require the radiant source to contribute significantly to the total

count rate if satisfactory results are to be obtained.

The imaging meteor radar system developed by *Morton and Jones* was used to study the structure of the Geminid meteor shower (see *Morton and Jones*, (1982) and *Jones and Morton*, 1982) and the Orionid meteor shower (see *Morton and Jones*, 1982) in high detail. The resolution of the contour maps of the Geminids was 0.6°. Other measurements of the Orionids with this system include the variation of the radiant activity with solar longitude, the motion of the radiant, the absolute particle flux and the mass distribution of the particles in the stream (see *Jones*, 1983). However, the system developed by *Morton and Jones* also produced spurious elongation of prominent features in the radiant maps. *Morton and Jones* refer to the elongation of these features as "astigmatism", and attributed it to the use of a narrow beam transmitter system (see *Morton and Jones*, 1982) for further details). It was shown by *Poole and Roux*, (1989), that these astigmatic distortions in the radiant map may be reduced by using an all sky radar instead of a narrow beam system. *Poole and Roux* observed and produced radiant maps for five showers: the Arietids, the η-Aquarids, the Orionids, the δ-Aquarids and the Geminids at a resolution limit of about 2°. Although *Poole and Roux* have improved the technique developed by *Morton and Jones*, they still report some evidence of astigmatic distortions in their radiant maps, the form of the astigmatism depending markedly on the radiant declination. They also report that the low level contours should not be interpreted as a reliable indicator of background sporadic meteor activity. This could only be achieved by the improvement of the computational algorithms.

6.1.4 Multistation radar systems

Multistation systems have been widely used in the past to determine meteor orbits. Most of these systems were based on the pioneering work of *Gill and Davies* (1956) and *Davies and Gill* (1960) which, according to *Hawkins* (1964), was based on an idea proposed by *Kaiser*. The system developed by *Gill and Davies* at Jodrell Bank used a transmitter and one receiver at the main site with, remote receiving sites located 3.5 km South and East of the main site. Signals received at the remote sites were amplified, and sent to the main site on HF links. At the main site, the echoes were displayed on cathode ray oscilloscopes and recorded on film. Velocities were measured from the Fresnel oscillations of the echoes, which *Gill and Davies* reported to be accurate to within 2 $km\,s^{-1}$. The path of the meteoroid was then computed from the measured time delays of the echo occurring at each receiving site; the accuracy of the associated radiant position was about 3°. The meteoroid orbit was computed according

to the method described by *Porter* (1952), and included an estimation of the deceleration of the meteoroid in the atmosphere. Other researchers who have used similar systems include: *Nilsson*, (1964a and 1964b); *Kascheyev and Lebedinets*, (1967); *Andrianov et al.*, (1970); *Cook et al.*, (1972); and *Gartrell and Elford*, (1975). The most comprehensive study was undertaken by the Harvard Radio Meteor Group (*e.g. Cook et al.*, 1972; *Sekanina*, 1976).

The chief limitation of multistation systems, described above, is that the technique can only be applied to the relatively small fraction of echoes where the Fresnel oscillations are evident and well defined. For example, *Davies and Gill* (1960) found that velocities could be determined from only 10% of all echoes observed. Some improvement is possible by using spaced CW systems where the sky-wave and ground-wave signals generate Fresnel oscillations prior to the t_0 point (McKinley, 1961). Such systems were used by *Nilsson* (1964a) and *Gartrell and Elford* (1975).

Baggeley et al. (1994) improved significantly upon the method of determining meteor orbits with their Advanced Meteor Orbit Radar Facility (AMOR). AMOR employs fan beams, narrow in azimuth, for transmission and reception. The azimuthal half-power beam-widths are 3.5°; the half-power beam-widths in elevation are 20.7° for the transmitting antenna and 26.7° for the receiving antennas. The transmitting and receiving beams are directed at an azimuth of 180° and have their maximum gains at elevations of 22.9° and 24.6° respectively. The azimuth of the observed meteor echoes are defined by the fan beam, while the elevation of the echo is determined from the phase comparison of signals received by a pair of antennas separated by 5 wavelengths in the North/South, direction. *Baggeley et al.* show that if the position of the echo is known, the velocity of the meteoroid and it's radiant may be determined from the measured time delays between commencement of the echo at each observing site alone. While Fresnel oscillations are not require in order to determine the velocity, they can be used when available to verify the technique. For these special situations, the derived Fresnel velocities were also used, together with the velocity as measured from the echo commencement times, to obtain deceleration of these meteoroids. The measured decelerations were then applied to the bulk of the echoes which did not display Fresnel oscillations and thus a "no-atmosphere" velocity determination made for each observation. The advantage of AMOR is that all meteor echoes observed may have their orbits determined, not just the relatively few showing Fresnel oscillations.

The advantage of multistation systems over single station monostatic systems is, of course, that they are able to measure the velocities and radiants, and hence make possible

the computation of the orbits for individual meteoroids. However, due to the requirement of at least three receivers situated several kilometers apart, multistation systems are much more expensive to build and maintain, and more difficult to run than single station systems.

6.2 Meteor Shower Radiant Determination with the Buckland Park VHF radar

6.2.1 Introduction

The procedure used to determine meteor shower radiants from meteor observations with the Buckland Park VHF radar makes use of the meteor radar response function. Although the theory of the meteor radar response function is not new (first fully formulated by *Elford*, 1964) the application of the response function of a single station radar for meteor shower determination has only been developed recently. This technique was first used by *Cervera et al.* (1993) and *Elford et al.* (1994) to identify the June Librids in 1992, the first time this shower had been identified using radar.

6.2.2 The expected rate response of meteor showers observed by the Buckland Park VHF radar

Figure 6.1 shows a contour plot the response function of the VHF radar for a beam tilted Eastward (az. 86°), 30° off vertical. The calculation of the response was performed at a meteoroid velocity of $30\,km\,s^{-1}$, and was normalised to its peak value. The contours are at levels of 20% (outermost contour), 40%, 60%, 80% and 95% (innermost contour). It should be noted that while the response function is dependent on the initial velocity of the meteor (see Chapter 4), the variation of the response function with velocity is only manifest in the effect on the sidelobes and the absolute response of the main beam. The shape of the response of the main beam remains largely unaffected, and as will be seen, it is only the form of the response that is important for the prediction of the time of occurrence of shower activity for a given meteor radiant. The response function displayed in Figure 6.1 was calculated for a typical velocity of $30\,km\,s^{-1}$, but in what follows it will be assumed to be typical of all velocities.

Superimposed over the response function are the loci of six meteor radiants with ticks indicating the time of their passage. The radiants have declinations varying in steps of 20°

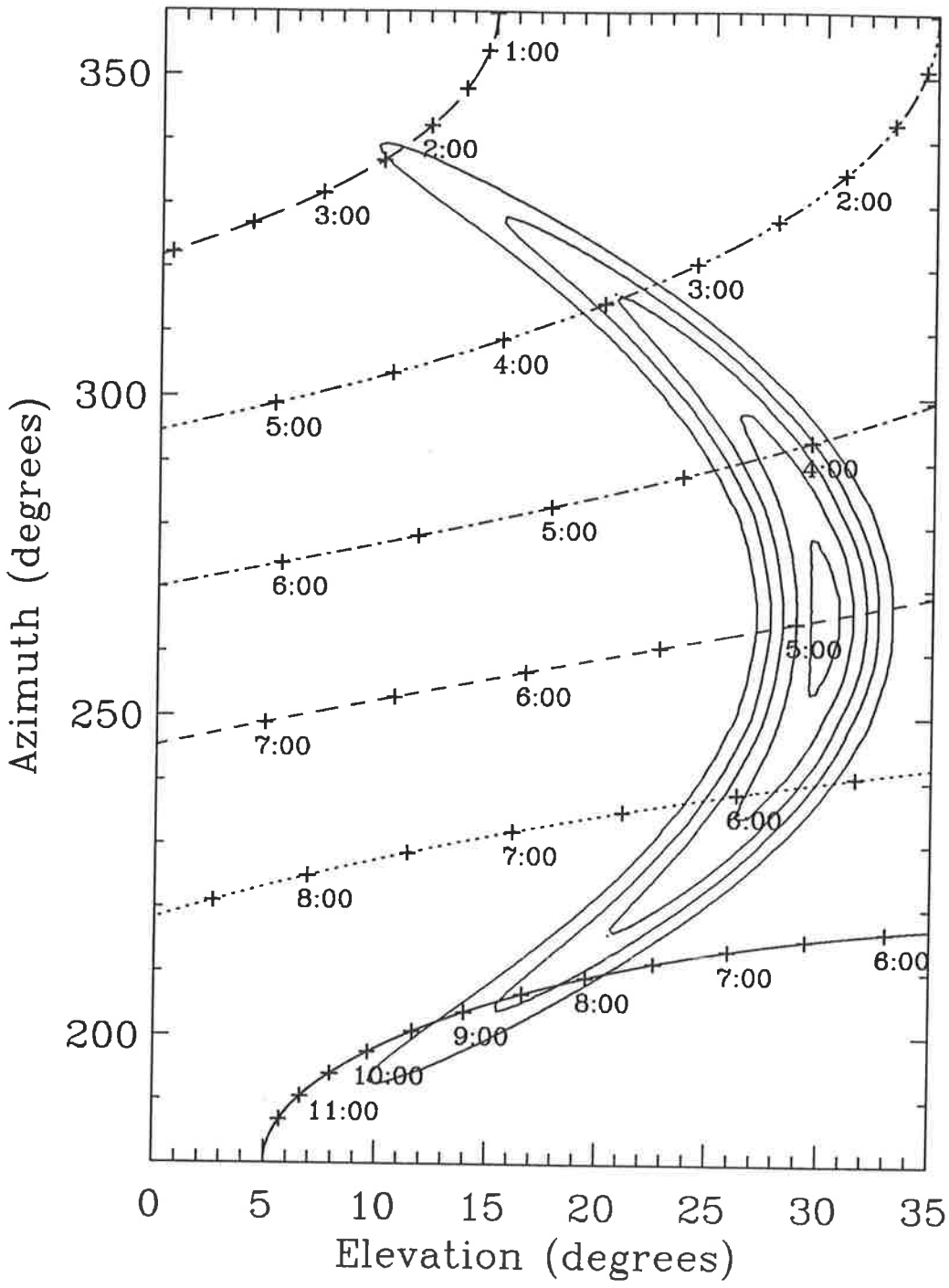

Figure 6.1: The response function for the VHF radar with 6 fictitious radiants superimposed. The radiants have declinations varying in steps of 20° from −60° (bottom solid line) to +40° (top long dashed line) and identical right ascensions. Tick marks indicate the time of passage of each radiant. The response function was calculated at a velocity of 30 $km\,s^{-1}$ and was normalised to its peak. The contours of the response function are at levels of 20% (outermost contour), 40%, 60%, 80% and 95% (innermost contour).

from $-60°$ (bottom solid line) to $+40°$ (top long dashed line). Their right ascensions are all identical as are their dates on which they occur. The declination of a radiant alone determines where the radiant will cross the response function, the right ascension governs only the time of passage of the radiant. Changing the date on which the radiant occurs, also changes the time of passage of the radiant according to the sidereal shift of cosmic sources, *i.e.* the radiant crosses the response function $3.93\,min$ earlier on each subsequent day. By by superimposing the locus of a particular shower on the response function, one can predict when the peak activity of the shower occurs. More formally, one can calculate the rate response of the shower radiant, and this is discussed below.

In Section 4.7, the theoretical diurnal variation in the sporadic meteor echo rates was found by convolving the sporadic radiant distribution $g(\theta_r, \phi_r)$ with the response function $n(\theta_r, \phi_r)$ *i.e.*:

$$n(t) = \int\int_{sky} n(\theta_r, \phi_r) g(\theta_r, \phi_r) d\Omega \; . \tag{6.1}$$

This same technique may be applied to meteor shower radiants using the radiant distribution of the shower instead of the sporadic radiant distribution. Assuming meteor showers are point sources, $g(\theta_r, \phi_r)$ is equal to the meteor shower radiant density in the radiant direction and zero elsewhere. The result, upon integration, is the expected count rate for the shower as a function of time. In Figure 6.2, the expected count rates for the six fictitious meteor shower radiants of Figure 6.1 are displayed. The shower radiants were assumed to be of unit density, and in each case the response function was normalised to its peak. Thus normalised count rates for the six fictitious meteor shower radiants were obtained. The 'lobe' structure displayed by these plots are due to the minor lobes in the response function which are not displayed in Figure 6.1. For low declinations, it can be seen that shower radiants remain in the beam of the radar for much longer durations. At a declination of $-60°$, the response "half-width", or the time during which the rate response is at-least half of the maximum, is about 75 minutes, this falls to 30 minutes for a declination of $-40°$ and 15 minutes at declination of $-20°$. Determinations of radiants of showers with declinations greater than $-40°$ would therefore be less accurate than for radiants closer to the ecliptic.

6.2.3 Determination of the meteor shower radiant coordinates

Although meteor radiants with different declinations take unique paths through the response function it is impossible to distinguish these radiants. For example, two meteor radiants with

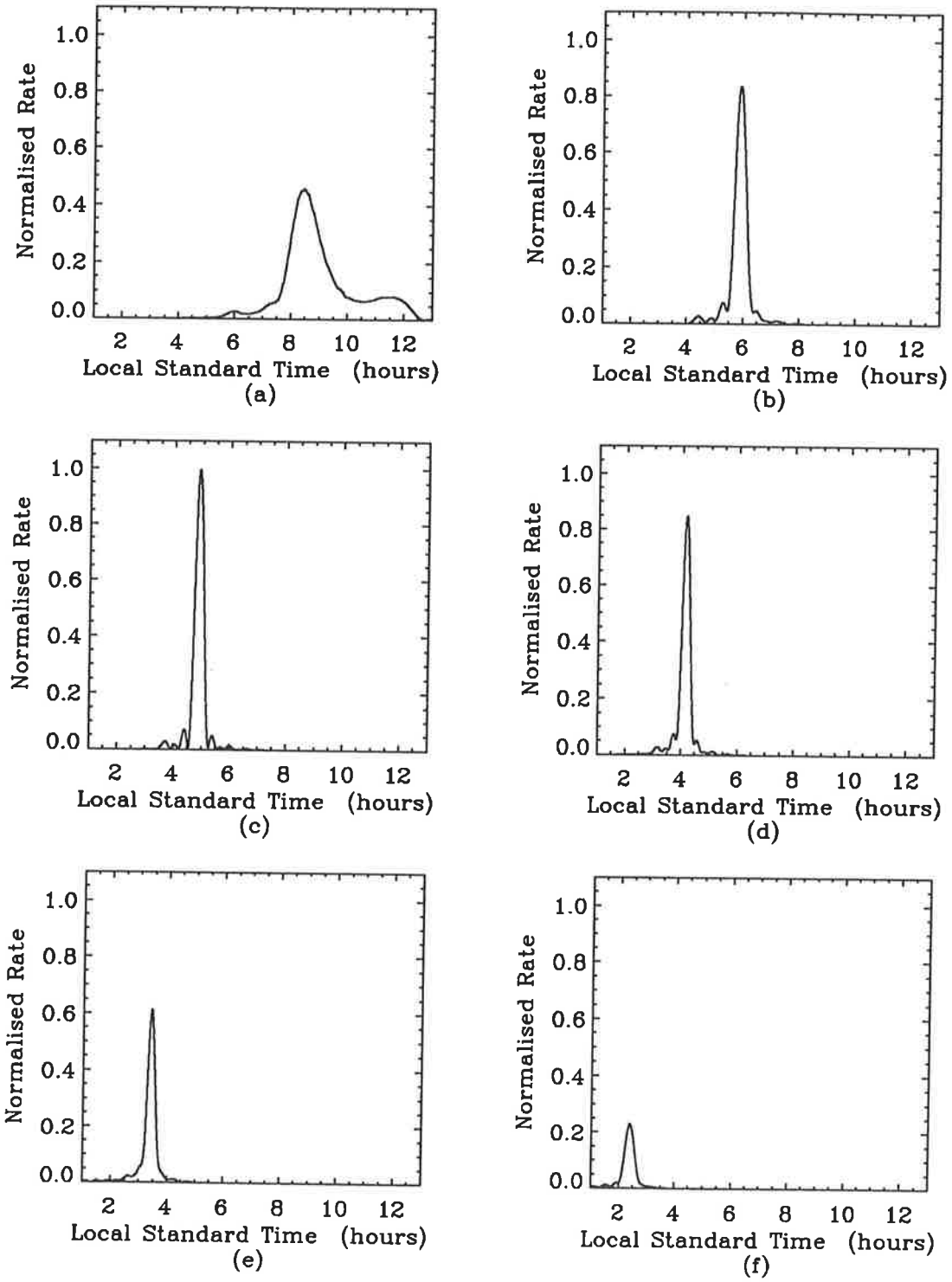

Figure 6.2: Expected normalised count rates for six fictitious radiants based upon the radiants intersecting the response function of the VHF radar for a beam directed 30° of zenith Eastwards (az. 86°). The coordinates of the radiants are as for Figure 4.1; panels a to f refer to the radiants with declinations from −60° through to +40° in successive 20° steps.

declinations of $-20°$ and $+20°$, would produce peak rates at the same time in the East beam of the radar, if the azimuth of the second radiant is advanced by 22.3° with respect to the first. Thus, unknown radiants are not able to be determine from observations with the beam directed at only one area of the sky. However, known meteor showers may by observed and studied (see *e.g. Cervera et al.*, 1993; *Elford et al.*, 1994), but one must be aware that other shower activity could cause elevated count rates at the same time as the shower in question. The only way to identify shower activity unambiguously is to use two beams directed to different areas of the sky and measure the time delay between observing the shower in the two beams (see Figure 6.3). This may achieved with the VHF radar by alternating the beam direction between West (az. 266°) and East (az. 86°) on a minute by minute basis. However, as the number of shower meteors will be halved in both beam, weak showers will be harder to detect if indeed they produce sufficient counts to distinguish the shower from the sporadic background. Also, one should note that the sporadic meteor rate will be different in the two beams as the respective response functions are crossed by the broad sources from the Apex, Helion and Anti-Helion directions.

Figure 6.3 shows a polar plot of the response functions for the East and West beams of the VHF radar. Superimposed are the loci of the six fictitious radiants from Figure 6.1, with solid circles denoting the hourly motion of these radiants. It can be seen that the time interval between the appearance of shower echoes in the two beams depends on the declination of the radiant. The time difference between the shower appearing in each beam is plotted against declination in Figure 6.4. By using Figure 6.4, the declination of meteor shower radiants may be determined, the precision of this value depending on how well the time of passage of the radiant across the response functions can be measured. The precision of the declination determination also depends on the declination itself, for example an error of ± 1 *min* in the measurement of the time of passage of the radiant corresponds to an error of $\pm 0.4°$ for declinations in the range $-20°$ to $+20°$, this decreasing to $\pm 0.2°$ for radiants with declinations of $-40°$ and $+40°$. However, showers with radiants at these larger declinations are more difficult to detect as they pass though sections of the response function which have lower sensitivities. This is shown in Figure 6.5, where the maximum normalised rate of meteor shower echoes as observed by the VHF radar, are plotted as a function of radiant declination. The reduced meteor counts for showers crossing the response function at the extremities reduces precision in the measurement of the time of passage of the shower.

Inspection of Figure 6.5 shows that the response in one of either of the two beams falls

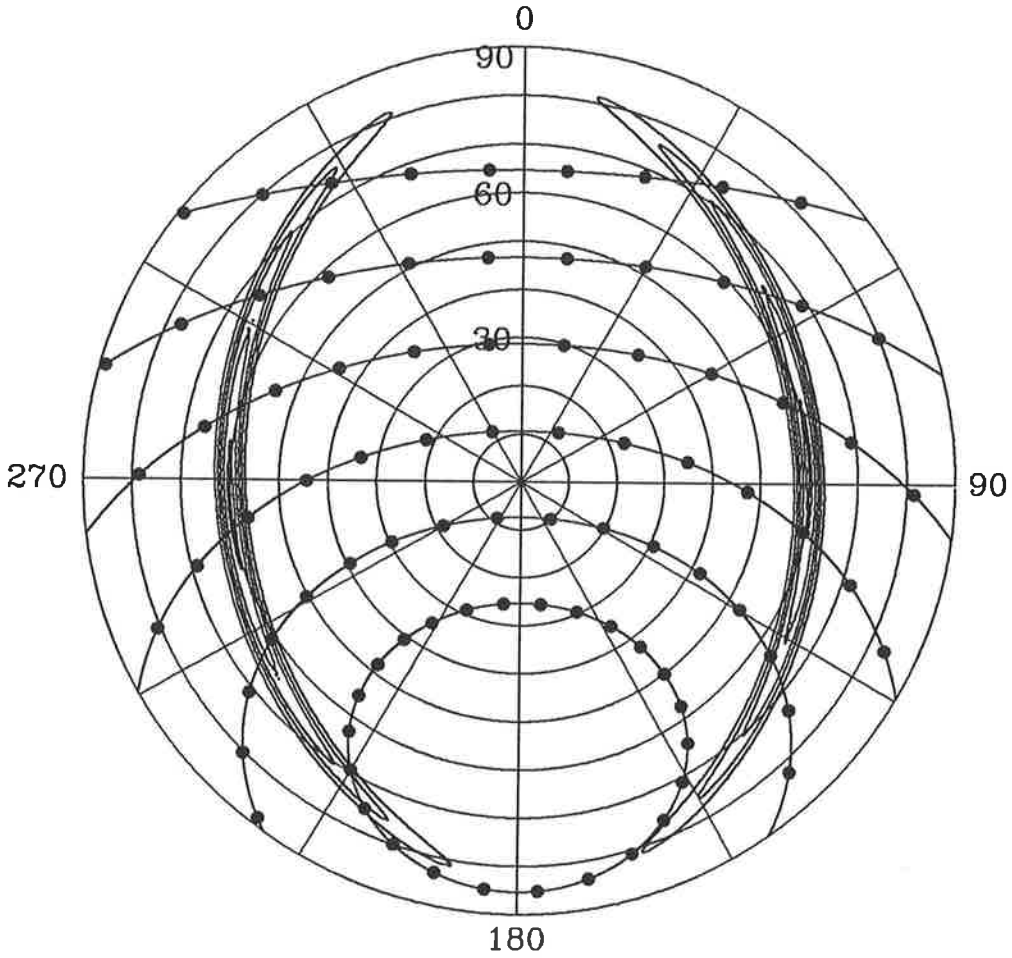

Figure 6.3: Polar contour plot of the response function for the VHF radar for beams tilted East and West. The radial coordinate is the off zenith angle and the polar coordinate is azimuth. The loci of six fictitious radiants are superimposed, their declinations vary from $-60°$ (circumpolar loop) through to $+40°$ in successive $20°$ steps. The hourly positions of the radiants are denoted by the solid circles.

to 50% at declinations of about $-57°$ and $+27°$. Thus this criterion can be used to define the range of declinations of radiants of typical showers that may be reasonably determined by the VHF radar. Strong meteor showers that may be detected at a sensitivity level of say 20% of the maximum response, would allow these radiants to be determined for declinations in the range from about $-60°$ to about $+40°$.

The right ascension of a meteor shower radiant is readily obtained from the time of maximum response of the shower in either the East or West beam once the declination has been determined. Figure 6.6 shows how the expected time of maximum echo rate of six fictitious showers (declinations of $-60°$ to $+40°$ in $20°$ steps), observed in the East beam, varies with the radiant right ascension. These curves were calculated for fictitious showers occurring on March 1^{st}, 1995. On subsequent days, the time of maximum echo rate will

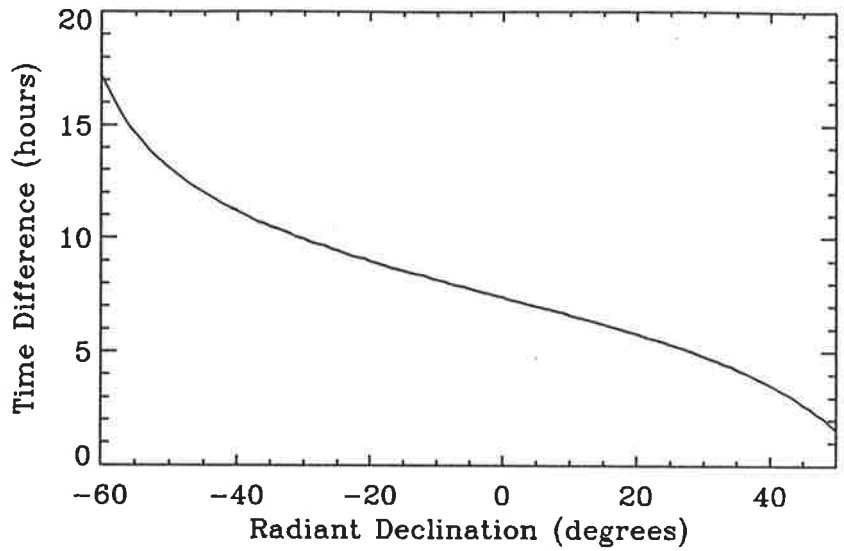

Figure 6.4: The time difference between the radiant maximum activity occurring in the East and West beams of the VHF radar as a function of the radiant declination.

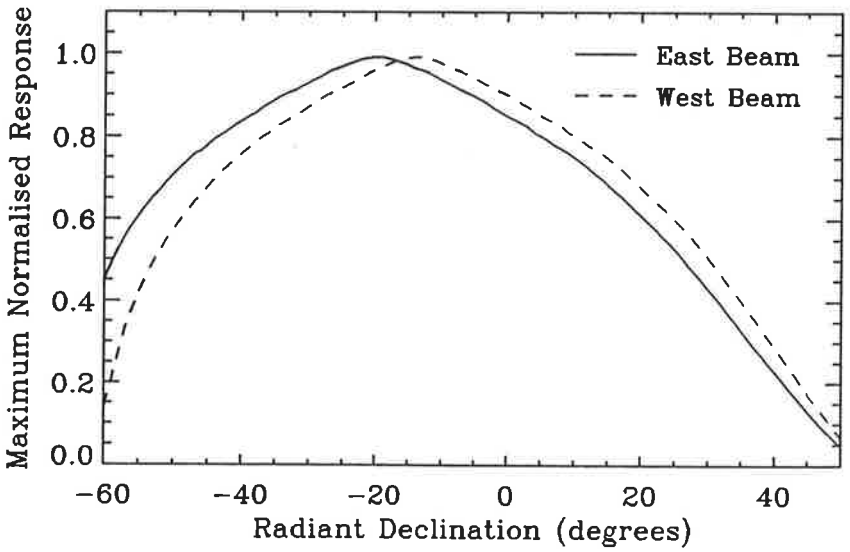

Figure 6.5: The maximum normalised response for meteor shower radiants crossing the East (solid line) and West (dashed line) response functions, displayed as a function of radiant declination

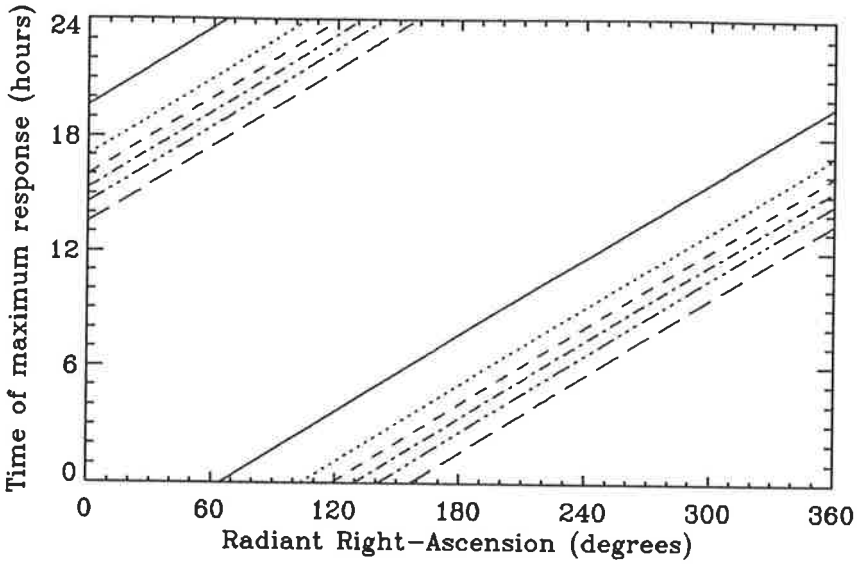

Figure 6.6: Time of maximum echo rate of six fictitious meteor showers detected in the East beam of the VHF, radar as a function of radiant right ascension. The radiant declinations are $-60°$ (solid line) through to $+40°$ (long dashed line) in $20°$ steps. These curves were calculated for March 1^{st}, 1995.

occur earlier due to the sidereal shift of the shower radiants, and thus these curves must be recalculated for each the day the meteor shower is detected. If the time of maximum response can be measured to within $1\,min$, the error associated with the right ascension determination is $\pm 0.25°$ (assuming there is zero error in the declination). Taking into account the error in the measurement of the meteor radiant declination, the error associated with the measurement of the right ascension increases to $\pm 0.45°$. As will be seen later, the time of maximum response for showers can generally be measured to within $\pm 1\,min$, therefore meteor shower radiants are able to be placed within a circle on the celestial sphere of radius less than $0.5°$.

6.3 Detection of the June Librids Meteor Shower

6.3.1 Introduction

The identification of the June Librids with the Buckland Park VHF radar was reported upon by *Cervera et al.* (1993) and *Elford et al.* (1994) and to the knowledge of the authors, this was the first identification since detection optically by Hoffmeister on June $8^{th} - 9^{th}$ 1937 (see *Hoffmeister*, 1948). The data was collected on June $6^{th} - 9^{th}$ 1992, which was prior to the upgrade of the VHF radar. During this period, the transmitted pulse power was $4\,kW$

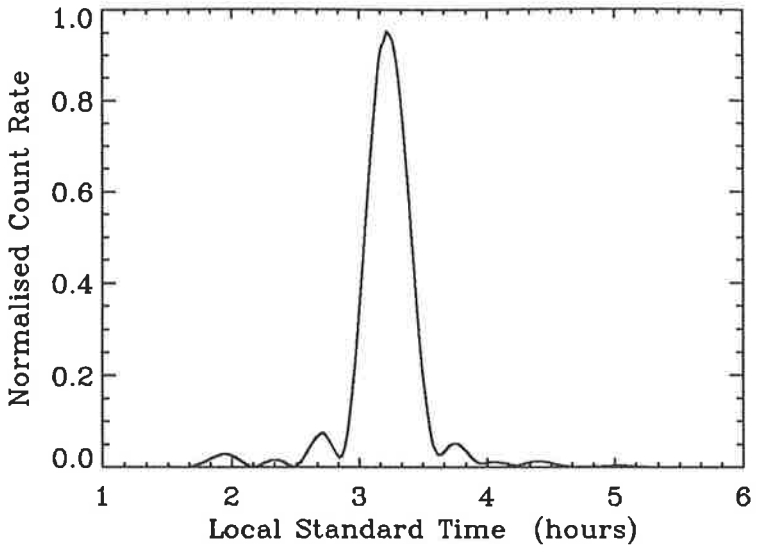

Figure 6.7: The expected normalised count rate for the June Librid shower in the East beam of the Buckland Park VHF radar.

and the time resolution of the raw data was limited to $1/64\,sec$ (see Chapter 2). Further the beam of the radar was directed only Eastwards due to a problem with the beam switching hardware. Although this was not the best configuration (alternating East-West is better for reasons already discussed), it was perhaps fortuitous as the shower was weak. If the beam had been switched between East and West on alternate minutes, only half the numbers of shower meteors would have been observed in either beam and most likely these would be swamped by the sporadic meteors. Since the beam was oriented only Eastwards, it was not possible to unambiguously identify the shower activity with the June Librids; however, the possibility of the activity being due to any other known meteor shower radiants was shown not to be tenable.

Figure 6.7 shows the expected rate response for the Librids meteor shower radiant traversing the response function for an Eastward pointing beam on June 7^{th} 1992. The peak of the expected rate response occurs at 03:13 local time, and thus if the June Librids were active on June 7^{th} 1992, an increase in the meteor rate would be expected at this time.

6.3.2 Observations and results

The time of occurrence of meteors observed during early June 1992 was binned into $12\,min$ bins. Figure 6.8 shows rate data from 3 data runs with the first bin centred at 15:00 local standard time (LST), 20 hours of data are shown in each panel. In the top panel, a peak rate

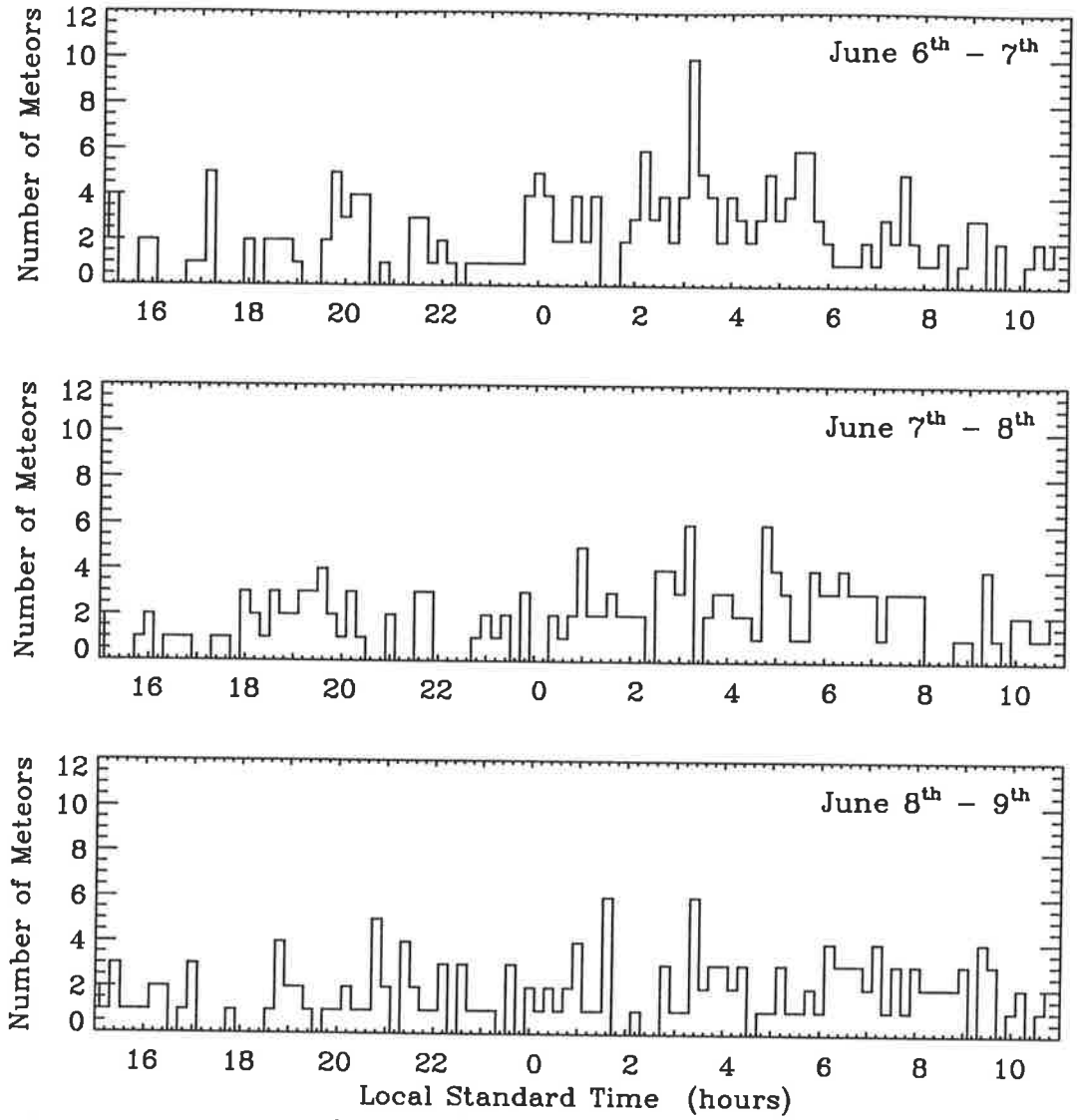

Figure 6.8: Meteor rates on $6^{th} - 7^{th}$, $7^{th} - 8^{th}$ and $8^{th} - 9^{th}$ of June 1992. The data is binned into 12 minute bins.

of 10 meteors may be seen at 03:12 LST on June 7^{th}. This is consistent with the June Librids being active on this day. On the subsequent two days, at 03:12 and 03:24 respectively, a rate of 5 meteors is observed in each case. These two rates do not appear significant, however they are equal to the peak rates on these two days. No appreciable rates were observed at around the same time on other days during early June.

The rate data from the relevant three days were superimposed with an appropriate shift in time to account for the sidereal shift in the radiant. The superimposed data was rebinned, again using $12\,min$ bins, and plotted in Figure 6.9. The shift was performed such that the data from the $7^{th} - 8^{th}$ and $8^{th} - 9^{th}$ were consistent in sidereal time with the data from the $6^{th} - 7^{th}$. Again in this plot, the peak rate is at 03:12. A significance test of the peak

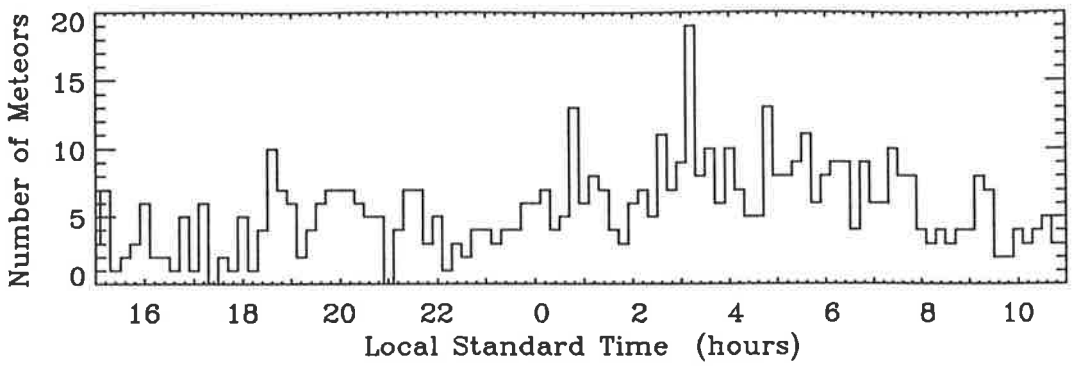

Figure 6.9: Superimposed meteor rate data from $6^{th} - 7^{th}$, $7^{th} - 8^{th}$ and $8^{th} - 9^{th}$ of June 1992. The data was shifted in time between days to correct the sidereal shift of the radiant and then binned into 12 minute bins.

of the superimposed rate data is now performed by generating an appropriate test statistic. Let r_p be the number of meteors contributing to the peak (in this case 19), r_i the number of meteors contributing to the i^{th} bin, and let the sample size (*i.e.* the number of bins) contributing to the test statistic be $2N + 1$, where N is the number of bins on either side of the peak. A test statistic, Z, may be formed as follows:

$$Z = \frac{r_p - \mu}{\sigma} , \tag{6.2}$$

where μ and σ are the sample mean and sample standard deviation respectively and are given by the usual expressions, *i.e.* :

$$\mu = \frac{1}{N} \sum_{i=p-N}^{p+N} r_i ,$$

$$\sigma = \left[\frac{1}{N-1} \sum_{i=p-N}^{p+N} (r_i - \mu)^2 \right]^{1/2} .$$

The choice of an appropriate value of N must be undertaken with care: a value which is too small will yield an unreliable value of Z due to poor statistics, while if N is too large the value obtained for μ and hence Z, will be influenced by the diurnal variation of the background sporadic meteor rates. As a consequence, a range of values of N was chosen (N=4, 6, 8, 10), which corresponded to sample sizes of 9, 13, 17 and 21 bins (1.8, 2.6, 3.4 and 4.2 hours in length respectively). Table 6.1 shows the results of the significance test. From this table it is clear that the peak is statistically significant at a high level of confidence. Although the peak is significant, it cannot be claimed that it is indeed due to the activity of the June Librids until the possibility of other shower activity causing the peak is excluded. This is considered below.

N	μ	σ	Z	Significance level
4	9.44	4.10	2.33	99.0%
6	8.46	3.71	2.84	99.8%
8	7.94	3.90	2.84	99.8%
10	7.90	3.49	3.18	99.9%

Table 6.1: Significance test of the peak observed in the superimposed rate data from $6^{th} - 9^{th}$ June 1992.

6.3.3 Discussion

Meteor showers occurring in early June that could cause the activity noted on the 7^{th} June 1992 include the χ-Scorpids, the Daytime Arietids, the Daytime ζ-Perseids, the Sagittariids, the θ-Ophiuchids and the June Lyrids. However, none of them are expected to be active at the time in question (*i.e.* around 03:12 LST) on the 7^{th} June. All of them, except for the χ-Scorpids, have expected peak rates occurring at least 3 hours later than the peak noted on the 7^{th} June. The χ-Scorpids are expected to peak at 03:54 LST in the East beam, however this is still over 40 *min* too late. Other showers from the lists of *Cook*, (1973), *Kronk*, (1988), and the International Meteor Organization (*McBeath*, 1993) do not produce meteor activity to within 2 *hr* either. The only known meteor shower radiant that is active at this time is the June Librids.

It appears then that the peak in the meteor rates at 03:12 LST on the 7^{th} June 1992 was due to the Librids. However it must be noted that these observations show that the Librids were detected 2 days earlier than by *Hoffmeister*, (1948), in 1937. Follow-up observations of the June Librids in 1993 were not possible due to equipment malfunction. During June 1994 the upgraded VHF radar was operated in the alternating East/West beam mode. There was no evidence for the activity of the June Librids in either beam of the radar.

6.4 Detection of the θ-Ophiuchids Meteor Shower

6.4.1 Introduction

During a meteor observing campaign in June 1994, significant meteor shower activity was detected on several days (with the appropriate sidereal shift in the time of passage), at times which corresponded to the expected time of passage of the Ophiuchids meteor shower radiant as given in the list of *Cook*, (1973). According to *Cook*, the θ-Ophiuchids are active from

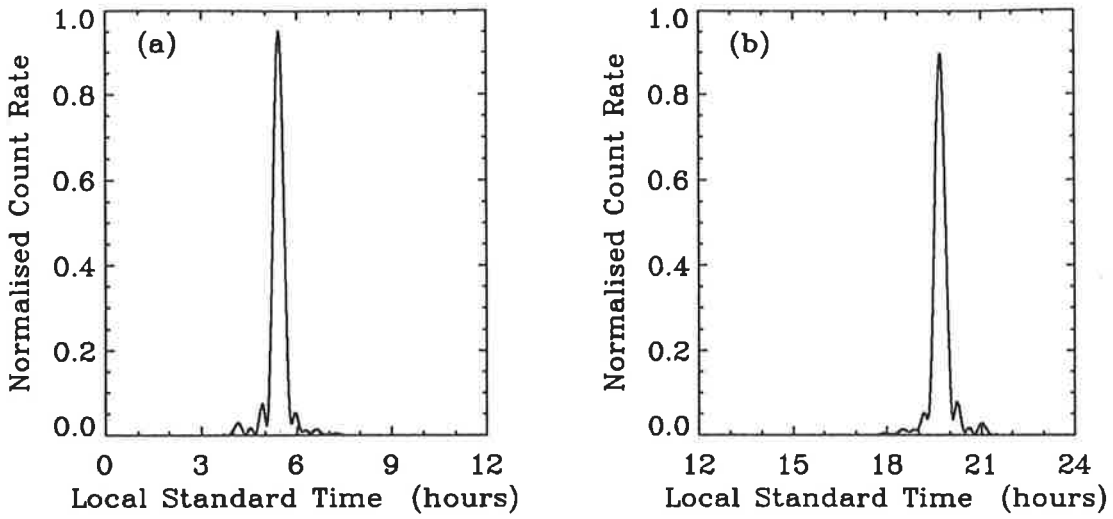

Figure 6.10: The expected normalised count rate for the θ-Ophiuchids meteor shower in (a) the East and (b) the West beams of the Buckland Park VHF radar.

the 6^{th} June to the 16^{th} June with maximum rates on the 13^{th}, and the right ascension and declination of the shower are 267° and −28° respectively. During this time the VHF radar was operated in the alternating East/West beam mode, with beam switching between East and West occurring each minute. The expected time of passage of the shower on the 13^{th} June 1994, is at 05:25 LST in the East beam, and at 19:42 LST in the West beam. Figure 6.10 shows the expected rate response of the θ-Ophiuchids on the 13^{th} June 1994 in the East and West beams.

6.4.2 Observations and results

In Figure 6.11 the meteor rate data obtained from the 11^{th} June 1994, is shown binned into 10 *min* bins. The smooth curve is a 10^{th} order polynomial fit to the rate data. This curve is taken to be representative of the mean background sporadic meteor rate, and tests of significance of any observed peaks are made relative to this mean background rate. The standard deviation of the observed rates about the mean background rate is first calculated as follows:

$$\sigma = \left(\frac{1}{N-1} \sum_{i=0}^{N} (r_i - \mu_i)^2 \right)^{1/2} , \tag{6.3}$$

where N is the number of bins, r_i is the rate level of the i_{th} bin and μ_i is the corresponding mean background rate. The significance of an observed peak is found by calculating how

many standard deviations the peak is above the mean, *i.e.*:

$$Z = \frac{r_p - \mu_j}{\sigma}, \tag{6.4}$$

where r_p is the rate of the peak to be tested which occurs in the j_{th} bin. This is similar to what was done for the Librids meteor shower discussed in Section 6.3.2, except here the meteor count rate is high enough to fit a curve to the rate data and thus obtain the background mean rate instead of varying the sample size and calculating a new constant background mean rate each time. The large peak observed at 05:40 LST in the East beam is significant to a high degree, being 7.03σ above the mean background rate. There are other minor peaks evident in the East beam data, the most notable occurring at 06:19, 12:49 and 13:49 LST, with significance levels of 2.01σ, 2.15σ and 2.32σ respectively. None of these peaks are repeated on other days either prior or subsequent to the data shown on this day. However, minor activity similar to that observed on the 11^{th} June, is evident on other days, although again they are not seen over several days at the same time. The West beam rate data from the 11^{th} June 1994 (Figure 6.11b) shows two significant peaks at around 20:00 LST. The first peak occurs at 19:26 with a significance of 3.60σ, the second occurs at 20:06 with a significance of 5.04σ. Again minor activity is evident, the most significant of these peaks occurring at 07:16 and 21:06 (2.04σ and 2.34σ respectively), which is not repeated on other days. On the basis of published radiant data, the θ-Ophiuchids, if active on the 11^{th} June, are expected to give enhanced meteor rates at 05:32 and 19:48 LST in the East and West beams respectively. This is $8\,min$ earlier than the peak in the rate data observed in the the East beam, and $18\,min$ earlier than the second significant peak observed in the West beam.

The rate data was examined on other days for evidence of the peaks shown in Figure 6.11 recurring. The data from each individual day is not shown, however Table 6.2 summarises the results. In the table, one can see that the peaks in the meteor rates detected in the East beam of the radar are organised into two distinct groups with three peaks contributing to each group. Each group has the expected sidereal time shift between the respective peaks except for the third peak of group A ($10^{th} June$), which occurs $4\,min$ later than expected. It is noted that the activity usually does not occur on successive days, but rather every third day. This is perhaps not surprising as the meteoroid stream may have "bright spots", *i.e.* the particles are clumped, so the shower appears only on the days when the Earth passes though each of the concentrations.

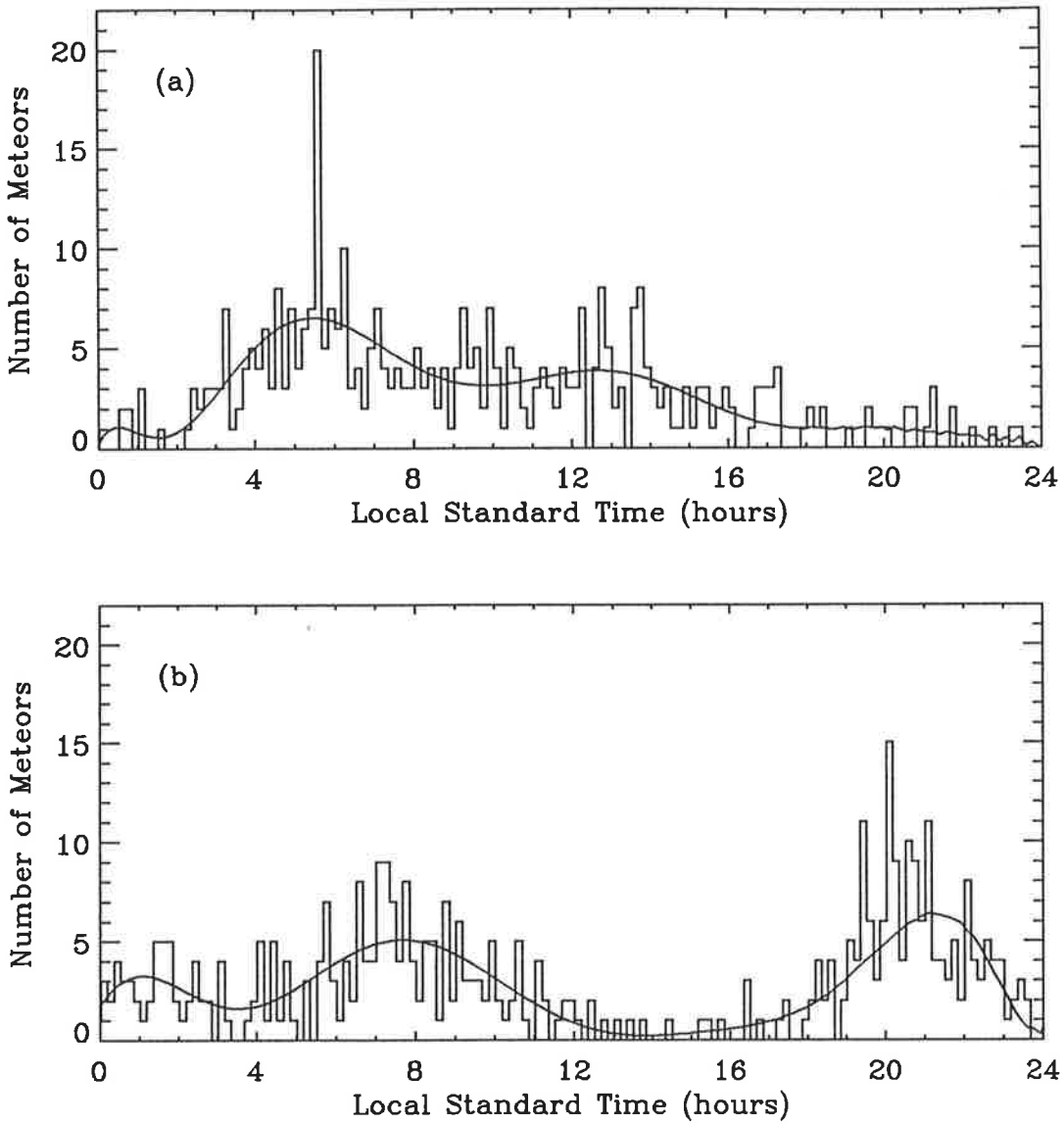

Figure 6.11: Histogram of meteor rate data on the 11^{th} June 1994 for (a) meteors observed in the East beam and (b) meteors observed in the Wast beam. The data is binned into 10 *min* bins, the smooth curves are 10^{th} order polynomial fits to the rate data and are taken to be representative of the mean background sporadic meteor rate.

The rate data for the West beam shows significant peaks only on one day *viz.* the 11^{th} June. The reason for this is not obvious and one possible explanation is elevated background noise levels at these times. Figure 6.12 shows the background noise in the East and West beams of the radar on a typical day in May 1994. The galactic centre is observed to pass through the East beam at about 02:30 LST and the West beam at around 04:00, as is expected. However, from around 16:00 to 20:00 LST an increase in the background noise level is observed in both beams of the radar (this is also seen at around 12:00 to 13:00 LST).

Day in	Group A (East)		Group B (East)		Group C (West)		Group D (West)	
June 1994	LST	sig.	LST	sig.	LST	sig.	time	sig.
6	05:34	5.04						
7	05:30	5.53						
8			05:52	5.21				
9								
10	05:22	5.91						
11			05:40	7.03	19.26	3.60	20:06	5.04
12								
13								
14			05:28	4.89				

Table 6.2: The time of occurrence (LST) and significance (units of σ above the mean background rate) of peaks in the meteor rate data from the $5^{th} - 14^{th}$ June, 1994. The peaks are grouped according to their evident sidereal shift in the time of occurrence on different days. The beam direction is noted in each case.

The increased noise levels at around these times (*i.e.* from 12:00 to about 20:00) is seen throughout May and most of June. The source of this noise remains unexplained, but the fact that it is seen simultaneously in both beams and at the same times over a period of almost 2 months, suggests that it is man-made interference. During the times when the noise is evident, the noise amplitude increased by a factor of about 2 (or a factor of 4 in noise power). Figure 4.17 (from Chapter 4) shows that an increase in the background noise power by this amount decreases the expected meteor count rate by almost half. As the increased levels in background noise occurs around the time the θ-Ophiuchids are expected to to be active in the West beam of the radar, the observation of this shower on only one day in the West beam (and also at a weaker level than in the East beam) is not surprising. While it is unfortunate that this is the case, the one day that the θ-Ophiuchids were observed in the West beam makes it possible to accurately determine the radiant.

The results displayed in Table 6.2 suggests that there are two centers of activity which may be associated with the θ-Ophiuchids. The next step in the analysis of the rate data is to combine the rate data for each group into one day (with the appropriate time shifts to take into account the sidereal shift of the radiants) and rebin. This is shown in Figure 6.13. The time shift for each group of meteor rate data was performed such that the data was consistent in sidereal time with the first day's data of that group (*i.e.* the 6^{th} June for group A, and the 8^{th} June for group B). From Figure 6.13, it may be seen that the group A meteors produce a significant ($6.63\,\sigma$) peak at 05:36 LST. There are several minor peaks that may be

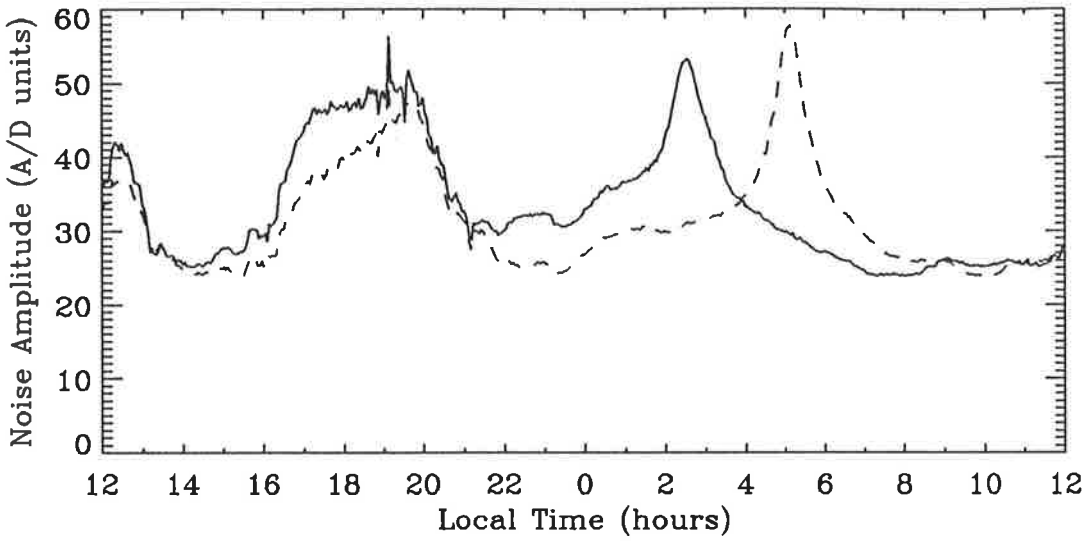

Figure 6.12: Background noise for a typical day in May 1994. The solid line is the noise observed in the East beam and the dashed line is the noise in the West beam. Note the elevated noise from about 16:00 LST to 20:00 LST in both beams, most likely due to a man-made source.

observed in this data, the most significant of these occurring at 06:06, 08:56, 09:37 and 10:37 LST (significance levels of 3.08, 2.38, 2.76 and 2.78σ respectively). The group B meteors produce a peak at 05:52 LST with a significance level of 7.32σ; no minor peaks of any note can be seen in this set of rate data.

In order to be able to sensibly compare the observed rate data in both the East and West beams with the expected time of passage of the θ-Ophiuchids, all relevant data must be sidereally shifted to the same day. This is performed and the results displayed in Table 6.3. An appropriated day must be chosen for this procedure, in this case the date chosen is the 11^{th} June. The reasons for this choice of date are as follows: 1) the shower appears in the West beam only on this day; 2) the maximum rate for the group B meteors occurs on this day; 3) this day is the central day for the period over which the group B meteors occur; and 4) the chosen date is close to the expected date of maximum activity, which occurs on 13^{th} June according to *Cook*, (1973). It should be noted that in Table 6.3 the earlier peak detected in the West beam (referred to as group C in Table 6.2) on the 11^{th} has been associated with the Group A set of peaks in the East beam (which occurs earlier that the group B set of peaks). Naturally it follows then that group D (*i.e.* the peak occurring later in the West beam) is then associated with the group B set of peaks. There is no reason to make this particular association (the reverse is equally valid), except here the two centres of

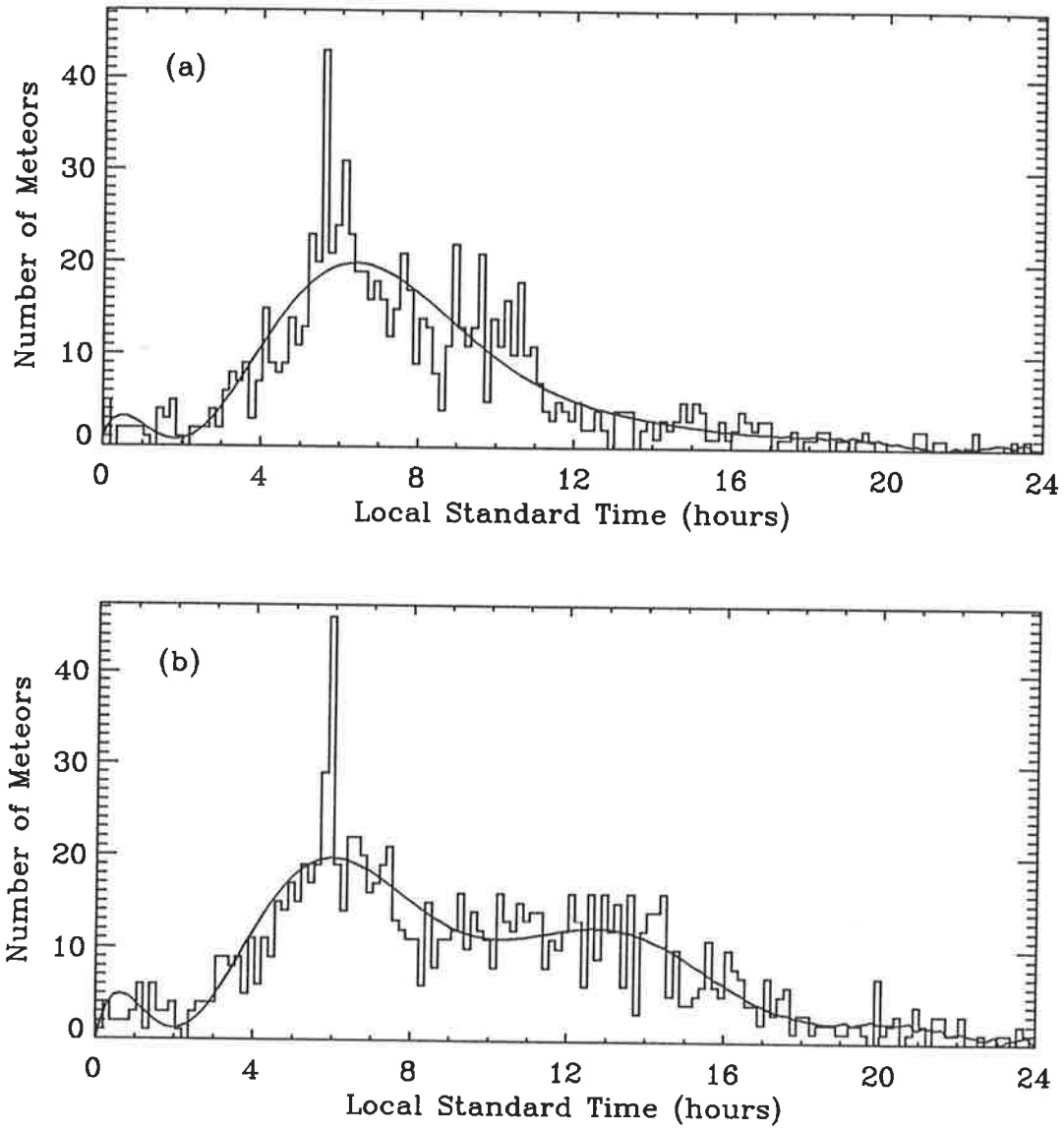

Figure 6.13: Superimposed meteor rate data from the θ-Ophiuchids meteor shower observed in the East beam for (a) group A (3 days), and (b) group B (3 days) meteors. The data is binned into 10 min bins, the smooth curves are 10^{th} order polynomial fits to the rate data and are taken to be representative of the mean background sporadic meteor rate. Appropriate time shifts were introduced to the data to account for the expected sidereal shift of the meteor shower radiants.

Data Set	Time of Occurrence (LST) East Beam		West Beam	
Group A	05:08	(6.63)	19:18	(3.60)
Group B	05:32	(7.32)	19:58	(5.04)
Expected	05:23		19:41	

Table 6.3: Time of occurrence of the peaks in the combined rate data and the expected time of passage of the θ-Ophiuchids. The data has been shifted sidereally to be consistent with the expected time which was calculated for the 11^{th} June 1994. The numbers in parentheses refers to the significance of the respective peaks (in units of σ above the mean).

shower activity occur consistently earlier (groups A and C) or later (groups B and D) than the expected time of passage of the θ-Ophiuchids, in both the East and West beams. This may be observed in Table 6.3. The group A centre of activity occurs $15\,min$ earlier than expected for the θ-Ophiuchids in the East beam and $23\,min$ earlier in the West beam. The group B centre of activity occurs $9\,min$ later and $17\,min$ later than expected for the East and West beams respectively.

Obviously if the two observed bursts of activity are to be uniquely associated with the θ-Ophiuchids shower being active, all other possible meteoroid streams must be shown to not produce meteor activity at these times. This is in fact the case. There are no other meteor showers active through May, June and July (from the lists of *Cook*, *Kronk*, and the International Meteor Organization) that, if active during the second week of June, would produce meteor activity within 1.5 hours of the times listed in Table 6.2. This being the case, it appears that the two bursts of meteor activity are indeed due to the θ-Ophiuchids, and thus raises the possibility that θ-Ophiuchids has two distinct radiant centres.

6.4.3 Determination of the shower radiant coordinates

The radiants of the two observed bursts of meteor activity will now be determined. As described in Section 6.2.3, the radiant coordinates are determined from the time of passage of the radiant through the East and West beams. For the two observed bursts of activity, the radiant coordinates have been calculated and are listed in Table 6.4 together with the radiant coordinates of the θ-Ophiuchids as given by *Cook's* list. Also shown in Table 6.4 are the averaged coordinates of the Group A and Group B bursts of meteor activity. As described in the previous section, it is equally valid to associate the earlier occurrence of the two peaks observed in the East beam with the second peak observed in the West beam (and

Data Set	R. A. (degrees)	Dec. (degrees)
Group A	262.3	-29.4
Group B	270.5	-26.4
Average	266.4	-27.9
Group A′	267.3	-22.4
Group B′	265.5	-32.6
Average	266.4	-27.5
θ-Ophiuchids[a]	267	-28

[a] *Cook*, 1973

Table 6.4: The right ascension and declination of the Group A and Group B bursts of meteor activity (together with their mean position), and the alternative Group A′ and Group B′ bursts (and their mean position). Also listed are the coordinates of the θ-Ophiuchids as given by *Cook*, (1973). See text for further details.

likewise the second peak in the East beam with the first peak in the West beam). This of course will change the radiant coordinates of the two bursts of activity. These coordinates have been calculated and are also listed in Table 6.4 (together with their average position), where they are referred to as Group A′ and Group B′ respectively.

Figure 6.14 displays all the radiant coordinates listed in Table 6.4 (Group A and Group B coordinates in Figure 6.14a and Group A′ and Group B′ coordinates in Figure 6.14b). One can see that either set of coordinates, describing the positions of the two bursts of meteor activity, are well removed from the coordinates of the θ-Ophiuchids as given by *Cook*; however, it is interesting to note that they do bracket the shower. Figure 6.14a shows the declinations of Groups A and B are fairly close to that of the θ-Ophiuchids, but their right ascensions differ by about 4°. The reverse is the case in Figure 6.14b for the Groups A′, B′. It is interesting to note that in both cases, the mean position of the two bursts is close to the radiant position of the θ-Ophiuchids as given in *Cook's* list; the difference of about 0.6° is within experimental error.

From the discussion in the last two paragraphs, it appears that the two bursts of meteor activity observed during early June are associated with the θ-Ophiuchids meteoroid stream and in fact indicates that the θ-Ophiuchids has two distinct centres of activity. To the best knowledge of the author, this has not been observed before. The radiant coordinates of the θ-Ophiuchids which appears in *Cook's* list were obtained from *Cook et al.* (1973) who summarised the observations of a number of researchers. A search by *Southworth and Hawkins* (1963), of *McCrosky and Posen's* (1961) sample of 2529 photographed meteors yielded 5 θ-Ophiuchid meteors. This was verified by *Lindblad* (1971a) and a further two

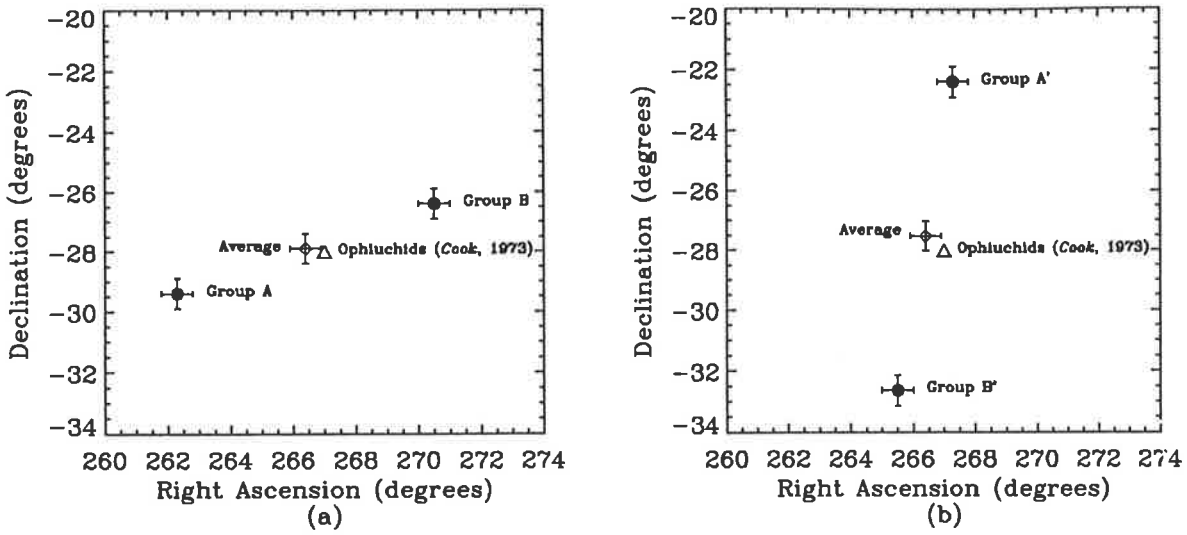

Figure 6.14: Plot of the radiant coordinates of (a) the Group A and Group B bursts of meteor activity observed during early June 1994 and (b) the alternative Group A′ and Group B′ bursts. In each figure the average position of the two bursts of activity and the coordinates of the θ-Ophiuchids, as given by *Cook* (1973), are also plotted.

meteors were added (*Lindblad*, 1971b) to bring the total to seven. Of these *Cook et al.* used only 4 to determine the mean orbital elements of the shower. Clearly there were insufficient data in these original observations to identify the two centres of activity displayed by the data presented here. More recent work by *Rogers and Keay* (1993), showed that the Newcastle meteor radar system operating at 25.6 *MHz* observed the θ-Ophiuchids in 1990 with maximum hourly rates of up to 80 meteors. However, due to limitations of their equipment they report that the quality of the data was too poor to enable any determination of the coordinates of the shower radiants they observed with any reasonable accuracy.

6.4.4 Velocity measurements of the θ-Ophiuchids meteors

The velocity distribution of the meteoroids contributing to the bursts of meteor activity discussed in sections 6.4.2 and 6.4.3 will now be examined. If the observed bursts of activity are indeed due to a meteor shower, then one would expect that these meteoroids encounter the Earth with the same velocity, and in fact close to the speed of 26.7 $km\,s^{-1}$, given by *Cook* (1973) for the θ-Ophiuchids. The method used to deduce the meteor velocities was the pre-t_0 phase technique described in Chapter 5 .

Figure 6.15 shows the velocity distribution of 111 meteors observed during the period of the bursts of meteor activity, that have been associated with the θ-Ophiuchids meteor shower (see Table 6.2). Of all the meteors examined, approximately 3/4 were able to have a velocity

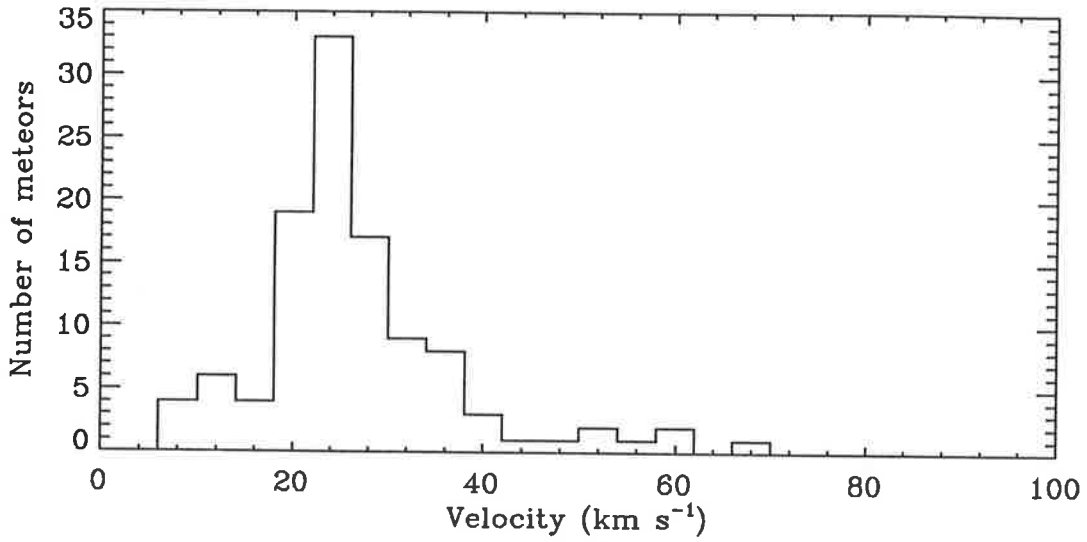

Figure 6.15: Velocity distribution of the meteors observed during the time of passage of the θ-Ophiuchids meteor shower. Meteors from each $10\,min$ bin of the rate data where the bursts of meteor activity are noted and associated with the θ-Ophiuchids (in either beam) are included. The bin size is $4\,km\,s^{-1}$, 111 meteors contribute.

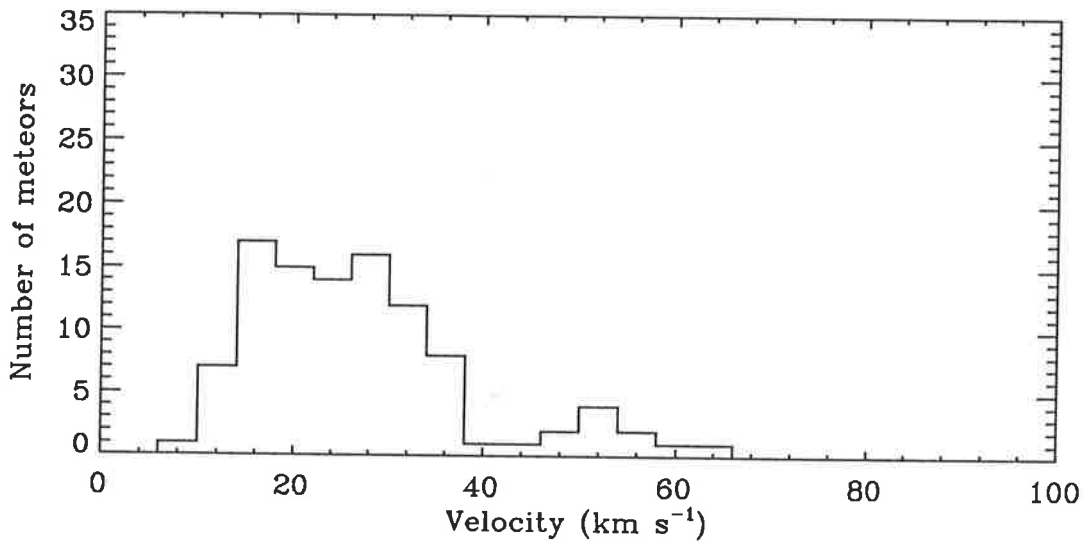

Figure 6.16: Velocity distribution of the meteors observed prior to the passage of the θ-Ophiuchids meteor shower. Meteors over a period starting from $60\,min$ before and extending to $30\,min$ before each burst of meteor activity associated with the θ-Ophiuchids from the data set. The bin size is $4\,km\,s^{-1}$, 102 meteors contribute.

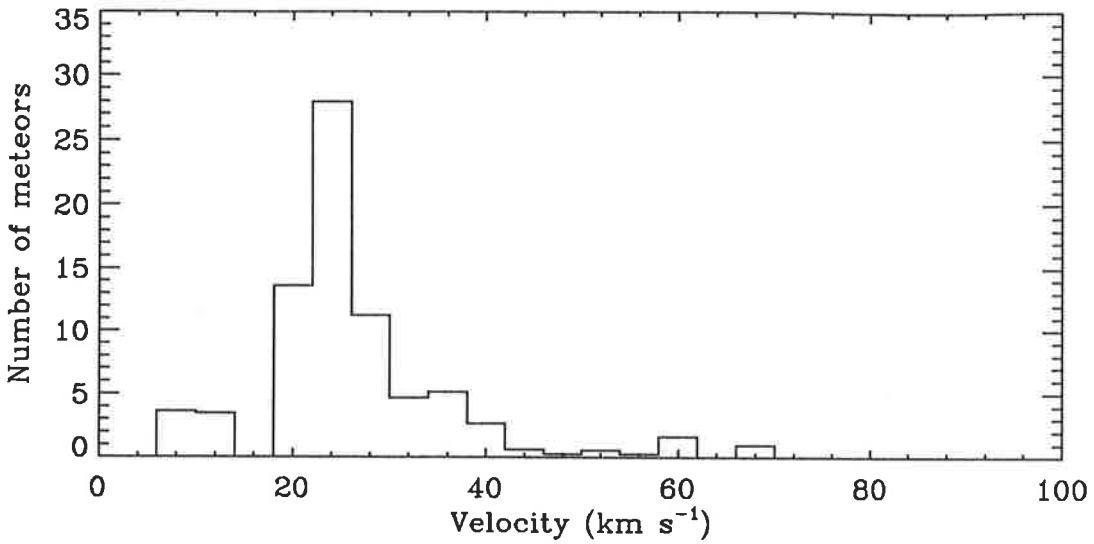

Figure 6.17: Velocity distribution of the meteors observed during the time of passage of the θ-Ophiuchids meteor shower with the sporadic distribution statistically removed. See text for details

determined, the others being either two weak or behaving in a manner that prevented a reliable velocity determination (see Chapter 5 for further details). The velocity distribution displayed in Figure 6.15 shows a large peak at $24\,km\,s^{-1}$, and this is to be compared with the expected velocity of $26.7\,km\,s^{-1}$. Also, the shower meteors show a spread in velocities of about $\pm 4\,km\,s^{-1}$ around the peak. The error in the velocity determination is, in most cases, of the order of 2-4%, so one would expect the spread in the measured velocities of shower meteors to be no more than $\pm 1\,km\,s^{-1}$. Both of the above points may be explained by the fact that (1) the deceleration of the meteoroids in the atmosphere has not been taken into account, and (2) the velocity distribution displayed in Figure 6.15 is contaminated by sporadic meteors.

The removal of sporadic meteor contamination from the velocity distribution of the bursts of meteor activity may be performed statistically. Figure 6.16 shows the velocity distribution of the meteors observed over the period starting from 60 *min* before and extending to 30 *min* before each observed burst of meteor activity associated with the θ-Ophiuchids. No bursts of meteor activity (*i.e.* showers) were evident during any of these periods. Again from all available meteors observed during these times approximately 3/4 were suitable for velocity determinations.

Figure 6.16 essentially shows the background velocity distribution of sporadic meteors

around the time of passage to the θ-Ophiuchids, assuming the velocity distribution of sporadics does not change significantly over a period of about 45 min. This is not an unreasonable assumption as in 45 min the Earth has rotated by only 11°, so that the velocity vector of the Earth's motion with respect to the 'look' direction has changed only by a small amount. As expected the velocity distribution of the sporadic meteors is clearly different to that of the bursts. Normalising the sporadic velocity distribution appropriately and subtracting this from the velocity distribution of the the bursts, removes the sporadic contamination statistically. The normalisation factor applied to the background sporadic distribution was 0.36. This was found from the consideration that the durations of each period of rate data, from which the meteors are selected for the background distribution, are about $25 - 30\,min$ compared to only $10\,min$ for the shower meteors. The velocity distribution of the bursts of meteor activity with the sporadic contamination removed is displayed in Figure 6.17

Now that the sporadic contamination has been removed from the bursts' velocity distribution, the effect of meteor deceleration may be accounted for, so as to yield the encounter speed of these meteoroids with the Earth. Before discussing the process for accounting for the effect of deceleration (Sections 6.4.5 and 6.4.6) it is important to establish that both groups of meteors are associated with a common stream by showing that they have the same velocity distribution. In Figure 6.18, the velocity distributions of the Group A, Group B and the combined Group A and B meteors are shown. Note, that only the meteors in observed in the East beam contribute to these plots. This is necessary as it is uncertain which bursts of meteor activity in the West beam should be associated with those in the East (as discussed in the previous section). Examination of Figure 6.18 shows that the velocity distributions of the two groups of meteors peak at the same velocity *viz.* $24\,km\,s^{-1}$. The two velocity distributions differ slightly, but the differences, are much less than the statistical errors involved due to the small sample sizes (39 and 44 meteors contributing to the respective distributions). The correlation coefficient between these two distributions is 0.85 which indicates they are well correlated and supports the hypothesis that the two groups of meteors are members of a common stream.

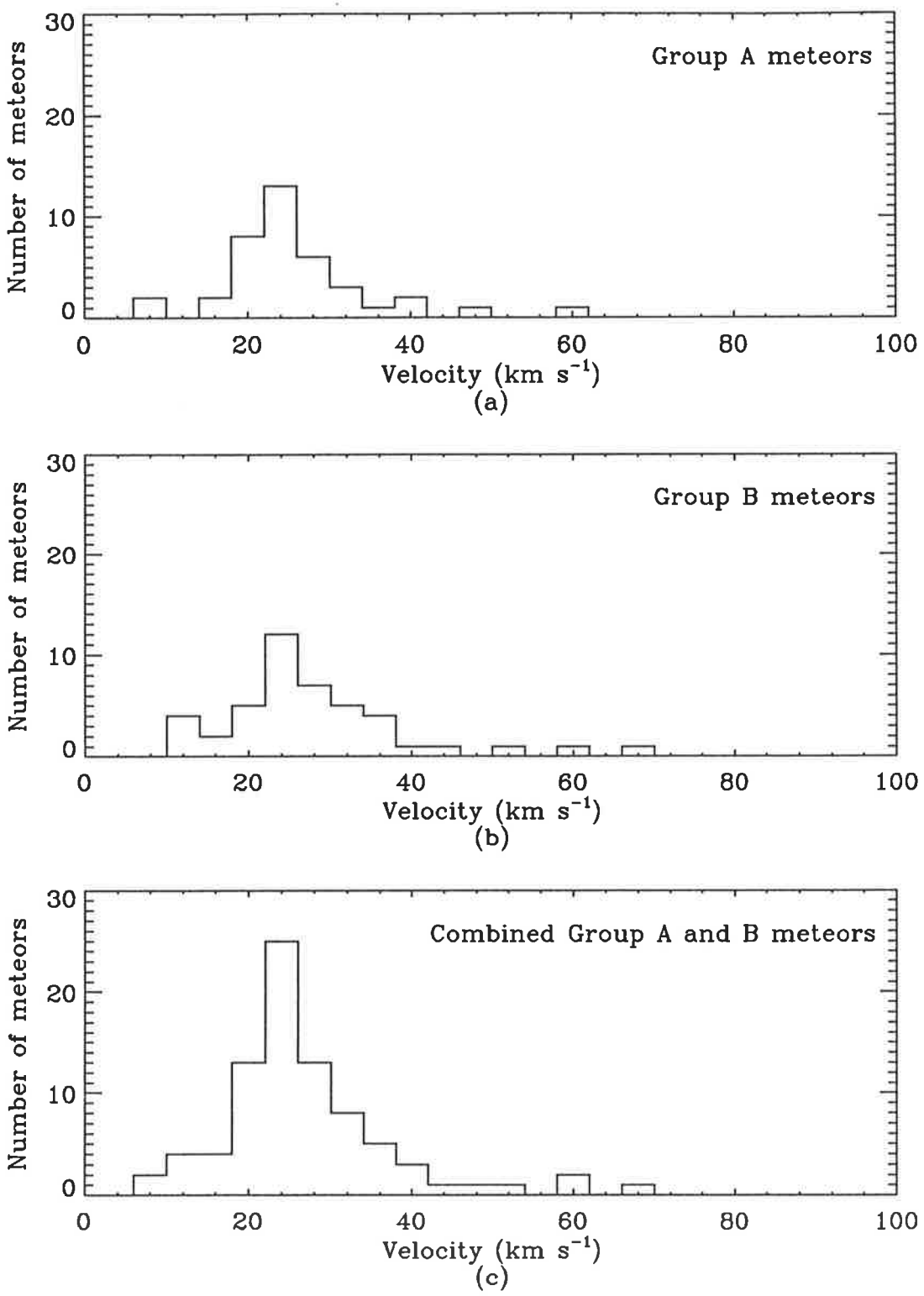

Figure 6.18: Velocity distribution of the (a) Group A, (b) Group B and (c) combined Group A and B meteors in the East beam (see text and Table 6.2). In each plot the binsize is $4\,km\,s^{-1}$, 39 and 44 meteors contribute to the Group A and Group B distributions respectively.

6.4.5 The corrected velocity of the θ-Ophiuchids: an attempt to account for meteoroid deceleration by examining the velocity-height profile

In the previous section, the velocity distribution of the shower meteors was observed to peak at a smaller value (by about $3\,km\,s^{-1}$) than that given by *Cook* (1973), and further the distribution exhibited a larger spread in values than expected. This was attributed to the deceleration of the meteoroids ablating in the atmosphere. Thus any estimate of the encounter velocity of the shower meteors with respect to the Earth requires analysis of the degree of deceleration. This will be attempted in this section.

In Chapter 5 it was found that measuring decelerations of individual meteoroids from the meteor echoes was only possible by comparing the velocity determined from post-t_0 amplitude oscillations with the velocity measured from the pre-t_0 phase information. This could only be applied in the few cases where the post-t_0 amplitude oscillations were evident, and even so was found to be prone to large errors associated with in the measurement of the post-t_0 amplitude oscillations. Also it was found that only strong echoes gave usable results, and thus using decelerations for only these meteors could introduce an undesirable selection bias. Given the unreliability and the sparseness of the deceleration measurements of individual meteors, a different approach to account for deceleration of the θ-Ophiuchids is considered.

Figure 6.19 displays the height of ablation of the observed shower meteors as a function of their velocity. The ellipse and the solid and dashed lines are described in the next paragraph. Note, as there is interest only in the shower meteors, the data displayed here is not only restricted to the times where the bursts of meteor activity is evident (see Table 6.2), but also to the meteors with velocities in the range from $18\,km\,s^{-1}$ to $30\,km\,s^{-1}$. This velocity range corresponds to the 3 highest bins in Figure 6.15, and meteors with velocities outside this range are considered not to be shower meteors and are therefore excluded. Of course there are background sporadic meteors occurring in the above velocity range. These are impossible to distinguish from the shower meteors, however an estimate of the upper limit on the number of the sporadic meteors may be established (addressed in the next paragraph). The scatter of the data points displays a distinct trend: as the height of ablation of the meteors increases, so too does the measured meteoroid velocity. This indicates that the shower meteors which experience the least deceleration occur at greater heights. The reason why this is the case may be explained by considering two identical meteoroids travelling with the same velocity

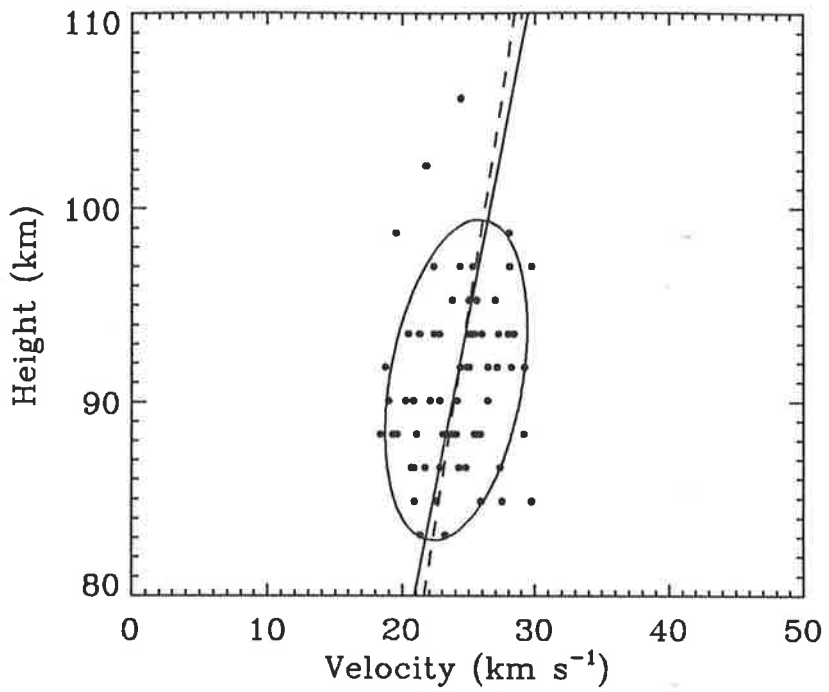

Figure 6.19: Velocity - height distribution of the observed shower meteors. Only meteors with velocities in the range from 18 $km\,s^{-1}$ to 30 $km\,s^{-1}$ are included. The ellipse is a fitted error ellipse to the data points at the 78% level. See text for details.

along paths which are parallel. If the second meteor is observed at a greater range, the observed height is likewise greater. However as the particles are the identical, so too are the ionization profiles, thus the second meteor is observed further back along the ionization profile where the deceleration is not as severe. Hence the observed trend in the shower meteors.

The observed trend in the velocity-height profile of the shower meteors immediately suggests a method to obtain the initial velocity of the meteoroids: extrapolate back to the maximum height where the shower meteors occur and take the velocity at this height as the 'pre-ablation' velocity. A classical deceleration argument may then applied (*Hughes*, 1978) to arrive at the initial velocity. The easiest (although crude) method of estimating the pre-ablation velocity, is to fit an ellipse to the data and take the point on the ellipse which is intersected by a line through the semi-major axis at the largest height. The ellipse fitted to the data displayed in Figure 6.19 is the most probable error ellipse (see *Chapman and Bartels*, 1962) calculated at the 78% level (an ellipse which contains 78% of the data points inside it) and the solid line is the line that intersects the points on the ellipse defined by its semi-major axis. The choice of level will be discussed shortly. Fitting an error ellipse to a

set of data is similar to obtaining a line of best fit to the data by another method (*eg.* a linear least squares fit). This may be seen in Figure 6.19, the solid line is very close to the dashed line which was obtained through a linear total regression analysis of the data. The only application for the error ellipse, in this case, is to help identify the point along the line of best fit, to the data, where the velocity measurement is to be made. This method is only approximate as it makes the assumption that the deceleration of the meteors is constant which is not true. However, to a first approximation it yields a reasonable estimate for the pre-ablation velocity.

The choice of level for the error ellipse (78%) was based upon the estimated fraction of meteors contributing to the data which are shower meteors. A total of 69 meteors comprise the data set, the background velocity distribution (see Figure 6.16) contains 45 meteors in the same velocity range as the shower velocity distribution. After scaling this number (as discussed previously) this becomes 15 meteors, therefore of the 69 meteors displayed in Figure 6.19, only 54 (or 78%) are expected to be shower meteors.

The choice of 78% will not exclude all sporadic meteors (as these will be somewhat randomly distributed), but this is probably the best estimate that can be made. This is vindicated by Figure 6.19: the error ellipse fits the data extremely well, only 6 points are well outside (and therefore are most likely sporadics or meteors detected in the sidelobes of the radar), with the other data points being fairly evenly distributed within or lying just outside the ellipse. The estimated pre-ablation velocity of the shower meteors is $26.4\,km\,s^{-1}$.

Figure 3.1 in Chapter 3 displays the theoretical altitude at the commencement of ablation as a function of meteoroid radius and initial velocity (after *Hughes*, 1978). From this diagram we see that a stony meteoroid with an initial velocity of $27\,km\,s^{-1}$ has a maximum starting height of 98–99 km. Inspection of Figure 6.19 reveals that 5 echoes occur at 97 km, none at 98 km, 2 at 99 km and 2 echoes above 102 km. As mentioned previously, the 2 echoes above 102 km, and the one at 99 km lying well outside the error ellipse are probably sporadics or meteors detected in the sidelobes. Thus, if these meteors are ignored, Figure 6.19 clearly shows that the height at which the θ-Ophiuchid meteoroids start to ablate is 98–99 km, and this is in agreement with the expected value from ablation theory.

Now, the velocity of the meteoroid immediately prior to commencement of ablation, V_p, is related to the initial velocity, V_∞, by the following expression (*Hughes*, 1978):

$$V_p = V_\infty exp\left(-\frac{3\mathcal{H}\Gamma\rho_a}{4R\rho_m cos\chi}\right) , \tag{6.5}$$

where $\mathcal{H}$ is the scale height of the atmosphere, Γ is drag coefficient, ρ_a the density of the atmosphere at the height where ablation commences, g is acceleration due to gravity, ρ_m and R are the density and radius of the meteoroid respectively, and χ is the zenith angle. Using $p = \rho_a g \mathcal{H}$ and $A(m/\rho_m)^{2/3} = \pi R^2$, where A is the shape factor and m the mass of the meteoroid, Equation 6.5 may be recast to give:

$$V_\infty = V_p exp\left(\frac{A\Gamma p}{g m^{1/3} \rho_m^{2/3} cos\chi}\right) . \tag{6.6}$$

Therefore, assuming a meteoroid density of about $3000\,kg\,m^{-3}$ (*i.e.* a stony particle) and using $\Gamma \approx 1$ and $A \approx 1.2$, then an initial velocity of $27.1\,km\,s^{-1}$ is obtained for a meteoroid with a mass of $10^{-9}\,kg$. This decreases to $26.7\,km\,s^{-1}$ and $26.6\,km\,s^{-1}$ for particles with masses of $10^{-8}\,kg$ and $5 \times 10^{-8}\,kg$ respectively.

As will be seen later, the masses of the θ-Ophiuchid meteoroids which produced meteors observable with the Buckland Park VHF radar are about $10^{-9}\,kg$ to $5 \times 10^{-8}\,kg$. Thus, a reasonable estimate of the initial velocity of the θ-Ophiuchids meteoroids is $26.8 \pm 0.3\,km\,s^{-1}$ which is in excellent agreement with the value given in *Cook's* list ($26.7\,km\,s^{-1}$).

6.4.6 An alternative method to account for deceleration: a theoretical approach based upon ablation theory

A simple theoretical approach to estimate the initial velocity of the individual meteoroids employing ablation theory, is now described. Also obtained from the process is the initial mass of the meteoroids and this is used later to investigate the mass distribution of the shower. The method relies on the electron line density of the trail being measured, and this requires the digitized output of the radar receiving system to be calibrated. This was achieved with a wide band white noise generator and observations of the background cosmic noise. The calibrated receiving system enabled the absolute returned echo power to be calculated from the digitized receiver output, whereupon the radar equation was employed to relate this to the electron line density of the trail. The assumption was made that the observed meteors were underdense which is reasonable on consideration of the limiting electron line density of meteor trails able to be observed by the radar.

The radar equation for underdense trails, which has already been discussed in detail in Chapter 3, is restated below:

$$P_R = 2.5 \times 10^{-32} q^2\, P_T\, G_T(\theta,\phi)\, G_R(\theta,\phi)\, \alpha_r\, \alpha_v\, \alpha_d \left(\frac{\lambda}{R}\right)^3 \left(\frac{C^2+S^2}{2}\right) , \tag{6.7}$$

where the various quantities have been described previously in Chapter 3. The returned echo power varies with time (through the $C^2 + S^2$ term) so a point along the trail close to the t_0 point must be chosen and the electron line density calculated at that point; the point at which the meteor echo power maximises is convenient. From equation 6.7, we see that the returned echo power attains its maximum value with $C^2 + S^2$ and it was shown previously that $C^2 + S^2$ maximises at $x = 1.21$ with a value of 2.682 (see Chapter 3). This value is used in the subsequent calculations with the radar equation.

In order to calculate the electron line density from the radar equation, the gain of the antenna is required and this is dependent upon the position of the meteor in the beam of the radar. It is impossible to determine where the meteor is in the beam of the radar, but a geometrical approach based on the response function is employed to resolve this. Consider the burst of activity due to the shower and in particular any meteor observed during the time of the shower. This meteor is observed a certain time before or after the peak activity, which may be related to the expected rate of the shower as calculated from a convolution of the radiant distribution (in this case a point source) with the radar response function (described earlier in this chapter). The rate at this time relative to the maximum value (meteors at centre of beam) is found and is applied as a correction factor for this particular meteor in the electron line density calculation. The radar equation, at the point where the returned echo power is a maximum, is thus modified as shown in the following equation:

$$q = 5.5 \times 10^{15} \frac{1}{r} \left(\frac{R}{\lambda}\right)^{3/2} P_{echo}^{1/2} (P_T \, G_T \, G_R \, \alpha_r \, \alpha_d \, \alpha_d)^{-1/2} \,, \tag{6.8}$$

where r is the correction factor obtained from the expected rate of the shower, P_{echo} is the maximum returned echo power and all other quantities are as before. The gains G_T and G_R take their maximum values (*i.e.* the centre of the beam).

Once the electron line density has been found, the ionization equation (see Chapter 4) is then used with the measured velocity to calculate the mass of the particle at the height at which the meteor was observed. The equations describing the ablation theory are then integrated from this height up to where the meteoroid began ablating (about 99 km for θ-Ophiuchid meteoroids). Thus the pre-ablation mass (*i.e.* initial mass) and the pre-ablation velocity of the meteoroid are found. Equation 6.6 is then applied to obtain the initial velocity of the meteoroid.

The initial velocity distribution of all the meteors observed during the passage of the shower is shown in Figure 6.20a, the distribution has a peak at 28 $km\,s^{-1}$. In Figure 6.20b, the

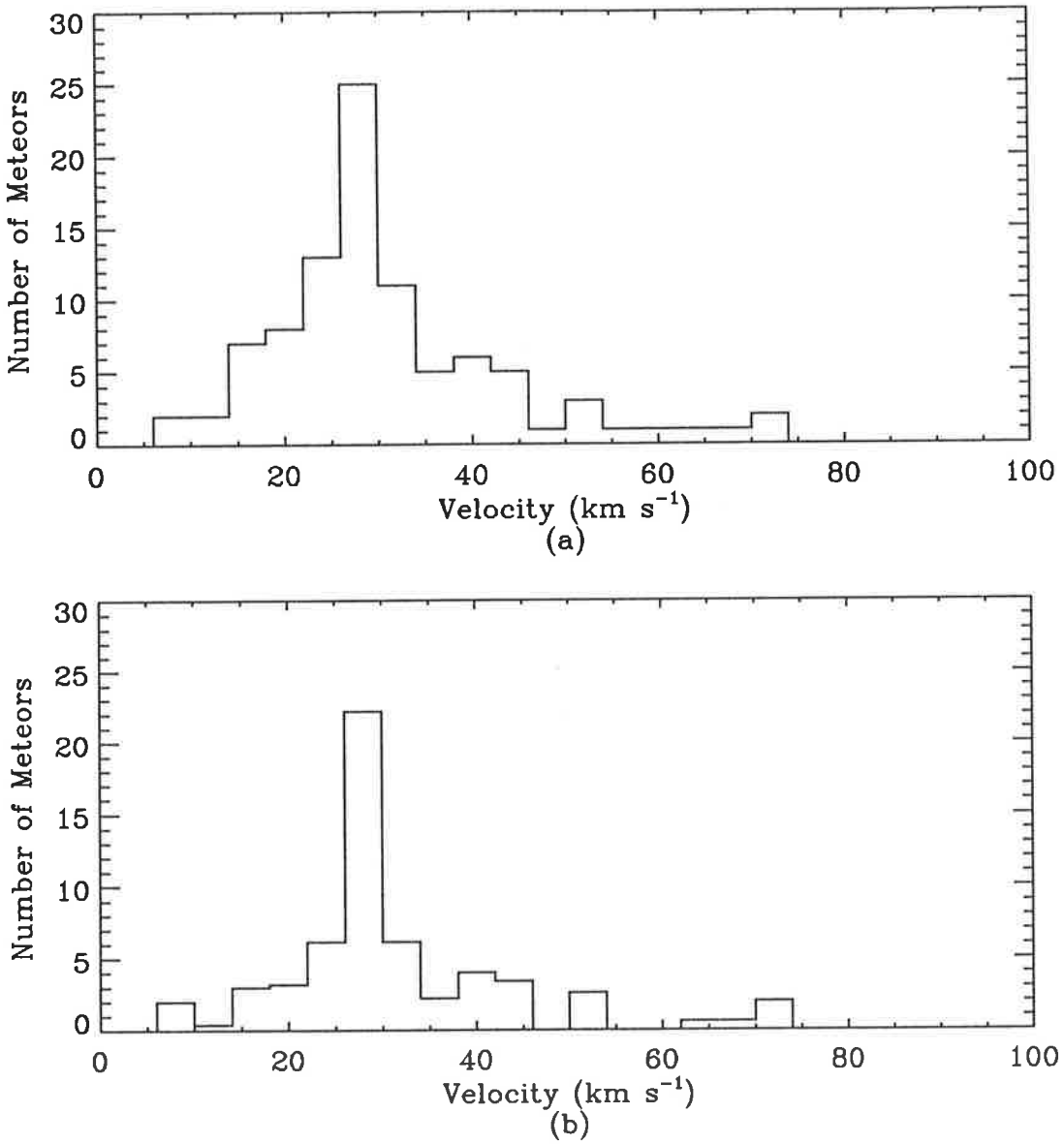

Figure 6.20: No atmosphere velocity distribution of the meteors observed during the time of passage of the θ-Ophiuchids meteor shower. The meteoroid velocities were corrected for deceleration using classical ablation theory (see text). Panel (a) displays the velocity distribution for all the meteors observed during the time of passage of the shower. In panel (b) the background velocity distribution has been subtracted, but apparently not sufficiently.

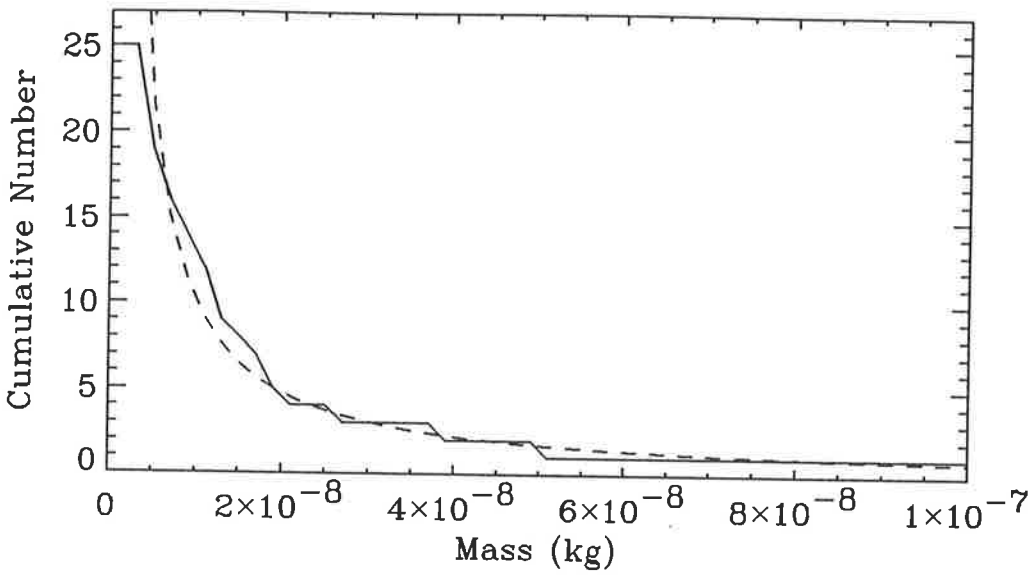

Figure 6.21: Cumulative mass distribution of the θ-Ophiuchids meteor shower (solid line) and the function $f(x) = x^c$, where $c = -1.1$ (dashed line).

background velocity distribution has been subtracted (although apparently not sufficiently). The peak initial velocity of the shower meteors occurs in the $28\,km\,s^{-1}$ bin.

6.4.7 The mass distribution of the θ-Ophiuchids

The method used to obtain the initial mass of the ablating meteoroids was explained in previous section and is the same process used to obtain the initial velocity. Figure 6.21 shows the initial mass distribution of the meteors detected during the time of passage of the θ-Ophiuchids with initial velocities in the range from 26 to $30\,km\,s^{-1}$ (*i.e.* the peak bin in the initial velocity distribution). The dashed line displays the function: $f(x) = x^c$, where $c = -1.1$ in this case. A value of -1.1 for c, gives the best fit to the data, thus the cumulative mass index for the θ-Ophiuchids over the mass range 1×10^{-9} to $5 \times 10^{-8}\,kg$ is -1.1.

Figure 6.22a shows the observed mass distribution of the remaining meteors (*i.e.* all those from outside the velocity range 26 to $30\,km\,s^{-1}$) from the time of passage of the θ-Ophiuchids. It is clear that the mass distribution is different to that in Figure 6.21, also the function $f(x) = x^c$ does not fit the data well for any value for c although a value of -0.6 gives the best fit. The reason for this is that these meteors are probably sporadics, whereas in Figure 6.21, most of the meteors are shower meteors. Sporadics meteors have a broad radiant distribution and are detected over a large area of the response function while the shower meteors are active over only a small portion of the meteor response function of

the radar (*i.e.* where the shower radiant crosses the response function). Hence, for shower meteors mass selection effects due to where the meteor is detected in the response function, are easily taken into account in the manner described in the previous section. Sporadics are not able to be corrected for mass selection effects in this manner, so that Figure 6.22a displays a mass distribution significantly corrupted by the polar diagram of the antenna. However, the response function may be employed to model the mass distribution expected to be observed by the radar for a given cumulative mass index. The dashed line in Figure 6.22a is the modelled mass distribution for an input cumulative mass index of -0.9, and one may observe that it agrees extremely well with the data.

The modelled mass distribution was obtained as follows. Recall from Chapter 4, the minimum detectable initial mass is required to be calculated for each radiant position over the sky, over all angles Φ in the echo plane and over all heights. A mass index was assumed and integration over the echo plane and height was carried out. This process is repeated here with a further step: convolution with the sporadic meteor radiant distribution at the time and date of observation. The number of meteors above a given mass which are expected to be detected are then binned according to the minimum detectable mass and thus the mass distribution expected to be observed by the radar is found. Note , integration of the response function over a suitable velocity distribution was also performed.

While the following is apparent from the previous discussion, it is reiterated here that Figure 6.21 displays the *actual* mass distribution of the shower meteors, whereas Figure 6.22a displays the mass distribution of the 'background' meteors as *observed* by the radar (*i.e* a mass mass distribution corrupted by the antenna polar diagram), and this may be modelled with the radar response function. Thus, the mass distributions of shower and sporadic meteors have been treated in a different manner.

Although the observed mass distribution displayed in Figure 6.22a has a modelled cumulative mass index of -0.9 and is most likely due to sporadic meteors, one must take care in interpreting this diagram as the contributing meteors were all detected during the passage of a shower and only certain velocities were selected. Thus, it is probably not entirely correct to say that this distribution is representative of the background distribution. For this reason, in Figure 6.22b the mass distribution of the meteors observed by the radar from an hour to half an hour prior to the passage of the θ-Ophiuchids is displayed. Again the dashed line is the model distribution obtained from the response function with an input cumulative mass index of -0.9, and is the best fit to the data.

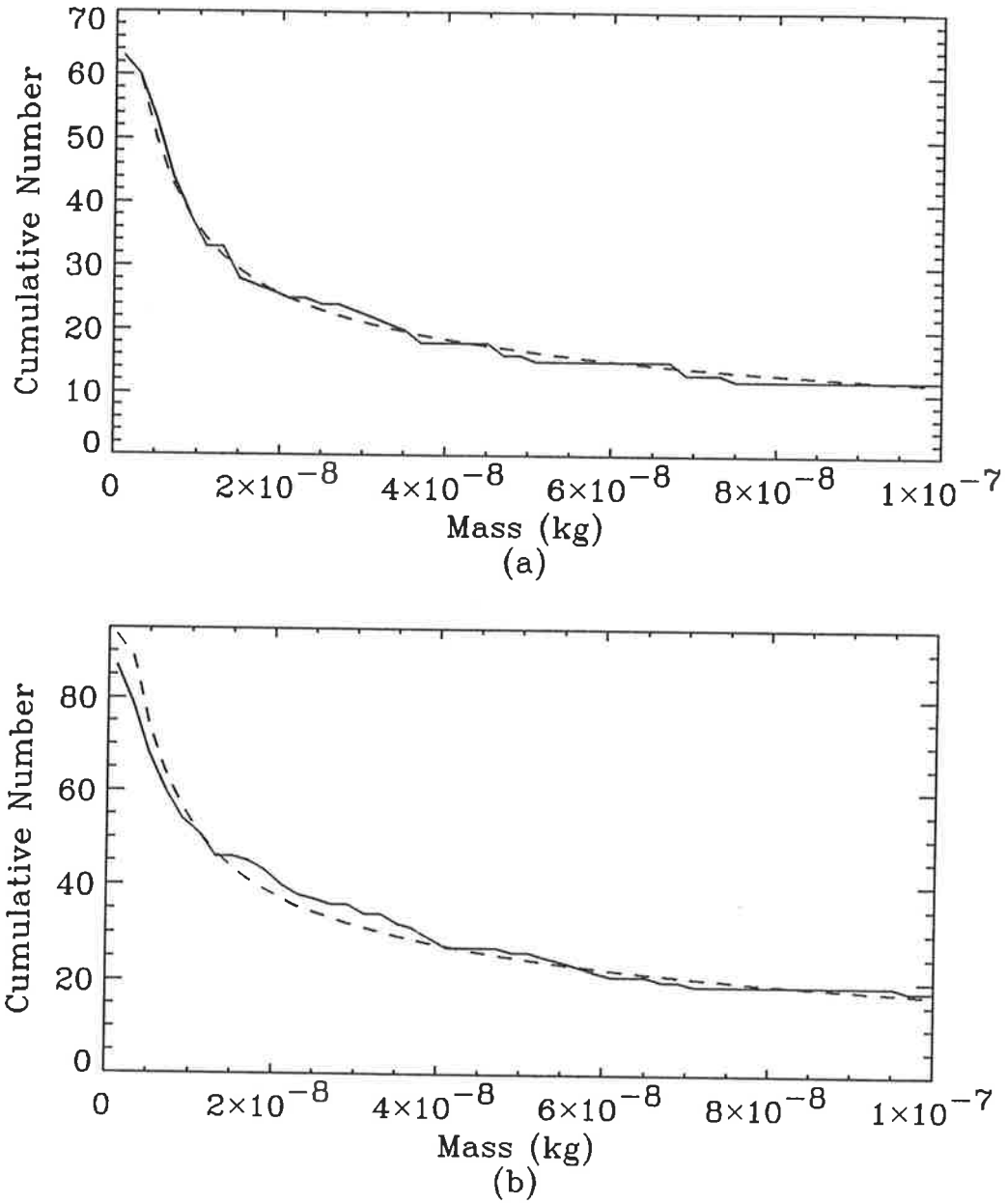

Figure 6.22: Observed mass distributions (solid lines) for (a) meteors detected during the time of passage of the θ-Ophiuchids meteor shower with initial velocities less than 26 $km\,s^{-1}$ and greater than 30 $km\,s^{-1}$ (i.e. meteors not associated with the shower), and (b) meteors observed from one hour to half an hour prior to the passage of the θ-Ophiuchids. In each case the dashed line is the best fit to to the data obtained from a model (see text for details), the input cumulative mass indices for the models were -0.9 in both cases.

It is clear then that the background sporadic meteors, around the time of passage of the θ-Ophiuchids meteor shower, have a cumulative mass index of -0.9 which agrees with previous observations at this mass range (see *e.g.* *Hughes*, 1973 and Chapter 4 for a brief discussion). Therefore the θ-Ophiuchids are observed to have a similar cumulative mass distribution to the background sporadic meteors.

The fact that the θ-Ophiuchids was found to have a similar cumulative mass distribution to the background sporadics, at the mass range where the VHF radar observes meteors, is an important result. If, for example, the cumulative mass index was closer to -2 at this mass range (as for many showers), then the θ-Ophiuchids probably would not have been detected by this radar. This will be discussed further in Section 6.5. One may postulate that because the θ-Ophiuchids has an abundance of small meteoroids, it has not been in existence long enough for these particles to be perturbed out of the stream's orbit, leaving only the larger meteoroids. Thus one may conclude that the θ-Ophiuchids is a relatively young meteor shower.

6.4.8 Conclusions

During early June 1994, significant meteor shower activity was observed at around 0600 hours LST. This was found to be consistent with the θ-Ophiuchids being active. Other meteor showers which occur during May, June or July are not expected to produce bursts of activity at around this time on the days in question. Thus it would appear that the observed increase in activity was due solely to the θ-Ophiuchids. The shower was active from the 6^{th} to the 14^{th} June; this is 2 days earlier than what is listed by *Cook* (1973). Also it was noted that the shower was not active on every day during this period, and this was attributed to the particles within the meteoroid stream not being uniformly distributed. Meteor shower rates observed in the narrow beam of the radar are expected to be subject to the non-uniformity of particles in a given meteoroid stream, thus the finer structure of the stream is being probed (although at this stage no useful information about this is able to be deduced).

It was noted that the shower activity comprised two temporally close bursts (some 25 min apart). This was attributed to the θ-Ophiuchids having two closely associated radiant centres whos coordinates were determined However, due to the ambiguity in associating each burst of activity with the correct burst in the alternate direction for the antenna beam, two equally likely sets of coordinates were obtained. These coordinates in the (R.A., dec.) coordinate frame are: (262.3°,−29.4°) and (267°,−28°) for the first possibility, and (267.3°,−22.4°)

and (265.5°,−32.6°) for the second. It was impossible to distinguish which set were the true coordinates. However, in both cases the average position of the two centres of activity agreed very closely with the radiant position as listed by *Cook* (1973).

The velocity of the shower meteoroids was calculated using the new technique developed in Chapter 5 and a velocity distribution obtained. The distribution exhibited a large peak above the background sporadic meteors (as expected for a shower) at about $24\,km\,s^{-1}$. This value represents the mean velocity of the shower meteors observed in the atmosphere. Attempts were made to account for meteoroid deceleration and these led to velocity estimates of about $26.4\,km\,s^{-1}$ at the onset of ablation, and $26.8 \pm 0.3\,km\,s^{-1}$ for the "no-atmosphere" or initial velocity.

The cumulative mass distribution of the shower meteors and the observed mass distribution of the background sporadics just prior to the passage of the shower were obtained. The mass distributions for the two cases were required to be treated differently. A geometrical approach involving the response function was employed to correct any corruption of mass distribution of the shower meteors due to the polar diagram of the radar antenna beam. Thus, the actual cumulative mass distribution of the shower meteors was able to be obtained, and a cumulative mass index of -1.1 was found for the θ-Ophiuchid meteoroid stream. It was not possible to perform this correction for the background sporadic meteors, but the meteor radar response function was employed to model the observed mass distribution of the sporadics. It was found that a input cumulative mass index of -0.9 gave the best fit of the model to the observed sporadic mass distribution. Using these results it was postulated that the θ-Ophiuchids is a relatively young shower where few of the small particles have been perturbed out of orbit.

6.5 Limitations and Advantages of the Technique

6.5.1 Identification of an anomaly

It is clear from the results presented earlier this chapter that the technique developed to observe meteor showers was successful in the detection of two showers *viz.* the June Librids in 1992 and the θ-Ophiuchids in 1994. The observations of the θ-Ophiuchids with the upgraded radar were particularly successful with velocity and mass distributions able to be obtained. It is of interest to note that previous observations of the θ-Ophiuchids indicate that it is a weak shower (see *e.g. Southworth and Hawkings*, 1963; *Lindblad*, 1971a, 1971b;

Cook et al., 1973), yet the observations presented in this chapter show that the shower is quite strong.

In stark contrast to the success of these observations is the non-detection of traditionally intense meteor showers, in particular the daytime-Arietids, the ζ-Perseids and the δ-Aquarids. There appears to be an anomaly: why are so-called weak showers detected, one of which appears quite intense, yet traditionally intense showers are not? An explanation is required, and again the radar response function is employed. Before this is done, a discussion on the variation of the mass index s of shower and sporadic meteors is required.

6.5.2 Previous measurements of the mass indices and incident fluxes for shower and sporadic meteors

It is assumed that the mass distribution of meteors is described by a power law, and this is justified from observation. The mass index is the exponent in the differential inverse mass power law, thus if $\nu(m)$ is the number of meteors incident in the Earth's atmosphere with masses between m and $m + dm$ the differential mass law is:

$$\nu(m) = K_1 m^{-s} , \tag{6.9}$$

where K_1 is a constant. Integrating this over mass, one obtains the usual cumulative mass law $N(m)$:

$$N(m) = \int_m^\infty K_1 m^{-s} dm = K m^{1-s} = K m^c , \tag{6.10}$$

where K is a constant and $c = 1 - s$. While these two laws are obviously equivalent, previous researchers used the differential (or incremental as it is sometimes referred to) form more often.

The work of *Weiss* (1961, 1963), examined the mass distributions for sporadic meteors and three showers (δ-Aquarids, η-Aquarids and Geminids) over three different radar magnitude ranges. *Weiss* summarises his results in a table which is reproduced here in Table 6.5 where the radar magnitude is related to the maximum electron line density of the meteor trails by the standard expression:

$$M_R = 40 - 2.5 log_{10} q , \tag{6.11}$$

and q is maximum the electron line density of the trail ($electrons/m$). *Hughes* (1978) found from summarising meteor data that $q\,(electrons/m)$ and $m_\infty\,(g)$ may be related via the

Shower	Mass index s (c)		
	$7.5 > M_r > 6.0$	$2.5 > M_r > 1.0$	$1.0 > M_r > 0.0$
η-Aquarids	1.6 (-0.6)	1.4 (-0.4)	2.0 (-1.0)
δ-Aquarids	1.5 (-0.5)	1.9 (-0.9)	2.7 (-1.7)
Geminids	1.5 (-0.5)	1.7 (-0.7)	2.7 (-1.7)
Sporadics	2.0 (-1.0)	2.5 (-1.5)	2.5 (-1.5)

Table 6.5: Values of mass distribution exponents s reproduced from *Weiss* (1961, 1963)

following general expression which is independent of velocity:

$$log_{10}q = 16.58 + log_{10}m_{\infty} \ , \tag{6.12}$$

and by using this expression the mass range over which *Weiss* observed meteors may be found. This was from 2.6×10^{-7} to $2.6 \times 10^{-4} kg$, or in terms of electron line density, from 1×10^{13} to 1×10^{16} $electrons/m$, where the upper end extends well into the overdense regime. Note that the mass index which *Weiss* observed for sporadic meteors brighter than +2.5 mag. (mass greater than 2.6×10^{-5} kg) agrees with the optical results for sporadic meteors in this range (see *eg. Hughes*, 1978). The range of radio magnitudes that the Buckland Park VHF radar is able to observe meteors extends from +13.6 to +6.1 mag. Thus the Buckland Park VHF radar is able to observe meteors some 6 magnitudes fainter than those detected by *Weiss*. One would expect, from the trends shown by *Weiss's* results, that at these fainter magnitudes, the mass indices of these showers would decrease further. This is a trend that is exhibited by many other showers. Consider Figure 6.23 (reproduced from *Elford*, 1967) which summarises the results of mass index measurements of various showers by *Browne et al.* (1956), *Weiss* (1961) and *Kaiser* (1961). This diagram clearly shows that at fainter magnitudes, the mass index these showers decreases to values much lower than that of the sporadic meteors. *Elford* states that for magnitudes greater than +8 all the showers have a value for the mass index well below that of the sporadics (s=2.0) and thus as the magnitude limit is extended to fainter meteors these showers must become swamped by the sporadic background.

In Figure 6.24, are summarised incident flux measurements for the sporadics and three showers from results published by *Elford* (1964), *Kaiser* (1953 1955, 1961), Lebedinets (1964) and Weiss (1957b). Clearly, at fainter magnitudes, the flux of the sporadics is greater and increases much more rapidly than the shower meteors listed. If one was to extrapolate the shower measurements to the limiting radio magnitude of the Buckland Park radar (+13.6

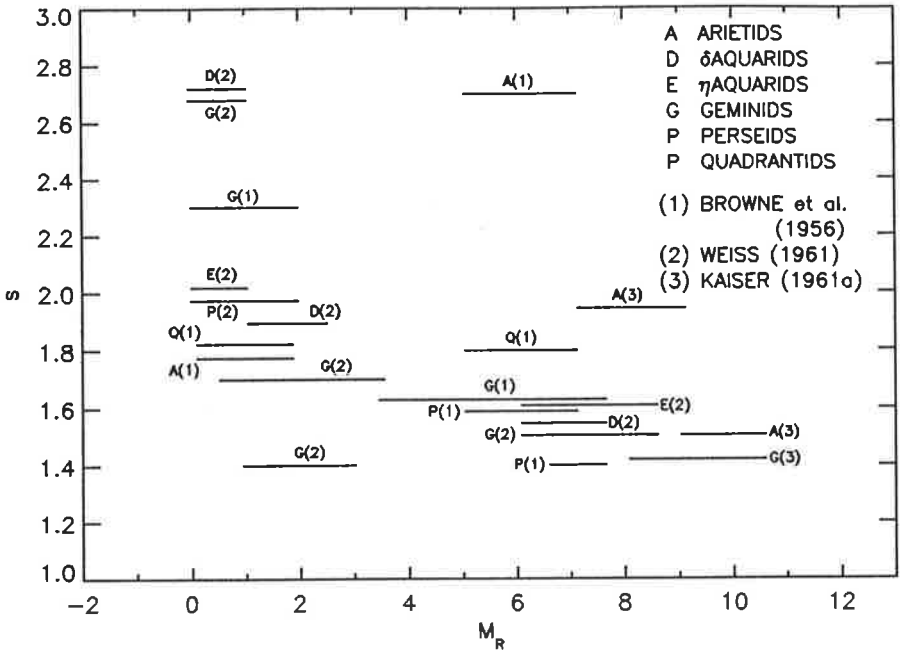

Figure 6.23: Values of the mass index s, for six meteor showers. The length of the line indicates the range of radio magnitudes appropriate to each determination (from *Elford*, 1967).

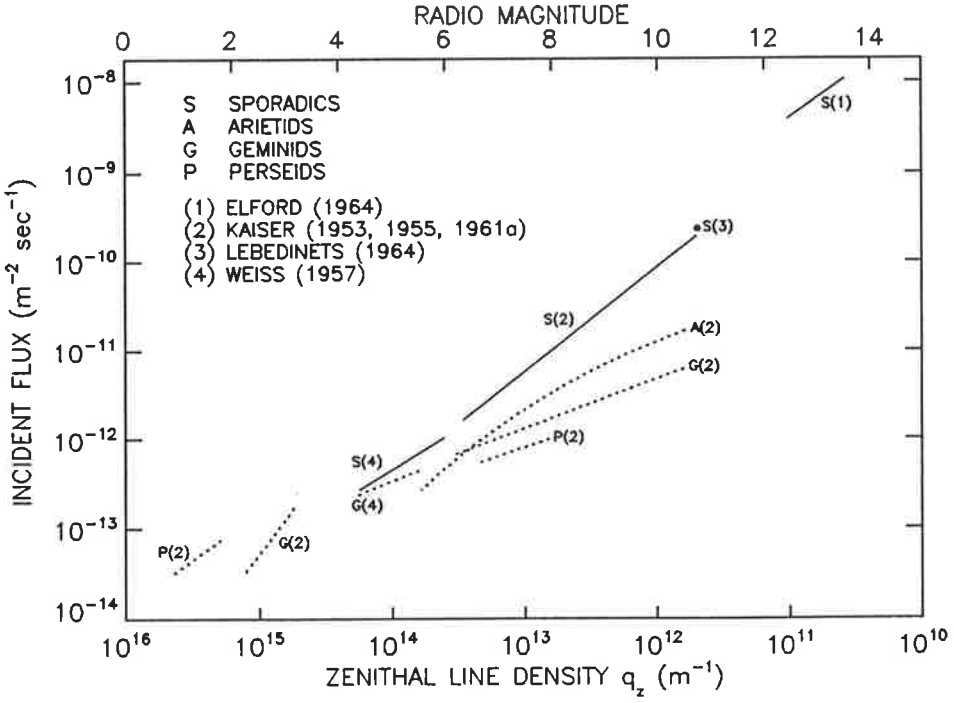

Figure 6.24: Mean incident flux over the whole Earth of meteoroids capable of producing zenithal electron line densities greater than q_z. Solid lines, sporadic flux; broken lines, shower flux (from *Elford*, 1967).

mag.), the sporadic flux is almost three orders of magnitude greater than the flux of the showers. Thus, these showers would not be detected by the Buckland Park VHF radar.

6.5.3 Calculation of the expected rate of the δ-Aquarids relative to the sporadic background

As a detailed test of the argument put forward in the previous section, the expected response of the δ-Aquarids with respect to the sporadic response will now be modeled for the VHF radar. This requires the response function calculation to be performed with an appropriate value of the cumulative mass index c. The results obtained by *Weiss* (1961, 1963) for the mass index will be used with the following assumptions: for $+6.0 > M_r > +2.5$ the mass index will be taken to be the average of the adjacent magnitude ranges (thus $c = -0.7$); and for $M_r < 7.5$, the mass index will be taken to be the value of the previous magnitude range (*i.e* $c = -0.5$). These assumptions are the best that can be made with the information available. The second assumption probably overestimates the value of the mass index for $M_r < 7.5$, given the trend for the mass index to decrease at fainter magnitudes. Thus the expected response obtained for the δ-Aquarids constitutes an upper limit.

The constant of proportionality in the cumulative mass law, K (see equation 6.10), is also required. As the interest is only in the expected response of the δ-Aquarids with respect to that of the sporadics, a value of K for the shower relative to the sporadics is only required, and this shall be denoted K_r. In Chapter 4 it was shown that incident flux $\mathcal{F}$, of meteoroids was given by:

$$\mathcal{F} = \pi K m^c \,, \tag{6.13}$$

thus the incident flux of the δ-Aquarids relative to the sporadics (denoted by $\mathcal{F}_r$) may be found and is given by the following equation:

$$\mathcal{F}_r = K_r m^{(c_a - c_s)} \,, \tag{6.14}$$

where c_a and c_s are the cumulative mass indices of the δ-Aquarids and the sporadics respectively. *Weiss* (1957b), found that the flux of the δ-Aquarids above a limiting electron line density of $10^{-14}\, electrons/m$ was about 40% of the sporadic flux. The corresponding radio magnitude is $M_r = +5.0$ mag. Using 6.14 and the assumed value for c_a of -0.7 at this magnitude, K_r is found to be 18.9. As c_a is assumed to be constant over the range $+6.0 > M_r > +2.5$, K_r is assumed to be constant also. $\mathcal{F}_r$ may be extrapolated down to $M_r = +6.0$ mag., and if this is done a value for $\mathcal{F}_r$ of 0.3 is found. Equation 6.14 is again

M_r	Mass range (kg)	Mass index c_a	Reference[a]	K_r	$\mathcal{F}_r$[b]
$< +7.5$	$< 2.6 \times 10^{-7}$	-0.5	assumed	292.0	0.15
+7.5 to +6.0	2.6×10^{-7} to 1.0×10^{-6}	-0.5	*Weiss* (1961)	292.0	0.30
+6.0 to +2.5	1.0×10^{-6} to 2.6×10^{-5}	-0.7	assumed	18.9	0.80
+2.5 to +1.0	2.6×10^{-5} to 1.0×10^{-4}	-0.9	*Weiss* (1961)	2.3	0.92
+1.0 to +0.0	1.0×10^{-4} to 2.6×10^{-4}	-1.7	*Weiss* (1961)	0.9	4.69

[a]Assumed values of c_a have interpolated from *Weiss* (1961).
[b]Relative cumulative flux above the upper mass limit of the given mass range.

Table 6.6: Values of the mass index used in the calculation of the expected response of the δ-Aquarids. Values of K_r and $\mathcal{F}_r$ are also tabulated.

used, but now the value of c_a is -0.5, and K_r is calculated to be 292.0 for $M_r < +6.0$ mag. This process is extended to the other mass ranges, establishing appropriate values of K_r at each step. Table 6.6 summarises the values of the mass index and K_r for each magnitude range and also gives the corresponding mass range (obtained from Equations 6.11 and Equations 6.12). The appropriate values for the mass index and K_r are then used in the response function calculations. The maximum expected response of the δ-Aquarids was found to be about 20 times smaller than the expected sporadic response at the same time.

Now that the response function of the δ-Aquarids relative to the sporadic response has been calculated, the expected number of shower meteors detected by the VHF radar, relative to the expected number of sporadic meteors, may be obtained. First the expected rate of the δ-Aquarids is calculated as described earlier in this chapter. The rate is then integrated over the period of time where the rate is at least 0.5 times the maximum value (about 20 min in duration). The total number of sporadic meteors are found over this period of time by integrating the expected rate of the sporadics over the relevant times. The expected rate of the sporadics was found by convolving the response function for the sporadics with the sporadic radiant distribution as described in Chapter 3. During the time of passage of the δ-Aquarids, on 29^{th} July 1994 (date of maximum activity as given by *Cook*, 1973), it was calculated that 8 times more sporadic meteors were expected to be detected than shower meteors. Thus, it is not surprising then that the δ-Aquarids were not detected with the Buckland Park VHF radar. Of the 15 to 20 meteors that were detected during the time of passage of the shower each day, only about 2 may be attributed to the δ-Aquarids.

6.5.4 Discussion

Clearly, from the discussions in this section, the mass range of meteors detectable by a meteor radar is very important in determining if a given shower will be detected. Meteor radars that observe meteors in the small mass range (say 1×10^{-9} to $1 \times 10^{-6}\,kg$) are unable to detect those showers which contain few small meteoroids as the sporadic meteor echoes swamp the shower meteor echoes. Examination of the mass index of a given shower helps to identify whether it will be able to be detected. If the mass index is much smaller that the sporadic mass index over the mass range where the radar observes meteors, then detection of the shower is unlikely. Modeling of the echo rates using the meteor radar response function, allows an estimate of the probability of the detection of the shower.

There is one situation where a shower may be detected even when it is weak compared with the sporadics. It the velocity of the shower meteors is high (*e.g.* η-Aquarids, Orionids) one might see an increase in the velocity distribution at high velocities. These showers might show up by the statistical removal of the background. An improved technique of shower detection is suggested where the rate and velocity data are examined in conjunction, possibly in the form of a two dimensional histogram.

Generally, it is observed that the sporadic mass index is constant over the range where most radars detect meteors, whereas the mass index for showers decreases at small masses thus indicating that showers are generally comprised of relatively larger particles. There are of course exceptions, for example the θ-Ophiuchid meteor shower was found to have a mass index similar to the sporadics in the small mass range. It may be postulated that the showers with few small meteoroids have had the smaller particles perturbed out of orbit and are thus older showers. Where this process has not had time to take effect, the showers, such as the θ-Ophiuchids, are probably younger.

Given that there appears to be two populations of meteor showers, those that have an abundance of small particles and those that don't, this immediately suggests that a range of meteor radars are required to study all cases. Narrow beam radars that are able to observe meteors in the small mass regime (such as the Buckland Park VHF radar) are excellent tools for studying meteoroids streams which have a large component of small meteoroids, but have limited application for the other showers where there are few small meteoroids. On the other hand, the wide beam meteor radars used in the past which observe brighter meteors are able to detect the showers which are comprised of mainly larger particles and are thus

the appropriate tool to use in the study of these showers.

6.6 Summary

This chapter has been concerned with the observation and study of meteor showers and an overview of previous techniques used to observe showers with meteor radars was given. The technique used to identify meteor showers with the Buckland Park VHF radar was described, and this required the response function of the radar to meteor backscatter to be calculated. The technique was first employed by *Cervera et al.* (1993) and *Elford et al.* (1994), to identify the June Librids in 1992 with the Buckland Park radar. The identification of new showers is also possible with this technique and this was described.

Observations of two meteor showers, the June Librids in 1992 and the θ-Ophiuchids in 1994, with the radar were described. A detailed study of the Librids was not possible due to hardware limitations of the radar system, however upgrades to the radar performed throughout 1993 (see Chapter 2) enabled the θ-Ophiuchids to be studied in detail. Velocity and mass distributions for this latter shower were obtained and it was found that the encounter velocity of the meteoroids agreed well with that given by *Cook* (1973). The cumulative mass index of the θ-Ophiuchids was found to have a value of -1.1, close to the value for sporadic meteors. This, relatively low value, was critical in the detection of the shower. It was also discovered that the θ-Ophiuchids actually has two distinct radiant centres, which to the best knowledge of the author has not been observed before. It appears that previous observations of this shower (*McCrosky and Posen*, 1961; *Southworth and Hawkins*, 1963; *Lindblad* 1971a, 1971b; and *Cook et al.*, 1973) were not detailed enough to establish the existence of the two radiant centres. However, due to a limitation of the present technique it was not possible to identify the radiant coordinates of the two centres of activity unambiguously; the best that could be achieved was to identify two equally likely sets of coordinates for the two radiants.

An apparent anomaly with the technique used to identify showers was noted: the Librids and θ-Ophiuchids are traditionally weak showers, yet the θ-Ophiuchids in particular appeared relatively intense, and traditionally intense showers were not observed at all! This required an explanation and the response function was employed to achieve this end. It was shown that because many showers have a mass index which decreases significantly at lower masses, these showers are swamped by the sporadic background if meteor observations are made in this mass regime, such is the case with the Buckland Park VHF radar. In particular it was

shown that during the time of passage of the δ-Aquarid meteor shower, some 8 times as many sporadic meteors are expected to be observed. The θ-Ophiuchids, on the other hand, was shown to have a mass index of -1.1 (similar to the sporadic mass index) in the low mass range, and it therefore was not swamped by the sporadics. Wide beam meteor radars generally have no problem in observing showers that have few small particles as these radars observe meteors produced from larger meteoroids. The wide beam of these radars means that the shower is observed for much longer periods due to the greater collecting area, and thus high counts are generally obtained for these showers. It was concluded that the appropriate radar system must be employed to observe and study a given shower: narrow beam high gain systems are appropriate for showers that have an abundance of small particles, and wide beam radars for older showers which contain few small particles.

Chapter 7

Conclusion

> And the sign flashed out its warning, In the words that it was forming
> And the sign said, "The words of the prophets are written on the subway walls"
>
> —*Sounds of silence, P. Simon and A. Garfunkel*

7.1 Summary and Conclusions

This thesis has been concerned with the observation and study of meteoric phenomena with the narrow beam VHF radar operated by the University of Adelaide. Although preliminary meteor observations had been carried out with this radar previously (*Steel and Elford*, 1991), in order to carry out further studies, both the transmitting and data acquisition systems were required to be upgraded. The RMS pulse power was increased from $4\,kW$ to $32\,kW$, whilst a new data acquisition system was constructed. In addition, the receiving system and the antenna array required substantial refurbishment.

It was shown in Chapter 3 that the Buckland Park VHF radar had several advantages over traditional meteor radars used in the past. These were the narrow pencil beam, high PRF, and the ability to record in-phase and in-quadrature data allowing the phase information of the echo to be investigated as well as the amplitude. The narrow beam constrains the response of the radar to meteor radiants from a narrow, well defined area of the sky allowing the positions of meteor shower radiants to be accurately determined. In addition, the narrow beam greatly increases the sensitivity of the system, even for low transmitted powers. For example, the Buckland Park radar was able to observe meteors as faint +13.6 Mag. The high PRF of the radar allowed high time resolution data to be obtained. This was important for detailed studies of the observed meteors, accurate determinations of meteor speeds, wind

drifts, and coherently averaging the raw data in the detection stage to allow fainter meteors to be detected. Finally, the phase coherent receivers, which enables the phase information of the echoes to be recorded as well as the amplitude, were vital to the development of a new technique for determining meteor speeds. This new technique proved to be far more powerful and versatile than previous methods.

The data presented in this thesis were collected during 1994 and early 1995, however the new meteor detection system came on line in September 1993. Data from this period were analysed to obtain atmospheric wind speeds in the meteor region using the drift of the meteor trail. The meteor drifts experiment formed part of a campaign, the object of which was the comparison of the winds derived from the meteor drifts with those obtained from the Full Correlation Analysis (FCA) of Spaced Antenna (SA) data with an MF radar situated at the same site. These results were not presented in the main body of this thesis, however see *Cervera and Reid* (1995) and Appendix A.

The meteor radar response function is a key element in the interpretation of meteor echoes collected with the Buckland Park VHF radar, and the derivation of the response function for the VHF system was extended from that of previous researchers (*Elford*, 1968; *Thomas et al.*, 1988). Previous derivations had assumed a constant ionization height profile of the meteors over a given height interval; here classical ablation theory was used to model the ionization profile. In addition, the response function calculation was based upon the cumulative mass distribution of meteors instead of cumulative number of meteors with electron line densities above a given value. As a consequence, the height distribution of meteors was not required for the model. Instead it was possible to obtain the expected height distribution as a function of the initial meteoroid speed. The full response function and expected height distribution were found by integrating over the speed distribution of meteors.

The response function was used to model various situations. For example, it was found that for the usual operation of the radar (beam tilted 30° off zenith), the number of meteors expected to be detected in the sidelobes was about 10%. When the off zenith beam tilt was reduced, the sidelobe response as expected, increased dramatically. The effect of reducing the radar operating frequency was also examined. As expected from *Steel and Elford* (1991), the height distribution peaked at higher altitudes with many more meteors expected to be observed by the lower frequency radars above 100 km.

The response function was used extensively throughout the thesis: (1) the expected height distribution was modelled and it agreed well with observation; (2) the diurnal variation and

the sporadic meteor radiant distribution were modelled at various times of the year; (3) application was made to the observation of meteor showers; (4) the mass distribution of sporadic meteors expected to be observed by the radar was modelled; and (5) finally the response function was also used to develop a new method of weighting shower echoes for the position of the echo in the antenna beam leading to accurate measurements of the mass distribution of shower meteoroids. In Chapter 3, it was shown that the response function could be used together with observations of the diurnal variation in the meteor echo rate to model the sporadic meteor radiant distribution throughout the year as a function of the meteor speed. This has not been possible in the past. Work of this nature is important to the understanding of how the sporadic meteors are distributed around the Earth's orbit, and also their origin.

A case study of the various types of meteors observed was undertaken. These included typical underdense and overdense meteors, rapidly diffusing meteors such that radio reflections were limited to less than a Fresnel zone length of trail, meteor echoes which displayed beating and saturation effects, head echoes, and long duration echoes which displayed severe distortion due to the background atmospheric winds. In the case of the rapidly diffusing meteors, the echoes resembled that of moving-ball targets.

The effects of receiver saturation and coherent averaging of the raw data was examined in detail. The effect of coherent averaging was to increase the signal-to-noise ratio with a reduction in the time resolution being the disadvantage. Through careful consideration of the trade-offs, it was decided that 16 point coherent averaging of the raw data, for the purposes of meteor detection, was appropriate. Once detected the raw unaveraged meteor echo was recorded. Receiver saturation, through a simple model, was shown to have only a minor effect on the phase information of the signal, even though the amplitude was strongly affected. In fact, it was found that even for cases of severe saturation, the phase information was correct at intervals of $\pi/4$; and the actual phase could be interpolated from the saturated signal and this could then be used to recover the amplitude.

A new robust method for the determination of meteor speeds was developed. This technique, which was based on the Fresnel diffraction theory of meteors, used the pre-t_0 phase information of the echo available from the phase coherent receivers, rather than the post-t_0 amplitude Fresnel oscillations used by previous diffraction methods. It was shown that this new technique was almost immune to the effects of diffusion and therefore the selection effects due to the rapid diffusion of high speed meteors ablating at high altitudes

were smaller than with the previous methods. Thus, greater numbers of meteors with large speeds were observed than had been done previously, and about 75% of all meteors observed were able to have speeds determined as opposed to only about 10% in the past (*i.e.* almost a factor of 8 increase in yield). These two features represent dramatic improvements over the previous diffraction methods. In addition, the phase information readily allowed the determination of speeds from weak echoes. This is very difficult, if not impossible, to achieve from analysis of the amplitude information. Thus, the selection biases against slow meteors are also much lower for the pre-t_0 phase technique. The high PRF's available with the radar was crucial in providing high time resolution data which enabled the speeds to be determined with a high degree of accuracy. Typical accuracies in the speed determinations were in the range from ± 0.5 to $\pm 5\%$.

The speed distribution of sporadic meteors was obtained from a data set of over 500 meteor spanning a period of 24 hours. It was observed that more meteors at the low and high ends of the distribution were evident than for previous distributions obtained from radio techniques. This was not surprising given that the velocity selection effects inherent in the new speed determination technique were smaller. The speed distribution was corrected for the various selection effects (such as ionization efficiency) and it was found that the result agreed very well with the corrected Harvard optical distribution over the entire velocity range. This was in contrast to the Harvard radio speed distribution which was up to two orders of magnitude lower than the optical results for the high speed meteors.

From the consideration that slow meteors were readily able to have speeds determined with the pre-t_0 phase technique, the possibility of the observation of meteors produced by the ablation of re-entering space debris was considered. Indeed a few meteors were observed with speeds less than the escape velocity of the Earth, but it was pointed out that this could have been due to limitations in the method used to obtain the initial speed prior to deceleration. Further work and a much larger sample of meteors would be required to show that ablating space debris may or may not be observed as a meteoric phenomenon.

A search for meteors with hyperbolic speeds, and therefore inter-stellar origins, was made with the obtained sample of meteor speeds. However, there was little evidence for them in the data set. Whether the study of hyperbolic meteors is feasible with the Buckland park radar will require further observations using a much larger sample (say 10,000 echoes). It should be noted that the effect of the height ceiling on VHF meteor observations is real and very limiting, with the detection of meteors generally restricted to heights below 100 km.

Thus, high speed meteoroids which ablate high in the atmosphere, are difficult to detect, and therefore it appears unlikely that Buckland park radar would be able to observe a statistically significant sample of hyperbolic meteors with the current setup of the system. However, the possibility of detecting hyperbolic meteors by observing the meteors travelling down the beam of the radar is a possible future application, and a brief discussion is given in the next section.

The observed mass distribution was obtained for the aforementioned sporadic meteor data set. This was found by integrating the equations describing ablation theory up in height until the initial mass was obtained. As this mass distribution was significantly corrupted by the polar diagram of the antenna, the response function was employed to model the expected mass distribution to be observed by the radar for various model mass indices. It was found that an input cumulative mass index of -0.9 gave the best fit to the observed distribution over a mass range of 10^{-9}–$10^{-6}\,kg$, and this value is in good agreement with previous measurements of the cumulative mass index with radar (about -1.0).

Observations of two showers, the June Librids in 1992 and the θ-Ophiuchids in 1994 were described. The narrow beam of the radar was an important feature in the detection and study of these showers. Radars with narrow beams have their response to meteor radiants restricted to a thin strip on the celestial sphere. Thus, from modelling with the response function, the time of passage of a given meteor radiant on a particular day may be accurately determined. A new technique was developed to accurately determine the radiant coordinates of unknown showers, and verify the positions of known ones. This involved the calculation of the response function for East and West pointing beams. The measured time delay between observing a shower in the two beams enabled the radiant declination to be accurately determined. The declination, once known, together with the observed time of passage of the shower then allowed the right ascension to be determined. This technique allowed the radiant position to be calculated to within about 0.5°.

Due to hardware limitations, the June Librids were not able to be studied in detail. However, upgrades to the radar performed throughout 1993 allowed a detailed study of the θ-Ophiuchids in 1994. It was shown that this shower is actually comprised of two distinct radiant centres, which to the best knowledge of the author has not been observed before. This was probably due to a prior lack of sufficiently detailed data on the θ-Ophiuchids. Unfortunately, due to a limitation of the present technique, it was not possible to unambiguously determine the positions of the radiants. The best that could be done was to identify

two equally likely sets of coordinates for the two radiants. The mean radiant position was calculated for both cases, and both mean positions were close and agreed very well with the radiant position determined from previous observations.

The cumulative mass index of the θ-Ophiuchids was found to be -1.1, close to the relatively low value of the sporadic population, and much smaller than for many other showers. The interpretation of this result was that at the θ-Ophiuchids meteor shower is essentially comprised of small particles, associated with a young stream, *i.e* the time frame for its existence not being sufficiently long to allow the perturbation of the small particles out of the stream.

The relatively low value for the cumulative mass index of the θ-Ophiuchids was critical for its detection. The narrow beam high gain antenna system of the Buckland Park VHF radar means that meteors produced from particles with masses as low as $10^{-9}\,kg$ are able to be observed. A consequence of this is that meteor streams which are comprised of primarily large particles are swamped by the sporadic background. For example it was calculated that the δ-Aquarids, a traditionally strong shower, had an expected rate some 8 times lower than the sporadics during the time of its passage. It was therefore not surprising that the radar did not discriminate this shower. The wide beam radar systems used in the past were able to observe these showers as the lower gain caused the mass limit to be much higher, and therefore these showers were not swamped by the sporadic population. The wide beams also allowed the showers to be observed for much longer (hours as opposed to about 20 min with the Buckland Park radar) and therefore high rates were obtained. However, these radars were not able to observe the low masses that the Buckland Park radar is capable of, and therefore the younger showers were not as well studied. It was therefore concluded that the appropriate radar system must be employed to study a given shower: narrow beam high gain systems for young streams with an abundance of small particles, wide beam radars for older streams which contain few small particles.

7.2 Further Work

In developing the response function of the Buckland Park VHF radar, the ionization profile of meteors as given by classical ablation theory was used. Classical ablation theory ignores the effects of thermal conduction, radiation, and heat capacity of the meteoroid; and the model of the meteor ionization profile could be improved by including these effects. While the

inclusion of these effects is simple in practice, current limits on the available computational time prohibits an iterative solution. An approximate analytical expression is required to be developed as was done for the classical ablation model in Chapter 4.

The effect of the geomagnetic field on the diffusion of the meteor trails was ignored, and this becomes important above heights of 95 km. The effect of the geomagnetic field above these heights is to suppress the radial diffusion of the trail orthogonal to the direction of the magnetic field lines. Thus, if the geometry of the situation is such that the radar observes the meteor trail in the direction where its diffusion has been suppressed, the lifetime of the trail is longer in duration than that expected if the magnetic field is not present. This effect is required to be considered and incorporated into the response function model. However, with a height ceiling of $\sim 100\,km$, the changes to the response function are only expected to be marginal.

Second order effects, such as the model of overdense meteors and the polarization of the radio waves with respect to the trail may also be considered. The model of the overdense meteors assumed a critical electron line density of $10^{14}\,electrons/m$ below which the meteor trails were considered fully underdense, and above fully overdense. However, *Poulter and Baggaley* (1977) show from a full-wave treatment of scattered radio signals from meteor trails that the transition from the underdense to the overdense case is a gradual one taking place over electron line densities from 10^{13} to $10^{15}\,electrons/m$. By considering the reflection coefficients calculated by *Poulter and Baggaley*, a more accurate treatment of the overdense case may be made. However, this is only a second order effect as the radar generally observes meteors well into the underdense regime (limiting electron line density of $\sim 10^{10}\,electrons/m$). The reflection coefficients may also be used to treat different polarizations of the radio waves with respect to the meteor trail, but again at low electron line densities this effect is small.

In Chapter 3 it was shown from the analysis and interpretation of the observed diurnal variation in meteor echo rates using the response function, that the sporadic radiant distribution during the period of observations, could be modelled. As expected, the preliminary results from this chapter showed that although the same features were present, the sporadic radiant distribution varied around the orbit of the Earth. These results, while demonstrating the technique, were limited in scope: only three months of the year were covered and there was no discrimination in terms of the speeds of the meteors. A data set of meteor observations spanning almost an entire year exists; and while the initial motivation for these long term observations was for the purpose of atmospheric wind determinations using the

meteor drifts technique, this data set may be analysed to produce models of the sporadic radiant distribution for each month of the year and for several speed regimes. Work of this nature is particularly important as the distribution of sporadic meteors around the orbit of the Earth may be described in better detail than has been previously possible.

The response function also lends itself to the investigation of the initial radius of the meteor train. The height distribution of meteor echoes as observed by radar is highly sensitive to the initial radius of the meteor; and as was shown in Chapter 4, the response function may be used to model the expected height distribution. Thus, as the initial radius is an important factor included in the response function calculation, the response function together with the observed height distribution may be employed to measure this parameter. The limited study presented in Chapter 4 supports the expression used by *Thomas et al.* (1988) for the initial radius, although a further investigation involving the examination of the height distribution of the meteors at various meteoroid speeds is desirable. This would enable the initial radius to accurately determined over the range of speeds of the meteoroids.

The speed distribution of sporadic meteors was obtained from only a relatively small sample of meteors. A much larger sample of meteors while giving a much better representation of the speed distribution of the sporadic population, would also allow a search for hyperbolic meteors. However as mentioned in the previous section the height ceiling effect would be a severe limiting factor. The study of the speed distribution for various times of the year (*i.e.* at different points around the Earth's orbit), would probably prove to be a more profitable exercise with the Buckland Park VHF radar.

Clearly the majority of meteoroids ablating in the atmosphere between 80 and 100 km are slow with speeds from 15 to 30 $km\,s^{-1}$. Slow meteoroids, in addition to producing meteors with lower electron line densities, ablate lower in the atmosphere and therefore are generally longer in duration. This suggests that the direction in which investigations into the improvement of the meteor detection criteria may be that of longer coherent integration times. This would increase the sensitivity of the system to weak meteor echoes, with the trade off being the reduced detectability of the high speed meteors ablating at high altitudes. A further possibility is to apply two sets of detection criteria to the raw data; one of which is sensitive to short duration echoes, the other to weak long duration echoes. As the meteor detection algorithm is required to operate in "real–time", the processor would need to be fast enough to handle both sets of detection criteria in a reasonable length of time. A further possibility for the improvement of the detection criteria is that of exploiting the

phase information of the echo as a detection trigger. As was shown in Chapter 3 the phase is a much better indicator of the presence of meteor backscatter, therefore an investigation into how this may be exploited should be undertaken.

The possibility of the detection of space debris was discussed. While meteors with speeds less than the escape velocity of the Earth were detected, it was uncertain whether these were in fact due to re-entering space debris or simply that the method used to correct the measured speed for deceleration was in error. Clearly further work is require in this area to resolve the issue. This would be comprised of two components: (1) improvement of the method of obtaining the initial meteoroid velocity, as discussed at the start of this section, and a careful examination of the validity of its application to slow meteors; and (2) a study of a much larger sample of meteors including observations with smaller off zenith beam tilts and careful interpretation of the results using the response function. From work of this nature it may be possible to estimate the influx of space debris to the Earth. However, it would probably be impossible to obtain the distribution of space debris in Earth orbit; a multi-station meteor orbit radar system would probably be required.

A new technique, which employed the response function, was developed in order to study meteor showers. It was found that the technique was able to determine the radiant of showers to within 0.5° and that the radar was particularly able to observe young streams which contain a large component of small meteoroids. Thus, an observing program designed to detect and study new relatively young meteor showers could be undertaken with the Buckland Park VHF radar employing the new shower radiant determination technique.

Novel meteor observations recently undertaken by *Taylor et al.* (1996) with the Buckland Park radar has shown that meteors may be detected travelling *down the beam* of the radar. Their preliminary results are particularly encouraging with highly accurate (to within 0.3%) velocities able to be determined. Accurate deceleration profiles of many of the meteors are also able to be obtained; and this is particularly important for the determination of the composition of these meteoroids. While the echo rate for meteors detected in this manner is low (typically 40–50 meteors a day), the technique lends itself particularly to the detection of high speed meteors ablating high in the atmosphere. Thus, the study of hyperbolic meteors is a real possibility with this technique. In addition, *Elford and Taylor* (1995) showed that from observation of these "down the beam" meteors using orthogonally polarized antenna arrays, the total electron content along the path of the meteor may be obtained by measuring the degree of Faraday rotation. Further work with the "down the beam" meteors has very

promising prospects.

Finally, a major upgrade to the Buckland Park VHF antenna array, which involves the installation of an orthogonal North/South CoCo antenna array, is underway. This is expected to be completed early in 1996 and will greatly increase the flexibility of the system with the antenna beam able to be pointed in the North and South cardinal directions as well as East and West. One application is in the study of meteor showers, where the shower radiant would be active in the beam of the radar for a much longer period of time. Indeed, with the proposed electronic system for switching in or out a series of phasing cables for each CoCo row, the beam will be able to track the radiant across the sky. Thus, detailed investigations of meteor showers will be able to be made.

Appendix A

On the Meteor Drift Technique and Comparisons with MF SA Wind Measurements

A.1 Introduction

A campaign to compare the atmospheric wind speeds determined from the drift of the meteor trails observed with a VHF radar and those obtained from the Full Correlation Analysis (FCA) of Spaced Antenna (SA) data with an MF radar (at the same site) was initiated on 10 September 1993. The results from this campaign were reported in a publication by the author (*Cervera and Reid*, 1995), but did not appear in the main body of this thesis. A copy of this paper is reproduced in Section A.2. The results from this campaign showed that while the two techniques were in good agreement below 90 km, above 90 km the SA winds underestimated the meteor winds. Several reasons as to why this might be the case were put forward; *e.g.* meteors detected in the sidelobes generally cause the meteor derived wind to be overestimated, and signal saturation in the MF receivers cause the FCA to underestimate the wind.

A second campaign, which involved the University of Colorado, was undertaken from June 29 to July 15, 1994. The objectives of this campaign were twofold: (1) to investigate the effect of signal saturation on the FCA of SA winds and perform a new MF/meteor wind comparison, and (2) to compare two meteor radar systems with the view to improving the wind estimates derived from both of them (*Valentic et al.*, 1996). The results from (1)

have been reported by *Vincent et al.* (1995), and their paper is reproduced in Section A.3. They found that signal saturation in the MF receivers does cause the FCA to underestimate the wind, and this usually occurs above 90 km. *Vincent et al.* conclude that the operating conditions, and the hardware controlling MF SA radars are required to be carefully examined.

Further investigations involving long term comparisons of meteor and MF wind data (about 10 months) are currently underway, and the initial results are promising.

A.2 Comparison of simultaneous wind measurements using colocated VHF meteor radar and MF spaced antenna radar systems

This is a reprint of the paper,

Cervera, M. A., and I. M. Reid, Comparison of simultaneous wind measurements using colocated VHF meteor radar and MF spaced antenna radar systems, *Radio Sci., 30*, 1245–1261, 1995.

Cervera, M. A. and Reid. I.M. (1995) Comparison of simultaneous wind measurements using colocated VHF meteor radar and MF spaced antenna radar systems.
Radio Science, v. 30 (4), pp. 1245-1261, July/August 1995.

NOTE: This publication is included in the print copy of the thesis held in the University of Adelaide Library.

It is also available online to authorised users at:

http://dx.doi.org/10.1029/95RS00644

A.3 Spaced antenna wind measurements: the effects of signal saturation

This is a reprint of the conference proceeding,

Vincent, R. A., I. M. Reid, D. A. Holdsworth, and M. A. Cervera, Spaced antenna wind measurements: the effects of signal saturation, *Wind observations in the middle atmosphere*, CNES–HQ Paris, Proceedings, 1994.

Vincent, R.A., Reid, I.M., Holdsworth, D.A. and Cervera, M.A. (1994) Spaced antenna wind measurements: the effects of signal saturation. In: *Wind Observations in the Middle Atmosphere Workshop 15/18 November 1994, CNES-HQ Paris, Proceedings*.

NOTE: This publication is included in the print copy of the thesis held in the University of Adelaide Library.

Appendix B

Single station identification of radar meteor shower activity: the June Librids in 1992

This is a reprint of the paper,

W. G. Elford, M. A. Cervera and D. I. Steel, Single station identification of radar meteor shower activity: the June Librids in 1992, *Mon. Not. R. Astron. Soc., 270*, 401–408, 1994.

Mon. Not. R. Astron. Soc. 270, 401–408 (1994)

Single station identification of radar meteor shower activity: the June Librids in 1992

W. G. Elford, M. A. Cervera and D. I. Steel*
Department of Physics and Mathematical Physics, University of Adelaide, GPO Box 498, Adelaide, SA 5001, Australia

Accepted 1994 April 29. Received 1994 April 22; in original form 1994 January 17

ABSTRACT
The use of a pencil-beam VHF radar to detect low-level activity from weak meteor showers is illustrated. Critical to this technique is a knowledge of the radar response function (a measure of its sensitivity variation with the radiant celestial coordinates). Our observations indicate that the June Librid shower, which had not been observed since 1937, was active in 1992.

Key words: techniques: radar astronomy – meteors, meteoroids.

1 INTRODUCTION

The determination of meteor radiants using a single station radar has been a long-term problem. By the use of such a radar, Clegg (1948) showed how, recognizing the specular reflection condition, the radiant of a shower could be found from the temporal change in the range of echoes obtained on a narrow-beam system, and this method was exploited by, for example, Hawkins & Almond (1952). Clegg altered the radar beam azimuth from day-to-day in order to determine the radiant, meaning that only showers lasting for several days could be studied, but Aspinall, Clegg & Hawkins (1951) showed how two fixed antennas directed to azimuths symmetric about the east–west direction could be used to determine radiants from a single day's data. Various other researchers have used the range-time envelope technique (for example, see Weiss 1955, 1960; McKinley 1961; Belkovich & Pupyshev 1968; Hughes 1972), but it suffers the severe drawback that weak showers are difficult to differentiate from the sporadic background, and concurrent showers are almost indistinguishable. A good knowledge of the antenna patterns of the radar is crucial. An improved method of analysis of the Clegg data, particularly applicable to occasions of high echo rate, was introduced by Keay (1957).

With a multistation system it is possible to determine the radiants and speeds of individual meteors, and thus to derive their heliocentric orbits, but such systems are costly, complex, and difficult to run (for example, see Davies & Gill 1960; Nilsson 1964; Andrianov, Pupysev & Sidorov 1970; Cook et al. 1972; Gartrell & Elford 1975). Such orbital systems were largely based upon the method of Gill & Davies (1956), which also made use of the condition of a specular reflection orientation of the meteor train being necessary to obtain a meteor echo. A variant upon this is the method of Baggaley et al. (1994), which constrains the radiant plane by the use of a beam narrow in azimuth but wide in elevation; the elevation angle then being independently measured by means of a phase pair of antennas.

The single station approach was reconsidered by Jones & Morton (1977) and Jones (1977) who showed, using visual and simulated data, that weak stream radiants for faint meteors could be determined monostatically, see also Steyaert (1984). Morton & Jones (1982), Jones & Morton (1982) and Jones (1983) developed this technique and applied it to an imaging radar, which was then used to produce meteor radiant maps, whilst Poole & Roux (1989) showed that, by using an all-sky radar rather than a narrow-beam system, astigmatic distortions in the radiant map produced could be alleviated. Returning to optical meteor data, which do not have the specular orientation restraint, Duffy, Hawkes & Jones (1987) used single station TV meteor data to show that shower parameters could be defined even for count rates as low as 5 per cent of the background.

Keay (1957) showed that the detection of showers and the measurement of their radiant coordinates, using the Clegg method, could be significantly improved by analysing only those echoes that occurred in a limited range interval centred on the most probable range. Plots of this limited echo rate as a function of time give 'partial rate curves', and the times of the maxima obtained with two antennas directed to different azimuths yield the radiant. As meteor shower echoes occur over a restricted height range, the selection of echoes from a limited range interval is equivalent to a reduction in beamwidth in the vertical plane. However, the application of the partial rate method of analysis requires echo rates in excess of 50 per hour.

*Also with the Anglo-Australian Observatory, Coonabarabran, NSW 2357, Australia.

The improvement in the resolution in meteor radiant measurements by Keay's modification of Clegg's method indicates that reduction in antenna beamwidth is a key factor. An extreme example is the observations of meteors carried out with the Millstone Hill radar at a frequency of 440 MHz by Evans (1965). The radar beamwidth was 2°.1 full-width half-power (FWHP), and shower meteors were selected by directing the beam at 90° in azimuth from the known shower radiant.

The original analysis of Clegg required the calculation of range-time envelopes for all possible showers, while in Keay's analysis theoretical rate-time curves were calculated from the range-time envelopes. In both cases, integrations were carried out over a region of the celestial sphere where the antennal polar diagram had a significant value.

An alternative procedure for determining rate-time curves was developed by Elford based on the 'response function' of the radar system (Elford 1964; Elford & Hawkins 1964). This latter procedure, discussed in Section 3, is more general than the Clegg/Keay method and is the basis for the analysis of the observations reported in this paper.

2 THE PRESENT RADAR SYSTEM

In this paper we have used data collected using a 54.1-MHz radar situated at Buckland Park (34°38′ S, 138°29′ E), about 40 km north of Adelaide, South Australia. This radar system was constructed in the 1980s for use as a MST (Mesosphere–Stratosphere–Troposphere) probe; details of the equipment are given by Vincent et al. (1987).

The main design criterion for this radar was the determination of winds and shears at 2–20 km altitudes; however, the pencil beam (FWHP ≈ 3°.2) may also be used for some types of meteor observation. Since 1986, we have made measurements of the heights of radar meteors, a program that is continuing with improved time resolution so as to demonstrate that the high-altitude ($h > 105$ km) meteors detected by us with adjacent 2- and 6-MHz radars may also be observed as very short-lived echoes at 54 MHz (Steel & Elford 1991).

In the data collection described here, the radar was run at a pulse repetition frequency (prf) of 1024 Hz and a power of 4 kW, with the beam directed to a zenith angle (z) of 30°, and an azimuth of either E4°N or W4°S.

The antenna used for both transmission and reception is a ~ 80 m × 80 m array of 32 parallel rows of linear antennas, each consisting of sets of crossed-over co-axial dipoles. The beam tilt ($z = 30°$) was achieved by introducing accumulating phase delays of $\lambda/4$ between the antenna rows. Note that the beam zenith angle is much smaller (elevation angle much larger) than that used in conventional meteor radars, which typically have antenna beams directed at elevations of 20°–30° ($z = 60°$–$70°$), and, with prfs of a few hundred Hz, collect data from ranges up to 1000 km or more. Our high-elevation beam limits the meteor count rate (typically ~ 20 per hour) to a value rather lower than is available with such systems, since a much smaller volume of the atmosphere is illuminated, but this geometry is critical in limiting the area of the celestial sphere (i.e. the radiant distribution) that is sampled at any time, since the meteor response function contours are limited in extent, as discussed in Section 3.

Coherent averaging of the signals' output by the phase-sensitive receivers (i.e. separate averaging of the in-phase and in-quadrature signals) over 16 sequential sweeps is carried out, rendering 64 samples per second from each range. Instrumental limitations determined that data could be collected in 42 distinct ranges from 86 to 127 km (i.e. heights from 74 to 110 km for $z = 30°$).

The radar transmitter is at present being upgraded to a pulse power of 32 kW, rendering a limiting radar meteor magnitude of about +8. In addition, an upgraded microprocessor system will allow higher prfs, lower numbers of integrations, and thus time discriminations at the millisecond level, and with the increased power the count rate will be much higher. Also, the present radar has a beam that may be tilted only along the line running from E4°N to W4°S, so that a limited range of declinations are accessible, whereas a planned extension will provide for an antenna array aligned north–south, allowing a much wider declination coverage. A north–south alignment will also put the long axis of the meteor response function (Section 3) along the same direction as the diurnal sweep of the radar across the sky, meaning that a shower radiant will remain observable for rather longer than in the present situation (data presented in Section 4) where the radiant quickly cuts orthogonally across the peak of the response function.

3 RADAR METEOR RESPONSE FUNCTION

If the parameters of a meteor radar system are known with sufficient precision, the theoretical echo rate for a point source radiant of unit strength can be determined for all positions of the radiant in elevation and azimuth. The result of such a calculation is a description of the response of the radar system to a radiant in any position in the sky, and is appropriately called the 'response function' of the system. The term was first used by Nilsson & Weiss (1962), although their calculation was restricted to the elementary case of a system whose response was assumed to be independent of azimuth.

A general procedure for calculating the response function of any meteor radar system was introduced by Elford (1964) and initially applied to a multistation system used in the Harvard Radar Meteor Project (Cook et al. 1972). Subsequently, the method was extended for the Jindalee over-the-horizon surveillance radar in central Australia by Thomas, Whitham & Elford (1988) by including additional propagation modes involving ground and F-region reflections. In the present context, we are only interested in the simplest case of monostatic backscatter.

The calculation of the response function is based on the fact that, for almost all meteor radars, scattering from the trails occurs specularly, so that the echoing points for meteors from a point radiant all lie in an 'echo plane' passing through the station and normal to the radiant direction. The geometry for a simple monostatic backscatter system is shown in Fig. 1, where the radiant is at elevation angle θ_r and azimuth angle ϕ_r, as seen from the radar site, and all possible reflection points P lie in the echo plane $ABCD$. For a given meteor shower, all trails are assumed to have the same height limits, $h \pm \Delta h$, and thus all occur within the strip formed by the intersection of the echo plane and these height limits.

Point P is within an area dS in the echo plane, which is at range R, elevation angle Θ and echo-plane azimuth angle Φ as measured in that plane (see Fig. 1). The rate of detection

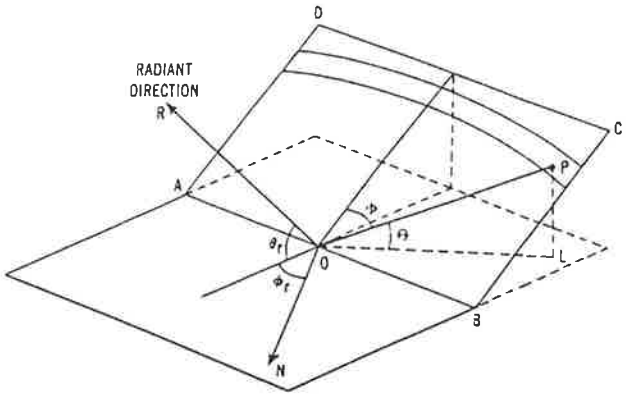

Figure 1. Geometry of the echo plane, from Elford (1964). The radiant direction R is defined by elevation angle θ_r and azimuth angle ϕ_r, relative to the radar site, 0. The reflection point P on the meteor train in the echo plane $ABCD$ is at elevation Θ and echo-plane azimuth Φ, measured directly using the radar equipment. The echo range allows height limits $h \pm \Delta h$ to be defined, shown by the curved strips crossing the echo plane.

of meteors within dS is found by first determining the minimum detectable line density q at this position, and then noting that the meteor flux associated with this line density is given by

$$N(q) = K(q \sec \chi)^c,$$

where χ is the zenith angle of the meteoroid path and the exponent c (which depends upon the meteoroidal mass distribution: see below) has a value of about -1. For the analysis that follows, we can put

$$\cos \chi = \sin \theta_r.$$

The total echo rate, n, is found by integrating over the echo-plane strip:

$$n = \iint N(q)\, \mathrm{d}S.$$

For underdense trails, the minimum detectable line density is given by (see e.g. McKinley 1961)

$$q = 4.5 \times 10^{15} (R/\lambda)^{3/2} (P_R)^{1/2} (P_T G_T G_R \eta)^{-1/2},$$

where R is the range, λ is the wavelength, P_T is the transmitted power, G_T and G_R are the power gains of the transmitting and receiving antennas, respectively, with respect to an isotropic radiator, and P_R is the minimum detectable echo power for the system.

The factor η is the fractional reduction in received echo power due to (i) the finite diameter of any section of the trail consequent on the initial ablation process and the diffusion that occurs during the time required to form the central scattering region of the trail; and (ii) diffusion during the interpulse period. This reduction factor is strongly height-dependent (Steel & Elford 1991).

The area element dS is given by

$$\mathrm{d}S = R\, \mathrm{d}R\, \mathrm{d}\Phi.$$

For a given mean height, h, R can be written in terms of Φ. Thus the summation in the echo plane[1] can be carried out in terms of Φ (Elford 1964; Thomas et al. 1988). The response function is therefore given by

$$n(\theta_r, \phi_r) = K \Delta h \int (G_T G_R)^{-c/2} f(\Phi) (\mathrm{cosec}\ \theta_r)^c\, \mathrm{d}\Phi.$$

The function $f(\Phi)$ is a slowly varying function of Φ, and for a narrow-beam system it can be approximated by a mean value when evaluating the integral in the echo plane.

By carrying out this calculation for every position of the echo plane defined by a grid of radiant points (θ_r, ϕ_r), the response function of the system can be tabulated as an array and thence interpolated to give a contour representation of the function.

The form of the response function is determined chiefly by the antennal radiation patterns represented by G_T and G_R. For the situation where (i) one antenna is used for both transmission and reception, so we can write $G = G_T = G_R$, and (ii) c has the value -1, the response function is

$$n(\theta_r, \phi_r) = K \Delta h \sin \theta_r \overline{f(\Phi)} \int G\, \mathrm{d}\Phi,$$

where the bar implies that the mean value of that function is taken. The above implies that the value of the integral is determined by the area under the curve defined by the section of the polar diagram lying in the echo plane. Thus, in this case, the response function is proportional to the fraction of the transmitted power contained in a thin planar wedge defined by echo planes whose normals have elevations θ_r and $\theta_r + \Delta\theta_r$.

While the antenna polar diagram is the dominant parameter in determining the response function of a meteor radar, the response shows a small but significant dependence on the distribution of the number of meteors as a function of the maximum electron line density in the trails (or the mass of the ablating meteoroids), as defined by the exponent c in the expression for the meteor flux. A comparison of the observed echo rates of a particular shower in selected range intervals with those predicted from a set of response functions with differing mass distribution indices can be used to estimate the mass index for the particular shower (Elford 1968).

For the antenna size and orientation and the beam tilt angle described in Section 2, the resulting meteor response function was calculated and is shown as a contour plot in Fig. 2, as a function of radiant elevation and azimuth. Here the beam was tilted east; for a west-tilted beam, the response function would be identical but rotated by 180° in azimuth. Note that, with a beam *zenith* angle of 30°, the specular reflection condition will lead to a peak (i.e. the location of the radiant with the highest detectability for the radar deployed as above) of the response function at an *elevation* angle of 30°. The azimuth of the peak is at 266° (86° for a west-directed beam), with the asymmetry of the plot being due to the antenna being oriented 4° away from due east–west. It is possible to carry out observations with the beam being switched (by electronically reversing the phase lags) from an easterly to a westerly direction from one minute to the next, so that the passage of a shower through the response function peak may be unambiguously detected since it will occur at one time in one beam and not in the other, with a reversal

[1]The echo-plane procedure was first proposed by Kaiser (1954), who subsequently developed a graphical method for calculating the echo rate: Kaiser (1960).

in this pattern some hours later. This will happen provided that the radiant is not at the periphery of the response function, since the azimuthal extent of the response function as shown in Fig. 2 is ~140° (to the 20 per cent of peak contour), so that the fact that the antennas are not aligned exactly east–west is not significant. In the initial observations described in this paper, however, all data were collected with the radar beam directed east only. Note that the response function traces the locus of the meteor echo plane on the celestial sphere.

We also plot in Fig. 2 three loci indicating the time-dependent positions in this reference frame for three meteor radiants. The central (solid) line refers to the Librid meteor shower (RA = 227°.2, Dec = −28°.3), which was optically observed by Cuno Hoffmeister on 1937 June 8–9, but, to the knowledge of the authors, not since (Hoffmeister 1948; Cook 1973; M. Gyssens & P. Roggemans, personal communication, 1992). The two other loci are for radiants with the same RAs, but Dec = −59° (bottom, dashed line), and Dec = +33° (top, broken line). These are the maximal and minimal declinations that intersect the response function down to a value of 20 per cent of the peak, indicating the region of the celestial sphere over which shower searches may be carried out with the presently available antenna array. On each of these three loci, tick marks show the local time (Australian Central Standard Time: ACST) at which the radiant would reach those topocentric coordinates at the time of year in question (June 7). We note that the passage of a shower radiant through the response function near the peak would take about 25 min across the 20 per cent contour levels, and about 15 min across the 60 per cent contour levels. This tells us how long to expect enhanced count rates for: up to 30 min for a strong shower (compared to the sporadic background) but only 10–15 min for a weak shower. In a more formal manner, we can calculate the expected (normalized) count rate variation with time for a shower as its radiant passes through the response function, and this we have done for the June Librid radiant in Fig. 3. We would expect to detect any activity from this shower almost exclusively around 03:12 ACST.

4 RESULTS

4.1 Was a shower detected?

The results presented here are limited to an initial set of data collected on 1992 June 6–9. We feel that these are worthy of publication, since they indicate that the June Librid shower was active in 1992, having only previously been observed (visually) in 1937.

As aforementioned, these data were all collected with the antenna beam directed solely east, rather than the east–west alternation that would have been optimal regarding shower activity identification (except that then only half the number of meteors would have been detected in that particular beam direction). In Fig. 4 we show, collected into 12-min bins, the number of meteors detected in each of three daily runs starting at 15:00 ACST on June 6, 7 and 8. In each case, 20 hours of data (100 bins) are plotted. Only a handful of meteors occur in most bins, but in reviewing these data we noted an apparent peak at bin number 61 on the first day (10 meteors in that bin), with 5 meteors in that bin on the subsequent two days, equalling the highest rate on those days. The question is whether these peaks are significant, and thus represent an active shower. We have previously plotted and published the June 6–7 data in 10-min bins, under which circumstance the peak is rather more noticeable (Cervera, Elford & Steel 1993), although in the present analysis we have rejected two of the 'meteors' included therein as being possible noise spikes. Bin 61 is centred on 03:12 ACST in each plot in Fig. 4.

We next plot, in Fig. 5, the superimposed data from three days, with a shift in time between the days so as to accommodate the expected sidereal shift in the radiant (e.g. Beech

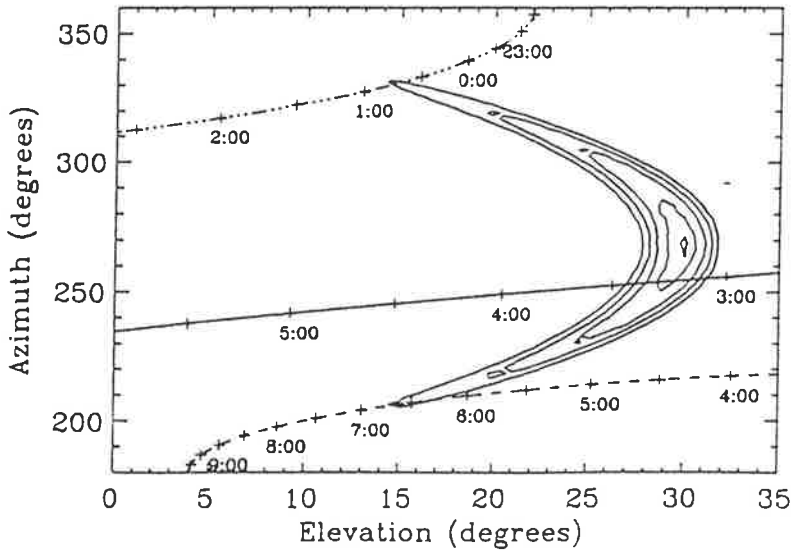

Figure 2. Contour plot of the response function of the Adelaide 54-MHz radar for a beam tilted 30° east of the zenith along the direction running from E4°N to W4°S. The contours are at 20, 40, 60, 80 and 95 per cent of the peak value. The other curves show the positions of three meteor radiants as functions of time; these radiants correspond to the June Librid shower radiant (RA = 227°.2, Dec −28°.3; central, solid line), and fictitious radiants at the same RA but at declinations of −59° (bottom, dashed line) and +33° (top, broken line). The Librid radiant passes through the response function at a level in excess of 80 per cent of the peak at about 03:12 local standard time (ACST).

1991). The shift is performed such that data from the 7th–8th and 8th–9th are consistent in sidereal time with the data from the 6th–7th. The peak is again in bin 61. We now do a statistical test upon the data in Fig. 5 to determine whether the peak is significant. Clearly, the significance level of any test will increase as we increase the number of samples (N) about the peak since the peak will contribute less to the mean, but in doing so the diurnal variation in the sporadic meteor influx will also contribute and confuse the issue (i.e. fewer sporadic meteors are expected before midnight and after 09:00 than at 06:00, say); we therefore restrict our analysis to meteors detected within two hours of the peak (i.e. N up to 21). The number of meteors contributing to the peak in Fig. 5 is $x_p = 19$. If x_i is the number of meteors in any bin i, and σ is the standard deviation of each sampling ($N = 9$, 13, 17 and 21), we obtain the results shown in Table 1. It appears that the peak is significant at a high confidence level.

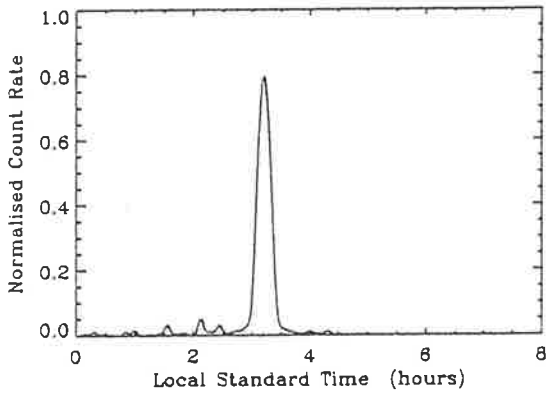

Figure 3. The expected normalized count rate for the June Librid shower as a function of time (0–8 h ACST), based upon the intersection of the radiant with the response function shown in Fig. 2.

4.2 Is the shower the June Librids?

Having determined that the peak is significant (i.e. that a shower was detected), we must next decide whether this is a

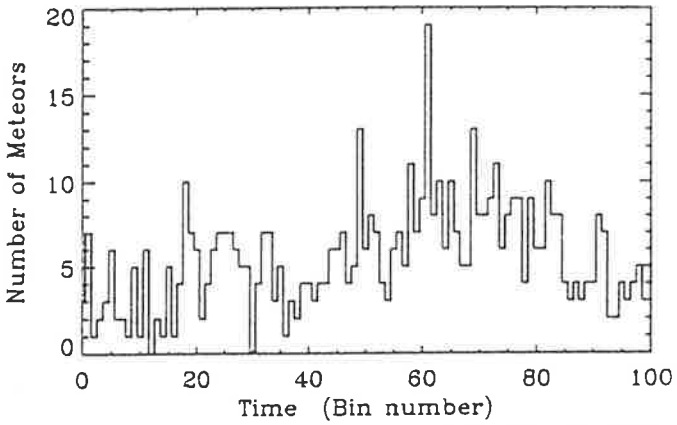

Figure 5. The data from Fig. 4 superimposed, but with a time shift between days to correct for the expected sidereal shift in the radiant of a meteor shower. The peak occurs at about 03:12 ACST on June 7. A total of 552 meteors contribute.

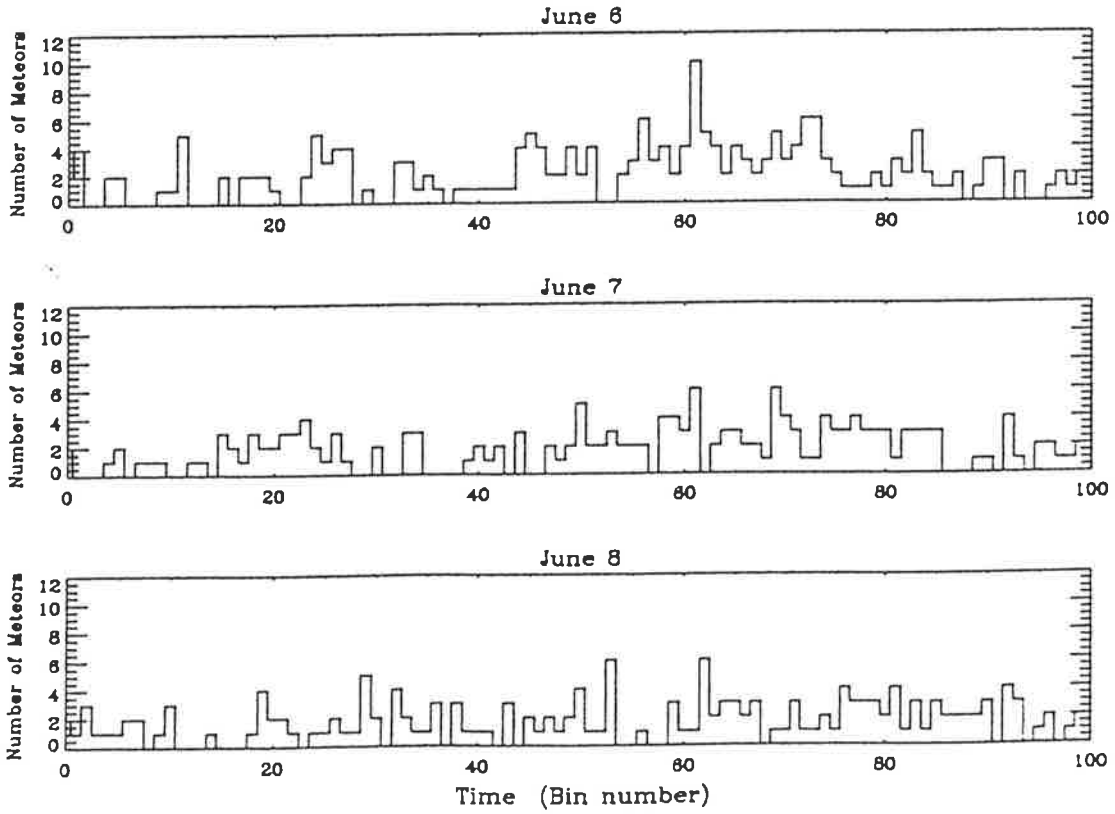

Figure 4. Meteor counts accumulated in 12-min bins for runs starting at 15:00 ACST on 1992 June 6, 7 and 8. Each plot covers 20 h.

known shower. As was mentioned above in connection with the radiants plotted in Fig. 2, a shower observed in 1937 by Hoffmeister (1948) and denoted the June Librids in the list of Cook (1973) would be expected to produce a discrete burst of detections at about 03:12 ACST in the beam tilted to the east in our radar set-up, if it were active at the time of the observations. This is in accord with the time of the detected peak shown in Fig. 5, so the possibility is raised that we did indeed detect June Librid activity in 1992.

We also need to show, however, that no other known shower would produce a peak at the time of day in question.

Table 1. Significance test upon the meteor counts up to 2 h from the peak in Fig. 5.

N	$\bar{x}_i$	σ	$(x_p - \bar{x}_i)/\sigma$	Significance level
9	9.44	4.10	2.33	99.0%
13	8.46	3.71	2.84	99.8%
17	7.94	3.90	2.84	99.8%
21	7.90	3.49	3.18	99.9%

At the end of the first week of June there are two strong daytime showers, the Arietids and the ζ Perseids, but these both have radiants too far north, and they transit at the wrong time of day – in the late morning, at about 10:00 and 11:00. What is required is a shower with a southern radiant and transit in the early hours. There are no such showers in the list of Cook (1973) apart from the June Librids, nor in the catalogue of Kronk (1988).

The International Meteor Organization (IMO) is developing a list of meteor showers based largely upon visual observations, including many weak showers that are yet to be confirmed (McBeath 1993); it is the confirmation of such showers that is the major aim of the publication of that list. In the IMO list, the only plausible candidate could be some part of the diffuse shower termed the Scorpiid/Sagittariid complex, which may be active from mid-April to the end of July. The zenithal hourly rate for this complex is only about 10, however, and this, along with a diffuse claimed radiant, has made it difficult to verify. At the dates in question, the complex would have a mean radiant near RA = 265°, Dec = −30°, resulting in the response function (Fig. 2) being crossed at about 06:15. For this complex, if it is real, to

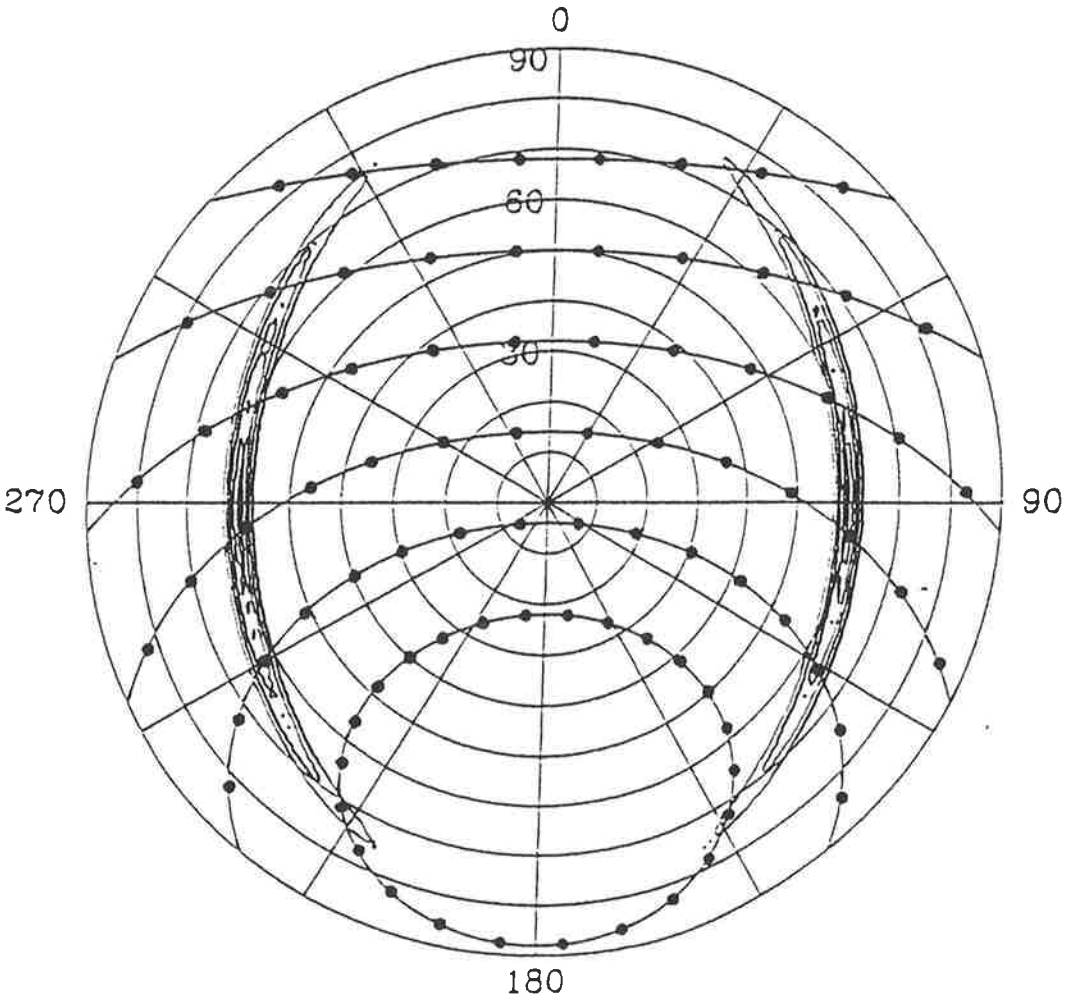

Figure 6. The response functions for the Adelaide 54-MHz radar for beams tilted east and west. In this plot, the azimuth is shown as the polar coordinate, and the zenith angle (the 90° complement of the elevation angle) is the radial coordinate. Any meteor radiant will therefore cross the plot from right to left during the day, passing through the separate response functions with a time separation that depends upon the radiant declination. The loci of six fictitious radiants are shown, with the black dots indicating the hourly motion of each. These have declinations varying in steps of 18° from −57° (circumpolar loop) to −33°.

produce the peak in Fig. 5, the radiant RA would need to be smaller by about 40°. For the Scorpiid/Sagittariid radiant, a peak around bins 75–80 in Fig. 5 would be predicted, should the activity be appreciable, and this is not seen in that plot. It therefore appears that no other known or suspected showers could explain the peak we detected, and it seems that the June Librids were active in 1992. In addition, we find no evidence for the existence of the Scorpiid/Sagittariid complex listed by McBeath (1993).

Whilst we are dealing here with only a handful of meteors (most likely only about 10 meteors from the June Librids were detected in these observations), the date of detection (peak on the night of June 6–7, Fig. 4) may seem to be two days earlier than that of Hoffmeister (1948), who observed the shower on 1937 June 8–9. This might suggest that nodal regression had been identified. Since Australia is at a far eastern longitude, and 1992 was a leap year, however, the solar longitudes at the times of observation in 1937 and 1992 are, in fact, within a degree of each other, and, in view of the count rates involved, it does not seem that any nodal movement may be concluded.

Obviously we would like to be able to confirm the June Librid activity in other years, but, unfortunately, equipment malfunction in the middle of 1993 meant that we were unable to collect data in that year. Follow-up observations are planned from 1994 onwards, with the beam alternation between east and west as described in Sections 3 and 5 being used.

5 APPLICABILITY OF THIS METHOD TO THE DETERMINATION OF UNKNOWN RADIANTS

We have seen above that the time of detection of meteors from a particular shower allows us to show that it is active, based upon the movement of the shower radiant through the response function of the radar operated with just one beam direction. If the beam direction were alternated between west and east, on a minute-by-minute basis, then the response function would alternate between sensitivity for radiants in the east (pre-transit) and in the west (post-transit). So long as the shower activity were sufficient to allow discrimination from the sporadic activity (and any other showers active at the time), it would then be possible to determine the radiant RA and Dec from the times of the two bursts of detections. One should note, however, that the sporadic meteor detection rate will be different for the two beams, particularly as the response function for each is crossed by the well-known Apex, Helion and Anti-Helion broad sources.

In Fig. 6, we show as a polar plot the response functions of the east and west beams of the 54-MHz radar. These are symmetric about a line running from E4°N to W4°S, due to the orientation of the radar. Overplotted are the paths taken by six fictitious radiants, with black dots denoting hourly positions. The radiant declinations vary between −57° (complete circumpolar loop) and +33° in 18° jumps. For example, for the radiant with Dec = −21°, shower activity would be detected in the west beam about 9 h before that in the east, in this imaginary case. The radiants take widely different periods to cross beween the two response function islands, with the period in each case being dependent upon the declination of the radiant; the time between bursts of meteor detections allows the shower declination to be determined. The mid-time indicates the time at which the radiant crossed the line running from N4°W to S4°E, and therefore allows the radiant right ascension to be defined. In consequence, this type of radar may be used to determine the radiants of unknown showers, even if these have low fluxes: in the example presented herein, only about 10 June Librids were detected in total.

ACKNOWLEDGMENTS

This work was supported by the Australian Research Council and the Defence Science and Technology Organization.

REFERENCES

Andrianov K. N. S., Pupysev U. A., Sidorov V. V., 1970, MNRAS, 148, 227
Aspinall A., Clegg J. A., Hawkins G. S., 1951, Phil. Mag., 42, 504
Baggaley W. J., Bennett R. G. T., Steel D. I., Taylor A. D., 1994, QJRAS, 35, 293
Beech M., 1991, QJRAS, 32, 245
Belkovich O. I., Pupyshev J. A., 1968, in Kresák L., Millman P. M., eds, Proc. IAU Colloq. 33, Physics and Dynamics of Meteors, Reidel, Dordrecht, p. 373
Cervera M., Elford W. G., Steel D. I., 1993, Štohl J., Williams I. P., eds, Meteoroids and their Parent Bodies, Slovak Academy of Sciences, Bratislava, p. 249
Clegg J. A., 1948, Phil. Mag., Ser. 7, 40, 614
Cook A. F., 1973, Evolutionary and Physical Properties of Meteoroids, NASA SP-319, Washington DC, p. 183
Cook A. F., Flannery M. R., Levy I. H., McCrosky R. E., Sekanina Z., Shao C.-Y., Southworth R. B., Williams J. T., 1972, Meteor Research Program, NASA CR-2109, Washington DC
Davies J. G., Gill J. C., 1960, MNRAS, 121, 437
Durfy A. G., Hawkes R. L., Jones J., 1987, MNRAS, 228, 55
Elford W. G., 1964, Harvard Radar Meteor Project Report No. 8, Cambridge, Massachusetts
Elford W. G., 1968, in Kresák L., Millman P. M., eds, Proc. IAU Colloq. 33, Physics and Dynamics of Meteors, Reidel, Dordrecht, p. 352
Elford W. G., Hawkins G. S., 1964, Harvard Radar Meteor Project Report No. 9, Cambridge, Massachusetts
Evans J. V., 1965, J. Geophys. Res., 70, 5395
Gartrell G., Elford W. G., 1975, Aust. J. Phys., 28, 591
Gill J. C., Davies J. G., 1956, MNRAS, 116, 105
Hawkins G. S., Almond M., 1952, MNRAS, 112, 219
Hoffmeister C., 1948, Meteorströme, Johann Ambriosius Barth, Leipzig
Hughes D. W., 1972, MNRAS, 155, 395
Jones J., 1977, Bull. Astron. Inst. Czechoslovakia, 28, 272
Jones J., 1983, MNRAS, 204, 765
Jones J., Morton J. D., 1977, Bull. Astron. Inst. Czechoslovakia, 28, 267
Jones J., Morton J. D., 1982, MNRAS, 200, 281
Kaiser T. R., 1954, MNRAS, 114, 39
Kaiser T. R., 1960, MNRAS, 121, 284
Keay C. S. L., 1957, Aust. J. Phys., 10, 471
Kronk G., 1988, Meteor Showers: A Descriptive Catalog, Enslow, New Jersey
McBeath A., 1993, Meteor Shower Calendar, International Meteor Organization, Mechelen, Belgium
McKinley D. W. R., 1961, Meteor Science and Engineering, McGraw-Hill, New York
Morton J. D., Jones J., 1982, MNRAS, 198, 737
Nilsson C. S., 1964, Aust. J. Phys., 17, 205
Nilsson C. S., Weiss A. A., 1962, Aust. J. Phys., 15, 1

Poole L. M. G., Roux D. G., 1989, MNRAS, 236, 645
Steel D. I., Elford W. G., 1991, J. Atmos. Terr. Phys., 53, 409
Steyaert C., 1984, Bull. Astron. Inst. Czechoslovakia, 35, 312
Thomas R. M., Whitham P. S., Elford W. G., 1988, J. Atmos. Terr. Phys., 50, 703
Vincent R. A., May P. T., Hocking W. K., Elford W. G., Candy B. C., Briggs B. H., 1987, J. Atmos. Terr. Phys., 49, 353
Weiss A. A., 1955, Aust. J. Phys., 8, 148
Weiss A. A., 1960, MNRAS, 120, 387

Appendix C

Meteor velocities: a new look at an old problem

This is a reprint of the paper,

W. G. Elford, M. A. Cervera and D. I. Steel, Meteor velocities: a new look at an old problem, *Earth, Moon and Planets*, in press, 1996.

W.G. Elford, M.A. Cervera and D.I. Steel (1996) Meteor velocities: A new look at an old problem.
Earth, Moon, and Planets, v. 68, (1-3), pp. 257-266,1995.

NOTE: This publication is included in the print copy of the thesis held in the University of Adelaide Library.

It is also available online to authorised users at:

http://dx.doi.org/10.1007/BF00671514

Appendix D

A comparison of meteor radar systems

This is a reprint of the paper,

T. Valentic, S. Avery, J. Avery, M. A. Cervera, R. A. Vincent, I. M. Reid, W. G. Elford, A comparison of meteor radar systems, *Radio Sci.*, in preparation, 1996.

A Comparison of Meteor Radar Systems at Buckland Park

T. A. Valentic,[1] J. P. Avery
Department of Electrical and Computer Engineering, University of Colorado, Boulder, Colorado

S. K. Avery[2]
Cooperative Institute for Research in Environmental Sciences, University of Colorado, Boulder, Colorado

M. A. Cervera, W. G. Elford, R. A. Vincent, I. M. Reid
Department of Physics and Mathematical Physics, University of Adelaide, Adelaide, Australia

Received _____; accepted _____

Submitted to *Radio Science*.

Short title: METEOR RADAR COMPARISON

---

[1]Also at Cooperative Institute for Research in Environmental Sciences, University of Colorado, Boulder, Colorado

[2]Also at Department of Electrical and Computer Engineering, University of Colorado, Boulder, Colorado

Abstract. This paper describes a comparison of two meteor radar systems operated simultaneously from June 29 to July 15, 1994 at the Buckland Park field station near Adelaide, Australia (35°S,138°E). Both meteor systems operate on a narrow-beam VHF wind profiler. The first meteor system was developed by the atmospheric physics group at the University of Adelaide. The second meteor system was the University of Colorado's meteor echo detection and collection (MEDAC) system. The goal of the campaign was to determine how closely the two similar meteor systems performed with regards to the detection of meteor trail echoes and the estimation of the doppler frequencies. Classification of the signals in the resulting data set showed that a number of the echoes were from sources other than underdense meteor trails, including a previously unrecognized class of echoes that appear to be from meteors traveling straight down the beam. When the non-underdense echoes were operated on by the doppler frequency estimators, widely varying estimates between the two systems were produced. Only when taking into careful consideration the details of the detection routines, the signal composition of the data set, and performance characteristics of the doppler estimators was the comparison satisfactory.

Introduction

Meteor wind radars have served as research tools for probing the dynamics of the upper mesosphere and lower thermosphere for over 40 years [*Elford*, 1993]. As a meteoroid ablates in the atmosphere, a long column of ionization forms which drifts with the prevailing wind. When first formed, such columns of ionization, or meteor trails, can strongly backscatter radar pulses in a direction at right angles to the axis of the trail. By measuring the doppler shift resulting from the motion of the meteor trail, a pulsed doppler radar can be used to profile the neutral winds in the meteor region.

Most modern meteor wind radars employ a wide aperture direction finding system to spatially locate the meteor trail. However, *Avery et al.* [1983] and *Tetenbaum et al.* [1986] demonstrated that meteor echoes could be detected with a narrow-beam VHF wind profiler. Because the beamwidths of these radars are on the order of a few degrees, the spatial location of a meteor trail is inferred from the pointing direction of the antenna's main lobe. At the University of Colorado, the meteor echo detection and collection (MEDAC) system was devised as a low-cost add-on to extract meteor echo data from wind profilers [*Wang et al.*, 1988; *Avery et al.*, 1990; *Valentic et al.*, 1995]. The MEDAC instrumentation package consists of custom-designed processing boards, a personal computer, and sophisticated control software. The system is passively attached to a host radar, sampling the baseband receiver outputs for the presence of meteor trails. This project was scientifically motivated by the potential upper atmosphere observations that could be obtained in the tropical Pacific due to the proliferation of wind profilers in the region. MEDAC packages have been deployed throughout the NOAA/CU trans-Pacific profiler network [*Gage et al.*, 1990] and above the arctic circle at the Early Polar Cap Observatory in Resolute Bay, Canada (74°N,101°W).

The University of Adelaide has reconfigured the Adelaide VHF radar at Buckland Park, Australia, (35°S,138°E) to investigate meteor height distributions [*Steel and Elford*, 1991], meteor shower radiant determinations [*Cervera et al.*, 1993; *Elford*

et al., 1994], MF wind comparisons [*Cervera and Reid*, 1995], and speeds of ablating meteoroids [*Elford et al.*, 1995]. While the MEDAC system consists of a stand-alone hardware/software combination, the Adelaide system operates as a special software program running on the base VHF hardware.

The two meteor systems could be operated simultaneously using the same radar, allowing for a comparison of the different detection and processing strategies. As the number of comparisons between dissimilar instruments is becoming more prevalent within the atmospheric community, we feel that it is important to show the difficulties that can arise even when comparing two very similar instruments measuring the same scattering phenomenon. As another means of comparison, a co-located MF radar was also operated during the campaign. This paper, however, only concentrates on the meteor comparison. A follow up paper will summarize the MF/meteor comparison.

Instrumentation Overview

The two meteor systems utilized the VHF radar at Buckland Park. This lower atmosphere wind profiler operates at 54.1 MHz [*Vincent et al.*, 1987] and was upgraded to a peak power of 32 kW in 1993. During the campaign, however, two non-operational modules limited the peak power to 28 kW. Data were collected over a line-of-sight range of 80 to 120 km with 2 km range resolution and a pulse repetition frequency of 1024 Hz. A 90 m square collinear coaxial (COCO) array was used for reception and transmission. The array of 32 north-south rows of 48 dipoles produced a beam of approximately 1.7° half-width when directed vertically. Appropriate phasing of the rows of antennas tilts the beam in an eastward or westward direction. During the campaign, the beam was tilted 30° off-zenith. At this angle, the beam width increases to about 1.9° half-width.

Both the MEDAC and Adelaide systems detect meteor echoes in real-time, storing the relevant data onto secondary long term storage, and performing the wind processing off-line. The Adelaide system began meteor detection by collecting 16 seconds of data

with its data acquisition system. The raw data were smoothed with a 16-point coherent average to improve the signal-to-noise ratio. The smoothing made detection of very short duration events (below 1/64 s) impossible, but allowed for detection of much weaker echoes. Because an accurate estimate of the doppler frequency required a time series of reasonable length, the trade off was valid. The signal amplitude was computed and a meteor judged to be present if the amplitude of two successive pulse returns was at least 4.5 times the mean noise level. This discrimination level was set such that, on average, one false detection due to random noise was detected per hour. Once an event was detected, the raw in-phase and in-quadrature data were stored from 0.5 s prior to and 2.5 s following the event.

The MEDAC/SC system used for the campaign consisted of a custom designed signal processing board used for data acquisition and meteor echo detection. An on-board TMS32025 signal processor executes the meteor detection code. A double buffered memory design allowed for simultaneous collection and detection of echoes. Data collection began with the sampling of the radar receiver's baseband output signal and the sampled values were stored into an input memory bank. Once the input bank was full, the TMS32025 began executing the detection routine. The first step was the determination of the background noise level by computing the average power for each range bin. The lowest average power was designated as the background noise floor. The detection threshold was then computed to be 4 dB above the noise floor. A window was then swept over the points in each range bin. If all of the points within the window exceed the threshold level, the range was tagged as containing a potential meteor echo. The window requirement filters out records containing momentary peaks in power due to noise. A typical window length is five points. However, for this campaign the window was disabled to determine how many of the echoes really were due to noise spikes. The TMS32025 then copies the data from all ranges which passed the detection criteria into an output memory bank for retrieval and long term storage by the host computer.

There are important differences between the two detection routines. First, data collection and processing occur sequentially in the Adelaide system. The collection takes 16 s and processing lasts no longer then 3 s. During the processing stage, there exists the opportunity to miss echoes. MEDAC has been designed to be a parallel processing system. The double buffered memory scheme allows for simultaneous collection and processing, yielding continuous coverage. The Adelaide detection routine also is inhibited for one second after an echo has been detected in a particular range gate, in order to avoid detecting the same meteor twice. MEDAC can detect events present at multiple ranges and times. An interesting difference deals with the decision to perform coherent averaging. The Adelaide system was much more adept at detecting weak meteor echoes, based on the 16-point coherent averaging and the use of 12-bit analog-to-digital converters. Both features improved the Adelaide system's sensitivity and thus the usable echo rate. MEDAC does not perform coherent averaging and uses 8-bit analog-to-digital converters, limiting MEDAC's sensitivity to weak signals. However, MEDAC was able to detect signals that were lost by the low-pass filter effect of the coherent averaging. Most of these signals tended to be short-duration echoes which can be broadly classified into two types: (a) echoes from trails observed orthogonally but subject to rapid diffusion at high altitudes, or (b) echoes from ionization near the head of trails when the meteoroid is coming almost directly down the beam. While not useful for wind determination, these other types of echoes are useful for studying astronomical and ionospheric aspects of meteors [*Cervera et al.*, 1995; *Elford and Taylor*, 1995; *Elford et al.*, 1995].

Initial Comparison

The two meteor systems were simultaneously operated from June 29 to July 15, 1994. During this time, MEDAC recorded 18,119 events and the Adelaide system detected 11,661 events. An event is any signal that passed the detection routines, but is

not necessarily an echo from a meteor trail.

The parameter of interest when using meteor trails for wind profiling is the line-of-sight doppler estimate, so this parameter was chosen as the basis of our initial comparison. Initially, both data sets were individually post-processed at the each institution and the results were directly compared. Figure 1 shows the comparison of line-of-sight doppler frequency estimates at 94 km for a single day during the campaign. The circles represent the estimates reported by the Adelaide system and the pluses reflect those estimates produced by the MEDAC post-processing. Had both systems detected exactly the same events and produced the same doppler estimates, each circle in Figure 1 would be overlaid with a plus. The actual result is much different. Although there are many cases where the two systems detect the same event and have similar estimates of the doppler frequency, there are a number of times when only one of the two systems detected a particular event. Additionally, there are cases where the estimates returned by each system are considerably different, even in regards to the sign of the estimate.

In an attempt to determine why the two systems produced different results at times, we proceeded to look closer at the individual echoes that were collected, classifying the raw data, and analyzing the effects of the different types of echoes on the doppler frequency estimators.

Echo Classifications

Radio echoes from meteor trails fall into two general categories: underdense and overdense [*McKinley*, 1961; *Sugar*, 1964]. Underdense trails have an electron density low enough such that secondary radiative and absorptive effects on the incident wave are negligible and the electrons can therefore be considered as an array of independent scatterers. When the diameter of the trail approaches the wavelength of the incident radiation, the returned echo power is severely attenuated due to interference between

reflections from the front end and rear portions of the trail. In contrast, overdense trails have an electron density high enough such that reflection of the incident wave is essentially that due to a solid metallic cylinder. As with metals, the overdense meteor trail has a "skin depth" which is defined as the distance at which the amplitude of the penetrating wave has fallen to e^{-1} of the surface amplitude. In either case, a maximum in the backscattered power occurs when the trail is perpendicular to the incident wave and encompasses the first Fresnel zone.

As an underdense trail diffuses, the echo power decays exponentially with a life-time typically less than a second. In contrast, echoes from overdense trails tend to maintain a constant amplitude for several seconds. On occasions, even longer duration echoes occur, but these become subject to significant fading as the trail becomes distorted by winds and turbulence.

To determine the different types of signals collected in the data sets, the MEDAC data were hand classified into ten different echo classes. The classes are summarized in Table 1 with examples shown in Figure 2. The first column of Figure 2 shows the time series recorded from the in-phase channel of the receiver. The second column contains the power profiles plotted on a normalized logarithmic scale. The third column contains plots of the instantaneous phase produced from the time series.

The first two echo classes contain echoes from underdense meteor trails. These echoes were subdivided into "strong" and "weak" groupings based on their signal-to-noise ratios. The motivation for this subdivision was to determine how well the doppler frequency estimators performed on weak signals. In both cases, the power profiles experience the expected exponential decay following the peak. The instantaneous phase plots are linear throughout the echo lifetime. The slope of the phase corresponds to the doppler frequency.

The third group of echoes corresponds to long duration trails, often associated with overdense echoes. Instead of the exponential decay in the power profile, clear fading is

present as a result of multiple scattering points along the trail. Although the phase plot in this example appears fairly linear, this is not always the case. Severe distortion of the trail can lead to unreliable estimates of the neutral wind.

The next group of echoes, clipped, are due to situations that caused the receiver to saturate. These large amplitude echoes were singled out to determine the number of time such events occurred and the impact on the doppler estimators. The frequency estimates proved to be quite robust in the presence of clipping.

The fifth echo class, noise spikes, are due to instrumental noise spikes. Potentially, these echoes could also be due to very short lived meteor echoes. The time series is too short to make a doppler determination, however.

The trail formation echo class consists of a number of very distinct echoes that are due to meteor trails experiencing rapid diffusion. Occurring at higher heights, these echoes have an effective scattering length less than a Fresnel zone. The result is a moving-ball target that produces a clearly parabolic trace in the instantaneous phase, often symmetric about the time of the peak in the power profile. The phase response illustrates the progression of the short duration trail, still moving at the speed of the parent meteoroid, through the beam. Zero doppler frequency will occur at the time of closest approach of the target; due to aliasing, a zero will also occur whenever the actual doppler frequency is an integer multiple of the pulse repetition freqeuncy. The power profile can be viewed as a cross-section of the antenna beam traced out by the trail.

The next echo class consists of echoes that have a trail formation signature followed by a body echo, which can either be underdense or long enduring.

The ninth echo class contains echoes that result from a meteoroid traveling down the beam. Unlike traditional trail echoes that are assumed to occur transverse to the beam, and thus are seen in only one or two range bins, these echoes appear as short bursts (about 0.05 s) in the time series over a number of ranges. The bursts appear to travel down in height with time. The left plot in Figure 3 shows the time series recorded

for a down-the-beam echo. It takes the echo 0.12 s to travel 7 km, resulting in a crude speed estimate of 58.3 km s^{-1}. Sporadic meteors entering the Earth's atmosphere are expected to have a speeds between 11 and 73 km s^{-1}. The instantaneous phase for these types of echoes is fairly linear during the burst at each height, not parabolic as with the traverse head echoes. The slope of the phase does decrease as the event decreases with height, indicating that the event is not directly head on, but passing through the beam at an angle to the bore direction. The frequency spectrum shown in the right plot of Figure 3 illustrates the same behavior deduced from the phase information. Deacceleration of the meteoroid can also cause this effect, but probably to a lesser extent. When the event is first detected at 100 km, the spectrum shows a signal near 400 Hz with a bandwidth of 200 Hz. By the time the event reaches 93 km, the doppler has decreased to -300 Hz and dispersed to a bandwidth of 400 Hz. These frequencies are clearly aliased, because the expected motion of the meteoroid produces doppler frequencies much larger than the Nyquist frequency.

The multiple echo class consists of traces that contained what appear to be two distinct events. Due to the collection methods, these echoes were stored as a single meteor trail.

The last echo class, unknown, is simply a group that contains echoes that could not be classified into other groups. These echoes were often clearly due to some sort of interference.

Collection Statistics

The distribution of ten signal classes in the MEDAC data set is shown in the top plot of Figure 4. Underdense echoes (strong and weak) account for nearly 40% of the total, while the burst events make up 30%. The noise spikes, which would have been eliminated had the detection window been active, make up 15% of the data. The remaining classes comprise less then 15% of the total. During post-processing, a number

of different checks are normally made to help eliminate the non-underdense echoes from propagating into the wind estimates.

Instead of performing the same hand classification on the Adelaide meteor data, an attempt was made to find those echoes in the Adelaide set that had matches in the MEDAC set. The first pass was done automatically with a algorithm that matched events occurring in the same direction and at the same range within four minutes of each other. The fairly wide time window was necessary because the system clocks drifted apart by approximately three minutes during the campaign. A side effect of this four minute window was that multiple MEDAC events mapped into the same Adelaide event. Another algorithm was then used to help determine which of these multiple events was the true match based on differences in the power profiles. Any time the algorithm was unsure about which echo to choose, a flag was set and these events were matched by hand. Finally, any matched events that exhibited more than 5 Hz difference in the estimates were examined by hand. The great majority of these were found to be non-matches that had managed to slip through the previous routines. The resulting distribution of the matched echoes is shown in on the bottom of Figure 4. A total of 8081 echoes (69%) out of the 11,661 Adelaide echoes had a match in the MEDAC data set. Nearly 64% of the matched echoes were from underdense meteor trails.

Figure 5 shows the time of day distributions for all the echo classes collected on the west beam for the MEDAC data set. The echoes that are plotted are those that passed successfully through the post-processing stage, meaning that there were a sufficient number of points from which to compute a doppler frequency estimate. Nearly 10% more echoes were seen on the eastward beam.

The distribution in height of the echoes, shown in Figure 5 matches the expected profile, with a peak near 93 km. The mean height peaks in the morning, around 0400 hours local time on the west beam and at 0900 hours on the east beam. Throughout the day, most noticeably on the west beam, the mean height decreases to its lowest point

at 1500 hours local time. The reduction in the mean height from its value in the early morning to its value in the late afternoon is as expected. The speeds of encounter of meteoroids with the Earth peak near 0600 hours local time, and the higher the speed of a meteoroid the greater the height of ablation.

The temporal distribution of the echo rate on both beams experiences a peak in the morning hours, as expected. However, the west beam also has a significant peak around 2000 hours local time. Recent modeling by *Cervera* [1995] predicts this bimodal distribution, as is shown on the right side of Figure 5. The model computes expected echo rates by convolving the radar's meteor response function [*Elford*, 1964; *Thomas et al.*, 1988; *Elford et al.*, 1994] with the sporadic meteor radiant density distribution as determined by *Elford and Hawkins* [1964] and modified by *Cervera* [1995]. It should be noted that this distribution was found by averaging meteor orbit data over eight months (January through August) and it is well established that sporadic meteor radiant distribution is not uniform over the orbit of the Earth. Nevertheless, the times at which the expected peak rates occur agree well with the data.

The time of day distribution of only the down-the-beam event echoes is shown in Figure 6. These events are clearly clustered in the morning hours. The west beam echo rate peaks at 0600 local time, while the east beam echo rate peaks two hours later at 0800 local time. The height profiles on both beams peak near 100 km, higher than the overall peak of 93 km. As is shown in Figure 4, the down-the-beam events make up 30% of all signals detected with the MEDAC system. Few, if any, such echoes were detected with the Adelaide system because of the pre-detection coherent averaging and the rejection of signals detected simultaneously in more than one range bin based on the assumption that they were due to noise.

Post-Processing

The real-time control programs of each meteor system are responsible solely for the detection of meteor echoes and storage of the relevant time series data. The post-processing stage analyzes these time series for the necessary parameters required for generating wind profiles. Because the meteor systems were developed separately, different design decisions were made with regards to the algorithms and estimators used. However, the overall processing methodologies are similar. The general steps are isolation of the meteor echo in the time series data and then estimation of the doppler frequency.

Isolating the echo within the time series is performed using the power profile of the echo. The echo is assumed to begin at the peak of the power profile, based on the assumption that the power returned from an underdense trail maximizes when the trail has just filled the first Fresnel zone. The MEDAC system tags this point as the start of the echo for processing, while the Adelaide system begins the echo processing approximately 15 ms after the peak, allowing any transients due to trail formation to settle out. The systems differed the most in determining the end of the echo. The Adelaide system uses the portion from the start until the power falls to 10% of the peak value. By comparison, the MEDAC system used all the power points from the start until the signal level returned to the mean noise level which applied when the echo was detected.

Once the echo has been isolated, the doppler frequency is computed. The Adelaide system uses a phase-slope estimator, based on the instantaneous phase computed from the time series data. Once the phase is computed, any 2π wrap around of the phase data is removed, so that the phase data becomes accumulative. A weighted linear least squares fit is then performed on the phase. The weights are based on the power, so that portions of the trail with lower signal-to-noise ratio contribute less. The resulting slope is an estimate of the doppler frequency due to the radial drift of the meteor trail.

The MEDAC system employs an alternative estimator, namely the poly-pulse pair [*Strauch et al.*, 1978], to determine the doppler frequency. This estimator uses the phase of the complex auto-correlation function $\angle r$, at lag m and sampling time T_s, and is defined as $\angle r[m] = \omega_d m T_s$, where ω_d is the doppler frequency. The auto-correlation phase is computed for a number of different lags, through which a line is then least-squares fitted to yield an estimate of the slope and thus the radial drift velocity of the trail.

Figure 7 illustrates the processing performed on a typical underdense meteor trail. The dotted lines in the time trace show the portion of the trail that was selected for processing. The poly-pulse pair estimator was run for five lags. The instantaneous phase was computed and unwrapped, then fit with a line according to Adelaide's processing methods. Additionally, the frequency spectrum is shown, in which a clearly defined peak is present. In general, the doppler estimators all return similar results for strong underdense meteor trails.

In contrast, Figure 8 shows the effects of applying doppler estimators to a down-the-beam event. The number of 2π rotations experienced by the phase increase dramatically; an order of magnitude higher than in the previous underdense example. This behavior is consistent with the interpretation that these echoes are from meteors coming down the beam. The dotted lines on the phase plots show the resulting fit produced by the estimators. The frequency spectrum represented by the Fourier transform contains a number of different frequencies, highlighting the difficulties experienced in estimating the doppler frequency.

Figure 9 presents a scatter plot comparing the results produced by the two different estimators for all the echoes in the underdense and down-the-beam echo classes. As was anticipated, the underdense echo frequency estimates are similar. However, a considerable difference arises for the burst echo events.

Figure 10 summarizes the results of running three different doppler frequency estimators on the echoes in each class. In addition to the poly-pulse pair and phase slope

estimators, a maximum likelihood estimator was used. This estimate is essentially the peak of the power spectrum [*Dowski*, 1983]. The deviation among the three estimators was computed for each echo, and the average deviation for each class was plotted in the bar graph. Again, the underdense meteor echoes produced the best results, with all three estimators producing estimates with average deviations of about ± 0.5 Hz. In contrast, the other classes of echoes have deviations between the estimators that range from 0.7 to 2.1 Hz. A possible discrimination mechanism against non-underdense meteor echoes is to use multiple frequency estimators and retain only those echoes where all the estimates are within ± 0.5 Hz.

Revisited Comparison

The comparison between the two systems can now be revisited. The plot on the top of Figure 11 shows the data from the same day that was examined previously in Figure 1, with the exception that only events that were found to be present in both data sets are now shown. In addition, each echo is color coded according to its classification. The doppler estimates were computed using the different estimators employed by each system. The comparison for the blue and green colored echoes, representing the underdense echo classes, is fairly good. Most of the points with considerable disagreement fall into the non-underdense meteor categories. However, there remains some underdense points in which there is still a significant difference in the resulting doppler estimate.

The bottom plot in Figure 11 shows the comparison again, only this time a single doppler estimator, the poly-pulse pair, was used on all the data. While the differences between the underdense echo estimates is further reduced in this case, there are still some occasions when the differences show an increase.

Figure 12 shows a histogram comparison of the differences between the doppler frequency estimates of each system. The plot on the left shows the results for the initial

comparison. The initial comparison contained all the points collected on each system, processed with the respective algorithms from each institution. Because no matching between events was done at this stage, the estimates on each system were binned into half-hour time intervals and the differences computed between these time bins. The mean and standard deviations are also shown on the graph. The initial comparison had a mean near -0.4 Hz with a standard deviation of 5.5 Hz. The plot on the right shows the estimate differences using only matched underdense echoes, allowing for a point-to-point comparison. The MEDAC post-processing routine was used on both data sets to eliminate any differences associated with different echo location and doppler estimation algorithms. Any differences at this point are solely due to different data acquisition hardware and collection strategies. The improvement is clear, with the mean difference now approaching 0.0 Hz and the standard deviation halved to 2.6 Hz.

Conclusions

Despite the fact that the meteor detection systems developed by the University of Colorado and the University of Adelaide operated simultaneously on the same signals received from a meteor radar, significant differences in the estimates of the derived parameters can arise. An acceptable level of similarity in outcomes was only achieved after the characteristics of the raw data and the performance of the doppler estimators were examined in greater detail. A direct result of the comparisons is a far better understanding of the radio scattering from meteor trails and the classes of echoes that occur when the meteors are detected with a VHF narrow beam radar.

A surprising and useful result of the experiment was the discovery of the "burst" events which correspond to meteoroids traveling straight down the beam. The astronomical applications of such events are considerable and are being explored [*Taylor*, 1995]. Further, *Elford and Taylor* [1995] have shown that by observing these echoes on two orthogonal antennas the electron density profile between 80 and 100 km may be

measured from the degree of Faraday rotation of these echoes.

Finally, each system benefited from improvements through the discovery of weak points in the detection and processing code that were only really highlighted through a comparison experiment such as this one. In a follow on paper, we will present the results of comparisons of meteor winds determined with the VHF radar and a co-located MF radar.

References

Avery, S. K., A. Riddle, and B. Balsley, Poker Flat Alaska, MST radar as a meteor radar, *Radio Sci.*, *18*, 1021–1027, 1983.

Avery, S. K., J. P. Avery, T. A. Valentic, S. E. Palo, M. J. Leary, and R. L. Obert, A new meteor echo detection and collection system: Chrismas Island mesospheric measurements, *Radio Sci.*, *25*, 657–669, 1990.

Cervera, M. A., Meteor observations with the upgraded Buckland Park pencil beam VHF radar, Ph.D. thesis, University of Adelaide, 1995.

Cervera, M. A., and I. M. Reid, Comparison of simultaneous wind measurements using co-located VHF meteor radar and MF spaced antenna radar systems, *Radio Sci.*, *30*(4), 1245, 1995.

Cervera, M. A., W. G. Elford, and D. I. Steel, in *Meteroids and their parent bodies*, edited by J. Stohl, and I. P. Williams, p. 249. Slovak Academy of Sciences, Bratislava, 1993.

Cervera, M. A., W. G. Elford, and D. I. Steel, A novel radar techdnique for the determination of meteor speeds and its significance in the interpretation of HF/VHF meteor backscatter. Conference on Solar and Terrestrial Physics, University of Adelaide, Sept. 25–29, 1995.

Dowski, E. R., Spectral estimation of randomly sampled signals with an application to atmospheric tidal determination, Master's thesis, University of Colorado, Boulder, 1983.

Elford, W. G., Calculation of the response function of the Harvard radio meteor project radar system, Research Report 8, Harvard College Observatory, 1964.

Elford, W. G., Radar observations of meteors, in *Meteoroids and their Parent Bodies*, edited by J. Stohl, and I. P. Williams, pp. 235–244. Astronomical Inst., Slovak Acad. Sci., Bratislava, 1993.

Elford, W. G., and G. S. Hawkins, Meteor echo rates and the flux of sporadic meteors, Research Report 9, Harvard College Observatory, 1964.

Elford, W. G., and A. D. Taylor, Measurement of electron densities in the lower ionosphere from Faraday rotation of radar meteor echoes. Conference on Solar and Terrestrial Physics, University of Adelaide, Sept. 25–29, 1995.

Elford, W. G., M. A. Cervera, and D. I. Steel, Single station identification of radar meteor shower activity: the June Librids in 1992, *Mon. Not. Royal Astr. Soc.*, *270*, 401–408, 1994.

Elford, W. G., M. A. Cervera, and D. I. Steel, Meteor velocities: a new look at an old problem, *Earth, Moon and Planets*, in press, 1995.

Gage, K. S., B. B. Balsley, W. E. Ecklund, R. F. Woodman, and S. K. Avery, Wind-profiling doppler radars for tropical atmospheric research, *EOS Transactions, American Geophysical Union*, *71*(50), 1851–1854, 1990.

McKinley, D. W. R., *Meteor Science and Engineering.* New York: McGraw-Hill, 1961.

Steel, D. I., and W. G. Elford, The height distribution of radio meteors: comparison of observations at different frequencies on the basis of standard echo theory, *J. Atmos. Terr. Phys.*, *53*, 409–417, 1991.

Strauch, R. G., R. Kropfli, W. Sweezy, and W. Moninger, Improved doppler velocity estimates by the poly-pulse pair method, in *18th Conference on Radar Meteorology*, pp. 376–380, Atlanta, GA. Am. Meteorol. Soc., 1978.

Sugar, G. R., Radio propogation by reflection from meteor trails, *Proceedings of the IEEE*, *52*(2), 117–136, 1964.

Taylor, A., Personal communication, 1995.

Tetenbaum, D., S. K. Avery, and A. Riddle, Observations of mean winds and tides in the upper atmosphere during 1980–1984 using the Poker Flat Alaska MST radar as a meteor radar, *J. Geophys. Res.*, *14*, 539–555, 1986.

Thomas, R. M., P. S. Whitham, and W. G. Elford, Response of high frequency radar to meteor backscatter, *J. Atmos. Terr. Phys.*, *50*(8), 703–724, 1988.

Valentic, T. A., J. P. Avery, and S. K. Avery, MEDAC/SC: A third generation meteor echo detection and collection system, *IEEE Trans. Geosci. Remote Sensing*, in press, 1995.

Vincent, R. A., P. T. May, W. K. Hocking, W. G. Elford, B. H. Candy, and B. H. Briggs, First results with the Adelaide VHF radar: spaced antenna studies of tropospheric winds, *J. Atmos. Terr. Phys.*, *49*, 353–366, 1987.

Wang, S. T., D. Tetenbaum, B. B. Balsley, R. L. Obert, S. K. Avery, and J. P. Avery, A meteor echo detection and collection system for use on VHF radars, *Radio Sci.*, *23*, 46–54, 1988.

This manuscript was prepared with the AGU LaTeX macros v3.1.

With the extension package 'AGU^{++}', version 1.2 from 1995/01/12

Figure Captions

Figure 1. Initial doppler frequency comparison between the MEDAC (pluses) and Adelaide meteor systems (circles).

Figure 2. Examples of time, power and phase plots for each of the different signal classes present in the MEDAC data set.

Figure 3. The left plot shows in-phase time series recorded for a down-the-beam event, while the right plot shows the corresponding frequency spectrum.

Figure 4. The top graph shows the distribution of echo classes within the MEDAC data set. The bottom graph shows the events seen simultaneously by both systems.

Figure 5. Time-height distribution for all the echo classes obtained with MEDAC on the west-pointing beam. The figure on the right is the expected distribution computed from an assumed sporadic meteor radiant distibution and the radar response function.

Figure 6. Time-height distributions of the burst event echoes on the east and west beams.

Figure 7. Stages in processing the data from a typical underdense meteor for the different doppler frequency estimators.

Figure 8. Stages in processing the data from a down-the-beam event for the different doppler frequency estimators.

Figure 9. Scatter plots showing the estimates returned for all the echoes in the underdense and burst echo classes using the phase slope and poly-pulse pair estimators.

Figure 10. Average deviation between the doppler frequency estimates produced by the phase slope, poly-pulse pair and maximum likelihood estimators for the different echo classes.

Figure 11. Comparison for one day of the campaign at a height of 94 km between matched events in the two data sets. The echoes have been color coded according to their classification. The data in the top plot for the Adelaide set was processed with the phase slope estimator, while the data for the MEDAC set was computed with using the poly-pulse pair method. The top plot shows the same data, but all the data were processed with the poly-pulse pair estimator.

Figure 12. Histogram comparison of the differences between the doppler frequency estimates of each system. The initial comparison includes all echoes detected on each system. The final comparison uses only underdense echoes present simultaneously on both systems.

Tables

Table 1. Echo classes and their meanings.

Class	Definition
Strong underdense	Underdense echoes with a clearly defined doppler frequency.
Weak underdense	Underdense echoes that appeared weak enough to give the frequency estimators some problems.
Overdense	An overdense echo is typically long in duration and experiences fading in the power profile. It can be strongly influenced by wind shear thus yielding unreliable wind measurements.
Clipped	Very strong echoes that caused the receivers to saturate.
Noise spike	Echoes due to noise spikes or very short lived meteor trails.
Trail formation echo	A signature resulting from a rapidly diffusing meteor trail that appears as a moving-ball target.
Trail formation and body	Echoes that exhibit both a head echo and an trail body echo.
Down the beam	Echoes from meteors coming straight down the beam.
Multiple Events	Traces which contain two or more unrelated events
Unknown	A generic class if an echo did not fit else where. Most of these echoes were simply noise.

Figures

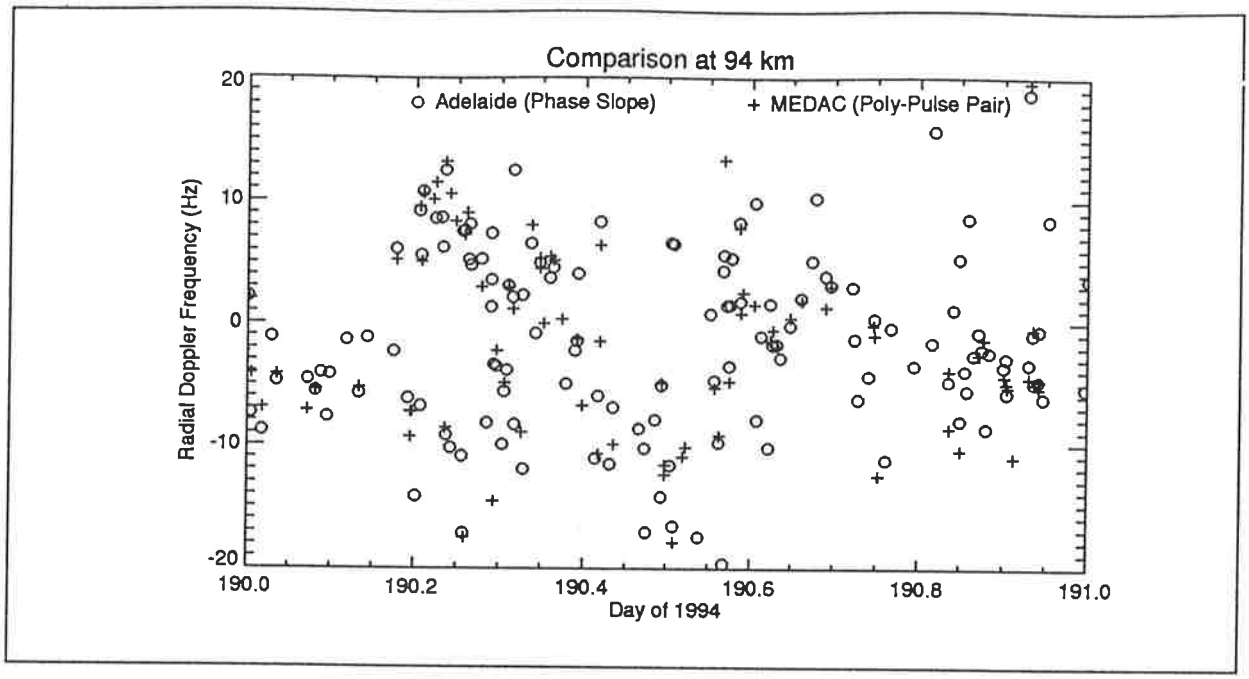

Figure 1. Initial doppler frequency comparison between the MEDAC (pluses) and Adelaide meteor systems (circles).

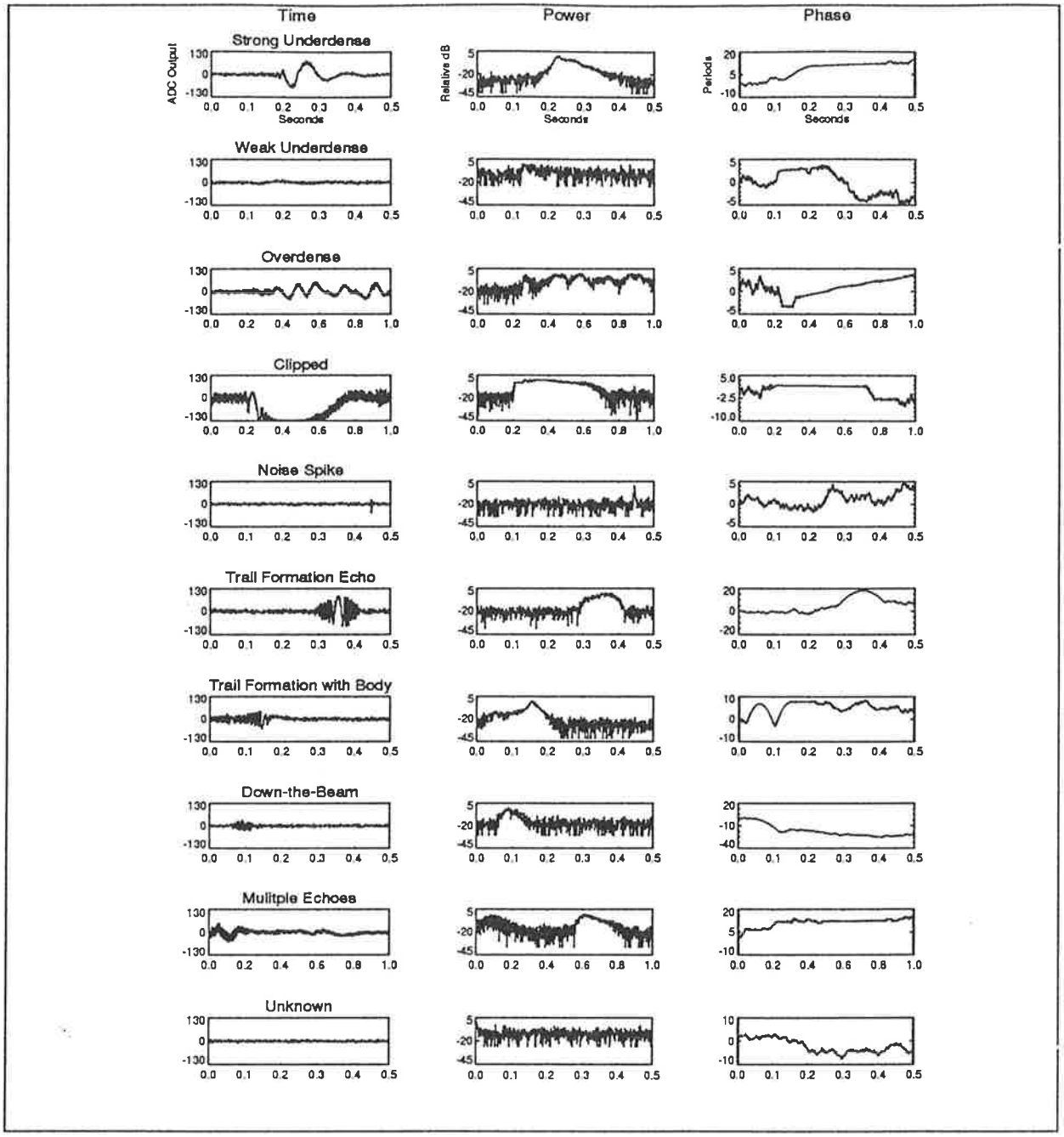

Figure 2. Examples of time, power and phase plots for each of the different signal classes present in the MEDAC data set.

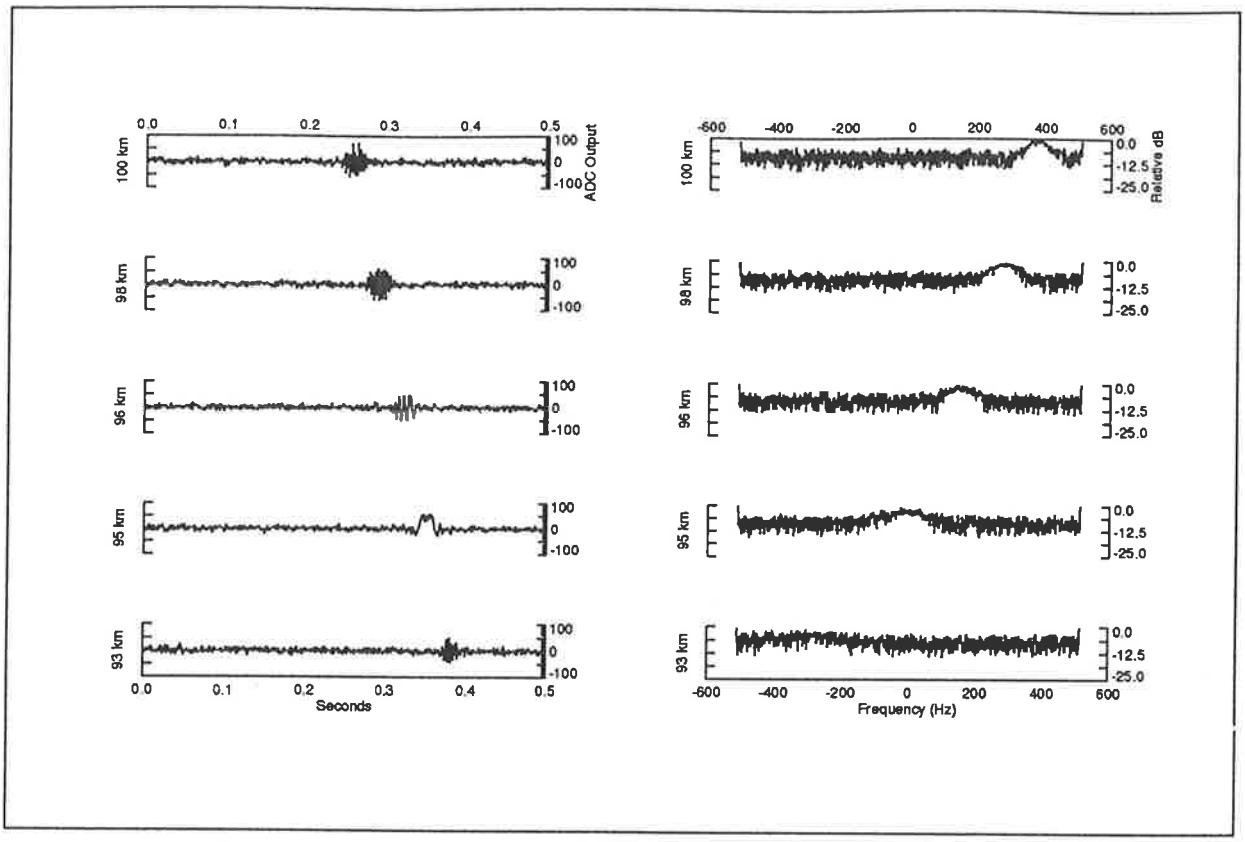

Figure 3. The left plot shows in-phase time series recorded for a down-the-beam event, while the right plot shows the corresponding frequency spectrum.

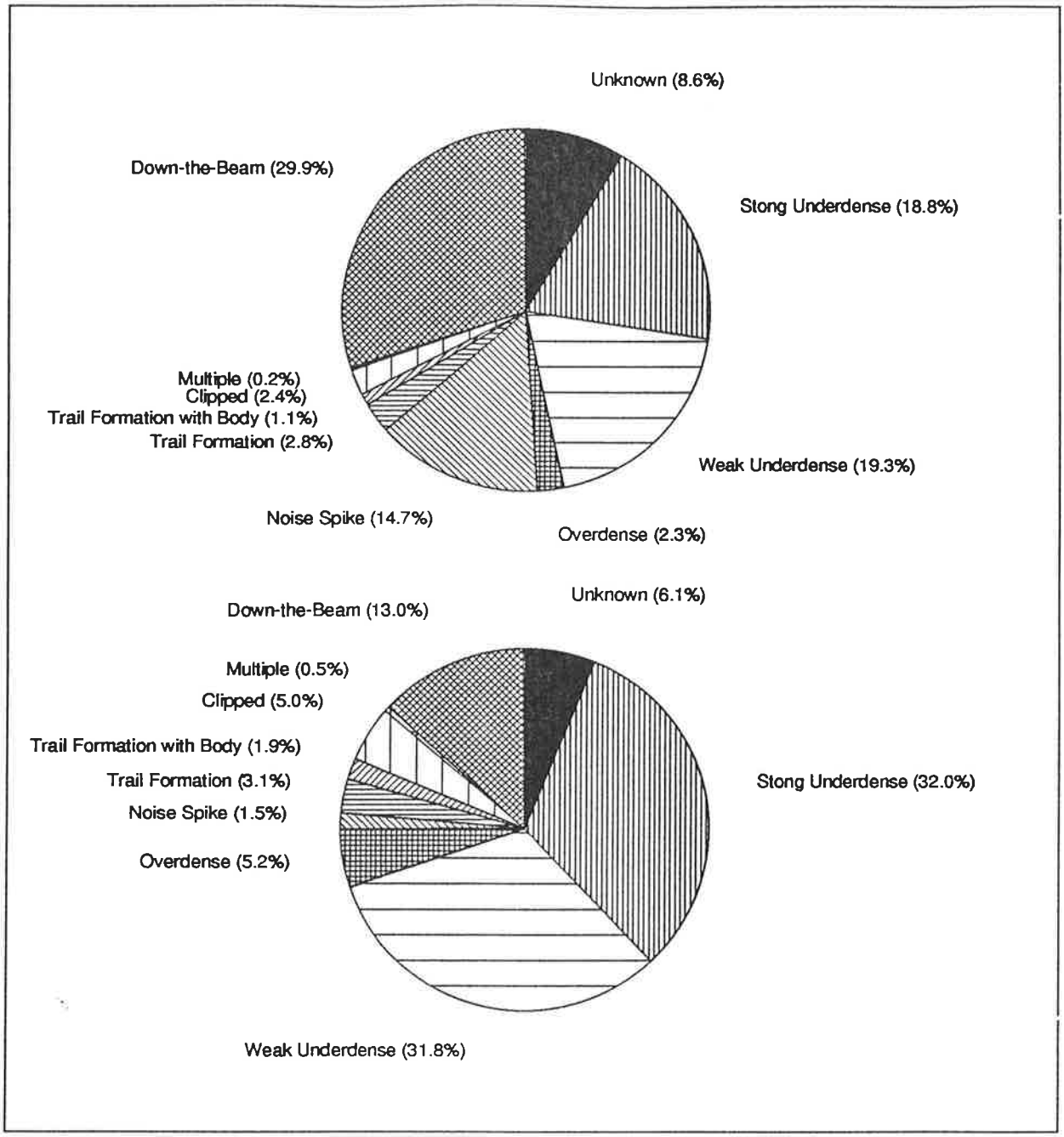

Figure 4. The top graph shows the distribution of echo classes within the MEDAC data set. The bottom graph shows the events seen simultaneously by both systems.

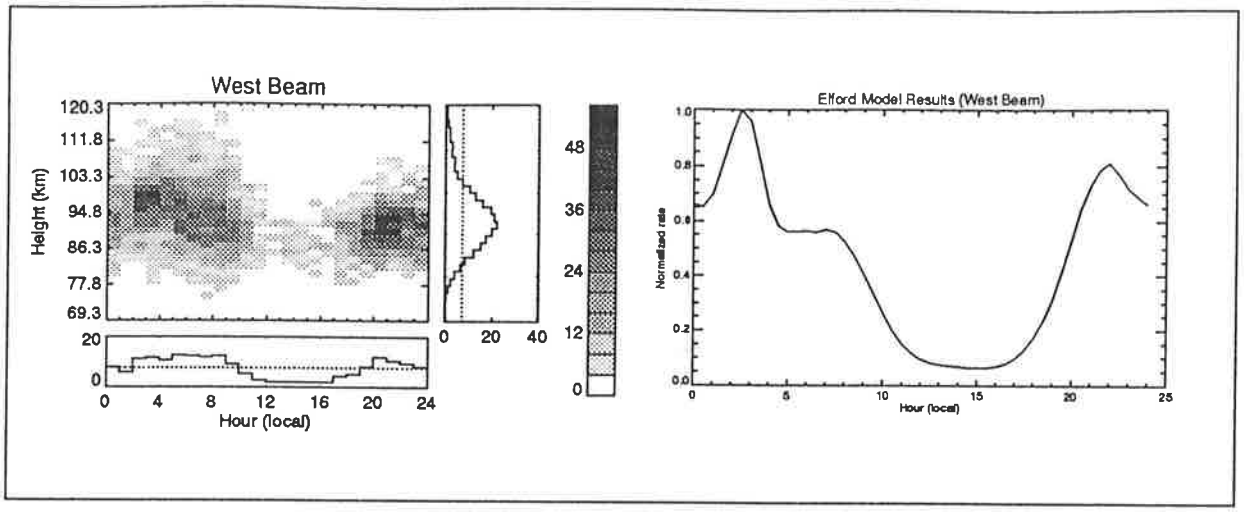

Figure 5. Time-height distribution for all the echo classes obtained with MEDAC on the west-pointing beam. The figure on the right is the expected distribution computed from an assumed sporadic meteor radiant distibution and the radar response function.

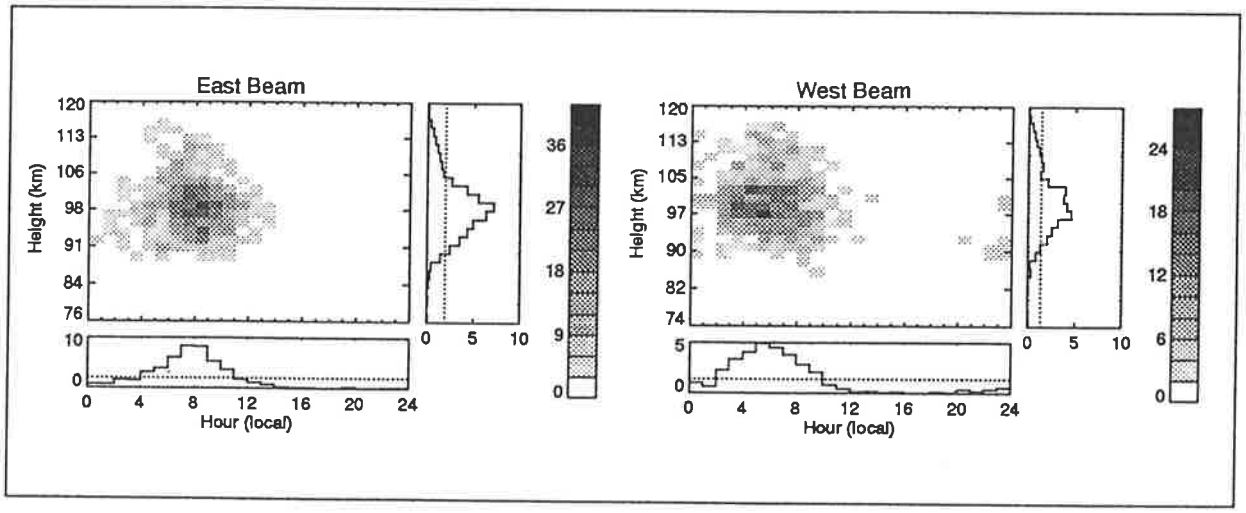

Figure 6. Time-height distributions of the burst event echoes on the east and west beams.

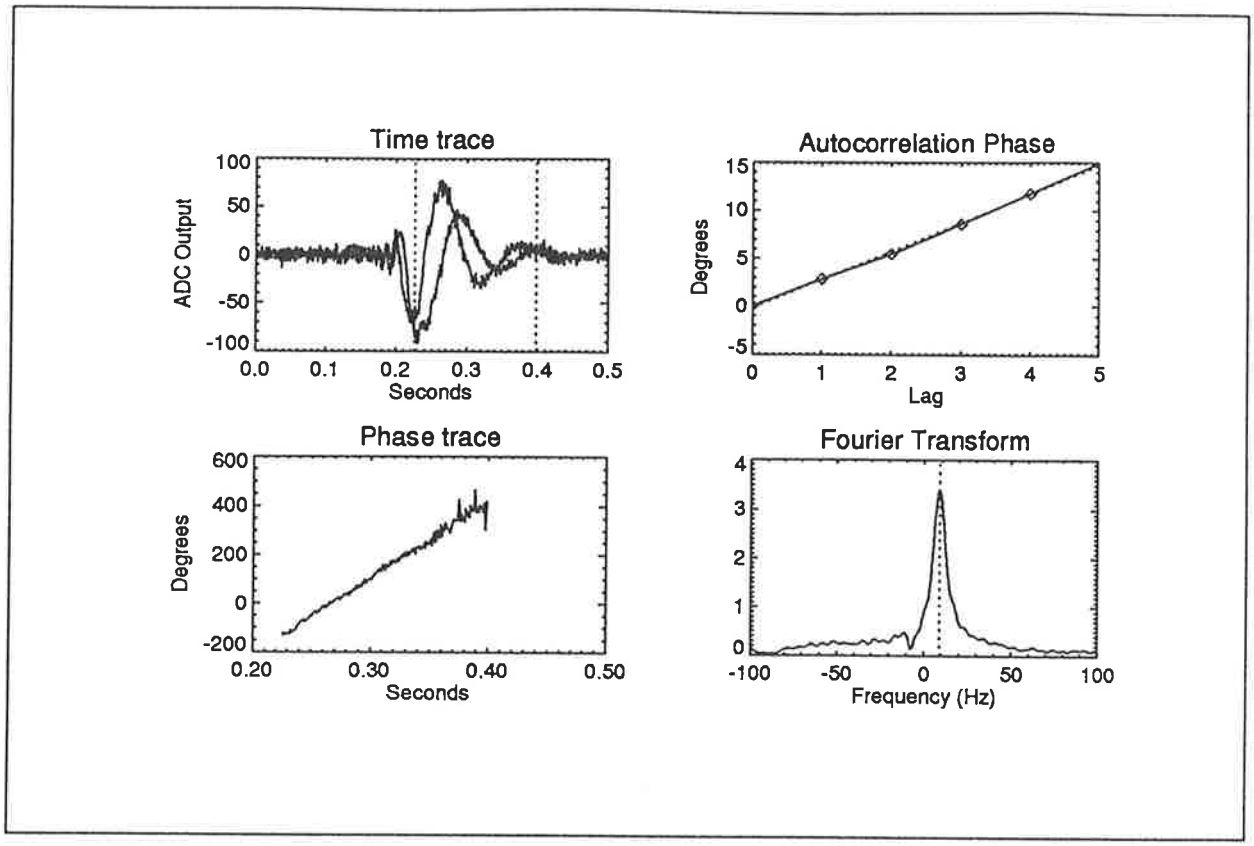

Figure 7. Stages in processing the data from a typical underdense meteor for the different doppler frequency estimators.

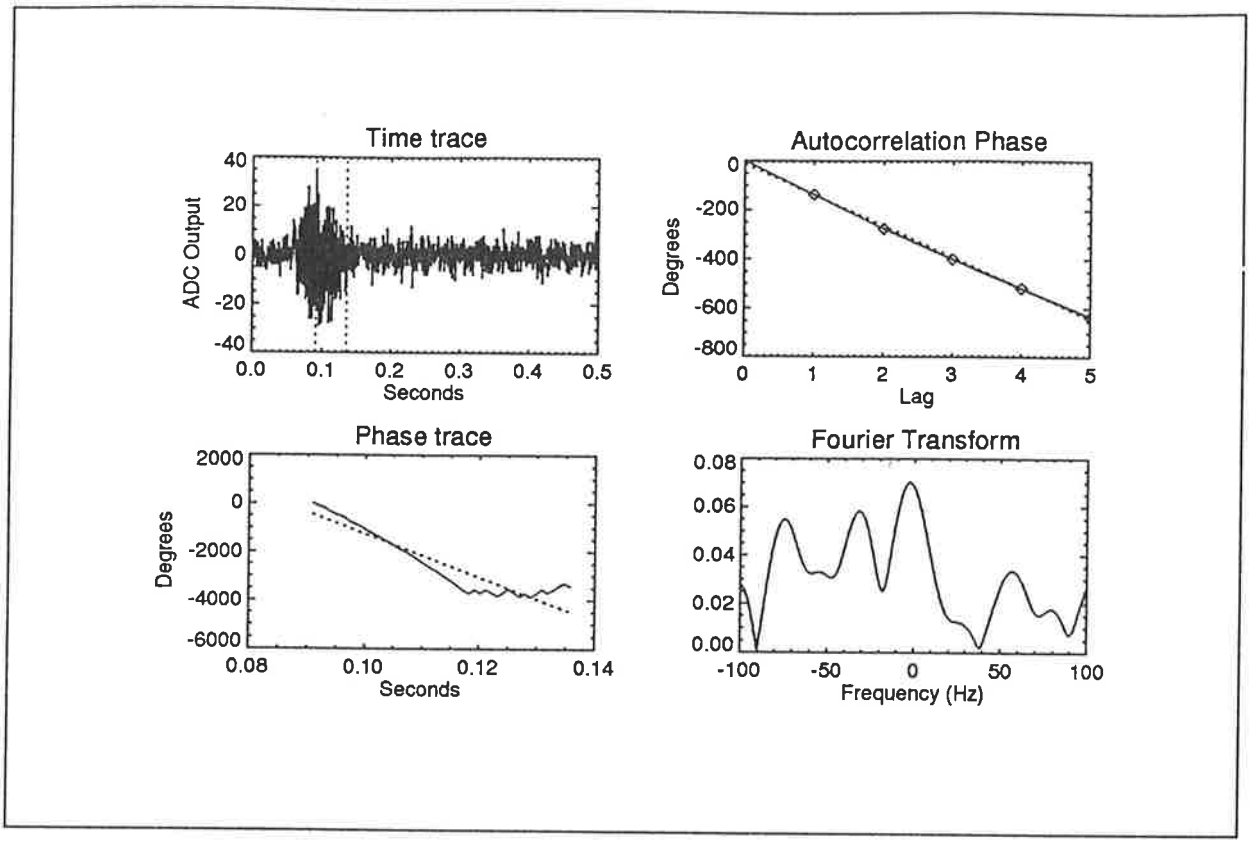

Figure 8. Stages in processing the data from a down-the-beam event for the different doppler frequency estimators.

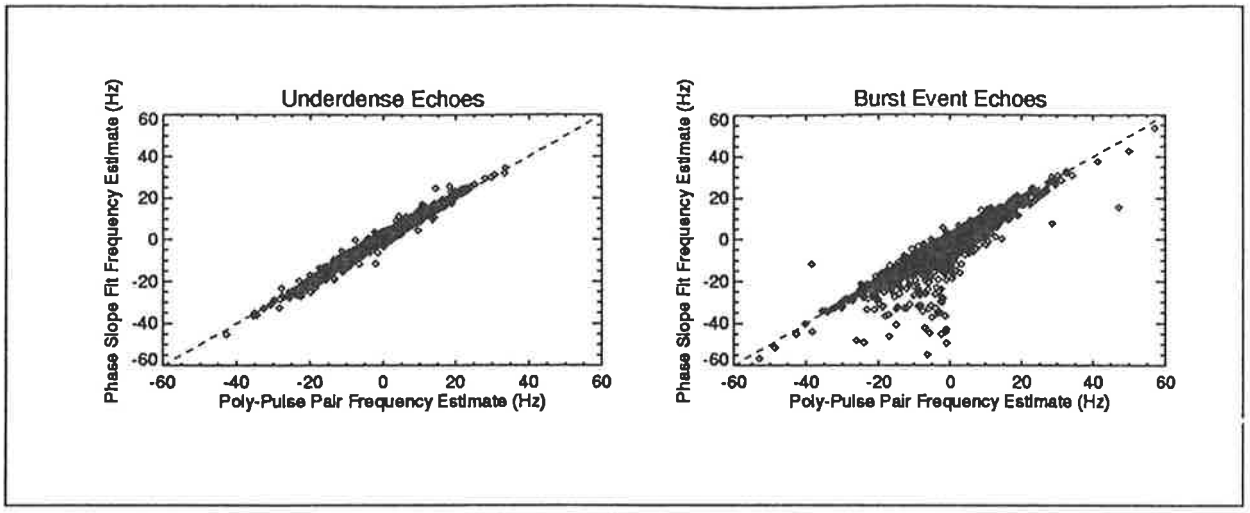

Figure 9. Scatter plots showing the estimates returned for all the echoes in the underdense and burst echo classes using the phase slope and poly-pulse pair estimators.

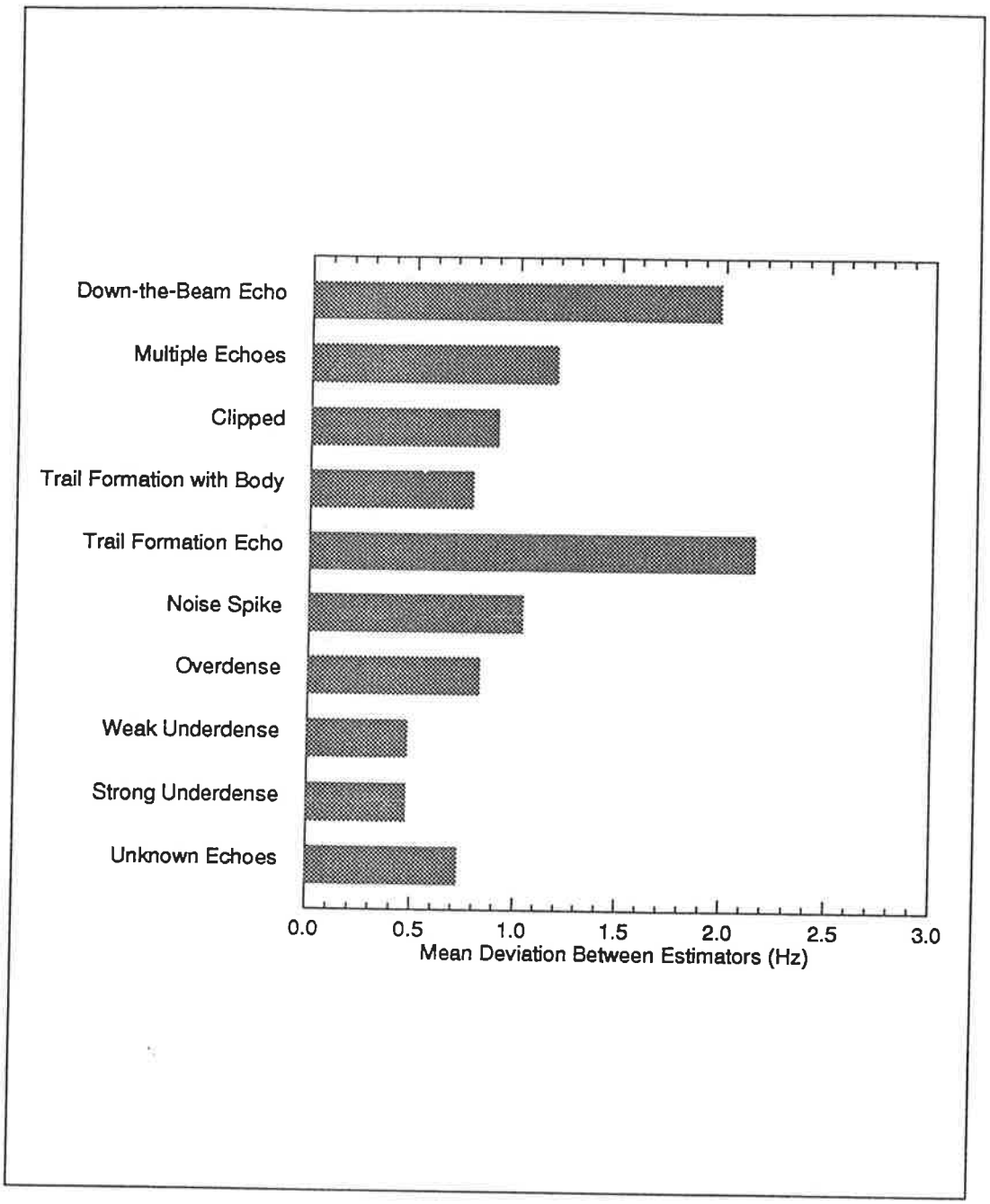

Figure 10. Average deviation between the doppler frequency estimates produced by the phase slope, poly-pulse pair and maximum likelihood estimators for the different echo classes.

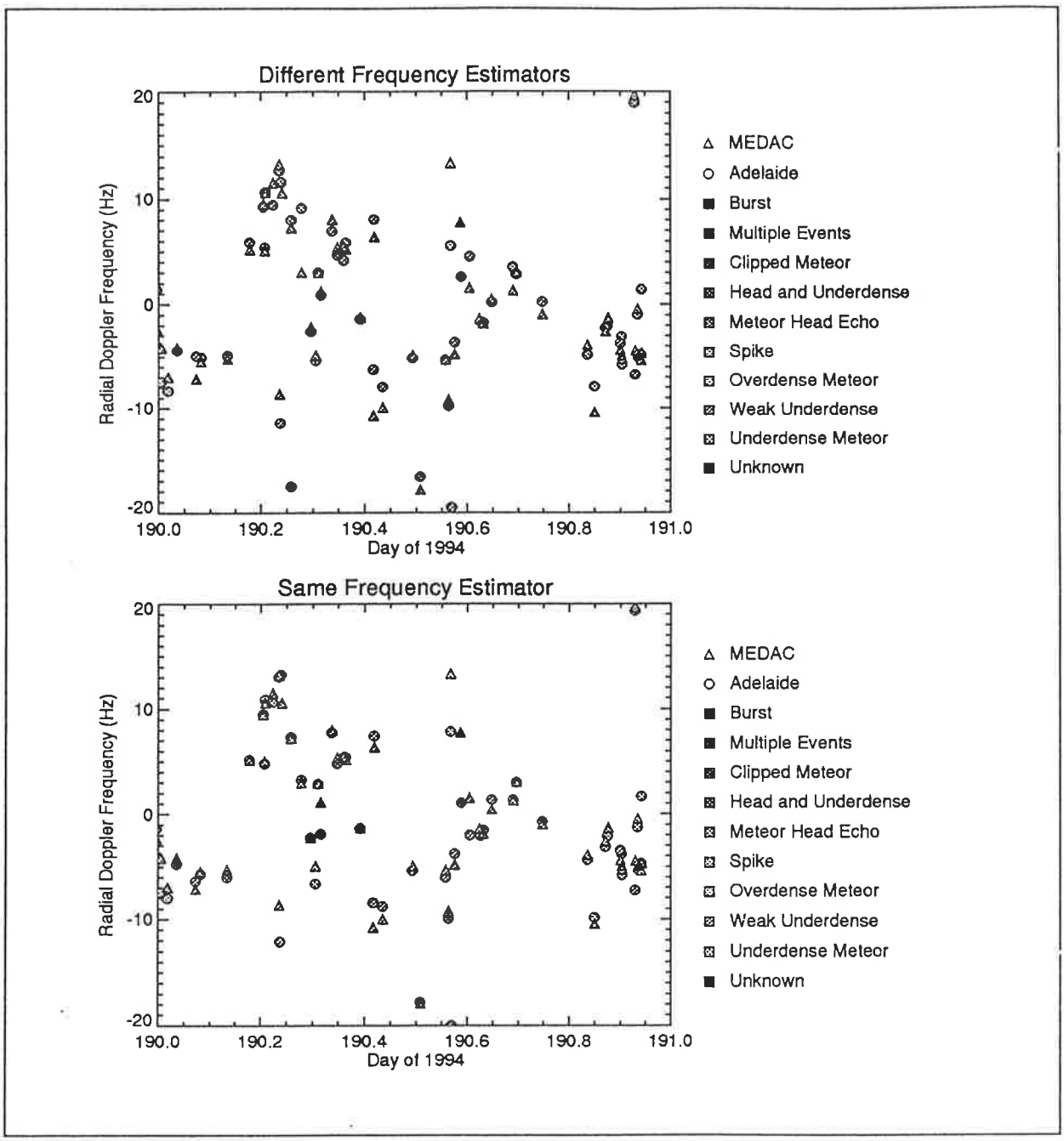

Figure 11. Comparison for one day of the campaign at a height of 94 km between matched events in the two data sets. The echoes have been color coded according to their classification. The data in the top plot for the Adelaide set was processed with the phase slope estimator, while the data for the MEDAC set was computed with using the poly-pulse pair method. The top plot shows the same data, but all the data were processed with the poly-pulse pair estimator.

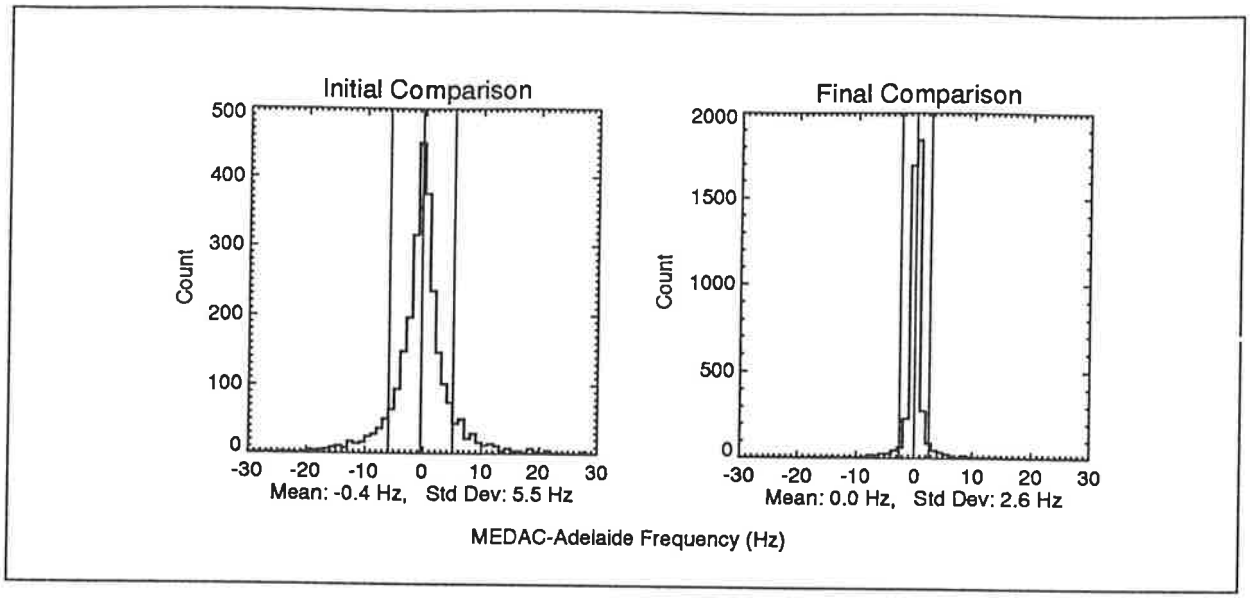

Figure 12. Histogram comparison of the differences between the doppler frequency estimates of each system. The initial comparison includes all echoes detected on each system. The final comparison uses only underdense echoes present simultaneously on both systems.

Appendix E

A new technique for radar meteor speed determination: inter–pulse phase changes from head echoes

This is a reprint of the paper,

Taylor, A. D., W. G. Cervera, W. G. Elford, D. I. Steel, A new method for radar meteor speed determination: inter-pulse phase changes from head echoes, *IAU Colloquium No. 150*, in press, 1996.

Taylor, A.D., Cervera, M.A., Elford, W.G. and Steel, D.I. (1996) A New Technique for Radar Meteor Speed Determination: Inter-Pulse Phase Changes from Head Echoes.
Physics, Chemistry, and Dynamics of Interplanetary Dust, ASP Conference Series, IAU Colloquium 150, v.104, pp. 75, 1996.

NOTE: This publication is included in the print copy of the thesis held in the University of Adelaide Library.

References

Alexander, W. M., and J. L. Bohn, Mariner 4: A study of the cumulative flux of dust particles over a heliocentric range of 1–1.56 AU, 1964–1967, *Space Research, XIV*, 749, Academie–Verlag, Berlin, 1974.

Andrianov, N. S., U. A. Pupyšev, and V. V. Sidorov, The distribution of orbit parameters and the changes in incident meteor particle flux density, *Mon. Not. R. astr. Soc., 148*, 227–237, 1970.

Arthur, J. S., J. C. Henry, G. C. Pettengill, and P. B. Sebring, The Millstone radar in satellite and missile tracking, *Ballistic Missiles and Space Technology, 3*, 81, Pergamon Press, New York, 1961.

Aspinall, A., J. A. Clegg, and G. S. Hawkings, A radio echo apparatus for the delineation of meteor radiants, *Phil. Mag., 42*, 504–514, 1951.

Avery, K. S., A. Riddle, and B. Balsley, Poker Flat Alaska, MST radar as a meteor radar, *Radio Sci., 18*, 1021–1027, 1983.

Avery, K. S., J. P. Avery, T. A. Valentic, S. E. Palo, M. J. Leary, and R. L. Obert, A new meteor echo detection and collection system: Christmas Island mesospheric wind measurements, *Radio Sci., 25,* 657–669, 1990.

Babadzhanov, P. B., Densities of meteoroids, *Meteoroids and their parent bodies*, J. Štohl and I. P. Williams (eds.), Bratislava: Slovak Acad. Sci., 295–302, 1993.

Baggaley W. J., The determination of the initial radii of meteor trains, *Mon. Not. R. astr. Soc., 147*, 231–243, 1970.

Baggaley W. J., Measurements of the velocity dependence of the initial radii of meteor trains, *Bull. Astron. Inst. Czechoslov., 31*, 308–311, 1980.

Baggaley W. J., Single wavelength measurements of the initial radii of radio meteor ionization columns, *Bull. Astron. Inst. Czechoslov., 32*, 345–349, 1981.

Baggaley W. J., and G. W. Fisher, Measurements of the initial radii of the ionization columns of bright meteors, *Planet Space. Sci., 28*, 575–580, 1980.

Baggaley, W. J., and T. H. Webb, Measurements of the ionization heights of sporadic radio-meteors, *Mon. Not. R. astr. Soc., 191*, 829–839, 1980.

Baggaley, W. J., A. D. Taylor, and D. I. Steel, The influx of meteoroids with hyperbolic heliocentric orbits, *Meteoroids and their parent bodies*, J. Štohl and I. P. Williams (eds.), Bratislava: Slovak Acad. Sci., 53–56, 1993.

Baggaley, W. J., R. G. T. Bennet, D. I. Steel, and A. D. Taylor, The advanced meteor orbit radar facility: AMOR, *Q. J. R. astr. Soc., 35*, 293–320, 1994.

Balsley, B. B., and W. L. Ecklund, A portable coaxial collinear antenna, *IEEE Transactions on Antennas and Propagation, 20*, 513–516, 1972.

Belkovič O. L., and J. A. Pupyšev, The variation of sporadic meteor radiant density and the mass law exponent over the celestial sphere, in *Physics and Dynamics of Meteors*, (Kresak L. and Millman P. M. Eds.) Reidel, Dordrecht, 373–381, 1968

Briggs, B. H., The analysis of spaced sensor records by correlation techniques, in *Handbook for MAP*, vol. 13, pp. 166–186, SCOSTEP Secr., Univ. of Ill., Urbana, 1984.

Briggs, B. H., G. J. Phillips, D. H. Shinn, The analysis of observations on spaced receivers of the fading of radio signals, *Proceedings of the Physical Society, 63B*, 106–121, 1950.

Briggs, B. H., W. G. Elford, D. G. Felgate, M. G. Golley, D. E. Rossiter, and J. W. Smith, Buckland Park aerial array, *Nature, 223*, 1321–1325, 1969.

Bronsten et al., The Physics of Meteoric Phenomena, Reidel, Dordrecht, 1983.

Browne, I. C., K. Bullough, S. Evans, T. R. Kaiser, Characteristics of radio echoes from meteor trails, II: The distribution of meteor magnitudes and masses, *Proc. Phys. Soc., 69B*, 83–87, 1956.

Brysk, H., and M. L. Buchannan, *Can. J. Phys., 43*, 28, 1965.

Cervera, M. A., and Reid, I. M., A preliminary comparison between meteor winds measured with the upgraded Buckland Park VHF radar and MF spaced antenna winds at the same site, *Step: Proceedings of the 6^{th} workshop on technical and scientific aspects of MST radar*, 412–416, 1994.

Cervera, M. A., and I. M. Reid, Comparison of simultaneous wind measurements using colocated VHF meteor and MF spaced antenna radar systems, *Radio Sci., 30*, 1245–1261, 1995.

Cervera, M. A., W. G. Elford, and D. I. Steel, Meteor observations with the Adelaide 54 MHz radar, *Meteoroids and their parent bodies*, J. Štohl and I. P. Williams (eds.), Bratislava: Slovak Acad. Sci., 249–252, 1993.

Cervera, M. A., W. G. Elford, and D. I. Steel, A novel radar technique for the determination of meteor speeds and its significance in the interpretation of HF/VHF meteor backscatter, *Conference on Solar and Terrestrial Physics*, University of Adelaide, Adelaide, Australia, 59–62, 1995.

Ceplecha, Z., Study of a bright meteor flare by means of emission curve of growth, *Bull. Astron. Inst. Czechoslov., 15*, 102, 1964.

Ceplecha, Z., Complete data on iron meteoroid (Meteor 36221), *Bull. Astron. Inst. Czechoslov., 17*, 195, 1966.

Ceplecha, Z., Meteor Spectra, in *Physics and Dynamics of Meteors*, (Kresak L. and Millman P. M. Eds.) Reidel, Dordrecht, 73–83, 1968.

Ceplecha, Z., Evidences from spectra of bright fireballs, *Evolution and physical properties of meteoroids, NASA SP–319*, 89–102, 1973.

Ceplecha, Z., Interactions of meteoroids with the atmosphere, *Meteoroids and their parent bodies*, J. Štohl and I. P. Williams (eds.), Bratislava: Slovak Acad. Sci., 287–294, 1993.

Chapman, S., and J. Bartels, Geomagnetism Vol. II (2nd ed.), Clarendon Press, Oxford, 1962

Clegg, J. A., Determination of meteor radiants by observation of radio echoes from meteor trails, *Phil. Mag., 39*, 577–594, 1948.

Clifton, K. S., Airborne meteor observations at high latitudes, *NASA TN D–6303*, 1971.

Clifton, K. S., Television studies of faint meteors, *J. Geophys. Res., 78*, 6511–6521, 1973.

Cook, A. F., M. R. Flannery, H. Levy II, R. E. McCrosky, Z. Sekanina, C.-Y. Shao, R. B. Southworth, J. T. Williams, Meteor reasearch program, *NASA Contractor Report, CR-2109*, Smithsonian Institution, Cambridge, Massachussetts, (1972)

Cook, A. F., A working list of meteoroid streams, *Evolution and physical properties of meteoroids, NASA SP–319*, 183–191, 1973.

Cook, A. F., B.-A. Lindblad, B. G. Marsden, R. E. McCrosky, and A. Posen, Yet another stream search among 2401 photographic meteors, *Smithsonian Contrib. Astrophys., 15*, 1–5, 1973.

Davies, J. G., and C. D. Ellyet, The diffraction of radio waves from meteor trails and the measurement of meteor velocities, *Phil. Mag., 40*, 614–626, 1949.

Davies, J. G., and J. C. Gill, Radio echo measurements of the orbits of faint sporadic meteors, *Mon. Not. R. astr. Soc., 121*, 437–462, 1960.

Eastwood, E., and K. A. Mercer, A study of transient radar echoes from the ionosphere, *Proc. Phys. Soc., 61*, 122-134, 1948.

Elford, W. G., Calculation of the response function of the Harvard Radio Meteor Project Radar System, *Harvard Radar Meteor Proj. Rep. 8*, Harvard Univ., Cambridge, Mass., 1964.

Elford, W. G., Incidence of meteors on the Earth derived from radio observations, *Meteor Orbits and Dust, NASA SP–13*, 121–131, 1967.

Elford, W. G., The influence of the atmosphere on radar meteor rates, in *Solid Particles in the Solar System*, (I. Halliday and B. A. McIntosh Eds.) Reidel, Holland, 101–104, 1980.

Elford, W. G., and G. S. Hawkins, Meteor echo rates and the flux of sporadic meteors, *Harvard Radar Meteor Proj. Rep. 9*, Harvard Univ., Cambridge, Mass., 1964.

Elford, W. G., G. S. Hawkins, and R. B. Southworth, The distribution of sporadic meteor radiants, *Harvard Radar Meteor Proj. Rep. 11*, Harvard Univ., Cambridge, Mass., 1964.

Elford, W. G., and D. Olsson-Steel, The height distribution of radio meteors: observations at 6 MHz, *J. Atmos. Terr. Phys., 50*, 811–818, 1988.

Elford, W. G., and A. Taylor, Measurement of electron densities in the lower ionosphere from Faraday rotation of meteor echoes, *Conference on Solar and Terrestrial Physics*, University of Adelaide, Adelaide, Australia, 27–29, 1995.

Elford, W. G., M. A. Cervera, and D. I. Steel, Single station identification of radar meteor shower activity: the June Librids in 1992, *Mon. Not. R. astr. Soc., 270*, 401–408, 1994.

Elford, W. G., M. A. Cervera, and D. I. Steel, Meteor velocities: a new look at an old problem, *Earth Moon and Planets*, in press, 1996.

Ellyett, C. D., and J. G. Davies, Velocity of meteors measured by diffraction of radio waves from trails during formation, *Nature, 161*, 596–597, 1948

Erikson, J. E., Velocity distribution of sporadic photographic meteors, *J. Geophys. Res., 73*, 3721–3726, 1968.

Evans, J. V., Radio-echo studies of meteors at 68-centimeter wavelength, *J. Geophys. Res., 70*, 5395–5416, 1965.

Evans, J. V., Radar observations of meteor deceleration, *J. Geophys. Res., 71*, 171–188, 1966.

Evans, J. V., and R. A. Brockelman, Radio echo studies of meteors at 68 *cm*, Part 1: Sporadic meteors, *Lincoln Lab. Tech. Rept. 332, DDC 439354*, Massachusetts Institute of Technology, Lexington, Massachusetts, 1963.

Evans, J. V., and R. A. Brockelman, Radio echo studies of meteors at 68 *cm*, Part 2: Shower meteors, *Lincoln Lab. Tech. Rept. 341, DDC 601518*, Massachusetts Institute of Technology, Lexington, Massachusetts, 1964.

Felgate, D. G., On the point source effect in the measurement of ionospheric drifts, *J. Atmos. Terr. Phys., 32*, 241–245, 1970.

Gartrell, G., Radio meteor astronomy , *PhD Thesis*, University of Adelaide, Adelaide, Australia, 1971.

Gartrell G., and W. G. Elford, Southern hemisphere meteor stream determinations, *Aust. J. Phys., 28*, 591–620, 1975.

Gill, J. C., and J. G. Davies, A radio echo method of meteor orbit determination, *Mon. Not. R. astr. Soc., 116*, 105–113, 1956

Greenhow, J. S., A radio-echo method for the investigation of atmospheric winds at altitudes of 80 to 100 km. *J. Atmos. Terr. Phys., 2*, 282–291, 1952.

Greenhow, J. S., and J. E. Hall, The variation of meteor heights with velocity and magnitude, *Mon. Not. R. astr. Soc., 121*, 174, 1960.

Halliday, I., Photographic fireball networks, *Evolution and physical properties of meteoroids, NASA SP–319*, 1–8, 1973.

Harvey, G. A., The NASA–LRC faint meteor spectra patrol, *NASA TN D–6298*, 1971.

Harvey, G. A., Spectral analysis of four meteors, *Evolution and physical properties of meteoroids, NASA SP–319*, 103–130, 1973a.

Harvey, G. A., NASA–LRC faint meteor spectra, *Evolution and physical properties of meteoroids, NASA SP–319*, 131–140, 1973b.

Harvey, G. A., Elemental abundance determination for meteors by spectroscopy, *J. Geophys. Res., 78,*, 3913–3926, 1973c.

Hawkes, R. L., and J. Jones, Television observations of faint meteors, 1. Mass distribution and diurnal rate variation, *Mon. Not. R. astr. Soc., 170*, 363, 1975a.

Hawkes, R. L., and J. Jones, A quantitative model for the ablation of dustball meteors, *Mon. Not. R. astr. Soc., 173*, 339–356, 1975b.

Hawkes, R. L., and J. Jones, Electro–optical meteor observation techniques and results, *Q. J. R. astr. Soc., 27*, 596–589, 1986.

Hawkins, G. S., The Physics and Astronomy of Meteors, Comets and Meteorites, McGraw–Hill, New York, 1964.

Hawkins, G. S., and M. Almond, Radio echo observations of the major night–time meteor streams, *Mon. Not. R. astr. Soc., 112*, 219–233, 1952.

Hawkins, G. S., and R. B. Southworth, The statistics of meteors in the Earth's atmosphere, *Smithsonian Contrib. Astrophys., 2*, 349–364, 1958.

Hawkins, G. S., and E. K. L. Upton, The influx rate of meteors in the earth's atmosphere, *Astrophys. J., 128*, 727–735, 1958.

Herlofson, N., The theory of meteor ionization, *Repts. Prog. Phys., 11*, 444–454, 1948.

Herlofson, N., Plasma resonance in ionospheric irregularities, *Arkiv För Fysik, 3*, 247–297, 1951.

Hey, J. S., and G. S. Stewart, Radar observations of meteors, *Proc. Phys. Soc., 59*, 858–883, 1947.

Hey, J. S., S. J. Parsons, and G. S. Stewart, Radar observations of the Giacobinid meteor shower, *Mon. Not. R. astr. Soc., 107*, 176–183, 1947.

Hoffmeister, Meteorströme, Johann Ambriosius Barth, Leipzig, 1948

Hughes, D. W., A radar determination of the right ascension and declination of the Quadrantid meteor stream, *Mon. Not. R. astr. Soc., 155*, 395–402, 1972.

Hughes, D. W., Meteors, in Cosmic Dust (McDonnell J. A. M., Ed.), 123–185, Wiley, Chichester, 1978.

Hughes, D. W., Meteoroids – an overview, *Meteoroids and their parent bodies*, J. Štohl and I. P. Williams (eds.), Bratislava: Slovak Acad. Sci., 15–28, 1993.

Jacchia, L. G., L. Copal, and P. M. Millman, A photographic study of the Draconid (Giacobinid) meteor shower of 1946, *Astrophys. J. III*, 104–133, 1950.

Jacchia, L. G., and F. L. Whipple, The Harvard photographic meteor program, *Vistas in Astronomy*, (Ed. A. Beer), Vol. 2, Pergamon, London, 1956.

Jacchia, L. G., F. Verniani, and R. E. Briggs, An analysis of the atmospheric trajectories of 413 precisely reduced photographic meteors, *Smithsonian Astrophys. Obs. Spec. Rept., 175*, 1965.

Jones, J., *Bull. Astron. Inst. Czechoslov., 28*, 272, 1977.

Jones, J., Radar observations of the Orionid meteor shower, *Mon. Not. R. astr. Soc., 204*, 765–776, 1983.

Jones, J., and J. G., Collins, On the validity of certain approximations in radio meteor echo theory, *Mon. Not. R. astr. Soc., 168*, 433–449, 1974.

Jones, J. and T. R. Kaiser, The effects of thermal radiation, conduction and meteoroid heat capacity on meteoric ablation, *Mon. Not. R. astr. Soc., 133*, 411–420, 1966.

Jones, J., and R. L. Hawkes, Television observations of faint meteors II: Light curves, *Mon. Not. R. astr. Soc., 171*, 159, 1975.

Jones, J., and J. D. Morton, *Bull. Astron. Inst. Czechoslov., 28*, 267, 1977

Jones, J., and J. D. Morton, High–resolution radar studies of the Geminid meteor shower, *Mon. Not. R. astr. Soc., 200*, 281–291, 1982.

Jones, J., J. B. A., Mitchell, B. A. McIntosh, Cluster ions and the meteor head echo, *Mon. Not. R. astr. Soc., 232*, 771–778, 1988.

Jones, J., and A. R. Webster, Visual and radar studies of meteor head echoes, *Planet. Space Sci., 39*, 873–878, 1991.

Jones, W., Theory of the initial radius of meteor trains, *Mon. Not. R. astr. Soc., 275*, 812–818, 1995.

Judasz, T. J., The coaxial colinear antenna: theoretical and experimental models, *PhD Thesis*, University of Colorado, Colorado, 1983.

Kaiser, T. R., Radio echo studies of meteor ionization, *Phil. Mag. Suppl., 2*, 493–544, 1953.

Kaiser, T. R., The incident flux of meteors and the total meteoric ionization, in *Meteors* (T. Kaiser Ed.), Pergamon Press, New York, 119–130, 1955.

Kaiser, T. R., The determination of the incident flux of radio meteors, *Mon. Not. R. astr. Soc., 121*, 284–298, 1960.

Kaiser, T. R., The determination of the incident flux of radio meteors. II sporadic meteors, *Mon. Not. R. astr. Soc., 123*, 265–271, 1961.

Kaiser, T. R., and R. L. Closs, Theory of radio reflections from meteor trails, *Phil. Mag., 43*, 1–32, 1952.

Kaiser, T. R., J. Jones, The ablation of solid meteoroids, *Physics and Dynamic of Meteors*, (Kresak L. and Millman P. M. Eds.) Reidel, Dordrecht, 205–205, 1968.

Kascheyev and Lebedinets, Radar studies of meteors, *Symposium on meteor orbits and Dust*, 183–199, 1967

Keay, C. S. L., Meteor radiant determination from high echo–rate observations, *Aust. J. Phys., 10*, 471–482, 1957.

Keitel, G. H., Certain mode solutions of forward-scattering by meteor trails, *Proc. Inst. Radio Engrs., 43*, 1481–1487, 1955.

Kraus, J. D., *Antennas*, 2nd ed., McGraw-Hill, New York, 1988.

Kronk, G., Meteor Showers: A Descriptive Catalogue, Enslow, New Jersey, 1988.

Langevin, Y., J. Kissel, J. L. Bertaux, and E. Chassefiere, First statistical analysis of 5000 mass spectra cometary grains obtained by PUMA1 (Vega 1) and PJA (Giotto) impact ionization mass-spectrometers in compressed modes, *Astron. Astrophys., 187*, 761–766, 1987.

Laurance, S. G., and D. E. Brownlee, A direct measurement of the terrestrial mass accretion rate of cosmic dust, *Nature, 323*, 136–138, 1986

Lebedinets, V. N., Density of meteoric matter in the vicinity of earth's orbit, from radar observations of meteors, *Soviet Astr., 7*, 549–558, 1964.

Lebedinets, V. N., Organic particles of cometary dust in space, *Adv. Space. Res., 11*, 149–153, 1991.

Lebedinets, V. N., and A. K. Sosnova, Radio reflections from meteor trails, *Physics and Dynamic of Meteors*, (Kresak L. and Millman P. M. Eds.) Reidel, Dordrecht, 27–44, 1968.

Lindblad, B.-A., A stream search among 865 precise photographic meteor orbits *Smithsonian Contrib. Astrophys., 12*, 1–13, 1971a.

Lindblad, B.-A., A computerized stream search among 2401 photographic meteor orbits *Smithsonian Contrib. Astrophys., 12*, 14–24, 1971b.

Love, S. G., and D. E. Brownlee, A direct measurement of the terrestrial mass accretion rate of cosmic dust, *Science, 262*, 550–553, 1993

Lovell, A. C. B., and J. A. Clegg, Characteristics of radio echoes from meteor trails. I: The intensity of radio reflections and electron density in the trail, *Proc. Phys. Soc., 60*, 491–498.

McBeath, A., Meteor Shower Calendar, International Meteor Organization, Mechelen, Belgium, 1993.

McCrosky, R. E. and A. Posen, Orbital elements of photographic meteors, *Smithsonian Contrib. Astrophys. 4*, 15–33, 1961.

McDaniel, E. W., and E. A. Mason, *Mobility and Diffusion of Ions in Gasses*, John Wiley, New York, 1973.

McKinley, D. W. R., Variation of meteor echo rates with radar system parameters, *Canad. J. Phys., 29*, 403–426, 1951.

McKinley, D. W. R., Effect of radar sensitivity on meteor echo durations, *Canad. J. Phys., 31*, 758–767, 1953.

McKinley, D. W. R., Meteor Science and Engineering, McGraw-Hill, New York, 1961.

McKinley, D. W. R., and P. M. Millman, A phenomenological theory of radar echoes from meteors, *Proc. Inst. Radio Engrs., 37*, 364–375, 1949.

McIntosh, M. A., The meteoric head echo, *J. Atmos. Terr. Phys., 24*, 311–315, 1962.

Mathews, J. D., M. P. Sulzer, C. A. Tepley, R. Bernard, J. L. Fellous, M. Glass, M. Massebuf, S. Ganguly, R. M. Harper, R. A. Behnke, and J. C. G. Walker, A comparison between thomson scatter and meteor radar wind measurements in the 65-105 km altitude region at Arecibo, *Planet. Space Sci., 29*, 341–348, 1981.

Manning, L. A., The strength of meteoric echoes from dense columns, *J. Atmos. Terr. Phys., 4*, 219–225, 1953.

Manning, L. A., and V. R. Eshleman, Meteors in the ionosphere, *Proc. Inst. Radio Engrs., 47*, 186–199, 1959.

Millman, P. M., Cometary Meteoroids, *From Plasma to Planet, Nobel Symposium 21*, (Almqvist and Wiskell Eds.), Interscience, New York, 1972.

Millman, P. M., A. F. Cook, and C. L. Hemenway, Image-orthicon spectra of Geminids in 1969, *Evolution and physical properties of meteoroids, NASA SP–319*, 147–151, 1973.

Morton, J. D., and J. Jones, A method for imaging radio meteor radiant distributions, *Mon. Not. R. astr. Soc., 198*, 737–746, 1982.

Nakamura, T., T. Tsuda, T. Tsutaumi, T. Kita, T. Uehara, S. Kato, and S. Fukao, Meteor wind observations with the MU radar, *Radio Sci., 26*, 857–869, 1991.

Nicol, E. J., J. MacFarlane, and R. L. Hawkes, Residual mass from atmospheric ablation of small meteoroids, *Plant. Space Sci., 33*, 315–320, 1985

Nilsson C. S., A radio survey of the orbits of meteors, *PhD Thesis*, University of Adelaide, Adelaide, Australia, 1962.

Nilsson C. S., A southern hemisphere radio survey of meteor streams, *Aust. J. Phys., 17*, 205–256, 1964a.

Nilsson C. S., The sextanid meteor stream, *Aust. J. Phys., 17*, 158–160, 1964b.

Olsson-Steel, D., and W. G. Elford, The height distribution of radio meteors: observations at 2 MHz, *J. Atmos. Terr. Phys., 50*, 243–258, 1987.

Olsson-Steel, D., and W. G. Elford, The use of meteor radars in the detection of infalling space debris, *IAU Colloquium No. 112: Light pollution, radio interference and space debris*, (D. L. Crawford Ed.), Astron. Soc. Pacific Conf. Ser. 17, 166–171, 1991.

Öpik, E., Results of the Arizona expedition for the study of meteors. III: Velocities of meteors observed visually, *Harvard Cir., 389*, 1934.

Pellinen-Wannberg, A., and G. Wannberg, Meteor observations with the European incoherent scatter UHF radar, *J. Geophys. Res., 99*, 11379–11390, 1994.

Peregudov, F. I., On the effect of meteor velocities on the hour number in radio-echo detection of meteors, *Soviet Astr., 2*, 833–838, 1958.

Pettengill, G. H., A new technique for investigation of meteor echoes at UHF, *J. Geophys. Res., 67*, 409–411, 1962.

Pettengill, G. H., and L. G. Kraft, Earth satellite observations made with the Millstone Hill radar, *Avionics Research: Satellites and Problems of Long Range Detection and Tracking*, 152, Pergamon Press, New York, 1960.

Pettengill, G. H., and V. C. Pineo, A preliminary investigation of meteor echoes at UHF, *Lincoln Lab., DDC 235669, H-67*, Massachusetts Institute of Technology, Lexington, Massachusetts, 1960.

Poole L. M. G., and D. G. Roux, Meteor radiant mapping with an all-sky radar, *Mon. Not. R. astr. Soc., 236*, 645–652, 1989.

Porter, J. G., Comets and Meteor Streams, Chapman and Hall, London, 1952.

Poulter, E. M., and W. J. Baggaley, Radio wave scattering from meteoric ionization, *J. Atmos. Terr. Phys., 39*, 757–768, 1977.

Poulter, E. M., and W. J. Baggaley, The applications of radio-wave scattering theory to radio-meteor observations, *Planet. Space Sci., 26*, 969–977, 1978.

Ratcliffe, J. A., Some aspects of diffraction theory and their application to the ionosphere, *Reports on Progress in Physics, 19*, 188, 1956.

Reid, I. M., B. G. W. Vandepeer, S. C. Dillon, B. M. Fuller, The new Adelaide medium frequency Doppler radar, *Radio Sci., 30*, 1177–1189, 1995.

Roberston, D. S., D. T. Liddy, and W. G. Elford, Measurements of winds in the upper atmosphere by means of drifting meteor trails I, *J. Atmos. Terr. Phys., 4*, 255–270, 1953.

Rogers, I. J., and C. S. L. Keay, Observations of some southern hemisphere meteor showers, *Meteoroids and their parent bodies*, J. Štohl and I. P. Williams (eds.), Bratislava: Slovak Acad. Sci., 273–276, 1993.

Röttger, J., The MST radar technique, in *Handbook for MAP*, vol. 13, pp. 187–232, SCOSTEP Secr., Univ. of Ill., Urbana, 1984.

Ruze, J., Physical limitations on antennas, *MIT Research Lab. Electronics Tech. Rept., 248*, 1952

Ruze, J., The effect of aperture errors on the antenna radiation pattern, *Proc. Symposium on Communication Theory and Antenna Design*, AFCRC Tech. Rept. 57–105, 1957

Sarma, T., and J. Jones, Double station observations of 454 TV meteors, *Bull. Astron. Inst. Czechoslov., 36*, 9–24, 1985.

Schiaparelli, J. V., *Note e riflessioni sulla theoria astronomica della stella cadenti* (in Italian), Stamferia, Firenze, 1866.

Sekanina, Z. and B. R. Southworth, Physical and dynamical studies of meteors, *NASA Contractor Report CR-2316*, Smithsonian Institution, Cambridge, Massachussetts, 1973.

Sekanina, Z. Statistical model of meteor streams IV. A study of radio streams from the synoptic year, *Icarus, 27*, 265–321, 1976.

Southworth, B. R., and G. S. Hawkins, Statistics of meteor streams, *Smithsonian Contrib. Astrophys., 7*, 261–285, 1963.

Steel, D. I., and W. G. Elford, The height distribution of radio meteors: Comparison of observations at different frequencies on the basis of standard echo theory, *J. Atmos. Terr. Phys., 53*, 409–417, 1991.

Stubbs, T. J., The measurement of winds in the *D*-region of the ionosphere by the use of partially reflected radio waves, *J. Atmos. Terr. Phys., 35*, 909–919, 1973.

Taylor, A. D., W.J. Baggaley, R. G. T. Bennett, and D. I. Steel, Radar measurements of very high velocity meteors with AMOR, *Planet. Space Sci., 42*, 135–140, 1994.

Taylor, A. D., The Harvard Radio Meteor Project velocity distribution reappraised, *Icarus, 116*, 154–155, 1995.

Taylor, A. D., Earth encounter velocities for interplanetary meteoroids, *Adv. Space. Res., 17*, 205–209, 1996.

Taylor, A. D., W. G. Cervera, W. G. Elford, D. I. Steel, A new method for radar meteor speed determination: inter-pulse phase changes from head echoes, *IAU Colloquium No. 150*, in press, 1996.

Thomas, R. M., and D. J. Netherway, Observations of meteors using an over-the-horizon radar, *Proc. Astr. Soc. Aust., 8*, 88–93, 1989.

Thomas, R. M., P. S. Whitham, and W. G. Elford, Response of high frequency radar to meteor backscatter, *J. Atmos. Terr. Phys., 50*, 703–724, 1988.

Valentic, T. A., J. P. Avery, and S. K. Avery, MEDAC/SC: A third generation meteor echo detection and collection system, *IEEE Trans. Geosci. Remote Sensing*, in press, 1995.

Valentic, T. A., J. P. Avery, S. K. Avery, M. A. Cervera, W. G. Elford, R. A. Vincent, and I. M. Reid, A comparison of meteor radar systems at Buckland Park, *Radio Sci.*, in press, 1996

Verniani, F., An analysis of the physical parameters of 5759 faint radio meteors, *J. Geophys. Res., 78*, 8429–8462, 1973.

Vincent, R. A., P. T. May, W. K. Hocking, W. G. Elford, B. H. Candy, and B. H. Briggs, First results with the Adelaide VHF radar: Spaced antenna studies of tropospheric winds, *J. Atmos. Terr. Phys. 49*, 353–366, 1987.

Vincent, R. A., I. M. Reid, D. A. Holdsworth, and M. A. Cervera, Spaced antenna wind measurements: the effects of signal saturation, *Wind observations in the middle atmosphere*, CNES–HQ Paris, Proceedings, 1995.

Weiss, A. A., Radio echo observations of meteors in the southern hemisphere, *Austr. J. Phys., 8*, 148–166, 1955.

Weiss, A. A., Meteor activity in the southern hemisphere, *Austr. J. Phys., 10*, 299–309, 1957a.

Weiss, A. A., The incidence of particles upon the earth, *Austr. J. Phys., 10*, 397–411, 1957b.

Weiss, A. A., Radio–echo observations of the southern hemisphere meteor shower activity from 1956 December to 1958 August, *Mon. Not. R. astr. Soc., 120*, 387–403, 1960.

Weiss, A. A., The distribution of meteor masses for sporadic meteors and three showers, *Austr. J. Phys., 14*, 102–119, 1961.

Weiss, A. A., Radio–echo measurements of meteor mass distributions, *Smithsonian Contrib. Astrophys., 7*, 41–43, 1963.

Wheeler, H. A., A vertical antenna made of transposed sections of coaxial cable, *IRE Conv. Rec., 4*, 160–164, 1956.

Whipple, F. L., Photographic meteor studies. IV: The Geminid shower, *Proc. Amer. Phil. Soc., 91*, 189–200, 1947.

Whipple, F. L., The Harvard photographic meteor program, *Sky and Telescope, 8*, No. 4, 1949.

Zhou, Q., Tepley, C. A., and M. P. Sulzer, Meteor observations by the Arecibo 430 *MHz* incoherent scatter radar–I. Results from time–integrated observations, *J. Atmos. Terr. Phys., 57*, 421–431, 1995.